ATMOSPHERIC AIR POLLUTION AND ITS ENVIRONMENTAL AND HEALTH EFFECTS

EDITED BY: Qiyuan Wang, Siwatt Pongpiachan, Jianhuai Ye, Hongmei Xu, Lang Liu and Qian Zhang

PUBLISHED IN: Frontiers in Environmental Science

frontiers Research Topics

frontiers

ISSN 1664-8714
ISBN 978-2-83250-381-2
DOI 10.3389/978-2-83250-381-2

About Frontiers

Frontiers is more than just an open-access publisher of scholarly articles: it is a pioneering approach to the world of academia, radically improving the way scholarly research is managed. The grand vision of Frontiers is a world where all people have an equal opportunity to seek, share and generate knowledge. Frontiers provides immediate and permanent online open access to all its publications, but this alone is not enough to realize our grand goals.

Frontiers Journal Series

The Frontiers Journal Series is a multi-tier and interdisciplinary set of open-access, online journals, promising a paradigm shift from the current review, selection and dissemination processes in academic publishing. All Frontiers journals are driven by researchers for researchers; therefore, they constitute a service to the scholarly community. At the same time, the Frontiers Journal Series operates on a revolutionary invention, the tiered publishing system, initially addressing specific communities of scholars, and gradually climbing up to broader public understanding, thus serving the interests of the lay society, too.

Dedication to Quality

Each Frontiers article is a landmark of the highest quality, thanks to genuinely collaborative interactions between authors and review editors, who include some of the world's best academicians. Research must be certified by peers before entering a stream of knowledge that may eventually reach the public - and shape society; therefore, Frontiers only applies the most rigorous and unbiased reviews.
Frontiers revolutionizes research publishing by freely delivering the most outstanding research, evaluated with no bias from both the academic and social point of view. By applying the most advanced information technologies, Frontiers is catapulting scholarly publishing into a new generation.

What are Frontiers Research Topics?

Frontiers Research Topics are very popular trademarks of the Frontiers Journals Series: they are collections of at least ten articles, all centered on a particular subject. With their unique mix of varied contributions from Original Research to Review Articles, Frontiers Research Topics unify the most influential researchers, the latest key findings and historical advances in a hot research area! Find out more on how to host your own Frontiers Research Topic or contribute to one as an author by contacting the Frontiers Editorial Office: frontiersin.org/about/contact

ATMOSPHERIC AIR POLLUTION AND ITS ENVIRONMENTAL AND HEALTH EFFECTS

Topic Editors:
Qiyuan Wang, Institute of Earth Environment, Chinese Academy of Sciences (CAS), China
Siwatt Pongpiachan, National Institute of Development Administration, Thailand
Jianhuai Ye, Southern University of Science and Technology, China
Hongmei Xu, Xi'an Jiaotong University, China
Lang Liu, Northwestern Polytechnical University, China
Qian Zhang, Xi'an University of Architecture and Technology, China

Citation: Wang, Q., Pongpiachan, S., Ye, J., Xu, H., Liu, L., Zhang, Q., eds. (2022). Atmospheric Air Pollution and Its Environmental and Health Effects. Lausanne: Frontiers Media SA. doi: 10.3389/978-2-83250-381-2

Table of Contents

frontiers in Environmental Science

ORIGINAL RESEARCH
published: 07 February 2022
doi: 10.3389/fenvs.2022.828408

The Burden of Neonatal Diseases Attributable to Ambient PM 2.5 in China From 1990 to 2019

Jia Yuan[1], Lu Shi[1], Hongbo Li[1], Jing Zhou[2], Lingxia Zeng[1], Yue Cheng[1] and Bei Han[1]**

[1]School of Public Health, Health Science Center, Xi'an Jiaotong University, Xi'an, China, [2]Department of Pediatrics, The Second Affiliated Hospital of Xi'an Jiaotong University, Xi'an, China

Background: Air pollution exposure is an environmental risk to public health. And the available data on relationships of air pollution and neonatal disease burden are scarce. This study assessed neonatal disease burden attributable to Particulate Matter 2.5 (PM 2.5) pollution in China.

Methods: This is a retrospective analysis with data from the GBD2019 database. Data of PM 2.5 pollution exposure levels and neonatal disease burden attributable to PM 2.5 in China from 1990 to 2019 were obtained from the Global Burden of Disease Study 2019 (GBD 2019); Data of PM2.5 concentration was collected from the Bulletin of the State of the Ecological Environment in China; Data of perinatal mortality was collected from the Chinese Maternal and Child Health Surveillance Network. Deaths, Disability-adjusted life years (DALYs), Year of life lost (YLLs), and Years lived with disability (YLDs) are primary indicators used to assess neonatal diseases burden. The correlation of PM2.5 pollution and neonatal death was analyzed. Average Annual Percentage Change (AAPC) and increment were used to assess exposure levels and disease burden trends.

Results: PM 2.5 pollution exposure level of newborns in China is much higher than global average, 32.08 per 100 people (95% UI: 26.57–38.06) in 2019 compared to 1990 (15.86 per 100 people, 95% UI: 6.83–30.88), with an increase of 102.27%. And it is statistically verified PM2.5 concentration was positively correlated with neonatal disease deaths ($r = 0.9534$, $p = 0.0009$) and DALYs ($r = 0.9534$, $p = 0.0009$). The overall disease burden of neonatal diseases attributed to PM 2.5 pollution in China has decreased from 1990 to 2019, with a decrement of 5738.34 deaths (decreased: 56.85%), 51.01 person/years (decreased: 56.84%) for DALYs, 51.23 person/years (decreased: 57.11%) for YLLs and an increase of 150.69 person/years (increased: 31.71%) for YLDs.

Conclusion: There exists positive correlation between environmental pollution and neonatal diseases in China. The number of neonatal disease deaths, DALYs, and YLLs due to PM 2.5 pollution showed a decreasing trend with the environmental pollution control. For the rising YLDs, there is a need to improve survival rates while focusing on prognosis of neonatal disease and reducing the burden of disease brought on by disability. Controlling environmental pollution is likely to help reduce neonatal disease burden, especially premature birth and neonatal encephalopathy.

Keywords: particulate matter pollution, PM 2.5, neonates, disease burden, GBD2019

OPEN ACCESS

Edited by:
Qiyuan Wang,
Institute of Earth Environment (CAS), China

Reviewed by:
Richard Ménard,
Environment and Climate Change, Canada
Xiao-San Luo,
Nanjing University of Information Science and Technology, China

****Correspondence:***
Yue Cheng
chengy@mail.xjtu.edu.cn
Bei Han
hanbei@mail.xjtu.edu.cn

Specialty section:
This article was submitted to Atmosphere and Climate, a section of the journal Frontiers in Environmental Science

Received: *03 December 2021*
Accepted: *17 January 2022*
Published: *07 February 2022*

Citation:
Yuan J, Shi L, Li H, Zhou J, Zeng L, Cheng Y and Han B (2022) The Burden of Neonatal Diseases Attributable to Ambient PM 2.5 in China From 1990 to 2019. Front. Environ. Sci. 10:828408. doi: 10.3389/fenvs.2022.828408

INTRODUCTION

Newborns' first 28 days of life (neonatal period) are the most vulnerable period for a child's survival, with approximately 2.5 million children dying each year in the first month of life (EF et al., 2017). Newborns may suffer from various diseases in this stage, such as prematurity, neonatal encephalopathy, jaundice, and sepsis. The main causes of newborns' death are preterm birth and intrapartum-related complications and infections, such as sepsis, meningitis, and pneumonia. The global neonatal mortality rate decreased from 3.66% in 1990 to 1.80% in 2017, with China decreasing from 2.95% in 1990 to 0.47% in 2017. In the United States, the neonatal mortality rate decreased from 0.58% in 1990 to 0.36% in 2017, while in Japan, it decreased from 0.25% in 1990 to 0.09% in 2017. In 2017, neonatal diseases were ranked ninth in the YLL ranking of the 25 leading causes of death of newborns in China (Zhou et al., 2019). Neonatal diseases are complex, and the mortality rate has decreased significantly with the development of medical and neonatal care; however, the potential for developmental disability cannot be ignored. The impact of neonatal disease on quality of life increases the burden of disease.

Air pollution has a negative impact on human health. Particulate Matter 2.5 (PM 2.5) is one of the main air pollutants. It has been shown that PM 2.5 pollution impacts maternal health during pregnancy and affects the outcome of birth, especially the birth weight and the preterm birth (Jacobs et al., 2017). Ambient particulate matter pollution was one of the top 4 risk factors for deaths and DALY percentages in China in 2017 where age-standardized Summary Exposure Values (SEV) have increased from 1990 to 2017, which is the largest change of age-standardized SEV among the top 10 risk factors in China (Zhou et al., 2019). The Chinese government has been actively combating air pollution over the past few years; even PM 2.5 pollution has been controlled strictly and its concentration has decreased obviously. Moreover, the long-term average absolute level of air pollution in China is still high, and the burden of disease due to those air pollution has decreased, but some areas are still on the rise (Huang et al., 2018; Yin et al., 2020; Zhang et al., 2021).

In recent years, the health effects of air pollution on newborns have received increasing attention. Therefore, this study aimed to assess the burden of neonatal diseases caused by PM 2.5 pollution in China from 1990 to 2019. Furthermore, to understand more systematically the burden of neonatal diseases attributable to PM 2.5 pollution in China and explore the pattern of change over the past 30 years; And the analysis results will provide a basis for rational allocation of health resources and the formulation of health policies.

MATERIALS AND METHODS

Data Sources

The 2019 Global Burden of Disease (GBD) project comprehensively assesses the disease burden for 87 risk factors in 204 countries and territories worldwide. The GBD publishes data on attributable mortality, disability-adjusted life years (DALYs), years of life lost (YLLs), and years lived with disability (YLDs) data. The current data is given for 1990–2019 (Murray et al., 2020). YLL was estimated by multiplying the estimated number of deaths by the patient's age with the standard life expectancy at that corresponding age. The YLD due to disease-induced disability was estimated by multiplying the disease prevalence with different disability weights, and the DALY was obtained by summing YLD and YLL (Liu et al., 2019). The rates were all age-standardized using the world standard population developed by the GBD research (Feigin et al., 2015).

In the GBD database, the primary data used to estimate mortality in China were obtained from the Chinese Center for Disease Control and Prevention, the Chinese Disease Surveillance Point System (DSPs), the Chinese Maternal and Child Health Surveillance Network, the Chinese Health Statistical Yearbook, and data from published and unpublished studies and reports (Luo et al., 2017). The GBD $PM_{2.5}$ values were derived from the integration of satellites combined with a chemical transport model, surface measurements, and geographical data at a $0.1^{\circ} \times 0.1^{\circ}$ (approximately 11 km × 11 km at the equator) resolution, and then aggregated to national-level population-weighted means to produce a national exposure estimate (Brauer et al., 2016; Cohen et al., 2017; Liu et al., 2021).

Data Analysis Parameters

The data used in this study was obtained from GBD 2019 through the Global Health Data Exchange query tool (GHDx, http://ghdx.healthdata.org/gbd-results-tool) with data refinement distinguishing between years, genders, attributions, and ages (Liu et al., 2021). The PM2.5 exposure data and the neonatal disease burden data attributable to PM2.5 from 1990 to 2019 were extracted from the GHDx. Deaths, DALYs, YLLs, and YLDs, were the main indicators used to assess the disease burden in newborns. Neonatal diseases are divided into five categories: neonatal preterm birth, neonatal encephalopathy due to birth asphyxia and trauma, hemolytic disease, neonatal jaundice, neonatal sepsis, and other neonatal infections and disorders.

The data on China's PM2.5 concentration comes from the Bulletin of the State of the Ecological Environment in China issued by the Ministry of Ecology and Environment of the People's Republic of China (https://www.mee.gov.cn/). The data on perinatal mortality in China comes from the Chinese Maternal and Child Health Surveillance Network (http://www.mchscn.cn/).

Statistical Analysis

The annual percentage change (APC) and average annual percentage change (AAPCs) were used to evaluate the change trend of PM2.5 exposure from 1990 to 2019. APCs were used to detect specific segments of the linear trend throughout the study. AAPCs were used to estimate the overall change. APC, AAPC, and its 95% CI were calculated using Joinpoint Regression Program 4.9.0.0, and differences were considered significant at $p < .05$.

GraphPad prism 5 was used to plot the figures and describe population exposure levels of PM2.5 pollution and its changes in

TABLE 1 | Trends in PM 2.5 exposure of the whole population globally and in China from 1990 to 2019 (SEV, 95%UI).

Year	Whole population		Neonates	
	Global	China	Global	China
1990	15.65 (10.62–21.58)	16.92 (7.57–30.64)	13.27 (8.22–19.58)	15.86 (6.83–30.88)
1991	15.82 (10.81–21.61)	17.47 (7.99–31.46)	13.38 (8.45–19.52)	16.31 (7.21–30.71)
1992	16.02 (11.06–21.71)	18.08 (8.54–32.19)	13.50 (8.63–19.60)	16.80 (7.71–30.61)
1993	16.24 (11.26–22.04)	18.75 (8.97–32.77)	13.65 (8.76–19.57)	17.34 (8.11–30.91)
1994	16.48 (11.49–22.28)	19.47 (9.45–33.45)	13.81 (8.95–19.66)	17.92 (8.70–31.39)
1995	16.73 (11.74–22.50)	20.23 (10.01–34.34)	14.00 (9.16–19.77)	18.56 (8.94–32.60)
1996	17.03 (12.08–22.63)	21.08 (10.90–34.64)	14.22 (9.37–19.89)	19.28 (9.71–33.12)
1997	17.43 (12.49–23.05)	22.08 (11.98–35.34)	14.53 (9.70–20.15)	20.11 (10.73–33.33)
1998	17.89 (12.98–23.52)	23.15 (13.39–36.02)	14.91 (9.97–20.57)	20.98 (11.62–34.56)
1999	18.34 (13.46–23.98)	24.19 (14.36–37.50)	15.27 (10.31–20.95)	21.83 (12.48–35.22)
2000	18.73 (13.70–24.45)	25.12 (15.26–38.25)	15.58 (10.64–21.36)	22.6 (13.13–35.62)
2001	19.01 (13.96–24.56)	25.92 (16.37–38.27)	15.78 (10.85–21.55)	23.26 (14.24–36.09)
2002	19.27 (14.28–24.61)	26.72 (17.61–38.25)	15.94 (11.03–21.53)	23.93 (14.92–36.25)
2003	19.53 (14.62–24.63)	27.54 (18.43–38.03)	16.13 (11.23–21.79)	24.64 (15.54–36.02)
2004	19.83 (14.95–24.87)	28.38 (19.00–38.93)	16.35 (11.45–21.85)	25.38 (16.36–36.80)
2005	20.17 (15.32–25.30)	29.25 (19.78–39.58)	16.64 (11.73–22.18)	26.13 (17.23–37.27)
2006	20.60 (15.73–25.50)	30.21 (21.74–38.97)	16.99 (12.19–22.26)	26.94 (18.55–36.50)
2007	21.15 (16.38–25.82)	31.38 (23.72–39.15)	17.44 (12.74–22.75)	27.91 (20.33–36.28)
2008	21.77 (17.06–26.28)	32.64 (25.40–39.47)	17.96 (13.29–23.20)	28.97 (21.98–36.18)
2009	22.40 (17.74–26.96)	33.88 (26.74–40.28)	18.50 (13.89–23.71)	30.04 (23.55–36.43)
2010	22.98 (18.28–27.62)	34.98 (27.90–41.25)	19.04 (14.40–24.30)	30.98 (24.61–37.40)
2011	23.64 (18.87–28.21)	36.10 (29.21–42.30)	19.74 (15.11–24.81)	31.97 (25.68–38.30)
2012	24.45 (19.64–28.95)	37.36 (30.42–43.49)	20.71 (16.03–25.85)	33.11 (26.84–39.42)
2013	25.27 (20.42–29.85)	38.54 (31.63–44.66)	21.63 (16.78–26.83)	34.17 (27.84–40.43)
2014	25.92 (21.01–30.52)	39.45 (32.57–45.67)	22.27 (17.37–27.66)	34.93 (28.56–41.14)
2015	26.19 (21.27–30.80)	39.83 (33.24–45.94)	22.72 (17.88–28.15)	35.22 (28.97–41.34)
2016	25.80 (20.97–30.21)	38.77 (32.44–44.65)	22.48 (17.80–27.72)	33.91 (28.03–39.90)
2017	25.41 (20.73–29.73)	37.53 (31.57–43.28)	21.99 (17.29–27.11)	32.44 (26.73–38.42)
2018	25.64 (21.01–29.90)	37.35 (31.64–43.08)	22.04 (17.42–27.04)	32.11 (26.58–38.02)
2019	26.22 (21.57–30.50)	37.57 (31.94–43.25)	22.60 (17.96–27.69)	32.08 (26.57–38.06)

China and globally from 1990 to 2017. And Pearson Correlation was analyzed to directly explore the correlation between PM2.5 pollution concentration and the neonatal death rate, also used to analyze the current level of mortality and disease burden attributable to PM 2.5 pollution among Chinese newborns from 1990 to 2019, as well as the magnitude of their changes.

RESULTS

Trends in PM 2.5 Exposure of the Whole Population

The PM 2.5 SEV in Global whole population increased from 15.65 (95% UI:10.62–21.58) per 100 population in 1990 to 26.22 (95% UI:21.57–30.50) per 100 population in 2019. Although a decreasing trend was observed from 2015 to 2017, the global average exposure level of PM 2.5 steadily increased between 1990 and 2019, with an increase of 71.20%. The global AAPC in PM 2.5 exposure level was 1.8% (95% CI: 1.7–1.9%) with an overall increasing trend. There existed a fastest increasing period from 2006 to 2014, with a statistically significant APC of 3.0% (95% CI: 2.9–3.1%).

Conversely, the PM 2.5 SEV in whole population of China was 16.92 (95% UI: 7.57–30.64) per 100 population in 1990, which is close to the global SEV, but has been increasing since then at a much higher rate than the global average. The SEV value increased to 37.57 (95% UI: 31.94–43.25) per 100 population in 2019, with a downward trend starting in 2015; however, an overall upward trend of 133% was observed from 1990 to 2019 and has remained high compared to the global average. The AAPC of PM 2.5 exposure level in China was 2.8% (95% CI: 2.6–2.9%). An overall increasing trend with the fastest increasing period being from 1995 to 1999 with an APC of 4.6% (95% CI: 3.5–5.7%) and a decreasing trend in 2014–2019 with an APC of −1.4% (95% CI: −1.9-0.9%), which was statistically significant (**Tables 1**, **2**; **Figure 1**).

Trends of Neonatal PM 2.5 Exposure Levels

The PM 2.5 SEV in Global newborns population increased from 13.27 (95% UI:8.22–19.58) per 100 people in 1990 to 22.60 (95% UI:17.96–27.69) per 100 people in 2019. The average exposure level showed an overall upward trend from 1990 to 2019 with an increase of 71.11%. The global AAPC in neonatal PM 2.5 exposure levels was 1.8% (95% CI: 1.5–2.1%). An overall increasing trend with the fastest increasing period being from 2010 to 2014 with a statistically significant APC of 4.3% (95% CI: 3.0–7.4%).

PM 2.5 exposure levels among Chinese newborns increased from 16.88 (95% UI: 7.55–30.62) per 100 people in 1990 to 32.08 (95% UI:26.57–38.06) per 100 people in 2019. A downward trend

TABLE 2 | The analysis of trends in PM 2.5 exposure of the whole population globally and in China from 1990 to 2019 according to the APC and the AAPC.

Location	Period	Index	General population			Neonates		
			Value	95% CI	*p* Value	Value	95% CI	*p* Value
Global	1990–1995	APC	1.3[a]	1.2–1.5	<.001	1.0[a]	0.5–4.1	.001
	1995–2000		2.3[a]	2.1–2.5	<.001	2.2[a]	1.5–6.2	<.001
	2000–2006		1.5[a]	1.4–1.7	<.001	1.2[a]	0.4–3.4	.005
	2006–2014		3.0[a]	2.9–3.1	<.001	2.8[a]	2.0–7.7	<.001
	2014–2017		−0.6	−1.3–0.0	.060	4.3[a]	3.0–7.4	<.001
	2017–2019		1.2[a]	0.5–1.9	.002	−.2	−0.7~-0.7	.522
	1990–2019	AAPC	1.8[a]	1.7–1.9	<.1	1.8[a]	1.5–2.1	<.1
China	1990–1995	APC	3.6[a]	3.1–4.2	<.001	3.1[a]	2.3–3.9	<.001
	1995–1999		4.6[a]	3.5–5.7	<.001	4.0[a]	3.2–4.8	<.001
	1999–2014		3.4[a]	3.3–3.5	<.001	3.3[a]	3.1–3.4	<.001
	2014–2019		−1.4[a]	-1.9~-0.9	<.001	−2.0[a]	-2.6~-1.5	<.001
	1990–2019	AAPC	2.8[a]	2.6–2.9	<.1	2.4[a]	2.2–2.6	<.1

[a]*Represents p < .05, the difference is statistically significant.*

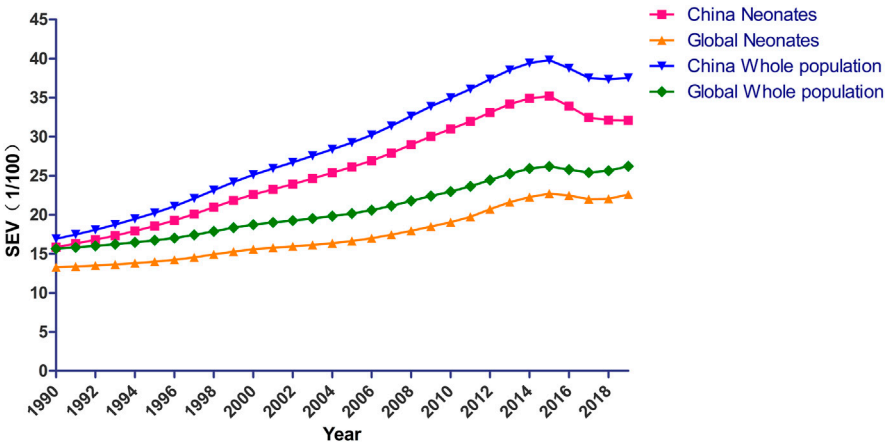

FIGURE 1 | Trends in PM 2.5 exposure of the whole population and newborns globally and in China from 1990 to 2019.

began in 2015; however, the overall trend over the period of 1990–2019 showed an upward trend with an increase of 102.27% and was beyond the global average. The mean AAPC in PM 2.5 exposure levels for newborns in China was 2.4% (95% CI: 2.2–2.6%). An overall increasing trend with the fastest increasing period from 1994 to 1999 with an APC of 4.0% (95% CI: 3.2–4.8%) and a decreasing trend from 2014 to 2019 with an APC of - 2.0% (95% CI: 2.6% to −1.5%), which is statistically significant. (**Tables 1**, **2**; **Figure 1**).

Correlation Analysis Between PM2.5 Concentration and Neonatal Disease Burden

The PM2.5 concentration is positively correlated with the burden of neonatal disease by Pearson Correlation analysis, showing that the data in GBD is consistent with the data from the China Maternal and Child Health Surveillance Network. Data from GBD shows that both neonatal disease deaths (r = 0.9534, p = 0.0009) and DALYs (r = 0.9534, p = .0009) in China are positively correlated with PM2.5 concentrations. Data obtained from the Chinese Maternal and Child Health Surveillance Network shows that the perinatal mortality rate is positively correlated with the concentration of PM2.5 (r = 0.9134, p = .004) (**Figure 2**).

Neonatal Disease Burden Attributable to PM 2.5 Pollution in China

From 1990 to 2019, the overall neonatal disease deaths, DALYs, and YLLs due to PM 2.5 pollution in China showed a decreasing trend, while YLDs showed an increasing trend (**Figure 2**). Compared to 1990, the number of deaths in 2019 decreased by 5738.34 cases, which is a decrement of 56.85%; DALYs decreased by 51.01, which is a decrement of 56.84%; YLLs decreased by 51.23, a 57.11% drop, and the YLDs increased by 150.69, which is an increment of 31.71%. Moreover, compared to

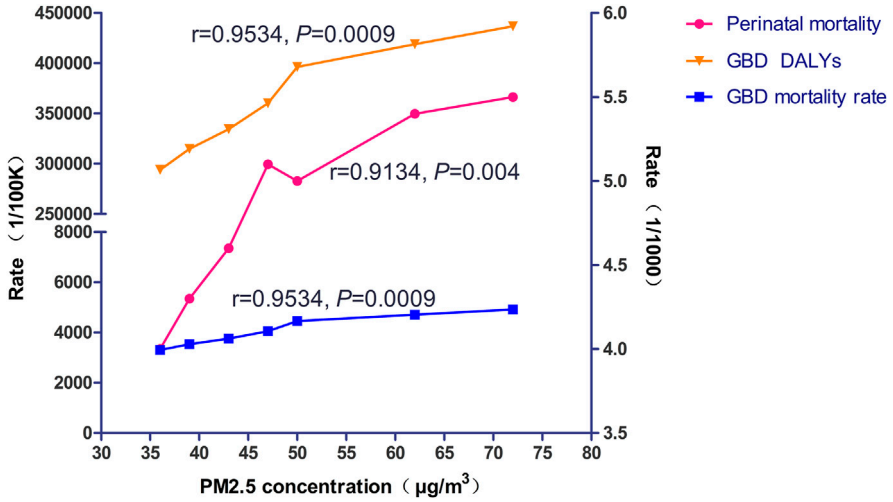

FIGURE 2 | Correlation between pm2.5 concentration and neonatal disease burden.

TABLE 3 | Neonatal disease burdens (in mortality, DALYs, YLDs, and YLLs) attributable to PM 2.5 exposure in China in 1990 and 2019.

	1990	2019	Increment	%
Mortality (person,95%UI)				
A	5476.80 (2537.60–9464.55)	2214.69 (1653.17–2782.82)	−3262.11	−59.56
B	3573.77 (1573.65–6351.33)	1484.47 (1111.38–1898.03)	−2089.30	−58.46
C	231.65 (103.94–413.66)	64.84 (47.92–84.61)	−-166.81	−72.01
D	166.3 (75.81-1–299.01)	164.91 (124.45–209.46)	−1.39	−0.84
E	645.5 (295.61–1131.09)	422.78 (315.76–544.35)	−222.72	−34.50
Total	10094.03 (4589.31–17883.13)	4351.69 (3282.10–5478.61)	−5738.34	−56.85
DALYs (person/10000/year,95%UI)				
A	48.69 (22.56–84.14)	19.71 (14.72–24.76)	−28.98	−59.52
B	31.76 (13.98–56.44)	13.19 (9.88–16.87)	−18.57	−58.47
C	2.06 (0.93–3.68)	0.58 (0.43–0.75)	−1.48	−71.84
D	1.48 (0.68–2.66)	1.48 (1.12–1.88)	−.00065	−0.04
E	5.74 (2.63–10.06)	3.77 (2.82–4.85)	−1.97	−34.32
Total	89.74 (40.80–158.97)	38.73 (29.24–48.76)	−51.01	−56.84
YLDs (person/year,95%UI)				
A	294.85 (129.99–521.18)	300.16 (209.60–407.37)	5.31	1.80
B	31.92 (11.13–75.18)	23.34 (13.31–37.56)	−8.58	−26.88
C	26.49 (9.73–63.81)	25.17 (9.16–65.39)	−1.32	−4.98
D	62.13 (22.61–129.12)	178.94 (108.98–265.40)	116.81	188.01
E	59.80 (27.39–105.86)	98.27 (66.42–135.02)	38.47	64.33
Total	475.19 (218.62–826.69)	625.88 (440.90–834.91)	150.69	31.71
YLLs (person/10000/year,95%UI)				
A	48.66 (22.55–84.10)	19.68 (14.69–24.73)	−28.98	−59.56
B	31.76 (13.98–56.44)	13.19 (9.88–16.87)	−18.57	−58.47
C	2.06 (0.92–3.68)	0.58 (0.43–0.75)	−1.48	−71.84
D	1.48 (0.67–2.66)	1.47 (1.11–1.86)	−.01	−0.68
E	5.74 (2.63–10.05)	3.76 (2.81–4.84)	−1.98	−34.49
Total	89.70 (40.78–158.90)	38.67 (29.16–48.68)	−51.23	−57.11

Note.: A, preterm birth; B, neonatal encephalopathy due to birth asphyxia and trauma; C, hemolytic disease and other neonatal jaundice; D, neonatal sepsis and other neonatal infections; E, Other neonatal disorders.

DALYs, Disability-adjusted life years; YLDs, Years lived with disability; YLLs, Years of life lost.

TABLE 4 | Different neonatal disease burdens and the rank in mortality, DALY, YLD, and YLL attributable to PM 2.5 exposure in China in1990 and 2019 (rate/100k).

Disease	Mortality				DALY				YLD				YLL			
	1990		2019		1990		2019		1990		2019		1990		2019	
	Rank	Rate	Rank	Rate	Rank	Rate	Rank	Rate	Rank	Rate	Rank	Rate	Rank	Rate	Rank	Rate
A	1	300.74	1	194.73	1	26738.98	1	17329.83	1	16.19	1	26.39	1	26722.79	1	17303.43
B	2	196.24	2	130.53	2	17439.53	2	11600.44	4	1.75	5	2.05	2	17437.78	2	11598.39
C	4	12.72	5	5.70	4	1131.59	5	508.71	5	1.45	4	2.21	4	1130.14	5	506.50
D	5	9.13	4	14.50	5	814.75	4	1304.04	2	3.41	2	15.73	5	811.34	4	1288.30
E	3	35.45	3	37.17	3	3152.71	3	3311.65	3	3.28	3	8.64	3	3149.42	3	3303.01

Note: A, Preterm birth; B, Neonatal encephalopathy due to birth asphyxia and trauma; C, Hemolytic disease and other neonatal jaundice; D, Neonatal sepsis and other neonatal infections; E, Other neonatal disorders; DALYs, Disability-adjusted life years; YLDs, Years lived with disability; YLLs, Years of life lost.

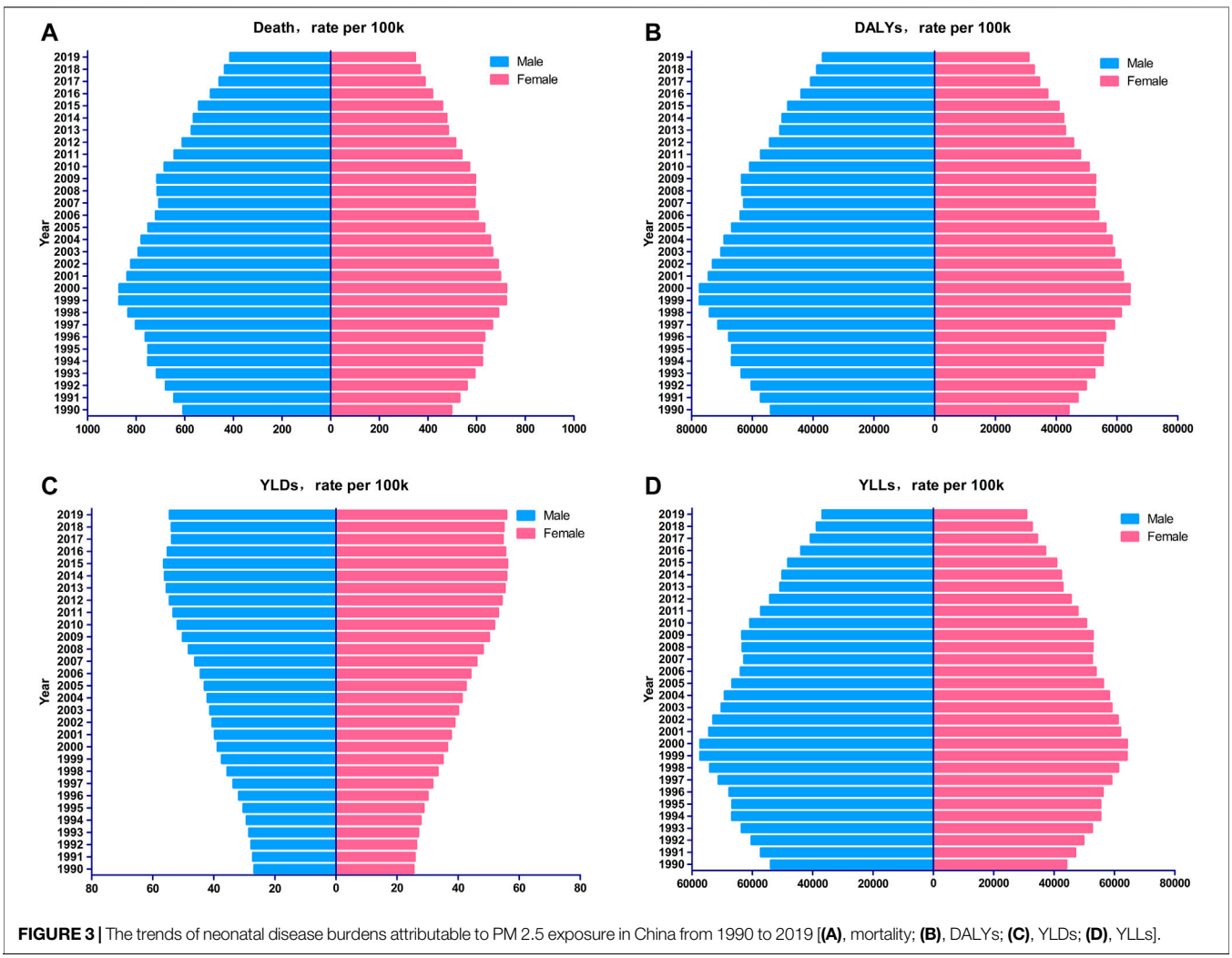

FIGURE 3 | The trends of neonatal disease burdens attributable to PM 2.5 exposure in China from 1990 to 2019 [**(A)**, mortality; **(B)**, DALYs; **(C)**, YLDs; **(D)**, YLLs].

1990, the number of deaths, DALYs, and YLLs for all types of neonatal diseases attributed to PM 2.5 pollution in China in 2019 decreased to various degrees, as shown in **Table 3**. YLDs indicators revealed a different scenario with increases of 5.31 person/years (1.8% increase), 116.81 person/years (188.01% increase), and 38.47 person/years (64.33% increase) for preterm birth, sepsis, and other infections and neonatal diseases, respectively; however, decreases of 8.58 person/years (26.88% decrease) and 1.32 person/years (4.98% decrease) for neonatal encephalopathy and hemolytic disease and jaundice, respectively were observed.

Mortality rate, DALY, YLL, and YLD rate of preterm neonatal birth due to PM 2.5 pollution in China in 1990 and 2019 is the highest among all types of neonatal diseases. Neonatal

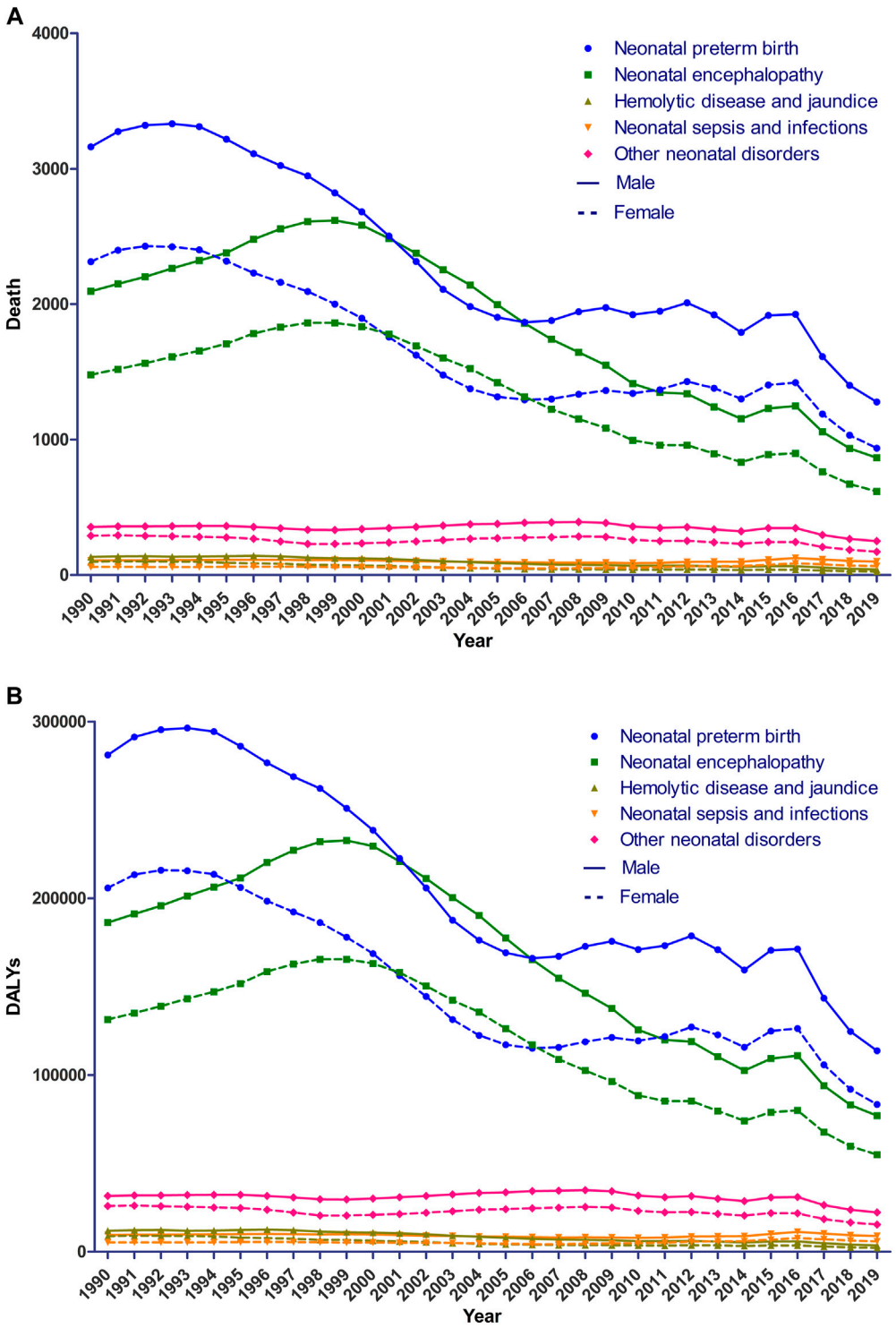

FIGURE 4 | The trends of different neonatal disease burdens in different genders attributable to PM 2.5 exposure in China from 1990 to 2019 [**(A)**, mortality; **(B)**, DALYs].

encephalopathy has the second highest mortality rate, DALY, and YLL. Sepsis and other infections had the second highest rate of YLD (**Table 4**).

The overall disease burden indicators for male infants are slightly higher than for female infants. The number of cases of death in 2019 was 2533.45 and 1818.24 for males and females, respectively. The mortality rates for males and females were 413.50 per 100K, and 346.58 per 100K, respectively. The DALYs were 225,449.84 person/years and 161,856.02 person/years for males and females, respectively (**Figure 3**). The burden of neonatal diseases attributable to PM 2.5 pollution in China decreases year to year, but the most predominant neonatal diseases are still preterm birth and neonatal encephalopathy (**Figure 4**).

DISCUSSION

As the source of various health problems, numerous scientific studies have explained the environmental risk to public health caused by particle exposure. And the available data on the relationships of particulate matter air pollution and neonatal disease burden, particularly in China, are scarce. This study assessed neonatal disease burden of attributable to PM 2.5 pollution in China from 1990 to 2019 using data related to PM 2.5 pollution exposure and neonatal disease obtained from the GBD research.

In this study, PM 2.5 pollution exposure levels among Chinese newborns were much higher than the global average and more than doubled in 2019 compared to 1990. Environmental PM2.5 concentration is positively correlated with neonatal disease burden. Though the overall disease burden of neonatal diseases attributed to PM 2.5 pollution in China has decreased from 1990 to 2019. Deaths, DALYs, and YLLs, decreased to various degrees, but YLDs for preterm birth, sepsis, and other infections and other neonatal diseases showed varying degrees of increase, which deserved more attention.

The global number of deaths attributable to PM 2.5 exposure in 2015 was 4.2 million, with 1.1 million deaths coming from China, accounting for more than a quarter of all deaths caused by PM 2.5 exposure. The mortality rate attributable to PM 2.5 pollution in China was 84.3 per 100K, more than four times that of the United States 18.5 per 100K people (Cohen et al., 2017). Globally, more than 250 million people live in highly polluted areas, primarily in east-central China and the Ganges Plains of India (Cheng et al., 2016). In 2013, China implemented the Action Plan for the Prevention and Control of Air Pollution, focusing on treatment mainly in the eastern and central regions (Huang et al., 2018). There is a decreasing trend of PM 2.5 exposure among Chinese newborns in 2014–2019 with an APC of–2.0% (95% CI: –2.6% to –1.5%, $p < .001$)., and there is a decreasing trend of mortality of neonatal diseases attributable to PM 2.5 in 2015–2019 with an APC of –6.4% (95% CI: –7.7% to –5.1%, $p < .001$). This study shows that the PM 2.5 exposure levels in China slowed down after 2013 and declined in 2015. Furthermore, the disease burden attributable to PM 2.5 pollution among newborns has also shown a significant decrease, However, China still has a severe PM 2.5 pollution problem and needs to further intensify its treatment and control efforts to reduce the damage of PM 2.5 pollution on population health.

Our research verified the data obtained in China and the GBD data, and the results showed that PM2.5 pollution does have a certain relationship with the burden of neonatal disease. One study found that short-term exposure to PM 2.5 adversely affects neonatal and postnatal mortality, specifically mortality related to respiratory causes (Yorifuji et al., 2016). A strong association between PM 2.5 and infant mortality has also been demonstrated for neonatal mortality in low- and middle-income countries (Anwar et al., 2019; Goyal et al., 2019). Several studies have also shown that PM 2.5 exposure during pregnancy or the postpartum period has adverse effects on neonatal health and results in adverse outcomes such as preterm birth, low birth weight, neonatal death, and impaired lung development (Proietti et al., 2013; Gauderman et al., 2015; Korten et al., 2017; Smith et al., 2017; Heft-Neal et al., 2018; Zhang et al., 2019; Macchi et al., 2021).

The leading causes of neonatal death are prematurity, birth-related complications, and infections such as sepsis, meningitis, and pneumonia. According the estimates from World Health Organization (WHO), 35% of all neonatal deaths in 2017 were due to complications of prematurity, 24% of deaths were related to delivery (intrapartum events), such as birth asphyxia, and 14% of deaths were due to sepsis or meningitis (Hug et al., 2019). From 1990 to 2017, there has been a significant improvement in neonatal survival globally, a 51% reduction in neonatal mortality, and a reduction in deaths from 5 million to 2.5 million per year (Hug et al., 2019). Despite this, 2.5 million newborns died in 2017 alone, with significant variation in neonatal mortality across regions and countries.

Preterm birth is an important global health issue. An estimated 15 million neonates are born preterm each year, and the rate of preterm birth has been steadily increasing worldwide (Blencowe et al., 2012). The World Health Organization's Birth Too Soon: Global Action Report on Preterm Birth, released on 02 May, 2012, states that 15 million preterm babies are born worldwide each year with more than 1 million dying soon after birth. Those who survive often endure a lifetime of accompanying illness (Hua et al., 2015). Preterm birth complications are the leading cause of death in children under 5 years of age. Approximately 1 million people died worldwide in 2015 (Liu et al., 2016). Air pollution has been shown to influence preterm birth (Sun et al., 2015; Li et al., 2017; Guan et al., 2019; Wang et al., 2020). This study shows that China has the highest mortality and disease burden of preterm births attributable to PM 2.5 pollution, with 197,100 person/years for DALYs, 300.16 person/years for YLDs, and 196,800 person/years for YLLs. It is suggested that the main contribution to the disease burden attributable to PM 2.5 neonatal preterm birth in China is currently YLL. Therefore, it is vital to target preterm birth complications with the necessary interventions to reduce deaths due to preterm birth.

Neonatal sepsis is an acute infectious disease with a very high morbidity and mortality rate. The widespread application of

antibiotics has led to a significant increase in drug-resistant strains of pathogenic bacteria (Jia et al., 2017). In 2019, the rate of neonatal sepsis and other infectious diseases YLD attributed to PM 2.5 pollution ranked second, increasing 142.31% compared to 1990. The death rate was the fourth highest, with a reduction of 14.29% compared to 1990. The results show that the burden of disability caused by neonatal sepsis is increasing, suggesting that early diagnosis, timely and rational antimicrobial drug treatment, as well as attention to its treatment prognosis leading to the possibility of disability should be achieved.

With improvements in obstetric and neonatal care, the number of children who survived high-risk neonatal illness with neurodevelopmental disorders and disabilities has increased. The risk of having at least one impairment during development after a perinatal injury is estimated to be approximately 40% (Kohli-Lynch et al., 2019). Sometimes, improper application of technical interventions, such as induction of labor without adequate monitoring during labor, may result in a higher incidence of injured survivors. In these settings, YLDs accounts for a larger proportion of the total DALYs (21% in East Asia/Pacific and Middle East/North Africa, and 9% in sub-Saharan Africa/South Asia) (Lee et al., 2013). This study found that the number of neonatal disease deaths, DALYs, and YLLs due to PM 2.5 pollution in China decreased from 1990 to 2019, while YLDs increased by 31.71% in 2019 compared to 1990. Developmental disabilities caused by neonatal diseases increase the burden of disease. It is suggested that reducing the burden of disease in the neonatal stage requires not only improving neonatal survival but also requires further attention. Moreover, we need to focus on the prognosis of neonatal diseases, paying attention to child developmental issues, and reducing the burden of disease caused by disability.

There have certain limitations in our research for using the available database. The data of PM2.5 concentration in China and the data of perinatal mortality in China are not detailed enough, and there are differences in the spatial distribution. Further cohort studies are needed to verify the relationship between PM2.5 pollution and neonatal disease burden.

CONCLUSION

This study assessed neonatal disease burden of attributable to PM 2.5 pollution in China from 1990 to 2019 using data related to PM 2.5 pollution exposure and neonatal disease obtained from the GBD research. The results show a high level of PM 2.5 pollution exposure in China. Environmental PM2.5 concentration is positively and strongly correlated with neonatal disease burden. With the control of PM2.5 pollution, although the burden of disease of newborns is reducing, the burden of disease caused by disability is increasing, which indicates that the long-term effects of PM2.5 exposure may contribute to the disability of newborns. The results of our study suggest that various measures should continue to be taken to improve air quality, and focus on the prognosis and developmental disabilities during improving the neonatal survival.

DATA AVAILABILITY STATEMENT

The original contributions presented in the study are included in the article/Supplementary Material, further inquiries can be directed to the corresponding authors.

AUTHOR CONTRIBUTIONS

All authors contributed to data interpretation, wrote and revised various parts of the paper. JY, LS, HL, and YC conducted the work presented here and performed data analysis; JY and BH drafted the manuscript. LZ, JZ, and YC revised the overall paper; YC and BH supervised the work. All authors read and approved the final manuscript.

FUNDING

This work was financially supported by the National Natural Science Foundation of China (82173526), and the Natural Science Basic Research Plan of the Shaanxi Province (2020JQ-547). The funding body played no role in the design of the study, in the collection, analysis, and interpretation of data, or in writing the manuscript.

ACKNOWLEDGMENTS

The authors thank AiMi Academic Services (www.aimieditor.com) for the English language editing and review services.

REFERENCES

Anwar, A., Ayub, M., Khan, N., and Flahault, A. (2019). Nexus between Air Pollution and Neonatal Deaths: A Case of Asian Countries. *Ijerph* 16 (21), 4148. doi:10.3390/ijerph16214148

Blencowe, H., Cousens, S., Oestergaard, M. Z., Chou, D., Moller, A.-B., Narwal, R., et al. (2012). National, Regional, and Worldwide Estimates of Preterm Birth Rates in the Year 2010 with Time Trends since 1990 for Selected Countries: a Systematic Analysis and Implications. *The Lancet* 379 (9832), 2162–2172. doi:10.1016/s0140-6736(12)60820-4

Brauer, M., Freedman, G., Frostad, J., van Donkelaar, A., Martin, R. V., Dentener, F., et al. (2016). Ambient Air Pollution Exposure Estimation for the Global Burden of Disease 2013. *Environ. Sci. Technol.* 50 (1), 79–88. doi:10.1021/acs.est.5b03709

Cheng, Z., Luo, L., Wang, S., Wang, Y., Sharma, S., Shimadera, H., et al. (2016). Status and Characteristics of Ambient PM2.5 Pollution in Global Megacities. *Environ. Int.* 89-90, 212–221. doi:10.1016/j.envint.2016.02.003

Cohen, A. J., Brauer, M., Burnett, R., Anderson, H. R., Frostad, J., Estep, K., et al. (2017). Estimates and 25-year Trends of the Global burden of Disease Attributable to Ambient Air Pollution: an Analysis of Data from the Global Burden of Diseases Study 2015. *The Lancet* 389 (10082), 1907–1918. doi:10.1016/s0140-6736(17)30505-6

Ef, U., Bank, W., and Division, U. P. (2017). *Levels and Trends in Child Mortality : Report 2017*.

Feigin, V. L., Krishnamurthi, R. V., Parmar, P., Norrving, B., Mensah, G. A., Bennett, D. A., et al. (2015). Update on the Global Burden of Ischemic and Hemorrhagic Stroke in 1990-2013: The GBD 2013 Study. *Neuroepidemiology* 45 (3), 161–176. doi:10.1159/000441085

Gauderman, W. J., Urman, R., Avol, E., Berhane, K., McConnell, R., Rappaport, E., et al. (2015). Association of Improved Air Quality with Lung Development in Children. *N. Engl. J. Med.* 372 (10), 905–913. doi:10.1056/NEJMoa1414123

Goyal, N., Karra, M., and Canning, D. (2019). Early-life Exposure to Ambient fine Particulate Air Pollution and Infant Mortality: Pooled Evidence from 43 Low- and Middle-Income Countries. *Int. J. Epidemiol.* 48 (4), 1125–1141. doi:10.1093/ije/dyz090

Guan, T., Xue, T., Gao, S., Hu, M., Liu, X., Qiu, X., et al. (2019). Acute and Chronic Effects of Ambient fine Particulate Matter on Preterm Births in Beijing, China: A Time-Series Model. *Sci. Total Environ.* 650, 1671–1677. doi:10.1016/j.scitotenv.2018.09.279

Heft-Neal, S., Burney, J., Bendavid, E., and Burke, M. (2018). Robust Relationship between Air Quality and Infant Mortality in Africa. *Nature* 559(7713), 254–258. doi:10.1038/s41586-018-0263-3

Hua, S., Wei-wei, L., Hong-yan, Y., Mai-geng, Z., Shi-wei, L., and Yi-chong, L. (2015). Burden of Neonatal Diseases in China,1990-2010. *DISEASE SURVEILLANCE* 30 (08), 663–667.

Huang, J., Pan, X., Guo, X., and Li, G. (2018). Health Impact of China's Air Pollution Prevention and Control Action Plan: an Analysis of National Air Quality Monitoring and Mortality Data. *Lancet Planet. Health* 2 (7), E313–E323. doi:10.1016/s2542-5196(18)30141-4

Hug, L., Alexander, M., You, D., Alkema, L., Alkema, L., Black, R., et al. (2019). National, Regional, and Global Levels and Trends in Neonatal Mortality between 1990 and 2017, with Scenario-Based Projections to 2030: a Systematic Analysis. *Lancet Glob. Health* 7 (6), E710–E720. doi:10.1016/s2214-109x(19)30163-9

Jacobs, M., Zhang, G., Chen, S., Mullins, B., Bell, M., Jin, L., et al. (2017). The Association between Ambient Air Pollution and Selected Adverse Pregnancy Outcomes in China: A Systematic Review. *Sci. Total Environ.* 579, 1179–1192. doi:10.1016/j.scitotenv.2016.11.100

Jia, Z., Bi, F., and Zhang, C. (2017). Distribution and Drug Resistance of Pathogens Isolated from Neonates with Septicemia. *Chin. J. Nosocomiology* 27 (1), 197–200.

Kohli-Lynch, M., Tann, C. J., and Ellis, M. E. (2019). Early Intervention for Children at High Risk of Developmental Disability in Low- and Middle-Income Countries: A Narrative Review. *Ijerph* 16 (22), 4449. doi:10.3390/ijerph16224449

Korten, I., Ramsey, K., and Latzin, P. (2017). Air Pollution during Pregnancy and Lung Development in the Child. *Paediatric Respir. Rev.* 21, 38–46. doi:10.1016/j.prrv.2016.08.008

Lee, A. C., Kozuki, N., Blencowe, H., Vos, T., Bahalim, A., Darmstadt, G. L., et al. (2013). Intrapartum-related Neonatal Encephalopathy Incidence and Impairment at Regional and Global Levels for 2010 with Trends from 1990. *Pediatr. Res.* 74, 50–72. doi:10.1038/pr.2013.206

Li, X., Huang, S., Jiao, A., Yang, X., Yun, J., Wang, Y., et al. (2017). Association between Ambient fine Particulate Matter and Preterm Birth or Term Low Birth Weight: An Updated Systematic Review and Meta-Analysis. *Environ. Pollut.* 227, 596–605. doi:10.1016/j.envpol.2017.03.055

Liu, C., Wang, B., Liu, S., Li, S., Zhang, K., Luo, B., et al. (2021). Type 2 Diabetes Attributable to PM2.5: A Global burden Study from 1990 to 2019. *Environ. Int.* 156, 106725. doi:10.1016/j.envint.2021.106725

Liu, L., Oza, S., Hogan, D., Chu, Y., Perin, J., Zhu, J., et al. (2016). Global, Regional, and National Causes of Under-5 Mortality in 2000-15: an Updated Systematic Analysis with Implications for the Sustainable Development Goals. *The Lancet* 388 (10063), 3027–3035. doi:10.1016/s0140-6736(16)31593-8

Liu, W., Liu, J., Liu, J., Song, Y., Zeng, X., Wang, X., et al. (2019). Burden of Lymphoma in China, 2006-2016: an Analysis of the Global Burden of Disease Study 2016. *J. Hematol. Oncol.* 12 (1). doi:10.1186/s13045-019-0785-7

Luo, L., Jiang, J., Zhang, G., Wang, L., Wang, Z., Yang, J., et al. (2017). Stroke Mortality Attributable to Ambient Particulate Matter Pollution from 1990 to 2015 in China: An Age-Period-Cohort and Spatial Autocorrelation Analysis. *Ijerph* 14 (7), 772. doi:10.3390/ijerph14070772

Macchi, C., Iodice, S., Persico, N., Ferrari, L., Cantone, L., Greco, M. F., et al. (2021). Maternal Exposure to Air Pollutants, PCSK9 Levels, Fetal Growth and Gestational Age - an Italian Cohort. *Environ. Int.* 149, 106163. doi:10.1016/j.envint.2020.106163

Murray, C. J. L., Aravkin, A. Y., Zheng, P., Abbafati, C., Abbas, K. M., Abbasi-Kangevari, M., et al. (2020). Global burden of 87 Risk Factors in 204 Countries and Territories, 1990-2019: a Systematic Analysis for the Global Burden of Disease Study 2019. *Lancet* 396 (10258), 1223–1249. doi:10.1016/S0140-6736(20)30752-2

Proietti, E., Röösli, M., Frey, U., and Latzin, P. (2013). Air Pollution during Pregnancy and Neonatal Outcome: A Review. *J. Aerosol Med. Pulm. Drug Deliv.* 26 (1), 9–23. doi:10.1089/jamp.2011.0932

Smith, R. B., Fecht, D., Gulliver, J., Beevers, S. D., Dajnak, D., Blangiardo, M., et al. (2017). Impact of London's Road Traffic Air and Noise Pollution on Birth Weight: Retrospective Population Based Cohort Study. *Bmj* 359, j5299. doi:10.1136/bmj.j5299

Sun, X., Luo, X., Zhao, C., Chung Ng, R. W., Lim, C. E. D., Zhang, B., et al. (2015). The Association between fine Particulate Matter Exposure during Pregnancy and Preterm Birth: a Meta-Analysis. *BMC Pregnancy Childbirth* 15. doi:10.1186/s12884-015-0738-2

Wang, Q., Li, B., Benmarhnia, T., Hajat, S., Ren, M., Liu, T., et al. (2020). Independent and Combined Effects of Heatwaves and PM2.5 on Preterm Birth in Guangzhou, China: A Survival Analysis. *Environ. Health Perspect.* 128 (1), 017006–17006. doi:10.1289/EHP5117

Yin, P., Brauer, M., Cohen, A. J., Wang, H., Li, J., Burnett, R. T., et al. (2020). The Effect of Air Pollution on Deaths, Disease burden, and Life Expectancy across China and its Provinces, 1990-2017: an Analysis for the Global Burden of Disease Study 2017. *Lancet Planet. Health* 4 (9), E386–E398. doi:10.1016/s2542-5196(20)30161-3

Yorifuji, T., Kashima, S., and Doi, H. (20162002-2013). Acute Exposure to fine and Coarse Particulate Matter and Infant Mortality in Tokyo, Japan (2002-2013). *Sci. Total Environ.* 551-552, 66–72. doi:10.1016/j.scitotenv.2016.01.211

Zhang, L., Liu, W., Hou, K., Lin, J., Song, C., Zhou, C., et al. (2019). Air Pollution Exposure Associates with Increased Risk of Neonatal Jaundice. *Nat. Commun.* 10. doi:10.1038/s41467-019-11387-3

Zhang, M. J., Su, F. C., Xu, Q. X., Zhang, R. Q., Wei, Y., and Xie, L. Z. (2021). Health Impact Attributable to the Control of PM2.5 Pollution in China during 2013-2017. *Huan Jing Ke Xue* 42 (2), 513–522. doi:10.13227/j.hjkx.202007012

Zhou, M., Wang, H., Zeng, X., Yin, P., Zhu, J., Chen, W., et al. (2019). Mortality, Morbidity, and Risk Factors in China and its Provinces, 1990-2017: a Systematic Analysis for the Global Burden of Disease Study 2017. *The Lancet* 394 (10204), 1145–1158. doi:10.1016/s0140-6736(19)30427-1

Conflict of Interest: The authors declare that the research was conducted in the absence of any commercial or financial relationships that could be construed as a potential conflict of interest.

Publisher's Note: All claims expressed in this article are solely those of the authors and do not necessarily represent those of their affiliated organizations, or those of the publisher, the editors and the reviewers. Any product that may be evaluated in this article, or claim that may be made by its manufacturer, is not guaranteed or endorsed by the publisher.

frontiers in Environmental Science

ORIGINAL RESEARCH
published: 09 February 2022
doi: 10.3389/fenvs.2022.814736

Effects of Different Aerosols on the Air Pollution and Their Relationship With Meteorological Parameters in North China Plain

Hujia Zhao[1], Ke Gui[2], Yanjun Ma[1], Yangfeng Wang[2], Yaqiang Wang[2], Hong Wang[2], Yuanyuan Dou[3], Yu Zheng[2], Lei Li[2], Lei Zhang[2], Yuqi Zhang[4], Huizheng Che[2] and Xiaoye Zhang[2]*

[1]Institute of Atmospheric Environment, China Meteorological Administration, Shenyang, China, [2]State Key Laboratory of Severe Weather (LASW) and Key Laboratory for Atmospheric Chemistry (LAC), Institute of Atmospheric Composition and Environmental Meteorology, Chinese Academy of Meteorological Sciences (CAMS), CMA, Beijing, China, [3]Weifang Municipal Linqu Ecology and Environment Monitoring Center, Weifang, China, [4]Liaoning Meteorological Service Center, Liaoning Meteorological Bureau, Shenyang, China

OPEN ACCESS

Edited by:
Qiyuan Wang,
Institute of Earth Environment (CAS), China

Reviewed by:
Yunfei Wu,
Institute of Atmospheric Physics (CAS), China
Qian Zhang,
Xi'an University of Architecture and Technology, China

***Correspondence:**
Hujia Zhao
tjzhj4659@sina.com

Specialty section:
This article was submitted to Atmosphere and Climate, a section of the journal Frontiers in Environmental Science

Received: 14 November 2021
Accepted: 18 January 2022
Published: 09 February 2022

Citation:
Zhao H, Gui K, Ma Y, Wang Y, Wang Y, Wang H, Dou Y, Zheng Y, Li L, Zhang L, Zhang Y, Che H and Zhang X (2022) Effects of Different Aerosols on the Air Pollution and Their Relationship With Meteorological Parameters in North China Plain. Front. Environ. Sci. 10:814736. doi: 10.3389/fenvs.2022.814736

Located in East Asia, the North China Plain (NCP) has a severe air pollution problem. In this study, variations in visibility, particulate matter (PM), gaseous pollutants, vertical meteorological parameters, and different types of aerosols and their optical properties were evaluated during an air pollution episode that occurred from 10 to 15 January 2019 in Tianjin over the NCP. The visibility was <10 km for approximately 96 h, and the concentrations of PM with an aerodynamic diameter of <2.5 μm ($PM_{2.5}$) and <10 μm (PM_{10}) increased to 300 and 400 μg/m^3, respectively. Because of the conversion of SO_2 to sulphate aerosol particles, the sulphur dioxide (SO_2) concentration decreased to a minimum of 10 μg/m^3. The continual deterioration of visibility was related to the high relative humidity and the boundary layer of <0.1 km. The southwest airflow (3.0–4.0 m/s) transported various pollutants from Hebei Province to the NCP. Higher mixing ratios of sulphate aerosols, organic aerosols, and black carbon aerosols were distributed over a 0.5-km-diameter area, and the maximum concentrations were approximately 90, 250–300, and 20 μg/kg, respectively. Higher mixing ratios of dust aerosols and sea salt aerosols were distributed within 1.5 km and 1.0–2.5 km, respectively, and their maximum concentrations were approximately 15 and 9 μg/kg, respectively. The findings are valuable for analysing the relationship between air quality and pollutant transport in the NCP.

Keywords: Pm, meteorological parameters, aerosol, aerosol optical depth, North China plain

INTRODUCTION

Aerosols can directly alter the energy balance of the earth–atmosphere system by absorbing and scattering solar radiation (Ackerman and Toon, 1981; Charlson et al., 1992; Hansen et al., 1997). Aerosols can facilitate the formation of cloud condensation nuclei, thereby causing changes in global and regional climates (Twomey et al., 1984; Hansen et al., 2000). Studies have investigated the environmental effects of aerosols, focusing on the problem of global climate change (Dubovik et al., 2002; Eck et al., 2005; Che et al., 2019; Gui et al., 2021a; Gui et al., 2021b).

In the past decade, $PM_{2.5}$ has become the main pollutant in the urban areas of China during haze events because of the rapid development of the economy, the expansion of urbanisation, and the acceleration of energy consumption (Che et al., 2009; Zhang et al., 2009; Wang et al., 2014). The regional degradation of visibility in urban agglomerations in China characterised by intensive anthropogenic activities has garnered widespread public attention (Che et al., 2007; Chang et al., 2009; Zhang et al., 2012). The Beijing–Tianjin–Hebei (BTH) region is the political and cultural centre of China and a crucial economic zone in northern China. In recent years, severe pollution caused by $PM_{2.5}$ in the BTH region has resulted in considerable public concern (Jin et al., 2016; Shen et al., 2019). Extreme haze episodes occur more frequently in the BTH region; moreover, several cities with poor air quality are located in this region (Che et al., 2014; Che et al., 2015). Studies have examined fine PM pollution in the BTH region because of its negative socioeconomic impacts (Gao et al., 2015; Zheng et al., 2015; Chen et al., 2017). During heavy pollution episodes, intercity transport is a crucial contributor to $PM_{2.5}$ pollution in this region (Hua et al., 2016; Chang et al., 2018). Studies have conducted model simulations to estimate the contributions of different source regions (Zhang et al., 2013; Sun et al., 2016; Zou et al., 2018). In addition to regional transport, local atmospheric circulation substantially contributes to high $PM_{2.5}$ pollution in the BTH region (Miao et al., 2015; Miao et al., 2017). Therefore, air pollution in the BTH region is mainly affected by local pollutant emission, specific regional topography, and regional pollutant transport.

Tianjin is the largest coastal city in the North China Plain (NCP; 117.2°E, 39.13°N). This city is the central functional area of the BTH region in China's Capital Economic Circle and a vital central city in the Bohai Economic Circle in northern China. Continuous increases in anthropogenic activities as well as vehicle exhaust and coal combustion are key factors of pollutant emissions in this region (Wu et al., 2015; Zhao et al., 2019). In addition, seasonal biomass burning substantially contributes to $PM_{2.5}$ pollution in Tianjin, thus affecting regional air quality (Andreae and Merlet, 2001; Yang et al., 2006; Chen et al., 2015). Tianjin Port, one of the world's largest container ports, is affected by pollutant emissions from ships. Furthermore, mesoscale atmospheric circulation considerably contributes to air pollution in coastal areas (Corbett et al., 2007; Dore et al., 2007; Yau et al., 2012).

Most studies on pollution events in Tianjin have focused on particle concentration evolution, chemical composition, and regional transport (Bai et al., 2021; Lang et al., 2021; Li et al., 2021). Very few studies have examined the vertical mixing ratios of different types of aerosols. Thus, we synchronously observed near-surface and boundary-layer meteorological factors and aerosols in the vertical direction to examine mechanisms through which aerosols with different chemical compositions affect regional air quality, thus causing severe pollution. The findings provide insights into the mechanisms of regional severe air pollution. We investigated a pollution event characterised by high $PM_{2.5}$ concentrations in the coastal city of Tianjin that occurred from 10 to 15 January 2019. Temporal variations in the concentrations of PM and gaseous pollutants as well as meteorological parameters, namely relative humidity (RH), temperature, wind speed (WS), and wind direction (WD), both near the surface and in the vertical direction, were examined. Moreover, potential sources contributing to $PM_{2.5}$ emission during the sampling period were determined using the weighted potential source contribution function (WPSCF)/ weighted concentration weighted trajectory (WCWT) model. In addition, we determined the effects of different types of aerosols and their contribution to aerosol extinction during the event. Multiple data sources were employed. The results may be used to formulate strategies for the prevention and control of local and regional air pollution in coastal areas during pollution events.

The remainder of the paper is organised as follows. Section 2 describes the study site and introduces the data used to analyse the temporal and vertical characteristics of pollution evolution. In Section 3, variations in pollutant concentrations, surface and vertical meteorological parameters, and potential $PM_{2.5}$ sources during the event were examined. Moreover, the spatial distributions of aerosol optical properties are discussed according to the aerosol type and their effects on aerosol extinction during the episode. Finally, conclusions are drawn in Section 4.

STUDY SITE AND DATA COLLECTION

Tianjin is a large port city in China with a thriving chemical industry. The combined effects of local accumulation, regional transport, and secondary aerosol formation have resulted in severe atmospheric pollution in this region (Han et al., 2014). As shown in **Figure 1**, Tianjin is located east of the Bohai Sea. Local circulation, such as sea–land breeze, affects air quality under stable weather conditions. Under the effect of sea–land breeze circulation, the dispersion of pollutants to distant locations is inhibited, leading to pollutant accumulation (Han et al., 2015; Han et al., 2018). During severe pollution events, a convergence flow field appears in Tianjin and its surrounding areas, leading to high local pollution levels.

Data collected from six meteorological stations in Tianjin, comprising the hourly mass concentrations of four crucial particles and gaseous pollutants, namely $PM_{2.5}$ (PM with an aerodynamic diameter of ≤2.5 μm), PM_{10} (PM with an aerodynamic diameter of ≤10 μm), SO_2, and NO_2, were obtained from the website of the China National Environmental Monitoring Centre (http://www.cnemc.cn). Furthermore, $PM_{2.5}$ data collected nationwide over the study period were used to present the spatiotemporal evolution of $PM_{2.5}$ in northern China. The time series analysis of the pollutants (**Figure 2**) is based on the average of data collected from the six stations.

Data on hourly horizontal visibility, temperature, WS, WD, pressure, and RH at the surface was obtained from the Tianjin meteorological station (No. 54527, 39.0819°N, 117.0533°E; 3.3 m above sea level). This information is stored in the database of the National Meteorological Information Centre of the China Meteorological Administration (http://data.cma.cn/site/index.html).

Using TrajStat software (http://www.meteothink.org/products/trajstat.html), 72-h back trajectories corresponding to

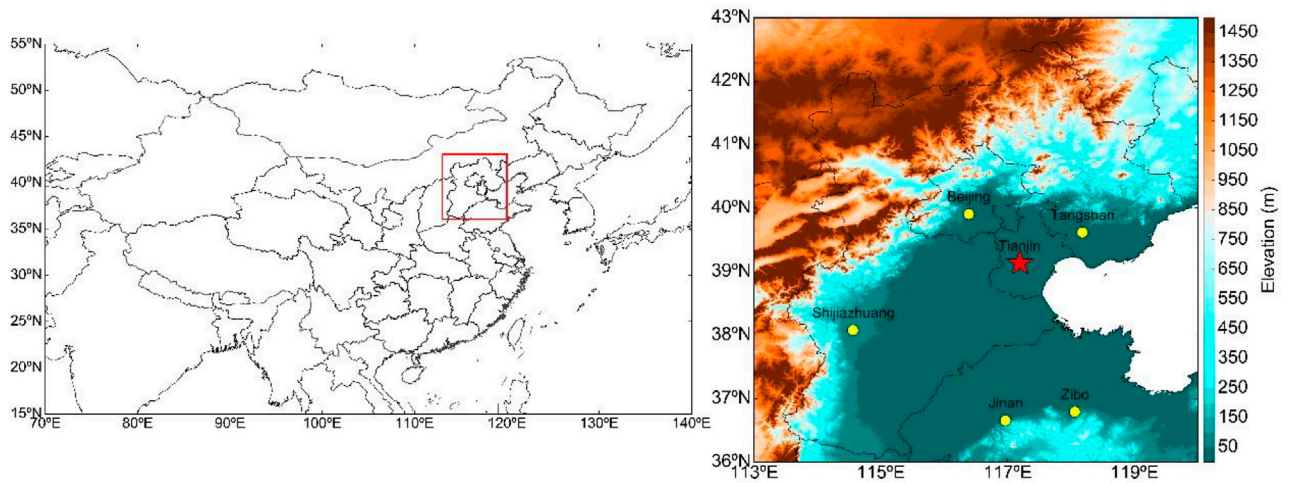

FIGURE 1 | Study site and its surrounding area in the NCP; the red star represents Tianjin.

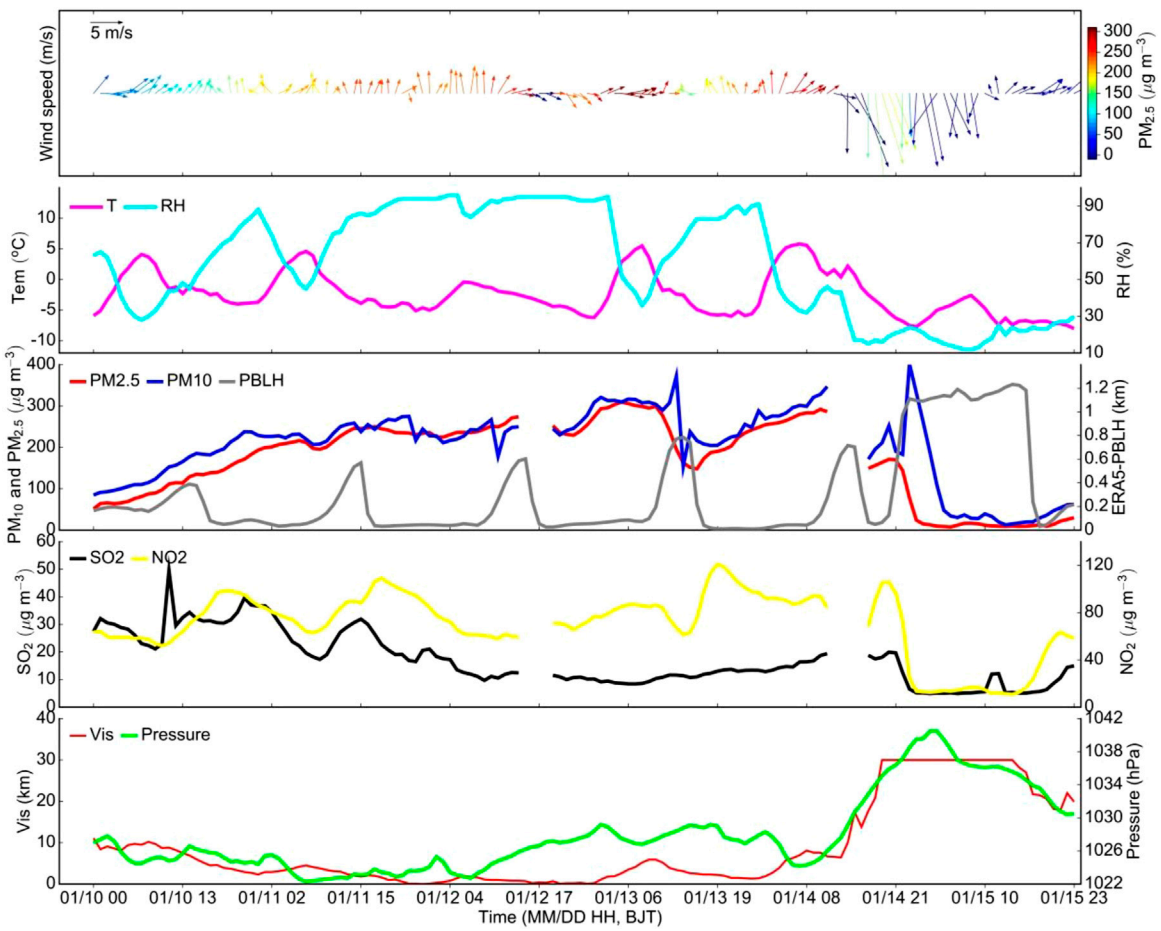

FIGURE 2 | Time series variations in visibility, PM, gaseous pollutants, PBL height, and meteorology parameters from 10 to 15 January 2019 in Tianjin.

the period from 11 to 14 January 2019 (with 6-h intervals) were calculated and clustered by a starting height of 500 m. Two weight function models, namely the WPSCF and WCWT, were used to investigate the spatial distribution of potential $PM_{2.5}$ sources for prevailing transport trajectories (Wang et al., 2006; Wang et al., 2009).

Potential source contribution function (PSCF) and concentration weighted trajectory (CWT) analyses of the study area (33.5°N–56.0°N, 85.0°E–117.5°E) were performed. A horizontal resolution grid of 0.5° × 0.5° was applied. To calculate the WPSCF and WCWT, global data assimilation system data with a resolution of 1° × 1° were used.

PSCF was analysed to calculate the probability that a source at latitude *i* and longitude *j*. The endpoints of the trajectory segment in each cell were obtained according to the results obtained by TrajStat and used to calculate the PSCF value of the grid cell. The following equation was employed:

$$\mathrm{PSCF_{ij}} = m_{ij}/n_{ij} \tag{1}$$

where n_{ij} is the total number of endpoints present in a cell (*i, j*) and m_{ij} is the number of sources with concentrations higher than the threshold criterion when trajectories pass through the cell (*i,j*). According to China's national ambient air quality standard (GB3095-2012: http://kjs.mep.gov.cn/hjbhbz/bzwb/dqhjbh/dqhjzlbz/201203/t20120302_224165.htm), the criterion value of a $PM_{2.5}$ source was set to 75 μg m^{-3}.

The weight function W_{ij} was multiplied by the PSCF value to reduce the effect of the smaller n_{ij}. The equation used was as follows:

$$\mathrm{WPSCF} = W_{ij} \times \mathrm{PSCF} \tag{2}$$

$$W_{ij} = \begin{cases} 1.00, & 3 < n_{ij} \\ 0.70, & 2 < n_{ij} \le 3 \\ 0.42, & 1 < n_{ij} \le 2 \\ 0.17, & n_{ij} \le 1 \end{cases} \tag{3}$$

The CWT analysis was performed to localize the major sources of $PM_{2.5}$. The C_{ij} value was multiplied by the same weight function W_{ij} as the PSCF to minimize the uncertainty of the CWT value.

The equation used was as follows:

$$C_{ij} = \frac{\sum_{k=1}^{M} C_k \times \tau_{ijk}}{\sum_{i=k}^{M} \tau_{ijk}} \times \mathrm{W}(i, j) \tag{4}$$

where C_{ij} is the weighted average concentration in a grid cell (*i, j*), C_k is the measured concentration at the sampling site during the residence time *k*, and τ_{ijk} is the residence time of the back trajectories corresponding to *k* in a grid cell (*i, j*).

To analyse variations in weather conditions during pollution episodes, two-dimensional data (horizontal 10-m wind field [WF]) and planetary boundary layer [PBL] height) and three-dimensional data (vertical WF, vertical RH, and vertical temperature) were obtained from the European Centre for Medium-Range Weather Forecasts Reanalysis v5 (ERA5), data from which have a resolution of 0.25 ° × 0.25 °. The time–height distributions of RH, temperature, and WF for Tianjin (**Figure 3**) were obtained by interpolating the three-dimensional meteorological data in the ERA5 to those collected by the station.

To examine regional aerosol extinction during the pollution episode, the spatial distributions of total aerosol optical depth (AOD) and different types of AOD (SO4AOD, DUAOD, OMAOD, BCAOD, and SSAOD), as well as the mixing ratios of sulphate aerosol, dust aerosol, organic matter aerosol, black carbon aerosol, and sea salt aerosol, were obtained from the Copernicus Atmosphere Monitoring Service Reanalysis (https://ads.atmosphere.copernicus.eu/cdsapp#!/dataset/cams-global-reanalysis-eac4?tab=overview) (Inness et al., 2019). The data have a resolution of 0.75° × 0.75°.

RESULTS AND DISCUSSION

Temporal Variations in Visibility, PM, and Gaseous Pollutants

Temporal variations in visibility, $PM_{2.5}$, PM_{10}, and gaseous pollutant concentrations during a severe pollution episode that occurred from 10 to 15 January 2019 in Tianjin are presented in **Figure 2**.

During this pollution event, visibility deteriorated significantly, dropping below 5 km and lasting for approximately 96 h. In the early stage of the pollution episode, visibility was approximately 10 km at 0000 China Standard Time (CST) on 10 January; subsequently, visibility continued to decline, falling to under 5 km on 11 January. Notably, on 12 January, with the intensification of pollution, visibility was <1 km and accompanied by poor air quality. At 1700 CST on 14 January, air quality improved and visibility significantly increased to approximately 30 km until 15 January at the end of the pollution.

At the start of the pollution event, on 10 January, the $PM_{2.5}$ concentration was approximately 50 μg/m^3. With the further evolution of pollution, the $PM_{2.5}$ concentration increased to approximately 200 μg/m^3 at 0000 CST on 11 January, reaching approximately 250 μg/m^3 on 12 January. On 13 January, with the continuous accumulation of pollutants, the $PM_{2.5}$ concentration increased to 300 μg/m^3. From night-time on 14 January to early morning on 15 January, the $PM_{2.5}$ concentration decreased substantially to approximately 20 μg/m^3. Compared with the influence of fine mode particles, the significant increase of PM_{10} mass concentration also reflects the important contribution of coarse particles to aerosol pollution in Tianjin. With the further exacerbation in pollution, the PM_{10} mass concentration increased to approximately 250 μg/m^3 at 0000 CST on 11 January, reaching approximately 300 μg/m^3 on 12 January. The PM_{10} mass concentration remained at the maximum of approximately 400 μg/m^3 on 13 and 14 January. This result reveals the strong effect of the substantial increase in coarse particle emission sources on air quality in Tianjin during this period. This phenomenon corresponded to the dust contribution, which will be discussed in Section 3.5. On 15 January, after the end of the pollution event, the PM_{10} concentration significantly decreased to approximately 20 μg/m^3.

Variations in the concentrations of SO_2 and NO_2, during the pollution event are displayed in **Figure 2**. In contrast to changes

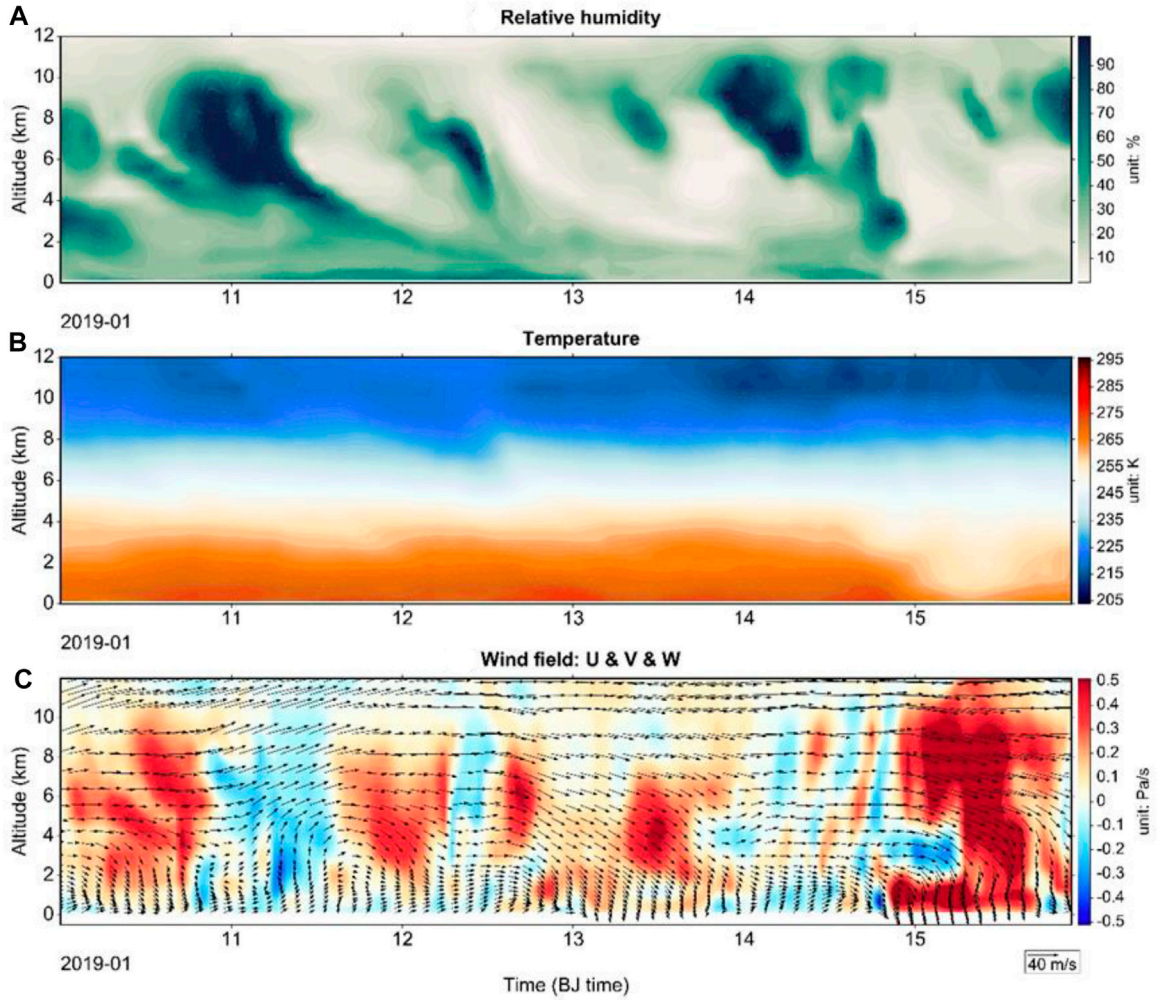

FIGURE 3 | Time–height distribution of **(A)** RH, **(B)** temperature, and **(C)** WF from 10 to 15 January 2019 in Tianjin.

in the PM mass concentration (which significantly increased during the pollution event), the SO_2 concentration exhibited a declining trend. The highest concentration of SO_2 (~30 μg/m^3) was observed in the early stage of pollution on 10 January. With the further evolution of pollution, the SO_2 concentration gradually decreased to approximately 20 μg/m^3 on 11 January. When visibility was less than 5 km on 12 and 13 January, the SO_2 concentration was at its lowest point of approximately 10 μg/m^3. With the increase in visibility and improvement in air quality, the maximum SO_2 concentration increased to approximately 20 μg/m^3 on 14 January. On 15 January, air quality improved further, and the SO_2 concentration remained low at <10 μg/m^3 as the pollutants diffused. The variation in the SO_2 concentration during the pollution event indicated the contribution of SO_2 to the transformation and generation of sulphate aerosol. The accumulation of sulphate aerosols was one of the main factors affecting the formation and transformation of pollutants and is discussed in Section 3.5. Therefore, the effects of the emission and concentration of SO_2 on air quality during air pollution should be investigated.

In contrast to the low SO_2 concentration observed during the pollution event, the NO_2 concentration remained at a certain level. The average NO_2 concentration was approximately 30 μg/m^3 from 10 to 14 January. The maximum daily NO_2 concentration was observed in the evening, between 1900 and 2100 CST. During this period, motor vehicle emissions increased substantially, and the NO_2 concentration increased to 40–50 μg/m^3. On 15 January, the NO_2 concentration dropped below 10 μg/m^3. This finding indicates that the NO_2 concentration was related to fossil fuel emissions from traffic sources (Dai et al., 2021). The results demonstrate that the main emission sources of gaseous pollutants in the NCP, including the energy, industry, transportation, residential, and port sectors, could contribute to specific aerosol concentrations in pollution events and affect air quality. NO_2 from vehicle exhaust and

SO_2 from fuel combustion can lead to an increase in the $PM_{2.5}$ concentration through precursor conversion.

Temporal Variations in Surface and Vertical Meteorological Parameters

Temporal variations in WS, temperature, RH, pressure, and PBL height during the study period (**Figure 2**) were evaluated to investigate the effects of meteorological conditions on air quality.

The $PM_{2.5}$ mass concentration increased to 200–250 μg/m^3 in the early morning of 11 and 12 January, and the average WS decreased to 1–2 m/s. Subsequently, the southwest airflow strengthened, and the pollutant concentration increased. The $PM_{2.5}$ mass concentration increased to approximately 300 μg/m^3 from the afternoon of 13 January to the morning of 14 January. On 14 and 15 January, the airflow from the northwestern and northeastern directions increased significantly, and the hourly WS was 8–10 m/s, contributing to aerosol dispersion and improved air quality. When pollution was at its most severe on 11 and 12 January, with the continuous deterioration of visibility, RH increased to approximately 90%. At the end of the pollution event, RH decreased to 30%–40%. The results reveal that the hygroscopic growth of aerosols under high RH significantly reduced visibility over the pollution episode. Temperatures increased as the pollution worsened; they were significantly higher on 13 January than on 12 January, with the highest temperature being 5°C. With the gradual reduction in the pollutant concentration, the average temperature began a reduction to approximately 0°C. The atmospheric boundary layer exhibited a significant diurnal fluctuation during the pollution process. With the further exacerbation of pollution, the nighttime and daytime height of the boundary layer was <0.1 km and approximately 0.7 km, respectively. On 15 January, with further improvements in visibility and air quality, the height of the boundary layer increased to 1.0–1.2 km. With the reduction in visibility, air pressure decreased to 1,022 hPa at 0800 CST on 11 January. At the end of the episode, air pressure increased to 1,042 hPa. These results indicate a positive correlation between visibility and air pressure. The low atmospheric pressure condition inhibited the upward dispersion of pollutants, leading to the accumulation of atmospheric pollutants near the surface, thus resulting in poor visibility.

We analysed vertical variations in meteorological parameters, namely RH, temperature, WS, and WD, at different heights during the pollution event (**Figure 3**). During the severe pollution period from 11 to 12 January, near-surface RH increased to approximately 50%–60%. With the further evolution of pollution, near-surface RH ranged between 70% and 80% on 13 January, and upper-atmosphere RH was close to 90%. At the end of the pollution event, on 14 January, near-surface RH decreased to approximately 20%, whereas near-surface RH was approximately 90% and distributed over approximate altitudes of 8–10 km. These results indicate that the pollution event was affected by the vertical distribution of RH. RH is a key factor that facilitates the transformation of SO_2 and NO_2 into sulphate and nitrate aerosols, respectively, through chemical reactions (Khoder 2002; Su et al., 2011). The temperature at an altitude of approximately 3 km was approximately 265 K from 9 to 13 January. On 14 January, the temperature dropped significantly to 255 K. The variation in the temperature distribution during the pollution period indicated that the combination of high temperature and RH is beneficial to the formation of secondary aerosols that exacerbate the level of aerosol pollution. The distribution of WF at different heights during the pollution process demonstrated that WS was low near the surface and that this altitude (0–2 km) was dominated by westerly airflow. With the evolution of pollution, airflow in the upper atmosphere exhibited a downward movement (~0.3 Pa/s), and airflow near the surface presented a weak downdraft of approximately 0.2 Pa/s on 11 January. As pollutant accumulation intensified on 12 January, a descending airflow was observed near the surface, with a positive rate of 0.3–0.4 Pa/s. In particular, a strong downdraft (0.5 Pa/s) appeared at an altitude of 2–6 km in the upper atmosphere. Pollutants were transported to the ground with the downdraft; this phenomenon increased the local pollutant concentration. On 13 January, the near-surface and upper-atmosphere flows were stable at approximately 0 Pa/s, leading to the accumulation of pollutants. At the end of the pollution event, the rapidly sinking northwest airflow, the speed of which was approximately 0.5 Pa/s, facilitated pollutant dispersion.

Spatial Distribution of Daily Averages of $PM_{2.5}$, WF, and PBL

Figure 4 depicts the spatial distribution of daily averages of $PM_{2.5}$ and WF as well as PBL.

On 10 January, the $PM_{2.5}$ mass concentration in Tianjin was approximately 100 μg/m^3. The highest concentration of $PM_{2.5}$ (approximately 190 μg/m^3) was observed in the southwest of Tianjin in Hebei Province. At that time, a southwest airflow, the speed of which was approximately 2.0 m/s, facilitated to the transport of pollutants to Tianjin. On 11 January, the spatial distribution of air pollutants in Tianjin and the southwest region intensified, and the $PM_{2.5}$ concentration in Tianjin and its surrounding areas increased to 200 μg/m^3. Moreover, the WF at 10 m, which was 1.0 m/s, was conducive to the initial accumulation of pollutants in Tianjin. During the severe pollution period on 12 January, the WF at 10 m indicated that the prevailing southwest airflow (3.0–4.0 m/s) transported various pollutants from Hebei Province to the NCP. Under the effect of the westerly airflow, a pollution belt characterised by the southwest–northeast transport of aerosols was formed. The centre of the high $PM_{2.5}$ mass concentration (approximately 300 μg/m^3) was observed in Baoding, Hebei Province. The daily average of the $PM_{2.5}$ concentration in Tianjin was approximately 250 μg/m^3 at that time. With an increase in westerly WS (~2 m/s), pollutants were transported to the eastern coast. The daily average of the $PM_{2.5}$ mass concentration in Tianjin remained high at nearly 200 μg/m^3 on 13 January. On 14 January, with the gradual strengthening of the northwest wind (4–5 m/s), pollution continued to spread to eastern China. At that time, the daily average of the $PM_{2.5}$ concentration in Tianjin was relatively low (approximately 190 μg/m^3). Under the control of a strong

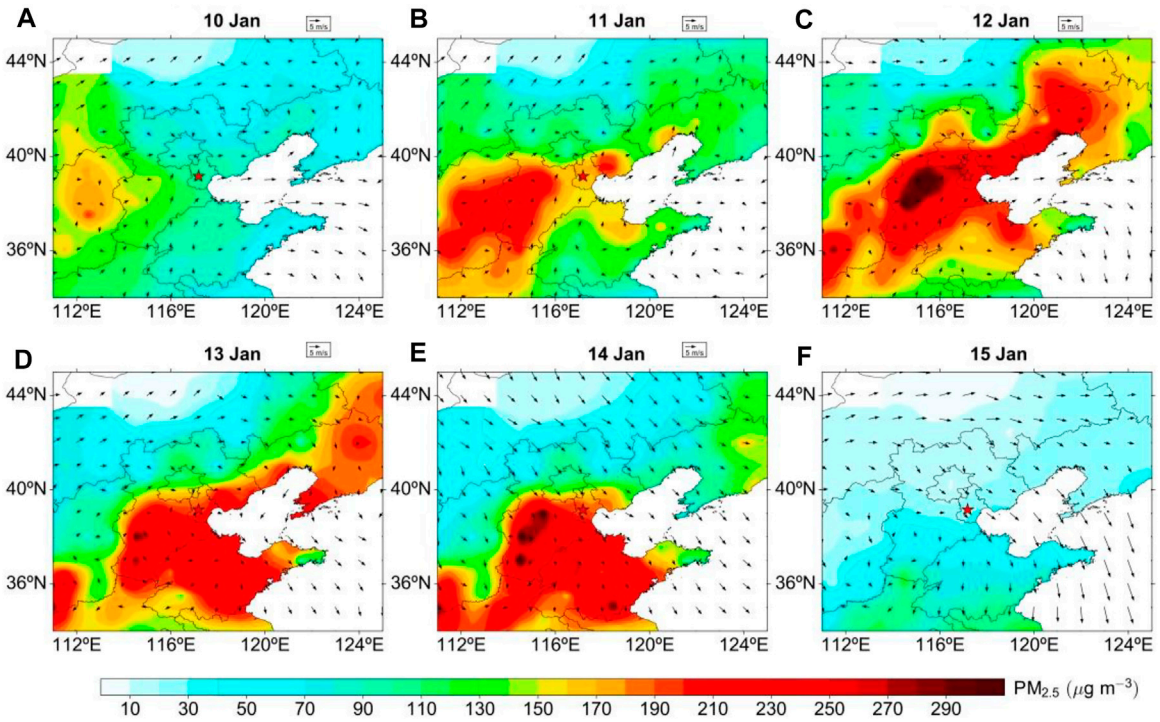

FIGURE 4 | Spatial distribution of daily $PM_{2.5}$ mass concentration and WF at 10 m from 10 to 15 January 2019 in Tianjin shown in **(A–F)**.

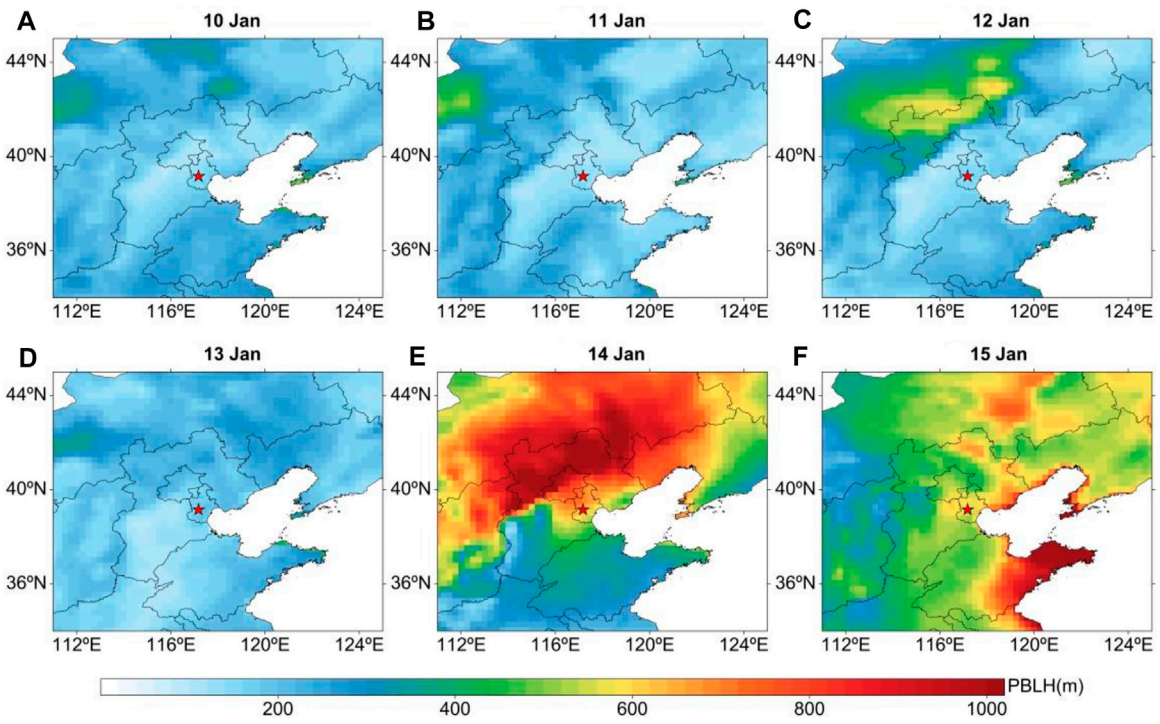

FIGURE 5 | Spatial distribution of daily PBL height from 10 to 15 January 2019 in Tianjin shown in **(A–F)**.

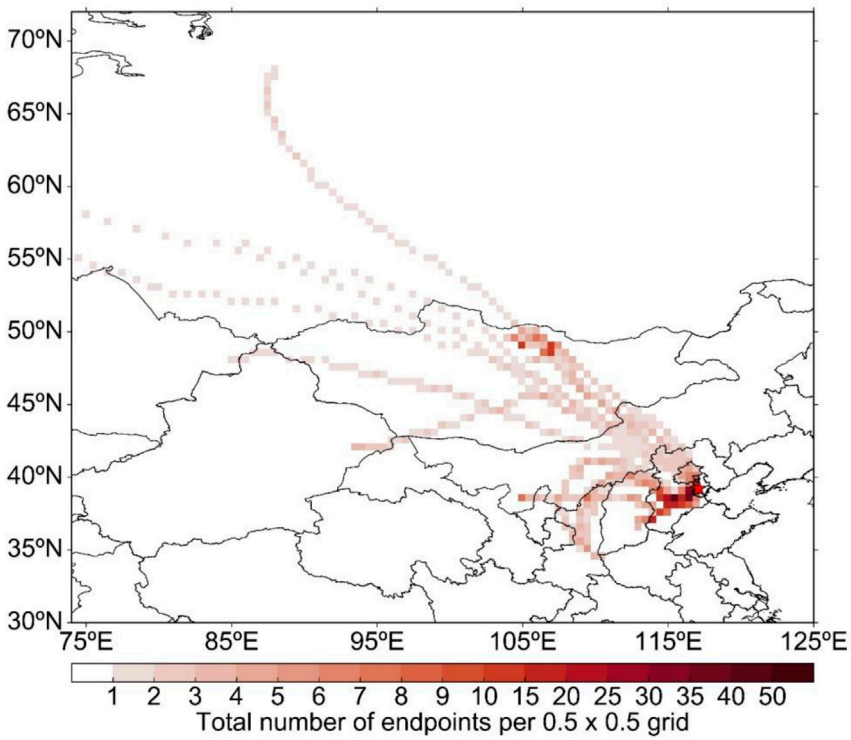

FIGURE 6 | Back trajectories for a 72-h period from 10 to 15 January 2019 in Tianjin, expressed as the total number of trajectory endpoints in each 0.5 × 0.5 grid box.

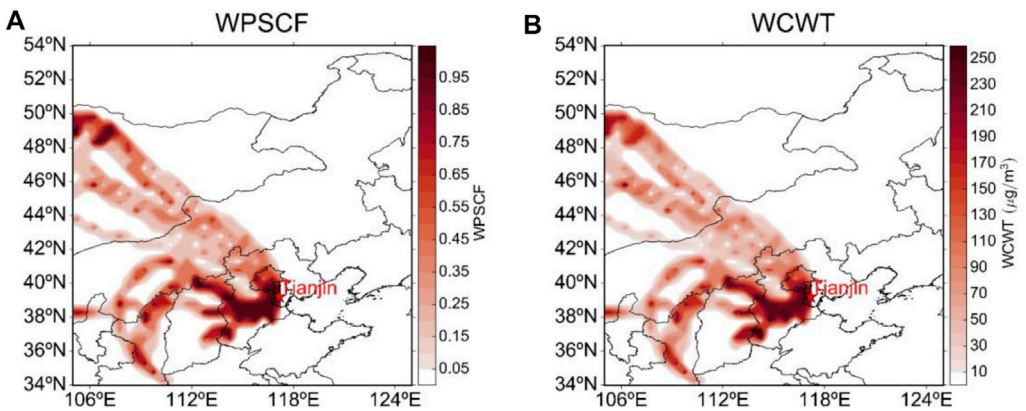

FIGURE 7 | $PM_{2.5}$ data obtained using the **(A)** WPSCF and **(B)** WCWT model for 10 to 15 January 2019 in Tianjin.

northwest airflow (4–5 m/s), pollutants were dispersed from Tianjin on 15 January. The daily average of the $PM_{2.5}$ concentration in Tianjin decreased to 30–50 μg/m^3. These results indicate that the WF plays a crucial role in the transport and dispersion of pollutants, including the spatial distribution of $PM_{2.5}$.

Considering the effect of the variation in the atmospheric boundary layer on air pollution, we examined the spatial variation in PBL during the pollution event.

As shown in **Figure 5**, the daily PBL height was approximately 200 m from 10 to 13 January. On 14 January, under the effect of the northwest airflow, the height of the atmospheric boundary layer in Tianjin significantly increased in the northwest direction, peaking at approximately 1,000 m. The average daily height of PBL in Tianjin increased to approximately 600 m on 14 January; this phenomenon was conducive to the dispersion of pollutants. Subsequently, the height of the boundary layer over the study area, centred in Tianjin, increased to approximately 600 m on 15 January.

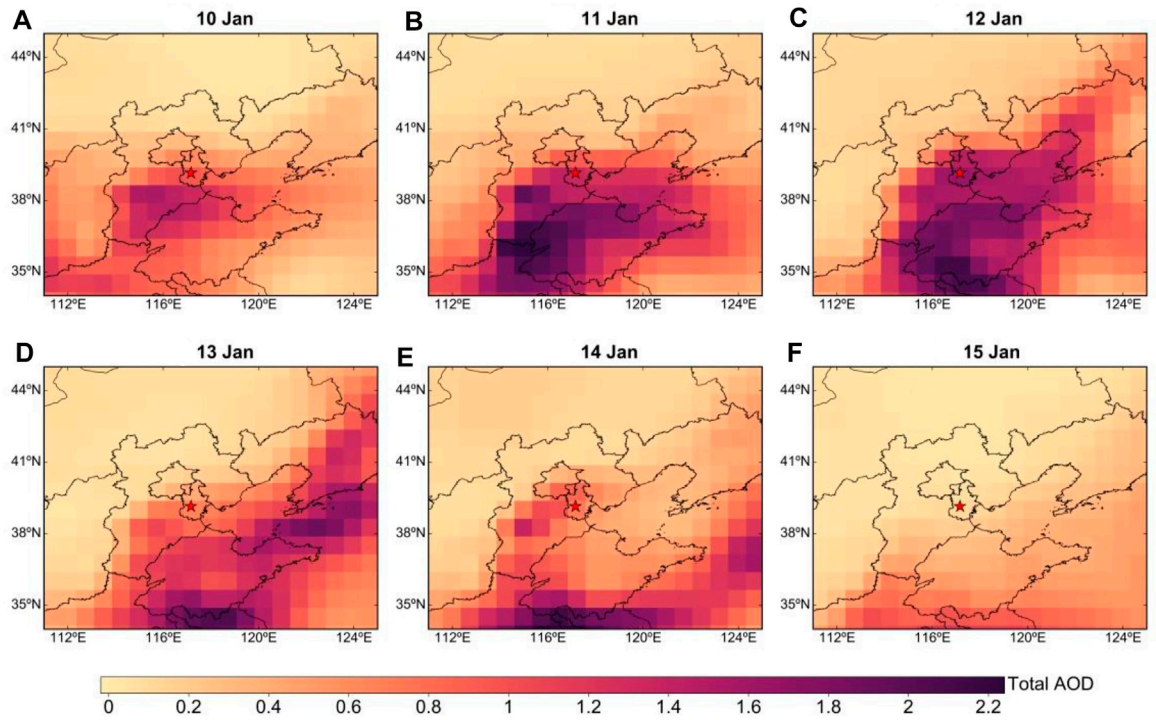

FIGURE 8 | Spatial distribution of daily AOD from 10 to 15 January 2019 in Tianjin shown in **(A–F)**.

We used 72-h back trajectories to investigate main potential sources during the pollution event. Moreover, the WPSCF and WCWT models were used to quantitatively analyse the local and regional contributions of pollutants (**Figure 6** and **Figure 7**).

The trajectories of air pollutants in Tianjin on 11 to 14 January were analysed. The major trajectories mainly originated from two directions during the pollution process. One was the northwest direction, with a long, fast-moving transport pattern at a high altitude of 3–4 km; the other was the southwest direction, with a short, slow-moving transport pattern at a low altitude of <400 m. The WPSCF value of >0.9 indicated that the most likely source areas for $PM_{2.5}$ pollution were Hebei Province, southwest of Tianjin, and most of the Shijiazhuang–Baoding area. A WCWT concentration of >200 μg/m^3 was observed in the southwest of Tianjin, indicating that Hebei Province was the main source region for $PM_{2.5}$ pollution in Tianjin during this pollution event.

Spatial Distribution of Daily AOD and AOD by Aerosol Type

The spatial distributions of total AOD and AOD by the aerosol type in the NCP during the pollution event are shown in **Figure 8** and **Figure 9**. The characteristics of aerosol extinction during the pollution event varied significantly.

On 10 January, the total AOD in Tianjin was 0.6–0.8, which is lower than that in the southwest region (~1.2). This result indicated that the main source of pollution in Tianjin was Hebei Province, which located in the southwest. On 11 January, the total AOD in Tianjin increased to exceed 1.0, and as aerosol extinction spread from the surrounding areas of Hebei Province to the Shandong Peninsula, the AOD increased to 2.0. With the further exacerbation of pollution, aerosol extinction significantly increased in Tianjin, and the AOD increased to approximately 1.5 on 12 January. At that time, the pollution zone expanded to the eastern coastal area, and the AOD exceeded 2.0. With the further evolution of pollution, aerosol extinction in Tianjin weakened, and the total AOD dropped below 0.5 on 13 January. The relatively high near-surface PM concentration of approximately 300 μg/m^3 indicated that aerosol pollution exerted a stronger effect at ground level. At that time, the total AOD in Hebei Province decreased to approximately 1.0, and severe pollution, as reflected by an AOD of >2.0, was observed in eastern China. With the eastward transport of pollutants, the AOD in Hebei Province, the source of pollution in the southwest of Tianjin, decreased to approximately 0.8 on 14 January.

We further discuss the contribution of different types of aerosols to aerosol extinction during the pollution event (**Figure 9**). On 10 January, the spatial distribution of SO4AOD in Tianjin was approximately 0.2, and the SO4AOD in the pollution source area in the southwest was approximately 0.5. On 11 January, the SO4AOD in Tianjin increased to approximately 0.5, and aerosol extinction in the surrounding area of Shijiazhuang, Hebei Province increased to 0.8. As pollution worsened, aerosol extinction increased significantly in Tianjin, and SO4AOD increased to approximately 0.6 on 12 January. On the same day, SO4AOD was high—more than 0.8—in the entire southwest–northeast line and the Bohai Sea. Sulphate aerosols are mainly emitted through anthropogenic

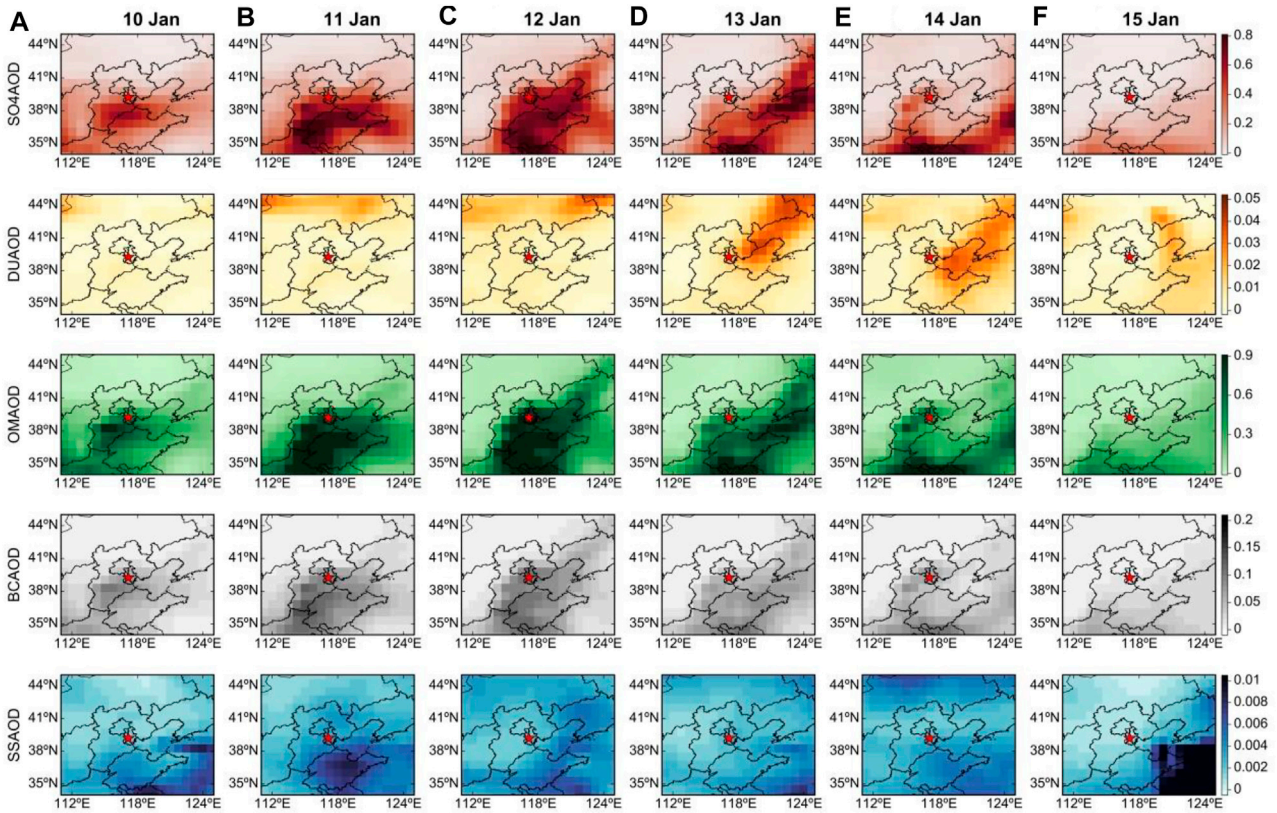

FIGURE 9 | Spatial distribution of daily AOD by aerosol type from 10 to 15 January 2019 in Tianjin shown in **(A–F)**.

activities conducted near ground level (Dai et al., 2021). Thus, the extinction of sulphate aerosols in the entire column decreased, whereas the near-surface PM concentration remained high. The SO4AOD distribution was higher on the east coast and in northeast plains. In the heavily polluted area, it was approximately 0.7. The distribution of SO4AOD (<0.1) was larger in the southwest of Tianjin. These results reveal the considerable effect of sulphate aerosol transport on the spatial distribution of aerosol extinction. According to the spatial distribution of DUAOD, dust particles from the northeast areas of Tianjin were found on 13 and 14 January. The effect of DUAOD on aerosol extinction was approximately 0.04 observed on 13 January, and the dust pollution zone spread to the east on 14 January. Changes in OMAOD showed a similar variation and spatial distribution as did SO4AOD during the pollution event. On 10 January, the highest OMAOD was approximately 0.3 in Tianjin. A higher OMAOD (~0.6) was observed in the southwest area of Tianjin during that period. On 11 January, OMAOD in Tianjin and the surrounding regions increased substantially to 0.9 with increased aerosol extinction. As pollution worsened, OMAOD remained constant at 0.9 on 12 January in Tianjin. On the same day, high OMAOD was noted in the entire BTH region, eastern coastal areas, and the Bohai Sea, with an OMAOD of >0.9. Because coal burning, vehicle exhaust, and biomass combustion are the main emission sources of OC, pollutants were concentrated near ground level, resulting in a high PM concentration (Pang et al., 2020); however, the extinction of organic carbon aerosols in the entire column was weakened. This phenomenon indicated the significant contribution of organic aerosols to the extinction of organic aerosols in the NCP that was related to the emission source. During the early stage of pollution, on 10 January, the highest in Tianjin in BCAOD (~0.05) was observed. The maximum BCAOD (~0.07) was detected in the surrounding regions in the southwest. On 11 January, the BCAOD in Tianjin increased to approximately 0.07, and aerosol extinction in the surrounding areas of Hebei Province increased to 0.1. With the further evolution of pollution, aerosol extinction in Tianjin significantly increased, and the BCAOD reached approximately 0.1 on 12 January. At that time, high BCAOD (>0.1) was observed in the entire southwest–northeast line and the Bohai Sea. This observation indicates the contribution of black carbon aerosols to atmosphere extinction in the column. Moreover, the contribution of SSAOD to aerosol extinction in Tianjin during the pollution process was nonsignificant, and the SSAOD remained at approximately 0.002.

Time–Height Evolution of Different Types of Aerosols

Figure 10 displays the time–height vertical structural evolution of different types of aerosols during the pollution episode.

At 1200 CST on 10 January 2019, sulphate aerosols were distributed near the surface at an altitude of 1.0 km, and the mixing ratio of sulphate aerosols near the surface was

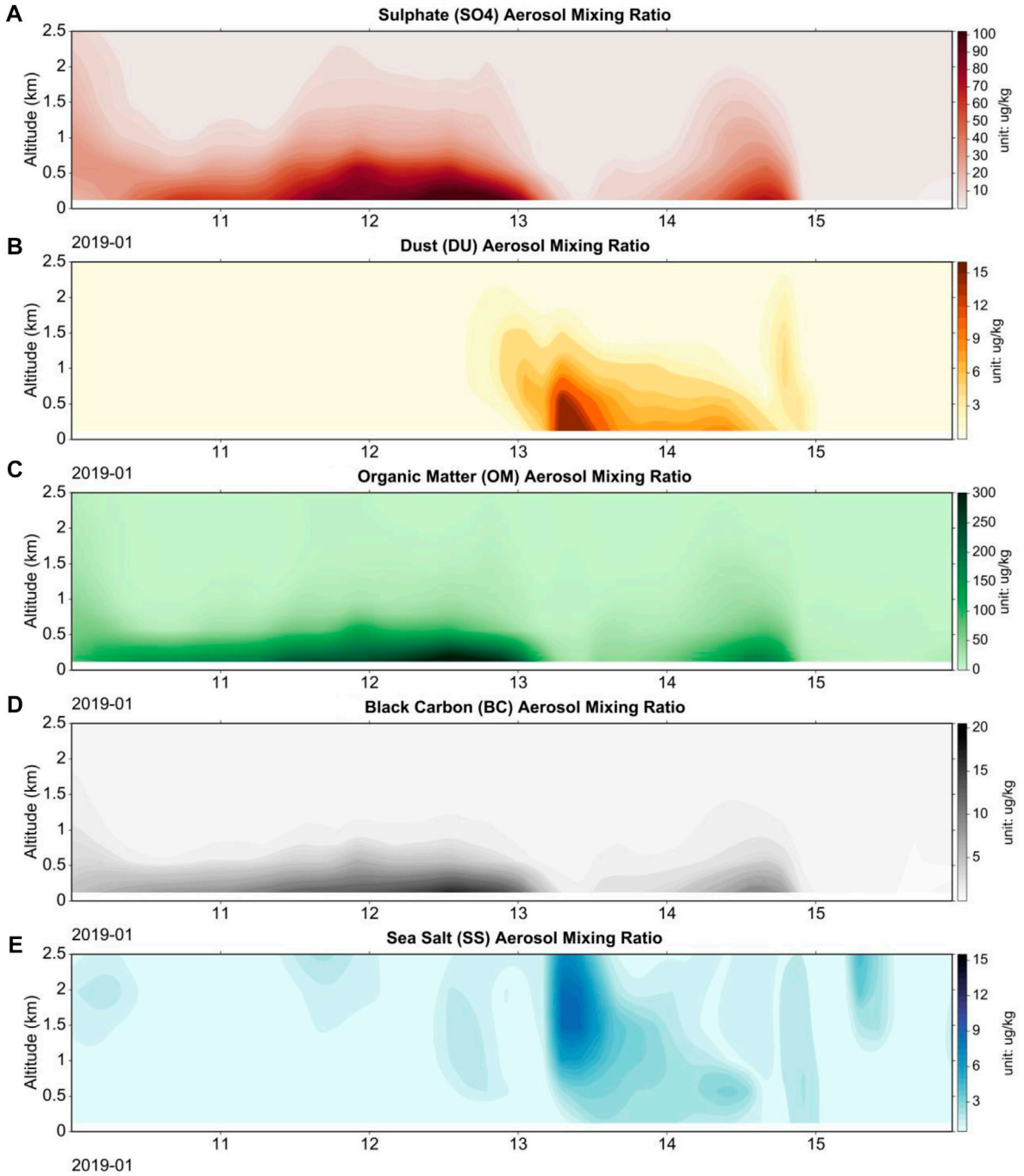

FIGURE 10 | Time–height distribution of mixing ratios by aerosol type **(A)** SO4, **(B)** DU, **(C)** OM, **(D)** BC, and **(E)** SS from 10 to 15 January 2019 in Tianjin.

40–50 μg/kg. On 11 January, the proportion of near-surface sulphate aerosols gradually increased, and the mixing ratio of sulphate aerosols within an altitude of 1.0 km significantly increased to 80–90 μg/kg. The distribution of sulphate aerosols gradually increased, and sulphate aerosol layers of different concentrations appeared at an altitude of 1–2 km, with a mixing ratio of 10–20 μg/kg. On 12 January, pollution continued to intensify, and the mixing ratio of near-surface sulphate aerosols remained high. The mixing ratio of sulphate aerosols within an altitude of 0.5 km was >90 μg/kg. As pollution evolved from 13 to 14 January, the mixing ratio and distribution of sulphate aerosols decreased both near the surface and at high altitudes, and the mixing ratio of sulphate aerosols decreased to 50–60 μg/kg within an altitude of 1 km near the surface. The variation in the mixing ratios of sulphate aerosols in the pollution event indicated the conversion of SO_2 to sulphate aerosols under

high RH, reflecting a crucial relationship with the variation in RH near the surface and at high altitudes. This finding was confirmed by the SO_2 emissions mentioned in Section 3.1.

Beginning on 13 January, dust aerosols were distributed from near the surface to an altitude of approximately 1.5 km. The mixing ratio of dust aerosols within 500 m near the surface was approximately 15 μg/kg, and the mixing ratio of dust aerosols at an altitude of 1.0–1.5 km was lower, at 3–6 μg/kg. Beginning on 14 January, with the reduction in dust aerosol pollution, the effect of dust aerosols gradually decreased within an altitude of 1 km, and the mixing ratio of dust aerosols near the surface decreased to 7–8 μg/kg within an altitude of 0.5 km. The presence of dust aerosols observed over the pollution event was consistent with the increase in PM_{10} emissions discussed in Section 3.1.

During the pollution event, organic aerosols had a high mixing ratio near the surface below an altitude of 0.5 km. The mixing ratio of organic aerosols on 10 January was approximately 100 μg/kg. With the evolution in pollution, the mixing ratio of organic aerosols near the surface gradually increased to 150–200 μg/kg on 11 January. With the intensification of pollution, the mixing ratio of near-surface organic aerosols reached a maximum of 250–300 μg/kg on 12 January. Furthermore, with the dispersion of pollution, the mixing ratio of organic aerosols decreased to approximately 150 μg/kg on 13 and 14 January. At the end of the pollution event on 15 January, organic aerosols disappeared. The vertical distribution of the mixing ratio of organic aerosols indicated that organic aerosols were mainly concentrated near the surface; this differed from the distribution of sulphate and dust aerosols in the upper atmosphere during the pollution event.

During the pollution episode, black carbon aerosols had a high mixing ratio near the surface below an altitude of 0.5 km. In the initial stage of pollution on 10 January, the mixing ratio of black carbon aerosols was approximately 5 μg/kg. With the further evolution of pollution, the mixing ratio of near-surface black carbon aerosols increased to 10–15 μg/kg on 11 January. As pollution continued to worsen, the mixing ratio of near-surface black carbon aerosols increased to 20 μg/kg on 12 January. With the dispersion of pollution, the mixing ratio of black carbon aerosols decreased to 10 μg/kg on 14 January. On 15 January, the black carbon aerosols had disappeared. The distribution of black carbon aerosols indicated that the effect of black carbon aerosols was mainly concentrated near the surface; this phenomenon is similar to that of organic carbon aerosols but different from the vertical distribution of sulphate and dust aerosols.

Because Tianjin is a coastal city, sea salt aerosols can cause a certain degree of air pollution. As shown in **Figure 10**, although the mixing ratio of sea salt aerosols was lower than that of other types of aerosols, it still was observed at an altitude of 1.0–2.5 km on 13 January. Combined with the time–height evolution of RH presented in **Figure 3**, the higher RH at a high altitude on 13 January was conducive to the hygroscopic growth of sea salt aerosols. With the vertical reduction in RH, the mixing ratio of sea salt aerosols decreased gradually. Because of the transport of water vapour in the atmosphere, sea salt aerosols were mainly distributed in the upper atmosphere and were strongly correlated with RH.

DISCUSSIONS AND CONCLUSION

With rapid economy development and massive anthropogenic emission, severe urban $PM_{2.5}$ pollution have occurred frequently in major cities over the BTH region and its surroundings in China. Some studies analyzed the variations of $PM_{2.5}$ and gaseous precursors and their chemical composition through *in situ* real-time comprehensive observation from measurement campaigns and simultaneously online measurements to examine the impact of meteorological conditions and pollutant emissions on air quality in these regions before and after the strictly controlled emissions. Dai et al. (2021) pointed out that SO_2 and NO_2 generated from vehicle emission and residential coal burning could be two major additional sources of environmental sulfate and nitrate during the haze episodes in Tianjin. Zhao et al. (2020) analyzed the long-range transport of dust and its impact on the pollution process that occurred in Tianjin by the westerly flow transported from northwestern China. Pang et al. (2020) investigated that $NO3^-$, $SO4^{2+}$, and $NH4^+$ was the main water-soluble ions contribute to $PM_{2.5}$ pollution in Tianjin during the heating season. Li et al. (2021) presented the important contribution of increased nitrate concentration to $PM_{2.5}$ during wintertime in Tianjin from 2014 to 2018. Shao et al. (2021) shown that nitrate aerosol was the most sensitive component to severe aerosol pollution under typical extremely unfavorable meteorological events in Tianjin.

In this study, an air pollution event in a typical city of the NCP was comprehensively analysed. In view of the core scientific problem of the whole process of the evolution of severe pollution, a comprehensive observation was conducted that overcame the limitation of a single observation data of near-surface stations. In particular, the temporal and spatial evolution of different composition aerosols was tracked. Temporal variations in visibility, PM mass concentration, PBL height, and vertical meteorological parameters as well as the spatial distributions of various types of aerosols and their optical properties were examined to determine aerosol pollution sources and regional transport characteristics during a pollution event from 10 to 15 January 2019 in Tianjin.

During this pollution event, the minimum visibility reached <5 km for approximately 96 h. The accumulative concentration of $PM_{2.5}$ and PM_{10} reached 300 and 400 $\mu g/m^3$, respectively. The variation in SO_2 exhibited a declining trend, indicating the contribution of SO_2 transformation to sulphate aerosols. The concentration of NO_2 remained at approximately 30 $\mu g/m^3$ which was significantly correlated with fossil fuel consumption and contributed to this pollution process.

The southwest airflow and low WS were dominant factors affecting PM accumulation and contributed to low visibility. With the continuous deterioration of visibility, RH increased to approximately 90%, thus aggravating pollution. A low PBL height of <0.1 km was observed during this period. The high RH

in the vertical direction facilitated the chemical transformation of SO_2 and NO_2 into sulphate and nitrate aerosols, respectively.

The prevailing southwest airflow transported various pollutants from Hebei Province to the NCP at a WS of 3.0–4.0 m/s, and the daily PBL height was approximately 200 m. A WPSCF of >0.9 and a WCWT of >200 μg/m^3 indicated that Hebei Province was the main source of $PM_{2.5}$ pollution in Tianjin during the pollution episode.

The total AOD in Tianjin increased to approximately 1.5 during the pollution episode. The effect of sulphate aerosols on the spatial distribution of aerosol extinction increased, with an SO4AOD of approximately 0.6. The extinction of organic aerosols in the NCP was related to the emission source, with the OMAOD remaining at approximately 0.9. The BCAOD increased to approximately 0.1 with the further evolution of pollution.

The mixing ratio of sulphate aerosols within an altitude of 0.5 km was >90 μg/kg. The mixing ratio of dust aerosols within 500 m of the surface was approximately 15 μg/kg. Black carbon and Organic aerosols had a high mixing ratio near the surface, below an altitude of 0.5 km. The mixing ratio of sea salt aerosols was correlated with higher RH and vertically distributed at 1.0–2.5 km.

The findings provide insights into the effect of near-surface pollutants and vertical meteorological parameters on air pollution in the NCP. Aerosol transformation process and transport mechanism in this region can be explored by analysing the contributions of different types of aerosols.

DATA AVAILABILITY STATEMENT

Publicly available datasets were analyzed in this study. This data can be found here: the Copernicus Atmosphere Monitoring Service Reanalysis (https://ads.atmosphere.copernicus.eu/cdsapp#!/dataset/cams-global-reanalysis-eac4?tab=overview).

AUTHOR CONTRIBUTIONS

HZ, HC and XZ contributed to conception and design of the study. KG, YM and YW organized the database. YW, HW and YD performed the statistical analysis. YZ, LL, LZ and YZ wrote sections of the manuscript. All authors contributed to manuscript revision, read, and approved the submitted version.

FUNDING

This work is financially supported by grant from National Natural Science Foundation of China (41875157 and 41825011 and 42030608 and 42175185), Basic Scientific Research Fund of Shenyang Institute of Atmospheric Environment (2021SYIAEZD3).

REFERENCES

Ackerman, T. P., and Toon, O. B. (1981). Absorption of Visible Radiation in Atmosphere Containing Mixtures of Absorbing and Nonabsorbing Particles. *Appl. Opt.* 20, 3661–3668. doi:10.1364/ao.20.003661

Andreae, M. O., and Merlet, P. (2001). Emission of Trace Gases and Aerosols from Biomass Burning. *Glob. Biogeochem. Cycles* 15, 955–966. doi:10.1029/2000gb001382

Bai, Y., Ni, Y., and Zeng, Q. (2021). Impact of Ambient Air Quality Standards Revision on the Exposure-Response of Air Pollution in Tianjin, China. *Environ. Res.* 198, 111269. doi:10.1016/j.envres.2021.111269

Chang, D., Song, Y., and Liu, B. (2009). Visibility Trends in Six Megacities in China 1973-2007. *Atmos. Res.* 94, 161–167. doi:10.1016/j.atmosres.2009.05.006

Chang, X., Wang, S., Zhao, B., Cai, S., and Hao, J. (2018). Assessment of Inter-city Transport of Particulate Matter in the Beijing-Tianjin-Hebei Region. *Atmos. Chem. Phys.* 18, 4843–4858. doi:10.5194/acp-18-4843-2018

Charlson, R. J., Schwartz, S. E., Hales, J. M., Cess, R. D., Coakley, J. A., Jr, Hansen, J. E., et al. (1992). Climate Forcing by Anthropogenic Aerosols. *Science* 255, 423–430. doi:10.1126/science.255.5043.423

Che, H., Xia, X., Zhao, H., Dubovik, O., Holben, B. N., Goloub, P., et al. (2019). Spatial Distribution of Aerosol Microphysical and Optical Properties and Direct Radiative Effect from the China Aerosol Remote Sensing Network. *Atmos. Chem. Phys.* 19, 11843–11864. doi:10.5194/acp-19-11843-2019

Che, H., Xia, X., Zhu, J., Li, Z., Dubovik, O., Holben, B., et al. (2014). Column Aerosol Optical Properties and Aerosol Radiative Forcing during a Serious Haze-Fog Month over north china plain in 2013 Based on Ground-Based Sunphotometer Measurements. *Atmos. Chem. Phys.* 14, 2125–2138. doi:10.5194/acp-14-2125-2014

Che, H., Xia, X., Zhu, J., Wang, H., Wang, Y., Sun, J., et al. (2015). Aerosol Optical Properties under the Condition of Heavy Haze over an Urban Site of Beijing, China. *Environ. Sci. Pollut. Res.* 22, 1043–1053. doi:10.1007/s11356-014-3415-5

Che, H., Zhang, X., Li, Y., Zhou, Z., Qu, J. J., and Hao, X. (2009). Haze Trends over the Capital Cities of 31 Provinces in China, 1981-2005. *Theor. Appl. Climatol.* 97, 235–242. doi:10.1007/s00704-008-0059-8

Che, H., Zhang, X., Li, Y., Zhou, Z., and Qu, J. J. (2007). Horizontal Visibility Trends in China 1981–2005. *Geophys. Res. Lett.* 34, 497–507. doi:10.1029/2007gl031450

Chen, H., Lin, Y., Su, Q., and Cheng, L. (2017). Spatial Variation of Multiple Air Pollutants and Their Potential Contributions to All-Cause, Respiratory, and Cardiovascular Mortality across China in 2015-2016. *Atmos. Environ.* 168, 23–35. doi:10.1016/j.atmosenv.2017.09.006

Chen, Y., Tian, C., Feng, Y., Zhi, G., Li, J., and Zhang, G. (2015). Measurements of Emission Factors of PM2.5, OC, EC, and BC for Household Stoves of Coal Combustion in China. *Atmos. Environ.* 109, 190–196. doi:10.1016/j.atmosenv.2015.03.023

Corbett, J. J., Winebrake, J. J., Green, E. H., Kasibhatla, P., Eyring, V., and Lauer, A. (2007). Mortality from Ship Emissions: a Global Assessment. *Environ. Sci. Technol.* 41, 8512–8518. doi:10.1021/es071686z

Dai, Q., Ding, J., Hou, L., Li, L., Cai, Z., Liu, B., et al. (2021). Haze Episodes before and during the COVID-19 Shutdown in Tianjin, China: Contribution of Fireworks and Residential Burning. *Environ. Pollut.* 286, 117252. doi:10.1016/j.envpol.2021.117252

Dore, A., Vieno, M., Tang, Y., Dragosits, U., Dosio, A., Weston, K., et al. (2007). Modelling the Atmospheric Transport and Deposition of sulphur and Nitrogen over the United Kingdom and Assessment of the Influence of SO2 Emissions from International Shipping. *Atmos. Environ.* 41, 2355–2367. doi:10.1016/j.atmosenv.2006.11.013

Dubovik, O., Holben, B., Eck, T. F., Smirnov, A., Kaufman, Y. J., King, M. D., et al. (2002). Variability of Absorption and Optical Properties of Key Aerosol Types Observed in Worldwide Locations. *J. Atmos. Sci.* 59, 590–608. doi:10.1175/1520-0469(2002)059<0590:voaaop>2.0.co;2

Eck, T. F., Holben, B. N., Dubovik, O., Smirnov, A., Goloub, P., Chen, H. B., et al. (2005). Columnar Aerosol Optical Properties at AERONET Sites in central Eastern Asia and Aerosol Transport to the Tropical Mid-Pacific. *J. Geophys. Res.* 110, D06202. doi:10.1029/2004jd005274

Gao, J. J., Tian, H. Z., Cheng, K., Lu, L., Zheng, M., Wang, S. X., et al. (2015). The Variation of Chemical Characteristics of PM2.5 and PM10 and Formation Causes during Two Haze Pollution Events in Urban Beijing, China. *Atmos. Environ.* 107, 1–8. doi:10.1016/j.atmosenv.2015.02.022

Gui, K., Che, H., Li, L., Zheng, Y., Zhang, L., Zhao, H., et al. (2021a). The Significant Contribution of Small-Sized and Spherical Aerosol Particles to the Decreasing Trend in Total Aerosol Optical Depth over Land from 2003 to 2018. *Engineering*. in press. doi:10.1016/j.eng.2021.05.017

Gui, K., Che, H., Zheng, Y., Zhao, H., Yao, W., Li, L., et al. (2021b). Three-dimensional Climatology, Trends, and Meteorological Drivers of Global and Regional Tropospheric Type-dependent Aerosols: Insights from 13 Years (2007-2019) of CALIOP Observations. *Atmos. Chem. Phys.* 21, 15309–15336. doi:10.5194/acp-21-15309-2021

Han, L., Zhou, W., Li, W., and Li, L. (2014). Impact of Urbanization Level on Urban Air Quality: A Case of fine Particles (PM 2.5) in Chinese Cities. *Environ. Pollut.* 194, 163–170. doi:10.1016/j.envpol.2014.07.022

Han, S., Liu, J., Hao, T., Zhang, Y., Li, P., Yang, J., et al. (2018). Boundary Layer Structure and Scavenging Effect during a Typical winter Haze-Fog Episode in a Core City of BTH Region, China. *Atmos. Environ.* 179, 187–200. doi:10.1016/j.atmosenv.2018.02.023

Han, S., Zhang, Y., Wu, J., Zhang, X., Tian, Y., Wang, Y., et al. (2015). Evaluation of Regional Background Particulate Matter Concentration Based on Vertical Distribution Characteristics. *Atmos. Chem. Phys.* 15, 11165–11177. doi:10.5194/acp-15-11165-2015

Hansen, J., Sato, M., Ruedy, R., Lacis, A., and Oinas, V. (2000). Global Warming in the Twenty-First century: An Alternative Scenario. *Proc. Natl. Acad. Sci.* 97, 9875–9880. doi:10.1073/pnas.170278997

Hansen, J., Sato, M., and Ruedy, R. (1997). Radiative Forcing and Climate Response. *J. Geophys. Res.* 102, 6831–6864. doi:10.1029/96jd03436

Hua, Y., Wang, S., Wang, J., Jiang, J., Zhang, T., Song, Y., et al. (2016). Investigating the Impact of Regional Transport on PM2.5 Formation Using Vertical Observation during APEC 2014 Summit in Beijing. *Atmos. Chem. Phys.* 16, 15451–15460. doi:10.5194/acp-16-15451-2016

Inness, A., Ades, M., Agustí-Panareda, A., Barré, J., Benedictow, A., Blechschmidt, A.-M., et al. (2019). The Cams Reanalysis of Atmospheric Composition. *Atmos. Chem. Phys.* 19, 3515–3556. doi:10.5194/acp-19-3515-2019

Jin, L., Luo, X., Fu, P., and Li, X. (2016). Airborne Particulate Matter Pollution in Urban China: a Chemical Mixture Perspective from Sources to Impacts. *Natl. Sci. Rev.* 4, 593–610. doi:10.1093/nsr/nww079

Khoder, M. I. (2002). Atmospheric Conversion of Sulfur Dioxide to Particulate Sulfate and Nitrogen Dioxide to Particulate Nitrate and Gaseous Nitric Acid in an Urban Area. *Chemosphere* 49, 675–684. doi:10.1016/s0045-6535(02)00391-0

Lang, J., Liang, X., Li, S., Zhou, Y., Chen, D., Zhang, Y., et al. (2021). Understanding the Impact of Vehicular Emissions on Air Pollution from the Perspective of Regional Transport: A Case Study of the Beijing-Tianjin-Hebei Region in China. *Sci. Total Environ.* 785, 147304. doi:10.1016/j.scitotenv.2021.147304

Li, X., Bei, N., Hu, B., Wu, J., Pan, Y., Wen, T., et al. (2021). Mitigating NOX Emissions Does Not Help Alleviate Wintertime Particulate Pollution in Beijing-Tianjin-Hebei, China. *Environ. Pollut.* 279, 116931. doi:10.1016/j.envpol.2021.116931

Miao, Y., Guo, J., Liu, S., Liu, H., Zhang, G., Yan, Y., et al. (2017). Relay Transport of Aerosols to Beijing-Tianjin-Hebei Region by Multi-Scale Atmospheric Circulations. *Atmos. EnvironmentEnviron* 165, 35–45. doi:10.1016/j.atmosenv.2017.06.032

Miao, Y., Liu, S., Zheng, Y., Wang, S., Chen, B., Zheng, H., et al. (2015). Numerical Study of the Effects of Local Atmospheric Circulations on a Pollution Event over Beijing-Tianjin-Hebei, China. *J. Environ. Sci.* 30, 9–20. doi:10.1016/j.jes.2014.08.025

Pang, N., Gao, J., Che, F., Ma, T., Liu, S., Zhao, P., et al. (2020). Cause of PM2.5 Pollution during the 2016-2017 Heating Season in Beijing, Tianjin, and Langfang, China. *J. Environ. Sci.* 95, 201–209. doi:10.1016/j.jes.2020.03.024

Shao, M., Dai, Q., Yu, Z., Zhang, Y., Xie, M., and Feng, Y. (2021). Responses in PM2.5 and its Chemical Components to Typical Unfavorable Meteorological Events in the Suburban Area of Tianjin, China. *Sci. Total Environ.* 788, 147814. doi:10.1016/j.scitotenv.2021.147814

Shen, Y., Zhang, L., Fang, X., Ji, H., Li, X., and Zhao, Z. (2019). Spatiotemporal Patterns of Recent PM2.5 Concentrations over Typical Urban Agglomerations in China. *Sci. Total Environ.* 655, 13–26. doi:10.1016/j.scitotenv.2018.11.105

Su, S., Li, B., Cui, S., and Tao, S. (2011). Sulfur Dioxide Emissions from Combustion in China: from 1990 to 2007. *Environ. Sci. Technol.* 45, 8403–8410. doi:10.1021/es201656f

Sun, Y., Chen, C., Zhang, Y., Xu, W., Zhou, L., Cheng, X., et al. (2016). Rapid Formation and Evolution of an Extreme Haze Episode in Northern China during winter 2015. *Sci. Rep.* 6, 27151. doi:10.1038/srep27151

Twomey, S. A., Piepgrass, M., and Wolfe, T. L. (1984). An Assessment of the Impact of Pollution on Global Cloud Albedo. *Tellus* 36B, 356–366. doi:10.1111/j.1600-0889.1984.tb00254.x

Wang, L. T., Wei, Z., Yang, J., Zhang, Y., Zhang, F. F., Su, J., et al. (2014). The 2013 Severe Haze over Southern Hebei, China: Model Evaluation, Source Apportionment, and Policy Implications. *Atmos. Chem. Phys.* 14, 3151–3173. doi:10.5194/acp-14-3151-2014

Wang, Y. Q., Zhang, X. Y., and Arimoto, R. (2006). The Contribution from Distant Dust Sources to the Atmospheric Particulate Matter Loadings at XiAn, China during spring. *Sci. Total Environ.* 368, 875–883. doi:10.1016/j.scitotenv.2006.03.040

Wang, Y. Q., Zhang, X. Y., and Draxler, R. R. (2009). TrajStat: GIS-Based Software that Uses Various Trajectory Statistical Analysis Methods to Identify Potential Sources from Long-Term Air Pollution Measurement Data. *Environ. Model. Softw.* 24, 938–939. doi:10.1016/j.envsoft.2009.01.004

Wu, H., Zhang, Y.-f., Han, S.-q., Wu, J.-h., Bi, X.-h., Shi, G.-l., et al. (2015). Vertical Characteristics of PM2.5 during the Heating Season in Tianjin, China. *Sci. Total Environ.* 523, 152–160. doi:10.1016/j.scitotenv.2015.03.119

Yang, H.-H., Tsai, C.-H., Chao, M.-R., Su, Y.-L., and Chien, S.-M. (2006). Source Identification and Size Distribution of Atmospheric Polycyclic Aromatic Hydrocarbons during rice Straw Burning Period. *Atmos. Environ.* 40, 1266–1274. doi:10.1016/j.atmosenv.2005.10.032

Yau, P. S., Lee, S. C., Corbett, J. J., Wang, C., Cheng, Y., and Ho, K. F. (2012). Estimation of Exhaust Emission from Ocean-Going Vessels in Hong Kong. *Sci. Total Environ.* 431, 299–306. doi:10.1016/j.scitotenv.2012.03.092

Zhang, Q., Streets, D. G., Carmichael, G. R., He, K. B., Huo, H., Kannari, A., et al. (2009). Asian Emissions in 2006 for the NASA INTEX-B mission. *Atmos. Chem. Phys.* 9, 5131–5153. doi:10.5194/acp-9-5131-2009

Zhang, R., Jing, J., Tao, J., Hsu, S.-C., Wang, G., Cao, J., et al. (2013). Chemical Characterization and Source Apportionment of PM2.5 in Beijing: Seasonal Perspective. *Atmos. Chem. Phys.* 13, 7053–7074. doi:10.5194/acp-13-7053-2013

Zhang, X. Y., Wang, Y. Q., Niu, T., Zhang, X. C., Gong, S. L., Zhang, Y. M., et al. (2012). Atmospheric Aerosol Compositions in China: Spatial/temporal Variability, Chemical Signature, Regional Haze Distribution and Comparisons with Global Aerosols. *Atmos. Chem. Phys.* 12, 779–799. doi:10.5194/acp-12-779-2012

Zhao, H., Wu, Z., Liu, J., and Wu, G. (2019). Two Air Pollution Events in the Coastal City of Tianjin, north China plain. *Atmos. Pollut. Res.* 10, 1780–1794. doi:10.1016/j.apr.2019.07.009

Zhao, L., Wang, W., Hao, T., Qu, W., Sheng, L., Luo, C., et al. (2020). The Autumn Haze-Fog Episode Enhanced by the Transport of Dust Aerosols in the Tianjin Area. *Atmos. Environ.* 237, 117669. doi:10.1016/j.atmosenv.2020.117669

Zheng, S., Pozzer, A., Cao, C. X., and Lelieveld, J. (2015). Long-term (2001-2012) Concentrations of fine Particulate Matter (PM2.5) and the Impact on Human Health in Beijing, China. *Atmos. Chem. Phys.* 15, 5715–5725. doi:10.5194/acp-15-5715-2015

Zou, Q., Cai, X., Guo, M., Song, Y., and Zhang, X. (2018). Long-term Mean Footprint and its Relationship to Heavy Air Pollution Episodes in Beijing. *Acta Sci. Nat. Univ. Pekin.* 54, 341–349. doi:10.13209/j.0479-8023.2017.134

Conflict of Interest: The authors declare that the research was conducted in the absence of any commercial or financial relationships that could be construed as a potential conflict of interest.

Publisher's Note: All claims expressed in this article are solely those of the authors and do not necessarily represent those of their affiliated organizations, or those of the publisher, the editors, and the reviewers. Any product that may be evaluated in this article, or claim that may be made by its manufacturer, is not guaranteed or endorsed by the publisher.

frontiers in Environmental Science

ORIGINAL RESEARCH
published: 09 February 2022
doi: 10.3389/fenvs.2021.816616

Gated Recurrent Unit Coupled with Projection to Model Plane Imputation for the PM2.5 Prediction for Guangzhou City, China

Muhammad Waqas Saif-ul-Allah[1], Muhammad Abdul Qyyum[2], Noaman Ul-Haq[3], Chaudhary Awais Salman[4] and Faisal Ahmed[1]**

[1]Process and Energy Systems Engineering Center-PRESTIGE, Department of Chemical Engineering, COMSATS University Islamabad, Lahore Campus, Lahore, Pakistan, [2]Department of Petroleum and Chemical Engineering, Sultan Qaboos University, Muscat, Oman, [3]Department of Chemical Engineering, COMSATS University Islamabad, Lahore Campus, Lahore, Pakistan, [4]School of Business, Society and Engineering, Mälardalen University, Västerås, Sweden

Air pollution is generating serious health issues as well as threats to our natural ecosystem. Accurate prediction of PM2.5 can help taking preventive measures for reducing air pollution. The periodic pattern of PM2.5 can be modeled with recurrent neural networks to predict air quality. To the best of the author's knowledge, very limited work has been conducted on the coupling of missing value imputation methods with gated recurrent unit (GRU) for the prediction of PM2.5 concentration of Guangzhou City, China. This paper proposes the combination of project to model plane (PMP) with GRU for the superior prediction performance of PM2.5 concentration of Guangzhou City, China. Initially, outperforming the missing value imputation method PMP is proposed for air quality data under consideration by making a comparison study on various methods such as KDR, TSR, IA, NIPALS, DA, and PMP. Secondly, it presents GRU in combination with PMP to show its superiority on other machine learning techniques such as LSSVM and two other RNN variants, LSTM and Bi-LSTM. For this study, data for Guangzhou City were collected from China's governmental air quality website. Data contained daily values of PM2.5, PM10, O_3, SOx, NOx, and CO. This study has employed RMSE, MAPE, and MEDAE as model prediction performance criteria. Comparison of prediction performance criteria on the test data showed GRU in combination with PMP has outperformed the LSSVM and other RNN variants LSTM and Bi-LSTM for Guangzhou City, China. In comparison with prediction performance of LSSVM, GRU improved the prediction performance on test data by 40.9% RMSE, 48.5% MAPE, and 50.4% MEDAE.

Keywords: PM2.5 prediction, project to model plane, LSTM, Bi-LSTM, GRU, Guangzhou city

OPEN ACCESS

Edited by:
Qian Zhang,
Xi'an University of Architecture and Technology, China

Reviewed by:
Ying ZHU,
Xi'an University of Architecture and Technology, China
Dongbin Wang,
Tsinghua University, China

****Correspondence:***
Chaudhary Awais Salman
chaudhary.awais.salman@mdh.se
Faisal Ahmed
faisalahmed@cuilahore.edu.pk

Specialty section:
This article was submitted to Atmosphere and Climate, a section of the journal Frontiers in Environmental Science

Received: *17 November 2021*
Accepted: *28 December 2021*
Published: *09 February 2022*

Citation:
Saif-ul-Allah MW, Qyyum MA, Ul-Haq N, Salman CA and Ahmed F (2022) Gated Recurrent Unit Coupled with Projection to Model Plane Imputation for the PM2.5 Prediction for Guangzhou City, China. Front. Environ. Sci. 9:816616. doi: 10.3389/fenvs.2021.816616

INTRODUCTION

The intrusion of foreign particles into the environment is identified as pollution that can make terrible changes in the natural environment. This intrusion could be natural or anthropogenic. Air is one of the most important resources of nature which is essential for humans, plants, and animals. Most of the developing countries are facing extreme challenges to control and reduce air pollution. Reasons of alarming levels of pollution are excessively increasing population, industries, and

automobiles (Sosa et al., 2017). Unfortunately, air pollution has become worst and intense over the time and has increased the death rates at such an alarming level that millions of people lose their lives every year. According to WHO, around 7 million people died because of air pollution in 2012 — one in eight deaths worldwide. This report claims 9 out of 10 people are inhaling air pollutants exceeding WHO standard limits (World Health Organization, 2021). According to the WHO's urban air quality statistics, 98% of cities having financial issues in low-income countries with populations greater than 100,000 do not meet WHO air quality instructions. Reducing air pollution might help millions of human lives from acute and chronic health disorders (Kampa and Castanas, 2008; Bustreo, 2012). In high-income countries, however, this percentage drops to 56% (Dora, 2016). Children, pregnant women, and people with respiratory and cardiovascular problems are more prone towards air pollution risks. Symptoms of air pollution on health might include wheezing, coughing, breathing problems, and in some extreme cases, mental health disorders (Kanner et al., 2021). Quality of life strongly depend upon the quality of air we inhale for breathing; a recent study has reported more vulnerability towards COVID-19 infection for humans as air pollution negatively affects the respiratory defense mechanism (Brauer et al., 2021).

Airborne particulate matters (PM) including PM10 (10 micron) and PM2.5 (2.5 micron) are the main contributor towards smog and disturb the human immune functionality and increases susceptibility to other infectious diseases (Sharma et al., 2021). A study has reported health issues of PM10, PM2.5, and O_3 as air-pollutants on children and has claimed adverse health problems for them (Zhang et al., 2019). The larger PM10 particles stick to mucosa and cause respiratory irritation, exacerbating lung infections and asthma (Wu et al., 2018). The finer particles of PM2.5 get into the internal respiratory tract, absorb through the pulmonary vein, and finally enter the bloodstream through the capillary network, which has a detrimental effect on the cardiovascular system (Xing et al., 2016). Recent study has reviewed health effects of short-term and long-term exposure to PM10 and PM2.5 and put forward the proof of morbidity and mortality related to different diseases (Lu et al., 2015; Kim et al., 2021). Air pollution is contributing to depletion of the ozone layer; acid rain and global climate change induce greater responsibility to human beings to protect the environment (Panda and Maity, 2021). Major air pollutants are chemical contaminants like carbon monoxide (CO), nitrogen dioxide (NO_2), lead (Pb), sulfur dioxide (SO_2), PM, and ozone (O_3) (Donald, 2021). International standards have described the standard ranges of Air Quality Index (AQI), and the concentration ($\mu g/m^3$) of PM2.5 in the environment in order of their intensities is given elsewhere (Omer, 2018). Rapid technological development and public demand lead to industrialization that is becoming a major cause of air pollution, and to curb the issue, multiple control methods/strategies need to be adopted (Wang et al., 2021). A very recent study found a convincingly positive relationship between PM2.5 and OCV (outpatient clinic visit) for hypertension in Guangzhou City in China (Lin et al., 2021). This study employed Cox-regression model to see the effects of PM2.5 on daily OCV for hypertension. Moreover, sensitive analysis study also pointed out PM2.5 daily mean and hourly peak concentration can be strong metrics for OCV. Owing to such serious medical and visibility concerns of PM2.5 concentration, research attention and practical measures on such issues are required in Guangzhou City, China. The concerned city has a 13.64 million population with reportedly high pollution rates. The official bodies of Guangzhou city have installed different air pollution sensors that constantly log SO_2, NO_2, O_3, CO PM10, and PM2.5 pollutant concentration. To avoid serious medical conditions and to take precautionary measures before time, reliable prediction models for pollutant concentration are employed.

There are many parameters that tend to affect air quality and can be recorded with sensitive devices and logged on different time series scales such as per hour, per day, etc. Complexity of the air quality parameters and other technical glitches cause missing values in the logged data. Commercial scale processes where a large number of variables are obtained might have 20–40% missing values.

Data containing missing values already loose quality of information and hence cannot be employed for effective model training (Kwak and Kim, 2017). In data preprocessing, the first step is to impute missing values using a suitable technique that should not disturb the quality of data. For multivariate data, principle component analysis (PCA) plays a significant role in data analysis and preprocessing (Bigi et al., 2021). In a study, the linear discriminant method has been employed and compared with the PCA technique for dimensionality reduction and results were evaluated by training different machine learning algorithms. The study concluded that Machine Learning algorithm with PCA performed better (Reddy et al., 2020). A study has also worked on data imputation that is centered on a PCA model that imputes the missing values by minimizing squared prediction error (SPE) (Wise and Ricker, 1991). Another study has investigated iterative algorithm (IA) for missing data imputation. This study has discussed the performance of iterative PCA, partial least square (PLS), and principal component regression (PCR) (Walczak and Massart, 2001). A novel PCA model building technique has also been reported with missing data imputation including data augmentation (DA) and nonlinear programming approach (NLP) along with the nonlinear iterative partial least squares (NIPALS) algorithm, IA, and trimmed score regression (TSR) (Folch-Fortuny et al., 2015). A study has discussed graphical user interface (GUI)-based data analysis and imputation methods such as DA, TSR, IA, projection to model plane (PMP), and NIPALS in the MATLAB environment (Folch-Fortuny et al., 2016).

Prediction of PM2.5 is an effective approach to improve the concern of the public about air quality. Many of the researchers provided the best contributions in improving the model capabilities to predict and identify the pollutants along with other quality variables (Oliveri Conti et al., 2017). A study discussed the mathematical and statistical models, and their coding methods were done by differential equation; drawbacks and amendments were done in alternative models introduced afterwards (Marriboyina, 2018). A study has put forward a

novel hybrid of the least square support vector machine (LSSVM), PCA-CS-LSSVM, for AQI prediction and reported better prediction efficiency than LSSVM and GRNN (Sun and Sun, 2017). Another study has worked on time series AQI prediction using the internet of things (IoT) and linear regression (LR) machine learning algorithms (Kumar et al., 2020). Neural network architecture has been evolving since the past decade and researchers have employed deep neural network (DNN) for AQI prediction. Neural network techniques such as multichannel ART-based neural network (MART), deep forward neural network (DFNN), and long short term memory (LSTM) have been used for AQI prediction and found LSTM has outperformed (Karimian et al., 2019). Keeping in mind the adverse effects of PM on human health as well as crops, a study has also employed the recurrent neural network (RNN) model as a time series prediction framework (Gul and Khan, 2020). Furthermore, considering the time series behavior of PM2.5, a recent study has discussed the LSTM-based PM2.5 prediction model and reported accurate and stable time series predictions (Li, 2021). For comparison purposes, this study has employed the back propagation model and proved LSTM superiority over it.

Data recorded on time basis contains sequences of pollutant concentration variation in the environment. Researchers have put efforts in developing time series deep learning models to predict the air pollutant concentration trend with time using LSTM and BILSTM. A recent study employed an LSTM neural network using time series data to predict PM10 concentration for major cities in China. This study reported superior performance of LSTM compared to statistical prediction and machine learning methods (Chen et al., 2021). More sophisticated and complex models tend to be more computationally expensive yet providing accurate predictions. However, the computationally expensive behavior of prediction models also needs attention. Certainly, there is a need to put more emphasis on deep learning models that are accurate and computationally feasible. Moreover, data preprocessing techniques such as outlier handling, missing data handling, feature extraction, etc., impact modeling efficiency.

Considering medical and other physical concerns, this work has dealt with input variables such as NO_2, SO_2, O_3, CO, and PM10 to predict the concentration of PM2.5 in the environment using different machine learning algorithms such as LSSVM, LSTM, Bi-LSTM, and GRU. Moreover, suitable parameters of each abovementioned model are then used in PM2.5 modeling. Researchers have developed and investigated different deep learning models, but this study aimed to investigate the abovementioned models for their accuracy, reliability, and computationally inexpensive behavior. The input variables that influence the concentration of PM2.5 were collected from the website of Guangzhou City in China and then preprocessed for missing values. Lastly, the comparison among different models has been carried out using error methods such as RMSE, MAPE, and MEDAE. The outperformed model is then suggested for PM2.5 prediction for taking precautionary measures in time.

GATED RECURRENT UNIT

A standard Artificial Neural Network (ANN) usually consists of three types of layers namely input layer, hidden layer, and output layer, respectively. Input, hidden and output layers are represented as x, h, and y. Recurrent neural network (RNN) is a special type of neural network architecture that has significance in learning sequential and time varying pattern (Cai et al., 2004). Because of the structure of RNN, a vanishing gradient problem comes in the way with large sequence input (Fei and Tan, 2018).

Hochreiter and Schmidhuber introduced LSTM back in 1997 to address the RNN vanishing gradient issue (Hochreiter and Schmidhuber, 1997). Four gates have been incorporated in a modified RNN memory cell to replace the RNN hidden state. The bidirectional LSTM (Bi-LSTM) variant of RNN was introduced in the same year as previous LSTM in 1997 (Schuster and Paliwal, 1997). It applies the previously explained two LSTMs in positive as well as negative time axis direction on input data. First, forward input sequence is propagated through LSTM. After this, reverse input sequence is propagated through the LSTM model. Bi-LSTM has certain advantages over single propagated LSTM such as good long-term learning capability and improved model prediction accuracy (Siami-Namini et al., 2019).

Gated recurrent unit (GRU) was introduced back in 2014, which performs a gating mechanism in RNN (Cho et al., 2014). GRU contains a modified LSTM-unit type hidden unit that has combined the input gate and forget gate into the update gate. The cellular and hidden states have also been considered while mixing the input and forget gate. The final model was simpler than LSTM and had fewer training parameters **Figure 1**.

The activation of hidden unit at time step is processed as follows:

$$r_t = \sigma(W_r h_{t-1} + U_r x_t) \tag{1}$$

Initially, r_t is calculated using **(1)** where σ represents logistic sigmoid function and W_r and U_r represent weight matrices. The new h_t is calculated by r_t with a tanh type layer:

$$\widetilde{h_t} = \tanh(W(r_t \times h_{t-1}) + U x_t) \tag{2}$$

In GRU, z_t replaces the remember gate along with the forget gate in LSTM. z_t is calculated as follows:

$$z_t = \sigma(W_z h_{t-1} + U_z x_t) \tag{3}$$

Finally, the hidden state gets updated as follows:

$$h_t = (1 - z_t)(h_{t-1}) + (z_t)\left(\widetilde{h_t}\right) \tag{4}$$

DATA ACQUISITION AND PREPROCESSING

In order to test imputation methods including KDR, IA, NIPALS, DA, and PMP, 2514 observations of six

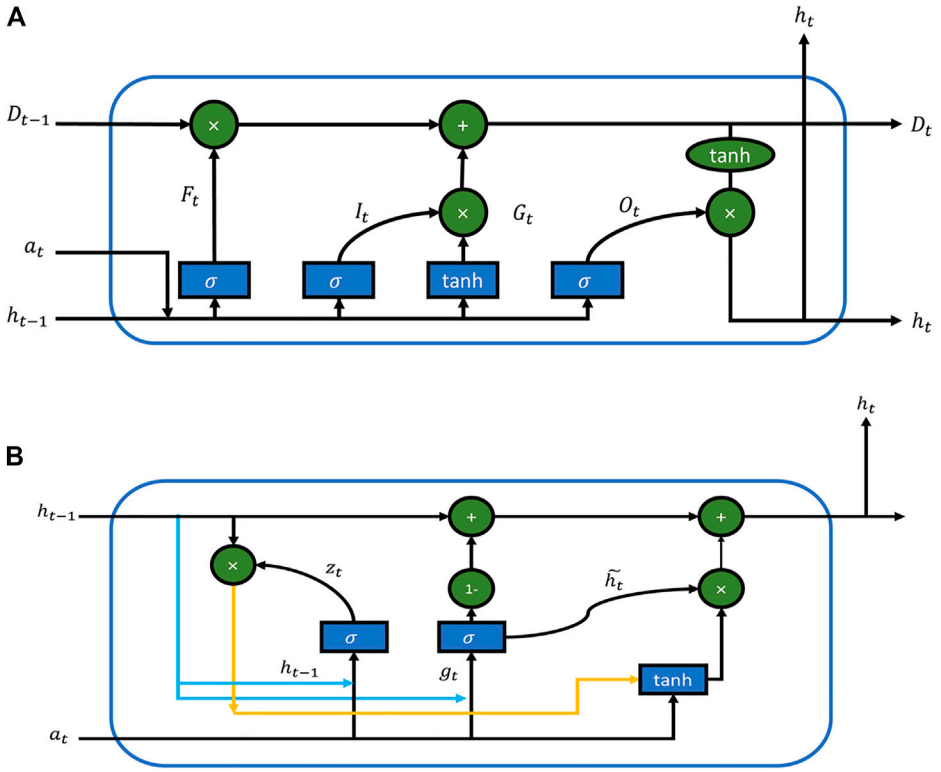

FIGURE 1 | Parameter comparison between **(A)** LSTM framework and **(B)** GRU framework.

TABLE 1 | Missing value imputation parameters

Imputation method	PCs	Tolerance	RMSE
KDR	6	10^{-10}	1.77
TSR	6	10^{-10}	1.77
IA	6	10^{-10}	2.66
NIPALS	6	10^{-10}	3.6
DA	6	10^{-10}	2.25
PMP	6	10^{-10}	1.22

parameters, PM2.5, PM10, SO_2, NO_2, O_3, and CO were used from Guangzhou air quality governmental website (The World Air Quality Project, 2020). The collected data contained ~2.5% missing values, and imputation was required with a suitable method. In order to select a suitable imputation method for this PM2.5 data, comparison experimentation was carried out. Firstly, all the rows with missing values were removed. The resulting new data were without missing values and run into random deletion of ~2.5% values of variables PM2.5, PM10, SO_2, NO_2, O_3, and CO overall.

Secondly, imputation methods including KDR, IA, NIPALS, DA, and PMP were employed to fill the missing values. After imputation, the imputed data results were compared using numerical errors for the abovementioned imputation methods. The criterion RMSE (**Eq. 5**) helped in opting the outperformed technique.

$$RMSE = \sqrt{\frac{\left(x_{actual-}\, x_{imputed}\right)^2}{N}} \tag{5}$$

Each method was allowed to iterate 5,000 times to impute missing data. The RMSE values obtained through comparison experimentation are tabulated in **Table 1**. KDR and TSR reported an RMSE value of 1.77 for overall imputed missing values. RSME values obtained by IA, NIPALS, and DA are 2.66, 3.6, and 2.25, respectively. Amongst all the methods, PMP showed better results with RMSE value equal to 1.22.

The outperformed method PMP was used to impute originally collected data. In order to summarize the impact of the individual variable on all other variables, correlation coefficients were obtained. For that, the correlation matrix was formed for imputed data that depicted the impact of individual input variables, i.e. PM10, SO_2, NO_2, O_3, and CO, in terms of correlation coefficients, on the output variable PM2.5 (**Figure 2**). The magnitude of the correlation coefficient shows the strength of correlation between two variables. The correlation matrix provided all possible correlations among all variables. Correlation coefficient ranges from −1 to +1. The coefficient value of −1 shows perfect inverse impact; 0 shows no impact, and +1 shows perfect direct impact. From the bottom left of **Figure 2**, it can be seen that output variable PM2.5 is strongly correlated with input variable PM10 with a coefficient value of 0.65. High coefficient value depicts that the

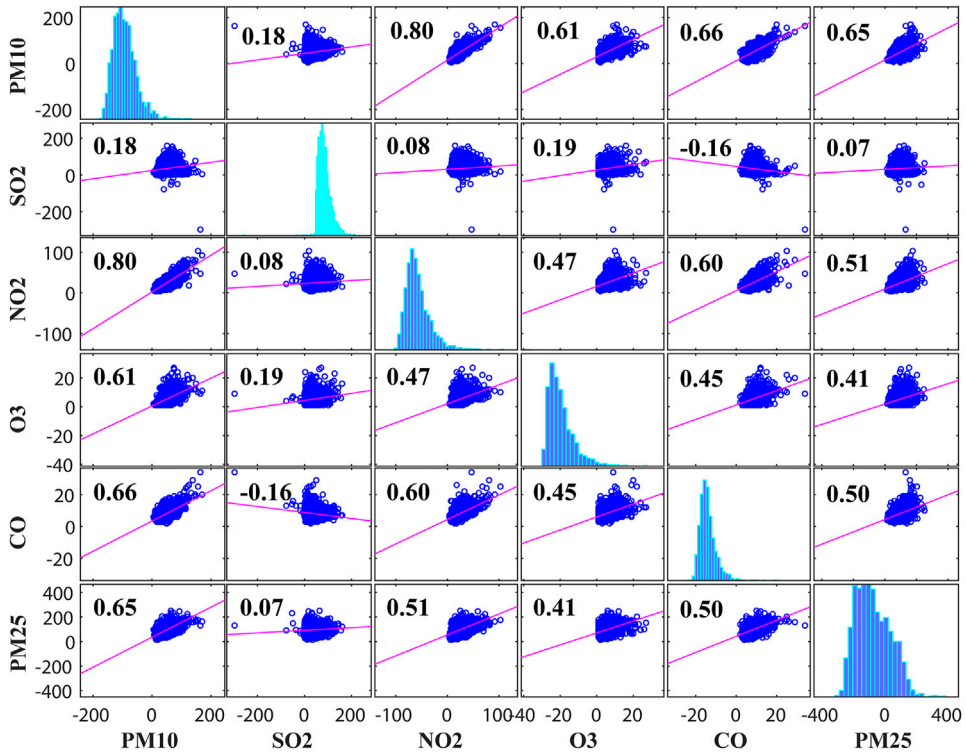

FIGURE 2 | Matrix of correlation among all variables.

TABLE 2 | Percentage wise data distribution in various ranges

Range	PM2.5%	PM10%	CO %	NOx %	Ozone %
Good	0	65.07	0.11	100	100
Moderate	2.3	34.8	3.9	0	0
Unhealthy for some	13.12	0.11	6.20	0	0
Unhealthy for all	74.5	0	10.7	0	0
Very unhealthy	9.94	0	56.24	0	0
Hazardous	0	0	22.8	0	0

change in concentration of PM10 will significantly affect the output variable PM2.5. Moreover, the output variable PM2.5 was least affected with the variation in SO_2 concentration that can be analyzed using the correlation coefficient in **Figure 2**. The correlation coefficient was very small, 0.07 between output variable PM2.5 and input variable SO_2. Removing SO_2 from the training data set for model training from the data under consideration would not significantly decrease the prediction performance of the model.

Moreover, the reported air pollutant safe limits (Agency, 2018) allow further analysis of the imputed data. A different coloring scheme with respect to the severity of individual pollutant concentration was employed to understand the distribution of data with their ranges (**Table 2**). The collected data contained approximately 80 months of PM2.5 and other pollutant data recorded on a per day basis.

Most of the PM2.5 data were found in an unhealthy range. Percentage-wise, data distribution in various ranges is given in **Table 2**. Out of 2514 total samples of PM2.5 collected for Guangzhou City, 0 samples were in green limit, 59 samples in yellow range, 330 samples in orange range, 1874 samples in red ranges, and 250 samples in purple range. PM10 data did not show much of the variation in ranges and categorized in safe or green ranges.

However, out of 2,514 total samples of PM10, 1,636 data points were in green range, 875 were in yellow, and 3 samples were in orange range that were collectively categorized in safe ranges. CO concentrations have shown variation in different ranges. Most of the data points were categorized in a not-safe range. Out of 2514 samples, three samples were in green range, 98 in yellow, 156 in orange, 269 in red, 1414 in purple, and 254 in maroon range. Moreover, most of the CO pollutant distributions were found in a very unhealthy range. NOx data and ozone data did not show any categorical variations. Almost all the data were in green range.

METHODOLOGY

The data were collected from the official Guangzhou air quality website that contained 2514 samples from Jan 2014 to Nov 2020 that contained missing values. To impute the missing values, various missing data imputation methods were employed and compared as shown in **Table 1**. This comparison study has been

discussed in the *Data acquisition and preprocessing* **section** in detail. The imputation method giving the least RMSE was selected to impute the original missing data. After the data was imputed, in order to select the most correlated variables with PM2.5, a correlation matrix was formed as shown in **Figure 2**. According to the figure, SO_2 was found least correlated with PM2.5 with the correlation coefficient 0.07. Owing to the insignificant impact of the SO_2 on PM2.5 for the data under consideration, it was decided that SO_2 can be removed from the input variables list. Afterwards, prior to model training, data standardization was carried out using **Eq. 6** to rescale the data for zero mean and unit variance. The standardized data were incorporated in model training where training input and corresponding output were termed as Xtrain and Ytrain. Training data with 2214 samples and validation data with 150 samples were devised for model training and validation, and 150 samples were devised for model testing. Furthermore, suitable parameters along with training data were employed to train these models, while the validation data were used to validate the model to check whether it is under-trained or over-trained. Subsequently, test data were fed to the trained model to evaluate the model prediction capability.

$$\text{standardized } (x_i) = \frac{x_i - \mu}{\sigma} \tag{6}$$

where x_i is the data value, μ represents the mean and σ represents standard deviation of the data. Moreover, RMSE, MAPE, and MEDAE were calculated using **Eqs. 7**, **8**, and **9** respectively, to evaluate model performance by comparing PM2.5 predictions with actual PM2.5 from testing data.

$$RMSE = \sqrt{\frac{1}{n}\sum_{i=1}^{n}(x_i - pred_i)^2} \tag{7}$$

$$MAPE = \frac{1}{n}\sum_{i=1}^{n}\left|\frac{x_i - pred_i}{x_i}\right| \tag{8}$$

$$MEDAE = \frac{1}{n}\sum_{i=1}^{n}\left|pred_i - x_i\right| \tag{9}$$

Here, x_i, $pred_i$, and n represent actual PM2.5 value, predicted PM2.5 value, and testing data sample size, respectively.

LSSVM-based model development

Data standardization was done using **Eq. 6** to scale it to zero mean and include unit variance in the data set. For LSSVM, two parameters, gamma and sigma, were selected after extensive trials, and set values came out to be 20 and 40, respectively.

LSTM-based model development

Input layer of LSTM contained four input units that were provided with training data to train the model. The training progressed using Adam algorithm. The Adam algorithm has the excellent capability to reach a globally optimal solution (Kingma and Ba, 2014). The Adam algorithm back-propagates the error to update the weights and biases of the LSTM to minimize the training error. Validation of the model training has also been performed to see if the model is under-trained or over-trained. The model was trained with 80 epochs. Moreover, necessary parameters for LSTM model training such as hidden units, dropout, initial learn rate, learn rate drop factor, learn rate, and drop period were set as 80, 0.9, 0.25, 1×10^{-6}, and 80, respectively. Finally, the test data were fed to obtain the prediction of the model.

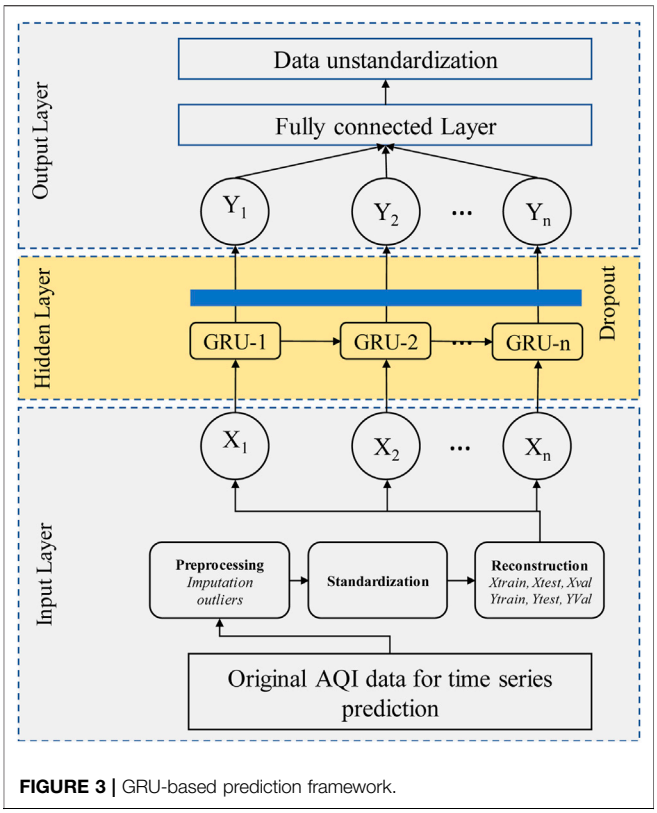

FIGURE 3 | GRU-based prediction framework.

Bi-LSTM-based model development

Bi-LSTM consists of two LSTMs that work in opposite direction, hence requiring more training time. The Adam algorithm was used to update the weights and biases of the Bi-LSTM to minimize the training error. The model was allowed to train for 80 epochs and validation of the model training was also carried out to see if the model was under-trained or over-trained. A dropout layer was also added to avoid overfitting while training the model. Moreover, necessary parameters for Bi-LSTM model training such as hidden units, dropout, initial learn rate, learn rate drop factor, and learn rate drop period were set as 80, 0.9, 0.75, 1×10^{-6}, and 80, respectively.

GRU-based model development

The GRU-based prediction model is shown in **Figure 3**. The GRU network trained the weights and biases while training to minimize the validation errors. The Adam algorithm was used for training due to its ability to reach the globally optimal solution effectively. The model was trained using 80 epochs and validation of the model training was also carried out to see if the model was under-trained or over-trained. A dropout layer was also added to avoid overfitting while training the model. If both training error and validation error decrease simultaneously, then the model is

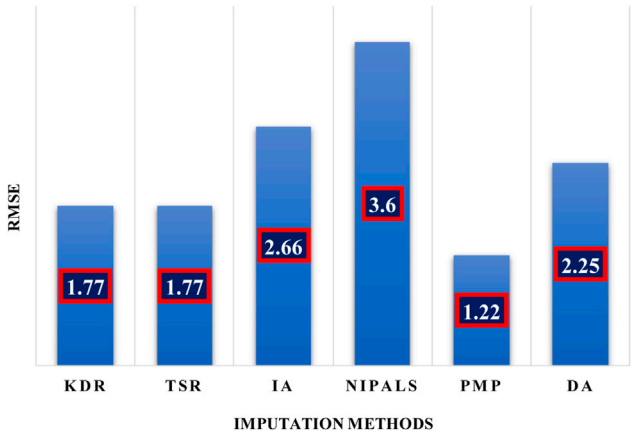

FIGURE 4 | Missing values imputation method comparison.

said to under-train. If training error decreases but validation error increases, the model is said to be over-trained. Moreover, necessary parameters for GRU model training such as hidden units, dropout, initial learn rate, learn rate drop factor, and learn rate drop period were set at 160, 0.9, 0.0009, 1, and 120, respectively.

RESULTS AND DISCUSSION

The acquisition of the PM2.5 data was described in the *Data acquisition and preprocessing* section along with missing data handling. Amongst all the methods employed for the data considered, KDR and TSR performed better with ~2.5% of missing value imputations (**Table 1**). Moreover, through imputation experiment, PMP was selected as the outperformed imputation method and, hence, used for the imputation of original collected PM2.5 missing data (**Figure 4**).

This study has employed time series predictive RNN models such as LSTM, Bi-LSTM, and GRU for prediction of PM2.5 using input variables of PM10, NO_2, O_3, and CO. The models were compared and evaluated on prediction error. RSME, MAE, and MAPE model evaluation techniques were used to evaluate model prediction performance.

After preparing data for model training, LSSVM, LSTM, Bi-LSTM, and GRU models were developed for PM2.5 prediction. The training and testing performances of the respective models are discussed afterwards.

Training performance of models

All models were trained with 2214 samples of the input variables PM10, NO_2, O_3, and CO and output variable PM2.5. The training data comprised almost 74 months of data. The training performance, in terms of RMSE, of all the models are given in **Table 3**.

LSSVM got trained with overall training RMSE of 29.4 (**Figure 5A**). The blue line in the upper graph shows the original values of PM2.5 of 74 months of data samples. The red line shows the trained PM2.5 values. It can be analyzed that the model training RMSE of 29.4 is significantly high. Moreover, the red-faced circles (**Figure 6A**) show the trained PM2.5 values in the form of scatter graph plotted against actual PM2.5 of 74 months of data. The red-faced circles were found distributed around the trend line (dashed diagonal line) and following it but not significantly, representing the deviation from the trend line at points. This was one of the reasons of high training RMSE, though the closeness of the red-faced circles with the trend line at various points also exhibits that the model was a good fit.

TABLE 3 | Model performance review

Models	Training RMSE	Validation RMSE	Testing RMSE
LSSVM	29.4	23.77	17.94
LSTM	17.32	13.87	10.82
Bi-LSTM	19.29	16.23	12.43
GRU	18.24	13.60	10.60

Seventy-four months of data were also employed to train the LSTM network, and training performance was plotted on a per day basis (**Figure 5B**). The solid blue line shows the actual PM2.5 from the training data and the red line shows the trained data by the model. It can be seen that model was able to learn the time series sequence very well and trained values showed relatively less RMSE 17.32.

Generally, it is not recommended to train the model as much in that trained values tightly fit the original data because overfitting takes away the generalizability of the model and future predictions get compromised drastically. Moreover **Figure 6B** was also plotted between original PM2.5 from 74 months of training data and trained data by the model. This scatter plot shows that the model was following the trend line with lesser deviation, which means the LSTM was able to learn time series sequence from the provided training data, and the closeness of red-faced circles with the trend line showed the superior learning capability of LSTM compared to LSSVM.

Figure 5C shows the training performance of the Bi-LSTM model with 74 months of PM2.5 training data. The upper plot shows the model has trained the time series sequences substantially from the provided training data. The Bi-LSTM model showed relatively poorer learning performance as compared to LSTM and showed the training RMSE of ~19.29. However, the model trained the time series sequence very well and was also able to show good performance in learning training data values.

Overall, the model showed relatively larger training error at every instance of training than LSTM. Moreover, **Figure 6C** shows that the trained data are distributed around the trend line with lesser deviation than that of LSSVM but greater deviation than that of LSTM. However, the trained data were found following the trend line very well showing better time series sequence learning capability as compared to LSSVM but not better than LSTM.

The GRU network has fewer parameters to train as compared to LSTM and Bi-LSTM (**Figure 1**). The GRU training looks similar to the LSTM network (**Figures 5B,D**). However,

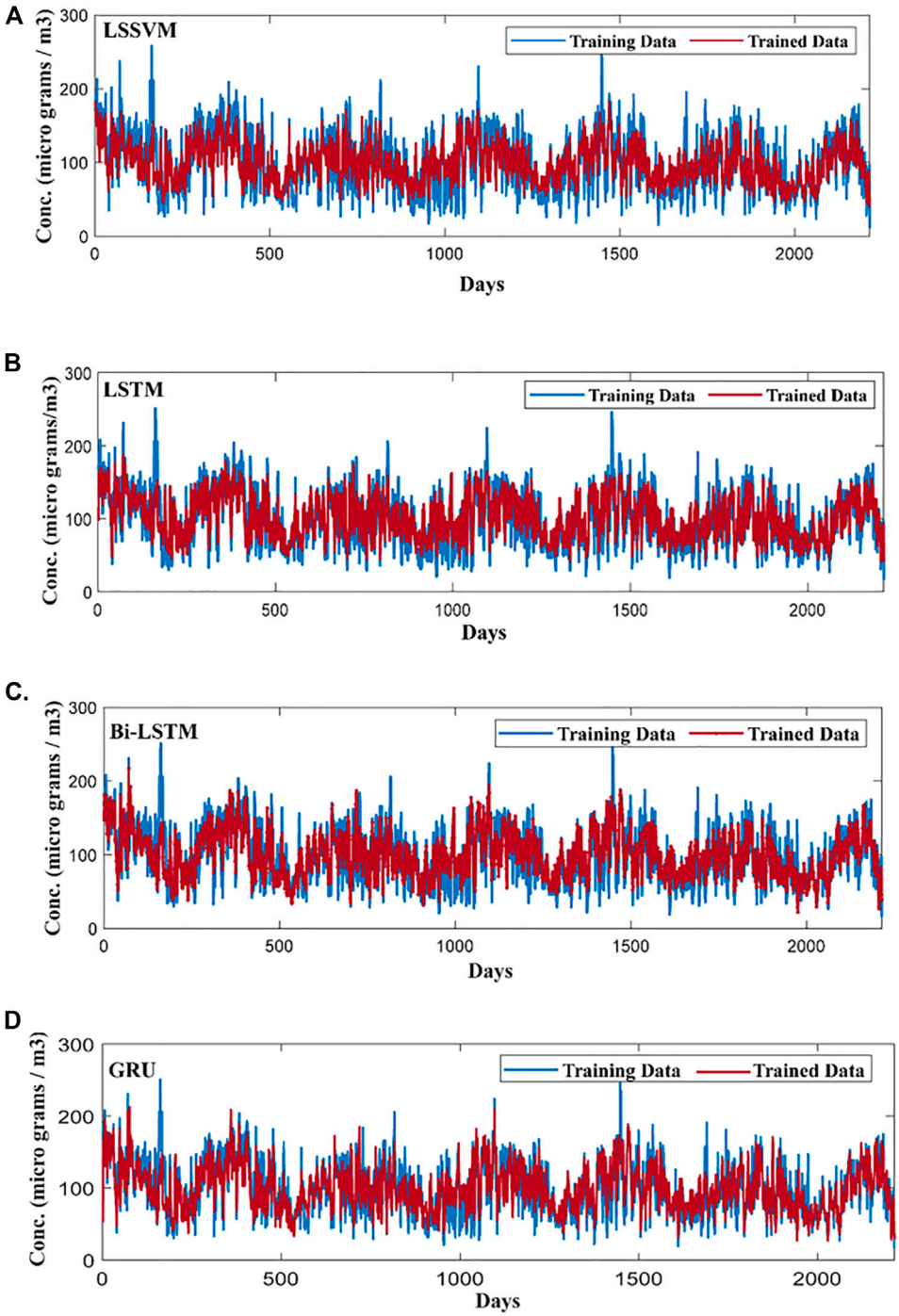

FIGURE 5 | (A) LSSVM model PM2.5 prediction on training data. **(B)** LSTM model PM2.5 prediction on training data. **(C)** Bi-LSTM model PM2.5 prediction on training data. **(D)** GRU model PM2.5 prediction on training data.

comparison showed that GRU model trained better than previously discussed models from the 74 months of training data and reported training an RMSE value of 18.24. **Figure 6D** also shows that the trained data was spread along the trend line, depicting good time series sequence learning capability of the model comparable to LSTM.

Moreover, comparison of RMSE of the models for training data shows that LSTM outperforms. However, it is important to note that lesser RMSE while training might not necessarily give lesser RMSE while testing. After training, models were validated with 150 samples (January 2020–June 2020) and validation RMSEs were

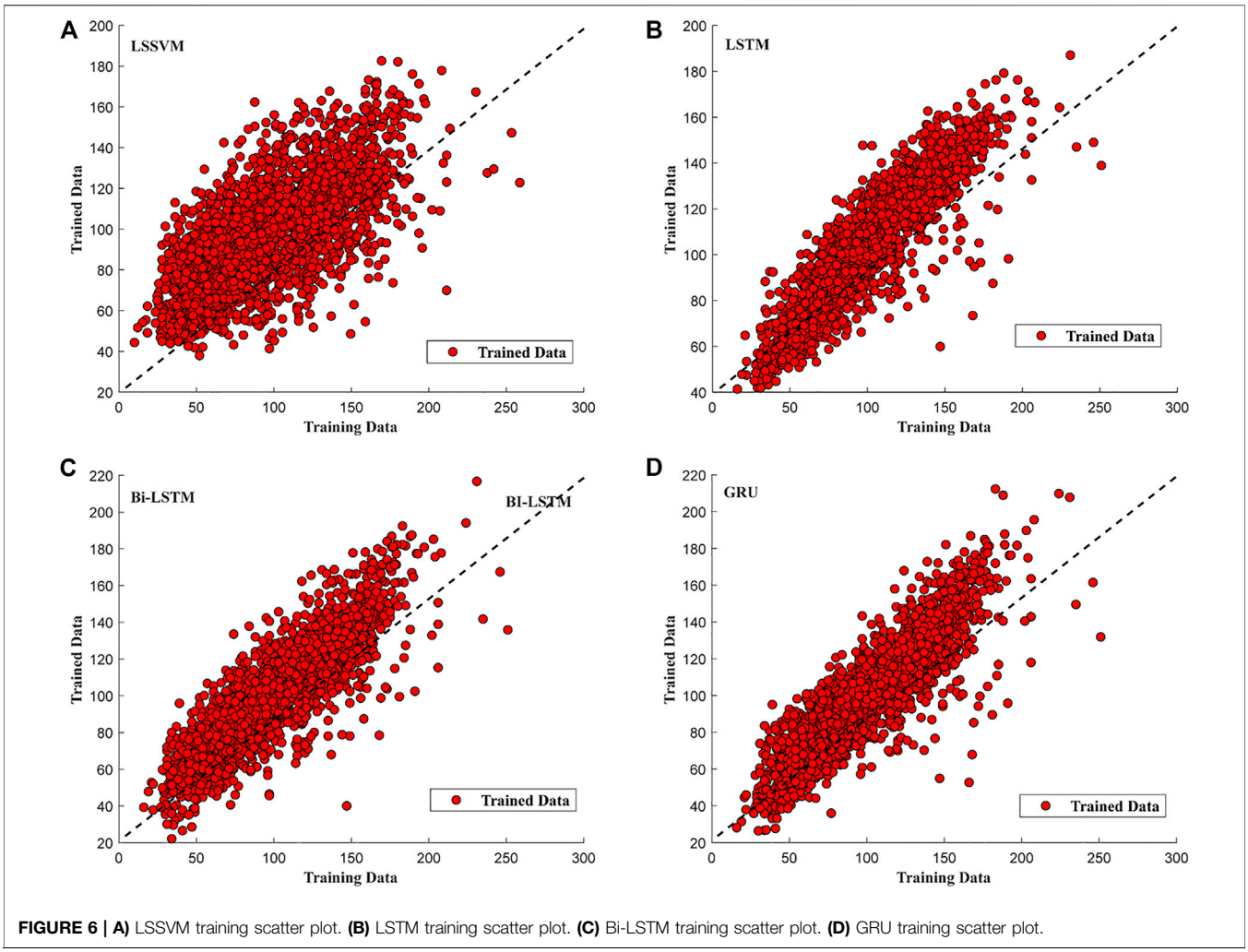

FIGURE 6 | A) LSSVM training scatter plot. **(B)** LSTM training scatter plot. **(C)** Bi-LSTM training scatter plot. **(D)** GRU training scatter plot.

TABLE 4 | PM2.5 models prediction errors with test data

Models	RMSE		MAPE		MEDAE	
	Value	% Diff [a]	Value	% Diff [a]	Value	% Diff [a]
LSSVM	17.94	–	21.40	–	11.70	–
LSTM	10.82	39.7%	15.57	27.2%	8.54	27%
Bi-LSTM	12.43	30.7%	14.29	33.2%	7.22	38.3%
GRU	10.60	40.9%	11.01	48.5%	5.80	50.4%

[a]*% diff refers to the percentage difference in RMSE, MAPE, and MEDAE, compared to that of LSSVM.*

reported in **Table 3**. Validation performance figures can be found in **Supplementary data**.

Testing performance of models

All models were trained and tested with four variables discussed in the *Data acquisition and preprocessing* section. The test data set contained 150 samples from July 2020 to November 2020 (5 months). Prediction performance criteria i.e., RMSE, MAPE, and MEDAE of the models under consideration are tabulated in **Table 4**. For the first 2 months (July, August) of LSSVM model prediction, performance was a bit poor (**Figure 7A**). For the next 2 months (Sep, Oct), the model showed a good trend following ability compared to previous 2 months of results. However, the model was found deviating from the actual trend for the end of October and start of the final month (November). The model reported overall prediction error using testing data as RMSE, MAPE, and MEDAE equal to 17.94, 21.40, and 11.70 respectively. From (**Figure 8A**) the scatter plot of predicted values was visualized against the actual PM2.5 testing values. Red-faced circles showed that the predicted values were getting far apart along the trend line representing the poor performance of the model. The model was not generalized enough to predict the PM2.5 values accurately.

The testing performance of the LSTM model is shown in (**Figure 7B**). For the first 2 months, some prediction values were found less accurate but were following the actual trend. For next 2 months, the model prediction followed the actual trend very well and predicted values were very close to the actual trend. For very few points, the model compromised the prediction in these months. However, for the last month the LSTM PM2.5 model was found losing its outstanding trend following capability as it had shown in

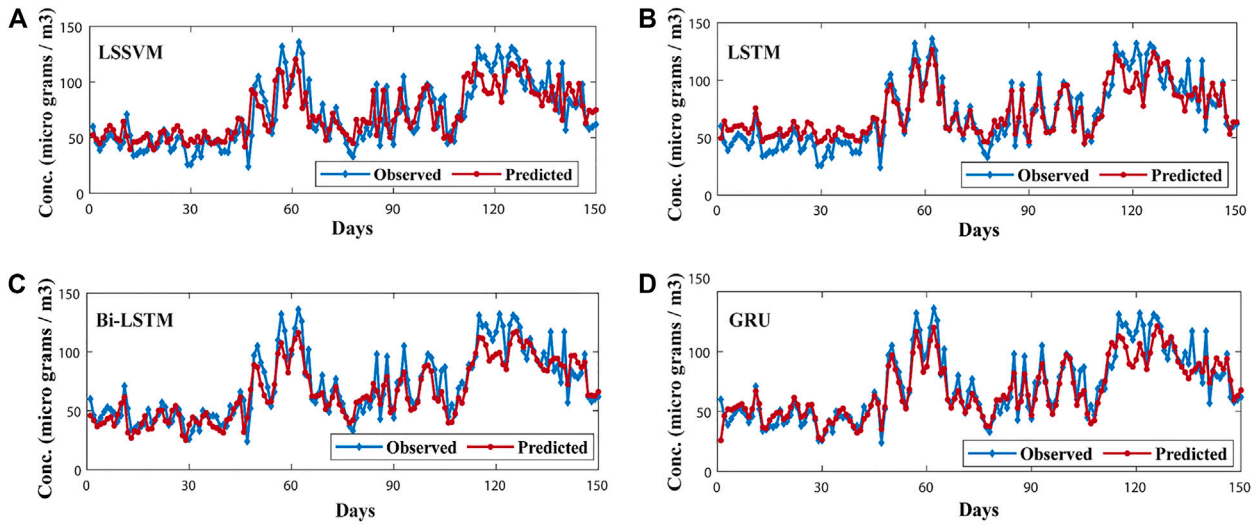

FIGURE 7 | (A) LSSVM model PM2.5 prediction on test data. **(B)** LSTM model PM2.5 prediction on test data. **(C)** Bi-LSTM model PM2.5 prediction on test data. **(D)** GRU model PM2.5 prediction on test data.

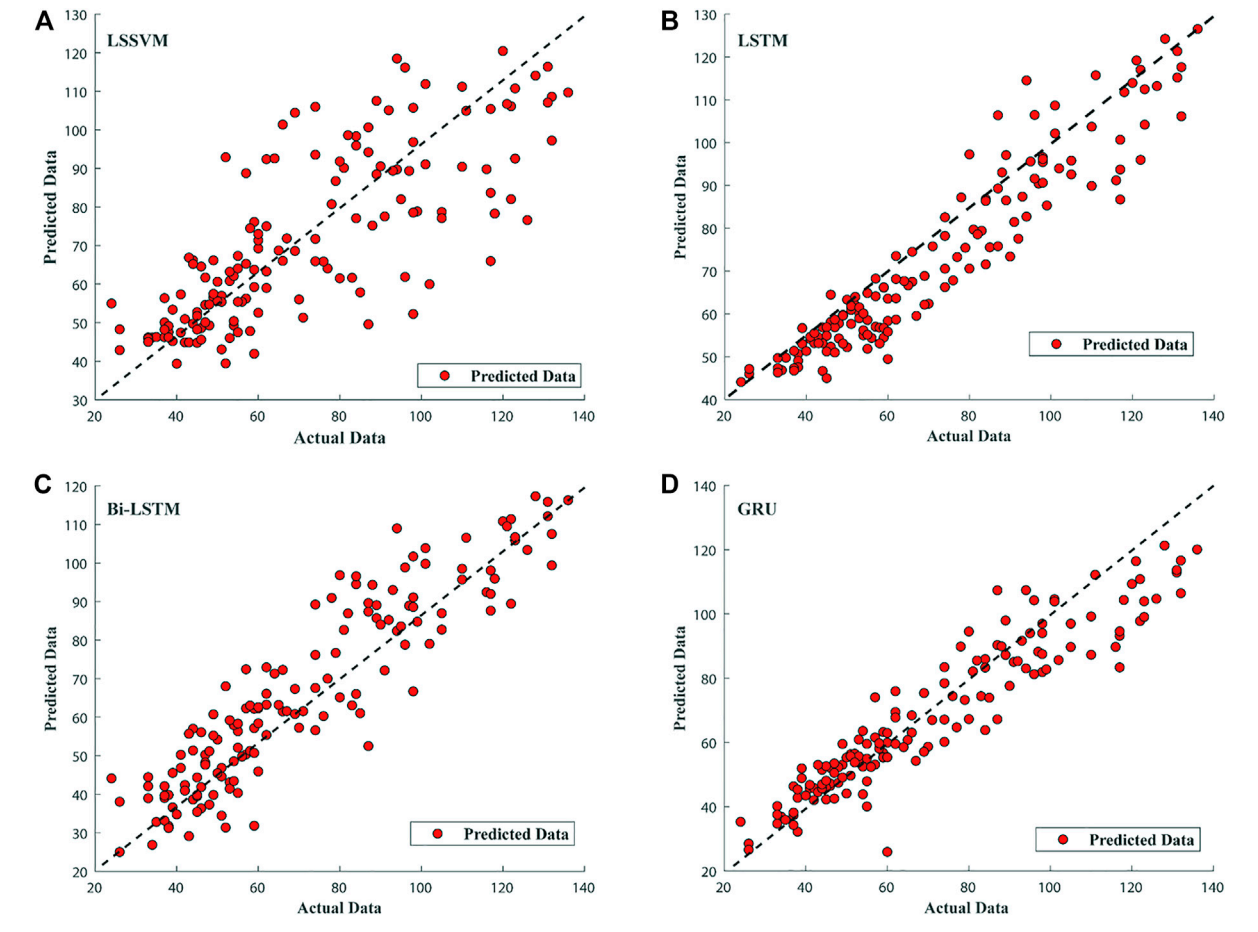

FIGURE 8 | (A) LSSVM model test data scatter plot. **(B)** LSTM model test data scatter plot. **(C)** Bi-LSTM test data scatter plot. **(D)** GRU model test data scatter plot.

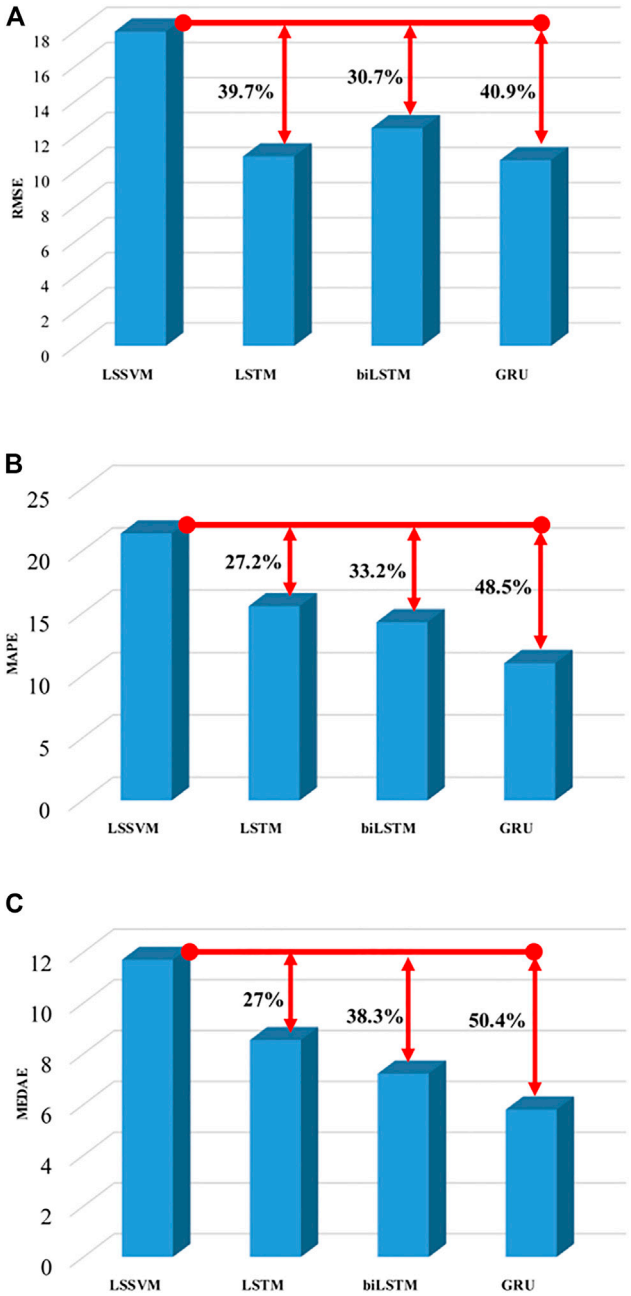

FIGURE 9 | Model performance improvement summary. **(A)** RMSE improvement summary. **(B)** MAPE improvement summary. **(C)** MEDAE improvement summary.

the previous 4 months **Figure 8B** shows the scatter plot of LSTM PM2.5 prediction against the actual testing values of PM25. The overall red-faced circles were found closely spread along the trend line compared to LSSVM representing good time series trend prediction of PM2.5 compared to that of the LSSVM model. The values of RMSE, MAPE, and MEDAE are 10.82, 15.57, and 8.54, respectively, which are 39.7%, 27.2%, and 27% lower than that of the LSSVM model, respectively, as shown in **Table 4** and **Figure 9**.

In case of Bi-LSTM, the actual trend following the ability of the model is shown in **Figure 7C**. The Bi-LSTM model predicted PM2.5 values accurately and actual trend following for the first 2 months was even better than LSTM. For the next 2 months, the prediction capability of the Bi-LSTM model was reduced compared to LSTM model. **Figure 8C** shows the Bi-LSTM prediction scatter plot against the actual PM2.5 testing values. In terms of overall prediction, the red-faced circles were closely spread along with the trend line, however, a bit far compared to LSTM model scatter plot. The Bi-LSTM model produced RMSE, MAPE, and MEDAE as 12.43, 14.29, and 7.22, respectively, which are 30.7%, 33.2%, and 38.3% lower than that of the LSSVM model, respectively, as shown in **Table 4** and **Figure 9**.

The GRU model with testing data set performed very well in terms of following the actual trend (**Figure 7D**). The model performance for the first 4 months of the testing data was significantly better than that of previously discussed models. The model displayed good prediction capability and followed the actual testing data trend accurately with close predicted values. However, for the last month the model lost excellent prediction performance but still predicted the actual trend effectively. However, in terms of overall prediction, the GRU model showed excellent performance with the testing data set as compared to previous models such as LSSVM, LSTM, and Bi-LSTM. **Figure 8D** shows the prediction performance of the GRU model in the scatter plot. The red-faced circles were found following the trend line excellently, better than that of LSSVM, LSTM, and Bi-LSTM.

The RMSE, MAPE, and MEDAE values are 10.60, 11.01, and 5.80 respectively, which are 40.9%, 48.5%, and 50.4% lower than those of the LSSVM model, respectively, as shown in **Table 4** and **Figure 9**.

The performance criteria values of the GRU model are the lowest among comparative models considered in this work. The results depicted that the GRU model outperformed the other PM2.5 prediction models with the least RMSE, MAPE, and MEDAE.

CONCLUSION

In this study, predictions of PM2.5 in Guangzhou City in China were performed with different machine learning models including LSSVM, LSTM, Bi-LSTM, and GRU. Originally collected data contained missing values ~2.5% of all data. Prior to model development, imputation experiment was run to shortlist the outperforming method among KDR, IA, NIPALS, DA, and PMP. Comparison experiment showed that PMP outperformed all other imputation methods with RMSE of 1.22. Therefore, the prediction models were developed in combination with PMP. The correlation result showed that SO_2 concentrations were badly correlated with PM2.5; therefore, the models were developed without SO_2 concentration in the data.

The RMSE, MAPE, and MEDAE of the LSSVM model with test data were produced to be 17.94, 21.4, and 11.7,

respectively. Compared to LSSVM, the LSTM improved the prediction performance by 39.7% RMSE, 27.2% MAPE, and 27% MEDAE. In the case of Bi-LSTM, it improved the prediction performance by 30.7%, 33.2%, and 38.3% compared to that of LSSVM, according to RMSE, MAPE, and MEDAE, respectively. Likewise, GRU improved the prediction performance by 40.9%, 48.5%, and 50.4% compared to LSSVM, according to RMSE, MAPE, and MEDAE, respectively. Based on the prediction performance improvement percentages, it can be concluded that GRU in combination with PMP was able to update its learnable parameters better and outperformed the LSSVM, LSTM, and Bi-LSTM for the prediction of PM2.5 data from Guangzhou City, China.

DATA AVAILABILITY STATEMENT

The original contributions presented in the study are included in the article/**Supplementary Material**; further inquiries can be directed to the corresponding authors.

AUTHOR CONTRIBUTIONS

Conceptualization, FA; methodology, MS; software, MQ; formal analysis, NU; investigation, MS and MQ; writing — original draft preparation, MS; project administration, FA; writing — review and editing, NU and CS; supervision, FA. All authors have read and agreed to the published version of the manuscript.

FUNDING

This work was funded by the Higher Education Commission Pakistan (HEC) under the National Research Program for Universities (NRPU), 2017, Project Number 8167.

SUPPLEMENTARY MATERIAL

The supplementary material for this article can be found online at: https://www.frontiersin.org/articles/10.3389/fenvs.2021.816616/full#supplementary-material

REFERENCES

Agency, U. S. E. P. (2018). *Technical Assistance Document for the Reporting of Daily Air Quality—the Air Quality Index (AQI)*. Geneva: World Health Orgaisation.

Bigi, F., Haghighi, H., De Leo, R., Ulrici, A., and Pulvirenti, A. (2021). Multivariate Exploratory Data Analysis by PCA of the Combined Effect of Film-Forming Composition, Drying Conditions, and UV-C Irradiation on the Functional Properties of Films Based on Chitosan and Pectin. *LWT.* 137, 110432. doi:10.1016/j.lwt.2020.110432

Brauer, M., Casadei, B., Harrington, R. A., Kovacs, R., Sliwa, K., Brauer, M., et al. (2021). Taking a Stand Against Air Pollution-The Impact on Cardiovascular Disease. *J. Am. Coll. Cardiol.* 77, 1684–1688. doi:10.1016/j.jacc.2020.12.003

Bustreo, D. F. (2012). *7 Million Premature Deaths Annually Linked to Air Pollution*. Geneva: World Health Orgaisation. Available at: https://www.who.int/mediacentre/news/releases/2014/air-pollution/en/#.WqBfue47NRQ.mendeley (Accessed December 20, 2019).

Cai, X., Zhang, N., Venayagamoorthy, G. K., and Wunsch, D. C. (2004). "Time Series Prediction with Recurrent Neural Networks Using a Hybrid PSO-EA Algorithm," in 2004 IEEE International Joint Conference on Neural Networks (IEEE Cat. No. 04CH37541), 1647–1652.

Chen, Y., Cui, S., Chen, P., Yuan, Q., Kang, P., and Zhu, L. (2021). An LSTM-Based Neural Network Method of Particulate Pollution Forecast in China. *Environ. Res. Lett.* 16 (4), 044006. doi:10.1088/1748-9326/abe1f5

Cho, K., van Merriënboer, B., Gulcehre, C., Bahdanau, D., Bougares, F., Schwenk, H., et al. (2014). Learning Phrase Representations Using RNN Encoder-Decoder for Statistical Machine Translation. Proceedings of the 2014 Conference on Empirical Methods in Natural Language Processing (EMNLP).

Donald, J. K. (2021). "Atmospheric Chemistry: An Overview—Ozone, Acid Rain, and Greenhouse Gases," in *Building STEM Skills Through Environmental Education*. Editors T. S. Stephen and D. Janese (Hershey, PA, USA: IGI Global), 172–218.

Dora, D. C. (2016). *Air Pollution Levels Rising in many of the World's Poorest Cities*. Geneva: World Health Organisation. Available at: https://www.who.int/news/item/12-05-2016-air-pollution-levels-rising-in-many-of-the-world-s-poorest-cities (Accessed December 22, 2019).

Fei, H., and Tan, F. (2018). Bidirectional Grid Long Short-Term Memory (BiGridLSTM): A Method to Address Context-Sensitivity and Vanishing Gradient. *Algorithms.* 11 (11), 172. doi:10.3390/a11110172

Folch-Fortuny, A., Arteaga, F., and Ferrer, A. (2015). PCA Model Building with Missing Data: New Proposals and a Comparative Study. *Chemometrics Intell. Lab. Syst.* 146, 77–88. doi:10.1016/j.chemolab.2015.05.006

Folch-Fortuny, A., Arteaga, F., and Ferrer, A. (2016). Missing Data Imputation Toolbox for MATLAB. *Chemometrics Intell. Lab. Syst.* 154, 93–100. doi:10.1016/j.chemolab.2016.03.019

Gul, S., and Khan, G. M. (2020). "Forecasting Hazard Level of Air Pollutants Using LSTM's," in *Artificial Intelligence Applications and Innovations*. Editors I. Maglogiannis, L. Iliadis, and E. Pimenidis (Berlin: Springer International Publishing), 143–153.

Hochreiter, S., and Schmidhuber, J. (1997). Long Short-Term Memory. *Neural Comput.* 9, 1735–1780. doi:10.1162/neco.1997.9.8.1735

Kampa, M., and Castanas, E. (2008). Human Health Effects of Air Pollution. *Environ. Pollut.* 151 (2), 362–367. doi:10.1016/j.envpol.2007.06.012

Kanner, J., Pollack, A. Z., Ranasinghe, S., Stevens, D. R., Nobles, C., Rohn, M. C. H., et al. (2021). Chronic Exposure to Air Pollution and Risk of Mental Health Disorders Complicating Pregnancy. *Environ. Res.* 196, 110937. doi:10.1016/j.envres.2021.110937

Karimian, H., Li, Q., Wu, C., Qi, Y., Mo, Y., Chen, G., et al. (2019). Evaluation of Different Machine Learning Approaches to Forecasting PM2.5 Mass Concentrations. *Aerosol Air Qual. Res.* 19, 1400–1410. doi:10.4209/aaqr.2018.12.0450

Kim, H., Byun, G., Choi, Y., Kim, S., Kim, S.-Y., and Lee, J.-T. (2021). Effects of Long-Term Exposure to Air Pollution on All-Cause Mortality and Cause-specific Mortality in Seven Major Cities of South Korea: Korean National Health and Nutritional Examination Surveys with Mortality Follow-Up. *Environ. Res.* 192, 110290. doi:10.1016/j.envres.2020.110290

Kingma, D., and Ba, J. (2014). "Adam: A Method for Stochastic Optimization," in International Conference on Learning Representations.

Kumar, R., Kumar, P., and Kumar, Y. (2020). Time Series Data Prediction Using IoT and Machine Learning Technique. *Proced. Computer Sci.* 167, 373–381. doi:10.1016/j.procs.2020.03.240

Kwak, S. K., and Kim, J. H. (2017). Statistical Data Preparation: Management of Missing Values and Outliers. *Korean J. Anesthesiol.* 70 (4), 407. doi:10.4097/kjae.2017.70.4.407

Li, Y. (2021). Time-series Prediction Model of PM2.5 Concentration Based on LSTM Neural Network. *J. Phys. Conf. Ser.* 1861 (1), 012055. doi:10.1088/1742-6596/1861/1/012055

Lin, X., Du, Z., Liu, Y., and Hao, Y. (2021). The Short-Term Association of Ambient fine Particulate Air Pollution with Hypertension Clinic Visits: A Multi-Community Study in Guangzhou, China. *Sci. Total Environ.* 774, 145707. doi:10.1016/j.scitotenv.2021.145707

Lu, F., Xu, D., Cheng, Y., Dong, S., Guo, C., Jiang, X., et al. (2015). Systematic Review and Meta-Analysis of the Adverse Health Effects of Ambient PM2.5 and PM10 Pollution in the Chinese Population. *Environ. Res.* 136, 196–204. doi:10.1016/j.envres.2014.06.029

Marriboyina, V. (2018). *A Survey on Air Quality Forecasting Techniques*. Geneva: World Health orgaisation.

Oliveri Conti, G., Heibati, B., Kloog, I., Fiore, M., and Ferrante, M. (2017). A Review of AirQ Models and Their Applications for Forecasting the Air Pollution Health Outcomes. *Environ. Sci. Pollut. Res.* 24 (7), 6426–6445. doi:10.1007/s11356-016-8180-1

Omer, A. (2018). *LahoreSmog, Just How Bad Is it? [Online]*. Lahore, Pakistan. Available at: https://medium.com/https://medium.com/pakistan-air-quality-initiative/lahoresmog-just-how-bad-is-it-81c0623cdb02 (Accessed December 20, 2020).

Panda, R., and Maity, M. (2021). Global Warming and Climate Change on Earth: Duties and Challenges of Human Beings. *Int. J. Res. Eng. Sci. Management.* 4 (1), 122–125.

Reddy, G. T., Reddy, M. P. K., Lakshmanna, K., Kaluri, R., Rajput, D. S., Srivastava, G., et al. (2020). Analysis of Dimensionality Reduction Techniques on Big Data. *IEEE Access.* 8, 54776–54788. doi:10.1109/access.2020.2980942

Schuster, M., and Paliwal, K. K. (1997). Bidirectional Recurrent Neural Networks. *IEEE Trans. Signal. Process.* 45, 2673–2681. doi:10.1109/78.650093

Sharma, J., Parsai, K., Raghuwanshi, P., Ali, S. A., Tiwari, V., Bhargava, A., et al. (2021). Emerging Role of Mitochondria in Airborne Particulate Matter-Induced Immunotoxicity. *Environ. Pollut.* 270, 116242. doi:10.1016/j.envpol.2020.116242

Siami-Namini, S., Tavakoli, N., and Namin, A. S. (2019). "The Performance of LSTM and BiLSTM in Forecasting Time Series," in 2019 IEEE International Conference on Big Data (Big Data)), 3285–3292.

Sosa, B. S., Porta, A., Colman Lerner, J. E., Banda Noriega, R., and Massolo, L. (2017). Human Health Risk Due to Variations in PM 10 -PM 2.5 and Associated PAHs Levels. *Atmos. Environ.* 160, 27–35. doi:10.1016/j.atmosenv.2017.04.004

Sun, W., and Sun, J. (2017). Daily PM 2.5 Concentration Prediction Based on Principal Component Analysis and LSSVM Optimized by Cuckoo Search Algorithm. *J. Environ. Manage.* 188, 144–152. doi:10.1016/j.jenvman.2016.12.011

The World Air Quality Project (2020). Air Pollution in Guangzhou: Real-time Air Quality Index Visual Map. Available at: https://aqicn.org/map/guangzhou (Accessed December 15, 2020).

Walczak, B., and Massart, D. L. (2001). Dealing with Missing Data. *Chemometrics Intell. Lab. Syst.* 58 (1), 15–27. doi:10.1016/s0169-7439(01)00131-9

Wang, K., Tong, Y., Yue, T., Gao, J., Wang, C., Zuo, P., et al. (2021). Measure-Specific Environmental Benefits of Air Pollution Control for Coal-Fired Industrial Boilers in China from 2015 to 2017. *Environ. Pollut.* 273, 116470. doi:10.1016/j.envpol.2021.116470

Wise, B., and Ricker, N. (1991). "Recent Advances in Multivariate Statistical Process Control: Improving Robustness and Sensitivity," in Proceedings of the IFAC. ADCHEM Symposium: Citeseer, 125–130.

World Health Organization (2021). Air Pollution [Online]. Available at: https://www.who.int/health-topics/air-pollution (Accessed November 13, 2020).

Wu, J.-Z., Ge, D.-D., Zhou, L.-F., Hou, L.-Y., Zhou, Y., and Li, Q.-Y. (2018). Effects of Particulate Matter on Allergic Respiratory Diseases. *Chronic Dis. translational Med.* 4 (2), 95–102. doi:10.1016/j.cdtm.2018.04.001

Xing, Y. F., Xu, Y. H., Shi, M. H., and Lian, Y. X. (2016). The Impact of PM2.5 on the Human Respiratory System. *J. Thorac. Dis.* 8 (1), E69–E74. doi:10.3978/j.issn.2072-1439.2016.01.19

Zhang, L., Morisaki, H., Wei, Y., Li, Z., Yang, L., Zhou, Q., et al. (2019). Characteristics of Air Pollutants inside and Outside a Primary School Classroom in Beijing and Respiratory Health Impact on Children. *Environ. Pollut.* 255, 113147. doi:10.1016/j.envpol.2019.113147

Conflict of Interest: The authors declare that the research was conducted in the absence of any commercial or financial relationships that could be construed as a potential conflict of interest.

Publisher's Note: All claims expressed in this article are solely those of the authors and do not necessarily represent those of their affiliated organizations, or those of the publisher, the editors and the reviewers. Any product that may be evaluated in this article, or claim that may be made by its manufacturer, is not guaranteed or endorsed by the publisher.

frontiers in Environmental Science

ORIGINAL RESEARCH
published: 18 February 2022
doi: 10.3389/fenvs.2022.836191

Increasing but Variable Trend of Surface Ozone in the Yangtze River Delta Region of China

*Keqin Tang[1], Haoran Zhang[1], Weihang Feng[2], Hong Liao[1], Jianlin Hu[1] and Nan Li[1]**

[1]*Jiangsu Key Laboratory of Atmospheric Environment Monitoring and Pollution Control, Jiangsu Collaborative Innovation Center of Atmospheric Environment and Equipment Technology, School of Environmental Science and Engineering, Nanjing University of Information Science and Technology, Nanjing, China,* [2]*Institute for Atmospheric and Earth System Research, Faculty of Science, University of Helsinki, Helsinki, Finland*

Surface ozone (O_3) increased by ~20% in the Yangtze River Delta (YRD) region of China during 2014–2020, but the aggravating trend is highly variable on interannual time and city-level space scales. Here, we employed multiple air quality observations and numerical simulation to describe the increasing but variable trend of O_3 and to reveal the main driving factors behind it. In 2014–2017, the governmental air pollution control action plan was mostly against $PM_{2.5}$ (mainly to control the emissions of SO_2, NO_x, and primary $PM_{2.5}$) and effectively reduced the $PM_{2.5}$ concentration by 18%–45%. However, O_3 pollution worsened in the same period with an increasing rate of 4.9 $\mu g\, m^{-3}\, yr^{-1}$, especially in the Anhui province, where the growth rate even reached 14.7 $\mu g\, m^{-3}\, yr^{-1}$. After 2018, owing to the coordinated prevention and control of both $PM_{2.5}$ and O_3, volatile organic compound (VOC) emissions in the YRD region has also been controlled with a great concern, and the O_3 aggravating trend in the same period has been obviously alleviated (1.1 $\mu g\, m^{-3}\, yr^{-1}$). We further combined the precursor concentration and the corresponding O_3 formation regime to explain the observed trend of O_3 in 2014–2020. The leading O_3 formation regime in 2014–2017 is diagnosed as VOC-limited (21%) or mix-limited (58%), with the help of a simulated indicator $HCHO/NO_y$. Under such condition, the decreasing NO_2 (2.8% yr^{-1}) and increasing VOCs (3.6% yr^{-1}) in 2014–2017 led to a rapid increment of O_3. With the continuous reduction in NO_x emission and further in ambient NO_x/VOCs, the O_3 production regime along the Yangtze River has been shifting from VOC-limited to mix-limited, and after 2018, the mix-limited regime has become the dominant O_3 formation regime for 55% of the YRD cities. Consequently, the decreases of both NO_x (3.3% yr^{-1}) and VOCs (7.7% yr^{-1}) in 2018–2020 obviously slowed down the aggravating trend of O_3. Our study argues that with the implementation of coordinated regional reduction of NO_x and VOCs, an effective O_3 control is emerging in the YRD region.

Keywords: ozone, YRD region, NO_2, O_3 formation regime, WRF-Chem

OPEN ACCESS

Edited by:
Hongmei Xu,
Xi'an Jiaotong University, China

Reviewed by:
Chunlei Cheng,
Jinan University, China
Qingyan Fu,
Shanghai Environmental Monitoring Center, China

****Correspondence:***
Nan Li
linan@nuist.edu.cn

Specialty section:
This article was submitted to Atmosphere and Climate, a section of the journal Frontiers in Environmental Science

Received: *15 December 2021*
Accepted: *10 January 2022*
Published: *18 February 2022*

Citation:
Tang K, Zhang H, Feng W, Liao H, Hu J and Li N (2022) Increasing but Variable Trend of Surface Ozone in the Yangtze River Delta Region of China. Front. Environ. Sci. 10:836191. doi: 10.3389/fenvs.2022.836191

INTRODUCTION

Tropospheric ozone (O_3) is a critical secondary air pollutant featured with strong oxidation (Thompson, 1992), which is produced via complicated photochemical reactions with volatile organic compounds (VOCs) and nitrogen oxides (NO_x, x = 1 and 2) acting as its precursors (Seinfeld and Pandis, 2006; Wang et al., 2017). A high concentration of O_3 may degrade air quality and pose health risks to humans, such as respiratory illness and premature birth (Barry et al., 2019; Ekland et al., 2021; Guan et al., 2021). Moreover, a severe O_3 pollution episode leads to premature mortality as well. A rise of 10 $\mu g\ m^{-3}$ in O_3 concentration would increase mortality by 2% (Lei et al., 2019). For the ecosystem, O_3 can impair plant production by getting into leaves through stomata (Ainsworth et al., 2012). Agricultural yields are also negatively impacted by O_3 with losses ranging from 6% to 15% for wheat products in China (Feng et al., 2015). At the same time, as an oxidant, the elevated O_3 also promotes the formation of secondary aerosols (Chen et al., 2020b; Feng et al., 2021). For example, the enhanced O_3 and secondary aerosols induced an unexpected haze event in Beijing during the COVID-19 lockdown (Huang et al., 2020; Le et al., 2020).

In 2013, China implemented the Air Pollution Prevention and Control Action Plan (APPCAP), which includes a series of measures for alleviating the current air pollution with particular attention to fine particulate matter ($PM_{2.5}$). The $PM_{2.5}$ pollution was, thus, effectively controlled with more than 30% of nationwide $PM_{2.5}$ reduced by the end of 2018 (Zhai et al., 2019). At the same time, O_3 concentration indicated an inverse trend. The average maximum daily average 8-h O_3 at the 90th percentile (MDA8-90) in 74 major cities increased by 20% from 2013 to 2017 in China. Major causes for the aggravated O_3 are summarized as follows. First, a decrease in NO_x and increase in VOC emissions (Zheng et al., 2018) facilitated the nonlinear production of O_3 in urban areas that belong to VOC-limited (Wang et al., 2017; Li et al., 2019c; Liu and Wang, 2020b). Second, enhanced radiation intensity and increased HO_2 radicals caused by the reduced $PM_{2.5}$ also posed a nonnegligible influence on O_3 pollution (Li et al., 2019a). Besides this, the meteorologically driven variability also contributed to the increase of O_3 (Liu and Wang, 2020a; Dang et al., 2021). From 2013 to 2017, humidity and wind speed drove an annual increase of 2.3 ppbv in O_3 over the Yangtze River Delta (YRD) region (Li et al., 2019b).

The rapid increase of O_3 in China since 2013 has been confirmed by many observational and model studies (Shen et al., 2019; Zhai et al., 2019; Chen et al., 2020c; Shen et al., 2020; Liu et al., 2021; Mousavinezhad et al., 2021). However, the upward trend has significant differences in different regions and different periods. Chen et al. (2021) revealed that annual O_3 concentration was in continuous increase across the YRD region during 2014–2019 but rose in volatility in the Pearl River Delta (PRD) region over the same period. In addition, the increment of O_3 in the YRD region is more obvious with a rate of 3.2 ppbv yr^{-1} from 50.7 to 66.3 ppbv, which is approximately four times that in the PRD region.

In this study, we used multiple air quality observations in conjunction with a regional chemical model, weather research and forecasting coupled with chemistry (WRF-Chem) to analyze the O_3 pollution in the YRD region from 2014 to 2020 with the aim of exploring the interannual and regional variations of O_3 and understanding the chemical principles behind it. Our study differs from previous studies in that 1) we combined surface air quality and meteorology observations, satellite remote sensing observations, numerical model simulation and an indicator-based approach to uncover the increasing but variable pattern of O_3 in the YRD region, and 2) we further explored and compared the chemical mechanisms and driving factors in different regions and at different stages.

MATERIALS AND METHODS

Observation

We adopted air quality monitoring measurements from 2014 to 2020 over the YRD region (**Figure 1**). Data was derived from the public website of the Ministry of Ecology and Environment (MEE) of China (http://106.37.208.233:20035/). MEE provides hourly *in situ* measurements of six criteria air pollutants, including $PM_{2.5}$, PM_{10}, NO_2, O_3, SO_2, and CO. A total of 127 sites from 26 cities in the YRD region were utilized for further analyses. Descriptions for the monitoring sites and cities can be found in **Supplementary Table S1**; **Supplementary Figure S1**. It is noted that the number of surface observational sites established by MEE continuously increased since 2013. We selected these sites with complete records during 2014–2020 for analyzing. Meanwhile, for measurements of the gaseous pollutants after September 2018, we converted the mass concentration under reference state into that under standard state in advance (https://www.mee.gov.cn/xxgk2018/xxgk/xxgk01/201808/t20180815_629602.html).

Moreover, we also obtained the hourly meteorological observation, including surface temperature, relative humidity, and wind speed from the open-source website (https://q-weather.info/) for assessing the meteorological conditions in the YRD region. Four meteorological stations located at the provincial cities of the YRD region were collected, including Shanghai, Nanjing, Hangzhou, and Hefei. Illustration of the meteorological stations used in this study is given in **Supplementary Table S2**; **Supplementary Figure S1**.

The WRF-Chem Model

WRF-Chem (Grell et al., 2005) is a regional air quality model developed by the National Center for Atmospheric Research (NCAR), Pacific Northwest National Laboratory (PNNL), and the National Oceanic and Atmospheric Administration (NOAA) of the United States. We applied WRF-Chem (v3.9.1) to simulate the summertime O_3 in July over the YRD region from 2014 to 2020. Each month-long simulation was spinned up for the last 2 days of the previous month. Spatially, two nested domains are configured (**Figure 1**). The parent domain covers the eastern China (100 × 100 grid cells) with a horizontal resolution of 18 km. The nested domain,

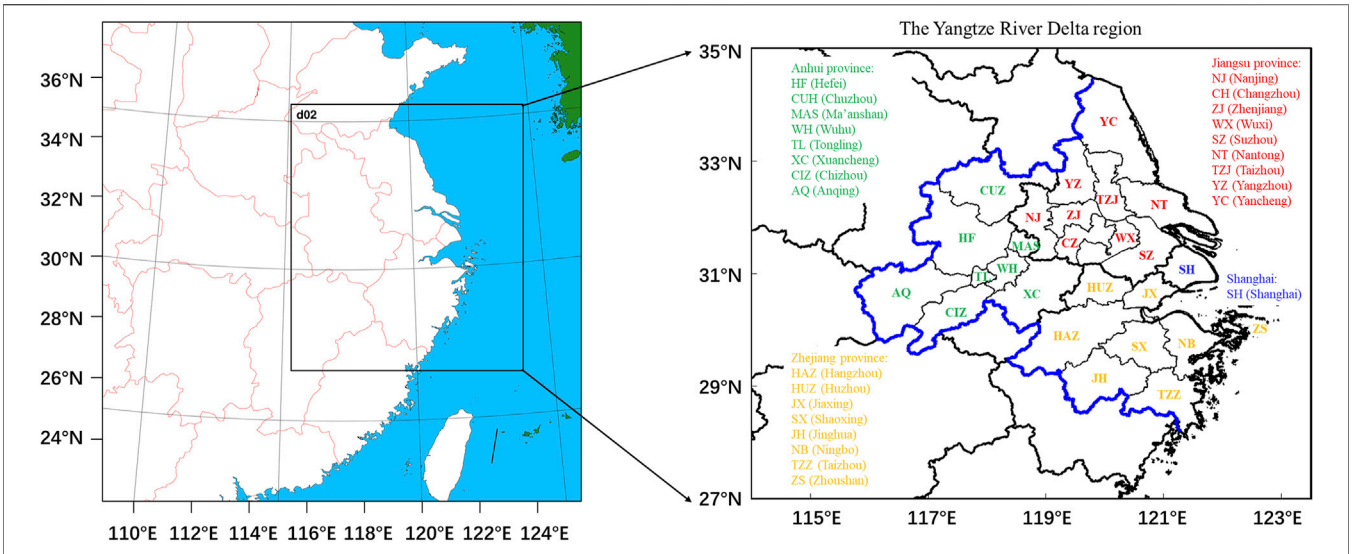

FIGURE 1 | Simulation domains of the WRF-Chem model used in this study (left). Right panel illustrates the YRD region as well as the locations of 26 cities in the YRD region. Names of the 26 cities are also labeled with colorful text in this panel.

whose horizontal resolution is 6 km, mainly includes the YRD region (145 × 166 grid cells). A total of 28 vertical layers extends from the ground to the height of 50 hPa. The bottom seven layers distribute below 1 km. The initial and boundary conditions of meteorological fields are determined by FNL reanalysis data sets by the National Centers for Environmental Prediction (NCEP) of the United States. Physical parameterization for describing subgrid processes, such as radiation, microphysics, and the surface layer are listed in **Supplementary Table S3**. For chemical species, the initial and boundary conditions are provided via the global chemical transport model MOZART (Emmons et al., 2010) and CAM-Chem (Emmons et al., 2020). Meanwhile, the Statewide Air Pollution Research Center (SAPRC99) mechanism is utilized for the gas phase reaction scheme in our study (Carter, 2000). For aerosols, we apply Model for Simulating Aerosol Interactions and Chemistry (MOSAIC) as the aerosol parameterization (Zaveri et al., 2008).

Multi-resolution Emission Inventory for China (MEIC) developed by Tsinghua University was adopted as the anthropogenic emission (Li et al., 2017). MEIC summarizes the 0.25° × 0.25° gridded emissions of SO_2, NO_x, CO, CO_2, NH_3, VOCs, EC, OC, $PM_{2.5}$, and PM_{10}. All species are categorized into five sectors, i.e., agriculture, industry, power, transportation, and residential activities. Online biogenic emissions were calculated by Model of Emissions of Gases and Aerosols from Nature (MEGAN, v2.0.4), which comprehensively took landcover, meteorology, and atmospheric chemical compositions into consideration (Guenther et al., 2006). Biomass burning emissions were provided by the Fire Inventory from NCAR (FINN). Combined with satellite retrieval constrains, FINN can generate high spatio-temporal resolution products of biomass burning emissions (Wiedinmyer et al., 2011).

TABLE 1 | Model performance in predicting meteorological parameters and air pollutants over the YRD region during the study period.

	Mean		IOA	MFB
	Simulation	Observation		
Meteorological parameter				
Temperature (K)	300.2	301.3	0.84	0%
Relative humidity (%)	79.5	79.1	0.85	1%
Wind speed ($m \cdot s^{-1}$)	3.1	2.9	0.64	9%
Air pollutant				
$PM_{2.5}$ ($\mu g \cdot m^{-3}$)	27.7	29.4	0.59	-17%
NO_2 (ppb)	14.4	12.6	0.62	12%
O_3 (ppb)	67.5	51.8	0.66	28%

O_3 Formation Regime

The ratio of formaldehyde (HCHO) to NO_y was utilized as the indicator (i.e., HCHO/NO_y) for diagnosing the formation regime of O_3 (Hu, 2021). In this indicator, HCHO can track the contribution of VOCs (Cao et al., 2018), which is a transient oxidation product of many VOCs and is positively correlated with peroxyl radicals. NO_y describes the impacts of multiple reactive nitrogenous compounds, including NO, NO_2, HONO, HNO_3, HO_2NO_2, N_2O_5, NO_3, peroxy acetyl nitrate (PAN), and other organic nitrates. Reactive nitrogen species play a central role in determining the levels of O_3 and hydroxyl radicals in the troposphere. In **Supplementary Figure S2**, NO_y is mainly concentrated in cities along the Yangtze River with 7.2 ppbv on average. Considering that photochemistry is the most active in the presence of abundant radiation, we, thus, investigated the O_3 formation regime from 12:00 to 16:00 (local time, UTC + 8). When HCHO/NO_y is less than 0.3, the O_3 formation regime is considered to be VOC-limited. NO_x controls O_3 production if the ratio is more than 0.72. Otherwise, it is expected to be under a mixed-limited condition, sensitive to changes both in NO_x and

VOCs. The threshold values were obtained by counting the distribution of the $HCHO/NO_y$ for different O_3 formation regimes in the YRD, which allow the $HCHO/NO_y$ sensitivity zone to be delineated in a way that is more consistent with the EKMA curve and accurately represents the sensitivity of O_3 to the precursors (Hu, 2021; Li, 2021).

MODEL EVALUATION

Reliable simulation of meteorological parameters and air pollutants could be the crucial premise for analyzing complicated causes of O_3 pollution. Comparisons between observation versus simulation are concluded in **Table 1**. To statistically quantify the model performance, we applied two following statistical metrics, i.e., index of agreement (IOA, varies from 0 to 1) and mean fractional bias (MFB, varies from −2 to 2). IOA and MFB are calculated based on **Eqs 1–2**, where *s, o*, and *N* represent simulation, observation, and the number of samples, respectively.

$$IOA = 1 - \frac{\sum_{i=1}^{N}(C_s - C_o)^2}{\sum_{i=1}^{N}\left(\left|C_s - \overline{C_o}\right| + \left|C_o - \overline{C_o}\right|\right)^2} \quad (1)$$

$$MFB = \frac{1}{N}\sum_{i=1}^{N}\frac{(C_o - C_m)}{\left(\frac{C_o + C_m}{2}\right)} \quad (2)$$

First, our model is capable of reproducing meteorological conditions, which is the key to simulate horizontal transportation, chemical transformation, and the removal of air pollutants. As shown in **Table 1**, the mean observed (simulated) temperature, relative humidity, and wind speed is averaged for 301.3 K (300.2 K), 79.1% (79.5%), and 2.9 m/s (3.1 m/s), respectively, in July from 2014 to 2020. Differences in terms of magnitudes between observation and simulation are quite small. All MFBs are less than 10% as well. IOAs for these meteorological parameters vary from 0.64 to 0.85, highlighting that our model has a good agreement with surface observations. The evaluation indicators of each city for each year can be found in the **Supplementary Table S4**. The city-level IOAs and MFBs varied in 0.6–0.9 and −0.1–0.3 except for the wind speed in 2016, which again confirmed the reasonable model performance.

Moreover, WRF-Chem reasonably reproduced the concentration levels of photochemical products. The mean observed summer O_3 and NO_2 concentrations are 51.8 and 12.6 ppbv averaged for 2014–2020. Simulations for these two species posed an overestimation by 28% and 12%, according to the hourly MFB index. Meanwhile, both hourly IOA values exceed 0.60, indicating that our model reasonably captures the temporal variations of O_3 and NO_2 as well. WRF-Chem also well simulates $PM_{2.5}$ with a predicted IOA of 0.59 as well as a MFB of −17%.

Supplementary Figures S3, S4 show scatterplots of simulations versus observations in daily MDA8 O_3 and NO_2 concentrations and their regression parameters in the 26 cities of the YRD region. The simulated O_3 demonstrates various model performance in different cities. The daily IOA of O_3 ranges from 0.55 (Hefei) to 0.83 (Shanghai) and the corresponding daily MFB poses a range from 13% (Shanghai) to 49% (Wuhu). Meanwhile, most of the fitted slopes of O_3 range from 0.9 to 1.3, further confirming that our model is reliable in reproducing concentrations of O_3. In addition, we verified the diurnal patterns of O_3 in all 26 cities of the YRD region as well. As shown in **Supplementary Figure S5**, both observation and simulation pose the same diurnal patterns with the peak O_3 concentration occurring between 12:00 and 16:00. The correlation coefficients (*R*) are more than 0.96, implying that diurnal variations of O_3 are successfully captured.

RESULTS AND DISCUSSION

Observed O_3 Pollution in the YRD Region From 2014 to 2020

We first analyzed the observed spatio-temporal variations of six air pollutants over the YRD region from 2014 to 2020. As illustrated in **Supplementary Figure S6**, regional mean O_3 concentration is 107.1 $\mu g\,m^{-3}$ in 2020, which increased by 18% compared with the concentration level in 2014. In contrast, concentrations of other five air pollutants sharply decreased over the study period. For example, the annual mean SO_2 shows a dramatic drop by 16.8 $\mu g\,m^{-3}$ from 2014 to 2020 with a relative reduction of 68%. At the same time, both $PM_{2.5}$ and PM_{10} concentrations are also reduced by more than 50%. It is precisely because of this decline that the dominant air pollutant in the YRD region has been changing from $PM_{2.5}$ to O_3. For NO_2, the variation trend generally showed a decrease with a rate of 0.8 $\mu g\,m^{-3}\ yr^{-1}$ even though an individual slight increase occurred in 2017. The changes of city-level pollutant concentrations are shown in **Supplementary Figure S7**. In addition, **Figure 2**; **Supplementary Figures S8–S12** show the frequency distribution of O_3, NO_2, $PM_{2.5}$, PM_{10}, CO, and SO_2 daily concentrations, respectively, which again emphasize that the concentration distribution of O_3 is changing from a low to a high value region while other pollutants show an opposite trend.

Based on the above analysis, we further find that the upward trend of O_3 is significantly different at different stages. In general, the increasing trend of O_3 concentration during 2014–2017 is more obvious in contrast to the years 2018–2020. Annual mean O_3 rapidly increased by 4.9 $\mu g\,m^{-3}\,yr^{-1}$ (5.5% yr^{-1}) during the period of 2014–2017, while in 2018–2019, the increasing trend slowed down, with the increase rate dropped to 1.1 $\mu g\,m^{-3}\,yr^{-1}$. Even in 2020, O_3 in many YRD cities has decreased by 0.1–14.3 $\mu g\,m^{-3}$ compared with 2019, mainly caused by the reduction of human activity and the more precipitation in 2020, especially in mobile sources and industry (Chen H. et al., 2020; Huang et al., 2021).

In addition, the upward trend of O_3 is also different in different regions of the YRD. As shown in **Figure 3**, the growth of O_3 in the Anhui Province is faster than that in other YRD regions. Especially during 2014–2017, the O_3 concentration in Anhui increased by a rate of 14.7 $\mu g\,m^{-3}\,yr^{-1}$—four times that in other provinces (i.e., Shanghai, Jiangsu, and Zhejiang, SJZ). Such trends can

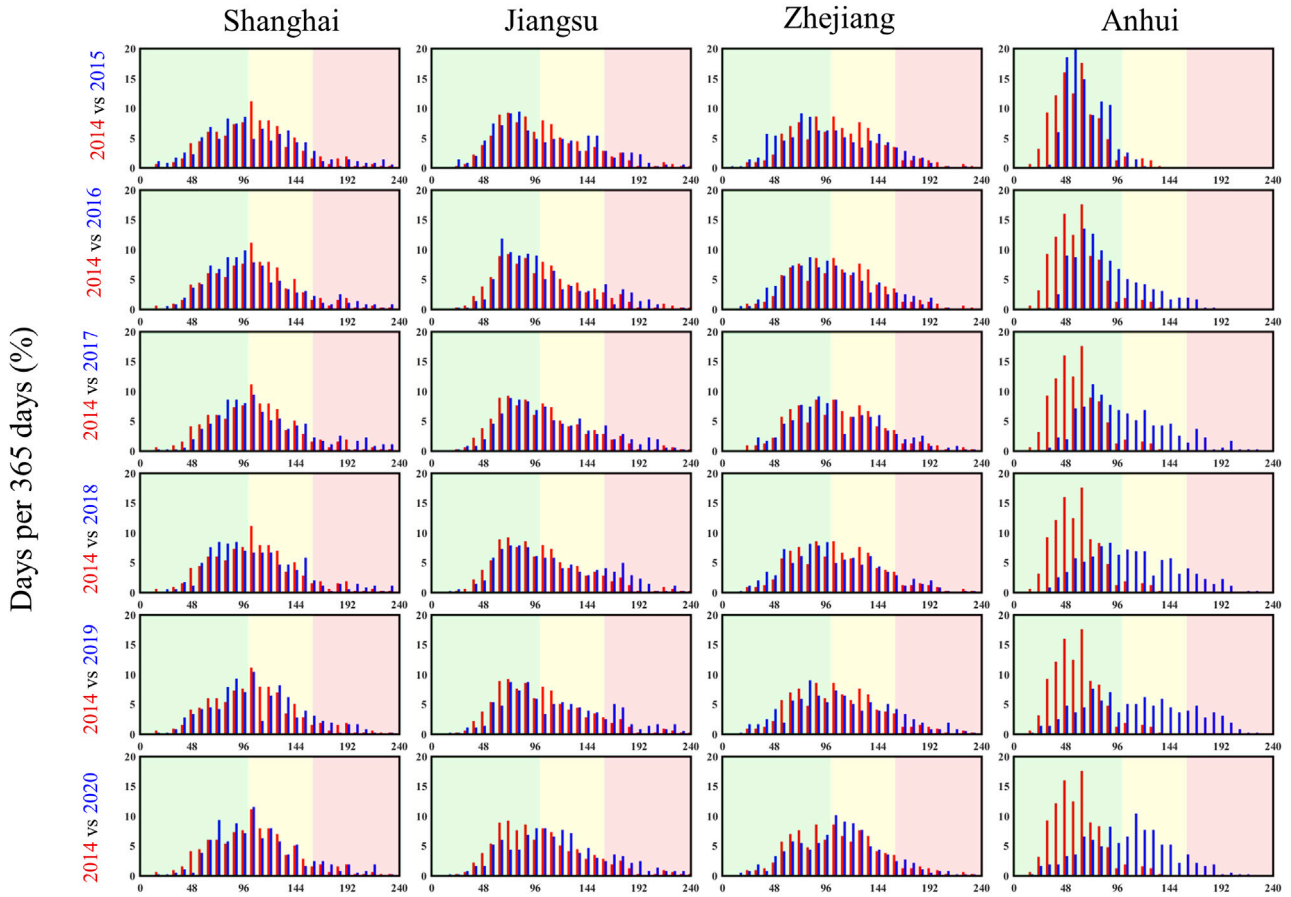

FIGURE 2 | Frequency distribution of the MDA8 O_3 concentration in the YRD region during the study period. Red bars represent the values of 2014. Blue bars indicate the values in the other year during 2015–2020. The colored shaded areas show different pollution levels according to the National Ambient Air Quality Standard of China.

also be observed on the city scale (**Supplementary Table S5**; **Supplementary Figure S7**). Hefei doubled its O_3 concentration between 2014 and 2017 while, in Shanghai, Nanjing, and Hangzhou, the increase was 9.7%–14.3%. To highlight the distinctive variation of O_3 in Anhui, we further compared the frequency distributions of O_3 in Anhui with that in other regions from 2014 to 2020 (**Figure 2**). In 2014, the O_3 concentration in Anhui was mostly concentrated around 50 μg m^{-3} while the city-level O_3 concentration in SJZ distributed in a range of 14.8–256.7 μg m^{-3}, and the average value was 80% higher than that in Anhui. However, after 2014, the O_3 in Anhui prominently increased with the frequency distribution rapidly moved to the high value scope (central at ~70 μg m^{-3}), and by 2018, it was close to other regions of YRD.

Driving Factors of Interannual Changes in O_3 From 2014 to 2020

We analyze the interannual variation of O_3 in the YRD region from 2014 to 2020 through two factors. One is the O_3 formation regime, and the other is the precursor (NO_x and VOCs) concentrations. The dual role of NO_x in O_3 generation results in the variation of O_3 formation regime. NO_x can either promote O_3 production through photochemical reactions with atomic oxygen (O), O_2, or mitigate O_3 formation by removing OH from the oxidation cycle. At the same time, ambient radical budget and weather conditions can also affect the O_3 generation regime (Li et al., 2019b; Liu and Wang, 2020a; Lin et al., 2020; Wang et al., 2020).

We employed $HCHO/NO_y$ as an indicator to diagnose the formation regime of O_3. **Figure 4** shows the spatial distributions of the indicator over the YRD region simulated by WRF-Chem. The surrounding areas of the Yangtze River (purple line) are mostly under VOC-limited, mainly due to the abundant NO_x emissions from industrial and shipping activities (An et al., 2021). In contrast, the south regions of YRD demonstrate a universal pattern of NO_x-limited. This could be attributed to the substantial biogenic VOCs emissions from the forest districts in Zhejiang province (Cao et al., 2021). Other YRD regions are mainly controlled by both NO_x and VOCs.

To better understand the fate of O_3 formation regime, we primarily explore the emission characteristics of NO_x and VOCs during this period. As shown in **Figure 5**, the NO_x emission over the YRD region was continuously reduced by a rate of 3.5% yr^{-1}

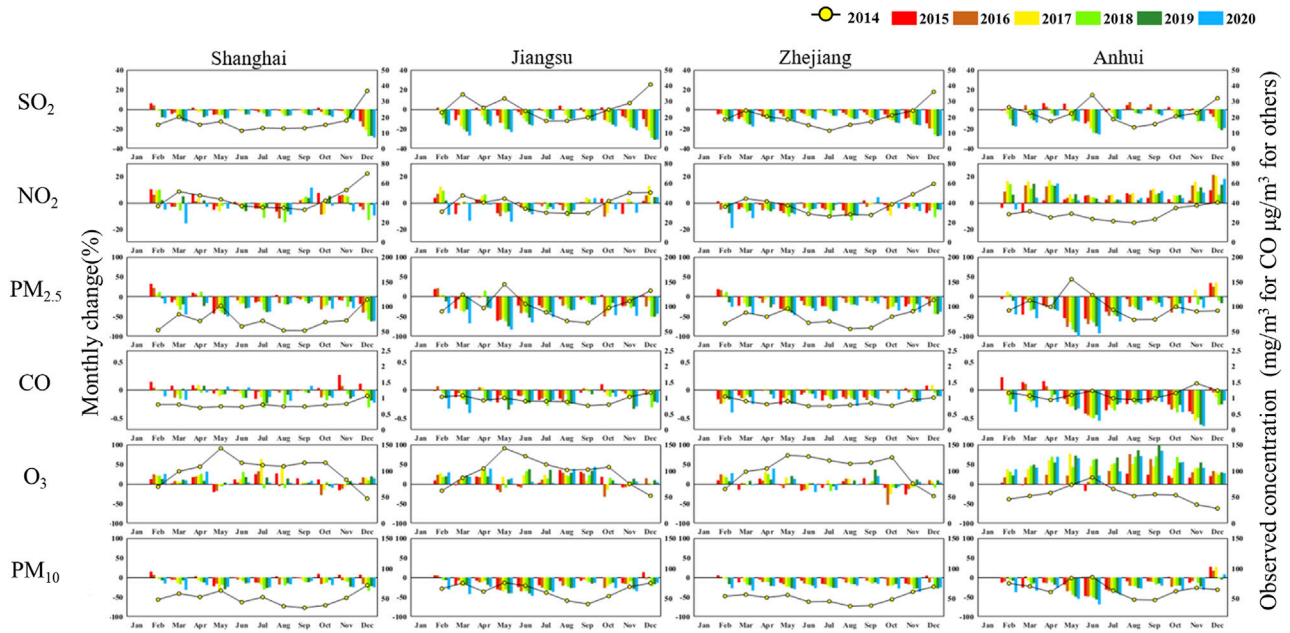

FIGURE 3 | Monthly variations of SO_2, NO_2, $PM_{2.5}$, CO, O_3, and PM_{10} concentrations over the YRD region in 2014 (filled dots). Also shown are the differences between 2014 and each of 2015–2020 (bars).

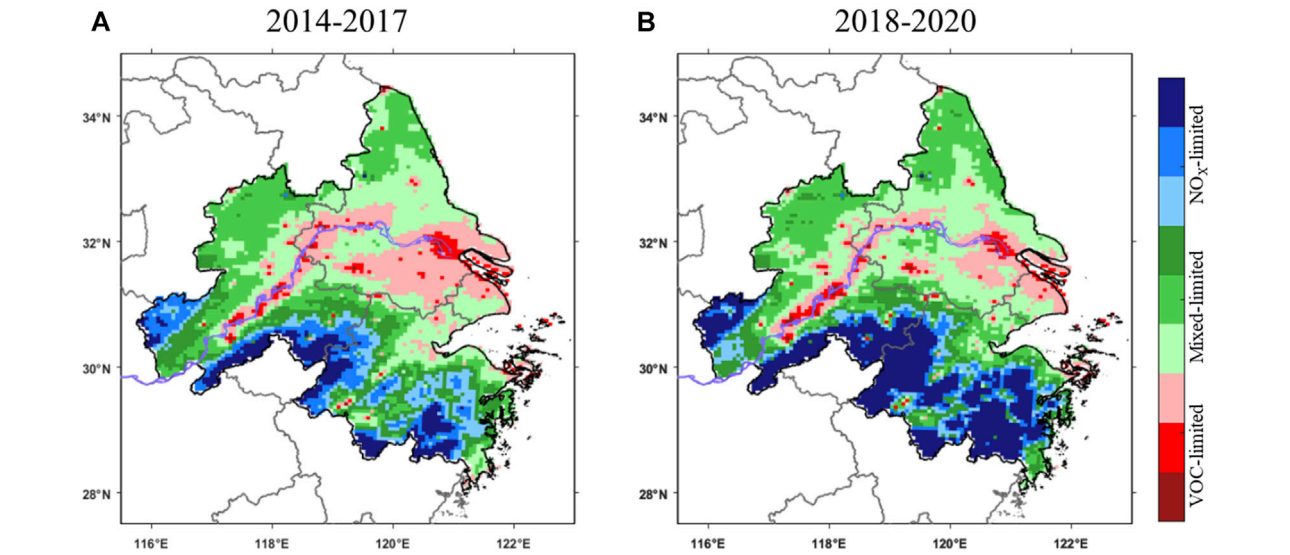

FIGURE 4 | Spatial distribution of the indicator ($HCHO/NO_y$) for diagnosing the O_3 formation regime over the YRD region in the summertime. **(A)** indicates 2014–2017, and **(B)** indicates 2018–2020. Red, green, and blue shaded areas represent VOC-limited, mix-limited, and NO_x-limited condition, respectively.

from 2014 to 2020, which was largely benefited from the APPCAP (http://www.gov.cn/zwgk/2013-09/12/content_2486773.htm). Unprecedented emission reductions due to COVID-19 in 2020 also enhance this trend (Wang G. et al., 2021; Li et al., 2021b; Hu et al., 2021).

However, during 2014 and 2017, the VOC emissions in the YRD region were not effectively controlled and even increased by 0.8% yr^{-1}. After 2018, with the implementation of strict VOC control (http://www.gov.cn/zhengce/content/2018-07/03/content_5303158.htm), VOC emissions began to decline, and in 2020, the VOC emissions in the YRD region dropped by 15.4% compared with the highest level in 2017. The decline in aromatics propene/ethene emission from the petrochemical industry as well as gasoline evaporation and vehicular emissions is the main

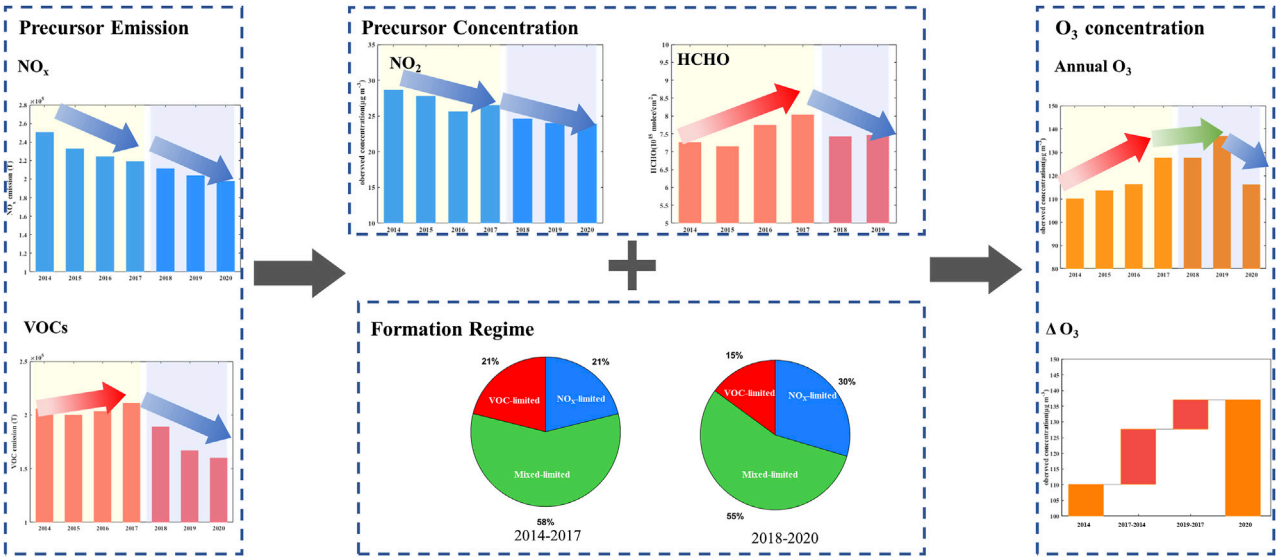

FIGURE 5 | The schematic diagram for illustrating changes of precursor emissions and concentrations, O_3 formation regime and O_3 concentration over the YRD region during the study period.

component of the reduction of VOCs emissions in 2020 (Wang M. et al., 2021; Qi et al., 2021). The distribution of emission variation also reveals similar trends with the whole region (**Supplementary Figure S13**). Emissions of NO_x in 2018–2020 decreased by 17.7%–50.8% compared to 2014–2017 in most regions of the YRD. VOCs emissions for 87.8% of YRD areas are reduced in 2018–2020 relative to 2014–2017.

With the changes in NO_x and VOCs emissions, the O_3 formation regime has also changed in response. In 2014–2017, most cities along the Yangtze River are in VOC-limited areas, and other regions are mainly under mix-limited except for the forested areas in southern Zhejiang. Since 2018, the original VOC-limited region has shifted to mix-limited (36%). It should be noted that there are still 15% areas controlled by VOC-limited over the YRD region.

In addition, the concentrations of NO_x and VOCs in the YRD region show a consistent trend as their emissions. As shown in **Figure 5**, the NO_2 concentration clearly demonstrates a continuous decreasing trend over the YRD region during 2014–2020. In term of VOCs, we employed the column density of HCHO via satellite retrievals to represent the interannual variations of VOCs (Li R. et al., 2021). The column density of HCHO shows an inverted "U" shape, which increases from 7.2×10^{15} molec cm^2 (2014) to 8.0×10^{15} molec·cm^2 (2017) and then drops to 7.4×10^{15} molec cm^2 (2020).

As a result of the changes of both O_3 formation regime and precursor concentrations, the O_3 concentration in the YRD region shows an increasing but variable trend during 2014–2020. Between 2014–2017, the declined NO_2 and the elevated VOCs, under the VOC-limited and mix-limited O_3 formation regime, led to a rapid increase of O_3. However, when it comes to 2018–2020, the VOCs began to slowly decline, and meanwhile, the formation regime shifted to more mix-limited so that the upward trend of O_3 has obviously slowed down and even appeared as a downward trend in 2020.

Explanation for Distinctive Variation of O_3 in Anhui

The main reason of the rapid growth of O_3 in Anhui, which is different from that in other regions, is the distinctive growth of NO_x during 2014–2017. The NO_2 in Anhui elevated with a rate of 2 μg m^{-3} yr^{-1} while, in other YRD regions, it posed a remarkable decline of 1.1 μg m^{-3} yr^{-1}. At the same time, the O_3 formation regime in Anhui was mostly controlled by NO_x-limited (24%) or mix-limited conditions (65%). It is also different from other YRD regions where more than 27% areas were controlled by VOC-limited condition. The ambient non-VOC-limited condition is conducive to generation of O_3 when NO_2 increases, via enhancing the "NO_x cycle" (Wang et al., 2017). In addition, the VOCs concentration in Anhui also increased in 2014–2017, which had not yet received much attention over the early stage. It intensified the O_3 production as well. Since 2018, the concentration of O_3 in Anhui (130.6 μg m^{-3}) reached the same level as other regions (122.9 μg m^{-3}).

DISCUSSION

Though the emission control strategy since 2018 is effective for slowing down the worsening O_3 pollution over the YRD region, there is still a long way to go to see continuous decline in O_3 concentration. Meanwhile, previous studies point out that the O_3 formation regime in other Chinese city clusters, such as the north China plain and PRD, are dominated by VOC-limited and changes toward mix-limited (Jiang et al., 2018; Wang et al.,

2019). To address this issue, a more efficient synergistic measure should be taken to control both NO_x and VOCs (Li et al., 2019c; Huang et al., 2020). O_3 concentration can be quickly reduced with a reasonable reduction ratio between these two precursors according to its nonlinear formation regime. In addition, it is also complicated to conduct the reduction of VOCs emissions. A comprehensive source apportionment for detailed VOCs speciation is necessary for planning better control policies (Wu and Xie, 2017).

Meanwhile, the mitigation of O_3 that is focused on other seasons except for summertime is also proved to be meaningful. Previous case studies of air quality, such as research during COVID-19 or summit exhibited that O_3 could increase resulting from the weakened titration of NO_x due to the reduction of its emissions (Le et al., 2020; Li K. et al., 2021; Zhang et al., 2021b). The elevated O_3 further facilitated the production of secondary aerosols and even led to haze events (Chang et al., 2020; Zhang et al., 2021a; Wang N. et al., 2021). Thus, controlling O_3 concentration during other nonwarm seasons also helps to eliminate the negative environmental impacts by O_3 and $PM_{2.5}$.

CONCLUSION

In this study, we employed multiple air quality observations and WRF-Chem simulation to describe the increasing but variable trend of O_3 concentration in the YRD region from 2014 to 2020, and further revealed the main factors that caused such trends. During the period of 2014–2020, the annual average O_3 concentration in the YRD region was 101 $\mu g\,m^{-3}$ with an increase from 93.4 $\mu g\,m^{-3}$ in 2014 to 107 $\mu g\,m^{-3}$ in 2020. The increase rate was 4.9 $\mu g\,m^{-3}\,yr^{-1}$ in the first 4 years, which was four times higher than that in 2018–2020. It should be noted that the O_3 concentration in Anhui significantly increased by 44.1 $\mu g\,m^{-3}$ during 2014–2017, twofold higher than that in the YRD region (13.0 $\mu g\,m^{-3}$). Since 2018, both Anhui and other regions in the YRD slowed down their increase in O_3.

We further analyzed the two main factors driving the interannual variation of O_3 in the YRD region, including precursor concentrations and the corresponding O_3 formation regime. With the help of the indicator $HCHO/NO_y$ simulated by WRF-Chem, we concluded that the O_3 production regime along the Yangtze River has shifted from VOC-limited to mix-limited. In 2014–2017, most cities along the Yangtze River were in VOC-limited areas, and other regions were mainly under mix-limited. After 2018, 36% areas that belong to the VOC-limited condition shifted to a mix-limited condition. Therefore, the alleviative NO_x and elevated VOCs under a VOC- and mix-limited O_3 formation regime generally contributed to the cumulative rise in O_3 concentration. However, since 2018, the drop of both precursors under the mix-limited O_3 formation regime alleviated the worsening O_3 pollution. Our work is of importance to understand the current O_3 pollution in a megacity cluster of China and offers an investigative insight for further alleviating O_3 pollution in the future.

DATA AVAILABILITY STATEMENT

The original contributions presented in the study are included in the article/**Supplementary Material**, further inquiries can be directed to the corresponding author.

AUTHOR CONTRIBUTIONS

Data curation, model simulation, visualization, and writing-original draft preparation, KT and HZ; Supervision, funding acquisition, writing-review and editing, NL, HL, and JH; Data curation, WF. All authors have read and agreed to the published version of the manuscript.

FUNDING

This work was supported by the National Key Research and Development Program of China (2019YFA0606804), the National Natural Science Foundation of China (41975171), the Major Research Plan of the National Social Science Foundation (18ZDA052).

SUPPLEMENTARY MATERIAL

The Supplementary Material for this article can be found online at: https://www.frontiersin.org/articles/10.3389/fenvs.2022.836191/full#supplementary-material

REFERENCES

Ainsworth, E. A., Yendrek, C. R., Sitch, S., Collins, W. J., and Emberson, L. D. (2012). The Effects of Tropospheric Ozone on Net Primary Productivity and Implications for Climate Change. *Annu. Rev. Plant Biol.* 63, 637–661. doi:10.1146/annurev-arplant-042110-103829

An, J., Huang, Y., Huang, C., Wang, X., Yan, R., Wang, Q., et al. (2021). Emission Inventory of Air Pollutants and Chemical Speciation for Specific Anthropogenic Sources Based on Local Measurements in the Yangtze River Delta Region, China. *Atmos. Chem. Phys.* 21 (3), 2003–2025. doi:10.5194/acp-21-2003-2021

Barry, V., Klein, M., Winquist, A., Chang, H. H., Mulholland, J. A., Talbott, E. O., et al. (2019). Characterization of the Concentration-Response Curve for Ambient Ozone and Acute Respiratory Morbidity in 5 US Cities. *J. Expo. Sci. Environ. Epidemiol.* 29 (2), 267–277. doi:10.1038/s41370-018-0048-7

Cao, H., Fu, T.-M., Zhang, L., Henze, D., Miller, C., Lerot, C., et al. (2018). Adjoint Inversion of Chinese Non-methane Volatile Organic Compound Emissions Using Space-Based Observations of Formaldehyde and Glyoxal. *Atmos. Chem. Phys. Discuss.* 18, 1–46. doi:10.5194/acp-2017-1136

Cao, J., Situ, S., Hao, Y., Xie, S., and Li, L. (2021). Enhanced Summertime Ozone and SOA from Biogenic Volatile Organic Compound (BVOC) Emissions Due to Vegetation Biomass Variability during 1981–2018 in China. *Atmos. Chem. Phys. Discuss.* 2021, 1–21. doi:10.5194/acp-2021-675

Carter, W. P. L. (2000). *Documentation of the SAPRC-99 Chemical Mechanism for VOC Reactivity Assessment*. California: University of California Riverside. Report to the California Air Resources Board, Contract 92-329. 95-308.

Chang, Y., Huang, R. J., Ge, X., Huang, X., Hu, J., Duan, Y., et al. (2020). Puzzling Haze Events in China during the Coronavirus (COVID-19) Shutdown. *Geophys. Res. Lett.* 47, e2020GL088533. doi:10.1029/2020GL088533

Chen, H., Huo, J., Fu, Q., Duan, Y., Xiao, H., and Chen, J. (2020a). Impact of Quarantine Measures on Chemical Compositions of PM2.5 during the COVID-19 Epidemic in Shanghai, China. *Sci. Total Environ.* 743, 140758. doi:10.1016/j.scitotenv.2020.140758

Chen, L., Xing, J., Mathur, R., Liu, S., Wang, S., and Hao, J. (2020b). Quantification of the Enhancement of PM2.5 Concentration by the Downward Transport of Ozone from the Stratosphere. *Chemosphere* 255, 126907. doi:10.1016/j.chemosphere.2020.126907

Chen, L., Zhu, J., Liao, H., Yang, Y., and Yue, X. (2020c). Meteorological Influences on PM2.5 and O3 Trends and Associated Health burden since China's Clean Air Actions. *Sci. Total Environ.* 744, 140837. doi:10.1016/j.scitotenv.2020.140837

Chen, X., Jiang, Z., Shen, Y., Li, R., Fu, Y., Liu, J., et al. (2021). Chinese Regulations Are Working—Why Is Surface Ozone over Industrialized Areas Still High? Applying Lessons from Northeast US Air Quality Evolution. *Geophys. Res. Lett.* 48 (14), e2021GL092816. doi:10.1029/2021gl092816

Dang, R., Liao, H., and Fu, Y. (2021). Quantifying the Anthropogenic and Meteorological Influences on Summertime Surface Ozone in China over 2012-2017. *Sci. Total Environ.* 754, 142394. doi:10.1016/j.scitotenv.2020.142394

Ekland, J., Olsson, D., Forsberg, B., Andersson, C., and Orru, H. (2021). The Effect of Current and Future Maternal Exposure to Near-Surface Ozone on Preterm Birth in 30 European Countries—An EU-wide Health Impact Assessment. *Environ. Res. Lett.* 16 (5). doi:10.1088/1748-9326/abe6c4

Emmons, L. K., Schwantes, R. H., Orlando, J. J., Tyndall, G., Kinnison, D., Lamarque, J.-F., et al. (2020). The Chemistry Mechanism in the Community Earth System Model Version 2 (CESM2). *J. Adv. Model. Earth Syst.* 12 (4), e2019MS001882. doi:10.1029/2019MS001882

Emmons, L. K., Walters, S., Hess, P. G., Lamarque, J. F., Pfister, G. G., Fillmore, D., et al. (2010). Description and Evaluation of the Model for Ozone and Related Chemical Tracers, Version 4 (MOZART-4). *Geosci. Model. Dev.* 3 (1), 43–67. doi:10.5194/gmd-3-43-2010

Feng, T., Zhao, S., Bei, N., Liu, S., and Li, G. (2021). Increasing Atmospheric Oxidizing Capacity Weakens Emission Mitigation Effort in Beijing during Autumn Haze Events. *Chemosphere* 281, 130855. doi:10.1016/j.chemosphere.2021.130855

Feng, Z., Hu, E., Wang, X., Jiang, L., and Liu, X. (2015). Ground-level O3 Pollution and its Impacts on Food Crops in China: a Review. *Environ. Pollut.* 199, 42–48. doi:10.1016/j.envpol.2015.01.016

Grell, G. A., Peckham, S. E., Schmitz, R., McKeen, S. A., Frost, G., Skamarock, W. C., et al. (2005). Fully Coupled "Online" Chemistry within the WRF Model. *Atmos. Environ.* 39 (37), 6957–6975. doi:10.1016/j.atmosenv.2005.04.027

Guan, Y., Xiao, Y., Wang, F., Qiu, X., and Zhang, N. (2021). Health Impacts Attributable to Ambient PM2.5 and Ozone Pollution in Major Chinese Cities at Seasonal-Level. *J. Clean. Prod.* 311, 127510. doi:10.1016/j.jclepro.2021.127510

Guenther, A., Karl, T., Harley, P., Wiedinmyer, C., Palmer, P. I., and Geron, C. (2006). Estimates of Global Terrestrial Isoprene Emissions Using MEGAN (Model of Emissions of Gases and Aerosols from Nature). *Atmos. Chem. Phys.* 6 (11), 3181–3210. doi:10.5194/acp-6-3181-2006

Hu, J. (2021). "Exploring the Applicability of Indicators for Determining Ozone Sensitivity (In Chinese)," in *The 3rd Workshop on Atmospheric Ozone Pollution Prevention and Control in China* (Shanghai, China: Chinese Society For Environmental Sciences).

Hu, X., Liu, Q., Fu, Q., Xu, H., Shen, Y., Liu, D., et al. (2021). A High-Resolution Typical Pollution Source Emission Inventory and Pollution Source Changes during the COVID-19 Lockdown in a Megacity, China. *Environ. Sci. Pollut. Res. Int.* 28 (33), 45344–45352. doi:10.1007/s11356-020-11858-x

Huang, C., An, J., Wang, H., Liu, Q., Tian, J., Wang, Q., et al. (2021). Highly Resolved Dynamic Emissions of Air Pollutants and Greenhouse Gas CO2 during COVID-19 Pandemic in East China. *Environ. Sci. Technology Lett.* 8 (10), 853–860. doi:10.1021/acs.estlett.1c00600

Huang, X., Ding, A., Gao, J., Zheng, B., Zhou, D., Qi, X., et al. (2020). Enhanced Secondary Pollution Offset Reduction of Primary Emissions during COVID-19 Lockdown in China. *Natl. Sci. Rev.* 8 (2), nwaa137. doi:10.1093/nsr/nwaa137

Jiang, M., Lu, K., Su, R., Tan, Z., Wang, H., Li, L., et al. (2018). Ozone Formation and Key VOCs in Typical Chinese City Clusters. *Chin. Sci. Bull.* 63 (12), 1130–1141. doi:10.1360/n972017-01241

Le, T., Wang, Y., Liu, L., Yang, J., Yung, Y. L., Li, G., et al. (2020). Unexpected Air Pollution with Marked Emission Reductions during the COVID-19 Outbreak in China. *Science* 369 (6504), 702–706. doi:10.1126/science.abb7431

Lei, R., Zhu, F., Cheng, H., Liu, J., Shen, C., Zhang, C., et al. (2019). Short-term Effect of PM2.5/O3 on Non-accidental and Respiratory Deaths in Highly Polluted Area of China. *Atmos. Pollut. Res.* 10 (5), 1412–1419. doi:10.1016/j.apr.2019.03.013

Li, K., Jacob, D. J., Liao, H., Qiu, Y., Shen, L., Zhai, S., et al. (2021a). Ozone Pollution in the North China Plain Spreading into the Late-winter Haze Season. *Proc. Natl. Acad. Sci. U S A.* 118 (10), e2015797118. doi:10.1073/pnas.2015797118

Li, K., Jacob, D. J., Liao, H., Shen, L., Zhang, Q., and Bates, K. H. (2019a). Anthropogenic Drivers of 2013-2017 Trends in Summer Surface Ozone in China. *Proc. Natl. Acad. Sci.* 116 (2), 422–427. doi:10.1073/pnas.1812168116

Li, K., Jacob, D. J., Liao, H., Shen, L., Zhang, Q., and Bates, K. H. (2019b). Anthropogenic Drivers of 2013-2017 Trends in Summer Surface Ozone in China. *Proc. Natl. Acad. Sci. U S A.* 116 (2), 422–427. doi:10.1073/pnas.1812168116

Li, K., Jacob, D. J., Liao, H., Zhu, J., Shah, V., Shen, L., et al. (2019c). A Two-Pollutant Strategy for Improving Ozone and Particulate Air Quality in China. *Nat. Geosci.* 12, 906–910. doi:10.1038/s41561-019-0464-x

Li, M., Wang, T., Xie, M., Li, S., Zhuang, B., Fu, Q., et al. (2021b1994). Drivers for the Poor Air Quality Conditions in North China Plain during the COVID-19 Outbreak. *Atmos. Environ.* 246, 118103. doi:10.1016/j.atmosenv.2020.118103

Li, M., Zhang, Q., Kurokawa, J. I., Woo, J. H., He, K., Lu, Z., et al. (2017). MIX: a Mosaic Asian Anthropogenic Emission Inventory under the International Collaboration Framework of the MICS-Asia and HTAP. *Atmos. Chem. Phys.* 17 (2), 935–963. doi:10.5194/acp-17-935-2017

Li, R., Xu, M., Li, M., Chen, Z., Zhao, N., Gao, B., et al. (2021c). Identifying the Spatiotemporal Variations in Ozone Formation Regimes across China from 2005 to 2019 Based on Polynomial Simulation and Causality Analysis. *Atmos. Chem. Phys.* 21 (20), 15631–15646. doi:10.5194/acp-21-15631-2021

Li, X. (2021). *Research On the Applicability of Ozone Sensitivity Determination Indicators in Jiangsu. Master*. Nanjing: Nanjing University of Information Science & Technology.

Lin, H., Wang, M., Duan, Y., Fu, Q., Ji, W., Cui, H., et al. (2020). O3 Sensitivity and Contributions of Different NMHC Sources in O3 Formation at Urban and Suburban Sites in Shanghai. *Atmosphere* 11 (3), 295. doi:10.3390/atmos11030295

Liu, H., Liu, J., Liu, Y., Yi, K., Yang, H., Xiang, S., et al. (2021). Spatiotemporal Variability and Driving Factors of Ground-Level Summertime Ozone Pollution over Eastern China. *Atmos. Environ.* 265, 118686. doi:10.1016/j.atmosenv.2021.118686

Liu, Y., and Wang, T. (2020a). Worsening Urban Ozone Pollution in China from 2013 to 2017 – Part 1: The Complex and Varying Roles of Meteorology. *Atmos. Chem. Phys.* 20 (11), 6305–6321. doi:10.5194/acp-20-6305-2020

Liu, Y., and Wang, T. (2020b). Worsening Urban Ozone Pollution in China from 2013 to 2017 – Part 2: The Effects of Emission Changes and Implications for Multi-Pollutant Control. *Atmos. Chem. Phys.* 20 (11), 6323–6337. doi:10.5194/acp-20-6323-2020

Mousavinezhad, S., Choi, Y., Pouyaei, A., Ghahremanloo, M., and Nelson, D. L. (2021). A Comprehensive Investigation of Surface Ozone Pollution in China, 2015–2019: Separating the Contributions from Meteorology and Precursor Emissions. *Atmos. Res.* 257, 105599. doi:10.1016/j.atmosres.2021.105599

Qi, J., Mo, Z., Yuan, B., Huang, S., Huangfu, Y., Wang, Z., et al. (2021). An Observation Approach in Evaluation of Ozone Production to Precursor Changes during the COVID-19 Lockdown. *Atmos. Environ.* 262, 118618. doi:10.1016/j.atmosenv.2021.118618

Seinfeld, J. H., and Pandis, S. N. (2006). *Atmospheric Chemistry and Physics: From Air Pollution to Climate Change*. Third edition. New York: John Wiley.

Shen, F., Zhang, L., Jiang, L., Tang, M., Gai, X., Chen, M., et al. (2020). Temporal Variations of Six Ambient Criteria Air Pollutants from 2015 to 2018, Their Spatial Distributions, Health Risks and Relationships with Socioeconomic Factors during 2018 in China. *Environ. Int.* 137, 105556. doi:10.1016/j.envint.2020.105556

Shen, L., Jacob, D. J., Liu, X., Huang, G., Li, K., Liao, H., et al. (2019). An Evaluation of the Ability of the Ozone Monitoring Instrument (OMI) to Observe Boundary Layer Ozone Pollution across China: Application to 2005–2017 Ozone Trends. *Atmos. Chem. Phys.* 19 (9), 6551–6560. doi:10.5194/acp-19-6551-2019

Thompson, A. M. (1992). The Oxidizing Capacity of the Earth's Atmosphere: Probable Past and Future Changes. *Science* 256 (5060), 1157–1165. doi:10.1126/science.256.5060.1157

Wang, G., Huang, K., Fu, Q., Chen, J., Huo, J., Zhao, Q., et al. (2021a). Response of PM2.5-bound Elemental Species to Emission Variations and Associated Health Risk Assessment during the COVID-19 Pandemic in a Coastal Megacity. *J. Environ. Sci.* 122, 115–127. doi:10.1016/j.jes.2021.10.005

Wang, G., Jia, S., Li, R., Ma, S., Chen, X., Wu, Z., et al. (2020). Seasonal Variation Characteristics of Hydroxyl Radical Pollution and its Potential Formation Mechanism during the Daytime in Lanzhou. *J. Environ. Sci.* 95, 58–64. doi:10.1016/j.jes.2020.03.045

Wang, M., Lu, S., Shao, M., Zeng, L., Zheng, J., Xie, F., et al. (2021b). Impact of COVID-19 Lockdown on Ambient Levels and Sources of Volatile Organic Compounds (VOCs) in Nanjing, China. *Sci. Total Environ.* 757, 143823. doi:10.1016/j.scitotenv.2020.143823

Wang, N., Lyu, X., Deng, X., Huang, X., Jiang, F., and Ding, A. (2019). Aggravating O3 Pollution Due to NOx Emission Control in Eastern China. *Sci. Total Environ.* 677, 732–744. doi:10.1016/j.scitotenv.2019.04.388

Wang, N., Xu, J., Pei, C., Tang, R., Zhou, D., Chen, Y., et al. (2021c). Air Quality during COVID-19 Lockdown in the Yangtze River Delta and the Pearl River Delta: Two Different Responsive Mechanisms to Emission Reductions in China. *Environ. Sci. Technol.* 55 (9), 5721–5730. doi:10.1021/acs.est.0c08383

Wang, T., Xue, L., Brimblecombe, P., Lam, Y. F., Li, L., and Zhang, L. (2017). Ozone Pollution in China: A Review of Concentrations, Meteorological Influences, Chemical Precursors, and Effects. *Sci. Total Environ.* 575, 1582–1596. doi:10.1016/j.scitotenv.2016.10.081

Wiedinmyer, C., Akagi, S. K., Yokelson, R. J., Emmons, L. K., Al-Saadi, J. A., Orlando, J. J., et al. (2011). The Fire INventory from NCAR (FINN): a High Resolution Global Model to Estimate the Emissions from Open Burning. *Geoscientific Model. Development* 4 (3), 625–641. doi:10.5194/gmd-4-625-2011

Wu, R., and Xie, S. (2017). Spatial Distribution of Ozone Formation in China Derived from Emissions of Speciated Volatile Organic Compounds. *Environ. Sci. Technol.* 51 (5), 2574–2583. doi:10.1021/acs.est.6b03634

Zaveri, R. A., Easter, R. C., Fast, J. D., and Peters, L. K. (2008). Model for Simulating Aerosol Interactions and Chemistry (MOSAIC). *J. Geophys. Res.* 113 (D13). doi:10.1029/2007jd008782

Zhai, S., Jacob, D. J., Wang, X., Shen, L., Li, K., Zhang, Y., et al. (2019). Fine Particulate Matter ($PM_{2.5}$) Trends in China, 2013–2018: Separating Contributions from Anthropogenic Emissions and Meteorology. *Atmos. Chem. Phys.* 19 (16), 11031–11041. doi:10.5194/acp-19-11031-2019

Zhang, H., Li, N., Tang, K., Liao, H., Shi, C., Huang, C., et al. (2021a). Estimation of Secondary PM2.5 in China and the United States Using a Multi-Tracer Approach. *Atmos. Chem. Phys. Discuss.* 2021, 1–36. doi:10.5194/acp-2021-683

Zhang, H., Tang, K., Feng, W., Yan, X., Liao, H., and Li, N. (2021b). Impact of Short-Term Emission Control Measures on Air Quality in Nanjing during the Jiangsu Development Summit. *Front. Environ. Sci.* 9, 693513. doi:10.3389/fenvs.2021.693513

Zheng, B., Tong, D., Li, M., Liu, F., Hong, C., Geng, G., et al. (2018). Trends in China's Anthropogenic Emissions since 2010 as the Consequence of Clean Air Actions. *Atmos. Chem. Phys.* 18 (19), 14095–14111. doi:10.5194/acp-18-14095-2018

Conflict of Interest: The authors declare that the research was conducted in the absence of any commercial or financial relationships that could be construed as a potential conflict of interest.

Publisher's Note: All claims expressed in this article are solely those of the authors and do not necessarily represent those of their affiliated organizations, or those of the publisher, the editors, and the reviewers. Any product that may be evaluated in this article or claim that may be made by its manufacturer, is not guaranteed or endorsed by the publisher.

frontiers in Environmental Science

ORIGINAL RESEARCH
published: 04 March 2022
doi: 10.3389/fenvs.2022.842237

Spatiotemporal Distributions of $PM_{2.5}$ Concentrations in the Beijing–Tianjin–Hebei Region From 2013 to 2020

Xiaohui Yang[1,2,3], *Dengpan Xiao*[1,2,3]*, *Huizi Bai*[3], *Jianzhao Tang*[3] *and Wei Wang*[1,2]*

[1]College of Geography Science, Hebei Normal University, Shijiazhuang, China, [2]Hebei Laboratory of Environmental Evolution and Ecological Construction, Shijiazhuang, China, [3]Institute of Geographical Sciences, Hebei Academy of Sciences, Hebei Engineering Research Center for Geographic Information Application, Shijiazhuang, China

Fine particulate matter ($PM_{2.5}$) seriously affects the environment, climate, and human health. Over the past decades, the Beijing–Tianjin–Hebei region (BTH) has been severely affected by pollutant gas and $PM_{2.5}$ emissions caused by heavy industrial production, topography, and other factors and has been one of the most polluted areas in China. Currently, the long-term, large-scale, and high spatial resolution monitoring $PM_{2.5}$ concentrations ([$PM_{2.5}$]) using satellite remote sensing technology is an important task for the prevention and control of air pollution. The aerosol optical depth (AOD) retrieved by satellites combined with a variety of auxiliary information was widely used to estimate [$PM_{2.5}$]. In this study, a two-stage statistical regression [linear mixed effects (LME) + geographically weighted regression (GWR)] model, combined with the latest high spatial resolution (1 km) AOD product and meteorological and land use parameters, was constructed to estimate [$PM_{2.5}$] in BTH from 2013 to 2020. The model was fitted annually, and the ranges of coefficient of determination (R^2), root mean square prediction errors (*RMSPE*), and relative prediction error (*RPE*) for the model cross-validation were 0.85–0.95, 7.87–29.90 μg/m^3, and 19.19%–32.71%, respectively. Overall, the model obtained relatively good performance and could effectively estimate [$PM_{2.5}$] in BTH. The [$PM_{2.5}$] showed obvious temporal characteristic within a year (high in winter and low in summer) and spatial characteristic (high in the southern plain and low in the northern mountain). During the investigated period of 2013–2020, the high pollutant areas ([$PM_{2.5}$] > 75 μg/m^3) in 2020 significantly narrowed compared to 2013, and the annual average [$PM_{2.5}$] in BTH fell below 55 μg/m^3, with a drop of 54.04%. In particular, the [$PM_{2.5}$] in winter season dropped sharply from 2015 to 2017 and declined steadily after 2017. Our results suggested that significant achievements have been made in air pollution control over the past 8 years, and they still need to be maintained. The research can provide scientific basis and support for the prevention and control of air pollution in BTH and beyond.

Keywords: $PM_{2.5}$ concentrations, aerosol optical depth, two-stage statistical regression model, spatiotemporal distribution, Beijing–Tianjin–Hebei region, Tianjin–Hebei region

OPEN ACCESS

Edited by:
Jianhuai Ye,
Southern University of Science and Technology, China

Reviewed by:
Jie Zhang,
University at Albany, United States
Xiaodong Xie,
Nanjing University of Information Science and Technology, China

***Correspondence:**
Dengpan Xiao
xiaodp@sjziam.ac.cn
Wei Wang
wangwei@hebtu.edu.cn

Specialty section:
This article was submitted to Atmosphere and Climate, a section of the journal Frontiers in Environmental Science

Received: *23 December 2021*
Accepted: *19 January 2022*
Published: *04 March 2022*

Citation:
Yang X, Xiao D, Bai H, Tang J and Wang W (2022) Spatiotemporal Distributions of $PM_{2.5}$ Concentrations in the Beijing–Tianjin–Hebei Region From 2013 to 2020. Front. Environ. Sci. 10:842237. doi: 10.3389/fenvs.2022.842237

INTRODUCTION

Fine particulate matter ($PM_{2.5}$, particles with aerodynamic diameter less than 2.5 μm) are suspended in the atmosphere as a composite of solid and liquid particles. It can carry toxic and harmful substances over long distances, crossing countries and geographic boundaries (Engel-Cox et al., 2013; Li et al., 2017). Epidemiological studies have shown that exposure to high $PM_{2.5}$ concentrations ([$PM_{2.5}$]) has adverse effects on human health, such as increasing morbidity and mortality of cardiopulmonary diseases (Chow et al., 2006; Gu et al., 2018; Riediker et al., 2018; Zhang et al., 2018). With the rapid economic and urbanization development, $PM_{2.5}$ has become a major air pollutant in China, especially in densely populated urban agglomerations, such as the Beijing–Tianjin–Hebei region (BTH) and the Yangtze River Delta region (He and Huang, 2018a; Wang G. et al., 2021). Therefore, studying the spatiotemporal patterns and trends of [$PM_{2.5}$] is conductive to taking accurate preventive measures against $PM_{2.5}$ pollution for policymakers and has important practical significance for air pollution control (Yan et al., 2021).

At present, $PM_{2.5}$ monitoring data mainly were derived from the ground monitoring network and aerosol optical depth (AOD) products generated by satellite sensors (van Donkelaar et al., 2006; Chudnovsky et al., 2014). AOD is a measure of the degree about which aerosols prevent light from penetrating the atmosphere and describes the reduction effect of aerosols on light. The AOD retrieved by visible channels is most sensitive to particles with sizes between 0.1 and 2 μm (close to the particle size of $PM_{2.5}$), which is an important theoretical basis for establishing the correlation between AOD and $PM_{2.5}$ (Kahn er al., 1998; Hu et al., 2013). Generally, satellite-derived AOD can provide valuable information for the estimation of ground-level $PM_{2.5}$ pollution due to its large spatial coverage, high spatial resolution, and reliable repeated measurement, especially suitable for those places without $PM_{2.5}$ monitoring station on the surface (Schaap et al., 2009; Yeganeh et al., 2017; Stowell et al., 2020). Recently, most of the AOD products used to predict [$PM_{2.5}$] were derived from the Moderate Resolution Imaging Spectroradiometer (MODIS), Visible Infrared Imaging Radiometer Suite (VIIRS), Multiangle Imaging SpectroRadiometer (MISR), and Advanced Himawari Imager (AHI) that the nominal spatial resolutions for AOD retrieved by their algorithms are 10 or 3 km, 17.6 or 4.4, 0.75 and 5 km, respectively (Lee et al., 2011; Hu et al., 2014a; Yao et al., 2018; Wang et al., 2020). However, the coarser resolution AOD products hinder the study of fine-scale [$PM_{2.5}$]. For example, the detailed spatial variability of $PM_{2.5}$ exposure was ignored at the urban scale (Hu et al., 2014b). A new high spatial resolution (1-km) MODIS Collection 6 (C6) daily AOD product (MCD19A2) was released in 2018, which was generated based on the Multi-Angle Implementation of Atmospheric Correction (MAIAC) algorithm and demonstrated excellent performance in estimating [$PM_{2.5}$] (Lyapustin et al., 2018; Zhang Z. et al., 2019; Choi et al., 2019).

Previous studies have established a variety of models to explore the relationship between station-based $PM_{2.5}$ observations and satellite-based AOD data, including scaling approach (Liu et al., 2004), semi-empirical (Wang and Christopher, 2003), and statistical regression models. Given their simplicity, fast process, and high performance, statistical regression models are widely used. These models ranged from simple linear regression (Engel-cox et al., 2004) in early study to advanced statistical models, such as linear mixed effects (LME) (Lee et al., 2011), generalized additive (GAM) (Liu et al., 2009), geographically weighted regression (GWR) (Hu et al., 2013), space-time LME (STLME) (Wang W. et al., 2021), geographically and temporally weighted regression (GTWR) (Bai et al., 2016), and time fixed effects regression (TEFR) (Yao et al., 2018). To improve prediction accuracy, various models have evolved from using AOD as the only predictor to a combination of multiple additional predictors [e.g., meteorological factors, human activities, and land use (LU) variables] (Gupta and Christopher, 2009; Hu et al., 2017). To reduce the deviation caused by a single model prediction, more complex models were then developed by combining two or more models, such as two-stage model (e.g., LME + GWR, LME + GAM, and TEFR + GWR) (Ma et al., 2016; Yao et al., 2019; Xue et al., 2020; Guo et al., 2021) and three-stage model [e.g., inverse probability weighting (IPW) + generalized additive mixed model (GAMM) + kriging with external drift (KED)] (Liang et al., 2018). In addition, some machine learning methods were employed to estimate [$PM_{2.5}$], such as random forest (RF) (Stafoggia et al., 2019; Zhao et al., 2020), artificial neural network (ANN) (Polezer et al., 2018), adaptive deep neural network (SADNN) (Chen et al., 2021), and support vector machine (SVM) (Moazami et al., 2016). However, the parameters in the machine learning models cannot explain the spatiotemporal relationship between $PM_{2.5}$ and AOD, owing to an unknown mechanism, causing the model to lack reasoning capability (Yang et al., 2021). The LME + GWR model is weak in dealing with nonlinear relationships between various predictors, but it can accurately capture the spatiotemporal variability of $PM_{2.5}$–AOD, which is better than the LME model and LME + GAM model (Zhang K. et al., 2019; Guo et al., 2021). Moreover, related studies indicated that adding interaction terms (quadratic terms) to the statistical regression models could better describe nonlinear effects (Xiao et al., 2017; He et al., 2020).

$PM_{2.5}$ estimation data with higher resolution and long-term series are of great significance for the analysis of small-scale air pollution (Lu et al., 2021). In this study, our main goal was to estimate the [$PM_{2.5}$] in the BTH and analyze its long-term spatiotemporal characteristics and trends. The specific objectives of this research were 1) to establish a suitable two-stage statistical regression model (LME + GWR), including adding quadratic terms and interaction terms in the model to account for the nonlinear relationship, and considering the influence of meteorological and LU information and AOD data in the BTH; 2) to estimate the daily [$PM_{2.5}$] distribution with 1-km spatial resolution in the BTH from 2013 to 2020; and 3) to analyze the spatiotemporal characteristics and trends of long-term [$PM_{2.5}$] on annual, seasonal, and monthly scales. The results can provide a reference for the joint prevention and control of particulate pollution in the study area.

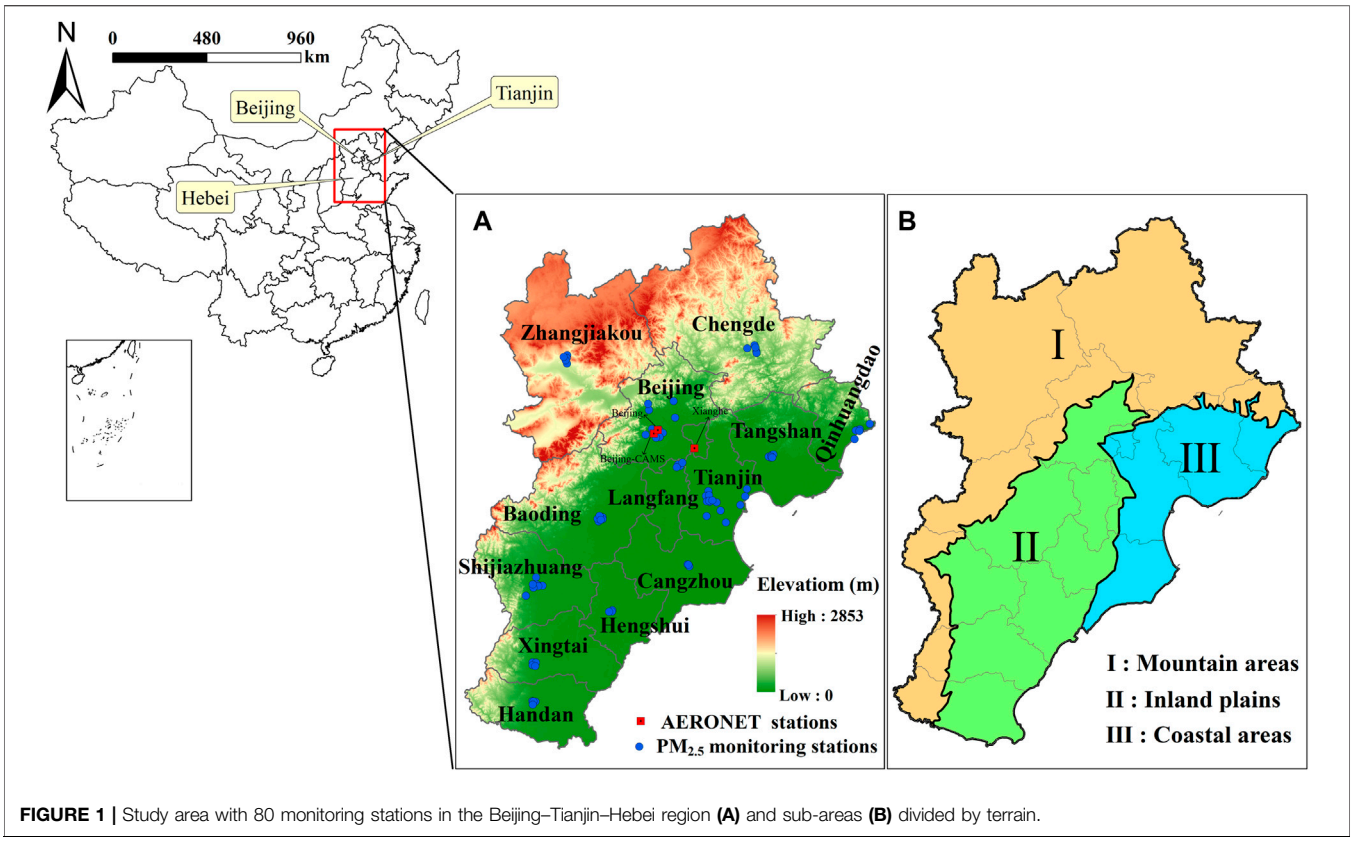

FIGURE 1 | Study area with 80 monitoring stations in the Beijing–Tianjin–Hebei region **(A)** and sub-areas **(B)** divided by terrain.

MATERIALS

Study Area

The BTH (113.45°E–119.85°E and 36.03°N–42.62°N) is one of the most important administrative, commercial, and cultural center in northern China, including Beijing and Tianjin, and 11 prefecture-level cities of Hebei Province (**Figure 1**). The region is densely populated and is a secondary industry that used coal as the main energy source emits various air pollutants, which causing relatively severe haze (Zhao et al., 2019). In particular, in the inland plains, coupled with unfavorable topography, it makes it more difficult for pollutants to spread (Lv et al., 2017). According to the statistics from the "China Environmental Bulletin" (http://www.cnemc.cn/jcbg/zghjzkgb/) during 2013–2020, the BTH included seven, eight, seven, six, six, five, four, and one, respectively, among the top 10 cities with poor air quality in China. Although the air quality in this region has improved during the past few years, we should still pay close attention to $PM_{2.5}$ pollution. Therefore, it is essential to analyze the spatiotemporal distribution and the trend of [$PM_{2.5}$].

$PM_{2.5}$ Monitoring Data and Predictor Variables

In addition to adding AOD to the model for [$PM_{2.5}$] prediction, it has been recognized that combining meteorological and LU information can significantly improve the model predictability (Hu et al., 2017; Wang G. et al., 2021). In this study, for the proposed two-stage statistical regression (LME + GWR) model, a main independent predictor (AOD) and eight auxiliary predictors [i.e., planetary boundary layer height (PBLH), 2-m air temperature (TEMP), 10-m wind speed (WS), relative humidity (RH, specific humidity calculated), surface pressure (PRS), precipitation (PRCP), forest coverage (FC), and urban coverage (UC)] were utilized through variables selection and multicollinearity diagnosis. The datasets covered the period from January 1, 2013, to December 31, 2020. The detail information about the datasets is shown in **Table 1**.

1) $PM_{2.5}$ data. The $PM_{2.5}$ hourly concentration of 80 monitoring stations in BTH was obtained from the National Urban Air Quality Real-time Release Platform. In the process of fitting the daily mean [$PM_{2.5}$], we eliminated the [$PM_{2.5}$] (i.e., <2 and >500 μg/m^3) that was not within the monitoring range of the National Ambient Air Quality Standard (NAAQS) (GB 3095-2012) to ensure the validity of the $PM_{2.5}$ data.
2) AErosol RObotic NETwork (AERONET) AOD. The AOD measured by AERONET was used as the true value to verify the accuracy of the AOD retrieved by remote sensing. The AERONET AOD data (version 3, level 2) from three sites (i.e., Beijing, Beijing-CAMS, and Xianghe) were collected in our modeling area (https://aeronet.gsfc.nasa.gov/), which were used to validate the MODIS MAIAC AOD.
3) One-kilometer AOD data. High-resolution AOD products are increasingly used to capture the fine-scale differences in the spatial distribution of [$PM_{2.5}$]. The emergence of the MAIAC algorithm provided a theoretical basis for constructing a high-resolution [$PM_{2.5}$] estimation model. The MAIAC Terra/

TABLE 1 | Information about data source, temporal and spatial resolution.

Variable		Temporal resolution	Spatial resolution	Data source
$PM_{2.5}$		hourly	site	http://106.37.208.233:20035/
AOD		daily	1 × 1 km	https://ladsweb.modaps.eosdis.nasa.gov/
Meteorological	PBLH	hourly	0.25° × 0.3125°	ftp://rain.ucis.dal.ca/ctm/
	TEMP, WS, RH, PRS, and PRCP	daily	0.1° × 0.1°	http://data.tpdc.ac.cn/zh-hans/data/ (2013–2018)
			0.0625° × 0.0625°	http://data.cma.cn/ (2019–2020)
Land use	FC	yearly	30 × 30 m	http://www.dsac.cn/DataProduct/
	UC			

PBLH is planetary boundary layer height; TEMP, WS, RH, PRS, and PRCP are 2-m air temperature, 10-m wind speed, relative humidity, surface pressure, and precipitation, respectively. FC and UC are forest coverage and urban coverage, respectively.

Aqua AOD (0.55 μm) products were available through the MODIS Collection-6 data record. The AERONET $AOD_{550\ nm}$ was calculated from the AOD at 675 and 440 nm using the Angstrom exponent. Simple linear regressions were carried out between the MAIAC Terra/Aqua AOD (0.55 μm) and AERONET $AOD_{550\ nm}$ at the AERONET sites for each year. The results show that the fitting with the coefficient of determination (R^2) in 0.81–0.91 was acceptable in all years (**Figure 2**). The root mean square prediction error (*RMSPE*) ranged from 0.10 to 0.25, 73.15%–83.74% of the samples falling within the interval of 1 × variance, and the slope of 0.95–1.17, which met the verification accuracy requirements.

4) Meteorological data. The hourly PBLH data were derived from the Goddard Earth Observing System Model 5-Forward-processing (GEOS5-FP). Other daily meteorological data (e.g., TEMP, WS, RH, PRS, and PRCP) were extracted from the National Tibetan Plateau Data Center (TPDC) and only cover the period from 2013 to 2018 (Yang and He, 2019). The daily data from 2019 to 2020 were downloaded from the National Meteorological Science Data Center. The meteorological data in the two periods have negligible influence on the model prediction results because they have similar spatial resolutions and need to be interpolated to the same resolution as MODIS MAIAC AOD.
5) LU data. LU data were downloaded from the Geographical Information Monitoring Cloud Platform (GIM Cloud). The study selected LU data in 2015 to represent the LU status from 2013 to 2020 and extracted the urban coverage and FC in the study area into the model.
6) Data integration. Considering to match the daily [$PM_{2.5}$], the daily PBLH data were represented by averaging the observation values obtained at two times during the transit of the MODIS satellite. The daily meteorological data were then resampled to the 1-km grid by the bilinear interpolation method. In addition, the UC and FC data with 30-m spatial resolutions were averaged over the 1-km grid.

METHODS

Collinearity Diagnosis

Considering the stability of the predictive model, the collinearity of the independent variables should be diagnosed. In this study, the variance inflation factor (VIF) and tolerance value (TV) were selected to diagnose the collinearity of the selected variables. The VIF and TV of all independent variables participating in the model satisfied VIF < 10 and TV > 0.1 for each year (**Table 2**), indicating that there was no collinearity problem among the independent variables and could be considered for model fitting.

Two-Stage Statistics Regression Model

A two-stage statistical regression model consisting of LME model and GWR model was used to simulate the spatiotemporal variation of the $PM_{2.5}$–AOD relationship. The LME model in the first stage was applied to correct the time-varying relationship of $PM_{2.5}$–AOD. The quadratic term of AOD (AOD^2) and the interaction between PBLH and AOD (PBLH × AOD) were added to the model to explain the nonlinear relationship between AOD and $PM_{2.5}$. The specific structure of the model is as follows:

$$\begin{aligned} PM_{2.5st} = {} & (\beta_0 + \theta_0) + (\beta_1 + \theta_1)AOD_{st} + (\beta_2 + \theta_2)AOD_{st}^2 \\ & + (\beta_3 + \theta_3)PBLH_{st} + (\beta_4 + \theta_4)WS_{st} \\ & + (\beta_5 + \theta_5)TEMP_{st} + (\beta_6 + \theta_6)RH_{st} + (\beta_7 + \theta_7)PRS_{st} \\ & + (\beta_8 + \theta_8)PRCP_{st} + \beta_9 \times PBLH_{st} \times AOD_{st} \\ & + \beta_{10} \times FC_s + \beta_{11} \times UC_s \\ & + \varepsilon_{st}\,(\theta_{1\sim8}) \sim N\left[(0,0,0,\psi)\right], \varepsilon_{st} \sim N(0,\sigma^2) \end{aligned} \quad (1)$$

where $PM_{2.5st}$ is the [$PM_{2.5}$] at station *s* on day *t*; AOD_{st} is the AOD of the grid cell in which the station *s* is positioned on day *t*; AOD^2st is the quadratic term for AOD at station *s* on day *t*; PBLH*st*, WS*st*, TEMP*st*, RH*st*, PRS*st*, and PRCP*st* are the planetary boundary layer height, wind speed at 10-m height, temperature at 2-m height, relative humidity, surface pressure, and precipitation at station *s* on day *t*, respectively; $PBLH_{st} \times AOD_{st}$ is the interaction between PBLH and AOD at station *s* on day *t*; FC_s and UC_s are the FC value and UC value at station *s*, respectively; β_0 and θ_0 are the fixed and random intercepts, respectively; β_1 and β_2 are the fixed slopes of square polynomials for AOD; β_3, β_4, β_5, β_6, β_7, β_8, β_{10}, and β_{11} are the fixed slopes of PBLH, WS, TEMP, RH, PRS, PRCP, FC, and UC; β_9 is the fixed slope of the interaction between PBLH and AOD; θ_1 and θ_2 are the daily random slopes of square polynomials for AOD; and θ_3–θ_8 are the daily random slopes of each meteorological variables, respectively.

The GWR model of the second stage was used to correct the spatial heterogeneity between $PM_{2.5}$ and AOD. The specific method was to model the residuals of the LME model. This GWR model was fitted once a day to account for temporal variability. In addition, the model using adaptive bandwidth selection methods calculated by

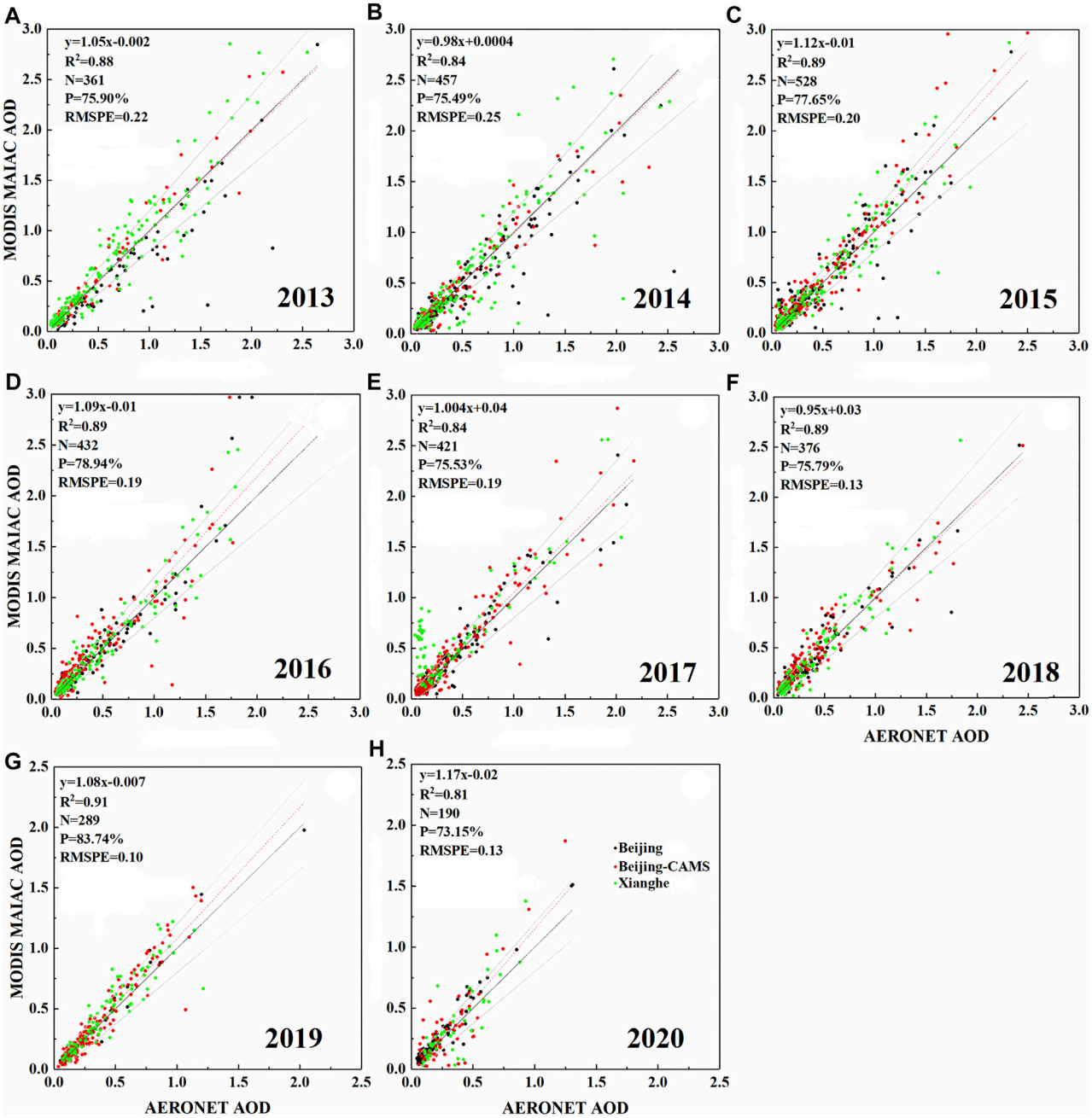

FIGURE 2 | Scatter plot of MODIS MAIAC AOD and AERONET AOD at 550 nm for the period of 2013–2020 **(A–H)**. The red dashed line is the regression line. The black line is a 1:1 line. The gray lines represent the expected error (EE) envelopes [±(0.05 + 20% × AERONET AOD)]. It also shows the coefficient of determination (R^2), the number of samples (N), the percentage in EE (P), and the root mean square prediction error (*RMSPE*).

minimizing the corrected Akaike Information Criterion (AIC) value. The specific expression is as follows:

$$PM_{2.5\_resi_{st}} = \beta_0(u_s, v_s) + \beta_1(u_s, v_s)AOD_{st} + \varepsilon_{st}\ \varepsilon_{st} \sim N(0, \sigma^2) \quad (2)$$

where $PM_{2.5}$_$resi_{st}$ is the residual value from the LME model at station s in day t; AOD_{st} is the AOD value at station s on day t; (u_s, v_s) is the spatial coordinates of the monitoring station s; and β_0 (u_s,v_s) and β_1 (u_s,v_s) represent the regression intercept and regression slope at station s, respectively.

For model verification, a 10-fold cross-validation (CV) method was conducted to detect the degree of overfitting of the model. The entire model-fitting dataset was randomly split into 10 subsets, with each subset containing approximately 10% of the dataset. In each CV time, we selected one subset as the testing sample and used the

TABLE 2 | The range of variance inflation factor (VIF) and tolerance value (TV) in the analysis of variable collinearity.

Predict variables	VIF	TV
AOD	1.18–1.64	0.60–0.84
PBLH	1.17–1.60	0.69–0.84
WS	1.15–1.28	0.68–0.86
TEMP	1.15–1.78	0.56–0.86
RH	1.41–1.88	0.52–0.82
PRS	1.24–1.50	0.66–0.80
PRCP	1.03–1.07	0.93–0.96
FC	1.30–1.48	0.67–0.76
UC	1.43–1.87	0.53–0.69

PBLH is planetary boundary layer height; TEMP, WS, RH, PRS, and PRCP are 2-m air temperature, 10-m wind speed, relative humidity, surface pressure, and precipitation, respectively. FC and UC are forest coverage and urban coverage, respectively.

remaining nine subsets to fit the model for prediction on the testing sample. This process was repeated 10 times to ensure that all the subsets were predicted. We fitted a linear regression was performed between the measured and predicted [$PM_{2.5}$], and the fitted R^2, slope, *RMSPE*, and relative prediction error (*RPE*) were evaluated the performance of the model. They represented by **Eqs. 3** and **4**, respectively.

$$RMSPE = \sqrt{\frac{\sum_{i=1}^{n}\left(y_{mod,i} - y_{obs,i}\right)^2}{n}} \quad (3)$$

$$RPE = \frac{RMSPE \times 100\%}{\bar{y}} \quad (4)$$

where $y_{mod,i}$ is the estimated $PM_{2.5}$ at site *i*; $y_{obs,i}$ is the observed $PM_{2.5}$ at site *i*; *n* is the total number of data samples; and $\bar{y}$ is the average of the observed $PM_{2.5}$.

The estimation process of the daily [$PM_{2.5}$] by the LME + GWR model is shown in **Supplementary Figure S1**.

RESULTS

Descriptive Statistics

As shown in **Table 3**, the daily minimum and maximum [$PM_{2.5}$] in the BTH were ranged from 2 to 3 μg/m^3 and from 371 to 499 μg/m^3, respectively, which indicated that the pollution degree of different areas in the BTH had considerable differences. The annual average [$PM_{2.5}$] during the investigated period from 2013 to 2020 in the BTH were 91.27, 85.93, 72.89, 68.22, 61.02, 53.53, 45.75, and 40.97 μg/m^3, respectively, indicating that the $PM_{2.5}$ pollution has been on a downward trend in the past 8 years. However, it still exceeded the limit (35 μg/m^3) of the national secondary standard for ambient air quality (GB3095-2012). The average annual AOD ranged from 0.37 to 0.69 during the same period. The great difference between the mean FC and UC reflected that most of the monitoring sites in the study area were located inside or around the city. In addition, the ranges of the meteorological variables from 2013 to 2020 are also shown in **Table 3**.

During the period from 2013 to 2020, the monthly [$PM_{2.5}$] monitored in the BTH demonstrated that the median monthly [$PM_{2.5}$] presented a U-shaped oscillation for each year (**Figure 3**). Overall, the [$PM_{2.5}$] displayed significant monthly differences, following the change pattern of "high in winter, low in summer, falling in spring and rising in autumn". In detail, [$PM_{2.5}$] displayed a downward trend from January to May, a general stability from June to September, and an upward trend from October to December. The reason for the highest monthly [$PM_{2.5}$] in December and January was the combined effect of coal-fired heating in winter and unfavorable meteorological conditions in the BTH, such as low air humidity and weak wind speed.

Model-Fitting and Validation

The comparison of LME + GWR model fitting (**Figure 4A**) and 10-fold CV results (**Figure 4B**) from 2013 to 2020 indicated that the model displayed excellent performance in capturing daily [$PM_{2.5}$]. For model fitting, the data distribution was concentrated toward the regression line. The R^2 ranged from 0.89 to 0.97, indicating that the two-stage model could effectively explain 89%–97% of the ground-level [$PM_{2.5}$] variation. The slope ranged from 0.89 to 1.04, indicating that only a small prediction bias remained in the model. In addition, the fitting results also displayed that the *RMSPE* and *RPE* were 6.85–24.60 μg/m^3 and 16.67%–26.94%, respectively. Compared with model fitting, the 10-fold CV results showed that the *CV-*R^2, *CV-RMSPE*, and *CV-RPE* ranged from 0.85 to 0.95, 7.87 μg/m^3 to

TABLE 3 | Statistical indicators of modeling variables.

Variables	Minimum	Maximum	Mean	Std. Deviation
$PM_{2.5}$ (μg/m^3)	2.00–3.00	371.00–499.00	40.97–91.27	34.18–77.23
AOD (unitless)	0.003–0.02	2.98–3.79	0.37–0.69	0.37–0.71
PBLH (m)	54.68–64.69	2,307.02–3,124.23	333.92–553.57	321.9–471.71
WS (m/s)	0.05–0.63	5.61–12.04	1.52–2.59	0.73–1.28
TEMP (°C)	–22.66–-12.85	31.58–33.97	9.83–12.88	10.30–11.57
RH	0.04–0.10	0.93–1.00	0.42–0.51	0.16–0.18
PRS (hPa)	866.01–891.61	1,016.94–1,042.73	997.25–1,006.12	27.10–33.92
PRCP (mm)	0	42.02–99.12	0.30–0.43	2.27–2.74
FC	0	0.68–0.75	0.03–0.05	0.11–0.14
UC	0	0.79–1.00	0.55–0.78	0.29–0.33

PBLH is planetary boundary layer height; TEMP, WS, RH, PRS, and PRCP are 2-m air temperature, 10-m wind speed, relative humidity, surface pressure, and precipitation, respectively. FC and UC are forest coverage and urban coverage, respectively.

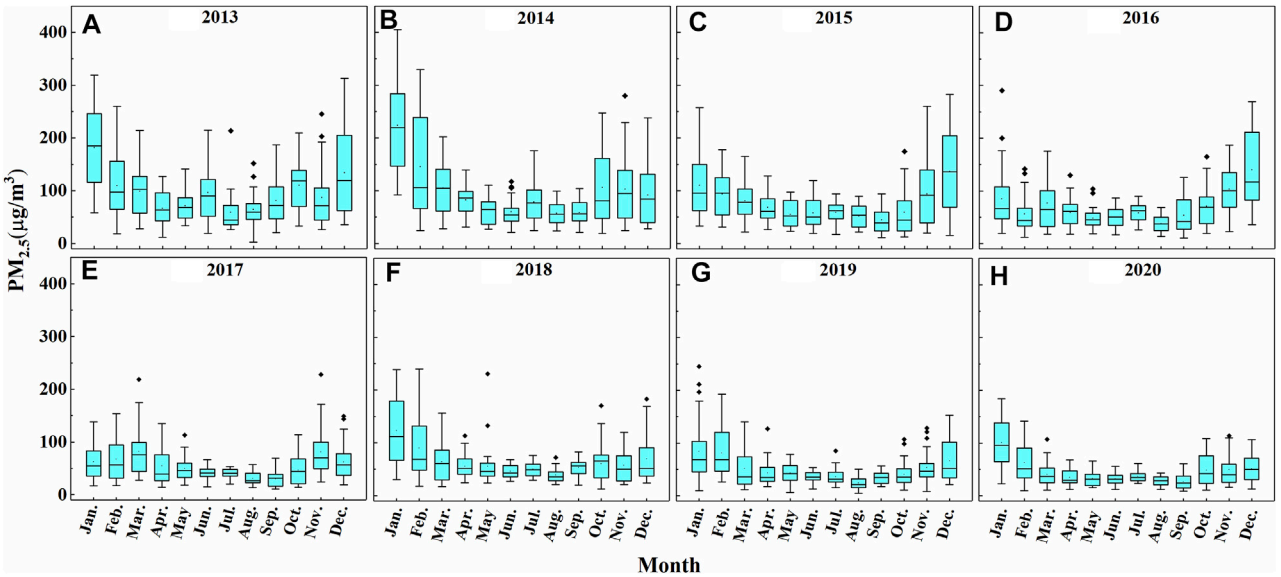

FIGURE 3 | The monthly mean observed $PM_{2.5}$ concentrations from 2013 to 2020 **(A–H)** in the Beijing–Tianjin–Hebei region.

29.90 μg/m^3, and 19.19–32.72%, respectively. The *CV-R*^{2} decreased, and *CV-RMSPE* and *CV-RPE* increased, indicating that the model had a slight overfitting. In addition, **Figure 4** shows that, when the measured [$PM_{2.5}$] exceeds 400 μg/m^3, the model had a slight "high value underestimation" phenomenon.

During the study period, the model performed best in 2020. Under the regression of the observed and predicted [$PM_{2.5}$] in the study area, *CV-R*^{2} was the highest at 0.95, and the *CV-RMSPE* and *CV-RPE* were the lowest at 7.87 μg/m^3 and 19.19%, respectively. This is mainly attributable to the government's series of "Air Pollution Prevention and Control Action Plans" (APPCAP), and the [$PM_{2.5}$] has been declining year by year. About 93.72% of [$PM_{2.5}$] data samples in 2020 were less than 100 μg/m^3. In contrast, the model performed the worst in 2013, with the lowest *CV-R*^{2} and the largest forecast uncertainty. The main reason was that more than 32.38% of the data samples were more than 100 μg/m^3, and relatively discrete data samples increased the difficulty of model fitting. Overall, the LME + GWR model that we have established was robust. Using the LME + GWR model combined with the 1-km MAIAC AOD product could excellently predict the daily near-surface [$PM_{2.5}$] with *CV-R*^{2} > 0.84, *CV-RMSPE* < 30 μg/m^3, and *CV-RPE* < 33% in the BTH.

Spatiotemporal Patterns of $PM_{2.5}$ Concentrations

Annual Variations

Figure 5 illustrated the annual mean [$PM_{2.5}$] estimated by the LME + GWR model, and ground-level observed [$PM_{2.5}$] from 2013 to 2020 in the BTH. The spatial variation pattern of [$PM_{2.5}$] estimated by the model was in good agreement with ground observations. The low-value areas of [$PM_{2.5}$] were located in the western and northern mountainous areas (Zone I), and the high-value areas were located in the middle and south of the BTH inland plain (Zone II). In general, the [$PM_{2.5}$] present a spatial distribution pattern of "low in the northern mountains and high in the southern plains". During the study period, the annual mean [$PM_{2.5}$] were 69.67, 65.31, 49.26, 51.17, 44.96, 43.11, 34.54, and 32.02 μg/m^3, respectively, and the overall $PM_{2.5}$ pollution level dropped significantly. Moreover, high-concentration areas ([$PM_{2.5}$] > 75 μg/m^3) have shrunk remarkably, and polluted cities were mainly concentrated in Handan, Xingtai, Shijiazhuang, and Baoding.

We adopted linear regression method to analyze the trends of annual mean [$PM_{2.5}$] in BTH. **Figure 6** illustrates the spatial distribution of the slope and significance level of [$PM_{2.5}$] from 2013 to 2020. Most of the mountain areas (Zone I) in the BTH failed the significance test ($p \geq 0.01$). The reason was speculated that the [$PM_{2.5}$] changed slightly during the study period. In addition, the [$PM_{2.5}$] level showed a significant decreasing trend ($p < 0.05$) in inland and coastal areas (Zone II and Zone III).

Seasonal Variations

$PM_{2.5}$ pollution in the BTH displayed strong seasonal variability. On the whole, the [$PM_{2.5}$] presented the seasonal variation characteristics of "high concentration in winter, low concentration in summer, and transition between spring and autumn" (**Figure 7**). During the study period in winter, the mean [$PM_{2.5}$] were 117.46, 84.24, 75.30, 72.72, 55.97, 52.75, 51.48, and 51.42 μg/m^3, respectively. There was a sharp decline in pollution from 2015 to 2017 and a steady decline after 2017. Compared with the [$PM_{2.5}$] in the winter of 2013, there was a decrease of 61 μg/m^3 (52%) in 2017 and 66 μg/m^3 (56%) in 2020. In addition, the annual and seasonal mean [$PM_{2.5}$] in the Zone II dropped the fastest compared with Zone I and Zone III (**Figure 8**).

Monthly Variations

During the study period, the estimated monthly [$PM_{2.5}$] of each year presented a U-shaped pattern (**Figure 9**), which was consistent with

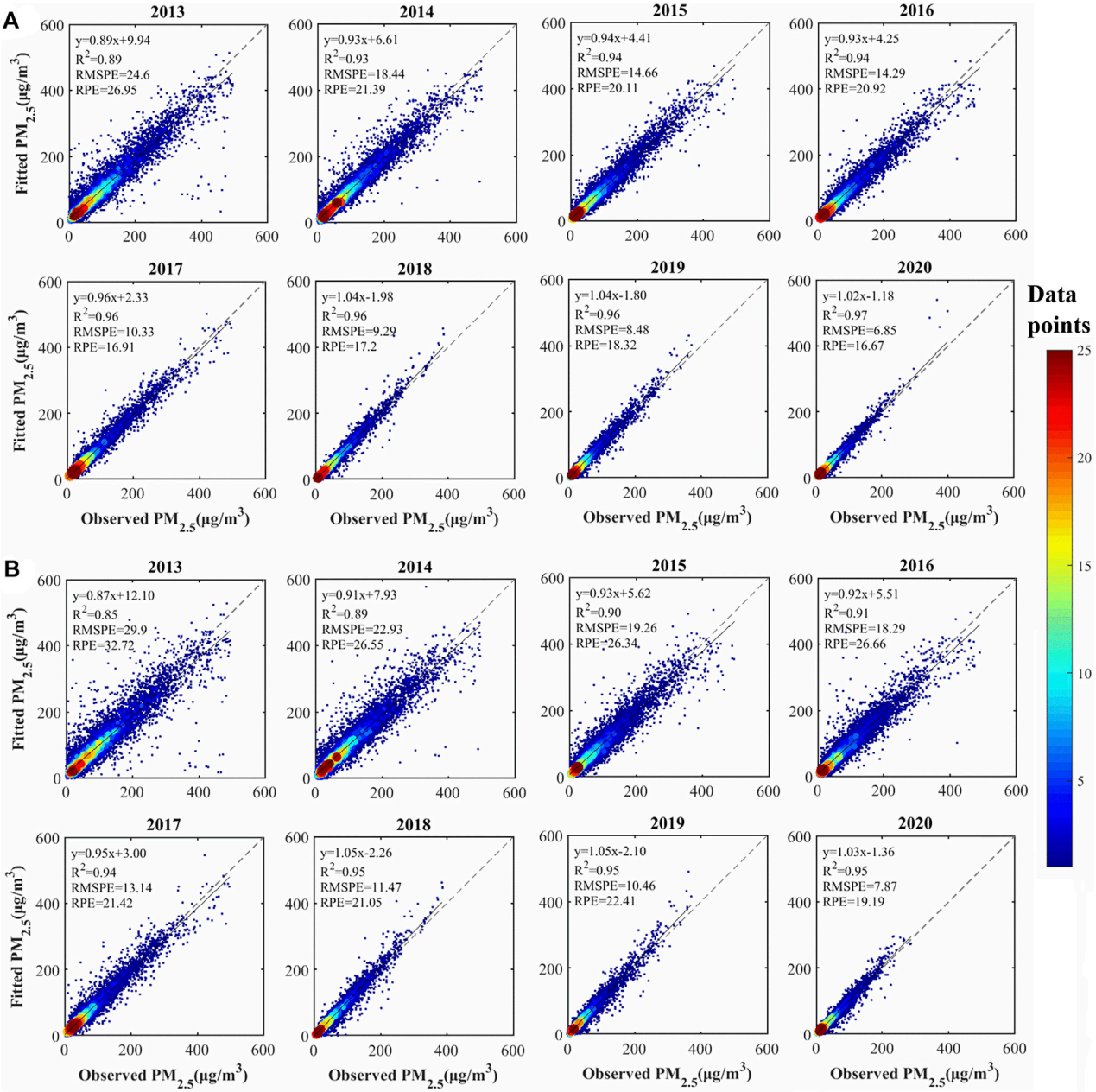

FIGURE 4 | Comparison of model fitting **(A)** and 10-fold cross-validation **(B)** results from 2013 to 2020.

the monthly measured [$PM_{2.5}$] distribution (**Figure 3**). January and December were the two months with the highest monthly mean [$PM_{2.5}$], which were related to coal-fired heating in the BTH. In addition, the low atmospheric humidity and temperature in these two months were also an important reason.

For the spatial distribution, the mean monthly [$PM_{2.5}$] had significant differences (**Figure 10**). The [$PM_{2.5}$] from May to September remained at a relatively low level. From October to February of the next year, cities in inland plain areas (e.g., Shijiazhuang, Baoding, Handan, and Xingtai) had the high-level [$PM_{2.5}$].

Figure 11 represents the daily fluctuations of [$PM_{2.5}$] based on station measurements and model estimates in Beijing and Shijiazhuang. The [$PM_{2.5}$] estimated by LME + GWR from 2013 to 2020 had excellent consistency with the monitoring station data and merely appeared a "high value underestimated" prediction deviation at few high concentrations (more than 400 μg/m^3). The fluctuation pattern of $PM_{2.5}$ pollution in Shijiazhuang was identical with Beijing. The peak values of [$PM_{2.5}$] were mainly distributed in winter, and the peak value in Shijiazhuang (the highest of 492.28 μg/m^3 appeared in 2014) was higher than that in Beijing (the highest of 463.52 μg/

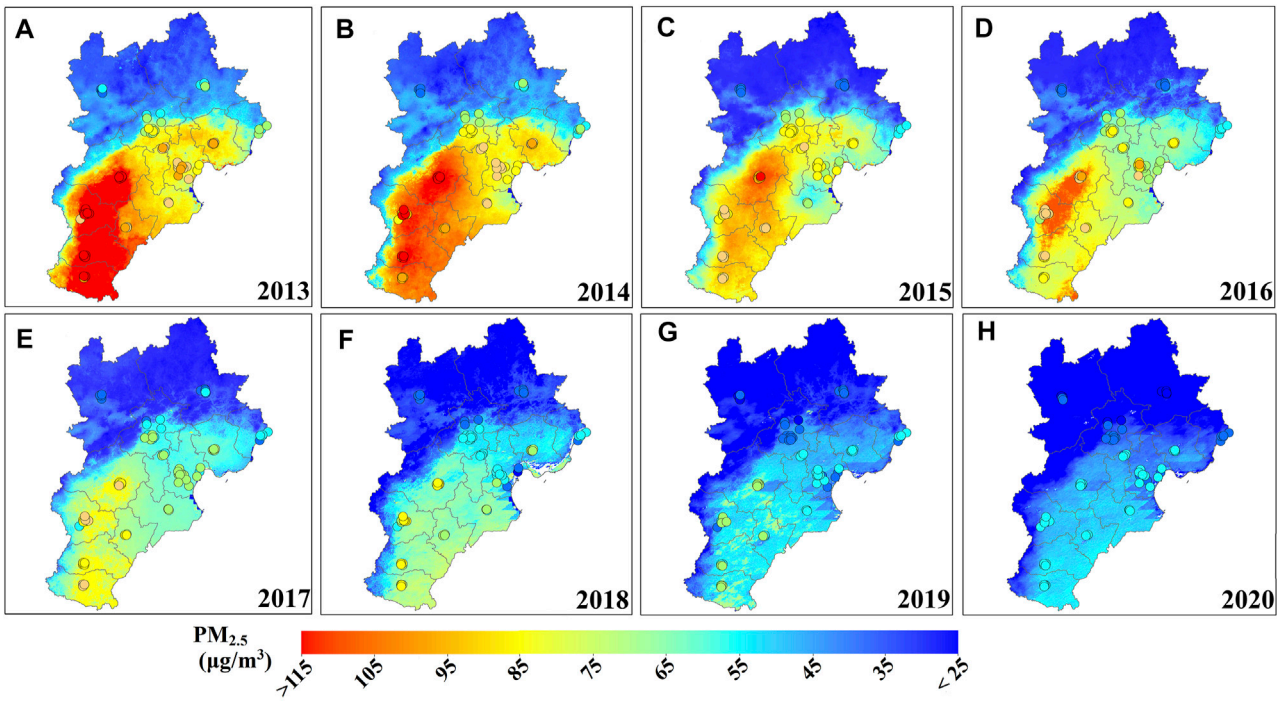

FIGURE 5 | The distribution of the annual mean estimated $PM_{2.5}$ concentrations and observed $PM_{2.5}$ concentrations in the Beijing–Tianjin–Hebei region during 2013–2020 **(A–H)**.

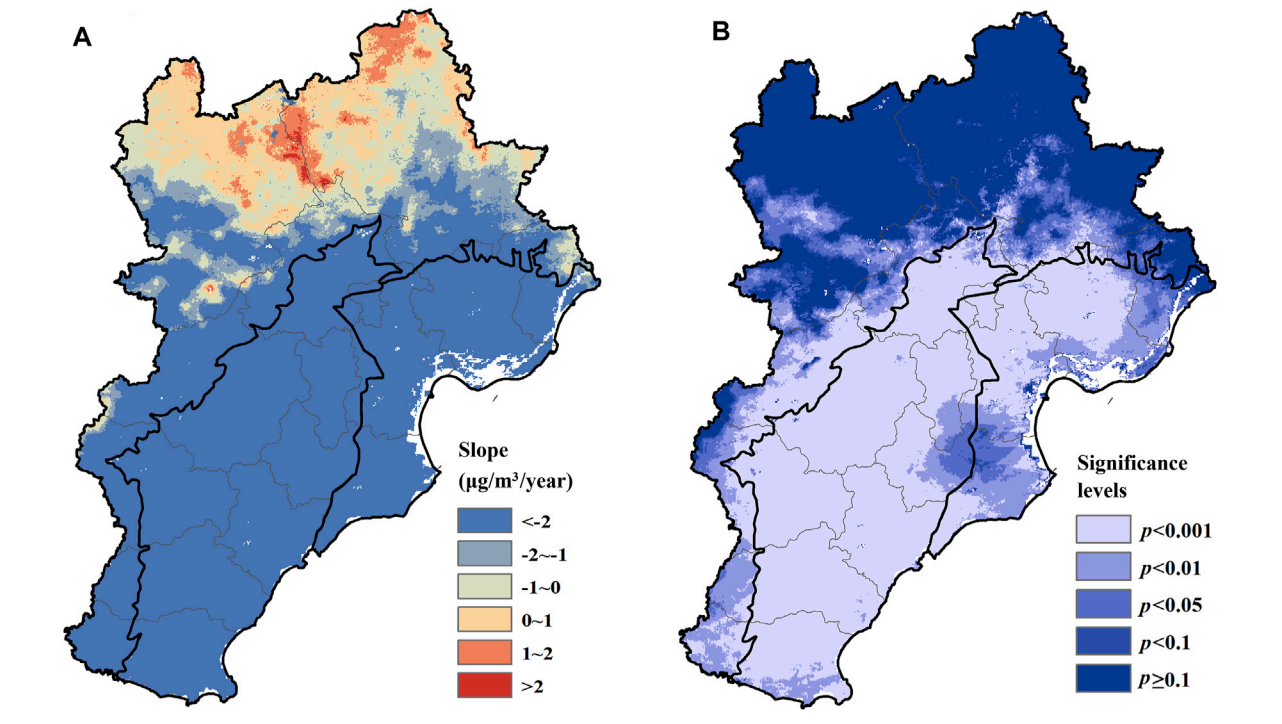

FIGURE 6 | Spatial distributions of the slope **(A)** and significance levels **(B)** of annual mean $PM_{2.5}$ concentrations in the Beijing–Tianjin–Hebei region from 2013 to 2020.

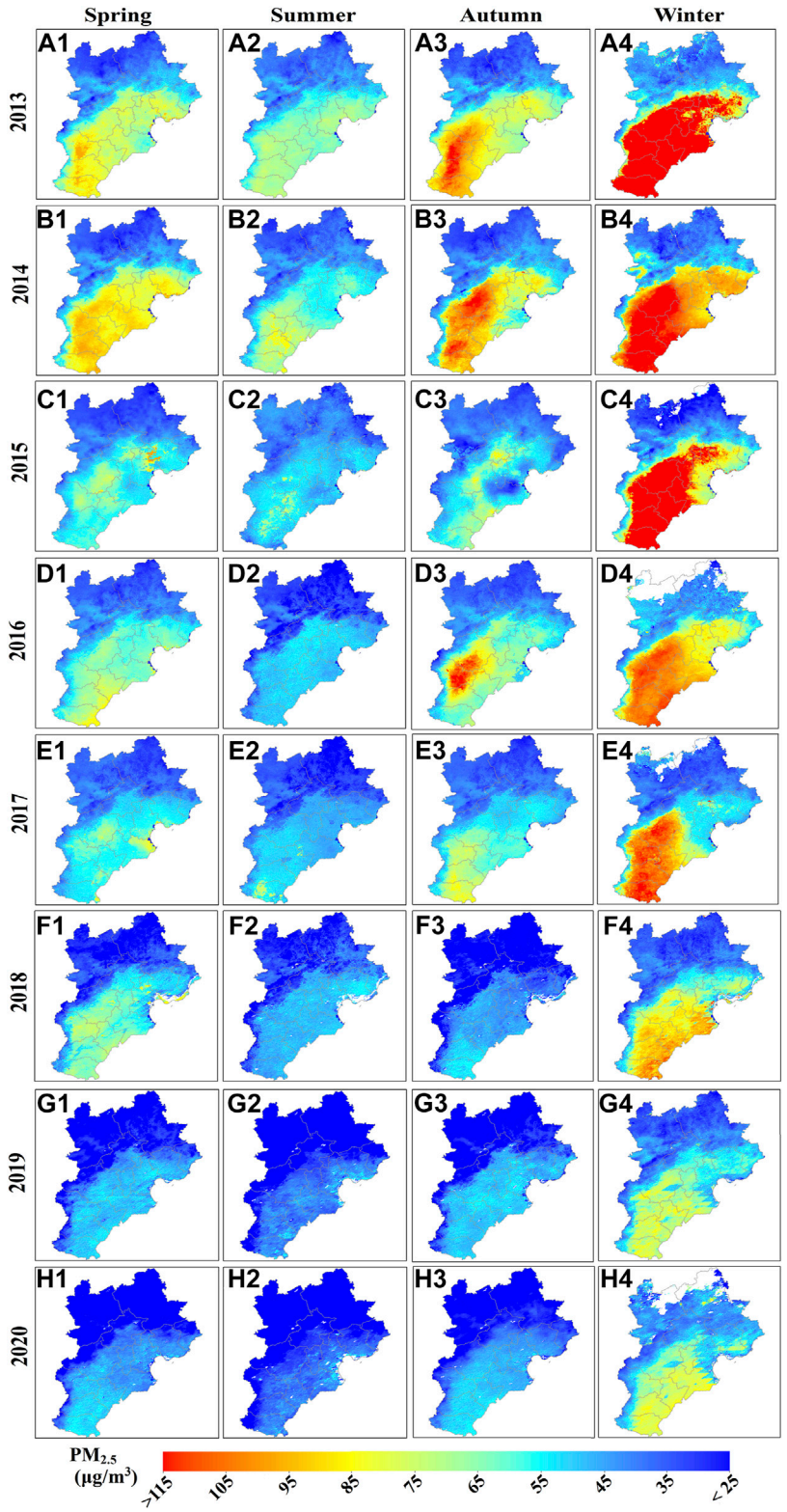

FIGURE 7 | Distribution of mean $PM_{2.5}$ concentrations in spring **(A1–H1)**, summer **(A2–H2)**, autumn **(A3–H3)**, and winter **(A4–H4)** in the Beijing–Tianjin–Hebei region during 2013–2020.

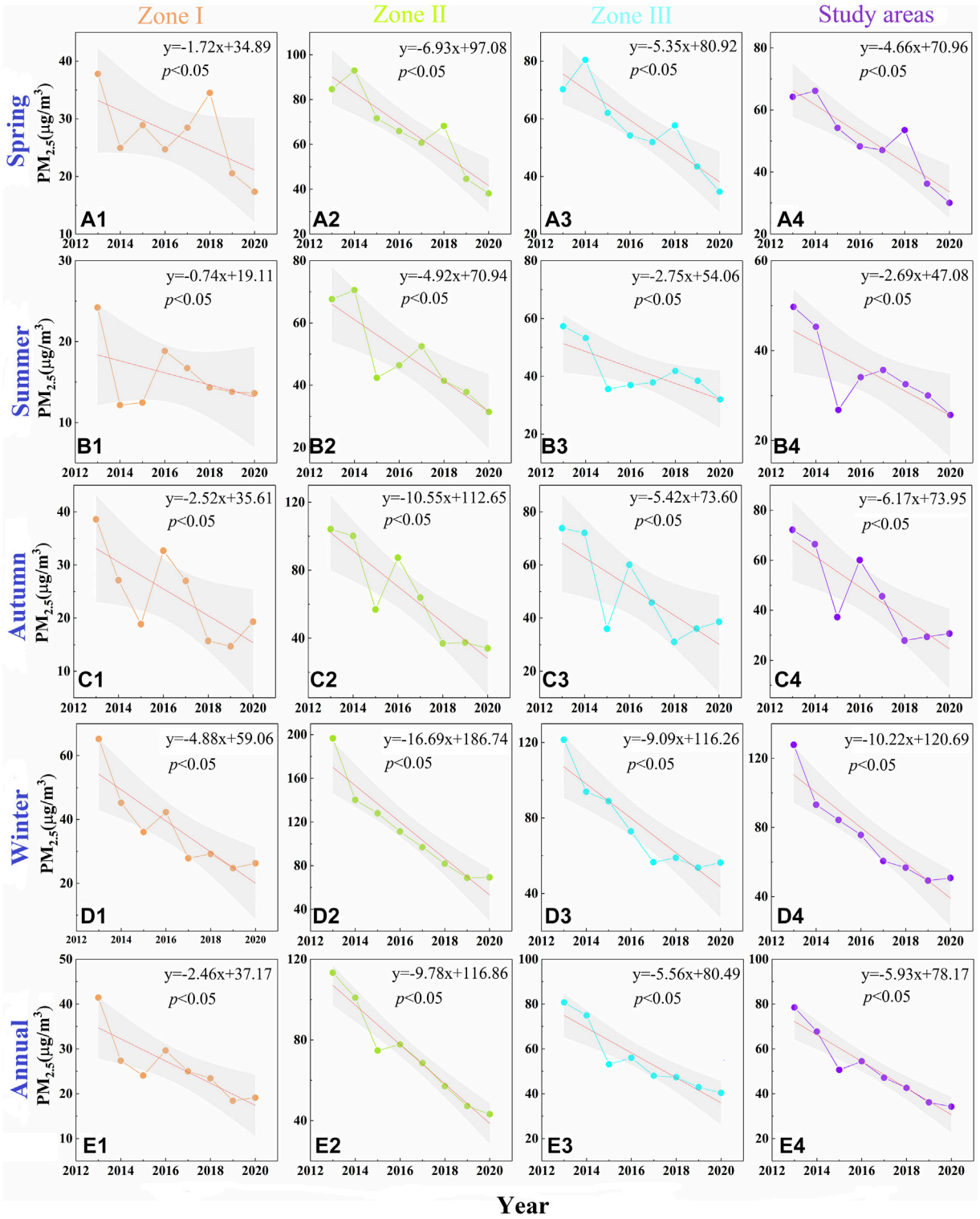

FIGURE 8 | Scatter plots of seasonal and annual trends of $PM_{2.5}$ concentrations in the Zone I **(A1–E1)**, Zone II **(A2–E2)**, Zone III **(A3–E3)**, and the Beijing–Tianjin–Hebei region **(A4–E4)** from 2013 to 2020. (The gray band represents the 95% confidence interval).

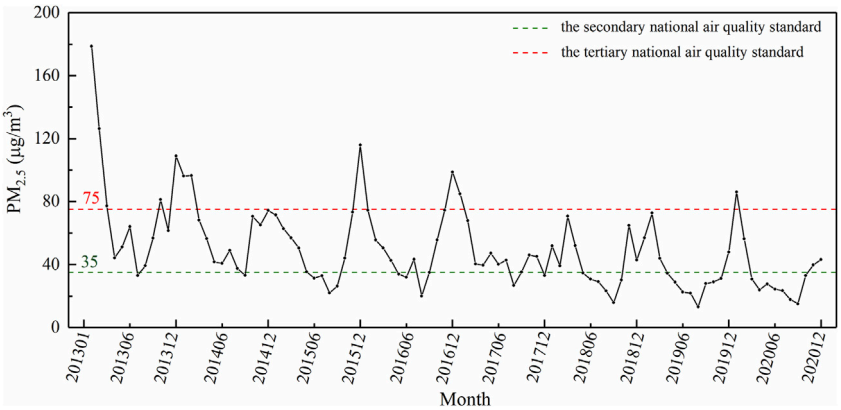

FIGURE 9 | Statistical variations of the monthly mean $PM_{2.5}$ concentrations in the Beijing–Tianjin–Hebei region from 2013 to 2020.

m^3 appeared in 2015). During the study period, the annual mean [$PM_{2.5}$] in Beijing were 57.54, 54.34, 54.30, 54.53, 54.38, 39.07, 30.87, and 30.09 μg/m^3, which were lower than 108.40, 91.61, 69.31, 74.48, 67.63, 53.63, 43.52, and 39.87 μg/m^3 in Shijiazhuang. However, $PM_{2.5}$ fell sharply in Shijiazhuang, with a drop of 63.21% from 2013 to 2020. In addition, the frequency of high pollution in Shijiazhuang in winter was higher than that in Beijing.

DISCUSSION

Causes Affecting the Spatiotemporal Distributions of $PM_{2.5}$

During the period from 2013 to 2020, [$PM_{2.5}$] in the BTH showed obvious spatiotemporal variations on different scales of annual, seasonal, and monthly. Overall [$PM_{2.5}$] in the BTH revealed a downward trend during the investigated period. Exploring the reasons for the decrease in the [$PM_{2.5}$] was inseparable from the national policy control, such as coal-to-gas and energy-saving transformation (Pan et al., 2021). In detail, the APPCAP implemented between 2013 and 2017 has successfully reduced [$PM_{2.5}$] (Yue et al., 2020), and the sharp decline in 2017 was closely related to the termination year of the APPCAP in 2017. Moreover, the [$PM_{2.5}$] in December 2015 and December 2016 were significantly higher than that in other years. The reason was that El Niño in 2015 enhanced the winter air pollution in northern China (Chang et al., 2016). The high concentration in the winter of 2016 might be influenced by anthropogenic factors (Ding et al., 2021). In addition, the [$PM_{2.5}$] in the winter of 2018–2020 decreased slowly compared with 2017, and the light-pollution areas (such as Langfang and Tangshan) slightly expanded. Furthermore, combined with the contribution of the suspension of work and production during new coronavirus disease (COVID-19) (Xian et al., 2021), the [$PM_{2.5}$] in the winter of 2020 dropped to 51.42 μg/m^3, which was the lowest [$PM_{2.5}$] in winter during the study period.

In the BTH, [$PM_{2.5}$] presented the significant seasonal variation characteristics of "high in winter, low in summer, and transition between spring and autumn", which were consistent with previous studies (Wu et al., 2016; Guo et al., 2021; Lu et al., 2021). The high [$PM_{2.5}$] in winter was concentrated in cities such as Shijiazhuang, Xingtai, and Handan. In the study areas, pollutant emissions were mainly due to the coal-fired heating and unfavorable meteorological conditions (Lv et al., 2017). Relevant studies have pointed out that the increase of boundary layer height and higher water vapor content in summer are the main reasons for the low [$PM_{2.5}$] (Qu et al., 2016; Ding et al., 2021). Moreover, the elevated [$PM_{2.5}$] levels in autumn were likely caused by the large scale straw burning in the rural areas and coal burning for heating in November (Duan et al., 2004; Lv et al., 2017). In addition, the spatiotemporal variation trends on the monthly scale follow the characteristics of seasonal changes, with the most polluted months appearing in December and January.

Comparisons With Other Studies in the Beijing–Tianjin–Hebei Region

In previous studies, the *CV-R^2* value range of the satellite-based ground [$PM_{2.5}$] estimation model for the BTH was 0.54–0.95 (**Table 4**). Among these, the [$PM_{2.5}$] estimation model based on MODIS MAIAC AOD (*CV-R^2* up to 0.82–0.95) has been found to perform better than other [$PM_{2.5}$] estimation models (a maximum *CV-R^2* of 0.83), owing to its superior spatial resolution. Under the same high spatial resolution of AOD, our model showed similar or even better performance than other machine learning models. The performance statistics of the LME + GWR model developed was also comparable with other studies conducted in the United States that used the MODIS MAIAC AOD data (*CV-R^2* up to 0.62–0.84) (Hu et al., 2014a, 2014b; Chudnovsky et al., 2014; Stowell et al., 2020). For model, the LME model cannot estimate the daily value of $PM_{2.5}$ at non-monitoring points, even if there are abundant data available. Models such as TEFR and STLME also have this shortcoming (Wu et al., 2016; Wang W. et al., 2021). In addition, machine learning methods that account for complex nonlinear relationships between different variables by adding hidden nodes and layers exhibited good performance in estimating [$PM_{2.5}$] (Ni et al., 2018; Stafoggia et al., 2019; Sun et al., 2019; Zhao et al., 2020; Ding et al., 2021). However, the

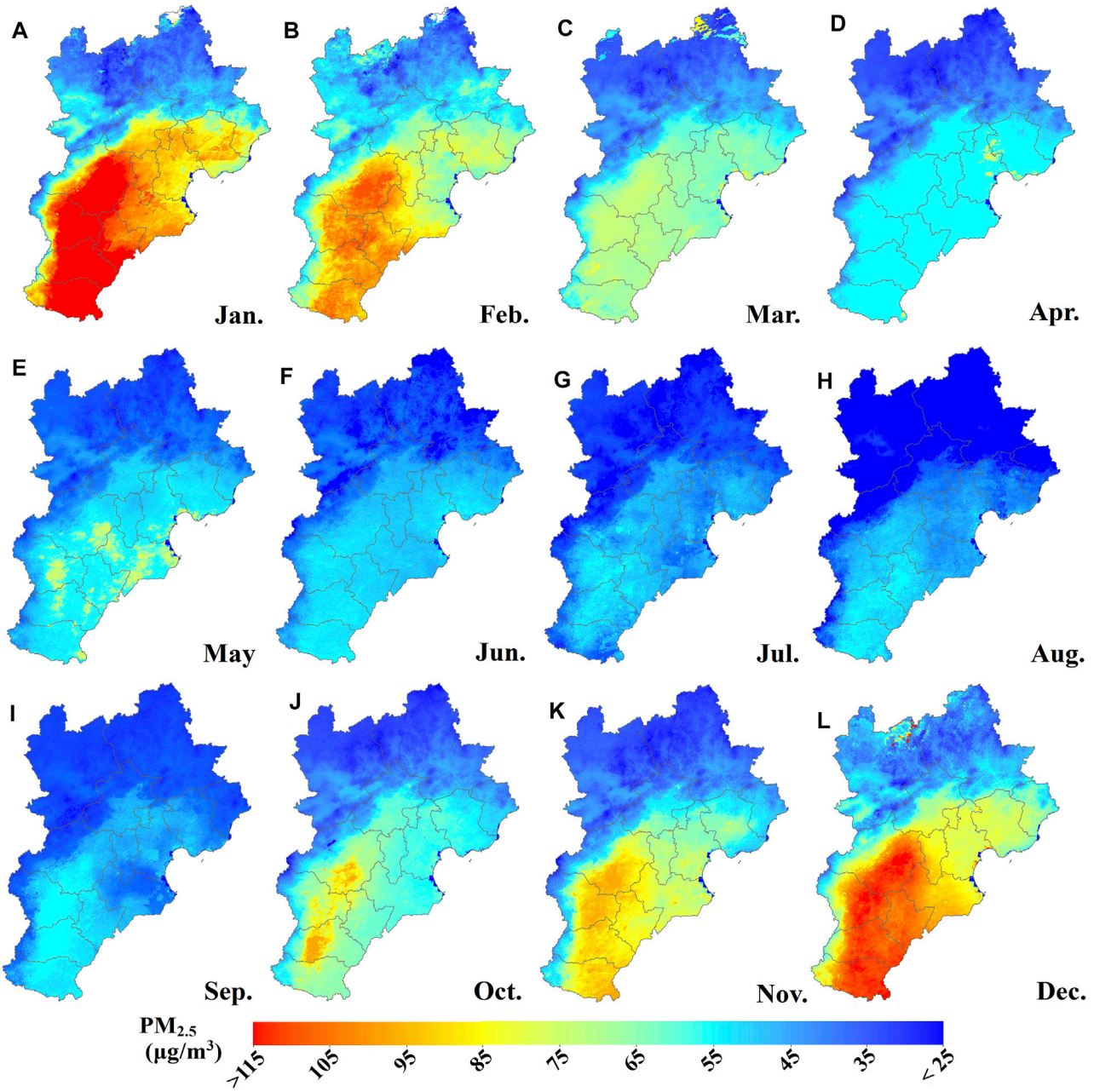

FIGURE 10 | Spatial distributions of monthly mean $PM_{2.5}$ concentrations **(A–L)** in the Beijing–Tianjin–Hebei region during 2013–2020.

addition of more hidden nodes and layers consumed a lot of time in estimating $PM_{2.5}$ load and produced different results for each training (Wang W. et al., 2021). Therefore, the LME + GWR model has certain advantages in terms of performance and stability. For AOD product, AHI AOD was commonly used to estimate hourly [$PM_{2.5}$] due to its high resolution. However, AHI cannot retrieve AOD at nighttime, and the quality is slightly inferior to MODIS AOD (Sun et al., 2019; Wang W. et al., 2021).

The model proposed in this study has many advantages. First, the high spatiotemporal resolution MAIAC Terra/Aqua fusion AOD data were employed in the model and achieved satisfactory performance. Second, the AOD quadratic term (AOD^2) and the interaction term of AOD and PBLH (PBLH×AOD) were introduced into the first-stage LME model to describe the nonlinear effect of the model. Third, we adopted the GWR model as the second-stage model to improve the spatial difference of the $PM_{2.5}$–AOD. The bisquare kernel bandwidth function and adaptive bandwidth method were selected owing to the difference between the daily sample data. After CV, the degree of overfitting was very small (compared with R^2, CV-R^2 was only reduced by 0.01–0.04).

However, the model still has some limitations. One limitation was the mismatch in spatial resolution between MODIS MAIAC AOD

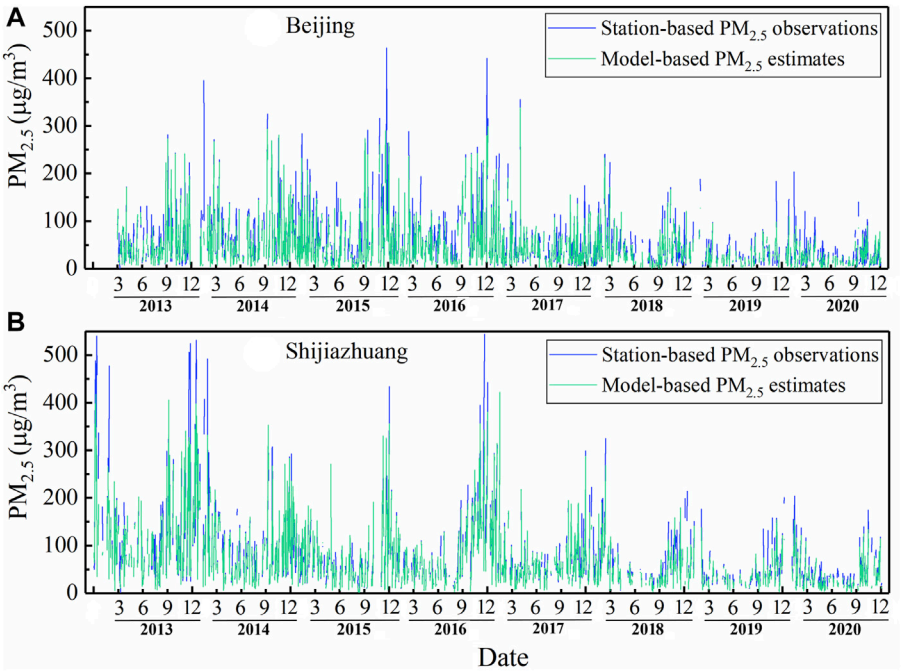

FIGURE 11 | Daily fluctuation in $PM_{2.5}$ concentrations based on station observations and model-based estimates in Beijing **(A)** and Shijiazhuang **(B)**.

TABLE 4 | Performances of previous studies on $PM_{2.5}$ estimates in the Beijing–Tianjin–Hebei region.

Related study	Spatial resolution (km)	Time period	Model	Model-fitting		Cross-validation		AOD source
				R^2	RMSPE	R^2	RMSPE	
Wang et al. (2019)	10	2017	LME	0.81	24.48	0.78	26.69	MODIS, NAQPMS
Wu et al. (2016)	6	2014	TEFR + GWR	0.88	13.05	0.71	19.29	VIIRS
Wang et al. (2021b)	5	2018	STLME	0.88	17.10	0.83	20.90	AHI
Ni et al. (2018)	3	2014–2016	BPNN	0.68	20.99	0.54	24.13	MODIS
He and Huang (2018b)	3	2013–2015	iGTWR	0.88	24.22	0.82	29.96	MODIS
Sun et al. (2019)	1	2017	DNN	0.91	14.27	0.84	19.90	AHI
Zhao et al. (2020)	1	2010-–2016	RF	0.86	23.48	0.83		MODIS
Ding et al. (2021)	1	2015–2019	CatBoost	-	-	0.88	17.79	MODIS
This study	1	2013–2020	LME + GWR	0.89–0.97	6.85–24.60	0.85–0.95	7.87–29.90	MODIS

BPNN, iGTWR, and DNN are the back propagation neural network model, improved geographically and temporally weighted regression model, and the deep neural networks model, respectively.

(0.01° × 0.01°) and meteorological parameters (0.1° × 0.1° and 0.0625° × 0.0625°). Although the bilinear interpolation method for meteorological factors has proved to have better performance than linear interpolation and nearest neighbor interpolation algorithms (Zhao et al., 2020), more meteorological products with high spatial resolution were still needed. Another limitation was that we only keep three data records in some days to bring into the model. Related studies have pointed out that the overfitting degree of the two-stage model incorporating GWR decreases with the increase in the number of matching data records per day (Hu et al., 2014a; Wu et al., 2016). Therefore, too few observations in some days would lead to the GWR model to overfitting. We will explore the optimal threshold that matches the minimum number of data records later. In addition, some studies have indicated that $PM_{2.5}$ monitoring stations mostly located in cities and suburbs, and the $PM_{2.5}$ estimation in mountainous and rural areas was relatively poor (Zeng et al., 2020; Ding et al., 2021). Our study area is in the BTH with characteristics of urban industrial conditions. In particular, Hebei Province that has many rural administrative units also has a large number of factories. Provincial monitoring sites with a larger coverage area should be added to future research to increase the regional representation of the sample.

CONCLUSION

In this study, the two-stage model (LME + GWR) that applied MODIS MAIAC AOD and measured [$PM_{2.5}$] and

meteorological and LU data as input variables was constructed to estimate the daily [$PM_{2.5}$] from 2013 to 2020 in the BTH. The LME + GWR model presented satisfactory performance ($CV\text{-}R^2$ was 0.85–0.95, *RMSPE* was 7.87–29.90 μg/m^3, and *RPE* was 19.19–32.71%) and provided a well-documented dataset for air pollution monitoring. During the investigated period from 2013 to 2020, $PM_{2.5}$ pollution in the BTH region has generally been on a downward trend. This decline is mainly due to anthropogenic factors such as pollution-preventing policies, but natural factors such as climate phenomenon (El Niño) also have a certain effect. In particular, in winter season, the [$PM_{2.5}$] exhibited relatively small fluctuations from 2013 to 2014, a sharp decline occurred from 2015 to 2017, and a steady decline from 2018 to 2020.

DATA AVAILABILITY STATEMENT

The original contributions presented in the study are included in the article/**Supplementary Material**, further inquiries can be directed to the corresponding authors.

AUTHOR CONTRIBUTIONS

DX and WW had the idea for the article and critically revised the work; XY performed the data processing and analysis; HB and JT gave many suggestions for this paper; XY, DX, and WW prepared the manuscript. All authors read and approved the final manuscript.

FUNDING

This work was supported by the National Natural Science Foundation of China (no.41471091) and the High-level Talents Training and Subsidy Project of Hebei Academy of Science (202201).

SUPPLEMENTARY MATERIAL

The Supplementary Material for this article can be found online at: https://www.frontiersin.org/articles/10.3389/fenvs.2022.842237/full#supplementary-material

REFERENCES

Bai, Y., Wu, L., Qin, K., Zhang, Y., Shen, Y., and Zhou, Y. (2016). A Geographically and Temporally Weighted Regression Model for Ground-Level PM2.5 Estimation from Satellite-Derived 500 M Resolution AOD. *Remote Sensing* 8 (3), 262. doi:10.3390/rs8030262

Chang, L., Xu, J., Tie, X., and Wu, J. (2016). Impact of the 2015 El Nino Event on Winter Air Quality in China. *Sci. Rep.* 6, 34275. doi:10.1038/srep34275

Chen, B., You, S., Ye, Y., Fu, Y., Ye, Z., Deng, J., et al. (2021). An Interpretable Self-Adaptive Deep Neural Network for Estimating Daily Spatially-Continuous PM2.5 Concentrations across China. *Sci. Total Environ.* 768, 144724. doi:10.1016/j.scitotenv.2020.144724

China, M. E. P. (2012). *Ambient Air Quality Standards. GB 3095-2012*. Beijing: China Environmental Science Press.

Choi, M., Lim, H., Kim, J., Lee, S., Eck, T. F., Holben, B. N., et al. (2019). Validation, Comparison, and Integration of GOCI, AHI, MODIS, MISR, and VIIRS Aerosol Optical Depth over East Asia during the 2016 KORUS-AQ Campaign. *Atmos. Meas. Tech.* 12 (8), 4619–4641. doi:10.5194/amt-12-4619-2019

Chow, J. C., Watson, J. G., Mauderly, J. L., Costa, D. L., Wyzga, R. E., Vedal, S., et al. (20062006). Health Effects of Fine Particulate Air Pollution: Lines that Connect. *J. Air Waste Manage. Assoc.* 56 (10), 1368–1380. doi:10.1080/10473289.2006.10464545

Chudnovsky, A. A., Koutrakis, P., Kloog, I., Melly, S., Nordio, F., Lyapustin, A., et al. (2014). Fine Particulate Matter Predictions Using High Resolution Aerosol Optical Depth (AOD) Retrievals. *Atmos. Environ.* 89, 189–198. doi:10.1016/j.atmosenv.2014.02.019

Ding, Y., Chen, Z., Lu, W., and Wang, X. (2021). A CatBoost Approach with Wavelet Decomposition to Improve Satellite-Derived High-Resolution PM2.5 Estimates in Beijing-Tianjin-Hebei. *Atmos. Environ.* 249, 118212. doi:10.1016/j.atmosenv.2021.118212

Duan, F., Liu, X., Yu, T., and Cachier, H. (2004). Identification and Estimate of Biomass Burning Contribution to the Urban Aerosol Organic Carbon Concentrations in Beijing. *Atmos. Environ.* 38, 1275–1282. doi:10.1016/j.atmosenv.2003.11.037

Engel-cox, J. A., Holloman, C. H., Coutant, B. W., and Hoff, R. M. (2004). Qualitative and Quantitative Evaluation of MODIS Satellite Sensor Data for Regional and Urban Scale Air Quality. *Atmos. Environ.* 38 (16), 2495–2509. doi:10.1016/j.atmosenv.2004.01.039

Engel-Cox, J., Kim Oanh, N. T., van Donkelaar, A., Martin, R. V., and Zell, E. (2013). Toward the Next Generation of Air Quality Monitoring: Particulate Matter. *Atmos. Environ.* 80, 584–590. doi:10.1016/j.atmosenv.2013.08.016

Gu, Y., Wong, T. W., Law, C. K., Dong, G. H., Ho, K. F., Yang, Y., et al. (2018). Impacts of Sectoral Emissions in China and the Implications: Air Quality, Public Health, Crop Production, and Economic Costs. *Environ. Res. Lett.* 13 (8), 084008. doi:10.1088/1748-9326/aad138

Guo, W., Zhang, B., Wei, Q., Guo, Y., Yin, X., Li, F., et al. (2021). Estimating Ground-Level PM2.5 Concentrations Using Two-Stage Model in Beijing-Tianjin-Hebei, China. *Atmos. Pollut. Res.* 12 (9), 101154. doi:10.1016/j.apr.2021.101154

Gupta, P., and Christopher, S. A. (2009). Particulate Matter Air Quality Assessment Using Integrated Surface, Satellite, and Meteorological Products: Multiple Regression Approach. *J. Geophys. Res.* 114, D14205. doi:10.1029/2008JD011496

He, Q., Gu, Y., and Zhang, M. (2020). Spatiotemporal Trends of PM2.5 Concentrations in central China from 2003 to 2018 Based on MAIAC-Derived High-Resolution Data. *Environ. Int.* 137, 105536. doi:10.1016/j.envint.2020.105536

He, Q., and Huang, B. (2018b). Satellite-based High-Resolution PM2.5 Estimation over the Beijing-Tianjin-Hebei Region of China Using an Improved Geographically and Temporally Weighted Regression Model. *Environ. Pollut.* 236, 1027–1037. doi:10.1016/j.envpol.2018.01.053

He, Q., and Huang, B. (2018a). Satellite-based Mapping of Daily High-Resolution Ground PM2.5 in China via Space-Time Regression Modeling. *Remote Sensing Environ.* 206, 72–83. doi:10.1016/j.rse.2017.12.018

Hu, X., Belle, J. H., Meng, X., Wildani, A., Waller, L. A., Strickland, M. J., et al. (2017). Estimating PM2.5 Concentrations in the Conterminous United States Using the Random Forest Approach. *Environ. Sci. Technol.* 51 (12), 6936–6944. doi:10.1021/acs.est.7b01210

Hu, X., Waller, L. A., Al-Hamdan, M. Z., Crosson, W. L., Estes, M. G., Jr, Estes, S. M., et al. (2013). Estimating Ground-Level PM2.5 Concentrations in the southeastern U.S. Using Geographically Weighted Regression. *Environ. Res.* 121, 1–10. doi:10.1016/j.envres.2012.11.003

Hu, X., Waller, L. A., Lyapustin, A., Wang, Y., Al-Hamdan, M. Z., Crosson, W. L., et al. (2014a). Estimating Ground-Level PM2.5 Concentrations in the Southeastern United States Using MAIAC AOD Retrievals and a Two-Stage Model. *Remote Sensing Environ.* 140, 220–232. doi:10.1016/j.rse.2013.08.032

Hu, X., Waller, L. A., Lyapustin, A., Wang, Y., and Liu, Y. (2014b). 10-year Spatial and Temporal Trends of PM2.5 Concentrations in the southeastern US Estimated Using High-Resolution Satellite Data. *Atmos. Chem. Phys.* 14 (12), 6301–6314. doi:10.5194/acp-14-6301-2014

Kahn, R., Banerjee, P., Mcdonald, D., and Diner, D. J. (1998). Sensitivity of Multiangle Imaging to Aerosol Optical Depth and to Pure-Particle Size Distribution and Composition over Ocean. *J. Geophys. Res.* 103 (D24), 32195–32213. doi:10.1029/98JD01752

Lee, H. J., Liu, Y., Coull, B. A., Schwartz, J., and Koutrakis, P. (2011). A Novel Calibration Approach of MODIS AOD Data to Predict PM2.5 Concentrations. *Atmos. Chem. Phys.* 11 (15), 7991–8002. doi:10.5194/acp-11-7991-2011

Li, T., Shen, H., Zeng, C., Yuan, Q., and Zhang, L. (2017). Point-surface Fusion of Station Measurements and Satellite Observations for Mapping PM2.5 Distribution in China: Methods and Assessment. *Atmos. Environ.* 152, 477–489. doi:10.1016/j.atmosenv.2017.01.004

Liang, F., Xiao, Q., Wang, Y., Lyapustin, A., Li, G., Gu, D., et al. (2018). MAIAC-based Long-Term Spatiotemporal Trends of PM2.5 in Beijing, China. *Sci. Total Environ.* 616-617, 1589–1598. doi:10.1016/j.scitotenv.2017.10.155

Liu, Y., Paciorek, C. J., and Koutrakis, P. (2009). Estimating Regional Spatial and Temporal Variability of PM 2.5 Concentrations Using Satellite Data, Meteorology, and Land Use Information. *Environ. Health Perspect.* 117 (6), 886–892. doi:10.1289/ehp.0800123

Liu, Y., Park, R. J., Jacob, D. J., Li, Q., Kilaru, V., and Sarnat, J. A. (2004). Mapping Annual Mean Ground-Level PM2.5concentrations Using Multiangle Imaging Spectroradiometer Aerosol Optical Thickness over the Contiguous United States. *J. Geophys. Res.* 109, a–n. doi:10.1029/2004jd005025

Lu, J., Zhang, Y., Chen, M., Wang, L., Zhao, S., Pu, X., et al. (2021). Estimation of Monthly 1 Km Resolution PM2.5 Concentrations Using a Random forest Model over "2 + 26" Cities, China. *Urban Clim.* 35, 100734. doi:10.1016/j.uclim.2020.100734

Lv, B., Hu, Y., Chang, H. H., Russell, A. G., Cai, J., Xu, B., et al. (2017). Daily Estimation of Ground-Level PM2.5 Concentrations at 4 Km Resolution over Beijing-Tianjin-Hebei by Fusing MODIS AOD and Ground Observations. *Sci. Total Environ.* 580, 235–244. doi:10.1016/j.scitotenv.2016.12.049

Lyapustin, A., Wang, Y., Korkin, S., and Huang, D. (2018). MODIS Collection 6 MAIAC Algorithm. *Atmos. Meas. Tech.* 11 (10), 5741–5765. doi:10.5194/amt-11-5741-2018

Ma, Z., Hu, X., Sayer, A. M., Levy, R., Zhang, Q., Xue, Y., et al. (2016). Satellite-Based Spatiotemporal Trends in PM 2.5 Concentrations: China, 2004-2013. *Environ. Health Perspect.* 124 (2), 184–192. doi:10.1289/ehp.1409481

Moazami, S., Noori, R., Amiri, B. J., Yeganeh, B., Partani, S., and Safavi, S. (2016). Reliable Prediction of Carbon Monoxide Using Developed Support Vector Machine. *Atmos. Pollut. Res.* 7 (3), 412–418. doi:10.1016/j.apr.2015.10.022

Ni, X., Cao, C., Zhou, Y., Cui, X., and P. Singh, R. (2018). Spatio-Temporal Pattern Estimation of PM2.5 in Beijing-Tianjin-Hebei Region Based on MODIS AOD and Meteorological Data Using the Back Propagation Neural Network. *Atmosphere* 9, 105. doi:10.3390/atmos9030105

Pan, X., Zhao, Y., and Wang, M. (2021). Impact of COVID-19 on Extremely Polluted Air Quality and Trend Forecast in Seven Provinces and Three Cities of China. *Front. Environ. Sci.* 9, 770900. doi:10.3389/fenvs.2021.770900

Polezer, G., Tadano, Y. S., Siqueira, H. V., Godoi, A. F. L., Yamamoto, C. I., de André, P. A., et al. (2018). Assessing the Impact of PM2.5 on Respiratory Disease Using Artificial Neural Networks. *Environ. Pollut.* 235, 394–403. doi:10.1016/j.envpol.2017.12.111

Qu, W., Wang, J., Zhang, X., Sheng, L., and Wang, W. (2016). Opposite Seasonality of the Aerosol Optical Depth and the Surface Particulate Matter Concentration over the North China Plain. *Atmos. Environ.* 127, 90–99. doi:10.1016/j.atmosenv.2015.11.061

Riediker, M., Franc, Y., Bochud, M., Meier, R., and Rousson, V. (2018). Exposure to Fine Particulate Matter Leads to Rapid Heart Rate Variability Changes. *Front. Environ. Sci.* 6, 2. doi:10.3389/fenvs.2018.00002

Schaap, M., Apituley, A., Timmermans, R. M. A., Koelemeijer, R. B. A., and de Leeuw, G. (2009). Exploring the Relation between Aerosol Optical Depth and PM2.5 at Cabauw, the Netherlands. *Atmos. Chem. Phys.* 9, 909–925. doi:10.5194/acp-9-909-2009

Stafoggia, M., Bellander, T., Bucci, S., Davoli, M., de Hoogh, K., de' Donato, F., et al. (2019). Estimation of Daily PM10 and PM2.5 Concentrations in Italy, 2013-2015, Using a Spatiotemporal Land-Use Random-forest Model. *Environ. Int.* 124, 170–179. doi:10.1016/j.envint.2019.01.016

Stowell, J. D., Bi, J., Al-Hamdan, M. Z., Lee, H. J., Lee, S.-M., Freedman, F., et al. (2020). Estimating PM2.5 in Southern California Using Satellite Data: Factors that Affect Model Performance. *Environ. Res. Lett.* 15 (9), 094004. doi:10.1088/1748-9326/ab9334

Sun, Y., Zeng, Q., Geng, B., Lin, X., Sude, B., and Chen, L. (2019). Deep Learning Architecture for Estimating Hourly Ground-Level PM2.5 Using Satellite Remote Sensing. *IEEE Geosci. Remote Sensing Lett.* 16 (9), 1343–1347. doi:10.1109/lgrs.2019.2900270

van Donkelaar, A., Martin, R. V., and Park, R. J. (2006). Estimating Ground-Level PM2.5using Aerosol Optical Depth Determined from Satellite Remote Sensing. *J. Geophys. Res.* 111, D21201. doi:10.1029/2005JD006996

Wang, G., Leng, W., Jiang, S., and Cao, B. (2021a). Long-Term Variation in Wintertime Atmospheric Diffusion Conditions over the Sichuan Basin. *Front. Environ. Sci.* 9, 763504. doi:10.3389/fenvs.2021.763504

Wang, J., and Christopher, S. A. (2003). Intercomparison between Satellite-Derived Aerosol Optical Thickness and PM2.5mass: Implications for Air Quality Studies. *Geophys. Res. Lett.* 30 (21), 2095. doi:10.1029/2003gl018174

Wang, Q., Zeng, Q., Tao, J., Sun, L., Zhang, L., Gu, T., et al. (2019). Estimating PM2.5 Concentrations Based on MODIS AOD and NAQPMS Data over Beijing-Tianjin-Hebei. *Sensors* 19 (5), 1207. doi:10.3390/s19051207

Wang, W., He, J., Miao, Z., and Du, L. (2021b). Space-Time Linear Mixed-Effects (STLME) Model for Mapping Hourly fine Particulate Loadings in the Beijing-Tianjin-Hebei Region, China. *J. Clean. Prod.* 292, 125993. doi:10.1016/j.jclepro.2021.125993

Wang, X., Sun, W., Zheng, K., Ren, X., and Han, P. (2020). Estimating Hourly PM2.5 Concentrations Using MODIS 3 Km AOD and an Improved Spatiotemporal Model over Beijing-Tianjin-Hebei, China. *Atmos. Environ.* 222, 117089. doi:10.1016/j.atmosenv.2019.117089

Wu, J., Yao, F., Li, W., and Si, M. (2016). VIIRS-based Remote Sensing Estimation of Ground-Level PM2.5 Concentrations in Beijing-Tianjin-Hebei: A Spatiotemporal Statistical Model. *Remote Sensing Environ.* 184, 316–328. doi:10.1016/j.rse.2016.07.015

Xian, T., Li, Z., and Wei, J. (2021). Changes in Air Pollution Following the COVID-19 Epidemic in Northern China: The Role of Meteorology. *Front. Environ. Sci.* 9, 654651. doi:10.3389/fenvs.2021.654651

Xiao, Q., Wang, Y., Chang, H. H., Meng, X., Geng, G., Lyapustin, A., et al. (2017). Full-coverage High-Resolution Daily PM2.5 Estimation Using MAIAC AOD in the Yangtze River Delta of China. *Remote Sensing Environ.* 199, 437–446. doi:10.1016/j.rse.2017.07.023

Xue, W., Zhang, J., Zhong, C., Ji, D., and Huang, W. (2020). Satellite-derived Spatiotemporal PM2.5 Concentrations and Variations from 2006 to 2017 in China. *Sci. Total Environ.* 712, 134577. doi:10.1016/j.scitotenv.2019.134577

Yan, J.-W., Tao, F., Zhang, S.-Q., Lin, S., and Zhou, T. (2021). Spatiotemporal Distribution Characteristics and Driving Forces of PM2.5 in Three Urban Agglomerations of the Yangtze River Economic Belt. *Ijerph* 18, 2222. doi:10.3390/ijerph18052222

Yang, K., and He, J. (2019). *China Meteorological Forcing Dataset (1979-2018)*. National Tibetan Plateau Data Center. doi:10.11888/AtmosphericPhysics.tpe.249369.file

Yang, W., He, Z., Huang, H., and Huang, J. (2021). A Clustering Framework to Reveal the Structural Effect Mechanisms of Natural and Social Factors on PM2.5 Concentrations in China. *Sustainability* 13 (3), 1428. doi:10.3390/su13031428

Yao, F., Si, M., Li, W., and Wu, J. (2018). A Multidimensional Comparison between MODIS and VIIRS AOD in Estimating Ground-Level PM2.5 Concentrations over a Heavily Polluted Region in China. *Sci. Total Environ.* 618, 819–828. doi:10.1016/j.scitotenv.2017.08.209

Yao, F., Wu, J., Li, W., and Peng, J. (2019). A Spatially Structured Adaptive Two-Stage Model for Retrieving Ground-Level PM2.5 Concentrations from VIIRS AOD in China. *ISPRS J. Photogrammetry Remote Sensing* 151, 263–276. doi:10.1016/j.isprsjprs.2019.03.011

Yeganeh, B., Hewson, M. G., Clifford, S., Knibbs, L. D., and Morawska, L. (2017). A Satellite-Based Model for Estimating PM2.5 Concentration in a Sparsely Populated Environment Using Soft Computing Techniques. *Environ. Model. Softw.* 88, 84–92. doi:10.1016/j.envsoft.2016.11.017

Yue, H., He, C., Huang, Q., Yin, D., and Bryan, B. A. (2020). Stronger Policy Required to Substantially Reduce Deaths from PM2.5 Pollution in China. *Nat. Commun.* 11, 1462. doi:10.1038/s41467-020-15319-4

Zeng, Q., Tao, J., Chen, L., Zhu, H., Zhu, S., and Wang, Y. (2020). Estimating Ground-Level Particulate Matter in Five Regions of China Using Aerosol Optical Depth. *Remote Sensing* 12, 881. doi:10.3390/rs12050881

Zhang, K., de Leeuw, G., Yang, Z., Chen, X., Su, X., and Jiao, J. (2019b). Estimating Spatio-Temporal Variations of PM2.5 Concentrations Using VIIRS-Derived AOD in the Guanzhong Basin, China. *Remote Sensing* 11 (22), 2679. doi:10.3390/rs11222679

Zhang, R., Di, B., Luo, Y., Deng, X., Grieneisen, M. L., Wang, Z., et al. (2018). A Nonparametric Approach to Filling Gaps in Satellite-Retrieved Aerosol Optical Depth for Estimating Ambient PM2.5 Levels. *Environ. Pollut.* 243 (Pt B), 998–1007. doi:10.1016/j.envpol.2018.09.052

Zhang, Z., Wu, W., Fan, M., Wei, J., Tan, Y., and Wang, Q. (2019a). Evaluation of MAIAC Aerosol Retrievals over China. *Atmos. Environ.* 202, 8–16. doi:10.1016/j.atmosenv.2019.01.013

Zhao, B., Wang, S., Ding, D., Wu, W., Chang, X., Wang, J., et al. (2019). Nonlinear Relationships between Air Pollutant Emissions and PM2.5-related Health Impacts in the Beijing-Tianjin-Hebei Region. *Sci. Total Environ.* 661, 375–385. doi:10.1016/j.scitotenv.2019.01.169

Zhao, C., Wang, Q., Ban, J., Liu, Z., Zhang, Y., Ma, R., et al. (2020). Estimating the Daily PM2.5 Concentration in the Beijing-Tianjin-Hebei Region Using a Random forest Model with a 0.01° × 0.01° Spatial Resolution. *Environ. Int.* 134, 105297. doi:10.1016/j.envint.2019.105297

Conflict of Interest: The authors declare that the research was conducted in the absence of any commercial or financial relationships that could be construed as a potential conflict of interest.

frontiers in Environmental Science

ORIGINAL RESEARCH
published: 17 March 2022
doi: 10.3389/fenvs.2022.857701

Comparative Study of Source Inversion Under Multiple Atmospheric Pollutant Emission Scenarios

Shushuai Mao[1], *Jianlei Lang*[1,2]*, *Tian Chen*[1], *Shuiyuan Cheng*[1] *and Feng Hu*[1]

[1]*Key Laboratory of Beijing on Regional Air Pollution Control, College of Environmental and Energy Engineering, Beijing University of Technology, Beijing, China,* [2]*Beijing Laboratory for Intelligent Environmental Protection, Beijing University of Technology, Beijing, China*

Source inversion is an effective approach for estimating air pollutant source parameters (e.g., source emission or source strength [Q_0], source horizontal location [x_0, y_0], and release height [z_0]) in industrial activities or accidents. Air pollution events in the real world generally correspond to complex application scenarios arising from unknown source parameters (i.e., Q_0, [Q_0, z_0], [Q_0, x_0, y_0], and [Q_0, x_0, y_0, z_0]) and atmospheric dispersion conditions. However, the source inversion characteristic law of these complex practical scenarios and the interaction mechanism between source location prior information and source strength inversion have not been revealed. In this study, the source inversion performance (accuracy and robustness) under the aforementioned scenarios was evaluated based on the Prairie Grass field experiments. Results indicated that the estimation accuracy of source strength was worse with an increase in the number of unknown source parameters with absolute relative deviations of 34.4, 46.0, 80.1, and 83.6% for a single parameter and double, triple, and quadruple parameters, respectively. Source strength inversion performance was obviously affected by location parameters; robustness was markedly reduced when source height was unknown, whereas accuracy was obviously reduced when source horizontal locations were unknown. Impacts of atmospheric conditions on different source parameters were distinct. Extreme atmospheric conditions (stability A and F) can obviously reduce the estimation accuracy of source strength for single and double parameter inversion scenarios, whereas unstable conditions (stability A, B, and C) can reduce the estimation accuracy of source strength for triple and quadruple parameter scenarios. Source inversion accuracy and robustness were generally poor under extremely stable conditions. This study can fill the knowledge gap in characteristic laws of source inversion under complex application scenarios and the interaction relationship between different unknown source parameters. The results of the influence law of location prior information on source strength inversion have important guiding significance to further improve the inversion accuracy of source strength in practical environmental managements.

Keywords: air pollution, source parameter estimation, inversion modeling, atmospheric dispersion conditions, multiple pollutant emission scenarios, small-scale regions

OPEN ACCESS

Edited by:
Hongmei Xu,
Xi'an Jiaotong University, China

Reviewed by:
Wei Sun,
Sun Yat-Sen University, China
Nan Li,
Nanjing University of Information Science and Technology, China

***Correspondence:**
Jianlei Lang
jllang@bjut.edu.cn

Specialty section:
This article was submitted to Atmosphere and Climate, a section of the journal Frontiers in Environmental Science

Received: *19 January 2022*
Accepted: *11 February 2022*
Published: *17 March 2022*

Citation:
Mao S, Lang J, Chen T, Cheng S and Hu F (2022) Comparative Study of Source Inversion Under Multiple Atmospheric Pollutant Emission Scenarios. Front. Environ. Sci. 10:857701. doi: 10.3389/fenvs.2022.857701

INTRODUCTION

As works promoting air pollution treatment and thereby ensuring the safety of life and property are given importance, air pollution events in small-scale regions triggered by conventional pollution discharge or accidents have caught the attention of governments and the public (Chen and Carter, 2020; Du et al., 2020; Lin et al., 2021; Liu et al., 2020; Wang et al., 2021). Accurately estimating unknown source emission information (or source parameters) is essential for rapidly promoting the refined control of air pollution or effective emergency response in sudden accidents (Mao et al., 2021; Zhou et al., 2021). However, capturing source emission information is difficult because pollutant emissions are generally abnormal or furtive (Bildirici, 2017; Jeričević et al., 2019).

To solve this problem, optimization inversion technologies have been proposed and proven promising for identifying unknown source parameters (e.g., source emission rate or source strength [Q_0], source horizontal location [x_0, y_0], and source release height [z_0]) of air pollution (Gao et al., 2009; Stohl et al., 2012; Wang et al., 2020; Zheng and Chen, 2010). The technology determines the unknown source information by solving an inversion model (or cost function) that minimizes the gap between the observed and simulated concentrations (Ma et al., 2018). The technical structure of the optimization source inversion mainly consists of two parts: inversion models and optimization algorithms. In the past decades, scholars have conducted meaningful research on source inversion. Algorithms such as gradient-based methods (e.g., least-squares; Singh and Rani, 2014; Singh and Rani, 2015), direct search methods (e.g., simulated annealing; Thomson et al., 2007), genetic algorithms (Cantelli et al., 2015; Hamblin, 2013; Haupt et al., 2006; Mao et al., 2020b), and hybrid algorithms (Cui et al., 2019; Wang et al., 2020) have been proposed to estimate the characteristics of source parameters. A few scholars have focused on the forms of cost functions (Ma et al., 2017; Wang et al., 2018), whereas Dong et al. (2020) found that the method involving the sum of deviation squares exhibited relatively better source inversion performance. However, the literature has mainly focused on theoretical research at the technical level. Notably, from the perspective of practical applications, optimization of source inversion is also vulnerable to external environmental factors (e.g., pollutant emission types and atmospheric dispersion conditions), except the aforementioned technical factors.

In the real world, pollutant-release scenarios are complex, and various types of pollutant emission events generally generate different source parameter inversion scenarios. For instance, conventional pollutants (e.g., volatile organic compounds and nitrogen oxides [NOx]) can be discharged *via* industrially organized or unorganized emissions, which correspond to inversion scenarios where the source location (e.g., horizontal location and release height) is known and unknown, respectively (Amoatey et al., 2019; Clappier and Thunis, 2020; Wang et al., 2019; Wei et al., 2014). For sudden accidents, hazardous gas releases from leakage accidents may occur near the surface or at a certain height. The release height of hazardous gas from fire accidents is generally difficult to determine because of the thermal lift (Koutsomarkos et al., 2021; Lei et al., 2021); however, the horizontal source location information might be known. These pollutant release types correspond to the different source inversion scenarios due to the difference in prior source location information available for different pollution event types. Meanwhile, Cervone and Franzese (2011), Cui et al. (2019), and Cantelli et al. (2015) found that, in the real world, optimization of source inversion is also affected by atmospheric dispersion conditions by influencing the simulation performance of forward dispersion models or the number of effective monitoring sensors utilized for source inversion. However, they only focused on the single inversion scenario where the source location is unknown (i.e, unknown source parameters are [Q_0, x_0, y_0, and z_0]) under different atmospheric conditions. The inversion characteristic law under other different complex practical application scenarios arising from unknown source parameters (i.e., Q_0, [Q_0, z_0], and [Q_0, x_0, and y_0]), atmospheric dispersion conditions, and the possible interaction mechanism between source location prior information and source strength inversion have not been revealed. This limits our understanding of the source inversion problem.

Consequently, the aim of this study was to comprehensively investigate the optimization of source inversion performance under multiple specific application scenarios. In an effort to reflect reality, 68 experiments from the Parris Grass field experiment dataset were used as the basic data (Barad, 1958). Four inversion models corresponding to four source inversion scenarios were established based on a relationship analysis between unknown source parameters and real air pollution events. Next, the source strength estimation performance (i.e., accuracy and robustness) under the four inversion scenarios was evaluated under different atmospheric dispersion conditions (i.e., Pasquill stability classes A, B, C, D, E, and F). The relationship between the performance of the source strength estimation and unknown source location parameters was revealed. Furthermore, the estimation performances of different location parameters were evaluated under different atmospheric conditions, and those of the same parameter under different application scenarios were compared. The results of this study can deepen the understanding of the impacts of external environmental factors on source inversion and provide a valuable reference for objectively evaluating and utilizing the source inversion results in practice.

METHODS

As mentioned in the introduction section, the core idea of the source inversion technology is determining the unknown source information by solving an inversion model that minimizes the gap between the observed and simulated concentrations (**Figure 1**). Thus, combined with this concept, the methodology section was divided into four sub-sections: forward dispersion model, source inversion model, basic field experimental data, and inversion performance evaluation method.

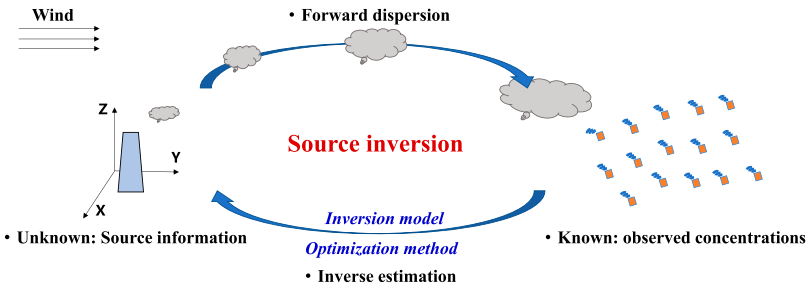

FIGURE 1 | Concept diagram of source inversion.

TABLE 1 | Dispersion parameter schemes established by BRRIGS.

Atmospheric conditions (Pasquill standard)	σ_y (m)	σ_z (m)
A (extremely unstable)	$0.22\cdot(x\text{-}x_0)\cdot(1 + 0.0001\cdot(x\text{-}x_0))^{-0.5}$	$0.20\cdot(x\text{-}x_0)$
B (stable)	$0.16\cdot(x\text{-}x_0)\cdot(1 + 0.0001\cdot(x\text{-}x_0))^{-0.5}$	$0.12\cdot(x\text{-}x_0)$
C (slightly stable)	$0.11\cdot(x\text{-}x_0)\cdot(1 + 0.0001\cdot(x\text{-}x_0))^{-0.5}$	$0.08\cdot(x\text{-}x_0)\cdot(1 + 0.0002\cdot(x\text{-}x_0))^{-0.5}$
D (neutral)	$0.08\cdot(x\text{-}x_0)\cdot(1 + 0.0001\cdot(x\text{-}x_0))^{-0.5}$	$0.06\ (x\text{-}x_0)\cdot(1 + 0.0015\cdot(x\text{-}x_0))^{-0.5}$
E (stable)	$0.06\cdot(x\text{-}x_0)\cdot(1 + 0.0001\cdot(x\text{-}x_0))^{-0.5}$	$0.03\ (x\text{-}x_0)\cdot(1 + 0.0003\cdot(x\text{-}x_0))^{-1}$
F (extremely stable)	$0.04\cdot(x\text{-}x_0)\cdot(1 + 0.0001\cdot(x\text{-}x_0))^{-0.5}$	$0.016\ (x\text{-}x_0)\cdot(1 + 0.0003\cdot(x\text{-}x_0))^{-1}$

Note: x_0 represents the horizontal downwind location parameter of the gas release source.

Forward Dispersion Model

A dispersion model with high efficiency and relatively high accuracy is generally required to conduct source inversion in small-scale regions in practice. From the viewpoint of practical applications (source term estimations and prediction concentrations) (MEPPRC, 2004; Senocak et al., 2008; Lushi and Stockie, 2011; Stockie, 2011; Ma et al., 2017; Ma et al., 2018), the Gaussian plume model was adopted in this study. According to the dispersion theory of the Gaussian model (Pasquill and Smith, 1983), the simulation concentration at any point in the downwind direction can be expressed as follows:

$$C(x,y,z) = \frac{Q_0}{2\cdot\pi\cdot u\cdot\sigma_{y_{(x-x_0)}}\cdot\sigma_{z_{(x-x_0)}}}\exp\left(-\frac{(y-y_0)^2}{2\cdot\sigma^2_{y_{(x-x_0)}}}\right)* \left[\exp\left(-\frac{(z-z_0)^2}{2\cdot\sigma^2_{z_{(x-x_0)}}}\right)+\exp\left(-\frac{(z+z_0)^2}{2\cdot\sigma^2_{z_{(x-x_0)}}}\right)\right], \quad (1)$$

where C(x,y,z) is the pollutant concentration (g/m^3) at the monitoring site (x,y,z) (m); Q_0, y_0, and z_0 represent the pollutant emission rate parameter (g/s), horizontal crosswind location parameter (m), and the release height parameter (m); u is the near-surface average wind speed (m/s); σ_y and σ_z represent the dispersion parameters in the horizontal and vertical directions, respectively, which are the functions of downwind distance ($x\text{-}x_0$). The BRRIGS scheme (Briggs, 1973) was used to calculate the dispersion parameters. See **Table 1** for further details.

Source Inversion Model

The widely used form of the sum of deviation squares (Zheng and Chen, 2010; Ma et al., 2018; Dong et al., 2020) was also used to construct the inversion models in this study, which is expressed as follows:

$$\min f = \sum_{n=1}^{n}\left(c_{obs,i} - c_{sim,i}\right)^2. \quad (2)$$

In **Eq 2**, $c_{obs,i}$ and $c_{sim,i}$ are the monitoring concentration and simulated concentration, respectively, of the sampling site i; and N is the number of sampling sites in the downwind.

As described in the introduction section, different pollutant release types may correspond to different prior source location information available. According to the difference in location prior information, the source emission estimation of hazardous pollutants can be divided into two main cases: the known release source location (i.e., only source strength is unknown) and the unknown release source location (i.e., source strength and certain location parameters are unknown). In the case of an unknown release source location, it can be further divided into 1) only the release height is unknown (e.g., emissions from fires or certain industrial smokestacks), 2) only the horizontal location is unknown (e.g., emissions from near-ground source leakages), and 3) horizontal location and height are both unknown (e.g., emissions from near-ground or elevated source leakages). Thus, four source emission estimation scenarios were determined based on the aforementioned analysis, and four corresponding source emission inversion models were built by combining **Eqs. 1**, **2**. The expressions under four source estimation scenarios are as follows:

Scenario 1. Only estimating source strength (single parameter estimation).

$$\min f = \sum_{n=1}^{n} \left\{ c_{obs,i} - \frac{Q'_0}{2\cdot\pi\cdot u\cdot\sigma_{y(x_i-x_0)}\cdot\sigma_{z(x-x_0)}} \exp\left(-\frac{(y-y_0)^2}{2\cdot\sigma^2_{y(x_i-x_0)}} \right) * \left[\exp\left(-\frac{(z_i-z_0)^2}{2\cdot\sigma^2_{z(x_i-x_0)}} \right) + \exp\left(-\frac{(z_i+z_0)^2}{2\cdot\sigma^2_{z(x_i-x_0)}} \right) \right] \right\}^2, \quad (3)$$

where Q'_0 is the unknown source parameter (i.e., the source strength) to be estimated.

Scenario 2. Estimating both source strength and release height (double parameter estimation).

$$\min f = \sum_{n=1}^{n} \left\{ c_{obs,i} - \frac{Q'_0}{2\cdot\pi\cdot u\cdot\sigma_{y(x_i-x_0)}\cdot\sigma_{z(x-x_0)}} \exp\left(-\frac{(y-y_0)^2}{2\cdot\sigma^2_{y(x_i-x_0)}} \right) * \left[\exp\left(-\frac{(z_i-z'_0)^2}{2\cdot\sigma^2_{z(x_i-x_0)}} \right) + \exp\left(-\frac{(z_i+z'_0)^2}{2\cdot\sigma^2_{z(x_i-x_0)}} \right) \right] \right\}^2, \quad (4)$$

where Q'_0 and z'_0 are the unknown source parameters (i.e., source strength and release height) to be estimated.

Scenario 3. Estimating both source strength and horizontal location (triple parameter estimation).

$$\min f = \sum_{n=1}^{n} \left\{ c_{obs,i} - \frac{Q'_0}{2\cdot\pi\cdot u\cdot\sigma_{y(x_i-x'_0)}\cdot\sigma_{z(x-x'_0)}} \exp\left(-\frac{(y-y'_0)^2}{2\cdot\sigma^2_{y(x_i-x'_0)}} \right) * \left[\exp\left(-\frac{(z_i-z_0)^2}{2\cdot\sigma^2_{z(x_i-x'_0)}} \right) + \exp\left(-\frac{(z_i+z_0)^2}{2\cdot\sigma^2_{z(x_i-x'_0)}} \right) \right] \right\}^2, \quad (5)$$

where Q'_0, x'_0, and y'_0 are the unknown source parameters (i.e., source strength, horizontal downwind location parameter, and horizontal crosswind location parameter, respectively) to be estimated.

Scenario 4. Estimating source strength, horizontal location, and release height (quadruple parameter estimation).

$$\min f = \sum_{n=1}^{n} \left\{ c_{obs,i} - \frac{Q'_0}{2\cdot\pi\cdot u\cdot\sigma_{y(x_i-x'_0)}\cdot\sigma_{z(x-x'_0)}} \exp\left(-\frac{(y-y'_0)^2}{2\cdot\sigma^2_{y(x_i-x'_0)}} \right) * \left[\exp\left(-\frac{(z_i-z'_0)^2}{2\cdot\sigma^2_{z(x_i-x'_0)}} \right) + \exp\left(-\frac{(z_i+z'_0)^2}{2\cdot\sigma^2_{z(x_i-x'_0)}} \right) \right] \right\}^2, \quad (6)$$

where Q'_0, x'_0, y'_0, and z'_0 are the unknown source parameters (i.e., source strength, horizontal downwind location parameter, horizontal crosswind location parameter, and release height parameter, respectively) to be estimated.

The aforementioned equations indicate that source inversion is an ill-posed and nonlinear optimization problem; however, the degrees of nonlinearity vary with specific unknown parameters. The genetic algorithm (GA) was selected as the optimization method of source inversion in this study owing to its excellent capability in global searching and robustness (Haupt, 2005; Haupt et al., 2006; Long et al., 2010). It mainly includes the process of individual evaluation iteration, selection, crossover and mutation, and finally produces a best solution through the continuous iterative evolution of population. The mutation (0.2) and crossover rates (0.5) in the GA were chosen based on previous studies (Haupt, 2005). The average change in the fitness function value less than the threshold value (10^{-6}) was set as the algorithm convergence termination criterion of the search process. One hundred independent calculations were performed for each experiment in order to reduce the influence of randomness on inversion results. **Figure 2** shows the flowchart of performance evaluation of source inversion in this study.

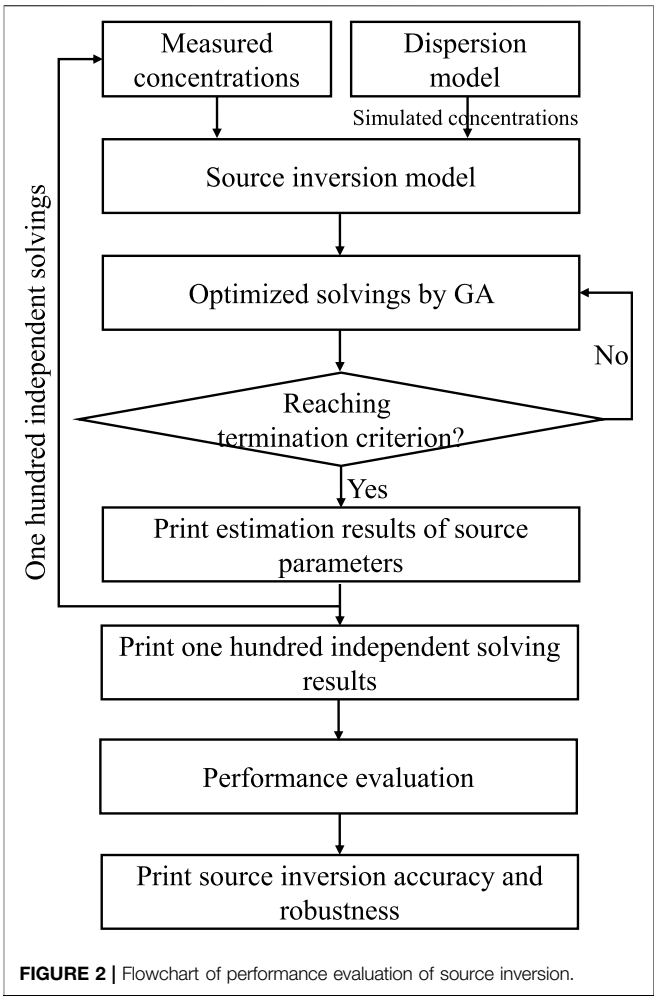

FIGURE 2 | Flowchart of performance evaluation of source inversion.

Field Experimental Data

Prairie Grass field experiments were conducted over a broad flat grassland in O'Neill, Nebraska, in 1956 (Barad, 1958). The overall roughness of the experimental site was approximately 6 cm. In total, 68 release experiments of SO_2 were performed, and each experiment lasted for 10 min (**Table 2**). SO_2 gas was continuously released as a point source at 0.46 or 1.5 m (the last six trials, i.e., numbers R63 to R68). The downwind sample collection adopted a semicircular arrangement of points and the base

TABLE 2 | Information of field experiments under different atmospheric conditions.

Atmospheric stability class	Serial number of the experiments
A (extremely unstable)	R15, R16, R25, R47, and R52.
B (unstable)	R1, R2, R7, R10, and R48S.
C (slightly unstable)	R5, R8, R9, R19, R27, R43, R44, R49, R50, and R62.
D (neutral)	R6, R11, R12, R17, R20, R21, R22, R23, R24, R29, R30, R31, R33, R34, R35S, R37, R38, R42, R45, R46, R48, R51, R54, R55S, R56, R57, R60, R61, R65, and R67.
E (stable)	R18, R28, R41, R66, and R68.
F (extremely stable)	R3, R4, R13, R14, R32, R35, R36, R39, R40, R53, R58, and R59.

line of the horizontal sampling network was oriented along a true east–west line to take advantage of the prevailing southerly winds. Five arcs at distances of 50, 100, 200, 400, and 800 m from the release source were set as sampling arcs, and approximately 600 sensors were scattered along the sampling arcs to monitor downwind concentrations with a sampling height of 1.5 m. The coverage area of each sampling layer was 180°; the first four layers of sampling points were arranged at intervals of 1°, and the fifth layer was arranged at intervals of 2°. Wind speeds and wind direction at the height of 2 m above the ground were measured during the experiments by the cup anemometers and the means of airfoil-type vanes, respectively. Cervone and Franzese (2011) divided the dataset into six subset data of different atmospheric conditions based on the Pasquill atmospheric stability classification standard. The number of field experiments under Pasquill atmospheric stability classes A (extremely unstable), B (unstable), C (slightly unstable), D (neutral), E (stable), and F (extremely stable) were 5, 5, 10, 31, 5, and 12, respectively. To reflect the effects of atmospheric conditions in the real world, all valid detection concentrations above the sensor detection limit were used for each experiment.

Inversion Performance Evaluation Method

The absolute value of the relative deviation (ARD) of the source strength and the absolute value of deviation (AD) of the source location parameters were introduced to characterize the accuracy of the source inversion.

$$ARD = \left|\left(E_{Q,J} - R_{Q,J}\right)\right| / R_{Q,J}, \tag{7}$$

$$AD = \left|E_{L,J} - R_{L,J}\right|, \tag{8}$$

where E represents the inversion value, R represents the real value, Q is the source strength, J represents the serial number of the test experiment, and L represents the source location parameter (x_0, y_0, and z_0).

The coefficient of variation (CV) was used to evaluate the robustness of the source inversion. The formula is as follows:

$$CV = \mu_{(Q,L)} / m_{(Q,L)}, \tag{9}$$

where μ represents the standard deviation of the inversion results (estimation values of source strength or source location) and m represents the mean value of the inversion results.

In this study, ARDs of the inversion results for 100 independent calculations for each field experiment were calculated first, then mean of 100 ARDs was taken as the result of each field experiment, and mean ARD of all field experiments for each atmospheric stability class was taken as the final result of each atmospheric stability class. The CV of each field experiment was calculated first based on the inversion results of 100 independent calculations, and the mean CV of all field experiments for each atmospheric stability class was taken as the final result of each atmospheric stability class.

RESULTS

Source Strength Estimation Under Multiple Scenarios

Figure 3 shows the change progress of the best fitness value with evolutionary generations for GA optimization under different inversion scenarios. From the figure, as evolution progressed, the fitness value gradually declined. The process for searching source parameters under each inversion scenario stopped when the fitness value was less than the threshold value (i.e., 10^{-6}). This indicates that the genetic algorithm can be successfully converged and efficiently applied to source parameter inversion.

Figure 4 shows the estimation accuracy and robustness of the source strength estimation under different inversion scenarios. **Figures 4A,B** show results for the single parameter and double parameter inversion. The atmospheric conditions had a similar effect on source strength inversion between the two inversion scenarios. Specifically, regarding the inversion accuracy, the comparable interquartile ranges, numerical distribution intervals of deviation data, mean values, and median values for these two scenarios under nearly all stability classes (except the stability class F) revealed that the impact of the pollutant release height parameter on the inversion accuracy of source strength was limited. The numerical distribution intervals of the deviations in the box under atmospheric stability classes A (extremely unstable condition) and F (extremely stable condition) were obviously higher than those under the other stability classes. These findings indicated that most experiments under stability classes A and F had large estimation deviations in source inversion. Notably, for the stability class A, the minimum and mean values of ARD under single (71.1 and 130.1%) and double (72.5 and 129.6%) parameter inversion were obviously larger than those of other stability classes. These aforementioned findings demonstrated that the inversion accuracy of source strength under extreme atmospheric conditions performed worse than the other conditions, wherein the inversion

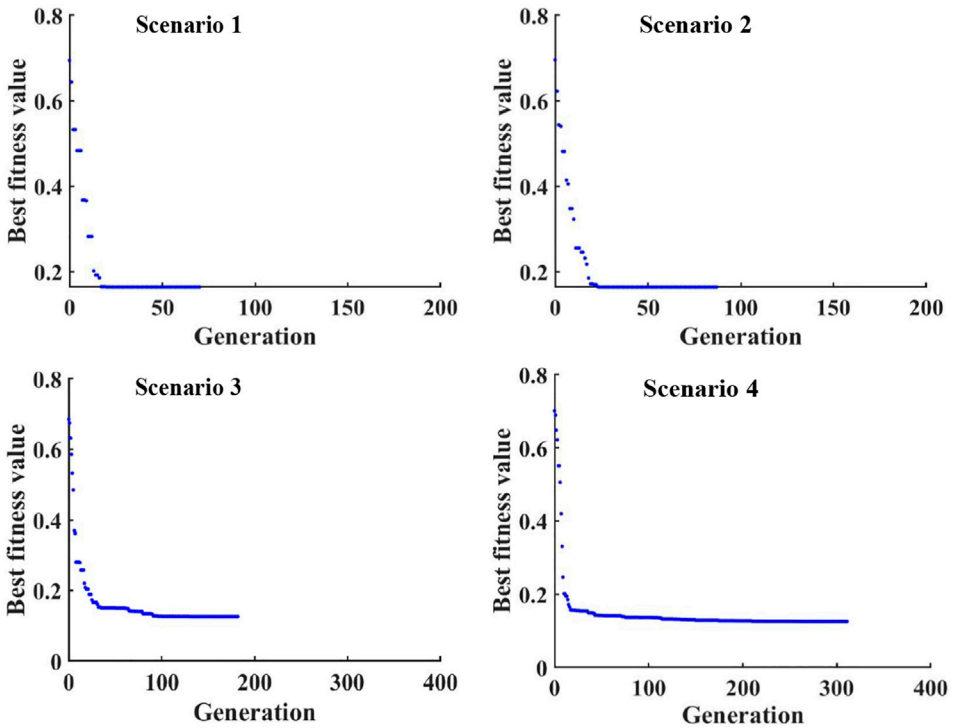

FIGURE 3 | Change progress of best fitness value with evolutionary generations for GA optimization under different inversion scenarios: Scenario 1: only estimating source strength (Q_0); (b) Scenario 2: estimating source strength (Q_0) and release height (z_0); Scenario 3: estimating both source strength (Q_0) and horizontal location (x_0, y_0); Scenario 4: estimating source strength (Q_0), horizontal location (x_0, y_0), and release height (z_0).

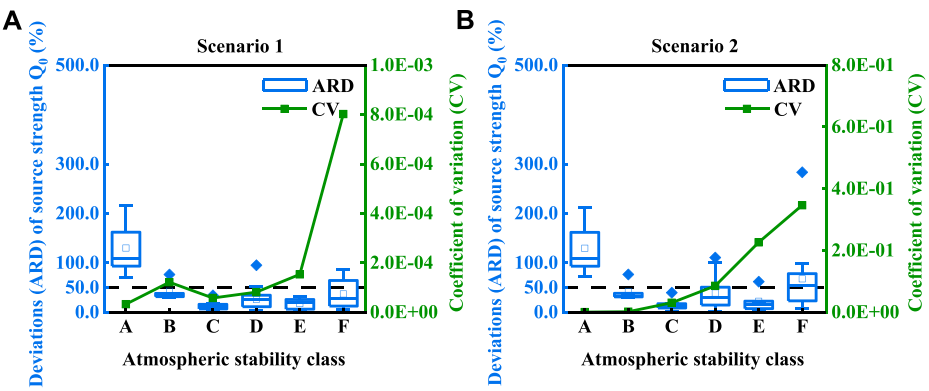

FIGURE 4 | Boxplots of the inversion accuracy index (ARD) and line charts of the inversion robustness index (CV) for source strength (Q_0) estimation under different application scenarios: **(A)** Scenario 1: only estimating source strength (Q_0), and **(B)** Scenario 2: estimating source strength (Q_0) and release height (z_0).

accuracy was the worst under extremely unstable atmospheric conditions. The worst inversion accuracy under extremely unstable atmospheric conditions might be the main reason for the significant decline in the simulation performance of the forward model for stability class A (Mao et al., 2020a). However, for the obviously large estimation deviations under extremely stable conditions, the reasons might have been mainly caused by the combined action of the poor simulation performance of the forward model (Mao et al., 2020a) and the fewer number of sensors with effective ground measurements owing to a smaller dispersion footprint (Cervone and Franzese, 2011; Cantelli et al., 2015). The aforementioned analysis indicated that the dominant factors that obviously reduced the inversion accuracy in two extreme atmospheric conditions were completely different. Additionally, there were obviously larger interquartile ranges of deviations under the atmospheric stability classes A

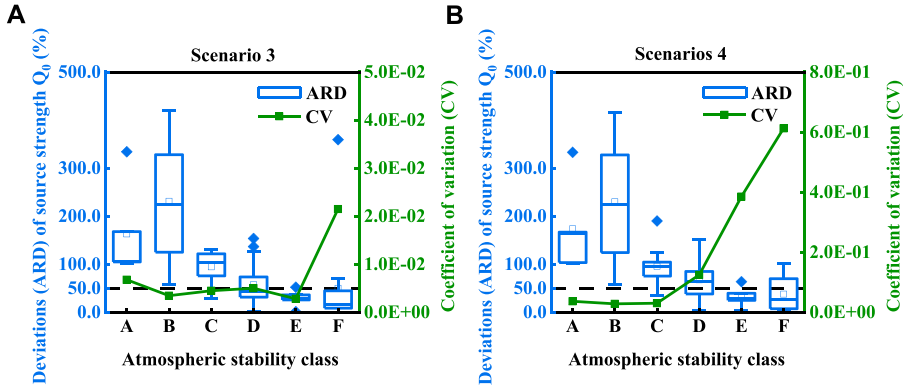

FIGURE 5 | Boxplots of the inversion accuracy index (ARD) and line charts of the inversion robustness index (CV) for source strength (Q_0) estimation under different application scenarios: **(A)** Scenario 3: estimating both source strength (Q_0) and horizontal location (x_0, y_0), and **(B)** Scenario 4: estimating source strength (Q_0), horizontal location (x_0, y_0), and release height (z_0).

(68.7 and 68.6% for single and double parameter inversion, respectively) and F (48.8 and 52.0% for single and double parameter inversion, respectively). This indicated that data in the box fluctuated greatly, representing a large difference in the inversion accuracy of different experiments under both stability classes. The reasons for large individual differences among these experiments in the inversion accuracy may also be attributed to the aforementioned factors. Conversely, the estimation accuracy of source inversion performed well under the stability classes B, C, D, and E because of small interquartile ranges and low numerical distribution intervals of inversion deviations, where the number of tested experiments with ARD less than 50.0% accounted for more than 75% in each stability class.

For robustness, CVs in all stability classes for single parameter inversion (<0.001) and double parameter inversion (<0.4) were both at a relatively low level. This suggested that the atmospheric conditions had only a limited impact on inversion robustness. There were slightly higher values of CVs under the atmospheric stability class F than under other stability classes. It indicated that the inversion robustness performed relatively worse under extremely stable atmospheric conditions. However, comparing the results of **Figures 4A,B**, the CV of the double parameter inversion was obviously higher than that of the single parameter inversion by more than an order of magnitude in each stability class. This phenomenon indicated that the inversion robustness of the source strength largely declined as the unknown parameter was added to the source height. **Figures 5A,B** show the results under inversion scenarios of triple and quadruple parameters. These figures reveal that the variation characteristics of the parameter inversion performance under atmospheric conditions under these two scenarios were also similar. Regarding accuracy, similar to single and double parameter scenarios, the comparable interquartile ranges, numerical distribution intervals of deviation data, mean values, and median values for these two scenarios under each stability class revealed that the vertical release height parameter had little influence on the inversion accuracy of source strength. The numerical distribution intervals of the deviation data in the box under unstable atmospheric conditions (stability classes A, B, and C) were obviously higher than those in the box under neutral (stability class D) and stable conditions (stability classes E and F), with most ARDs larger than 50.0%. However, the interquartile ranges (202.8 and 203.2% for triple and quadruple parameter inversion, respectively), and minimum values of ARD (225.2 and 225.0% triple and quadruple parameter inversion, respectively) under the stability class B were much larger than those of the other two unstable stability classes. This finding suggests that the inversion accuracy for unstable atmospheric conditions was obviously worse than that for extremely unstable and slightly unstable dispersion conditions. However, what seems to be contradictory is that the inversion accuracy under unstable conditions (stability class B) was obviously worse than that under extremely unstable conditions (stability class A). This phenomenon was also found by Cui et al. (2019) where the source inversion performance was evaluated under different stability classes based on another optimization algorithm (PSO-NM). Cervone and Franzese et al. (2011) summarized the calculated error between the simulated and observed concentrations under all the 68 Prairie Grass field experiments and found that four out of the five experiments had a remarkably larger margin of errors between the simulated and observed concentrations under the stability class B. Meanwhile, Cantelli et al. (2015) investigated the relationship between the averaged wind direction standard deviation and distance errors of source location inversion and found that the worst inversion performance of source location was associated with high values of the measured averaged wind direction standard deviation. It is worthy to note that this phenomenon had no relation with single and double parameter scenarios. This might be related to the fact that the horizontal location parameter increased the complexity of solving nonlinear problems. Thus, in summary, the large uncertainty of inversion results under unstable conditions may be attributed to two factors including the large simulation error of the forward model due to insufficient description for the turbulent characteristics of the dynamic wind

field by the model itself and the nonlinear degree variation with the addition of unknown horizontal location parameters. On the whole, from unstable to slightly stable atmospheric conditions (i.e., stability classes A–E), the inversion accuracy generally tended to increase because the interquartile ranges, mean values, and median values all showed a decreasing tendency. This finding indicates that the inversion accuracy gradually improved with the stabilization of atmospheric conditions. However, large interquartile ranges and the mean value of ARD occurred when the atmospheric dispersion condition developed to an extremely stable state (i.e., the stability class F). This finding indicated that the extremely stable condition increased the uncertainty of the inversion deviations of the source strength. Our results of atmospheric condition influence based on the classical GA method are basically consistent with those based on improved algorithms (PSO-NM, Cui et al., 2019; non-Darwinian evolutionary algorithm, Cervone and Farnese, 2011) when applied to the same Prairie Grass experiments and under the same inversion scenarios. However, different conclusions stating that the inversion accuracy under the A and B classes performed relatively well were drawn by Catelli et al. (2015). This is mainly caused by the difference in evaluation methods of inversion results. In the study by Cantelli et al., the inversion performance was evaluated by comparing the number of experiments in which the inversion deviation exceeded a certain value under different stability degrees, whereas the inversion performance was evaluated by calculating the mean value of the inversion deviation of all experiments in the present and previous studies (i.e., Cui et al., 2019; Cervone and Franzese, 2011).

Comparing the different scenarios, the mean ARDs of 68 experiments were 34.4, 46.0, 80.1, and 83.6% for single parameter, double parameters, triple parameters, and quadruple parameters, respectively. This indicated that the estimation accuracy of source strength gradually worsened with an increase in the number of unknown source parameters. Additionally, by comparing the scenarios of single and double parameters and the scenarios of triple and quadruple parameters, it was obviously found that source release height had a minimal effect on the estimation accuracy; whereas, by comparing the scenarios of single and triple parameters and the scenarios of double and quadruple parameters, it was obviously found that source horizontal location largely affected the estimation accuracy. This indicated that the unknown source horizontal location parameters were important factors influencing the accuracy of source strength inversion and source release height only had limited influence.

For robustness, there were obviously higher values of CVs under the atmospheric stability class F (0.02 and 0.61 for the triple and quadruple parameter inversions, respectively) than those of other stability classes. This phenomenon is similar to the single and double parameter inversions. The robustness performed worse in the case of quadruple parameter inversion than in the case of triple parameter inversion under each stability class because the CVs were obviously larger (0.037, 0.028, 0,03, 0.124, 0.385, and 0.613 for the stability classes A, B, C, D, E, and F, respectively) when four parameters were both estimated. Notably, a remarkable picture occurred when we compared the robustness of the source strength estimation under all scenarios: CVs had more than one order of magnitude and were smaller under triple parameter inversion than under double and quadruple parameter inversion in all atmospheric conditions except for the stability classes A and B; and although the CVs of quadruple parameter inversion were generally higher than those of double parameter inversion, they were of the same order of magnitude as those of double parameter inversion. These findings indicated that the inversion robustness did not necessarily deteriorate as expected with an increase in the number of unknown parameters, whereas, it was obviously affected by the type of the unknown source location parameter. In other words, the inversion robustness was more susceptible to source release height parameter in the source strength estimation and relatively insensitive to horizontal positional parameters.

Source Location Estimation Under Multiple Scenarios

Accurately locating pollutant sources is also important in some scenarios, especially in the case of toxic gas release caused by an accidental leak or terrorist acts (Ma et al., 2018). **Figure 6** shows the estimation deviations and CV for source location parameters (i.e., x_0, y_0, z_0) estimation under different inversion scenarios. **Figure 6A** shows the results of the inversion performance indicators of horizontal location x_0 under triple and quadruple parameter inversion. Regarding accuracy, the variation characteristics of inversion deviations under the effects of atmospheric conditions were similar for these two inversion scenarios. The magnitude of the deviation values was very close under each stability class (A, B, C, D, E, and F) for triple parameter inversion (14.6, 74.2, 21.5, 27.4, 20.4, and 94.7 m) and quadruple parameter inversion (14.7, 73.9, 19.0, 27.6, 23.3 and 99.4 m). Obviously, the estimation accuracy of location x_0 changed little with the addition of release height parameters. This indicated that the inversion accuracy of location x_0 was insensitive to the source release height. The higher numerical distribution intervals of the deviation data, larger mean values, and median values for the stability classes B and F than for other stability classes suggested that the inversion accuracy was obviously worse in unstable and extremely stable atmospheric conditions. The relatively larger interquartile ranges for the stability classes B and F indicated that there were larger fluctuations of inversion deviation for different experiments. These findings for location x_0 were similar to source strength Q_0. The inversion accuracy performed relatively well with low numerical distribution intervals (most ADs <50.0 m) for stability classes A, C, D, and E. For robustness, all CVs were at a low level, with values less than 0.1. This finding indicated that the inversion robustness performed well in estimating the location x_0. However, there were large differences in the robustness. The CV of each stability class (A, B, C, D, E, and F) was obviously higher for quadruple parameter inversion (0.102, 0.021, 0.045, 0.093, 0.061, and 0.137) than that of triple parameter inversion (0.060, 0.005, 0.020, 0.080. 0.014, and 0.020). This finding indicated that the inversion robustness of location parameter

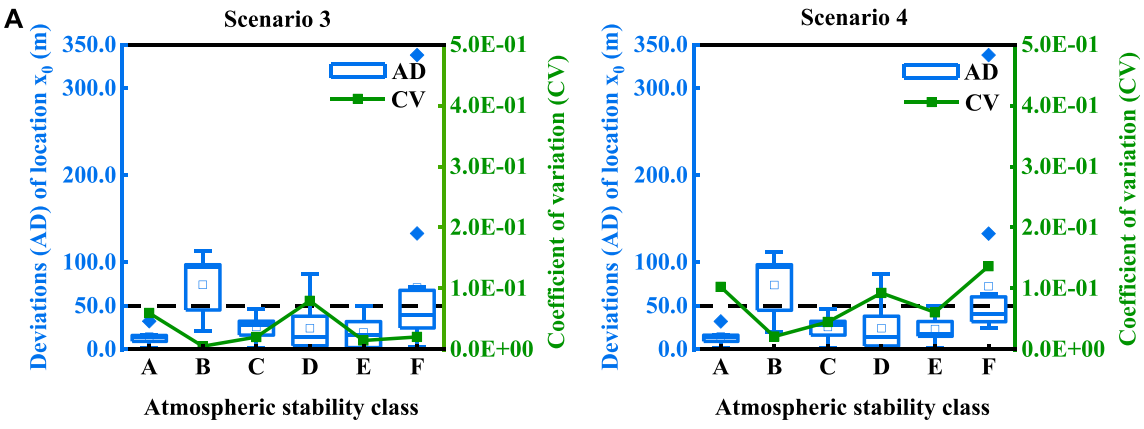

Comparison of inversion performance indicators of horizonal location x_0

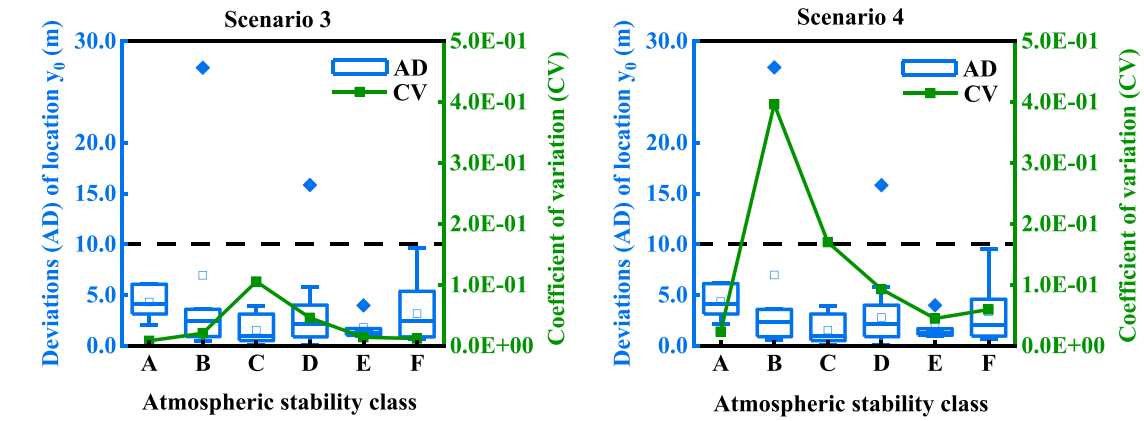

Comparison of inversion performance indicators of horizonal location y_0

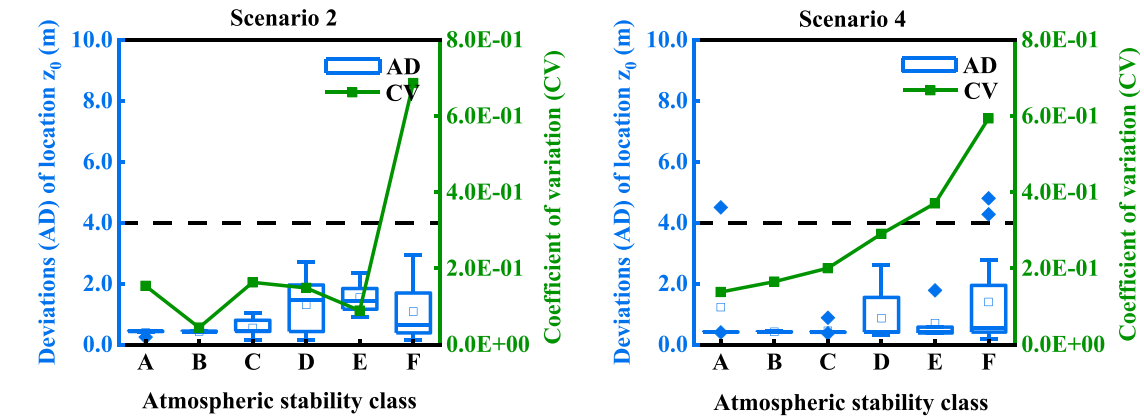

Comparison of inversion performance indicators of vertical height z_0

FIGURE 6 | Boxplots of the inversion accuracy index (AD) and line charts of the inversion robustness index (CV) for source location (i.e., x_0, y_0, and z_0) estimation. **(A)** Comparison of inversion performance indicators of the horizontal location parameter x_0, **(B)** comparison of inversion performance indicators of the horizontal location parameter y_0, and **(C)** comparison of inversion performance indicators of the vertical height parameter z_0.

x_0 was obviously affected by the unknown source height parameter. **Figure 6B** shows the comparison results of the inversion performance indicators of the horizontal location y_0. Overall, the variation characteristics of the inversion accuracy with atmospheric conditions were consistent for the two inversion scenarios. Interquartile ranges and minimum values of inversion deviations were comparable for the triple and quadruple parameter inversion scenarios. Compared with parameter x_0, inversion deviations were obviously reduced, with deviations less than 10.0 m in most experiments. For robustness, the largest CVs for triple parameter inversion and quadruple parameter inversion were obtained in stability classes C (0.11) and B (0.40), respectively. Overall, CVs of the triple parameter inversion were slightly lower than those of the quadruple parameter inversion in most atmospheric conditions. **Figure 6C** shows the comparison results of the inversion performance indicators of the source release height z_0. There were only slight differences between the double parameter inversion and quadruple parameter inversion scenarios in accuracy under each atmospheric stability class, and the deviations under the two inversion scenarios were very low (< 4.0 m). Regarding robustness, similar decline characteristics of the robustness with the atmospheric condition variation occurred, and the highest CVs (0.69 and 0.59 for triple and quadruple parameter inversions, respectively) occurred under extreme conditions (stability class F).

DISCUSSION

The practical application and popularization of optimized source inversion technology must overcome substantial challenges because complex, real air pollution accident scenes generally correspond to different source inversion scenarios. This study investigated the performance variation law of optimization source inversion in small-scale regions (<1 km) under multiple scenarios involving different atmospheric conditions (stability class A–F) and unknown source parameters (source strength and location) and further explored the influencing mechanism of different location parameters on the estimation performance of source strength. The results showed that atmospheric conditions had different impacts on the source strength inversion under different parameter inversion scenarios. Extreme atmospheric conditions (stability classes A and F) can obviously reduce the estimation accuracy of source strength for single and double parameter inversion scenarios. However, the dominant factors that reduced the inversion accuracy in two extreme atmospheric conditions were completely different. Thereinto, the poor inversion accuracy under stability class A may mainly be attributed to poor model simulations. However, the poor performance under the stability class F was caused by the combined actions of the poor model simulations and the fewer available sensors. However, for triple and quadruple parameter scenarios, the estimation accuracy of the source strength was worse under unstable atmospheric conditions (stability classes A, B, and C) than that under other atmospheric conditions. Thereinto, a contradiction occurred stating that the inversion accuracy under unstable conditions (stability class B) was worse than that under extremely unstable conditions. This large uncertainty of inversion results may be attributed to the combined effects of the increase in the complexity of nonlinearity problem with the addition of horizontal location parameters and poor model simulation performance caused by the insufficient description for the dynamic wind field. Relationship analysis between estimation performance of source strength and source location revealed that source strength inversion performance was affected by location parameters; robustness was markedly reduced when source height was unknown, whereas accuracy was obviously reduced when source horizontal location parameters were unknown.

These new findings in this article can fill the knowledge gap in the characteristic laws of optimized source inversion technology under complex application scenarios and the interaction relationship between different unknown source parameters. The results of the influence mechanism of source location prior information on source strength have important guiding significance to further improving the inversion accuracy of source strength in practical environmental management. Additionally, this study quantified the uncertainty of the inversion results under multiple specific scenarios based on sufficient experimental data. This can provide a reference for pollutant emission estimation in small-scale flat terrains (e.g., small-scale industrial parks distributed in flat rural or suburban areas) in real applications. However, the limitations of this study should be investigated in further research. For example, the number of experiments used in some atmospheric stability classes (i.e., stability A, B, and E) was small. This may have caused uncertainties in the results. For a limited number of searching problems (less than four variables) in this study, the GA may not be the optimal method in searching solutions when the factors such as solving efficiency, absolute accuracy, and so on were considered. Thus, a more appropriate optimization method should be selected according to the requirements in actual research studies or real-world applications. Furthermore, the conclusions may provide a limited application reference in practice for more complex scenarios (e.g., urban and long-range scale) because the basic dataset used is from a flat grassland terrain on a small scale, and the dispersion model is a relatively simple Gaussian model where the pollution dispersion process under complex terrains cannot be well described. Additionally, this study did not focus on the secondary chemical transformation of pollutants; therefore, the study results may not be successfully applied to secondary pollutants.

CONCLUSION

This study investigated the estimation performance of source optimization inversion under multiple application scenarios involving different atmospheric dispersion conditions and inversion parameters. Four source inversion models were constructed based on typical application scenarios of source estimation. The genetic algorithm was selected as the optimization inversion method, and the Prairie Grass dataset,

including 68 experiments, was selected as the basic data to evaluate the estimation performance. The results showed that the atmospheric conditions obviously affected the source strength inversion performance. The atmospheric conditions had similar effect characteristics on the source strength inversion for the single and double parameter inversion scenarios. The source inversion performed poorly with regard to the estimation accuracy of source strength under extremely unstable (stability class A) and stable (stability class F) atmospheric conditions. However, the robustness of source strength estimation was obviously poor under only extremely unstable atmospheric conditions (stability class F). For the triple and quadruple parameter inversion scenarios, similar performances were also shown; that is, the inversion accuracy of the source strength was worse under unstable atmospheric conditions (stability classes A, B, and C) than under other atmospheric conditions. As for robustness, similar to the single and double parameter inversions, there were obviously high values of the CV under the atmospheric stability class F. Comparative results of the four inversion scenarios indicated that the estimation accuracy of source strength declined with an increase in the number of unknown source parameters. The estimation accuracy of the source strength obviously declined when the horizontal location parameters were unknown, and the estimation robustness of the source strength greatly declined when the source height parameter was unknown. The results of location parameter inversion showed that, for parameter x_0, the variation characteristics of inversion accuracy under different atmospheric conditions were essentially consistent for the two scenarios. The robustness of source inversion is vulnerable to the unknown source height parameter, whereas the inversion accuracy is not sensitive to the unknown source height. There were obviously smaller estimation deviation distribution ranges for the parameters y_0 and z_0 than for the parameter x_0. Furthermore, there was a little difference in the accuracy of the two parameters y_0 and z_0 under different inversion scenarios. Regarding robustness, related to the parameter y_0, the performance was relatively worse owing to the addition of an unknown source height parameter. Regarding the parameter z_0, similar decline characteristics of robustness occurred with variations in atmospheric conditions; the highest CVs occurred under extreme conditions (stability class F). This study can deepen the understanding of the impacts of external environmental factors on source inversion and provide a reference for pollutant emission estimation and location tracking of air pollution events in small-scale flat terrains in practice.

DATA AVAILABILITY STATEMENT

Publicly available datasets were analyzed in this study. These data can be found here: Barad, M.L. (1958). PROJECT PRAIRIE GRASS, A FIELD PROGRAM IN DIFFUSION. Air Force Cambridge Research Center, Bedford, United States, pp. 300.

AUTHOR CONTRIBUTIONS

LJ contributed to the conception and design of the study. SM organized the database and wrote the first draft of the manuscript. TC and SC edited the manuscript. FH performed the statistical analysis. All authors contributed to manuscript revision, read, and approved the submitted version.

FUNDING

This research was financially supported by the National Key R&D Program of China (No. 2017YFC0209905) and Beijing Nova Program (Z201100006820098) of the Beijing Municipal Science and Technology Commission.

ACKNOWLEDGMENTS

The authors are grateful to the reviewers for their insightful comments. In addition, we greatly appreciate the Beijing Municipal Education Commission for supporting this work.

REFERENCES

Amoatey, P., Omidvarborna, H., Baawain, M. S., and Al-Mamun, A. (2019). Emissions and Exposure Assessments of SOX, NOX, PM10/2.5 and Trace Metals from Oil Industries: A Review Study (2000-2018). *Process Saf. Environ. Prot.* 123, 215–228. doi:10.1016/j.psep.2019.01.014

Barad, M. L. (1958). *PROJECT PRAIRIE GRASS, A FIELD PROGRAM IN DIFFUSION*. Bedford, USA: Air Force Cambridge Research Center, 300.

Bildirici, M. E. (2017). The Effects of Militarization on Biofuel Consumption and CO 2 Emission. *J. Clean. Prod.* 152, 420–428. doi:10.1016/j.jclepro.2017.03.103

Briggs, G. A. (1973). *Diffusion Estimation for Small Emissions*. Oak Ridge, TN: Atmospheric Turbulence and Diffusion Laboratory, NOAA. ATDL Contribution File NO.79.

Cantelli, A., D'orta, F., Cattini, A., Sebastianelli, F., and Cedola, L. (2015). Application of Genetic Algorithm for the Simultaneous Identification of Atmospheric Pollution Sources. *Atmos. Environ.* 115, 36–46. doi:10.1016/j.atmosenv.2015.05.030

Cervone, G., and Franzese, P. (2011). Non-Darwinian Evolution for the Source Detection of Atmospheric Releases. *Atmos. Environ.* 45, 4497–4506. doi:10.1016/j.atmosenv.2011.04.054

Chen, H., and Carter, K. E. (2020). Hazardous Substances as the Dominant Non-methane Volatile Organic Compounds with Potential Emissions from Liquid Storage Tanks during Well Fracturing: A Modeling Approach. *J. Environ. Manage.* 268, 110715. doi:10.1016/j.jenvman.2020.110715

Clappier, A., and Thunis, P. (2020). A Probabilistic Approach to Screen and Improve Emission Inventories. *Atmos. Environ.* 242, 117831. doi:10.1016/j.atmosenv.2020.117831

Cui, J., Lang, J., Chen, T., Cheng, S., Shen, Z., and Mao, S. (2019). Investigating the Impacts of Atmospheric Diffusion Conditions on Source Parameter Identification Based on an Optimized Inverse Modelling Method. *Atmos. Environ.* 205, 19–29. doi:10.1016/j.atmosenv.2019.02.035

Dong, J., Du, W., Wang, B., and Xu, Q. (2020). Investigating Impacts of Cost Functions to Atmospheric Dispersion Modeling and Source Term Estimation in Turbulent Condition. *CIESC J.* 71 (3), 1163–1173. (Chinese). doi:10.11949/0438-1157.20191550

Du, L., Wang, H., and Xu, H. (2020). Analysis of Spatial-Temporal Association and Factors Influencing Environmental Pollution Incidents in China. *Environ. Impact Assess. Rev.* 82, 106384. doi:10.1016/j.eiar.2020.106384

Gao, Z., Desjardins, R. L., and Flesch, T. K. (2009). Comparison of a Simplified Micrometeorological Mass Difference Technique and an Inverse Dispersion Technique for Estimating Methane Emissions from Small Area Sources. *Agric. For. Meteorology* 149, 891–898. doi:10.1016/j.agrformet.2008.11.005

Hamblin, S. (2013). On the Practical Usage of Genetic Algorithms in Ecology and Evolution. *Methods Ecol. Evol.* 4, 184–194. doi:10.1111/2041-210X.12000

Haupt, S. E. (2005). A Demonstration of Coupled Receptor/dispersion Modeling with a Genetic Algorithm. *Atmos. Environ.* 39, 7181–7189. doi:10.1016/j.atmosenv.2005.08.027

Haupt, S. E., Young, G. S., and Allen, C. T. (2006). Validation of a Receptor-Dispersion Model Coupled with a Genetic Algorithm Using Synthetic Data. *J. Appl. Meteorology Climatology* 45, 476–490. doi:10.1175/JAM2359.1

Jeričević, A., Gašparac, G., Mikulec, M. M., Kumar, P., and Prtenjak, M. T. (2019). Identification of Diverse Air Pollution Sources in a Complex Urban Area of Croatia. *J. Environ. Manage.* 243, 67–77. doi:10.1016/j.jenvman.2019.04.024

Koutsomarkos, V., Rush, D., Jomaas, G., and Law, A. (2021). Tactics, Objectives, and Choices: Building a Fire Risk index. *Fire Saf. J.* 119, 103241. doi:10.1016/j.firesaf.2020.103241

Lei, J., Miao, X., Liu, Z., Liu, N., and Zhang, L. (2021). Lifted Flame in Fire Whirl: An Experimental Investigation. *Proc. Combustion Inst.* 38, 4595–4603. doi:10.1016/j.proci.2020.07.087

Lin, Y.-C., Lai, C.-Y., and Chu, C.-P. (2021). Air Pollution Diffusion Simulation and Seasonal Spatial Risk Analysis for Industrial Areas. *Environ. Res.* 194, 110693. doi:10.1016/j.envres.2020.110693

Liu, Y., Han, F., Liu, W., Cui, X., Luan, X., and Cui, Z. (2020). Process-based Volatile Organic Compound Emission Inventory Establishment Method for the Petroleum Refining Industry. *J. Clean. Prod.* 263, 121609. doi:10.1016/j.jclepro.2020.121609

Long, K. J., Haupt, S. E., and Young, G. S. (2010). Assessing Sensitivity of Source Term Estimation. *Atmos. Environ.* 44, 1558–1567. doi:10.1016/j.atmosenv.2010.01.003

Lushi, E., and Stockie, J. M. (2010). An Inverse Gaussian Plume Approach for Estimating Atmospheric Pollutant Emissions from Multiple point Sources. *Atmos. Environ.* 44, 1097–1107. doi:10.1016/j.atmosenv.2009.11.039

Ma, D., Tan, W., Zhang, Z., and Hu, J. (2017). Parameter Identification for Continuous point Emission Source Based on Tikhonov Regularization Method Coupled with Particle Swarm Optimization Algorithm. *J. Hazard. Mater.* 325, 239–250. doi:10.1016/j.jhazmat.2016.11.071

Ma, D., Tan, W., Wang, Q., Zhang, Z., Gao, J., Wang, X., et al. (2018). Location of Contaminant Emission Source in Atmosphere Based on Optimal Correlated Matching of Concentration Distribution. *Process Saf. Environ. Prot.* 117, 498–510. doi:10.1016/j.psep.2018.05.028

Mao, S., Lang, J., Chen, T., Cheng, S., Cui, J., Shen, Z., et al. (2020a). Comparison of the Impacts of Empirical Power-Law Dispersion Schemes on Simulations of Pollutant Dispersion during Different Atmospheric Conditions. *Atmos. Environ.* 224, 117317. doi:10.1016/j.atmosenv.2020.117317

Mao, S., Lang, J., Chen, T., Cheng, S., Wang, C., Zhang, J., et al. (2020b). Impacts of Typical Atmospheric Dispersion Schemes on Source Inversion. *Atmos. Environ.* 232, 117572. doi:10.1016/j.atmosenv.2020.117572

Mao, S., Lang, J., Chen, T., and Cheng, S. (2021). Improving Source Inversion Performance of Airborne Pollutant Emissions by Modifying Atmospheric Dispersion Scheme through Sensitivity Analysis Combined with Optimization Model. *Environ. Pollut.* 284, 117186. doi:10.1016/j.envpol.2021.117186

Mepprc (2004). *Technical Guidelines for Environmental Risk Assessment on Projects (HJ/T 169-2004)*. (Chinese) Available from: http://kjs.mep.gov.cn/hjbhbz/bzwb/other/pjjsdz/200412/W020110127329297430823.pdf.

Pasquill, F., and Smith, F. (1983). *Atmospheric Diffusion*. Ellis Horwood Limited.

Senocak, I., Hengartner, N. W., Short, M. B., and Daniel, W. B. (2008). Stochastic Event Reconstruction of Atmospheric Contaminant Dispersion Using Bayesian Inference. *Atmos. Environ.* 42, 7718–7727. doi:10.1016/j.atmosenv.2008.05.024

Singh, S. K., and Rani, R. (2014). A Least-Squares Inversion Technique for Identification of a point Release: Application to Fusion Field Trials 2007. *Atmos. Environ.* 92, 104–117. doi:10.1016/j.atmosenv.2014.04.012

Singh, S. K., and Rani, R. (2015). Assimilation of Concentration Measurements for Retrieving Multiple point Releases in Atmosphere: A Least-Squares Approach to Inverse Modelling. *Atmos. Environ.* 119, 402–414. doi:10.1016/j.atmosenv.2015.08.063

Stockie, J. M. (2011). The Mathematics of Atmospheric Dispersion Modeling. *SIAM Rev.* 53, 349–372. doi:10.1137/10080991x

Stohl, A., Seibert, P., Wotawa, G., Arnold, D., Burkhart, J. F., Eckhardt, S., et al. (2012). Xenon-133 and Caesium-137 Releases into the Atmosphere from the Fukushima Dai-Ichi Nuclear Power Plant: Determination of the Source Term, Atmospheric Dispersion, and Deposition. *Atmos. Chem. Phys.* 12 (5), 2313–2343. doi:10.5194/acp-12-2313-2012

Thomson, L. C., Hirst, B., Gibson, G., Gillespie, S., Jonathan, P., Skeldon, K. D., et al. (2007). An Improved Algorithm for Locating a Gas Source Using Inverse Methods. *Atmos. Environ.* 41, 1128–1134. doi:10.1016/j.atmosenv.2006.10.003

Wang, Y., Huang, H., Huang, L., and Zhang, X. (2018). Source Term Estimation of Hazardous Material Releases Using Hybrid Genetic Algorithm with Composite Cost Functions. *Eng. Appl. Artif. Intelligence* 75, 102–113. doi:10.1016/j.engappai.2018.08.005

Wang, X., Lei, Y., Yan, L., Liu, T., Zhang, Q., and He, K. (2019). A Unit-Based Emission Inventory of SO2, NOx and PM for the Chinese Iron and Steel Industry from 2010 to 2015. *Sci. Total Environ.* 676, 18–30. doi:10.1016/j.scitotenv.2019.04.241

Wang, Y., Chen, B., Zhu, Z., Wang, R., Chen, F., Zhao, Y., et al. (2020). A Hybrid Strategy on Combining Different Optimization Algorithms for Hazardous Gas Source Term Estimation in Field Cases. *Process Saf. Environ. Prot.* 138, 27–38. doi:10.1016/j.psep.2020.02.029

Wang, Y., Zhang, R., Worden, S., Cao, H., and Li, C. (2021). Public Participation in Environmental Governance Initiatives of Chemical Industrial parks. *J. Clean. Prod.* 305, 127092. doi:10.1016/j.jclepro.2021.127092

Wei, W., Cheng, S., Li, G., Wang, G., and Wang, H. (2014). Characteristics of Ozone and Ozone Precursors (VOCs and NOx) Around a Petroleum Refinery in Beijing, China. *J. Environ. Sci.* 26, 332–342. doi:10.1016/S1001-0742(13)60412-X

Zheng, X., and Chen, Z. (2010). Back-calculation of the Strength and Location of Hazardous Materials Releases Using the Pattern Search Method. *J. Hazard. Mater.* 183, 474–481. doi:10.1016/j.jhazmat.2010.07.048

Zhou, W., Zhao, X., Cheng, K., Cao, Y., Yang, S.-H., and Chen, J. (2021). Source Term Estimation with Deficient Sensors: Error Analysis and mobile Station Route Design. *Process Saf. Environ. Prot.* 154, 97–103. doi:10.1016/j.psep.2021.08.001

Conflict of Interest: The authors declare that the research was conducted in the absence of any commercial or financial relationships that could be construed as a potential conflict of interest.

frontiers | Frontiers in Environmental Science

ORIGINAL RESEARCH
published: 07 April 2022
doi: 10.3389/fenvs.2022.864897

Response of Summer Ozone to Precursor Emission Controls in the Yangtze River Delta Region

Yu-Hao Mao[1,2], Shukun Yu[1], Yongjie Shang[1], Hong Liao[1,2] and Nan Li[1]*

[1]*Jiangsu Key Laboratory of Atmospheric Environment Monitoring and Pollution Control/Jiangsu Collaborative Innovation Center of Atmospheric Environment and Equipment Technology, School of Environmental Science and Engineering, Nanjing University of Information Science and Technology (NUIST), Nanjing, China,* [2]*Key Laboratory of Meteorological Disaster, Ministry of Education (KLME)/ Collaborative Innovation Center on Forecast and Evaluation of Meteorological Disasters (CIC-FEMD)/International Joint Research Laboratory on Climate and Environment Change (ILCEC), NUIST, Nanjing, China*

Surface ozone concentrations in the Yangtze River Delta (YRD) region in China have shown a significant increase with the dramatic reduction of anthropogenic nitrogen oxide (NO_x) emissions since 2013. As the nonlinearity between ozone and its precursors (i.e., NO_x and volatile organic compounds (VOCs)) varies greatly in time and space, we quantify the monthly changes of surface ozone with the co-control of NO_x and VOCs anthropogenic emissions in the YRD region from May to October 2017 by using the GEOS-Chem model. Model evaluations show that the GEOS-Chem model exhibits good performance to simulate ozone concentrations in the region. For May–September 2017, most areas in the YRD region are under a transitional regime, but the regions with high anthropogenic emissions including Shanghai and southern Jiangsu are under a VOCs-limited regime. In October, basically, the entire YRD region is under a VOCs-limited regime. Generally, reducing VOCs emissions only is the most effective method for ozone control in the YRD. Nanjing is under a VOCs-limited regime in May, June, September, and October, and under a transition regime from July to August. The VOCs/NO_x emission reduction ratio of 1:1 is effective for ozone mitigation in Nanjing (Shanghai) in May, June, and September (for May–September); the corresponding ratio is 2:1 in October. Hangzhou belongs to a transitional regime from May to September and is under a VOCs-limited regime in October. Reducing NO_x emissions only would control ozone in Hangzhou from May to September, while the VOCs/NO_x emission reduction ratio of 1:1 is favorable to reduce ozone concentrations in October. During high pollution days on July 22–27, 2017, the three cities belong to a transitional regime and reducing NO_x emissions only is generally the most effective way to control high ozone pollution. GEOS-Chem tagged ozone simulation shows that ozone problem in the region is caused by the joint effect of local generation and regional and long-distance transport. Local generation (19.0–50.7%) is generally the largest contributor to monthly mean ozone concentrations in Jiangsu and Shanghai, Zhejiang, and central eastern China; the contribution of ozone from regions outside the YRD is larger in spring and autumn (42–76.0%) than in summer (23.3–51.8%). Since the annual VOCs (NO_x) anthropogenic emissions in the region have shown a decline by 8% (11%) from 2017 to 2020 and would continue to reduce by 10% (10%) by 2025 according to the Chinese government requirement, the growth of ozone would be stopped in the

OPEN ACCESS

Edited by:
Qiyuan Wang,
Institute of Earth Environment, (CAS), China

Reviewed by:
Peng Wang,
The Hong Kong Polytechnic University, China
Haofei Yu,
University of Central Florida, United States

***Correspondence:**
Yu-Hao Mao
yhmao@nuist.edu.cn

Specialty section:
This article was submitted to Atmosphere and Climate, a section of the journal Frontiers in Environmental Science

Received: *29 January 2022*
Accepted: *11 March 2022*
Published: *07 April 2022*

Citation:
Mao Y-H, Yu S, Shang Y, Liao H and Li N (2022) Response of Summer Ozone to Precursor Emission Controls in the Yangtze River Delta Region. Front. Environ. Sci. 10:864897. doi: 10.3389/fenvs.2022.864897

YRD for May–September but likely to continue in October. Our study thus would provide a scientific base for guiding the effective emission reduction strategies to control ozone pollution in the YRD region.

Keywords: ozone, precursor emissions, VOCs/NOx, source contribution, Yangtze River Delta

HIGHLIGHTS

- Yangtze River Delta is changing from a VOCs-limited regime to a transition regime.
- VOCs emission reduction is the key to control ozone pollution in the YRD region.
- Ozone decreases effectively with VOCs/NO_x emission reduction ratio larger than 1:1.
- Regional transport is a larger contributor to ozone in spring and fall than in summer.

INTRODUCTION

Ozone is the main component of photochemical smog, mainly generated by the reaction of volatile organic compounds (VOCs) and nitrogen oxides (NO_x) in the sunlight (NRC, 1991). Because of its strong oxidative capacity and the formation of OH radicals, ozone pollution enhances the oxidation of the background atmosphere (Seinfeld and Pandis, 1998). The ground-level ozone is considered as an air pollutant as it can severely harm public health and damage the ecosystem (Krupa and Manning, 1988; Bell et al., 2006).

With the rapid development of economics and the fast process of industrialization and urbanization in China, ozone pollution is becoming more and more severe in recent years. Yangtze River Delta (YRD) located on the east coast of China is one of the most economically developed and densely populated regions in China. The ozone pollution in the YRD region is thus particularly serious and ozone concentrations measured by the China National Environmental Monitoring Center have increased significantly since 2013 (e.g., Lu et al., 2018; Lu et al., 2020; Li M et al., 2021). A report on the Ministry of Ecology and Environment of China (https://www.mee.gov.cn/hjzl/sthjzk/zghjzkgb/) showed that the 90th percentile of daily maximum 8 h average (MDA8) ozone concentrations reached 152 $\mu g\,m^{-3}$ in the YRD region in 2020 and that the number of days with ozone as the primary pollutant accounted for 50.7% of all the polluted days. Nanjing, Shanghai, and Hangzhou are economically developed cities in the YRD region; ozone pollution problem of these cities has attracted much public attention (e.g., An et al., 2015; Gao et al., 2017; Li K et al., 2017).

VOCs and NO_x are important precursors of ozone, the emissions of which are major factors influencing ozone concentration (Ding et al., 2019; Yu et al., 2019). Anthropogenic emissions in China have shown dramatic changes in the recent 2 decades due to rapid economic growth and urbanization as well as energy structure changes and strict emission controls (Wu et al., 2016; Liu et al., 2017; Wang et al., 2019; Liang et al., 2020). In 2013, Chinese government put forward "Air Pollution Prevention and Control Action Plan" (APPCAP, http://www.gov.cn/zhengce/content/2013-09/13/content_4561.htm) and implemented strict emission control measures to reduce anthropogenic emissions for 2013–2017. NO_x anthropogenic emissions have decreased by 19.1% from 2013 to 2017 and continue to decline after 2017 (Liu et al., 2017; Zheng et al., 2018; Zheng et al., 2021). Different from NO_x emissions, VOCs anthropogenic emissions remain stable for 2013–2017, but begin to decline after 2017 (Ma et al., 2019; Zheng et al., 2018; Zheng et al., 2021). Previous studies (e.g., Xue et al., 2014; An et al., 2015; Gao et al., 2017) have shown that the reduction of NO_x anthropogenic emissions could not effectively alleviate ozone pollution in the YRD region, largely due to the strong nonlinear relationship between ozone and its precursors (e.g., Li K et al., 2017; Lu H et al., 2019; Xu et al., 2021).

Chemical transport models (CTM) are widely used to determine ozone sensitivity to its precursors (e.g., Kanaya et al., 2009; Wang et al., 2019; Wei et al., 2019). Based on sensitivity simulations, exploring the changes on ozone concentrations under different VOCs/NO_x emission reduction ratios is useful for formulating appropriate and effective ozone reduction strategies (e.g., Wang et al., 2019; Wang et al., 2020; Su et al., 2021). Previous studies have shown that the YRD region was generally under a VOCs-limited regime or a transitional regime (e.g., Wang et al., 2019; Li L et al., 2021; Yang et al., 2021). The VOCs/NO_x anthropogenic emission reduction ratio larger than 2:1 was generally effective to control ozone concentrations in the YRD region (e.g., Wang et al., 2019; Wang et al., 2020). Due to the significant reduction of NO_x anthropogenic emissions from 2013, the sensitivity of ozone to its precursors is changing dramatically which would significantly affect ozone control strategies.

Ozone has a lifetime of several days to weeks in the free troposphere (Lin et al., 2008). Ozone pollution is thus not only related to local source emissions of ozone precursors but also influenced by regional transport (Zheng et al., 2010; Gong et al., 2020). By using a tagged ozone simulation in GEOS-Chem, Gong et al. (2020) found that ozone transport from central eastern China contributed 36% to the enhanced daily mean ozone concentrations during the persistent ozone pollution episodes in North China in May–July of 2014–2018. Based on the ozone source apportionment technology of WRF/CMAx, Li L et al. (2019) found that regional transport was a significant source of ozone in urban regions in the YRD region and contributed 38.7–111.1 $\mu g\,m^{-3}$ to daily average MDA8 ozone concentrations in May, August, and October of 2015.

To our knowledge, previous studies on ozone–NO_x–VOCs sensitivity and ozone control strategies have largely focused on

the whole summer season, a certain month, or high ozone pollution days (e.g., Xu et al., 2017; Li K et al., 2017; Wang et al., 2020; Zhang et al., 2020). Due to the strong nonlinearity between ozone and its precursors in time and space, it is thus necessary to systematically analyze the ozone–NO_x–VOCs sensitivity and control strategies of NO_x and VOCs anthropogenic emissions for different months, different cities, and high pollution days to guide the effective ozone mitigation in the YRD region. In this study, we aim to quantify the changes of surface ozone with the control of NO_x and VOCs anthropogenic emissions at different reduction ratios in the YRD region (28.2°N~34.5°N, 115.8°E~123.4°E) using the GEOS-Chem CTM. We mainly focus on three big cities (Nanjing, Shanghai, and Hangzhou) in the region from May to October in 2017, the final year of implementation of the APPCAP action plan. To explore the reasons for the differences in monthly sensitivity of ozone–NO_x–VOCs, we further quantify the ozone contributions from different regions to monthly mean surface ozone concentrations in the YRD region using the GEOS-Chem tagged ozone technique. We introduce the observation data and the sensitivity simulations of the GEOS-Chem model in **Section 2**. We evaluate model results with observation data from the China National Environmental Monitoring Center in **Section 3**. In **Section 4**, we evaluate the ozone–NO_x–VOCs sensitivity in the YRD region and the changes in ozone concentrations with the reduction of NO_x and VOCs anthropogenic emissions. In **Section 5**, we quantify the contributions of ozone from different regions to surface ozone concentrations in the YRD region. We conclude in **Section 6**.

METHODS

Observations

In this study, we obtain the observations of hourly ozone concentrations for May–October 2017 from the China National Environmental Monitoring Center (http://106.37.208.233:20035/). There are 10 monitoring sites in Shanghai, 11 in Hangzhou, and 9 in Nanjing. The sampling measurements and techniques comply with the Chinese national ambient air quality monitoring technical regulations HJ/T193-2005. According to ambient air quality standard GB 3095-2012, the MDA8 ozone concentrations are calculated if at least 6 hourly averages are recorded in every 8 h and more than 14 8-hour averages are available from 8:00 to 24:00 local time.

Model Description and Simulations

The GEOS-Chem global CTM is driven by assimilated meteorological data from the Goddard Earth Observing System (GEOS) of the NASA Global Modeling and Assimilation Office (GMAO) (Bey et al., 2001). Here, we use GEOS-Chem version 11-01 (http://wiki.geos-chem.org/GEOS-Chem_v11-01) driven by MERRA-2 meteorological data with spatial horizontal resolutions of 2 × 2.5 ° globally and 0.5 × 0.625 ° nested over Southeastern Asia (11°S~55°N, 60°E~150°E), reduced 47 vertical levels from the surface to 0.01 h Pa, and a temporal resolution of 1 h.

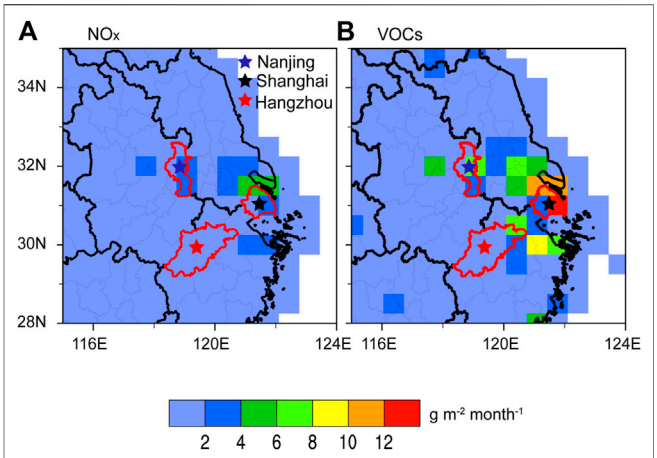

FIGURE 1 | Monthly anthropogenic **(A)** NO_x emissions and **(B)** VOCs emissions (g m^{-2} $month^{-1}$) from the MEIC inventory in the Yangtze River Delta (YRD) region averaged for May–October 2017. Red enclosed areas indicate Nanjing, Shanghai, and Hangzhou, respectively.

We conduct full-chemistry NO_x–O_x–Hydrocarbon-aerosol model simulations. We use the Linoz scheme for ozone production in the stratosphere (McLinden et al., 2000) and the nonlocal planetary boundary layer (PBL) mixing scheme for vertical mixing of air tracers in the PBL (Holtslag and Boville, 1993; Lin and McElroy, 2010). Dry deposition is calculated based on the resistance-in-series scheme (Wesely, 1989). The wet deposition for water-soluble aerosols and gas is described by Liu et al. (2001) and Amos et al. (2012).

The Harvard–NASA Emission Component (HEMCO) is used to process emissions in the GEOS-Chem model (Keller et al., 2014). Global anthropogenic emissions are from the Emissions Database for Global Atmospheric Research (EDGAR). The Global anthropogenic VOCs emissions are from the REanalysis of TROpospheric chemical composition (RETRO) inventory, but C_2H_6 and C_3H_8 are overwritten by the emission inventory developed by Xiao et al. (2008). The regional anthropogenic emissions are taken from the European Monitoring and Evaluation Project (EMEP) for Europe (Auvray and Bey, 2005), the Big Bend Regional Aerosol and Visibility Observational emission inventory (BRAVO) for Mexico (Kuhns et al., 2005), the Canadian Criteria Air Contaminant emission inventory (CAC) for Canada, the National Emission Inventory (NEI) for the United States, and the MIX emission inventory over East and South Asia (Li M et al., 2017).

Particularly, we used monthly anthropogenic emissions in China from the Multi-resolution Emission Inventory for China (MEIC) with a horizontal resolution of 0.5 ° × 0.667 ° for 2017. The annual NO_x anthropogenic emissions in MEIC are 3,666 Gg in the YRD region (including Jiangsu, Shanghai, Zhejiang, and Anhui provinces) in 2017 and reduce by 19.1% from 2013 to 2017; NMVOCs emissions are 5,593 Gg and increased by 3.3% from 2013 to 2017 (http://meicmodel.org/). **Figure 1** shows monthly anthropogenic NO_x and VOCs emissions of the MEIC inventory in the YRD region averaged for May–October 2017. The spatial distributions of NO_x and VOCs emissions in the

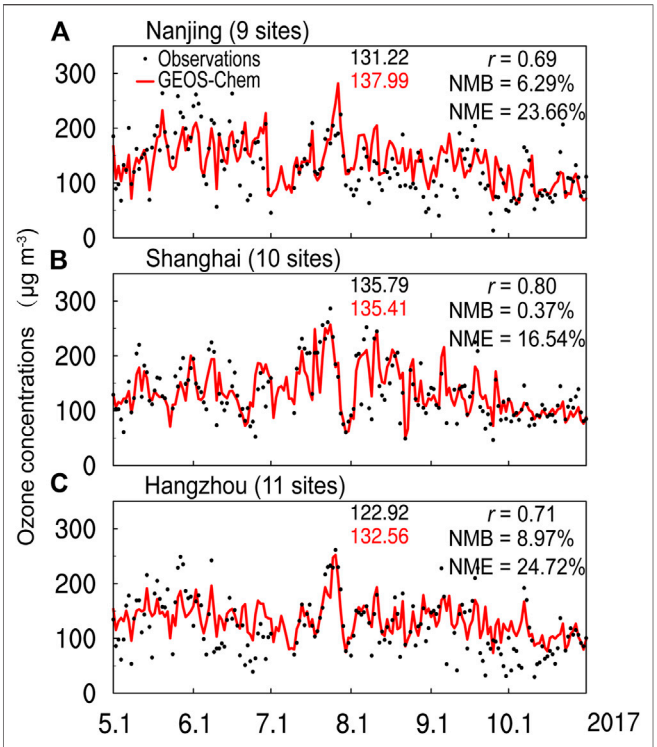

FIGURE 2 | Observed (black) and simulated (red) daily maximum 8 h average (MDA8) ozone concentrations (μg m^{-3}) averaged for stations at **(A)** Nanjing (9 sites), **(B)** Shanghai (10 sites), and **(C)** Hangzhou (11 sites) from May to October 2017. Also shown are observed and simulated mean ozone concentrations for the time period, correlation coefficients (*r*), normalized mean bias (NMB), and normalized mean errors (NME) between model results and observations. All the correlation coefficients pass the two-tailed *t*-test with 95% confidence interval.

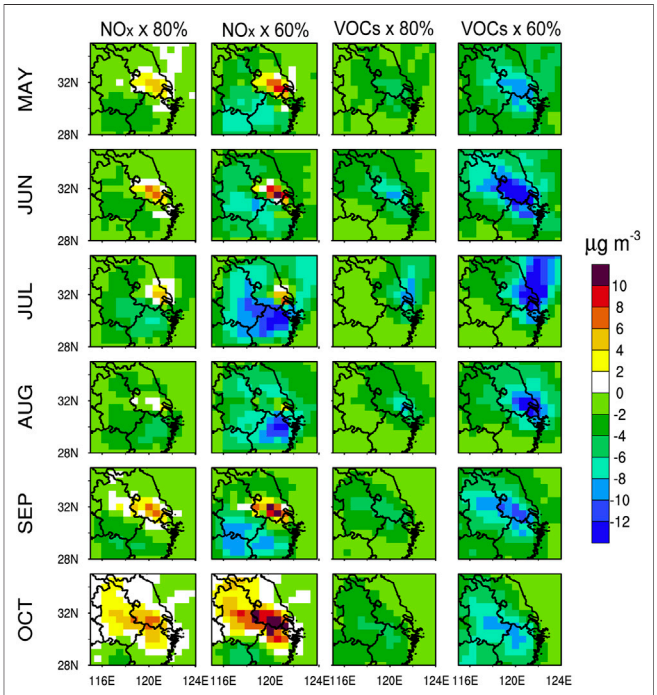

FIGURE 3 | Differences in monthly mean daily maximum 8 h average (MDA8) ozone concentrations (μg m^{-3}) between sensitivity simulations with reduced anthropogenic NO_x (left two columns) or VOCs (right two columns) emissions and the standard model simulation from May to October 2017. Anthropogenic NO_x or VOCs emissions in the Yangtze River Delta (YRD) region reduced by 20 and 40%.

YRD region are generally similar. The regions with high emissions are mainly concentrated in Shanghai and southern Jiangsu. Among the three cities of Nanjing, Shanghai, and Hangzhou, NO_x and VOCs emissions are the highest in Shanghai (3 g m^{-2} $month^{-1}$ and 2.4 g m^{-2} $month^{-1}$, respectively) and the lowest in Hangzhou (0.6 g m^{-2} $month^{-1}$ and 0.5 g m^{-2} $month^{-1}$, respectively).

A number of natural emissions are also implemented in the model. We used biomass burning emissions from the Global Fire Emissions Database version 4 (GEFD v4) with a horizontal resolution of 0.25 ° × 0.25 ° and a spatial resolution of 1 month (van der Werf et al., 2017). Biogenic VOCs emissions are from the MEGAN version 2.1 (MEGAN v2.1) (Guenther et al., 2012). Lightning and soil NO_x emissions are also included in the model following Lu X et al. (2019).

We simulate ozone concentrations in the YRD region from February to October 2017 with the first 3 months for spin-up. Our analysis centers on 2017, the final year of implementation of the APPCAP action plan and also the latest year currently available for the MEIC emission inventory. In addition to a standard simulation with all emissions unchanged, we also conduct simulations to study the sensitivities of NO_x and VOCs to ozone formation and the effective emission reduction ratio of VOCs/NO_x for ozone control in the YRD region. Empirical Kinetic Modeling Approach (EKMA) isopleths of ozone concentrations under different emissions of precursors are commonly used method to reflect ozone-NO_x-VOCs sensitivity (e.g., Xing et al., 2011; Guo et al., 2019). In order to obtain the EKMA isopleths, we conduct 24 sensitivity simulations with anthropogenic NO_x and VOCs emissions in the YRD region reduced by 20, 40, 60, and 80%, respectively.

The ratio of formaldehyde (HCHO) to nitrogen dioxide (NO_2) (HCHO/NO_2, FNR) has been widely used to evaluate ozone–NO_x–VOCs sensitivity (e.g., Jin and Holloway, 2015; Xu et al., 2021). To examine the ozone–NO_x–VOCs sensitivity obtained from the EKAM isopleths, we calculate FNR using monthly mean HCHO and NO_2 column concentrations from the GEOS-Chem simulations. FNR > 2 indicates a NO_x-limited regime, FNR < 1 reflects a VOCs-limited regime, and FNR between 1 and 2 is considered as a transitional regime (Martin et al., 2004).

The offline tagged ozone technique in the GEOS-Chem CTM is used to quantify the contributions of ozone from different source regions to monthly mean ozone concentrations in the YRD region. We run tagged ozone simulation with a spatial horizontal resolution of 2 ° × 2.5 ° globally (the only resolution available) by using 3-D ozone production rates and loss frequencies archived from the full-

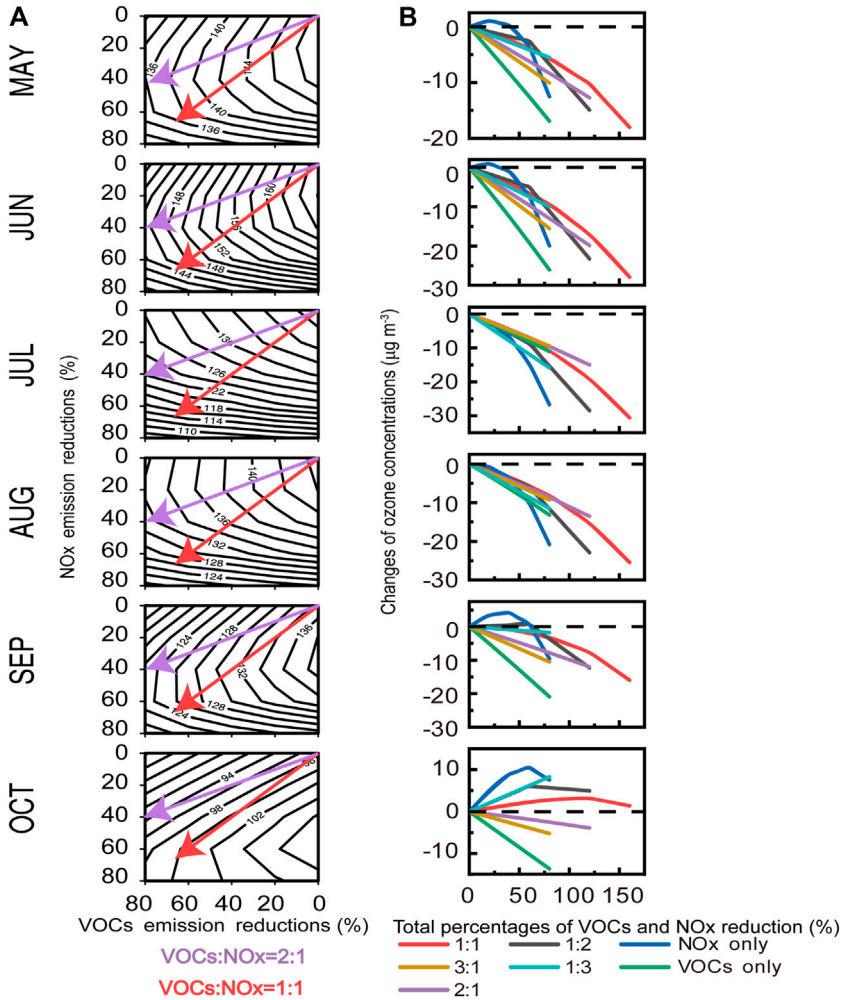

FIGURE 4 | (A) Empirical kinetic modeling approach (EKMA) isopleths of monthly mean daily maximum 8 h average (MDA8) ozone concentrations (μg m^{-3}) in Nanjing for May–October 2017. Red and purple arrows represent VOCs and NO_x anthropogenic emissions simultaneously reduced by 1:1 and 2:1, respectively. **(B)** Differences in monthly mean MDA8 ozone concentrations between sensitivity simulations and standard model simulation in Nanjing for May–October 2017. Sensitivity simulations include VOCs anthropogenic emissions reduction only, NO_x anthropogenic emissions reduction only, and reduction of VOCs and NO_x anthropogenic emissions simultaneously by 1:1, 1:2, 1:3, 2:1, and 3:1.

chemistry standard simulation. We consider eight regions in China and one region representing the rest of the world (**Supplementary Figure S1**). We tag the generated ozone from the surface to the 38th vertical layer in the model (~48 hPa altitude) from nine regions. Generally, the sum of these nine tagged ozone concentrations in the YRD region is equal to the simulated ozone concentration in this region.

MODEL EVALUATIONS

Previous studies have shown that the GEOS-Chem model with the MEIC emission inventory reasonably captured observed ozone concentrations in China (e.g., Li K et al., 2019; Sun et al., 2019). We further compare in **Figure 2**, observed and GEOS-Chem simulated MDA8 ozone concentrations at stations in Nanjing, Shanghai, and Hangzhou. Observations are averaged for the measurement stations in each region, and the model results are sampled at the corresponding locations of the measurement stations. The GEOS-Chem model is generally in good performance to simulate ozone concentrations in three regions. The differences in MDA8 ozone concentrations between simulations and observations are 6.77 μg m^{-3} in Nanjing, −0.38 μg m^{-3} in Shanghai, and 9.64 μg m^{-3} in Hangzhou, respectively, averaged for May–October 2017.

We further used correlation coefficients (r), normalized mean bias (NMB), and normalized mean errors (NME) (Emery et al.,

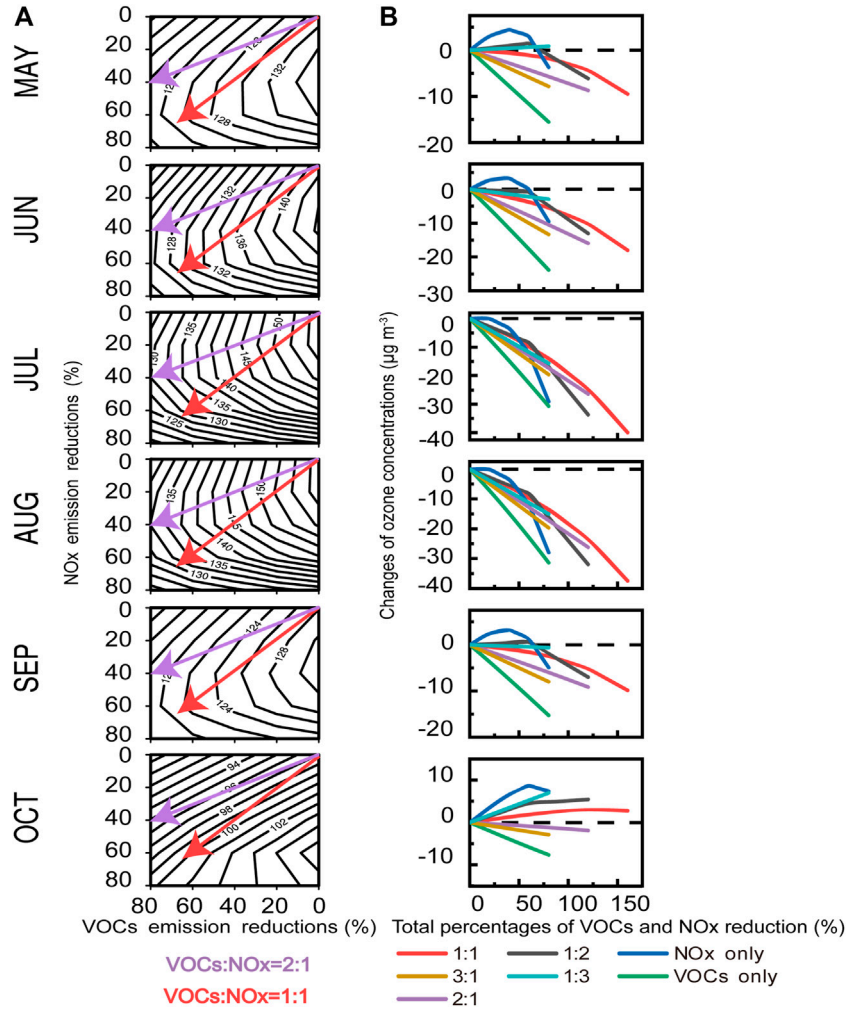

FIGURE 5 | Same as **Figure 4**, but for Shanghai.

2017) between simulated and observed ozone concentrations to evaluate the model performance.

$$r = \frac{\sum_{i=1}^{N}\left(c_m - \overline{c_m}\right)\left(c_o - \overline{c_o}\right)}{\sqrt{\sum_{i=1}^{N}\left(c_m - \overline{c_m}\right)^2 \sum_{i=1}^{N}\left(c_o - \overline{c_o}\right)^2}} \quad (1)$$

$$\mathrm{NMB} = \frac{\sum_{i=1}^{N}(c_m - c_o)}{\sum_{i=1}^{N} c_o} * 100\% \quad (2)$$

$$\mathrm{NME} = \frac{\sum_{i=1}^{N}|c_m - c_o|}{\sum_{i=1}^{N} c_o} * 100\% \quad (3)$$

where c_o is the observed MDA8 ozone concentration averaged for stations in each region (μg m^{-3}), c_m is the corresponding simulated MDA8 ozone concentration (μg m^{-3}), and N is the number of the observation days from May to October 2017.

Simulated ozone concentrations largely capture the day-to-day variations of observations with the correlation coefficients in the range of 0.69–0.80 at the stations in Nanjing, Shanghai, and Hangzhou. All the correlation coefficients pass the two-tailed *t*-test with 95% confidence interval. The model performance criteria for MDA8 ozone concentrations have been met when both the NMB and NME are less than or equal to approximately ±15% and +25%, respectively (Emery et al., 2017). The NMB and NME of simulated and observed MDA8 ozone concentrations are 0.37–8.97% and 16.54–24.72% at the stations in Nanjing, Shanghai, and Hangzhou, which are within the model performance criteria.

Model performance is further evaluated by the monthly correlation coefficients between observations and model results in Nanjing, Shanghai, and Hangzhou for May–October 2017 (**Supplementary Figure S2**). Generally, monthly correlation coefficients averaged for the three areas are highest in July (r = 0.87), May (0.75), and August (0.73), but lowest in October (0.5). For each city, model performance is best in Nanjing in May and June, in Shanghai from August to October, and in Hangzhou in July.

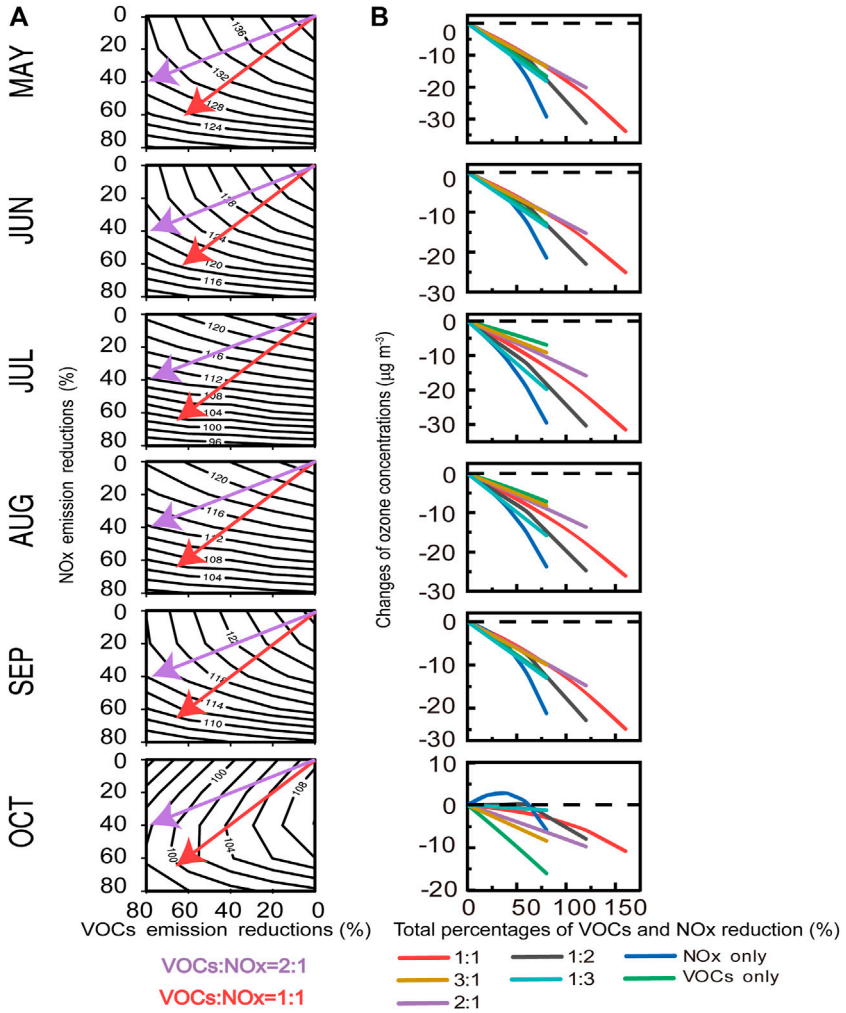

FIGURE 6 | Same as **Figure 4**, but for Hangzhou.

We also conduct the GEOS-Chem simulation at a horizontal resolution of 0.25 × 0.3125 ° with the same model configuration as those at 0.5 × 0.625 °. The differences of simulated MDA8 ozone concentrations between 0.5 × 0.625° and 0.25 × 0.3125 ° model simulations are only −0.03, 5.67%, and 0.51%, respectively, for correlation coefficients, NMB, and NME averaged for three cities during May–October 2017. Considering the problem of computing time cost, we thus conduct sensitivity simulations at 0.5 × 0.625 °.

RESPONSE OF OZONE TO PRECURSOR CONTROLS

The sensitivity of ozone to its precursors varies significantly over time and location (e.g., Tang et al., 2017; Wei et al., 2019; Yang et al., 2021). **Figure 3** shows the changes in the monthly mean MDA8 ozone concentrations for May to October 2017 from sensitivity simulations with anthropogenic NO_x or VOCs emissions in the YRD region reduced by 20 and 40%, compared to the ozone concentrations from the standard model simulation. The sensitivities of ozone concentrations to anthropogenic NO_x emissions show large differences in space and time. From May to September, ozone concentrations decrease with the reduction of NO_x emissions in northern Jiangsu and most areas of Zhejiang and Anhui. The ozone concentrations decrease by more than 6 μg m^{-3} in southwestern YRD region from May to September when the reduction of NO_x emissions reaches 40%. In May, June, and September, ozone concentrations yet increase in the regions with high anthropogenic emissions including Shanghai and southern Jiangsu; the increases of ozone concentrations are largest in Suzhou by ~8 μg m^{-3} with the reduction of NO_x emissions by 40%. From July to August, reducing NO_x emission is effective for most of the YRD regions, except for a small part of southeast Jiangsu and northern Shanghai. In October, most of the YRD region shows increased ozone concentrations with decreased NO_x emissions, except for the

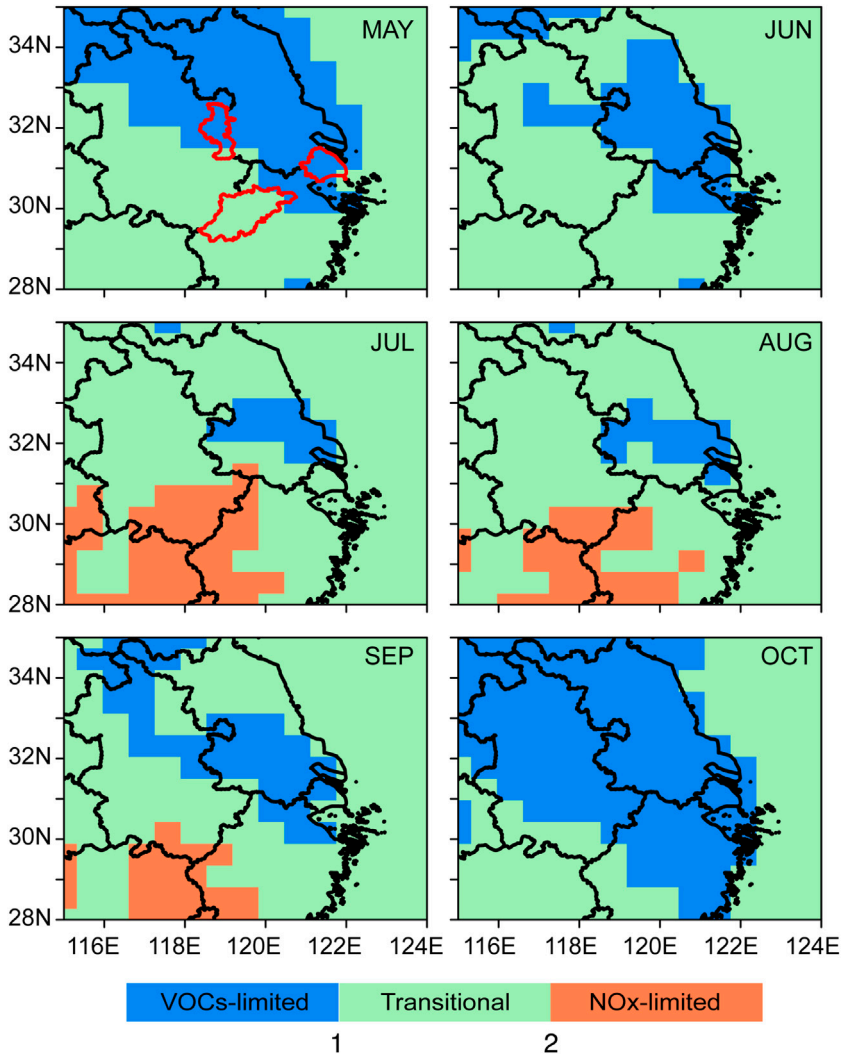

FIGURE 7 | Sensitivity regimes of ozone–NO_x–VOCs defined by $HCHO/NO_2$ ratios (FNR) in the Yangtze River Delta (YRD) region from May to October 2017. Red enclosed areas indicate Nanjing, Shanghai, and Hangzhou, respectively.

southwestern YRD region including southern part of Anhui and Zhejiang.

Compared to cutting NO_x emissions, the reduction of VOCs emissions is more effective to control the ozone concentrations in the entire YRD region, where the ozone concentrations decrease with the reduction of VOCs emissions from May to October. The ozone concentrations are most sensitive to VOCs emissions in Shanghai and southern Jiangsu, which decrease by more than 8 μg m^{-3} with the reduction of VOCs emissions by 40% from May to September.

Combined with the changes in ozone concentrations due to the reduction of NO_x or VOCs emissions, most of the regions in the YRD are controlled by a transitional regime for May–September 2017 while under a VOCs-limited regime in October. The regions with high anthropogenic emissions including Shanghai and southern Jiangsu are controlled by a VOCs-limited regime in May, June, September, and October. From July to August, the VOCs-limited regions shrink to only small part of southeast Jiangsu and northern Shanghai. Previous studies have also shown that the YRD region is changing from a VOCs-limited regime to a transition regime due to the reduction of NO_x anthropogenic emissions in recent years (e.g., Jin and Holloway, 2015; Wang et al., 2019).

To further investigate the ozone sensitivity to its precursors for Nanjing, Shanghai, and Hangzhou and the changes of ozone concentrations under different VOCs/NO_x emission reduction ratios, **Figure 4**, **Figure 5**, and **Figure 6** show the EKMA isopleths of monthly MDA8 ozone concentrations from May to October 2017 for the three cities. **Figure 4**, **Figure 5**, and **Figure 6** (**Supplementary Figure S3**) show the differences in monthly mean MDA8 ozone concentrations between sensitivity simulations (including VOCs emissions reduction only, NO_x emissions reduction only, and reduction of VOCs and NO_x

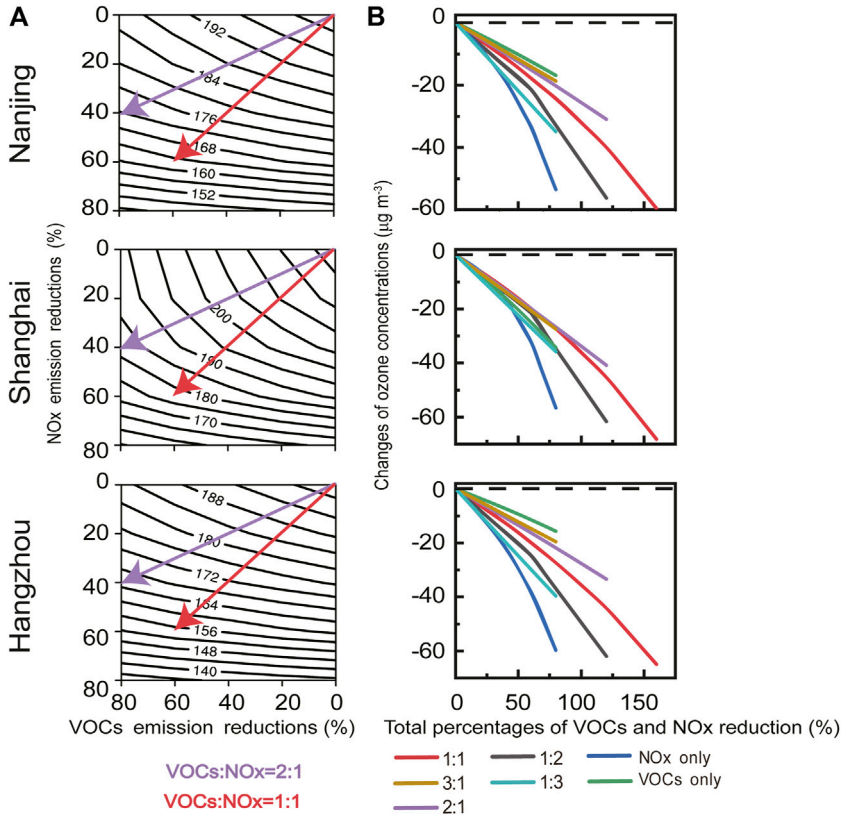

FIGURE 8 | Same as **Figure 4**, but for high pollution events from July 22 to 27, 2017 in Nanjing, Shanghai, and Hangzhou, respectively.

emissions simultaneously by 1:1, 1:2, 1:3, 2:1, and 3:1) and the standard model simulation in Nanjing, Shanghai, and Hangzhou for May–October 2017. In the three cities, reducing VOCs emissions is generally an effective approach to control ozone concentrations. When VOCs emissions are reduced by 40%, ozone concentrations from May to October would decrease by 5.3–12.3 μg m^{-3} (3.8–7.5%) in Nanjing, 4.0–14.5 μg m^{-3} (4.1–9.3%) in Shanghai, and 3.2–7.9 μg m^{-3} (2.5–7.2%) in Hangzhou.

In Nanjing, ozone concentrations are more sensitive to the VOCs emissions in May, June, September, and October, when ozone concentrations would decrease by 6.8–12.3 μg m^{-3} (5.6–7.5%) with the VOCs emissions reduced by 40%. Nanjing would turn into a transition regime when NO_x emissions reduce by more than 20% for May–June, by 40% in September, and by 60% in October. The VOCs/NO_x emission reduction ratio of 1:1 is effective for ozone mitigation in May, June, and September; the corresponding ratio is 2:1 in October. Nanjing belongs to a transition regime from July to August when controlling ozone would be achieved by reducing VOCs emissions only, NO_x emissions only, or both NO_x and VOCs emissions. For near-term ozone control in July and August, the VOCs emissions reduction only is the most effective method; while for a long-term control strategy, the NO_x emissions reduction only is more effective. Ozone concentrations in July and August would decrease by 3.7–6.9 μg m^{-3} (2.6–5.0%) with the reduction of NO_x emissions by 40%.

Shanghai is generally under a VOCs-limited regime from May to October. Ozone concentrations always decrease with the reduction in VOCs emissions; ozone concentrations would decrease by 4.0–14.5 μg m^{-3} (4.1–9.3%) with the VOCs emissions reduced by 40% from May to October. In July and August, Shanghai closes to a transition regime. Ozone concentrations would decrease when NO_x emissions reduce by 40% in May, June, and September, by 20% in July and August, and by 60% in October. The effective VOCs/NO_x emission reduction ratios for controlling ozone concentrations are larger than 1:1 for May–September and 2:1 in October, which are close to those in Nanjing.

Hangzhou belongs to a transitional regime from May to September and a VOCs-limited regime in October, when Hangzhou would become a transition regime with the NO_x emission reduced by more than 60%. Ozone concentrations would decrease by 1.5–33.8 μg m^{-3} (1.2–25.1%) in Hangzhou from May to September under all emission reduction scenarios. In May, June, and September, the VOCs emissions reduction only below 40% is the most effective way for near-term ozone control; while the NO_x emissions reduction only above 40% is more effective as a long-term control strategy. The NO_x

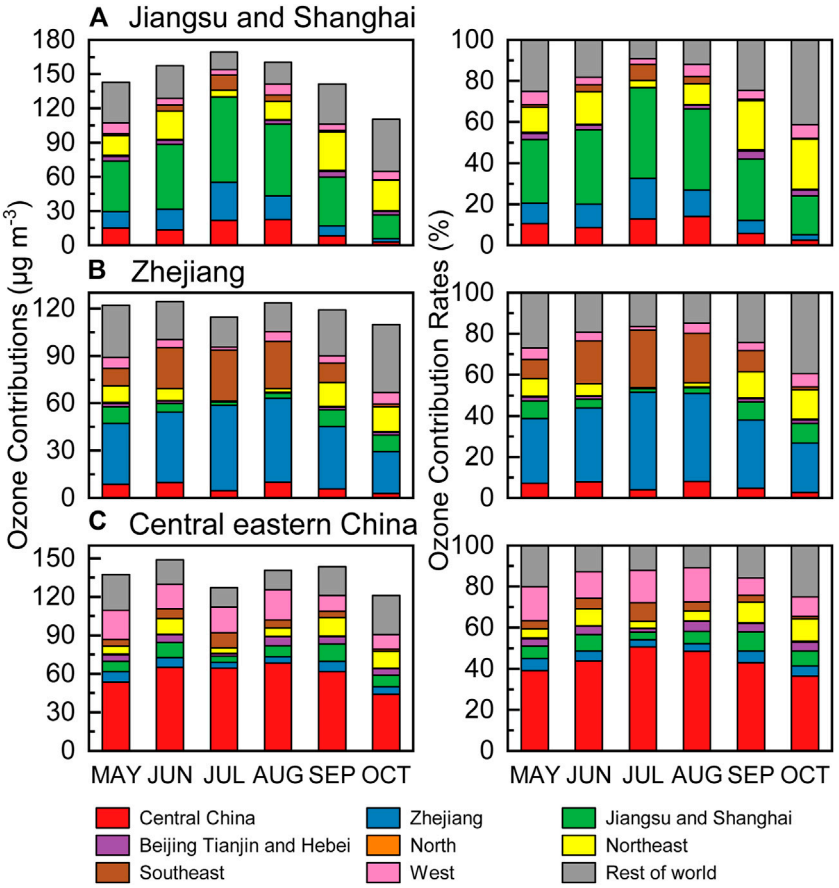

FIGURE 9 | Ozone contributions from different source regions to monthly mean surface ozone concentrations in three regions: **(A)** Jiangsu and Shanghai, **(B)** Zhejiang, and **(C)** central eastern China from May to October 2017.

emission reduction only scenario is generally the effective way to control ozone concentrations in July and August, when ozone concentrations decrease by 8.6–11.2 μg m^{-3} (6.8–8.9%) with the NO_x emissions reduced by 40%.

Figure 7 shows sensitivity regimes of ozone–NO_x–VOCs defined by FNR in the YRD region for May–October 2017. Generally, the ozone–NO_x–VOCs sensitivities in the YRD indicted by FNR are consistent with those from the model sensitivity simulations and the EKAM isopleths. From May to September, most areas of the YRD region belong to a transition regime; while southern Jiangsu, Shanghai, and northern Zhejiang are under a VOCs-limited regime. In October, basically, the whole YRD region belongs to a VOCs-limited regime. Nanjing and Shanghai are under a VOCs-limited regime in May, June, September, and October and parts of the cities are in a transition regime in July and August. Hangzhou generally belongs to a transition regime for May–September and parts of the city are under a NO_x-limited regime.

We further analyze the sensitivity of ozone to its precursors and the changes of ozone under different VOCs/NO_x emission reduction ratios in Nanjing, Shanghai, and Hangzhou during high pollution event (**Figure 8**). We choose the high ozone pollution period from July 22 to 27, 2017, when the observed daily MDA8 ozone concentrations exceed the national air quality standard of 160 μg m^{-3} (https://www.mee.gov.cn/ywgz/fgbz/bz/bzwb/dqhjbh/dqhjzlbz/201203/W020120410330232398521.pdf) simultaneously in Nanjing, Shanghai, and Hangzhou. The NMB and NME of simulated and observed MDA8 ozone concentrations during this period are −14.9 to 11.4% and 14.9–18.7% at the stations in three cities, which are within the model performance criteria. Ozone concentrations under all emission reduction scenarios would decrease by 3.8–59.7 μg m^{-3} (1.9–29.4%) in Nanjing, 6.1–68.3 μg m^{-3} (2.7–30.6%) in Shanghai, and 3.4–65.0 μg m^{-3} (1.7–32.7%) in Hangzhou. The three cities all belong to a transitional regime during high pollution days and NO_x emissions reduction only is generally the most effective method to control long-term ozone concentrations. When NO_x emissions reduce by 40%, the reduction of ozone concentrations in high pollution days are larger than those averaged in July by 11.8 μg m^{-3} in Nanjing, 12.9 μg m^{-3} in Shanghai, and 10.8 μg m^{-3} in Hangzhou. In Shanghai, the VOCs emissions reduction would be the most effective for near-term ozone control.

Our results of ozone–NO_x–VOCs sensitivity are broadly consistent with previous studies (e.g., Xu et al., 2017; Li K et al., 2017; Yang et al., 2021), but provide updated and detailed information about monthly ozone sensitivity to its precursors and the effective emission reduction ratios of VOCs/NO_x to control ozone in the three cities. Generally, the three cities are under a VOCs-limited regime or a transitional regime during the summer season and changing to a transitional regime gradually. Previous observational and modeling studies have shown that ozone concentrations would decrease in the YRD region when VOCs/NO_x emission reduction ratio was greater than 2:1 (e.g., Wang et al., 2019; Wang et al., 2020). With the reduction of NO_x emissions from 2013, our results show that VOCs/NO_x emission reduction ratio of 1:1 is in favor of effective ozone control in the region for May–September, and NO_x emission reduction only is an effective way to control ozone concentrations during the high pollution event in July.

OZONE CONTRIBUTIONS FROM DIFFERENT SOURCE REGIONS

In **Figure 9**, we qualify the contributions of ozone from nine defined regions to monthly mean surface ozone concentrations in the YRD region for May–October 2017 using the GEOS-Chem tagged ozone technique. We focus on the contributions to monthly mean surface ozone concentrations in three regions, Jiangsu and Shanghai (**Figure 9A**), Zhejiang (**Figure 9B**), and central eastern China (**Figure 9C**), generally belonging to the YRD region. Locally generated ozone is the largest contributor to monthly mean surface ozone concentrations in the three regions for May–September 2017, ranging from 42.4 to 74.7 $\mu g\,m^{-3}$ (30.0–44.1%) in Jiangsu and Shanghai, 38.5–54.2 $\mu g\,m^{-3}$ (31.5–47.4%) in Zhejiang, and 53.6–68.3 $\mu g\,m^{-3}$ (39.0–50.7%) in central eastern China. The control of local source emissions is thus important to control ozone concentrations in the YRD region.

For Jiangsu and Shanghai region (**Figure 9A**), ozone from adjacent areas, i.e., Zhejiang and central eastern China are the second (20.6–33.7%) and third (21.6–22.4%) largest contributors in July and August. For other months, ozone from the rest of world also shows large contributions to surface ozone concentrations in Jiangsu and Shanghai in May (25.1%), June (18.1%), September (24.7%), and October (41.4%), indicating that regional and long-distance transport is also a significant contributor to surface ozone in Jiangsu and Shanghai. For Zhejiang region (**Figure 9B**), ozone from nearby southeast is the second largest contributor for the summer months of June to August (20.9–28.0%). Ozone from the rest of world accounts for 27.0% of surface ozone concentrations in Zhejiang in May, 24.4% in September, and 39.3% in October. For the central eastern China region (**Figure 9C**), ozone contributions from the rest of the world to the surface ozone in central eastern China are the second largest in spring and autumn months (20.2% in May, 15.7% in September, and 25.1% in October). For the summer months of June to August, ozone transport from the adjacent west regions contributes the second largest fraction of surface ozone (12.9–16.6%) in central eastern China.

Previous studies have shown that ozone pollution is a regional problem and regional transport has large contribution to the ozone within the YRD region (e.g., Gao et al., 2016; Li L et al., 2019). Our results also show that regional and long-range transport is also a significant contributor to surface ozone in the YRD. Ozone from regions outside the YRD accounts for 23.3–76.0% of surface ozone in Jiangsu and Shanghai, 46.3–63.8% in Zhejiang, 41.9–51.3% in central eastern China, which are larger in spring and autumn than in summer. The largest regional transport in October (51.3–76.0%) would affect the sensitivity of ozone to its locally emitted precursors, which show significant differences compared with those for May–September. The large regional transport will therefore affect the effectiveness of local precursor emission reduction on ozone control.

DISCUSSION AND CONCLUSION

We used the GEOS-Chem model to analyze ozone sensitivity to its precursors in the YRD region from May to October 2017. We aimed to quantify the changes of surface ozone with the control of NO_x and VOCs anthropogenic emissions at different reduction ratios in three big cities in the YRD region (Nanjing, Shanghai, and Hangzhou). The GEOS-Chem model was generally in good performance to simulate ozone concentrations in the three cities with correlation coefficients, NMB, and NME values in the range of 0.69–0.80, 0.37–8.97% and 16.54–24.72%, respectively, which were all within the model performance criteria.

We conducted sensitivity simulations by reducing anthropogenic NO_x and VOCs emissions by 20, 40, 60, and 80% in the YRD region, and evaluated the ozone–NO_x–VOCs sensitivity in the YRD region. Most areas in the YRD region were under a transitional regime for May–September 2017 while under a VOCs-limited regime in October. The regions with high anthropogenic emissions including Shanghai and southern Jiangsu were under a VOCs-limited regime for May–October; the VOCs-limited regions for July–August shrank to only a small part of southeast Jiangsu and northern Shanghai. Generally, compared to reducing NO_x emissions, VOCs emissions reduction was more effective to control ozone concentrations in the entire YRD region.

We further evaluated ozone sensitivity to its precursors and compared changes of ozone concentrations between sensitivity simulations and standard model simulation in Nanjing, Shanghai, and Hangzhou. Nanjing was under a VOCs-limited regime in May, June, September, and October and under a transition regime from July to August. The VOCs/NO_x emission reduction ratio of 1:1 was effective for ozone mitigation in Nanjing in May, June, and September; the corresponding ratio was 2:1 in October. Shanghai was generally under a VOCs-limited regime for May–October

and closed to a transition regime for July–August. The effective VOCs/NO_x emission reduction ratios for controlling ozone concentrations in Shanghai was larger than 1:1 for May–September and 2:1 in October. Hangzhou belonged to a transitional regime from May to September and was under a VOCs-limited regime in October. Reducing NO_x emission was the effective method to control ozone in Hangzhou from May to September, while the VOCs/NO_x reduction ratio of 1:1 was favorable to reduce ozone concentrations in October. During high pollution days on July 22–27, 2017, the three cities belong to a transitional regime and reducing NO_x emissions only is generally the most effective way to control high ozone pollution.

We used tagged ozone simulation to quantify contributions of ozone from eight regions to monthly mean ozone concentrations in Jiangsu and Shanghai, Zhejiang, and central eastern China from May to October 2017. Generally, locally generated ozone was the largest contributor to monthly mean ozone concentrations in Jiangsu and Shanghai (30.0–44.1%) and Zhejiang (31.5–47.4%) from May to September, while in central eastern China (36.4–50.7%) from May to October. Ozone transport from adjacent regions was also a major contributor for June–August. Ozone from regions outside the YRD were larger in spring and autumn than in summer, and accounted for 23.3–76.0% of surface ozone in Jiangsu and Shanghai, 46.3–63.8% in Zhejiang, and 41.9–51.3% in central eastern China. Ozone in the YRD region was therefore caused by the joint effect of local source and transport of ozone from adjacent and long-distance regions.

Due to the strict and effective emission reduction policies of the Chinese government, annual anthropogenic NO_x emissions continued to reduce in the YRD from 2017, and anthropogenic VOCs emissions have begun to show a decline. Compared to the MEIC emission inventory in 2017, the annual anthropogenic VOCs (NO_x) emission in 2020 reduced by 8% (11%) in the YRD region (Zheng et al., 2021). The VOCs/NO_x emission reduction ratio was thus about 1:1. According to our discussions in Sect.4, the joint reduction of VOCs and NO_x emissions with the VOCs/NO_x reduction ratio larger than 1:1 would be conducive to ozone mitigation in the YRD region. The report on the Ministry of Ecology and Environment of China has shown that 90th percentile of MDA8 ozone concentrations in the YRD region has decreased by 10.6% from 2017 to 2020. In November 2021 (https://www.mee.gov.cn/zcwj/zyygwj/), the Chinese government has put forward specific requirements for ozone control to reduce anthropogenic VOCs and NO_x emissions by 10% by 2025 compared with 2020. The ozone concentration in the YRD would further show a decline by 2025, especially from May to September. However, ozone concentrations are likely to continue to rise in October, especially when weather conditions are unfavorable and regional and long-range transport are significant.

Our study may provide a scientific base for guiding effective control strategies for ozone pollution. In the present study, we evaluated the ozone sensitivity to only anthropogenic precursor emissions in a monthly time scale, which may not meet the requirements of controlling daily maximum ozone concentrations due to the strong nonlinear relationship between ozone and its precursors. NO_x emissions are mainly from vehicles, industry, and power plants, while VOCs emissions are from solvent use, industry, vehicles, and residences. Future studies include the ozone sensitivity to precursor emissions from different emission sectors and ozone sensitivity on daily or hourly bases under different weather patterns would be more valuable for emission mitigation measures.

DATA AVAILABILITY STATEMENT

The original contributions presented in the study are included in the article/**Supplementary Material**, further inquiries can be directed to the corresponding author.

AUTHOR CONTRIBUTIONS

Conceptualization, methodology, writing—review and editing, and supervision: Y-HM; formal analysis, writing—original draft, and visualization: SY; data curation: YS; conceptualization: HL and NL.

FUNDING

This work was supported by the National Key Research and Development Plan (2018YFC0213800) and the China Postdoctoral Science Foundation (2017M620218, 2018T110526).

ACKNOWLEDGMENTS

The GEOS-Chem model is managed by the Atmospheric Chemistry Modeling group at Harvard University with support from the NASA ACMAP program.

SUPPLEMENTARY MATERIAL

The Supplementary Material for this article can be found online at: https://www.frontiersin.org/articles/10.3389/fenvs.2022.864897/full#supplementary-material

REFERENCES

Amos, H. M., Jacob, D. J., Holmes, C. D., Fisher, J. A., Wang, Q., Yantosca, R. M., et al. (2012). Gas-particle Partitioning of Atmospheric Hg(II) and its Effect on Global Mercury Deposition. *Atmos. Chem. Phys.* 12, 591–603. doi:10.5194/acp-12-591-2012

An, J., Zou, J., Wang, J., Lin, X., and Zhu, B. (2015). Differences in Ozone Photochemical Characteristics between the Megacity Nanjing and its Suburban Surroundings, Yangtze River Delta, China. *Environ. Sci. Pollut. Res.* 22, 19607–19617. doi:10.1007/s11356-015-5177-0

Auvray, M., and Bey, I. (2005). Long-range Transport to Europe: Seasonal Variations and Implications for the European Ozone Budget. *J. Geophys. Res.* 110, D11303. doi:10.1029/2004JD005503

Bell, M. L., Peng, R. D., and Dominici, F. (2006). The Exposure-Response Curve for Ozone and Risk of Mortality and the Adequacy of Current Ozone Regulations. *Environ. Health Perspect.* 114, 532–536. doi:10.1289/ehp.8816

Bey, I., Jacob, D. J., Yantosca, R. M., Logan, J. A., Field, B. D., Fiore, A. M., et al. (2001). Global Modeling of Tropospheric Chemistry with Assimilated Meteorology: Model Description and Evaluation. *J. Geophys. Res.* 106, 23073–23095. doi:10.1029/2001jd000807

Ding, D., Xing, J., Wang, S., Chang, X., and Hao, J. (2019). Impacts of Emissions and Meteorological Changes on China's Ozone Pollution in the Warm Seasons of 2013 and 2017. *Front. Environ. Sci. Eng.* 13, 1–9. doi:10.1007/s11783-019-1160-1

Emery, C., Liu, Z., Russell, A. G., Odman, M. T., Yarwood, G., and Kumar, N. (2017). Recommendations on Statistics and Benchmarks to Assess Photochemical Model Performance. *J. Air Waste Manage. Assoc.* 67, 582–598. doi:10.1080/10962247.2016.1265027

Gao, J., Zhu, B., Xiao, H., Kang, H., Hou, X., and Shao, P. (2016). A Case Study of Surface Ozone Source Apportionment during a High Concentration Episode, under Frequent Shifting Wind Conditions over the Yangtze River Delta, China. *Sci. Total Environ.* 544, 853–863. doi:10.1016/j.scitotenv.2015.12.039

Gao, W., Tie, X., Xu, J., Huang, R., Mao, X., Zhou, G., et al. (2017). Long-term Trend of O3 in a Mega City (Shanghai), China: Characteristics, Causes, and Interactions with Precursors. *Sci. Total Environ.* 603-604, 425–433. doi:10.1016/j.scitotenv.2017.06.099

Gong, C., Liao, H., Zhang, L., Yue, X., Dang, R., and Yang, Y. (2020). Persistent Ozone Pollution Episodes in North China Exacerbated by Regional Transport. *Environ. Pollut.* 265, 115056. doi:10.1016/j.envpol.2020.115056

Guenther, A. B., Jiang, X., Heald, C. L., Sakulyanontvittaya, T., Duhl, T., Emmons, L. K., et al. (2012). The Model of Emissions of Gases and Aerosols from Nature Version 2.1 (MEGAN2.1): An Extended and Updated Framework for Modeling Biogenic Emissions. *Geosci. Model. Dev.* 5, 1471–1492. doi:10.5194/gmd-5-1471-2012

Guo, H., Chen, K., Wang, P., Hu, J., Ying, Q., Gao, A., et al. (2019). Simulation of Summer Ozone and its Sensitivity to Emission Changes in China. *Atmos. Pollut. Res.* 10, 1543–1552. doi:10.1016/j.apr.2019.05.003

Holtslag, A. A. M., and Boville, B. A. (1993). Local versus Nonlocal Boundary-Layer Diffusion in a Global Climate Model. *J. Clim.* 6, 1825–1842. doi:10.1175/1520-0442(1993)006<1825:lvnbld>2.0.co;2

Jin, X., and Holloway, T. (2015). Spatial and Temporal Variability of Ozone Sensitivity over China Observed from the Ozone Monitoring Instrument. *J. Geophys. Res. Atmos.* 120, 7229–7246. doi:10.1002/2015jd023250

Kanaya, Y., Pochanart, P., Liu, Y., Li, J., Tanimoto, H., Kato, S., et al. (2009). Rates and Regimes of Photochemical Ozone Production over Central East China in June 2006: A Box Model Analysis Using Comprehensive Measurements of Ozone Precursors. *Atmos. Chem. Phys.* 9, 7711–7723. doi:10.5194/acp-9-7711-2009

Keller, C. A., Long, M. S., Yantosca, R. M., Da Silva, A. M., Pawson, S., and Jacob, D. J. (2014). HEMCO v1.0: A Versatile, ESMF-Compliant Component for Calculating Emissions in Atmospheric Models. *Geosci. Model. Dev.* 7, 1409–1417. doi:10.5194/gmd-7-1409-2014

Krupa, S. V., and Manning, W. J. (1988). Atmospheric Ozone: Formation and Effects on Vegetation. *Environ. Pollut.* 50, 101–137. doi:10.1016/0269-7491(88)90187-X

Kuhns, H., Knipping, E. M., and Vukovich, J. M. (2005). Development of a United States-Mexico Emissions Inventory for the Big Bend Regional Aerosol and Visibility Observational (BRAVO) Study. *J. Air Waste Manage. Assoc.* 55, 677–692. doi:10.1080/10473289.2005.10464648

Li, K., Jacob, D. J., Liao, H., Shen, L., Zhang, Q., and Bates, K. H. (2019). Anthropogenic Drivers of 2013-2017 Trends in Summer Surface Ozone in China. *Proc. Natl. Acad. Sci. U.S.A.* 116, 422–427. doi:10.1073/pnas.1812168116

Li, K., Chen, L., Ying, F., White, S. J., Jang, C., Wu, X., et al. (2017). Meteorological and Chemical Impacts on Ozone Formation: A Case Study in Hangzhou, China. *Atmos. Res.* 196, 40–52. doi:10.1016/j.atmosres.2017.06.003

Li, L., An, J., Huang, L., Yan, R., Huang, C., and Yarwood, G. (2019). Ozone Source Apportionment over the Yangtze River Delta Region, China: Investigation of Regional Transport, Sectoral Contributions and Seasonal Differences. *Atmos. Environ.* 202, 269–280. doi:10.1016/j.atmosenv.2019.01.028

Li, L., Xie, F., Li, J., Gong, K., Xie, X., Qin, Y., et al. (2021). Diagnostic Analysis of Regional Ozone Pollution in Yangtze River Delta, China: A Case Study in Summer 2020. *Sci. Total Environ.* 812, 151511. doi:10.1016/j.scitotenv.2021.151511

Li, M., Wang, T., Shu, L., Qu, Y., Xie, M., Liu, J., et al. (2021). Rising Surface Ozone in China from 2013 to 2017: A Response to the Recent Atmospheric Warming or Pollutant Controls? *Atmos. Environ.* 246, 118130. doi:10.1016/j.atmosenv.2020.118130

Li, M., Zhang, Q., Kurokawa, J.-i., Woo, J.-H., He, K., Lu, Z., et al. (2017). MIX: A Mosaic Asian Anthropogenic Emission Inventory under the International Collaboration Framework of the MICS-Asia and HTAP. *Atmos. Chem. Phys.* 17, 935–963. doi:10.5194/acp-17-935-2017

Liang, X., Sun, X., Xu, J., and Ye, D. (2020). Improved Emissions Inventory and VOCs Speciation for Industrial OFP Estimation in China. *Sci. Total Environ.* 745, 140838. doi:10.1016/j.scitotenv.2020.140838

Lin, J.-T., and McElroy, M. B. (2010). Impacts of Boundary Layer Mixing on Pollutant Vertical Profiles in the Lower Troposphere: Implications to Satellite Remote Sensing. *Atmos. Environ.* 44, 1726–1739. doi:10.1016/j.atmosenv.2010.02.009

Lin, J.-T., Wuebbles, D. J., and Liang, X.-Z. (2008). Effects of Intercontinental Transport on Surface Ozone over the United States: Present and Future Assessment with a Global Model. *Geophys. Res. Lett.* 35, L02805. doi:10.1029/2007GL031415

Liu, F., Beirle, S., Zhang, Q., van der A, R. J., Zheng, B., Tong, D., et al. (2017). NOx Emission Trends over Chinese Cities Estimated from OMI Observations during 2005 to 2015. *Atmos. Chem. Phys.* 17, 9261–9275. doi:10.5194/acp-17-9261-2017

Liu, H., Jacob, D. J., Bey, I., and Yantosca, R. M. (2001). Constraints from210Pb and7Be on Wet Deposition and Transport in a Global Three-Dimensional Chemical Tracer Model Driven by Assimilated Meteorological fields. *J. Geophys. Res.* 106, 12109–12128. doi:10.1029/2000JD900839

Lu, H., Lyu, X., Cheng, H., Ling, Z., and Guo, H. (2019). Overview on the Spatial-Temporal Characteristics of the Ozone Formation Regime in China. *Environ. Sci. Process. Impacts* 21, 916–929. doi:10.1039/c9em00098d

Lu, X., Hong, J., Zhang, L., Cooper, O. R., Schultz, M. G., Xu, X., et al. (2018). Severe Surface Ozone Pollution in China: A Global Perspective. *Environ. Sci. Technol. Lett.* 5, 487–494. doi:10.1021/acs.estlett.8b00366

Lu, X., Zhang, L., Chen, Y., Zhou, M., Zheng, B., Li, K., et al. (2019). Exploring 2016-2017 Surface Ozone Pollution over China: Source Contributions and Meteorological Influences. *Atmos. Chem. Phys.* 19, 8339–8361. doi:10.5194/acp-19-8339-2019

Lu, X., Zhang, L., Wang, X., Gao, M., Li, K., Zhang, Y., et al. (2020). Rapid Increases in Warm-Season Surface Ozone and Resulting Health Impact in China since 2013. *Environ. Sci. Technol. Lett.* 7 (4), 240–247. doi:10.1021/acs.estlett.0c00171

Ma, T., Duan, F., He, K., Qin, Y., Tong, D., Geng, G., et al. (2019). Air Pollution Characteristics and Their Relationship with Emissions and Meteorology in the Yangtze River Delta Region during 2014-2016. *J. Environ. Sci.* 83, 8–20. doi:10.1016/j.jes.2019.02.031

Martin, R. V., Fiore, A. M., and Van Donkelaar, A. (2004). Space-based Diagnosis of Surface Ozone Sensitivity to Anthropogenic Emissions. *Geophys. Res. Lett.* 31, L06120. doi:10.1029/2004GL019416

McLinden, C. A., Olsen, S. C., Hannegan, B., Wild, O., Prather, M. J., and Sundet, J. (2000). Stratospheric Ozone in 3-D Models: A Simple Chemistry and the Cross-Tropopause Flux. *J. Geophys. Res.* 105, 14653–14665. doi:10.1029/2000JD900124

NRC (1991). *Rethinking the Ozone Problem in Urban and Regional Air Pollution*. Washington, DC: The National Academies Press. doi:10.1016/0021-8502(93)90076-l

Seinfeld, J. H., and Pandis, S. N. (1998). From Air Pollution to Climate Change. *Atmos. Chem. Phys.* 1326, 429–443. doi:10.1080/00139157.1999.10544295

Su, F., Xu, Q., Wang, K., Yin, S., Wang, S., Zhang, R., et al. (2021). On the Effectiveness of Short-Term Intensive Emission Controls on Ozone and Particulate Matter in a Heavily Polluted Megacity in central China. *Atmos. Environ.* 246, 118111. doi:10.1016/j.atmosenv.2020.118111

Sun, L., Xue, L., Wang, Y., Li, L., Lin, J., Ni, R., et al. (2019). Impacts of Meteorology and Emissions on Summertime Surface Ozone Increases over central Eastern China between 2003 and 2015. *Atmos. Chem. Phys.* 19, 1455–1469. doi:10.5194/acp-19-1455-2019

Tang, G., Zhu, X., Xin, J., Hu, B., Song, T., Sun, Y., et al. (2017). Modelling Study of Boundary-Layer Ozone over Northern China - Part I: Ozone Budget in Summer. *Atmos. Res.* 187, 128–137. doi:10.1016/j.atmosres.2016.10.017

van der Werf, G. R., Randerson, J. T., Giglio, L., Van Leeuwen, T. T., Chen, Y., Rogers, B. M., et al. (2017). Global Fire Emissions Estimates during 1997-2016. *Earth Syst. Sci. Data* 9, 697–720. doi:10.5194/essd-9-697-2017

Wang, M., Chen, W., Zhang, L., Qin, W., Zhang, Y., Zhang, X., et al. (2020). Ozone Pollution Characteristics and Sensitivity Analysis Using an Observation-Based Model in Nanjing, Yangtze River Delta Region of China. *J. Environ. Sci.* 93, 13–22. doi:10.1016/j.jes.2020.02.027

Wang, N., Lyu, X., Deng, X., Huang, X., Jiang, F., and Ding, A. (2019). Aggravating O3 Pollution Due to NOx Emission Control in Eastern China. *Sci. Total Environ.* 677, 732–744. doi:10.1016/j.scitotenv.2019.04.388

Wei, W., Li, Y., Ren, Y., Cheng, S., and Han, L. (2019). Sensitivity of Summer Ozone to Precursor Emission Change over Beijing during 2010-2015: A WRF-Chem Modeling Study. *Atmos. Environ.* 218, 116984. doi:10.1016/j.atmosenv.2019.116984

Wesely, M. L. (1989). Parameterization of Surface Resistances to Gaseous Dry Deposition in Regional-Scale Numerical Models. *Atmos. Environ. (1967)* 23, 1293–1304. doi:10.1016/0004-6981(89)90153-4

Wu, R., Bo, Y., Li, J., Li, L., Li, Y., and Xie, S. (2016). Method to Establish the Emission Inventory of Anthropogenic Volatile Organic Compounds in China and its Application in the Period 2008-2012. *Atmos. Environ.* 127, 244–254. doi:10.1016/j.atmosenv.2015.12.015

Xiao, Y., Logan, J. A., Jacob, D. J., Hudman, R. C., Yantosca, R., and Blake, D. R. (2008). Global Budget of Ethane and Regional Constraints on U.S. Sources. *J. Geophys. Res.* 113, D21306. doi:10.1029/2007jd009415

Xing, J., Wang, S. X., Jang, C., Zhu, Y., and Hao, J. M. (2011). Nonlinear Response of Ozone to Precursor Emission Changes in China: A Modeling Study Using Response Surface Methodology. *Atmos. Chem. Phys.* 11, 5027–5044. doi:10.5194/acp-11-5027-2011

Xu, J., Huang, X., Wang, N., Li, Y., and Ding, A. (2021). Understanding Ozone Pollution in the Yangtze River Delta of Eastern China from the Perspective of Diurnal Cycles. *Sci. Total Environ.* 752, 141928. doi:10.1016/j.scitotenv.2020.141928

Xu, Z., Huang, X., Nie, W., Chi, X., Xu, Z., Zheng, L., et al. (2017). Influence of Synoptic Condition and holiday Effects on VOCs and Ozone Production in the Yangtze River Delta Region, China. *Atmos. Environ.* 168, 112–124. doi:10.1016/j.atmosenv.2017.08.035

Xue, L. K., Wang, T., Gao, J., Ding, A. J., Zhou, X. H., Blake, D. R., et al. (2014). Ground-level Ozone in Four Chinese Cities: Precursors, Regional Transport and Heterogeneous Processes. *Atmos. Chem. Phys.* 14, 13175–13188. doi:10.5194/acp-14-13175-2014

Yang, L., Yuan, Z., Luo, H., Wang, Y., Xu, Y., Duan, Y., et al. (2021). Identification of Long-Term Evolution of Ozone Sensitivity to Precursors Based on Two-Dimensional Mutual Verification. *Sci. Total Environ.* 760, 143401. doi:10.1016/j.scitotenv.2020.143401

Yu, Y., Wang, Z., He, T., Meng, X., Xie, S., and Yu, H. (2019). Driving Factors of the Significant Increase in Surface Ozone in the Yangtze River Delta, China, during 2013-2017. *Atmos. Pollut. Res.* 10, 1357–1364. doi:10.1016/j.apr.2019.03.010

Zhang, K., Li, L., Huang, L., Wang, Y., Huo, J., Duan, Y., et al. (2020). The Impact of Volatile Organic Compounds on Ozone Formation in the Suburban Area of Shanghai. *Atmos. Environ.* 232, 117511. doi:10.1016/j.atmosenv.2020.117511

Zheng, B., Tong, D., Li, M., Liu, F., Hong, C., Geng, G., et al. (2018). Trends in China's Anthropogenic Emissions since 2010 as the Consequence of Clean Air Actions. *Atmos. Chem. Phys.* 18, 14095–14111. doi:10.5194/acp-18-14095-2018

Zheng, B., Zhang, Q., Geng, G., Chen, C., Shi, Q., Cui, M., et al. (2021). Changes in China's Anthropogenic Emissions and Air Quality during the COVID-19 Pandemic in 2020. *Earth Syst. Sci. Data* 13, 2895–2907. doi:10.5194/essd-13-2895-2021

Zheng, J., Zhong, L., Wang, T., Louie, P. K. K., and Li, Z. (2010). Ground-level Ozone in the Pearl River Delta Region: Analysis of Data from a Recently Established Regional Air Quality Monitoring Network. *Atmos. Environ.* 44, 814–823. doi:10.1016/j.atmosenv.2009.11.032

Conflict of Interest: The authors declare that the research was conducted in the absence of any commercial or financial relationships that could be construed as a potential conflict of interest.

Publisher's Note: All claims expressed in this article are solely those of the authors and do not necessarily represent those of their affiliated organizations, or those of the publisher, the editors, and the reviewers. Any product that may be evaluated in this article, or claim that may be made by its manufacturer, is not guaranteed or endorsed by the publisher.

frontiers | Frontiers in Environmental Science

ORIGINAL RESEARCH
published: 27 April 2022
doi: 10.3389/fenvs.2022.872226

The Effect of Banning Fireworks on Air Quality in a Heavily Polluted City in Northern China During Chinese Spring Festival

Dexin Liu[1,2], *Wanlong Li*[1], *Jianbiao Peng*[3] *and Qingxia Ma*[1,2,4]*

[1]College of Geography and Environmental Science, Henan University, Kaifeng, China, [2]Key Laboratory of Geospatial Technology for Middle and Lower Yellow River Regions, Henan University, Ministry of Education, Kaifeng, China, [3]School of Environment, Henan Normal University, Xinxiang, China, [4]Henan Key Laboratory of Integrated Air Pollution Control and Ecological Security, Kaifeng, China

OPEN ACCESS

Edited by:
Qiyuan Wang,
Institute of Earth Environment (CAS), China

Reviewed by:
Yichen Wang,
Northwestern Polytechnical University, China
Zhisheng Yao,
Institute of Atmospheric Physics (CAS), China

***Correspondence:**
Qingxia Ma
mqx@henu.edu.cn

Specialty section:
This article was submitted to Atmosphere and Climate, a section of the journal Frontiers in Environmental Science

Received: 09 February 2022
Accepted: 07 March 2022
Published: 27 April 2022

Citation:
Liu D, Li W, Peng J and Ma Q (2022) The Effect of Banning Fireworks on Air Quality in a Heavily Polluted City in Northern China During Chinese Spring Festival. Front. Environ. Sci. 10:872226. doi: 10.3389/fenvs.2022.872226

Air pollution has a negative impact on the ecological environment as well as on the health of people. Setting off fireworks and firecrackers lead to a significant deterioration in air quality in a short period of time. The firework prohibition policy of 2016 in Zhengzhou City provides an opportunity to investigate the effect of banning fireworks on air quality during the Spring Festival. The Air Quality Index and the concentrations of $PM_{2.5}$, PM_{10}, SO_2, NO_2, CO and O_3 during the Spring Festival between 2014 and 2019 in Zhengzhou City were analyzed. The results show that: There were small fluctuations in precipitation, air pressure, wind speed, temperature and relative humidity during the Spring Festival from 2014 to 2019. The air quality index in the Spring Festival in 2016 was significantly lower than that in 2014 and 2015, and the air quality in 2018 and 2019 showed greater improvements. The sudden increases in pollutants concentrations has been weakened, showing an obvious "peak-shaving" effect during the traditional heavy pollution period, New Year's Eve to the first day of the first lunar month. In 2014 and 2015 years, the concentrations of $PM_{2.5}$ and PM_{10} reached their peaks at 1:00 a.m. on the first day of the new year, and fluctuated in the ranges of 259–271 μg/m³ and 380–384 μg/m³, respectively. The concentrations of $PM_{2.5}$ and PM_{10} were 44 and 100 μg/m³, respectively in 2016, 40 and 80 μg/m³ in 2018 during the same period. In addition, the ban implemented has the most obvious impact on $PM_{2.5}$ and PM_{10}. Compared with the Spring Festival in 2014, the concentrations of $PM_{2.5}$ and PM_{10} increased by 19.15 and 18.64% in 2015, decreased by 18.38% and 15.90% in 2016, and decreased by 16.83% and 26.05% in 2018. Therefore, banning fireworks and firecrackers will help to improve the air quality during the Spring Festival in Zhengzhou City to a certain extent.

Keywords: Chinese spring festival, fireworks, air quality, China, pollutants

1 INTRODUCTION

Due to a rapid increase in heating, traffic, industrial emissions and the stable synoptic conditions especially during the cold winter, air pollution has become a major environmental problem that get special attention from the general public (Sahu and Sahu, 2019; Xu et al., 2020). Air pollution not only cause adverse effects on the development of regional economies (Zhou et al., 2019; Xu et al., 2020), but also has a negative impact on the ecological environment and health (Doherty et al., 2017; Hanaoka and Masui, 2019). Studies found that high concentrations of air pollutants may cause cardiovascular disease, chronic obstructive pulmonary disease, respiratory disease and chronic kidney disease (Shakerkhatibi et al., 2015; Todorović et al., 2019; Lin et al., 2020), resulting in a large number of deaths every year throughout the world (Sharma et al., 2019). With the rapid development of economy, severe air pollution engulfed in the winter in China (Zhou et al., 2019); Many studies proposed that coal combustion, industrial emissions, transportation and dust are the main sources of air pollutants in China (Ye et al., 2016; Ge et al., 2018; Wang et al., 2021; Wang et al., 2022); Chinese Spring Festival is an important holiday when a large number of people return to their hometowns causing many factories shut-down, and the traffic volume decreases significantly in megacities. However, setting off fireworks and firecrackers is a great tradition during this festival, which lead to a significant deterioration in air quality but crucially in a short period of time (Saha et al., 2014; Zhao et al., 2014; Lai and Brimblecombe, 2017; Wang et al., 2019; Kumar et al., 2016; Zhang et al., 2017; Greven et al., 2019; Zhang et al., 2020).

The main components of firecrackers are black powder, including potassium nitrate, sulfur powder, charcoal powder, and some of them contain potassium chlorate. When making fireworks, inorganic salt and magnesium powder are added (Wang et al., 2007; Zhang et al., 2017). Therefore, setting off large numbers of fireworks and firecrackers will inevitably cause the concentration of gas pollutants, particulate pollutants, and toxic substances to rise rapidly in a short period of time, resulting in adverse effect on the health and safety of people (Ji et al., 2018; Greven et al., 2019; Zhang et al., 2020). Setting off fireworks and firecrackers is a traditional custom that has been part of celebrating the Spring Festival in China for more than 1000 years (Kumar et al., 2016; Ye et al., 2016; Zhang et al., 2017). Haze still formed in megacities during the Spring Festival, although most enterprises shut down or half shut down, and traffic activities sharply reduce, resulting in a significant reduction in local pollution sources and emissions. The haze pollution could be attributed to intermittent and centralized fireworks and firecrackers during the Spring Festival, due to the chemicals making up their construction (Wang et al., 2019; Zhang et al., 2020).

Setting off fireworks and firecrackers was prohibited in Zhengzhou in 2016 during the spring festival. This inaugural prohibition policy applied to the five districts of Zhongyuan, Erqi, Jinshui, Guancheng and Huiji; as well to the four development zones of Zhengzhou Airport Economy Zone, Zhengdong New District, Zhengzhou Economic and Technological Development Zone and Zhengzhou National High&New Technology Industries Development Zone. In 2018, the policy was in effect strengthened through expansion if its scope to include the heavily built-up areas of wider Zhengzhou to include Xinzheng City, Xinmi City, Dengfeng City, Xingyang City, Zhongmu County and Shangjie District. The implementation of the policy which effectively closed down one specific source of air pollution during the Spring Festival, therefore, provided a unique opportunity in Zhengzhou to investigate the impact of fireworks on atmospheric environmental quality and comment on the efficacy of such policies on improving environmental air quality in general.

Scholars have researched into the impact of fireworks on atmospheric environmental quality. Saha et al. (2014) found that over an urban metropolis in India, an increase in air pollutant concentration, from large amounts of fireworks set off there during the Deepawali Festival, is related to the climate and environmental change patterns in the region. Among these pollutants, the increase in Particle Pollutant concentrations was significance (Kumar et al., 2016). In central London, the total concentration of $PM_{2.5}$ at night is higher than average daytime values, exceeding national ambient air quality standards (NAAQS), and the risk of $PM_{2.5}$-PTEs at night during fireworks activities is higher than that during daytime (Hamad et al., 2015). Case crossover studies have shown a positive correlation between fireworks and mortality, as well as PM_{10}, during the Dutch New Year celebrations (Greven et al., 2019). Many studies reported the relationship between fireworks and air pollution in Beijing (Wang et al., 2007), Tianjin (Xie et al., 2019), Nanning (Li et al., 2017), Lanzhou (Zhao et al., 2014)and Chengdu (Zhang et al., 2016; Wu et al., 2018)in China. The research usually involves on-line monitoring during combustion (Zhang et al., 2016; Wu et al., 2018), air pollution status determinations in different periods of the Spring Festival (Zhang et al., 2016), and the impact of fireworks combustion on air pollutants (Jing et al., 2014; Zhao et al., 2014; Zhang et al., 2017).

Obviously, the above research mainly focuses on the impact of fireworks on the overall atmospheric environmental quality of cities in the absence of no-burn or firework prohibition policies, and there are relatively few comparative studies before and after the implementation of such policies. Moreover, the time spans of existing studies are also relatively short, often within a year, and therefore, long-term sequence comparative studies are lacking. The firework prohibition policy was implemented in 2016 and expanded and strengthened in 2018 Based on the air quality monitoring data in Zhengzhou City from 2014 to 2019, We study the effects of banning fireworks and firecrackers on the air quality index and air pollutants such as $PM_{2.5}$, PM_{10}, NO_2, SO_2, O_3, CO during the Spring Festival to provide a scientific basis for the prohibition of setting off fireworks and firecrackers during the Chinese Spring Festival in other areas of the country.

2 STUDY AREA

Zhengzhou City (112°42′E to 114°14′E, 34°16′N to 34°58′N) is located in the eastern part of the Qinling Mountains, in the

transition zone between the second and third levels of the national geographic steps. Its altitude is generally high in the southwest whilst low in the northeast and experiences a temperate continental monsoon climate with poor rainfall and low wind speed. In winter, static wind and inversions are easily formed, which is well recognized as being detrimental to the movement and diffusion of air-based pollutants (Guo et al., 2019).

Zhengzhou is densely populated as a result of the city's rapid expansion which has also brought about increasing levels of air pollution. According to statistics, by the end of 2017, Zhengzhou had a permanent population of 9.88 million, with an annual GDP of 919.377 billion yuan, hosting some 133 industrial enterprises consuming in excess of 10,000 tons of standard coal annually, accounting for 17.7% of the province's total consumption, of which its industrial energy consumption has been dominated by coal for a significant amount of time (Wang and Xia, 2018). At the same time, Zhengzhou is not only the main city of the Central Plains urban agglomeration, but also the important transportation hub of "2 + 26 cities" in Beijing, Tianjin, Hebei and its surrounding areas (Guo et al., 2019).

As already alluded to in the introduction, Zhengzhou has a long history of culture in which fireworks and firecrackers have been used for thousands of years in traditional customs associated with events such as the spring festival. This use of fireworks in a significant coal burning area which is meteorologically predisposed to retain air pollution are the main reasons for this study's interest in choosing Zhengzhou as the study area (**Figure 1**).

3 MATERIALS AND METHODS

The air quality index and pollutant quality concentration data (including AQI, $PM_{2.5}$, PM_{10}, NO_2, SO_2, O_3, CO) are crucial to the analysis in this study, and are sourced from the state control station of Zhengzhou Environmental Protection Bureau for the period 2014 to 2019. The pollutant quality concentration and meteorological factor data are from http://www.tianqihoubao.com/ and https://www.aqistudy.cn/historydata/ in 2020. In these data sets, for dates where there are missing or partially missing data, the data average for the month in which the date occurred are used in replacement.

According to the ambient air quality standard GB3095-2012 (20160101) (Xie et al., 2019), the following definitions are used: "daily average" refers to the arithmetic mean of 24-h average concentration of a natural day; "quarterly average" refers to the arithmetic mean of daily average concentration in a calendar quarter; and "annual average" refers to the arithmetic mean of daily average concentration in a calendar year. Referencing the lunar calendar, Spring comprises the months March, April and May (92 days); summer comprises June, July and August (92 days); autumn comprises September, October and November (91 days); and winter comprises December as well as January and February of the following year (90 days for no leap year and 91 days for leap year).

According to the revised National Ambient Air Quality Standard (NAAQS-2012) issued by China's Ministry of Environmental Protection (now known as the Ministry of Ecology and Environment) (Ye et al., 2016; Zhou et al., 2019), AQI is a dimensionless index used to quantitatively describe air quality. As shown in **Table 1**, AQI is divided into six grades, depending on its value range, where each grade has an associated severity categorization and description. The larger the value range is, means a higher grade which implies the air pollution is more serious and of greater harm to human health. It is, therefore, suitable for characterizing the short-term air quality status and change trend of the city.

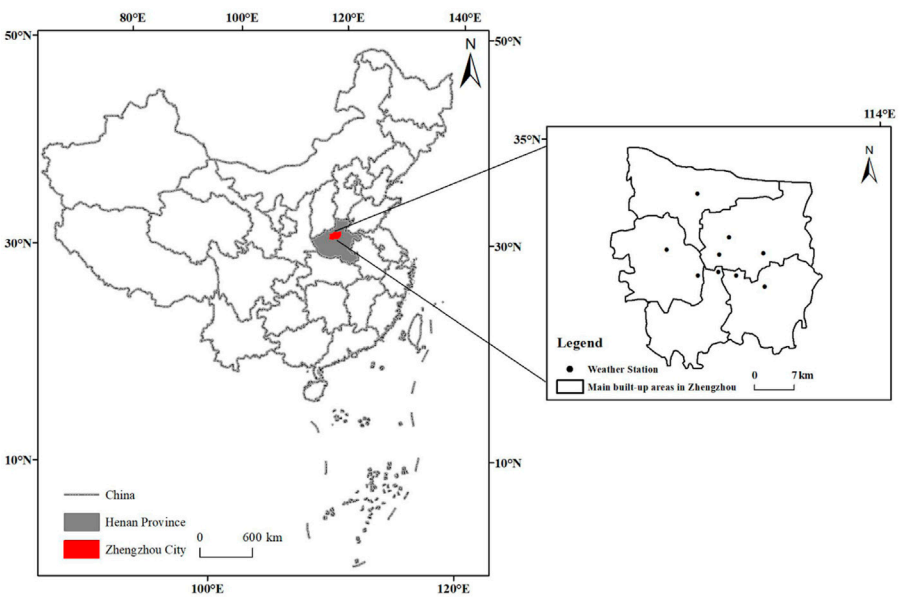

FIGURE 1 | Distribution map of meteorological observation stations in zhengzhou city.

TABLE 1 | AQI values, grade, and description.

AQI Value	Grade	Description
0–50	I	Good
51–100	II	Moderate
101–150	III	Unhealthy for sensitive people
151–200	IV	Unhealthy
201–300	V	Very unhealthy
301–500	VI	Hazardous

4 RESULTS

4.1 Air Quality Characteristics of Zhengzhou During the Spring Festival

The air quality index data for Zhengzhou City during the Spring Festival (from the 27th December to the 6th January) from 2014 to 2019 were used to establish the change trend in AQI average during the Spring Festivals as shown in **Figure 2**. The change trend of the AQI in Zhengzhou City during the Spring Festival shows a double peak trend of first rising and then falling, while the AQI in winter shows a double valley trend of first falling and then rising. The lowest AQI during a Spring Festival occurs in 2019 and can be classified as Grade III, that is "Moderate"; the second lowest occurred in 2018 (AQI = 141); whilst the highest occurred in 2017 (AQI = 197) and can be categorized as grade IV; the second highest in 2015 (AQI = 194), also a Grade IV but is higher than the average annual AQI. This is mainly because Zhengzhou started to implement its firework prohibition policy in 2016, but in 2017 there was a significant increase in the AQI, a reflection of inadequacies in the policy. However, in 2018, with the further expansion of the scope of the policy, the AQI decreased, and decreased further in 2019, the lowest it has been in recent history. This policy change is also the main reason for the opposite trend between AQI during the Spring Festival and AQI in winter.

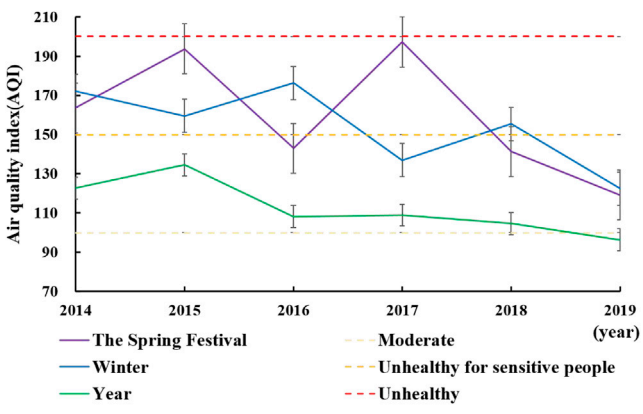

FIGURE 2 | AQI change trend of Zhengzhou during Spring Festival from 2014 to 2019.

2016 is the first year of Zhengzhou's policy implementation prohibiting fireworks, and it is also a turning point for the improvement of its air quality as evidenced in the decrease of 26.17% in the AQI during the Spring Festival in 2016 compared with the same period in 2015, as well as being significantly lower than the average value in winter. Hence, the banning of setting off fireworks and firecrackers during the Spring Festival had a great impact on the atmospheric environment quality. The AQI reached 197 during the Spring Festival in 2017, which is significantly higher than the winter average and close to being categorized as in the Unhealthy grade. This mainly resulted from the realization in 2017 of limitations in the prohibition policy that provided exemptions for certain districts and the problem was further compounded through significant levels of firework theft and their subsequent illegal setting off.

The AQI in 2018 decreased by 28.43% compared with the same period in 2017, moving from the Unhealthy for sensitive people grade to the Moderate grade. This is because the prohibition policy was strengthened in 2018 through expansion of its jurisdiction from the original five districts and four development zones to include the built-up areas surrounding the wider city. The AQI index further decreased significantly during the Spring Festival of 2019, reaching its lowest level (AQI = 119) in recent years.

The distribution of the air quality grades for Zhengzhou during the Spring Festivals from 2014 to 2019 are shown in **Table 2**. The air quality levels from the 27th December to the

TABLE 2 | Distribution of air quality grades during the Spring Festival of Zhengzhou from 2014 to 2019.

Date (Lunar)	Dec 27th	Dec 28th	Dec 29th	Dec 30th	Jan 1st	Jan 2ed	Jan 3rd	Jan 4th	Jan 5th	Jan 6th
2014	111	134	179	240	261	240	260	98	63	52
2015	333	181	219	162	192	126	154	147	199	225
2016	155	57		58	91	166	232	244	243	41
2017	260	283	318	221	184	256	67	89	147	149
2018	52	70	123	72	182	227	233	104	183	169
2019	79	143	143	84	163	308	87	57	69	62
Good (I)	Moderate (II)	Unhealthy for sensitive people (III)	Unhealthy (IV)	Very unhealthy (V)	Hazardous (VI)					

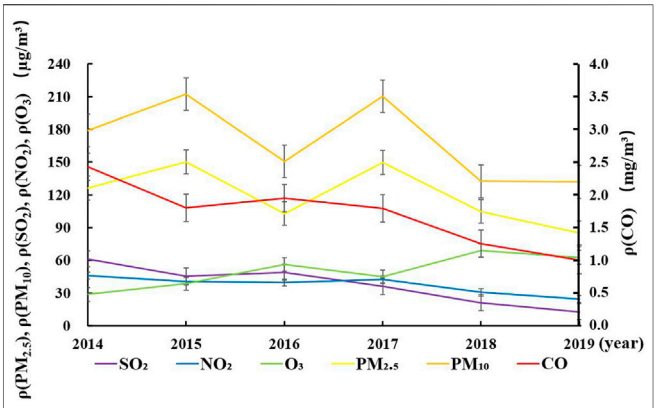

FIGURE 3 | Annual change trend of average concentration of main pollutants in Zhengzhou during the Spring Festival from 2014 to 2019.

1st January from 2014 to 2015 are all between III-VI. After the implementation of Zhengzhou's firework prohibition policy in 2016, the air quality has significantly improved, ranking at level II for four consecutive days. With the relaxation of the prohibition policy in 2017, the air quality level from the 27th December to the 1st January remains high, and only after the 3rd January does it reduce. With the strengthening of the prohibition policy during the Spring Festival, Zhengzhou's air quality from the 27th of December to the 1st January in 2018, significantly improved compared with 2017. Finally, the air quality obviously improved from the 27th December 2019 to the 1st January, while the air quality from the third day to the 6th January is eminently an improvement from that of previous years, a result that is attributed to the further strengthening of the prohibition policy, and corresponds to the results of annual AQI mean changes during the Spring Festival in Zhengzhou. The results indicated that the prohibition of fireworks and firecrackers plays an important role in improving the air quality of Zhengzhou during the Spring Festival, especially from the 27th December to the 1st January.

4.2 Daily Variation Characteristics of Pollutant Concentrations

The combustion of fireworks and firecrackers has an effect on the airborne concentrations of gas pollutants, particulate pollutants, heavy metals and toxic substances. The daily variations of pollutant concentrations were stduied in Zhengzhou during Spring Festival over three periods: firstly, from 2014 to 2015 which is before the implementation of the initial firework prohibition policy in 2016; secondly, from 2016 to 2017 during the initial implementation of the policy; and thirdly, from 2018 to 2019 after the implementation of the strengthened prohibition policy in 2018.

4.2.1 Variation Characteristics of Pollutant Concentrations Before the Prohibition Policy (2014–2015)

As shown in **Figure 3**, the average concentrations of $PM_{2.5}$ and PM_{10} increased during the Spring Festivals from 2014 to 2015. In 2014, the average concentration of $PM_{2.5}$ and PM_{10} were 126.18 and 178.97 μg/m³, respectively; whilst in 2015, they were 150.34 and 212.33 μg/m³, respectively; both exceeding the national secondary atmospheric standard. Secondly, as shown in **Figure 4**, from a local point of view, the $PM_{2.5}$ concentration reached a peak on the 1st January in 2014 at 210.75 μg/m³, and peaked again on the 3rd January at 210.38 μg/m³; whilst the PM_{10} concentration peaked on the 2nd January at 381.30 μg/m³. In 2015, the first peaks of $PM_{2.5}$ (283.17 μg/m³) and PM_{10} (333.63 μg/m³) occurred on the 27th of December, whereas the second peak of $PM_{2.5}$ (174.67 μg/m³) occurred on the 6th

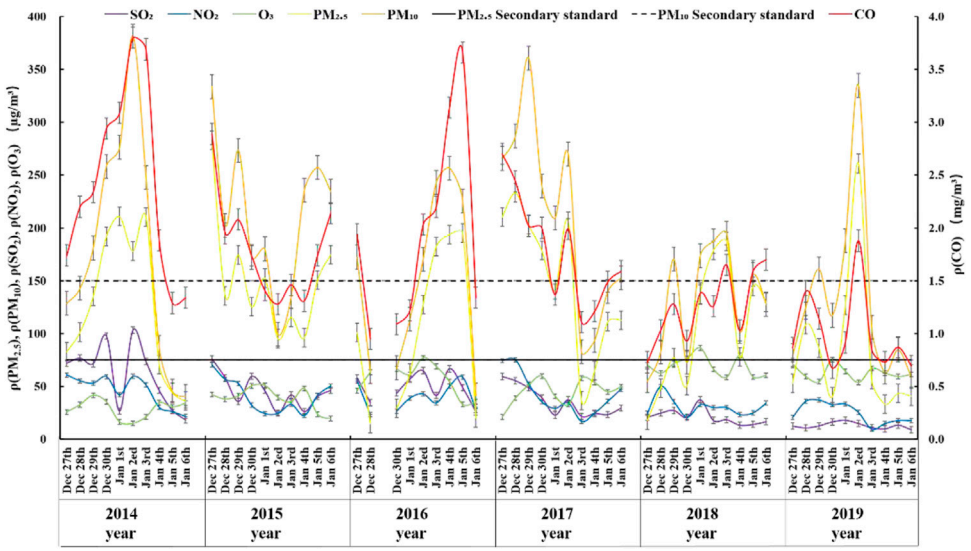

FIGURE 4 | Daily trend of average concentration of main pollutants in Zhengzhou during the Spring Festival from 2014 to 2019.

January, and the second peak of PM_{10} (257.21 μg/m³) occurred on the 5th January.

The average concentrations of SO_2 and NO_2 decreased during the Spring Festival from 2014 to 2015. In 2014, the average concentration of SO_2 and NO_2 were 61.36 and 45.96 μg/m³, respectively; whilst in 2015, they were 45.55 and 40.85 μg/m³, respectively. Secondly, from a local point of view, the concentrations of SO_2 and NO_2 in 2014 reached their respective first troughs of 26.71 and 42.21 μg/m³ on the 1st January, and troughed again on the 6th January at 18.38 and 21.63 μg/m³, respectively. In 2015, the troughs for SO_2 occurred on the 2nd January, whilst that of NO_2 was still on the 1st January.

Before the prohibition policy came into effect, the average concentration of CO decreased during the Spring Festivals of 2014 and 2015, whilst that of O_3 increased. The average concentrations in 2014 and 2015 of CO are 2.43 mg/m³, 1.80 mg/m³ and of O_3 are 28.75 and 38.90 μg/m³, respectively. The CO concentration first increased slowly, reaching a peak of 3.69 mg/m³ on the 3rd January in 2014, then decreased rapidly to its lowest value on the 6th January. CO concentrations showed a general downward trend, which troughed on the 2nd January in 2015 at 1.28 mg/m³ and again on the 4th January at 1.31 mg/m³. In 2014, the O_3 concentration peaked on the 29th December and on the 1st January, and in 2015, it peaked mainly on the 1st and 4th January. The high concentrations of pollutants mainly occur on the 1st and 2nd January, and also on the 5th and 6th January, which also confirms that New Year's Eve, the 1st and 5th January (commonly known as the fifth day break) are the peak periods for setting off fireworks during the Spring Festival (Pang et al., 2020).

4.2.2 Variation Characteristics of Pollutant Concentrations During the Initial Prohibition Period (2016–2017)

As shown in **Figure 3** the average concentrations of $PM_{2.5}$ and PM_{10} showed an upward trend from 2016 to 2017. In 2016, the average concentration of $PM_{2.5}$ and PM_{10} were 102.98 and 150.52 μg/m³, respectively, and in 2017, they were 149.88 and 210.20 μg/m³, respectively. Compared with 2015, the average concentrations of $PM_{2.5}$ and PM_{10} decreased by 31.50% and 29.11%, respectively. As shown in **Figure 4**, the average concentrations of $PM_{2.5}$ and PM_{10} in 2016 (the first year of prohibition policy) troughed at 14.67, 63.79 μg/m³, respectively on 28 December and troughed again on the 6th January. The first trough in 2017 is on the 1st January, and the second trough occurred on the 3rd January.

The average concentrations of SO_2 and NO_2 during the Spring Festival before the prohibition policy came into effect in 2016 and 2017 show a slight upward trend. In 2016, the average concentrations of SO_2 and NO_2 were 49.08, 39.70 μg/m³, respectively, and in 2017, they were 36.22 and 42.61 μg/m³, respectively. The trend of SO_2 and NO_2 changes in 2016 are similar, troughing on the 28th December, and on the 3rd and 6th January. In 2017, the trend of SO_2 and NO_2 is similar, troughing on the 1st and the 3rd January.

The average concentrations of CO decreased during the Spring Festival from 2016 to 2017, while O_3 increased. The average concentrations of CO in 2016 and 2017 are 1.95 and 1.79 mg/m³, respectively, whilst the average concentrations of O_3 are 56.22 and 45.02 μg/m³, respectively. In 2016 (the first year of the prohibition policy), the CO concentrations troughed at0.95 mg/m³ on the 28th December and at 1.34 mg/m³ on the 6th January, whilst in 2017, the CO concentrations troughed at 1.37 mg/m³ and 1.11 mg/m³ on the 1st and 3rd January. In 2016, the O_3 concentrations peaked on the 2nd January at 76.92 μg/m³, and in 2017, it peaked on Spring Festival's Eve at 59.75 μg/m³ and on the 3rd January at 57.67 μg/m³.

4.2.3 Variation Characteristics of Pollutant Concentrations After Expansion of the Prohibition Policy (2018–2019)

As shown in **Figure 3**, after the implementation of the expanded prohibition policy, the average concentrations of $PM_{2.5}$ and PM_{10} in Zhengzhou during the Spring Festival showed a slight downward trend. In 2018, the average concentrations of $PM_{2.5}$ and PM_{10} were 104.94 and 132.34 μg/m³, respectively, and in 2019, they were 85.01 and 131.88 μg/m³, respectively. As shown in **Figure 4**, from a local point of view, in 2018 (scope of prohibition policy expanded) the first peaks of $PM_{2.5}$ and PM_{10} occurred on the 29 December at 77.04 and 170.67 μg/m³, respectively; whilst the second peak occurred on the 3rd January at 187.29 and 195.08 μg/m³, respectively. However, in 2019, $PM_{2.5}$ and PM_{10} concentrations reach their respective peaks of 260.96 and 334.83 μg/m³ after the 2nd January, and they decrease rapidly, from the 3rd to the 6th January when they become lower than the national secondary atmospheric standard.

The average concentrations of SO_2 and NO_2 during the Spring Festivals of 2018 and 2019 show a slight downward trend. The average concentrations of SO_2 and NO_2 in 2018 are 21.13 and 30.65 μg/m³, respectively, and in 2019 are 12.90 and 24.53 μg/m³, respectively. The trend of SO_2 and NO_2 changes is similar. In 2018, SO_2 peaked on the 29th December, the first day of January and then again on the sixth day of January; whilst NO_2 peaked on the 28th December, the first and sixth days of January. In 2019, SO_2 peaked on the first and fifth days of January, and NO_2 peaked on the 29th December and 5th January.

The average concentrations of CO and O_3 during the Spring Festivals from 2018 to 2019 show a slight downward trend. The average concentrations of CO in 2018 and 2019 are 1.26 mg/m³ and 1.00 mg/m³, respectively; whilst the average concentrations of O_3 in 2018 and 2019 are 69.10 and 62.83 μg/m³, respectively. In 2018, the CO concentration reached its first trough of 0.93 mg/m³ on New Year's Eve, its second trough of 1.03 mg/m³ on the 4th January, whereas in 2019, it reached its first trough of 0.68 mg/m³ on Spring Festival's Eve, and its second trough of 0.70 mg/m³ on the 6th January. In 2018, O_3 concentrations reached troughs of 58.58, 60.67 μg/m³ on the 3rd and 6th January. Whereas, in 2019, it reached troughs of 54.33 μg/m³ on the 29th December and 2nd January.

4.3 Impact of the Prohibition Policy on Hourly Variation Characteristics

The hourly variations in the average concentrations of the major pollutants in Zhengzhou from New Year's Eve to the 1st January

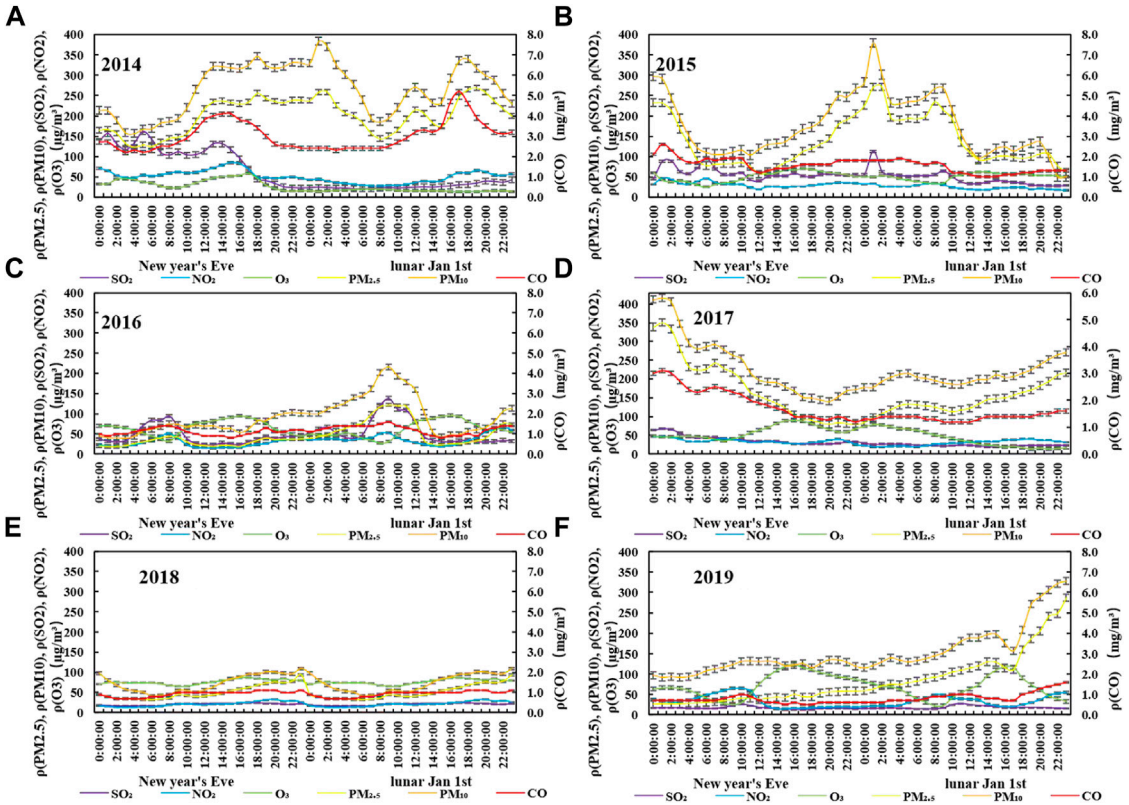

FIGURE 5 | Hourly variation of the average concentration of main pollutants from New Year's Eve to the 1st January in 2014–2019.

in 2014 and 2015 are shown in **Figures 5A,B**, respectively. The concentrations of $PM_{2.5}$ and PM_{10} on New Year's Eve in 2014 are initially at relatively low levels but from 03:00–09:00 their respective concentrations exceed 200 μg/m³ and 300 μg/m³, and between 0:00–01:00 on the 1st January, they reached their respective peaks of 259 and 384 μg/m³. Between 02:00–05:00, the concentrations of $PM_{2.5}$ and PM_{10} began to decline. However, at 06:00 the concentration of PM_{10} was still above 240 μg/m³ but by 18:00 it peaked again at 340 μg/m³. An hour later at 19:00, $PM_{2.5}$ peaked again at 269 μg/m³.

In 2015, between 05:00–17:00 on New Year's Eve, the concentrations of $PM_{2.5}$ and PM_{10} were at low levels. Compared with the same period of the Spring Festival in 2014, the rising speed of pollutant concentrations are slightly delayed, and the time to reach their peaks lagged slightly. The $PM_{2.5}$ concentration exceeded 200 μg/m³ at 23:00 on New Year's Eve but at 01:00 on the 1st January it peaked at 271 μg/m³. At the same time, the PM_{10} concentration also peaked at 380 μg/m³, exceeding 300 μg/m³ for the first time. After 01:00 the $PM_{2.5}$ and PM_{10} concentrations rapidly decreased until about 12:00 when their concentrations remained at relatively low levels. In addition, in 2014 and 2015, the timings of the $PM_{2.5}$ and PM_{10} concentration peaks are in good agreement with the traditional peak period for setting off fireworks, and the response results are obvious.

The firework prohibition policy was implemented for the first time, on the 1st January 2016 in Zhengzhou City as well as in five districts, four development zones and built-up districts of counties (cities) in the wider Zhengzhou region. In 2016, the air quality of New Year's Eve was in the two grades of excellent and good. As can be seen in **Figure 5C**, the concentrations of $PM_{2.5}$, PM_{10}, SO_2, NO_2 and CO peaked at 09:00 on the 1st January with respective concentrations of 122, 216, 138, and 52 μg/m³ and 1.6 mg/m³; these peaks are significantly delayed compared with the peak timings of pollutants in 2014–2015 prior to the implementation of the prohibition policy covering the Spring Festival, The results are consistent in that, after the implementation of the policy the peak value of pollutants decreased (Zhang et al., 2020). The concentration of O_3 peaked at 14:00–18:00 on the 1st January, while other pollutants troughed at this time, an observation that is mainly attributed to a series of photochemical reactions involving oxygen, nitrogen oxides and volatile organic compounds in the air under the action of natural light. Compared with the same period in 2014, the respective pollutant concentration decreased by 52.90%, 43.75%, 11.54%, 38.82%, 69.23% and 53.45%; and compared with the same period in 2015, the respective pollutant concentrations decreased by 54.98%, 43.16%, 22.12%, 10.64%, 38.46% and 65.71%. This essentially shows the net effect of the prohibition policy during the Spring Festival in Zhengzhou, the

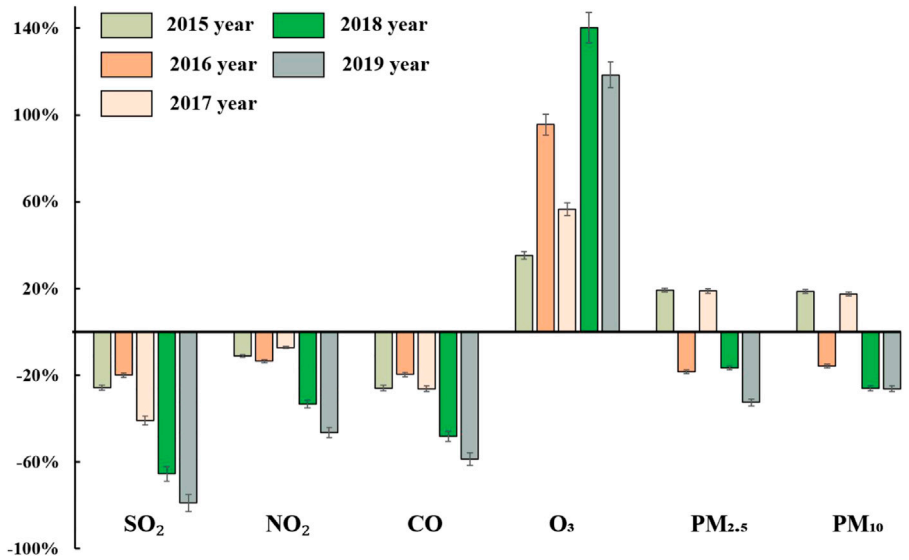

FIGURE 6 | average concentration changes of these pollutants from 2015 to 2019 compared to those during Spring Festival periods 2014.

concentration of various pollutants has decreased significantly, and the air quality has been improved significantly.

The change characteristics of pollutants concentrations in 2017 are quite different from those in 2014–2016 (**Figure 5D**). On New Year's Eve, from 00:00–03:00, the concentration of each pollutant is at a high level. On New Year's Eve, from 03:00–12:00 and on the 1st January, from 17:00–23:00, the concentration of each pollutant is still at a high level, while from 13:00 to 16:00 on the 1st January, the concentration of each pollutant became relatively low; From 23:00 on New Year's Eve to 02:00 on the 1st January, fireworks were set off intensively, but the concentration of pollutants in 2017 was not high. This shows that the policy has played a role in restraining the traditional high concentration stage of pollutants in 2017. It may also be that some residents illegally set off fireworks and firecrackers but deliberately avoided do so in the peak period.

On New Year's Eve and the 1st January in 2018, as can be seen in **Figure 5E**, the concentrations of pollutants were generally low. $PM_{2.5}$ and PM_{10} took the lead in reaching respective troughs of 32 and 41 μg/m³ at 06:00 on New Year's Eve, both of which exceeded the national level II standard. After that, the concentrations gradually increased, reaching respective peaks of 93 and 109 μg/m³ at 23:00. Compared with the same period in 2014 (before the prohibition policy), their respective concentrations decreased by 61.09% and 67.07%. After that, they only reached troughs at 06:00 on the 1st January, and then began to rise slowly, reaching respective peaks of 93 μg/m³and 109 μg/m³ at 23:00, which is a respective decrease of 124 μg/m³ and 162 μg/m³ compared with the same period in 2017, showing a very large reduction ratio.

Concentrations of $PM_{2.5}$ and PM_{10} on New Year's Eve 2019 are relatively low and do not exceed the national secondary air quality standard (**Figure 5F**). However, with the arrival of the 1st January, the concentrations of pollutants gradually increased, and the increasing range became larger and larger. The first peaks appeared between 14:00–15:00 on the 1st January, whilst the second peaks for $PM_{2.5}$ and PM_{10} of 287 μg/m³and 328 μg/m³, respectively occurred at 23:00, and are 54.70% and 39.63% higher than their respective first peaks. In addition, the changes of other gas pollutants concentrations are not obvious.

5 DISCUSSION

In order to further explore the relationship between the release of fireworks and the concentration of various pollutants, the average concentration of various pollutants during the Spring Festival from 2015 to 2019 was compared with that of 2014 and found in **Figure 6**, the implementation of the ban on combustion has the most significant impact on $PM_{2.5}$ and PM_{10} (Lorenzo et al., 2021; ten Brink et al., 2019; Tian et al., 2014). In 2015, the concentrations of $PM_{2.5}$ and PM_{10} were increased by 19.15 and 18.64%, respectively, compared with 2014. In 2016, the first year of the ban on combustion, the concentrations of $PM_{2.5}$ and PM_{10} decreased by 18.38% and 15.90%, respectively, compared with 2014. Compared with 2014, the increase in 2017 was 18.78% and 17.45%, respectively, which was caused by the decline in the implementation of the ban on combustion policy and the intensity of the ban. In 2018, with the further expansion of the scope of the ban and the strengthening of the ban, the concentrations of $PM_{2.5}$ and PM_{10} gradually decreased from 2018 to 2019, and dropped to the lowest in 2019, decreasing by 32.63% and 26.31%, respectively. The implementation of the non-combustion policy has little effect on the reduction of SO_2, NO_2 and CO concentrations, that is, fireworks and firecrackers are not the main cause of their pollution during the Spring Festival, but are determined by the types of pollutants produced by the discharge. With the implementation of the combustion ban policy, the pollutant

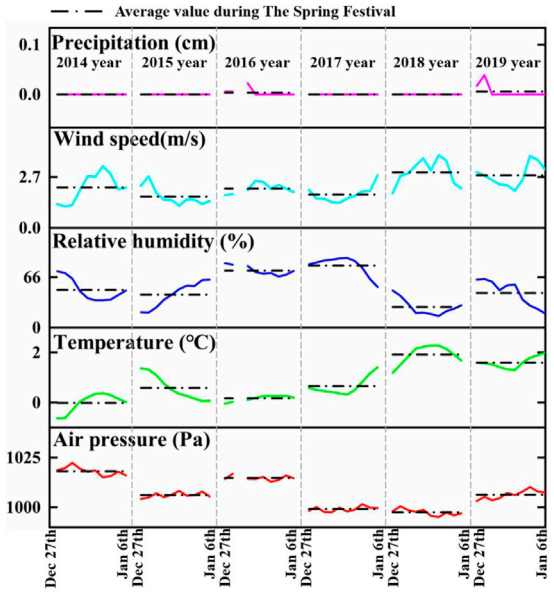

FIGURE 7 | Various meteorological elements change trend of Zhengzhou during Spring Festival half month from 2014 to 2019.

concentration from 2015 to 2019 showed a downward trend year by year, from 61.36, 45.96, and 2.43 mg/m^3 in 2014–2019, reaching a minimum value of 12.90, 24.53 and 1.00, respectively. When the combustion ban policy was initially implemented in 2016 and further strengthened in 2018, there was no significant trend change in SO_2, NO_2 and CO concentrations. The implementation of the ban on combustion has no effect on the change of O_3 concentration. From 2015 to 2019, the O_3 concentration increased significantly compared with 2014.

In order to further analyze the phenomenon of the sudden increase of pollutant concentrations during the Spring Festival, the meteorological element data during the Spring Festival from 2014 to 2019 were used to analyze the fluctuation trend. In **Figure 7**, the inter-annual variation of precipitation and air pressure during the Spring Festival from 2014 to 2019 was not obvious. Only a small amount of precipitation occurred on The New Year's Eve in 2016 and on the 28th and 29th of the first month of 2019, and the air pressure was mainly fluctuation at 995–1022 Pa. Among them, the air pressure only fluctuated between 998 and 1002 Pa from 2017 to 2018, with the smallest variation. The wind speed, relative humidity and temperature are slightly larger than those of precipitation and air pressure. The wind speed is similar from 2014 to 2017, and the annual average wind speed fluctuates between 1.7 and 2.1 m/s during the Spring Festival. The wind speed is similar from 2018 to 2019, and the average wind speed varies between 2.8 and 2.9 m/s during the Spring Festival. The overall relative humidity changed slightly. The relative humidity was the lowest at 27% during the Spring Festival in 2018. The average relative humidity during the Spring Festival from 2016 to 2017 was similar, at 75% and 81%, respectively. The relative humidity in 2014, 2015 and 2019 was relatively concentrated, respectively. 50%, 43%, 46%. The changes in temperature and wind speed are roughly similar. The temperatures in 2018 and 2019 are similar and higher than those in other years. The average temperature during the Spring Festival is 1.9 and 1.6°C, respectively, and the temperature fluctuates from −0.6 to 1.4°C from 2014 to 2017.

6 CONCLUSION

Based on air pollution data from 2014 to 2019, this study analyzed the characteristics of concentration changes of various air pollutants during the Spring Festival in Zhengzhou City for six consecutive years, to investigate the impact of the fireworks and firecracker prohibition policy, that came into effect in 2016, on the air environmental quality. The conclusions of the study are as follows:

Banning fireworks and firecrackers significantly improved Zhengzhou's air quality. There were small fluctuations in precipitation, air pressure, wind speed, temperature and relative humidity during the Spring Festival from 2014 to 2019. The AQI (143) of the Spring Festival in Zhengzhou in 2016 (the first year of the ban) was significantly better than that in 2014 (164) and 2015 (194). With the further implementation of the embargo policy, the air quality in 2018 and 2019 showed obvious improvements, decreasing to 141 and 119, respectively. The turning point for air quality improvement came in 2016, which coincided with the initial implementation of the policy. At the same time, the ban has effectively slowed down the sudden increase in pollutant concentrations from New Year's Eve to the first day of the first lunar month during the traditional heavy pollution period, showing an obvious "peak shaving" effect. In 2014, the concentrations of $PM_{2.5}$ and PM_{10} reached their first peaks at 1:00 a.m. on the first day of the new year, at 259 and 384 g/m^3, respectively. In 2015, the peaks were also reached at 1:00 on the first day of the first lunar month, at 271 and 380 g/m^3, respectively. During the same period, the $PM_{2.5}$ and PM_{10} concentrations were 44 and 100 μg/m^3, respectively in 2016, and 40 and 80 μg/m^3 in 2018. In addition, the implementation of the ban on combustion has the most obvious impact on $PM_{2.5}$ and PM_{10}. During the Spring Festival of 2015, which was not banned from burning, compared with 2014, the concentrations of $PM_{2.5}$ and PM_{10} increased by 19.15% and 18.64%, respectively. In 2016, they decreased by 18.38% and 15.90%, respectively, compared with 2014. In 2018, the concentrations of PM2.5 and PM10 decreased by 16.83% and 26.05%, respectively, compared with 2014.

DATA AVAILABILITY STATEMENT

The raw data supporting the conclusion of this article will be made available by the authors, without undue reservation.

AUTHOR CONTRIBUTIONS

DL: data curation, methodology, software, formal analysis, and writing–original draft. WL: methodology, investigation, and data

curation. JP: resources. QM: writing–review and editing and supervision.

FUNDING

This work was funded by National Natural Science Foundation of China (42105071), China Postdoctoral Science Foundation (2019M652520) and Program for Innovative Talents of Zhongyuan Postdoctoral.

ACKNOWLEDGMENTS

We are grateful to Dr John Turnbull for helping to improve the manuscript with comments on a draft of the paper.

REFERENCES

Doherty, R. M., Heal, M. R., and O'Connor, F. M. (2017). Climate Change Impacts on Human Health over Europe through its Effect on Air Quality. *Environ. Health* 16, 118. doi:10.1186/s12940-017-0325-2

Ge, B., Wang, Z., Lin, W., Xu, X., Li, J., Ji, D., et al. (2018). Air Pollution over the North China Plain and its Implication of Regional Transport: A New Sight from the Observed Evidences. *Environ. Pollut.* 234, 29–38. doi:10.1016/j.envpol.2017.10.084

Greven, F. E., Vonk, J. M., Fischer, P., Duijm, F., Vink, N. M., and Brunekreef, B. (2019). Air Pollution during New Year's Fireworks and Daily Mortality in the Netherlands. *Sci. Rep.* 9, 5735. doi:10.1038/s41598-019-42080-6

Guo, M. M., Jiang, N., Wang, S. B., Duan, S. G., and Zhang, R. Q. (2019). Analysis of Air Pollution Characteristics and Meteorological Conditions in Zhengzhou from 2014 to 2017. *Huan Jing Ke Xue* 40, 3856–3867. doi:10.13227/j.hjkx.201901118

Hamad, S., Green, D., and Heo, J. (2015). Evaluation of Health Risk Associated with Fireworks Activity at Central London. *Air Qual. Atmos. Health* 9, 735–741. doi:10.1007/s11869-015-0384-x

Hanaoka, T., and Masui, T. (2019). Exploring Effective Short-Lived Climate Pollutant Mitigation Scenarios by Considering Synergies and Trade-Offs of Combinations of Air Pollutant Measures and Low Carbon Measures towards the Level of the 2 °C Target in Asia. *Environ. Pollut.* 261, 113650. doi:10.1016/j.envpol.2019.113650

Jing, H., Li, Y.-F., Zhao, J., Li, B., Sun, J., Chen, R., et al. (2014). Wide-range Particle Characterization and Elemental Concentration in Beijing Aerosol during the 2013 Spring Festival. *Environ. Pollut.* 192, 204–211. doi:10.1016/j.envpol.2014.06.003

Ji, D. Y., Cui, Y., Li, D. W., He, J., Wang, L. L., Zhang, H. L., et al. (2018). Characterization and source identification of fine particulate matter in urban Beijing during the 2015 Spring Festival. *Sci. Total Environ.* 628-629, 430–440. doi:10.1016/j.scitotenv.2018.01.304

Kumar, M., Singh, R. K., Murari, V., Singh, A. K., Singh, R. S., and Banerjee, T. (2016). Fireworks Induced Particle Pollution: A Spatio-Temporal Analysis. *Atmos. Res.* 180, 78–91. doi:10.1016/j.atmosres.2016.05.014

Lai, Y., and Brimblecombe, P. (2017). Regulatory Effects on Particulate Pollution in the Early Hours of Chinese New Year, 2015. *Environ. Monit. Assess.* 189, 467. doi:10.1007/s10661-017-6167-0

Li, J., Xu, T., Lu, X., Chen, H., Nizkorodov, S. A., Chen, J., et al. (2017). Online Single Particle Measurement of Fireworks Pollution during Chinese New Year in Nanning. *J. Environ. Sci.* 53, 184–195. doi:10.1016/j.jes.2016.04.021

Lin, S. Y., Ju, S. W., Lin, C. L., Hsu, W. H., Lin, C. C., Ting, I. W., et al. (2020). Air Pollutants and Subsequent Risk of Chronic Kidney Disease and End-Stage Renal Disease: A Population-Based Cohort Study. *Environ. Pollut.* 261, 114154–154. doi:10.1016/j.envpol.2020.114154

Lorenzo, G. R., Bañaga, P. A., Cambaliza, M. O., Cruz, M. T., Azadiaghdam, M., Arellano, A., et al. (2021). Measurement Report: Firework Impacts on Air Quality in Metro Manila, Philippines, during the 2019 New Year Revelry. *Atmos. Chem. Phys.* 21, 6155–6173. doi:10.5194/acp-21-6155-2021

Pang, N., Gao, J., Zhao, P., Wang, Y., Xu, Z., and Chai, F. (2020). Impact of fireworks control on air quality in four Northern Chinese cities during the Spring Festival. *Atmos. Environ.* 117958. doi:10.1016/j.atmosenv.2020.117958

Saha, U., Talukdar, S., Jana, S., and Maitra, A. (2014). Effects of Air Pollution on Meteorological Parameters during Deepawali Festival over an Indian Urban metropolis. *Atmos. Environ.* 98, 530–539. doi:10.1016/j.atmosenv.2014.09.032

Sahu, C., and Sahu, S. K. (2019). Ambient Air Quality and Air Pollution index of Sambalpur: a Major Town in Eastern India. *Int. J. Environ. Sci. Technol.* 16, 8217–8228. doi:10.1007/s13762-019-02383-7

Shakerkhatibi, M., Dianat, I., Asghari Jafarabadi, M., Azak, R., and Kousha, A. (2015). Air Pollution and Hospital Admissions for Cardiorespiratory Diseases in Iran: Artificial Neural Network versus Conditional Logistic Regression. *Int. J. Environ. Sci. Technol.* 12, 3433–3442. doi:10.1007/s13762-015-0884-0

Sharma, R., Kumar, R., Sharma, D. K., Son, L. H., Priyadarshini, I., Pham, B. T., et al. (2019). Inferring Air Pollution from Air Quality index by Different Geographical Areas: Case Study in India. *Air Qual. Atmos. Health* 12, 1347–1357. doi:10.1007/s11869-019-00749-x

ten Brink, H., Otjes, R., and Weijers, E. (2019). Extreme Levels and Chemistry of PM from the Consumer Fireworks in the Netherlands. *Atmos. Environ.* 212, 36–40. doi:10.1016/j.atmosenv.2019.04.046

Tian, Y. Z., Wang, J., Peng, X., Shi, G. L., and Feng, Y. C. (2014). Estimation of the Direct and Indirect Impacts of Fireworks on the Physicochemical Characteristics of Atmospheric PM10 and PM2.5. *Atmos. Chem. Phys.* 14, 9469–9479. doi:10.5194/acp-14-9469-2014

Todorović, M. N., Radenković, M. B., Rajšić, S. F., and Ignjatović, L. M. (2019). Evaluation of Mortality Attributed to Air Pollution in the Three Most Populated Cities in Serbia. *Int. J. Environ. Sci. Tech.* 16, 7059–7070. doi:10.1007/s13762-019-02384-6

Wang, Y., Zhuang, G., Xu, C., and An, Z. (2007). The Air Pollution Caused by the Burning of Fireworks during the Lantern Festival in Beijing. *Atmos. Environ.* 41, 417–431. doi:10.1016/j.atmosenv.2006.07.043

Wang, S. Y., and Xia, C. Y. (2018). *Henan Statistical yearbook[M]*, 978-7-5037-8537-5. Beijing: China Statistics Press, 7–8.

Wang, S. S., Yu, R. L., Shen, H. Z., Wang, S., Hu, Q. C., Cui, J. Y., et al. (2019). Chemical characteristics, sources, and formation mechanisms of PM2.5 before and during the Spring Festival in a coastal city in Southeast China. *Environ. Pollut.* 251, 442–452. doi:10.1016/j.envpol.2019.04.050

Wang, Y., Liu, C., Wang, Q., Qin, Q., Ren, H., and Cao, J. (2021). Impacts of Natural and Socioeconomic Factors on PM2.5 from 2014 to 2017. *J. Environ. Manage.* 284, 112071. doi:10.1016/j.jenvman.2021.112071

Wang, Y., Wu, R., Liu, L., Yuan, Y., Liu, C., Hang Ho, S. S., et al. (2022). Differential Health and Economic Impacts from the COVID-19 Lockdown between the Developed and Developing Countries: Perspective on Air Pollution. *Environ. Pollut.* 293, 118544. doi:10.1016/j.envpol.2021.118544

Wu, K., Duan, M., Liu, H., Zhou, Z., Deng, Y., Song, D., et al. (2018). Characterizing the Composition and Evolution of Firework-Related Components in Air Aerosols during the Spring Festival. *Environ. Geochem. Health* 40, 2761–2771. doi:10.1007/s10653-018-0141-9

Xie, Z., Li, Y., Qin, Y., and Zheng, Z. (2019). Optimal Allocation of Control Targets for PM2.5 Pollution in China's Beijing-Tianjin-Hebei Regions. *Pol. J. Environ. Stud.* 28, 3941–3949. doi:10.15244/pjoes/97358

Xu, Y., Liu, H., and Duan, Z. (2020). A Novel Hybrid Model for Multi-step Daily AQI Forecasting Driven by Air Pollution Big Data. *Air Qual. Atmos. Health* 13, 197–207. doi:10.1007/s11869-020-00795-w

Ye, C., Chen, R., and Chen, M. (2016). The Impacts of Chinese Nian Culture on Air Pollution. *J. Clean. Prod.* 112, 1740–1745. doi:10.1016/j.jclepro.2015.04.113

Zhang, X. C., Shen, H. F., Li, T. W., and Zhang, L. P. (2020). The Effects of Fireworks Discharge on Atmospheric PM2.5 Concentration in the Chinese Lunar New Year. *Int. J. Environ. Res. Public Health* 17(24). doi:10.3390/ijerph17249333

Zhang, X., Shen, H., and Li, T. (2016). "Effect Characteristics of Chinese New Year Fireworks/firecrackers on PM $_{2.5}$ Concentration at Large Space and Time Scales," in Proceeding of the 2016 4thInternational Workshop on Earth Observation and RemoteSensing Applications, Guangzhou, July 2016 (IEEE), 179–182.

Zhang, J., Yang, L., Chen, J., Mellouki, A., Jiang, P., Gao, Y., et al. (2017). Influence of Fireworks Displays on the Chemical Characteristics of PM2.5 in Rural and

Suburban Areas in Central and East China. *Sci. Total Environ.* 578, 476–484. doi:10.1016/j.scitotenv.2016.10.212

Zhao, S., Yu, Y., Yin, D., Liu, N., and He, J. (2014). Ambient Particulate Pollution during Chinese Spring Festival in Urban Lanzhou, Northwestern China. *Atmos. Pollut. Res.* 5, 335–343. doi:10.5094/apr.2014.039

Zhou, X., Santana Jiménez, Y., Pérez Rodríguez, J. V., and Hernández, J. M. (2019). Air Pollution and Tourism Demand: A Case Study of Beijing, China. *Int. J. Tourism Res.* 21, 747–757. doi:10.1002/jtr.2301

Conflict of Interest: The authors declare that the research was conducted in the absence of any commercial or financial relationships that could be construed as a potential conflict of interest.

Publisher's Note: All claims expressed in this article are solely those of the authors and do not necessarily represent those of their affiliated organizations, or those of the publisher, the editors and the reviewers. Any product that may be evaluated in this article, or claim that may be made by its manufacturer, is not guaranteed or endorsed by the publisher.

frontiers | Frontiers in Environmental Science

ORIGINAL RESEARCH
published: 30 May 2022
doi: 10.3389/fenvs.2022.907735

Chemical Compositions in Winter $PM_{2.5}$ in Changzhou of the Yangtze River Delta Region, China: Characteristics and Atmospheric Responses Along With the Different Pollution Levels

Zhuzi Zhao, Ning Sun, Wenlin Zhou, Shuaishuai Ma, Xudong Li, Malong Li, Xian Zhang, Shishi Tang and Zhaolian Ye**

School of Chemical and Environmental Engineering, Jiangsu University of Technology, Changzhou, China

OPEN ACCESS

Edited by:
Lang Liu,
Northwestern Polytechnical University, China

Reviewed by:
Cheng Hu,
Nanjing Forestry University, China
Jun He,
The University of Nottingham Ningbo, China

***Correspondence:**
Zhuzi Zhao
zhaozz@jsut.edu.cn
Zhaolian Ye
bess_ye@jstu.edu.cn

Specialty section:
This article was submitted to Atmosphere and Climate, a section of the journal Frontiers in Environmental Science

Received: *30 March 2022*
Accepted: *25 April 2022*
Published: *30 May 2022*

Citation:
Zhao Z, Sun N, Zhou W, Ma S, Li X, Li M, Zhang X, Tang S and Ye Z (2022) Chemical Compositions in Winter $PM_{2.5}$ in Changzhou of the Yangtze River Delta Region, China: Characteristics and Atmospheric Responses Along With the Different Pollution Levels. Front. Environ. Sci. 10:907735. doi: 10.3389/fenvs.2022.907735

Changzhou, a typical industrial city located in the center of the Yangtze River Delta (YRD) region, has experienced serious air pollution in winter. However, Changzhou still receives less attention compared with other big cities in YRD. In this study, a four-month $PM_{2.5}$ sampling campaign was conducted in Changzhou, China from 1 November 2019, to 1 February 2020. The period covers the entire wintertime and includes first week of the Level 1 response stage of the lockdown period due to the outbreak of COVID-19. The mean $PM_{2.5}$ concentrations were 67.9 ± 29.0 μg m^{-3}, ranging from 17.4 to 157.4 μg m^{-3}. Secondary inorganic ions were the most abundant species, accounting for 37 and 50% during the low and high $PM_{2.5}$ pollution periods, respectively. Nitrogen oxidation ratio (NOR) during the high PM concentration level period was twice the low PM concentration period whereas sulfur oxidation ratio (SOR) showed a less significant increase. This represents that nitrate formation is potentially the predominant factor controlling the occurrence of PM pollution. The analysis of NOR, SOR as functions of relative humidity (RH) and ozone (O_3) concentrations suggest that the sulfate formation was mainly through aqueous-phase reaction, while nitrate formation was driven by both photochemistry and heterogeneous reaction. And, excess ammonium could promote the formation of nitrate during the high PM period, indicating that ammonia gas played a critical role in regulating nitrate. Furthermore, a special period-Chinese New Year overlapping first week of COVID-19 lockdown period, offered a precious window to study the impact of human activity pattern changes on air pollution variation. During the special period, the average $PM_{2.5}$ mean concentration was 60.4 μg m^{-3}, which did not show in a low value as expected. The declines in nitrogen oxide (NOx) emissions led to rapid increases in O_3 and atmospheric oxidizing capacity, as well as sulfate formation. The chemical profiles and compositions obtained during different periods provide a scientific basis for establishing efficient atmospheric governance policies in the future.

Keywords: secondary formation, oxidation capacity, anthropogenic emission, different periods, $PM_{2.5}$

1 INTRODUCTION

As one of the most economically developed zones with high energy consumption in China, the Yangtze River Delta (YRD) region has experienced serious air pollution problems in recent years (Fu et al., 2013). The temporal distribution showed the highest $PM_{2.5}$ concentration is found in winter, heavily affected by prevailing northerly and westerly winds (Qian et al., 2021). Hence, in-depth investigation at typical heavily polluted cities in the YRD region in winter is critical, assisting the formulation of efficient regional pollution control strategies (Ye et al., 2019).

At the end of the year 2019, the tragic coronavirus disease (COVID-19) pandemic occurred. To combat the rapid dispersion of the virus, many national lockdown policies were implemented in China to keep social distance. Quarantine measures have effectively alleviated the spread of the epidemic, and simultaneously resulted in declines in anthropogenic emissions from industry and transportation, and import and export of goods (Chen H. et al., 2020). Such a shutdown serves as a natural experiment to evaluate air-quality responses to a marked emissions reduction, and also to assess the interplay between emission, atmospheric chemistry, and meteorological conditions (Le et al., 2020). For example, Li et al. (2020) found that the implemented lockdown policy caused approximately 80% and 20–40% emission reductions for the traffic and the industrial sectors, respectively, corresponding to a reduction of $>20\ \mu g\ m^{-3}$ $PM_{2.5}$ compared to that during the pre-lockdown period. However, despite primary emissions being significantly reduced during the lockdown period, the air quality in some megacities has not been improved as expected due to the complex responses in terms of aerosol chemistry, with the variations of precursors and meteorological conditions (Sun et al., 2020).

Changzhou, a typical industrial city located in the center of the YRD region, has suffered haze pollution, especially in wintertime (Ma et al., 2019; Ye et al., 2019). To reduce air pollution, the establishment of effective pollution control strategies is important. However, there are many challenges such as the requirement of accurate apportionment of predominant sources and distinguishing primary emissions or secondary formations (Huang et al., 2014). In this study, we present the major chemical compositions of $PM_{2.5}$ and the concentrations of gaseous pollutants in urban Changzhou from 1 November 2019 to 1 February 2020. The period covers the entire wintertime and includes the first week of the Level 1 response stage of the lockdown period. It should be noted that the Chinese New Year (abbreviated as CNY, also as known as the Spring Festival) overlapped with the Level I response period. The YRD region hosted the first level of response started on 24 January 2020. The government actively executed epidemic prevention actions and control steps to the cities, including the adoption of compulsory measures following the law that prohibit all large-scale mass activities (Li et al., 2020). During the Level 1 response period, the number of people accessed and vehicles passed by the public places decreased substantially, and there were large-scale stoppages or even closures for the industrial factories, construction sites, and catering enterprises (Li et al., 2020). Due to the strict lockdown policy in Changzhou starting on February 2nd, no more offline sampling could be continuously carried out. Even though this circumstance, the samples collected in the days before the complete city lockdown could still provide a precious window to study how the air quality responds to the quick decline of anthropogenic emissions in Changzhou.

As the above description, we studied the temporal characteristics of $PM_{2.5}$ and its chemical compositions, gaseous pollutants, and meteorological factors during the wintertime. In addition, we investigated the characteristics of chemical compositions during different periods as well as the responses to the lockdown policies. Furthermore, the influence factors to the concentrations of air pollutants were interpreted to demonstrate the relationships between the meteorological conditions, emissions of primary pollutants, secondary species formation, etc. Our findings could assist to understand the winter haze formation, the impacts of different pollutants abatement, and the development of effective control strategies in this typical industrial city.

2 EXPERIMENT AND METHOD

2.1 Site Description

Changzhou, is located in central-south Jiangsu Province, geographically in the center of the YRD region, China (**Figure 1**). The Beijing-Hangzhou Canal runs through the city. To the south of the city is Lake Taihu, the third-largest freshwater lake in China. Moreover, the Yangtze River lies to the north of Changzhou. Abundant water sources around the city supply plentiful moisture in the air, leading to a humid atmosphere in Changzhou throughout the year.

The sampling site locates in the western part of downtown Changzhou where situates on the rooftop of a four-story building inside the campus of the Jiangsu University of Technology (31.7°N, 119.9°E). It is approximately 10 m above ground level. The location represents a typical urban monitoring site, surrounded by school and residential areas with medium-scaled population and middle traffic volume. There were no major industrial or constructive activities nearby during the observation period.

2.2 Measurements

2.2.1 Ambient $PM_{2.5}$ Sampling and Chemical Analyses

Ambient daily $PM_{2.5}$ samples (from 10:00 to 09:50 next day local time) were collected on Ø47 mm quartz-fiber filters (Whatman Ltd., Maidstone, United Kingdom) using a mini-volume air sample (Mini_TAS, Arimetric, Oregon, United States) at a flow rate of ~5 $L\ min^{-1}$. Before sampling, all filters were pre-combusted at 900°C for 4 h to remove organic contaminants. A total of 92 $PM_{2.5}$ filter samples were collected from 1 November 2019, to 1 February 2020. No more sampling could be continuous beyond February 1st due to the strict lockdown policies

FIGURE 1 | Map of Jiangsu province (filled with blue in the left panel) and Changzhou (red dot in the red panel). The observation site photos were displayed in the bottom right panel. (Maps downloaded from the website http://bzdt.ch.mnr.gov.cn/index.html.).

conducted in Changzhou. Mass concentrations, carbonaceous fractions, major inorganic ions, and elements were measured with an electronic microbalance balance, DRI OCEC analyzer, DX-600 ion chromatography and Epsilon-5 PANalytical ED-XRF, repectively. The details of sampling and analyses could be found in supplementary.

2.2.2 Air Quality Data and Meteorological Data

Hourly concentrations of the six pollutants (including SO_2, NO_2, CO, O_3, $PM_{2.5,}$ and PM_{10}) were achieved from the website of the Ministry of Ecology and Environment of the People's Republic of China (http://datacenter.mep.gov.cn). In this study, the citywide hourly and daily concentrations of the target air pollutants were calculated by averaging the hourly and daily data from all monitoring sites.

Meteorological data in Changzhou were obtained from the China Meteorological Administration and used to interpret the influence on air pollution. The observations include 2-m temperature (T), 10-m wind speed (WS) and wind direction (WD), and sea level pressure (P) available every 3 h at 02:00, 05: 00, 08:00, 11:00, 14:00, 17:00, 20:00, and 23:00 LT, as well as 2-m RH (RH) available every hour.

2.3 Data Analysis

2.3.1 Secondary Organic Carbon Calculation

For secondary organic carbon (SOC) calculation, most studies estimated SOC using the EC-tracer method (Turpin and Huntzicker, 1995), which applies the following equation.

$$SOC = OC - EC \times (OC/EC)_{primary\ or\ minimum} \quad (1)$$

Here, we used Minimum R Squared (MRS) method for the $(OC/EC)_{primary}$ calculation according to Wu and Yu (2016). Briefly, this method derives $(OC/EC)_{primary}$ through calculating a hypothetical set of $(OC/EC)_{primary}$ and SOC followed by seeking the minimum of the coefficient of correlation (R^2) between SOC and EC. The hypothetical $(OC/EC)_{primary}$ that generates the minimum R^2 (SOC, EC) then represents the actual $(OC/EC)_{primary}$ ratio if variations of EC and SOC are independent and $(OC/EC)_{primary}$ is relatively constant. In comparison, the MRS is identified as more accurate than the conventional subset percentile or minimum OCEC ratio approaches (Wu et al., 2016). Therefore, MRS was employed for the SOC calculation in this study.

2.3.2 Sulfur Oxidation Ratio and Nitrogen Oxidation Ratio Calculation

To assess the degrees of the secondary formation of SO_4^{2-} and NO_3^-, sulfur oxidation ratio (SOR) and nitrogen oxidation ratio (NOR) was calculated by the following equation.

$$SOR = \frac{n - SO_4^{2-}}{n - SO_4^{2-} + n - SO_2}; NOR = \frac{n - NO_3^-}{n - NO_3^- + n - NO_2} \quad (2)$$

where $n\text{-}SO_4^{2-}$ and $n\text{-}NO_3^-$ are the molar concentrations of SO_4^{2-} and NO_3^-, $n\text{-}SO_2$ and $n\text{-}NO_2$ are the molar concentrations of SO_2 and NO_2, respectively.

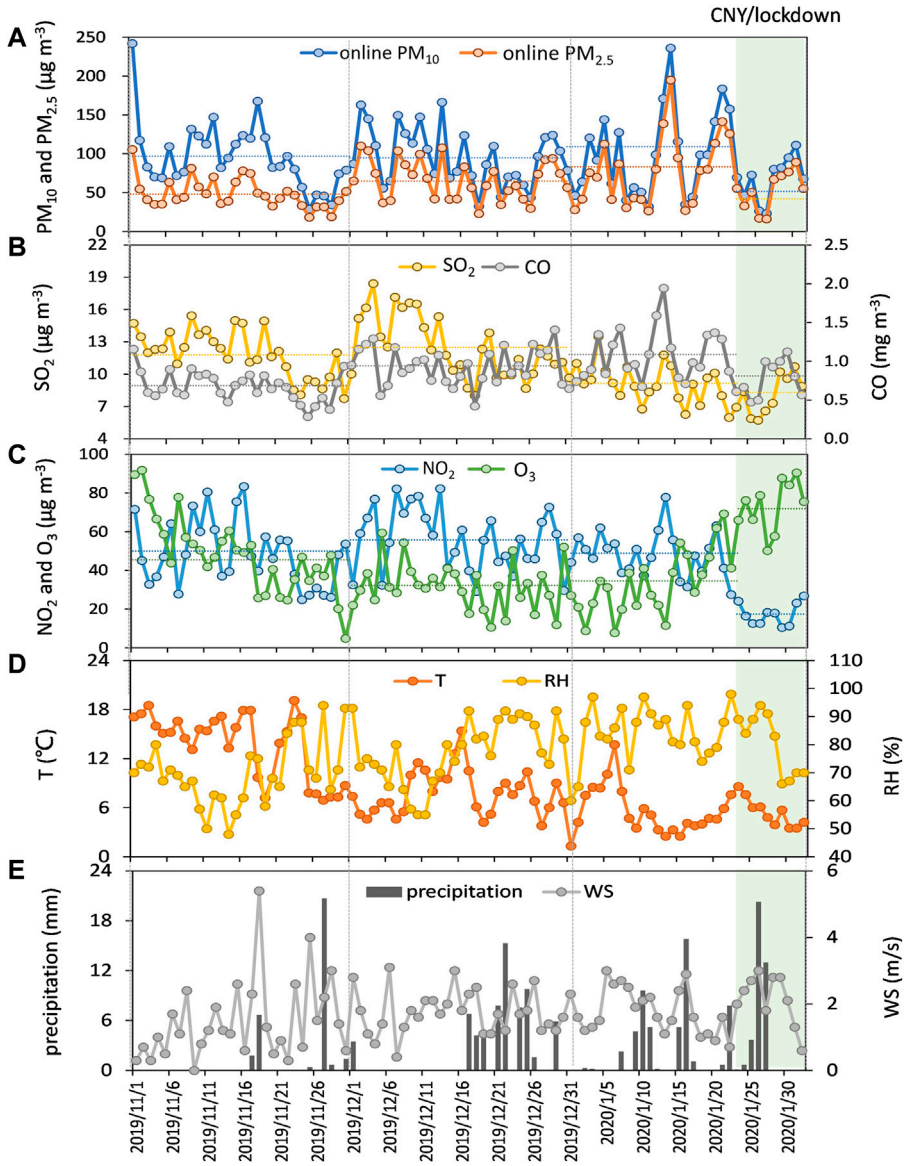

FIGURE 2 | Time series of **(A)** PM_{10} and $PM_{2.5}$ concentrations, **(B)** SO_2 and CO concentrations, **(C)** NO_2 and O_3 concentrations, **(D)** temperature and relative humidity, and **(E)** precipitation and wind speed from 1 November 2019 to 1 February 2020 (The dotted lines represent the mean concentrations for each pollutant).

3 RESULTS

3.1 Comparison of Online and Offline $PM_{2.5}$ Measurements

To cross-check the reliability of the offline sampling, data comparison between online monitoring and offline gravimetric analysis for $PM_{2.5}$ was performed, and the results are presented in Supplementary Figure S1. Notably, the online $PM_{2.5}$ data with 1 h resolution were integrated to calculate the average for 24 h, corresponding to the offline filter collection. Good linearity (r^2 = 0.97) was found between the online and offline approaches. Besides, the linear regression that passed through the origin of the plot yielded a slope of 1.053, indicating that the concentrations were relatively close. Therefore, the two approaches produced the $PM_{2.5}$ results in a good agreement.

3.2 General Characteristics of Atmospheric Pollutants

3.2.1. Online Measure for Six Criteria Pollutants

Figures 2A–C illustrate the time series of six criteria pollutants (i.e., $PM_{2.5}$, PM_{10}, SO_2, NO_2, CO, and O_3) and the meteorological parameters including temperature, relative humidity, wind speed, and precipitation during the sampling period. The CNY from

January 23rd to February 2nd was highlighted by the light green column. In general, the trends of PM_{10} and $PM_{2.5}$ are consistent with each other, showing peaks in mid-January. The $PM_{2.5}$ concentration levels ranged from 16.1 to 194.8 μg m^{-3}. An arithmetic mean of 61.6 ± 31.6 μg m^{-3} was found during the observation period, lower than the 24-h averaged Chinese $PM_{2.5}$ Grade II standard of 75 μg m^{-3} but greatly exceeded the Grade I standard of 35 μg m^{-3} (GB3095-2012). It should be noted that relatively low $PM_{2.5}$ concentrations were seen in November 2019 (48.7 ± 19.2 μg m^{-3}), and increased 1.3 and 1.4 fold in December and January, respectively. Compared to the $PM_{2.5}$, the PM_{10} concentration levels from November to January are relatively stable, showing the monthly averages of 90.1–96.1 μg m^{-3} (<10% difference). In another word, the monthly averaged $PM_{2.5}/PM_{10}$ ratios increased from 0.53 (November) to 0.69 (December) and 0.77 (January), indicating particles might be more influenced by crustal matters in November while the fine particles played an important role in January.

For the gaseous precursor species, the average concentrations of NO_2 and CO at the monitoring site were 47.6 μg m^{-3} and 0.9 mg m^{-3}, respectively, which are lower than the daily Grade I means of 50 μg m^{-3} and 4 mg m^{-3} for NO_2 and CO, respectively, established by the National Ambient Air Quality Standard (NAAQS) of China. Daily mean SO_2 concentrations ranged from 5.7 to 18.4 μg m^{-3}, much lower than the daily average SO_2 Grade I value (50 μg m^{-3}) from the NAAQS, indicating the implementation of the clean air policy since 2013 has substantially reduced the ambient SO_2 concentration in China (Zhang et al., 2019). The correlation of CO was well consistent with that of $PM_{2.5}$ (R^2 = 0.69, figure not shown), while the correlation between SO_2 and $PM_{2.5}$ was weak (R^2 = 0.11). CO is often used as a primary emission indicator due to its lifetime against oxidation by OH radicals (DeCarlo et al., 2010), thus the significant correlation between CO and $PM_{2.5}$ reflected the influence of primary combustion emissions during the sampling period.

Each species showed a different pattern during the sampling periods. As shown in **Figure 2**, in January (before Jan. 24th), major peaks of particulate matter coincided with high levels of CO and NO_2, NO_2 in November, and NO_2 and SO_2 in December. Overall, there was a doward trend of PM_{10}, $PM_{2.5}$, NO_2, SO_2 and CO in the CNY that overlapped the COVID-19 lockdown period. Compared with the first 3-week mean in January, NO_2 plummeted 65% due to the sharp decrease from the traffic sector, while SO_2 and CO reduced by 10% and 26%, respectively. The decreases of particulate matter are not obvious as expected (33% for online PM_{10} and 32% for online $PM_{2.5}$). These phenomena suggested the variations of dominant emission sources or formation mechanisms at the different phases. In contrast to the changes to these pollutants, O_3 increased by a factor of 2.13. The increase of O_3 could be attributed to insufficient NO for its uptake via the titration effect (Pei et al., 2020). More further discussions on the gaseous pollutants variations in different phrases were conducted in **Section 3.3.1**.

3.2.2 Offline $PM_{2.5}$ and Its Chemical Compositions

The time series of offline $PM_{2.5}$ and major chemical species (OC, EC, sulfate, nitrate, ammonium, Fe) are shown in **Figure 3**. The mean offline $PM_{2.5}$ concentrations were 67.9 ± 29.0 μg m^{-3}, ranging from 17.4 to 157.4 μg m^{-3}. Such levels were close to that observed in Changzhou in February 2017 (68.9 μg m^{-3}) (Ye et al., 2019) but significantly lower than that (126.9 ± 50.4 μg m^{-3}) in December 2015 to January 2016 in Changzhou (Ye et al., 2016). As mentioned in **Section 3.2.1**, the offline $PM_{2.5}$ mass also exhibited a well-defined trend, with higher mass concentrations observed during January and relatively low values in November.

Supplementary Table S1 summarizes the statistical data for the water-soluble ions, carbonaceous fractions concentrations in $PM_{2.5}$. For the carbonaceous fractions, the overall average concentrations of OC and EC were 12.4 ± 4.5 μg m^{-3} and 2.8 ± 1.8 μg m^{-3}, respectively. A moderate correlation between OC and EC was observed (r = 0.66, figure not shown). The ratios of OC to EC ranged from 1.8 to 13.6, with an average of 5.3 ± 2.1, suggesting complex sources for OC likely include both primary emission and also secondary formation (Ye et al., 2016). As shown in Supplementary Figure S2, the $(OC/EC)_{primary}$ was 2.62, 1.78, and 2.71 in November, December, and January, respectively. Correspondingly, the estimated SOC was 6.0 ± 4.5 μg m^{-3} during the sampling period, accounting for ~49.7% of OC. SOC/OC ratios were 45.4, 56.4, and 40.4 and 64.4% in November, December, January (before Jan. 24th) and the special period (Jan. 24th to Feb. 1st), respectively, demonstrating the importance of secondary aerosol formation, especially in December and the special period. A positive correlation between SOC/OC ratio and RH was observed in November and December (r = 0.44, figure not shown). That indicated that SOC formed at elevated levels of RH was likely part of water-soluble. However, in January, the SOC/OC ratio was not well correlated with RH. For the CNY overlapping lockdown period, high SOC/OC ratios could be explained by 1) the significant reduction of primary emissions leading to the relatively high contributions from secondary components; and 2) the enhancement of atmospheric oxidizing capacity and consequently strong photochemical processes due to the high levels of O_3.

The sum of the concentrations of the water-soluble ions was 39.2 ± 18.4 μg m^{-3}, accounting for ~57.8% of the total $PM_{2.5}$ mass. Among the water-soluble ions, Nitrate accounted for the largest fraction, with an average concentration of 15.8 ± 10.0 μg m^{-3}, followed by SO_4^{2-}, NH_4^+, Na^+, Ca^{2+} and Cl^-, with averages of 9.2 ± 4.5, 5.2 ± 4.0, 4.0 ± 0.6, 1.7 ± 0.5 and 1.6 ± 0.9 μg m^{-3}, respectively. The concentrations of other ions (i.e., K^+, Mg^{2+}, F^-, and NO_2^-) were relatively low. The fraction of the secondary inorganic compounds (sulfate, nitrate, and ammonium, namely as SNA) had the highest contributions (~72.9% of total ions). Ion mass balance calculations were used to evaluate the acid-base balance of aerosol. The average ratio of anions and cations (AC ratio) was 0.85 (averages of 0.77, 0.89, and 0.88 for November, December, and January,

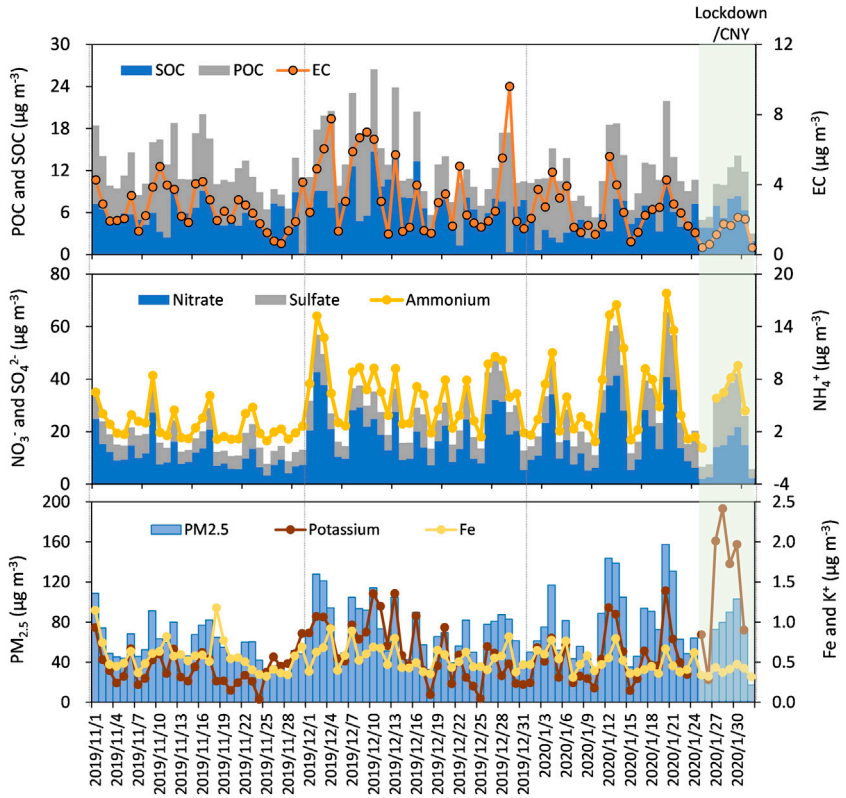

FIGURE 3 | Daily variation of major chemical compositions in $PM_{2.5}$ at the sampling site.

respectively), suggesting that Changzhou $PM_{2.5}$ was alkaline in the 2019 winter.

We further estimated the average aerosol acidity level ($[H^+]_{total}$) and *in-situ* acidity ($[H^+]_{in\text{-}situ}$) by E-AIM model, which described in Section 2.3.3 in supplement. The *in-situ* acidity of aerosols is an important parameter, because it could affect many acidity-dependent heterogeneous chemical processes (e.g., the oxidation of SO_2, the hydrolysis of N_2O_5) on the aerosol surfaces. On average, the aerosol acidity levels in Changzhou (164 nmol m^{-3}) were comparable with those in Shanghai (157 nmol m^{-3}) (Zhao et al., 2015), but higher than those in Lanzhou (59 nmol m^{-3}) and Guangzhou (90 nmol m^{-3}) (Pathak et al., 2011). And the *in-situ* acidity was 90.3 nmol m^{-3}, accounting for 55% of $[H^+]_{total}$. Previous study revealed that the $[H^+]_{in\text{-}situ}$ was related to water content. In high levels of aerosol water content conditions, H_2SO_4 and $H_SO_4^-$ molecules would release more $[H^+]$. But overall, it also dilutes the $[H^+]$ concentrations (moles per mole of aerosol water), making the aerosol less acidic (Pathak et al., 2004; Pathak et al., 2009). Thus, a large fraction of aerosol acidity releasing as *in-situ* acidity may related to the high levels of aerosol water content.

Among all species as shown in **Figure 3**, NH_4^+, NO_3^-, SO_4^{2-}, K^+, and EC showed low levels in November but some fluctuations from December to January. Comparatively, Fe remained stable (0.54 ± 0.17 μg m^{-3}) throughout the entire observation period. $PM_{2.5}$ showed three prominent peaks (December 1 ~ 4, January 12 ~14, and January 20 ~ 21, respectively), which coincided with relatively high loadings of secondary inorganic ions (NH_4^+, NO_3^- and SO_4^{2-}), OC, EC, and K^+, indicating both contributions of direct combustion emissions and secondary aerosol formation during these episodes. However, from December 7th to 13th, the high $PM_{2.5}$ mass co-varied with high loadings of POC, EC, and K^+, but moderate loading of secondary inorganic ions, suggesting the primary combustion emissions played a more important role in $PM_{2.5}$ pollution these days. In addition, the concentration K^+ substantially rose in the Chinese New Year within the lockdown period. More frequent fireworks occurred for the celebrations. Major oxidizers in the fireworks include KNO_3 or $KClO_4$, which are common constitutes used to generate green flames and are widely used as coloring agents and stabilizers (Zhang et al., 2017). Besides, $Sr(NO_3)_2$ can be used to generate red color fireworks, while Cu can produce blue flames and be used as a catalyzer (Kong et al., 2015). These elements are important fireworks constitutes, thus exhibited significant correlations with K^+ as shown in Supplementary Figure S3. Therefore, we concluded that K^+ was more influenced by the traditional fireworks rather than biomass burning during this period.

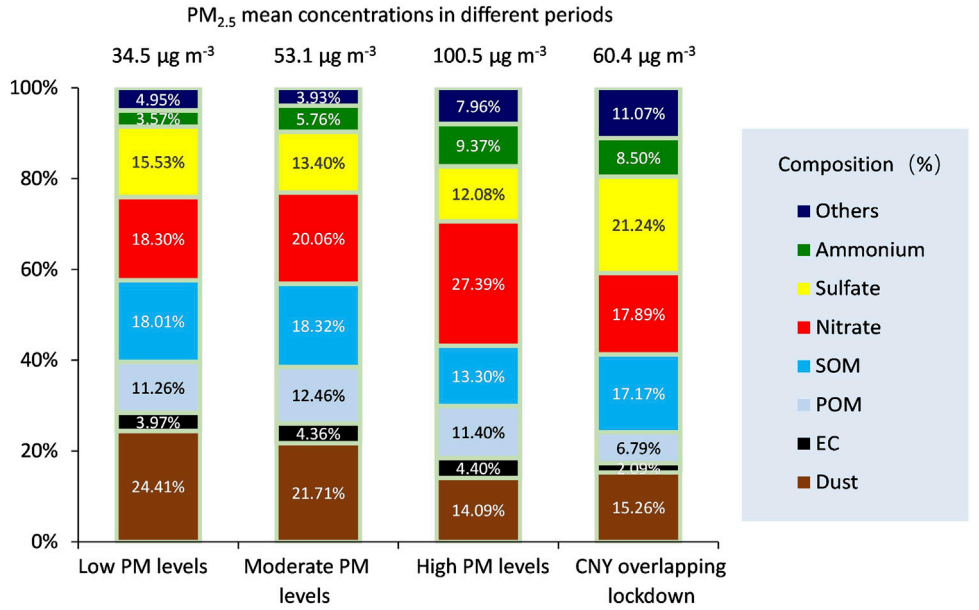

FIGURE 4 | Material balance during different PM concentration level periods. [The campaign was divided into three levels depending on the threshold values of the $PM_{2.5}$ concentrations as Low (≤35 μg m^{-3}), moderate (35–75 μg m^{-3}) and high (>75 μg m^{-3}) PM concentration levels. And the CNY overlapping lockdown period was separately listed.].

3.3 Characteristics of Chemical Compositions in Different Phases

The study was divided into three phases based on the $PM_{2.5}$ daily mass concentration thresholds established by the NAAQS as follows: low PM levels (clean) phase ($PM_{2.5} \leq 35\ \mu g\ m^{-3}$, 6 days), moderate PM levels phase ($35 < PM_{2.5} \leq 75\ \mu g\ m^{-3}$, 48 days) and high PM levels phase ($PM > 75\ \mu g\ m^{-3}$, polluted phase, 30 days). In addition, the local coronavirus broke out in Wuhan, China at the end of 2019 and was confirmed to be human-to-human transmission on 20 January 2020. Since then, several provincial administrative units in China have declared the highest level of public health emergency response and imposed national lockdown policies within a week (Pei et al., 2020). During the lockdown period, emissions from the traffic sector, industrial activities, construction sites, and eateries were markedly reduced (Pei et al., 2020). Therefore, the CNY covered lockdown period (9 days) was separately listed as the special changeover of anthropogenic emissions.

3.3.1 Variations of Gaseous Pollutants

For gaseous pollutants, the average concentrations of SO_2, NO_2, and CO were 12.4 μg m^{-3}, 62.1 μg m^{-3}, and 1.1 mg m^{-3} during the high PM levels phase, which were 1.5, 2.0, and 2.1 times higher than those of the clean phase, respectively. Among these, the increases of NO_2 and CO were more remarkable, while the variation of SO_2 was not obvious, indicating the importance of vehicle emissions on the polluted days. In contrast, O_3 declined from 43.4 μg m^{-3} during the clean phase to 36.9 μg m^{-3} during more polluted phases. This could be attributed to the higher mass concentration of particles that weaken the radiation, as a result of the concentration of photochemical oxidants decreased (Zhang et al., 2018). The gaseous pollutants showed different responses to the COVID-19 lockdown. As previous studies revealed, the COVID-19 lockdown indeed helped reduce NO_x levels with a substantial decrease in traffic volume and closure of small to middle sizes enterprises (Li et al., 2020; Pei et al., 2020). In Changzhou, the concentration of NO_2 plunged to 16.6 μg m^{-3} during the special period, even 50% lower than that during the low PM level phase. The concentration level of SO_2 is relatively steady (8.1 μg m^{-3}), comparable with that during the low PM level phase.

3.3.2 Material Balance of $PM_{2.5}$

The average chemical compositions of $PM_{2.5}$ during different phases are presented in **Figure 4**, grouping as, secondary inorganic aerosols (i.e., sulfate, nitrate, and ammonium), EC, primary organic matter (POM), secondary organic matter (SOM), and others. The dust was calculated by dividing the measured elemental Fe concentration by 4% based on its composition in the Asian dust and Chinese loess (Zhang et al., 2003). Most studies estimated OM by OC with the empirical conversion factors ranging from 1.4 to 2.2 shown in the literature (Turpin and Lim, 2001). In this study, OM was divided into POM and SOM to assess the relative contributions of primary or secondary OM to $PM_{2.5}$ during different phases. The POM concentrations were calculated as 1.2 times POC, while SOM concentrations were estimated as SOC multiplied by 1.8 because of the aerosol aging. The conversion factors were chosen based on the assumption that hydrocarbon-like organic aerosols were considered as the dominant aspect of the POM, while

oxygenated organic aerosols were a priority in SOM because of the aging process.

Overall, $PM_{2.5}$ mean concentrations were 34.5, 53.1, 100.5, and 60.4 $\mu g\,m^{-3}$ during the low, moderate, high PM level phases and the special period, respectively. The quantified compounds were reconstructed for ~95.0, 96.1, 92.0, and 88.9% of the measured $PM_{2.5}$ mass during the different periods. The chemical compositions showed no obvious differences (approximately ±10%) between the low PM and moderate PM concentration phases (**Figure 3**), suggesting the primary emissions and secondary formations have not altered greatly between the two phases. From the clean to polluted phases, the compositions of different components varied. For example, the dust in $PM_{2.5}$ decreased from 24.4 to 14.1%, while the fractions of ammonium and nitrate showed 2.6-fold and 1.5-fold increases, respectively. POM and EC had consistent contributions from the clean to the polluted phase indicating primary combustion emissions were steady. The proportion of SOM to $PM_{2.5}$ declined from 26.1% (low PM level phase) to 13.3% (high PM level phase). SOA aerosol is a product of photochemical reactions (Zheng et al., 2013) while O_3 is the crucial oxidant for the formation of SOA (Jimenez et al., 2009). Along the pollution periods, with the increase of particles, the concentration of photochemical oxidants decreased, and the photochemical reactions weakened, consequently, the concentration of SOM decreased.

Major compositions of $PM_{2.5}$ showed significantly different patterns during the CNY overlapping lockdown period. Firstly, under a low emission scenario with the quarantine policy, the concentrations of POM and EC dropped by almost half compared with those during other phases, accounting for 6.8 and 2.1% of $PM_{2.5}$ only. Secondly, the percentage of SOM to $PM_{2.5}$ was 17.2%, lower than that of the clean phase but higher than that of polluted phases. However, there was a considerable rise in the SOM/POM ratio, from 1.2 to 1.6 during different PM level phases to 2.5 during the special period, suggesting the important contribution of SOA while the anthropological activities were terminated. Lastly, the proportion of sulfate increased obviously and became dominant (21.2%), while the proportion of nitrate decreased noticeably.

4 DISCUSSIONS

Many factors influenced the concentration levels of air pollutants and the process of haze evolution, including meteorological conditions, emissions of primary pollutants, the conversion rate of secondary species, regional transport, etc. These factors will be discussed thoroughly in the following section.

4.1 Meteorological Influences

Meteorological conditions pose important effects on air quality. A previous study revealed that strong winds and precipitation would be effective in reducing air pollution (Liu et al., 2020). And, RH is generally regarded as one of the main factors facilitating the formation of secondary inorganic ions, which highly contributed to the episode events (Wu et al., 2019; Ye et al., 2019; Chen C. et al., 2020). A previous study conducted in Changzhou found that high $PM_{2.5}$ concentrations typically appeared at high RH and low WS (Ye et al., 2019). **Figures 1D,E** displayed the major meteorological parameters (temperature, RH, WS, and precipitation) during the sampling period. The geography of Changzhou (e.g., lakes and rivers) sustain the RH at high levels. The mean temperature, RH and WS were 8.9 ± 4.7°C, 76.9 ± 12.2% and 1.7 ± 0.9 $m\,s^{-1}$, respectively, demonstrating relatively high moisture and poor air diffusion. The averaged WS were 2.6, 1.7, 1.4, and 2.2 $m\,s^{-1}$ during the low, moderate, high PM concentration phases and the special period, respectively, demonstrating that relatively low WS favored the accumulation of atmospheric pollutants such as airborne particles. And the relatively low PM concentrations were observed on the rainy days due to the wet scavenging effect. The high humidity environment could serve as reaction media promoting the secondary inorganic ions formation. The impact of RH on the secondary species formations will be further discussed in Section 4.1.2.

In addition, the regional sources and transport of air pollutants affect the local air quality (Xu et al., 2016). The 72 h air mass back trajectories starting 500 m above ground level at 00:00 UTC were calculated using the Hybrid single-particle Lagrangian integrated trajectory (HYSPLIT 4) model developed by the National Oceanic and Atmospheric Administration (NOAA) Air Resource Laboratory. The calculated back trajectories were conducted by cluster analysis (Supplementary Figure S4) to obtain the main transport pathway of air masses. During the moderate PM concentration level phase (Supplementary Figure S4B), moist air mass trajectories were in cluster 3 (accounting for 46.2% of the total clusters) from the north, passing through highly industrialized and densely populated areas (i.e., Hebei and Shandong Province). Approximately 36.5% of air masses transport originated from the Yellow Sea and the East China Sea, which expectedly brought relatively clean air to Changzhou. The rapid air masses (cluster 1 and cluster 2, a sum of 17.3%) came from the northwest, sweeping across the northern region of Xingjiang Province and the northwest region of Inner Mongolia. With strong wind and declined temperatures, these factors consequently reduced the pollution in Changzhou to some extent. During the clean phase (Supplementary Figure S4A), it can be seen that nearly all air masses originated from Mongolia, passed through the Yellow Sea and the East China Sea with fast speed before reaching Changzhou. Comparatively, during the polluted phases (Supplementary Figure S4C), the air masses mainly came from local areas (Cluster 3, 36.4%), or the nearby provinces (cluster 4 from the southwest: 24.2%; cluster 1 from the northwest: 33.3%). These slow air masses represent the stable synoptic conditions these days, which limited the vertical and horizontal diffusions of pollutants, trapped the gas precursors and primary emission pollutants, and finally favored the secondary formation and the accumulation of atmospheric pollutants. Only 6.1% of clusters came from the north with relatively fast speed.

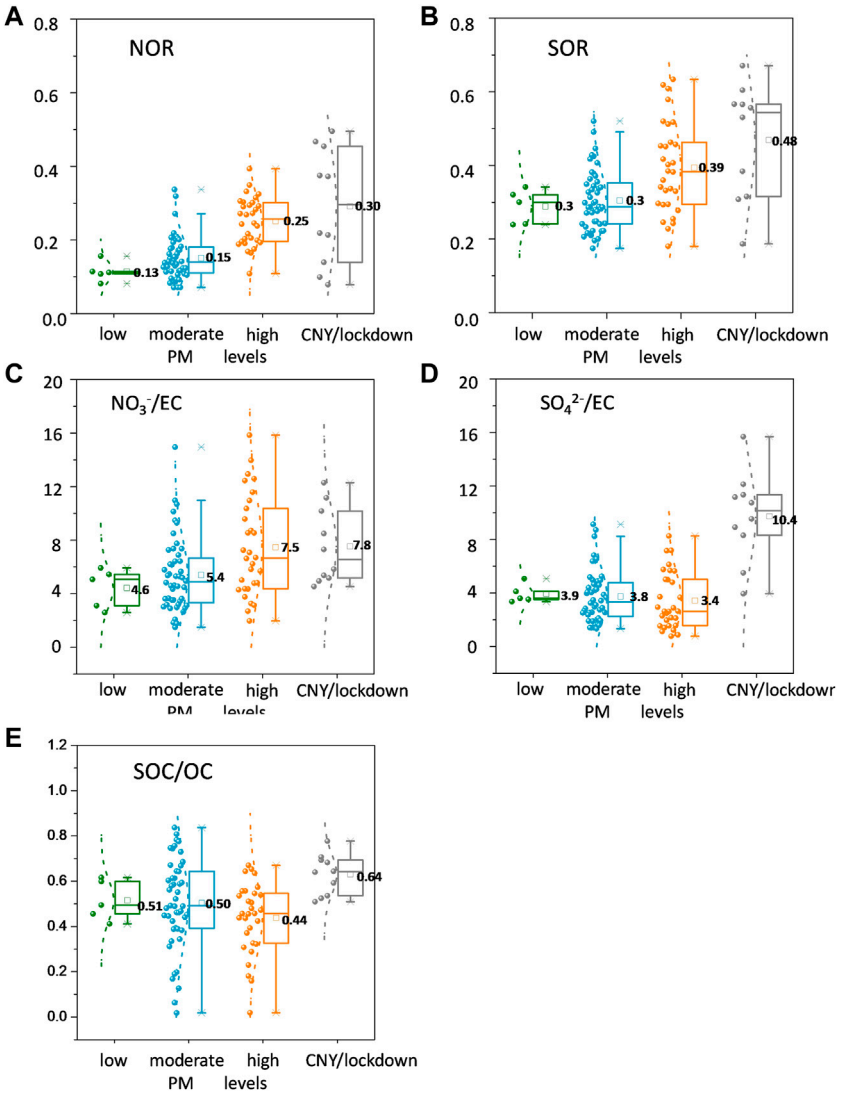

FIGURE 5 | Box and whisker plots of variation of **(A)** NOR, **(B)** SOR, **(C)** NO_3^-/EC, **(D)** SO_4^{2-}/EC and **(E)** SOC/OC in different phases. The mean (the small box), median (horizontal line), 25th and 75th percentiles (lower and upper box), and the 10th and 90th percentiles (lower and upper whiskers) are shown in the plots.

4.2 Conversion of Secondary Species

4.2.1 Characteristics of Secondary Formation Indicators

In general, direct emissions from the sources as well as reactions between primary pollutants in the atmosphere contribute to the generation of ambient PM (Chang et al., 2011). In **Section 3.3.2**, we found that the secondary inorganic ions drove the haze formation in Changzhou, consistent with the findings in the previous local studies (Li et al., 2017; Seo et al., 2017). Sulfate and nitrate are the major constituents of $PM_{2.5}$ which are mainly formed through atmospheric oxidation of SO_2 emitted mainly from coal burning, and NOx emitted from vehicle exhaust and power plants in urban areas, respectively (Huang et al., 2014; Ye et al., 2019). To evaluate the gas-to-particle partitioning and secondary conversion degree, NOR (nitrogen oxidation ratio) and SOR (sulfur oxidation ratio) were used the conversion degree of NO_2 and SO_2 (Xu et al., 2017; Tang et al., 2021). Literature reported that SOR and NOR less than 0.1 represent primary emissions, and greater than 0.1 represent the significant oxidation of primary pollutants (NO_2 and SO_2) (Zhang et al., 2013; Liu et al., 2020). The average NOR and SOR were 0.20 ± 0.10 and 0.35 ± 0.12 respectively, suggesting sulfate and nitrate mainly formed from the secondary transformation. As shown in **Figure 5**, the NOR during the high PM level period was twice that during first week in lockdown period, whereas SOR only showed a slight increase from 0.30 to 0.39, indicating the higher oxidation rate of NO_2 in more polluted airs. During the special period, NOR increased gently to 0.30 and SOR surged to 0.48. This could be explained by that SO_2 and NOx competed to react with OH radicals to form sulfate and nitrate, respectively, in the photochemical reaction system. During the special period, a substantial decrease in NOx emissions resulted in a large

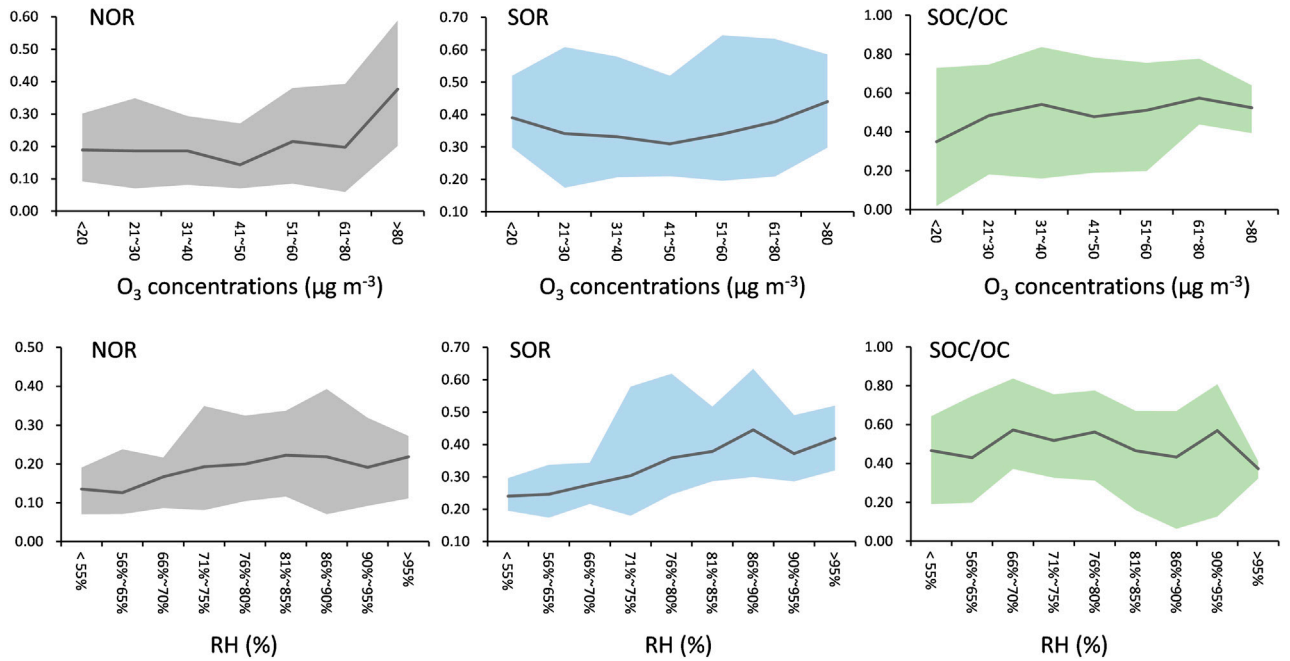

FIGURE 6 | Variations of species (NOR, SOR and SOC/OC) as functions of RH and O_3 concentrations. The solid lines represent the average values, and the shaded areas indicate the variation range.

increase of O_3 as well as the atmospheric oxidizing capacity (Chen H. et al., 2020; Chang et al., 2020). When NOx is reduced but the oxidation capacity is kept constant, SO_2 could participate more in photochemical reactions and form sulfate (Chen H. et al., 2020).

Besides, considering the variability of EC only controlled by emission intensity and atmospheric physical processes (such as the dilution/mixing effects at different boundary layer height), the EC-scaled concentrations of chemical species were used to isolate chemical processes from physical processes (Zhang et al., 2018). To assess the role of chemical outputs, the EC-scaled NO_3^- and SO_4^2 were calculated and shown in **Figures 5C,D**. The EC-scaled NO_3^- showed obvious differences from that of SO_4^{2-} during different periods. Along the low PM concentration to high PM concentration period, NO_3^-/EC ratio showed a rise from 4.6 to 7.5, while SO_4^{2-}/EC ratio reduced mildly from 3.9 to 3.4, illustrating the increasing chemical production of NO_3^- but constant chemical production of SO_4^{2-}. The phenomenon could be explained by the limited and low SO_2 levels in Changzhou. However, during the special period, NO_3^-/EC ratio remained constant, but SO_4^{2-}/EC ratio rose sharply to 10.4. Significantly reduction of NO_2 from the large decrease of vehicle emissions and the closure of small and middle-sized enterprises. Different mechanisms of sulfate and nitrate formation might be the major reason for their variations of EC-scaled concentrations. Here, the contributions of SOC to OC during different periods were also discussed. The trend of SOC/OC was close to that of SO_4^{2-}/EC, with a slight decrease from the clean (0.51) to polluted (0.44) periods, and a leap during the lockdown (0.64) period. The weakening of photochemical reactions caused by the aggravation of haze led to the reduction of SOA in $PM_{2.5}$ (Zhang et al., 2018).

4.2.2 Formation Mechanisms of Secondary Species

As discussed above, the secondary conversion of gaseous precursors contributed a lot to the pollution events. Nitrate and sulfate form chemically from the oxidation of SO_2 and NO_2 through two major pathways: 1) homogeneous gas-phase oxidation of SO_2 and NO_2 by OH radicals, and 2) heterogeneous reactions on the particle surfaces (Cheng et al., 2016; Tian et al., 2016; Chen X. et al., 2020). RH was generally regarded as one of the main factors facilitating the formation of haze through heterogonous reaction (Cheng et al., 2016), while O_3 was commonly regarded as an indicator of the atmospheric oxidation capacity or photochemical reaction (Ye et al., 2019; Chen H. et al., 2020).

We conducted further analysis of NOR, SOR, and SOC/OC as functions of RH and O_3 concentrations to explore the underlying mechanism. As shown in **Figure 6**, SOR and NOR showed a positive relationship with RH, reached the maximum at 86–90%, and then decreased when RH exceeded 90%. It is noted that SOC/OC oscillated with RH increased. This suggests the contributions of aqueous-phase reaction on both the sulfate and nitrate formations under humid conditions because the heterogeneous reaction positively correlated with high RH. In contrast, no obvious relationship was found between SOC formation and RH. In addition, the increasing trend of SOR was more pronounced than that of NOR, indicating more importance of

heterogeneous reactions to the secondary transformation of SO_4^{2-}. Previous studies suggested that high levels of NO_2 and transition metals promoted the conversion of SO_2 to SO_4^{2-} by aqueous-phase oxidation during winter haze rather than gas-phase oxidation (Sun et al., 2013; He et al., 2014; Ma et al., 2018). This could be ascribed with the weak photochemical activities resulting in insufficient production of oxidants (e.g., OH and H_2O_2 radicals) for gas-phase oxidation (Zheng et al., 2015). Those days with RH exceeded 90% were always associated with rainy, reversibly reducing the particulates concentrations efficiently, and thus led to the decreases of SOR and NOR.

It is found that SOC/OC was more sensitive when O_3 was in relatively low concentrations (ranged from <20 to 40 $\mu g\ m^{-3}$). It stayed at a stable level when O_3 concentration levels rose >40 $\mu g\ m^{-3}$. Comparatively, the NOR remained stable under a low O_3 environment and rose substantially when O_3 was higher than 40 $\mu g\ m^{-3}$, while the SOR did not show obvious dependence with the variation of O_3 concentrations. This suggests important contributions of photochemical reaction to SOC formation under relatively low O_3 conditions, and the nitrate formation was driven by both photochemistry reaction and heterogeneous reaction during our sampling campaign.

4.2.3 Important Role of Ammonium

Ammonia is an important alkaline gas in the atmosphere which could react with acidic compounds including H_2SO_4, HNO_3, and HCl to generate ammonium sulfate, ammonium nitrate, and ammonium chloride through gas phase and aqueous phase reactions (Zhao et al., 2015). As discussed in **Section 3.3.2**, from the clean to the polluted periods, the fractions of ammonium and nitrate increased from 18.3 to 27.4% and 3.57–9.37%, respectively (**Figure 4**), indicating that the co-increase of these two species had contributed to the aggravation of atmospheric pollution in Changzhou.

The formations of sulfate and nitrate were related to the existed amount of ammonium, namely, ammonia-rich (AR) or ammonia-poor (AP) conditions (Zhao et al., 2015), which estimated by ammonium to sulfate molar ratio (AR conditions: $[NH_4^+]/[SO_4^{2-}]$> 1.5; AP conditions: $[NH_4^+]/[SO_4^{2-}]$<1.5). It assumes that in AP conditions, all the NH_3 is used to neutralize H_2SO_4 formed NH_4HSO_4 and $(NH_4)_2SO_4$. Under AR conditions, the excess NH_4^+ could transfer HNO_3 to NH_4NO_3 (Li et al., 2013; Griffith et al., 2015). In Changzhou, the average molar ratio of ammonium to sulfate was 1.4 ± 0.7, suggesting that the aerosol environment was generally at AP condition. About 61.7% of the samples in Changzhou in winter were ammonia-poor, indicating sulfate and nitrate were not neutralized by ammonium completely. Hence, sulfate and nitrate might have other ways to be chemically formed such as the heterogeneous reactions with crustal and marine species in $PM_{2.5}$ (Li et al., 2013). Secondly, the comparisons among the different periods reveal that the $[NH_4^+]/[SO_4^{2-}]$ molar ratios were 0.6 ± 0.1, 1.1 ± 0.4, 2.1 ± 0.5, and 0.8 ± 0.4 during the low, moderate, high PM concentration levels, and the special periods, respectively. The higher value during the polluted periods represents that SO_4^{2-} and NO_3^- could be neutralized by NH_4^+ and particulate sulfate and nitrate could be formed by gas-phase reactions of acid precursors with NH_3. In addition, the *in-situ* acidity were 100.83 nmol m^{-3} (69.5% of the $[H^+]_{total}$), 90.68 nmol m^{-3} (60.4% of the $[H^+]_{total}$), 79.90 nmol m^{-3} (46.0% of the $[H^+]_{total}$) and 116.04 nmol m^{-3} (52.8% of the $[H^+]_{total}$) in low PM, moderate PM, high PM and the special period, respectively, as shown in Supplementary Figure S5. The lower concentrations $[H^+]_{total}$ and $[H^+]_{in\text{-}situ}$ obtaining in the polluted period indicated the important role of ammonium in neutralization in this period.

We further calculated the excess ammonium during the high PM concentration period using the below equation (Tian, et al., 2016).

$$[NH_4^+]_{excess} = ([NH_4^+]/[SO_4^{2-}] - 1.5) \times [SO_4^{2-}] \quad (3)$$

The concentration is of excess ammonium well correlated with the nitrate concentrations ($R^2 = 0.61$) as shown in Supplementary Figure S6. This indicates that the formation of nitrate was strongly associated with ammonium formation. Previous studies revealed that with the participation of ammonia during the daytime, NO_2 reacts with OH radicals to form nitric acid, which is efficiently converted into particulate NO_3^-. O_3 produced by NO_2 photolysis during the daytime is consumed by the nighttime oxidation of NO_2 to N_2O_5, which advances nitrate formation in the particle phase (Lu et al., 2019; Chen X. et al., 2020). This could be a possible reason for the high NO_3^- formation and contributions during the polluted periods.

4.4 Air Pollution Control Strategies in Changzhou

The four months observation in winter 2019 offers an opportunity to obtain the chemical compositions during different periods in Changzhou. And the CNY overlapped lockdown period provided a precious window to study how the air quality responds to the quick decline of anthropogenic emissions, which would be the critical basis to make atmospheric governance policies in the future (Pei et al., 2020).

For the elaboration and discussed in the above sections, the secondary inorganic ions were the most abundant species in $PM_{2.5}$ in urban Changzhou, accounting for 37 to ~50% during the clean and the polluted periods, respectively. Since NO_3^- contributed to a majority of the secondary inorganic ion formation during the high PM period in winter, reducing nitrate formation should rank as the highest priority for air pollution mitigation. Thus, the NOx emission control needs to be strengthened. Improvements on the denitrification technology for both industries and motor vehicle exhausts must be advocated (Niu et al., 2016). In addition, excess ammonium promoted the formation of nitrate during the high PM concentration period, indicating the critical role of NH_3 in regulating atmospheric nitrate. Given NH_4^+ plays a vital role in the formation of fine inorganic secondary particles, particularly in the winter season (Sharma et al., 2007), there is a need to identify and regulate the ammonia emissions in Changzhou.

The SO_2 emissions as well as ambient sulfate formation have shown a considerable drop since 2006 due to the nationwide

implementation of flue gas desulphurization controls (Wang et al., 2013). After the execution in Changzhou, the sulfate contributions to $PM_{2.5}$ are usually limited to ~15% during the normal period. However, during the CNY covered lockdown period, the plummet of NOx emissions led to the rapid increase of O_3 and the atmospheric oxidizing capacity, resulting in a leap of sulfate formation through photochemical reactions. This is similar to a "seesaw effect" between nitrate and sulfate. The benefit of nitrate reduction completely could be offset due to the significant increase of sulfate. Therefore, more attention should be paid to the impacts with the elevation of O_3 while NOx emissions are reduced.

5 CONCLUSION

In this study, we evaluated the air quality and chemical compositions in the atmosphere of urban Changzhou, China during periods with different $PM_{2.5}$ levels and the first week of city lockdown due to the outbreak of COVID-19. The analyses of NOR, SOR as functions of RH and O_3 concentrations reveal that sulfate formation mainly from the aqueous-phase reaction, while nitrate formation was driven by both photochemistry and heterogeneous reaction. In addition, the concentrations of excess ammonium linearly correlated with nitrate concentration, indicating that the formation of nitrate was strongly associated with ammonium.

Under the low $PM_{2.5}$ emission scenario during the CNY overlapping city lockdown, NO_2 plummeted 65% due to the traffic sector being markedly reduced. However, there were gentle to moderate declines in SO_2 and CO, as well as PMs. For the chemical compositions in $PM_{2.5}$, POM and EC dropped significantly, well representing the remarkable reduction of primary emissions. The proportion of sulfate increased obviously and became dominant in $PM_{2.5}$, whereas nitrate decreased observably. The declines of NOx emissions led to the rapid increase of O_3 and the atmospheric oxidizing capacity, promoting sulfate formation through photochemical reactions. This finally offset the benefit of nitrate reduction. Our study illustrates a clear picture of the characteristics and responses of chemical compositions in $PM_{2.5}$ during different periods in Changzhou in winter. The findings would serve as a critical basis for the establishment of atmospheric governance policies in the future.

DATA AVAILABILITY STATEMENT

The original contributions presented in the study are included in the article/**Supplementary Material**, further inquiries can be directed to the corresponding authors.

AUTHOR CONTRIBUTIONS

Conceptualization, ZZ and ZY; methodology, NS, DL and ST; formal analysis, ML and XZ; writing original draft preparation, ZZ and NS; writing review and editing, WZ, SM, and ZY; funding acquisition, ZZ, and ZY. All authors contributed to manuscript revision, read, and approved the submitted version.

FUNDING

State Key Laboratory of Loess and Quaternary Geology, Institute of Earth Environment, CAS (Number: SKLLQG1944); Jiangsu Innovation and Entrepreneurship Talents Plan 2020 (Number: (2020)30865); Jisangsu University of Technology, Program of Zhongwu Scientific research and innovation team (Number: 202101002).

SUPPLEMENTARY MATERIAL

The Supplementary Material for this article can be found online at: https://www.frontiersin.org/articles/10.3389/fenvs.2022.907735/full#supplementary-material

REFERENCES

Chang, L. T.-C., Tsai, J.-H., Lin, J.-M., Huang, Y.-S., and Chiang, H.-L. (2011). Particulate Matter and Gaseous Pollutants during a Tropical Storm and Air Pollution Episode in Southern Taiwan. *Atmos. Res.* 99 (1), 67–79. doi:10.1016/j.atmosres.2010.09.002

Chang, Y., Huang, R. J., Ge, X., Huang, X., Hu, J., Duan, Y., et al. (2020). Puzzling Haze Events in China during the Coronavirus (COVID-19) Shutdown. *Geophys. Res. Lett.*, e2020GL088533.

Chen, C., Zhang, H., Li, H., Wu, N., and Zhang, Q. (2020a). Chemical Characteristics and Source Apportionment of Ambient PM1.0 and PM2.5 in a Polluted City in North China Plain. *Atmos. Environ.* 242, 117867. doi:10.1016/j.atmosenv.2020.117867

Chen, H., Huo, J., Fu, Q., Duan, Y., Xiao, H., and Chen, J. (2020b). Impact of Quarantine Measures on Chemical Compositions of PM2.5 during the COVID-19 Epidemic in Shanghai, China. *Sci. Total Environ.* 743, 140758. doi:10.1016/j.scitotenv.2020.140758

Chen, X., Wang, H., Lu, K., Li, C., Zhai, T., Tan, Z., et al. (2020c). Field Determination of Nitrate Formation Pathway in Winter Beijing. *Environ. Sci. Technol.* 54 (15), 9243–9253. doi:10.1021/acs.est.0c00972

Cheng, Y., Zheng, G., Wei, C., Mu, Q., Zheng, B., Wang, Z., et al. (2016). Reactive Nitrogen Chemistry in Aerosol Water as a Source of Sulfate during Haze Events in China. *Sci. Adv.* 2 (12), e1601530. doi:10.1126/sciadv.1601530

Decarlo, P. F., Ulbrich, I. M., Crounse, J., De Foy, B., Dunlea, E. J., Aiken, A. C., et al. (2010). Investigation of the Sources and Processing of Organic Aerosol over the Central Mexican Plateau from Aircraft Measurements during MILAGRO. *Atmos. Chem. Phys.* 10 (12), 5257–5280. doi:10.5194/acp-10-5257-2010

Fu, X., Wang, S., Zhao, B., Xing, J., Cheng, Z., Liu, H., et al. (2013). Emission Inventory of Primary Pollutants and Chemical Speciation in 2010 for the Yangtze River Delta Region, China. *Atmos. Environ.* 70, 39–50. doi:10.1016/j.atmosenv.2012.12.034

Griffith, S. M., Huang, X. H. H., Louie, P. K. K., and Yu, J. Z. (2015). Characterizing the Thermodynamic and Chemical Composition Factors Controlling PM 2.5 Nitrate: Insights Gained from Two Years of Online

Measurements in Hong Kong. *Atmos. Environ.* 122, 864–875. doi:10.1016/j.atmosenv.2015.02.009

He, H., Wang, Y., Ma, Q., Ma, J., Chu, B., Ji, D., et al. (2014). Mineral Dust and NOx Promote the Conversion of SO2 to Sulfate in Heavy Pollution Days. *Sci. Rep.* 4, 4172. doi:10.1038/srep04172

Huang, R-J., Zhang, Y., Bozzetti, C., Ho, K-F., Cao, J-J., Han, Y., et al. (2014). High Secondary Aerosol Contribution to Particulate Pollution during Haze Events in China. *Nature* 514, 218-222. doi:10.1038/nature13774

Jimenez, J. L., Canagaratna, M. R., Donahue, N. M., Prevot, A. S. H., Zhang, Q., Kroll, J. H., et al. (2009). Evolution of Organic Aerosols in the Atmosphere. *Science* 326 (5959), 1525–1529. doi:10.1126/science.1180353

Le, T., Wang, Y., Liu, L., Yang, J., Yung, Y. L., Li, G., et al. (2020). Unexpected Air Pollution with Marked Emission Reductions during the COVID-19 Outbreak in China. *Science* 369 (6504), 702–706. doi:10.1126/science.abb7431

Li, H., Ma, Y., Duan, F., He, K., Zhu, L., Huang, T., et al. (2017). Typical Winter Haze Pollution in Zibo, an Industrial City in China: Characteristics, Secondary Formation, and Regional Contribution. *Environ. Pollut.* 229, 339–349. doi:10.1016/j.envpol.2017.05.081

Li, L., Li, Q., Huang, L., Wang, Q., Zhu, A., Xu, J., et al. (2020). Air Quality Changes during the COVID-19 Lockdown over the Yangtze River Delta Region: An Insight into the Impact of Human Activity Pattern Changes on Air Pollution Variation. *Sci. Total Environ.* 732, 139282. doi:10.1016/j.scitotenv.2020.139282

Li, X., Wang, L., Ji, D., Wen, T., Pan, Y., Sun, Y., et al. (2013). Characterization of the Size-Segregated Water-Soluble Inorganic Ions in the Jing-Jin-Ji Urban Agglomeration: Spatial/temporal Variability, Size Distribution and Sources. *Atmos. Environ.* 77, 250–259. doi:10.1016/j.atmosenv.2013.03.042

Liu, X., Pan, X., Wang, Z., He, H., Wang, D., Liu, H., et al. (2020). Chemical Characteristics and Potential Sources of PM2.5 in Shahe City during Severe Haze Pollution Episodes in the Winter. *Aerosol Air Qual. Res.* 20 (12), 2741–2753. doi:10.4209/aaqr.2020.03.0124

Lu, K., Fuchs, H., Hofzumahaus, A., Tan, Z., Wang, H., Zhang, L., et al. (2019). Fast Photochemistry in Wintertime Haze: Consequences for Pollution Mitigation Strategies. *Environ. Sci. Technol.* 53 (18), 10676–10684. doi:10.1021/acs.est.9b02422

Ma, J., Chu, B., Liu, J., Liu, Y., Zhang, H., and He, H. (2018). NO Promotion of SO2 Conversion to Sulfate: An Important Mechanism for the Occurrence of Heavy Haze during Winter in Beijing. *Environ. Pollut.* 233, 662–669. doi:10.1016/j.envpol.2017.10.103

Ma, T., Duan, F., He, K., Qin, Y., Tong, D., Geng, G., et al. (2019). Air Pollution Characteristics and Their Relationship with Emissions and Meteorology in the Yangtze River Delta Region during 2014-2016. *J. Environ. Sci.* 83, 8–20. doi:10.1016/j.jes.2019.02.031

Niu, X., Cao, J., Shen, Z., Ho, S. S. H., Tie, X., Zhao, S., et al. (2016). PM2.5 from the Guanzhong Plain: Chemical Composition and Implications for Emission Reductions. *Atmos. Environ.* 147, 458–469. doi:10.1016/j.atmosenv.2016.10.029

Pathak, R. K., Wang, T., Ho, K. F., and Lee, S. C. (2011). Characteristics of Summertime PM2.5 Organic and Elemental Carbon in Four Major Chinese Cities: Implications of High Acidity for Water-Soluble Organic Carbon (WSOC). *Atmos. Environ.* 45 (2), 318–325. doi:10.1016/j.atmosenv.2010.10.021

Pathak, R. K., Wu, W. S., and Wang, T. (2009). Summertime PM_{2.5} Ionic Species in Four Major Cities of China: Nitrate Formation in an Ammonia-Deficient Atmosphere. *Atmos. Chem. Phys.* 9 (5), 1711–1722. doi:10.5194/acp-9-1711-2009

Pathak, R., Louie, P. K. K., and Chan, C. K. (2004). Characteristics of Aerosol Acidity in Hong Kong. *Atmos. Environ.* 38 (19), 2965–2974. doi:10.1016/j.atmosenv.2004.02.044

Pei, Z., Han, G., Ma, X., Su, H., and Gong, W. (2020). Response of Major Air Pollutants to COVID-19 Lockdowns in China. *Sci. Total Environ.* 743, 140879. doi:10.1016/j.scitotenv.2020.140879

Qian, W., Wang, X., Huang, R., Wu, J., Xiao, Y., Hu, M., et al. (2021). *Regional Transport of PM2.5 and O3 Based on Complex Network Method and Source Apportionment Technology in the Yangtze River Delta*. China.

Seo, J., Kim, J. Y., Youn, D., Lee, J. Y., Kim, H., Lim, Y. B., et al. (2017). On the Multiday Haze in the Asian Continental Outflow: the Important Role of Synoptic Conditions Combined with Regional and Local Sources. *Atmos. Chem. Phys.* 17 (15), 9311–9332. doi:10.5194/acp-17-9311-2017

Sharma, M., Kishore, S., Tripathi, S. N., and Behera, S. N. (2007). Role of Atmospheric Ammonia in the Formation of Inorganic Secondary Particulate Matter: A Study at Kanpur, India. *J. Atmos. Chem.* 58 (1), 1–17. doi:10.1007/s10874-007-9074-x

Sun, Y., Lei, L., Zhou, W., Chen, C., He, Y., Sun, J., et al. (2020). A Chemical Cocktail during the COVID-19 Outbreak in Beijing, China: Insights from Six-Year Aerosol Particle Composition Measurements during the Chinese New Year Holiday. *Sci. Total Environ.* 742, 140739. doi:10.1016/j.scitotenv.2020.140739

Sun, Y., Wang, Z., Fu, P., Jiang, Q., Yang, T., Li, J., et al. (2013). The Impact of Relative Humidity on Aerosol Composition and Evolution Processes during Wintertime in Beijing, China. *Atmos. Environ.* 77 (0), 927–934. doi:10.1016/j.atmosenv.2013.06.019

Tang, M., Liu, Y., He, J., Wang, Z., Wu, Z., and Ji, D. (2021). *In Situ* continuous Hourly Observations of Wintertime Nitrate, Sulfate and Ammonium in a Megacity in the North China Plain from 2014 to 2019: Temporal Variation, Chemical Formation and Regional Transport. *Chemosphere* 262, 127745. doi:10.1016/j.chemosphere.2020.127745

Tian, M., Wang, H., Chen, Y., Yang, F., Zhang, X., Zou, Q., et al. (2016). Characteristics of Aerosol Pollution during Heavy Haze Events in Suzhou, China. *Atmos. Chem. Phys.* 16 (11), 7357–7371. doi:10.5194/acp-16-7357-2016

Turpin, B. J., and Huntzicker, J. J. (1995). Identification of Secondary Organic Aerosol Episodes and Quantitation of Primary and Secondary Organic Aerosol Concentrations during SCAQS. *Atmos. Environ.* 29 (23), 3527–3544. doi:10.1016/1352-2310(94)00276-q

Turpin, B. J., and Lim, H.-J. (2001). Species Contributions to PM2.5 Mass Concentrations: Revisiting Common Assumptions for Estimating Organic Mass. *Aerosol Sci. Technol.* 35 (1), 602–610. doi:10.1080/02786820119445

Wang, Y., Zhang, Q. Q., He, K., Zhang, Q., and Chai, L. (2013). Sulfate-nitrate-ammonium Aerosols over China: Response to 2000-2015 Emission Changes of Sulfur Dioxide, Nitrogen Oxides, and Ammonia. *Atmos. Chem. Phys.* 13 (5), 2635–2652. doi:10.5194/acp-13-2635-2013

Wu, C., Huang, X. H. H., Ng, W. M., Griffith, S. M., and Yu, J. Z. (2016). Inter-comparison of NIOSH and IMPROVE Protocols for OC and EC Determination: Implications for Inter-protocol Data Conversion. *Atmos. Meas. Tech.* 9 (9), 4547–4560. doi:10.5194/amt-9-4547-2016

Wu, C., and Yu, J. Z. (2016). Determination of Primary Combustion Source Organic Carbon-To-Elemental Carbon (OC/EC) Ratio Using Ambient OC and EC Measurements: Secondary OC-EC Correlation Minimization Method. *Atmos. Chem. Phys.* 16 (8), 5453–5465. doi:10.5194/acp-16-5453-2016

Wu, L., Sun, J., Zhang, X., Zhang, Y., Wang, Y., Zhong, J., et al. (2019). Aqueous-phase Reactions Occurred in the PM2.5 Cumulative Explosive Growth during the Heavy Pollution Episode (HPE) in 2016 Beijing Wintertime. *Tellus B Chem. Phys. Meteorology* 71 (1), 1620079. doi:10.1080/16000889.2019.1620079

Xu, J.-S., Xu, H.-H., Xiao, H., Tong, L., Snape, C. E., Wang, C.-J., et al. (2016). Aerosol Composition and Sources during High and Low Pollution Periods in Ningbo, China. *Atmos. Res.* 178-179, 559–569. doi:10.1016/j.atmosres.2016.05.006

Xu, J.-S., Xu, M.-X., Snape, C., He, J., Behera, S. N., Xu, H.-H., et al. (2017). Temporal and Spatial Variation in Major Ion Chemistry and Source Identification of Secondary Inorganic Aerosols in Northern Zhejiang Province, China. *Chemosphere* 179, 316–330. doi:10.1016/j.chemosphere.2017.03.119

Ye, S., Ma, T., Duan, F., Li, H., He, K., Xia, J., et al. (2019). Characteristics and Formation Mechanisms of Winter Haze in Changzhou, a Highly Polluted Industrial City in the Yangtze River Delta, China. *Environ. Pollut.* 253, 377–383. doi:10.1016/j.envpol.2019.07.011

Ye, Z., Liu, J., Gu, A., Feng, F., Liu, Y., Bi, C., et al. (2016). Chemical Characterization of Fine Particular Matter in Changzhou, China and Source Apportionment with Offline Aerosol Mass Spectrometry. *Atmos. Chem. Phys. Discuss.*, 1–46.

Zhang, C., Litao Wang, L., Qi, M., Ma, X., Zhao, L., Ji, S., et al. (2018). Evolution of Key Chemical Components in PM2.5 and Potential Formation Mechanisms of Serious Haze Events in Handan, China. *Aerosol Air Qual. Res.* 18 (7), 1545–1557. doi:10.4209/aaqr.2017.10.0386

Zhang, F., Xu, L., Chen, J., Chen, X., Niu, Z., Lei, T., et al. (2013). Chemical Characteristics of PM2.5 during Haze Episodes in the Urban of Fuzhou, China. *Particuology* 11 (3), 264–272. doi:10.1016/j.partic.2012.07.001

Zhang, J., Yang, L., Chen, J., Mellouki, A., Jiang, P., Gao, Y., et al. (2017). Influence of Fireworks Displays on the Chemical Characteristics of PM2.5 in Rural and

Suburban Areas in Central and East China. *Sci. Total Environ.* 578, 476–484. doi:10.1016/j.scitotenv.2016.10.212

Zhang, Q., Zheng, Y., Tong, D., Shao, M., Wang, S., Zhang, Y., et al. (2019). Drivers of Improved PM 2.5 Air Quality in China from 2013 to 2017. *Proc. Natl. Acad. Sci. U.S.A.* 116 (49), 24463–24469. doi:10.1073/pnas.1907956116

Zhang, X. Y., Gong, S. L., Arimoto, R., Shen, Z. X., Mei, F. M., Wang, D., et al. (2003). Characterization and Temporal Variation of Asian Dust Aerosol from a Site in the Northern Chinese Deserts. *J. Atmos. Chem.* 44 (3), 241–257. doi:10.1023/a:1022900220357

Zhao, M., Qiao, T., Huang, Z., Zhu, M., Xu, W., Xiu, G., et al. (2015). Comparison of Ionic and Carbonaceous Compositions of PM 2.5 in 2009 and 2012 in Shanghai, China. *Sci. Total Environ.* 536, 695–703. doi:10.1016/j.scitotenv.2015.07.100

Zheng, G. J., Duan, F. K., Su, H., Ma, Y. L., Cheng, Y., Zheng, B., et al. (2015). Exploring the Severe Winter Haze in Beijing: the Impact of Synoptic Weather, Regional Transport and Heterogeneous Reactions. *Atmos. Chem. Phys.* 15, 2969–2983. doi:10.5194/acp-15-2969-2015

Conflict of Interest: The authors declare that the research was conducted in the absence of any commercial or financial relationships that could be construed as a potential conflict of interest.

frontiers | Frontiers in Environmental Science

ORIGINAL RESEARCH
published: 30 May 2022
doi: 10.3389/fenvs.2022.893408

Baseline of Surface and Column-Integrated Aerosol Loadings in the Pearl River Delta Region, China

Xuehua Fan[1], Xiangao Xia[1,2], Hongbin Chen[1,2], Yanliang Zhu[1†], Jun Li[1], Honglong Yang[3] and Hongyan Luo[3]*

[1]Key Laboratory of Middle Atmosphere and Global Environment Observation, Institute of Atmospheric Physics, Chinese Academy of Sciences, Beijing, China, [2]Collaborative Innovation Center on Forecast and Evaluation of Meteorological Disasters, Nanjing University of Information Science & Technology, Nanjing, China, [3]Shenzhen National Climate Observatory, Meteorological Bureau of Shenzhen Municipality, Shenzhen, China

Much attention has been paid to the rapid variation of aerosol loading in the urban areas of the Pearl River Delta (PRD) region. The baseline of aerosol loading in this rapidly developing region is critical in evaluating how and why the aerosol level has evolved, which absolutely requires long-term observations. Based on long-term observations of aerosol optical depth (AOD), visibility, and particulate matter (PM) mass concentrations at Xichong (114.56°E, 22.49°N), a background site in the PRD region, the variabilities of aerosol loading at multiple temporal scales are revealed. The means (±σ) of AOD, visibility, PM_{10}, $PM_{2.5}$, and PM_1 are 0.38 ± 0.07, 12.6 ± 2.3 km, 23.7 ± 12.6 μg/m^3, 19.7 ± 11.0 μg/m^3, and 16.1 ± 10.1 μg/m^3, respectively, which show that aerosol loading at the Xichong site is much lower than that in urban and suburban sites. Significant decreases in PM_{10}, $PM_{2.5}$, and PM_1 mass concentrations are observed with magnitudes up to −2.13, −1.82, and −1.37 yr^{-1}, respectively, at a 95% confidence level. The decrease in aerosol loadings at Xichong is attributed to the strict environmental regulations for improving air quality. Higher AOD and PM (lower visibility) values are observed during the early spring months as a result of long-range transport of biomass burning from Southeastern Asia. Diurnal variations of PM and visibility are dominantly determined by those of boundary layer height and relative humidity. PM mass concentrations show a generally negative (positive) correlation with visibility (AOD) at Xichong, but the correlations are weak with the R^2 of 0.22 and 0.54, respectively. Low visibility and high aerosol loading are generally associated with very weak easterly and southerly winds. Understanding of variability of surface particle concentration and column-integrated aerosol loading at this background site in the PRD region would provide a scientific basis for the adoption of pollution prevention and control measures.

Keywords: air quality, visibility, PM mass concentration, AOD, background site, Pearl River Delta

OPEN ACCESS

Edited by:
Jianhuai Ye,
Southern University of Science and Technology, China

Reviewed by:
Shunyao Wang,
Shanghai University, China
Lei Shu,
Southern University of Science and Technology, China

****Correspondence:***
Xuehua Fan
fxh@mail.iap.ac.cn

†ORCID ID:
Yanliang Zhu
orcid.org/0000-0002-9898-5375

Specialty section:
This article was submitted to Atmosphere and Climate, a section of the journal Frontiers in Environmental Science

Received: *10 March 2022*
Accepted: *19 April 2022*
Published: *30 May 2022*

Citation:
Fan X, Xia X, Chen H, Zhu Y, Li J, Yang H and Luo H (2022) Baseline of Surface and Column-Integrated Aerosol Loadings in the Pearl River Delta Region, China. Front. Environ. Sci. 10:893408. doi: 10.3389/fenvs.2022.893408

INTRODUCTION

The Pearl River Delta (PRD) region has experienced a rapid urbanization process for the past 40 years. High population densities and developed industries have resulted in severe air pollution in the PRD region. Analysis of the long-term (1954–2006) trend of visibility in an urban site in the PRD region showed that visibility has dramatically deteriorated since the 1980s as a result of a rapid increase in fine particle loading (Wu et al., 2007; Deng et al., 2008a).

To characterize the air pollution and improve the understanding of chemical and radiative processes in the atmosphere of the PRD, a couple of intensive field campaigns were performed, for example, the Program of Regional Integrated Experiments on Air Quality over the PRD of China (PRIDE-PRD) was conducted in 12 urban sites and 2 super sites from 4 Oct. to 5 Nov. 2004 (Hu et al., 2008; Liu et al., 2008; Zhang et al., 2008), in Jul. 2006 (Liu et al., 2010; Yue et al., 2013), and from 19 Oct. to 18 Nov. 2008 (Ma et al., 2017). The major contributor to air pollution is particulate matter (PM) in PRD, mainly fine particulate matter ($PM_{2.5}$) emitted from fossil fuel, biomass burning, and urban construction (Cao et al., 2003; Wu et al., 2007). In addition to local anthropogenic emissions which are major driving forces for poor air quality, the smoke plume of agricultural residue burning in Southeastern Asia is also transported to the downwind PRD that often occurs during dry seasons such as early spring (Deng et al., 2008b).

The air pollution in the PRD region has attracted attention from both the scientific community and policymakers. A series of air pollution control measures have been undertaken, and the air quality has been improved since 2014 (Yu et al., 2009; Wang G. et al., 2019; Wu et al., 2019). These previous studies mainly focused on observations of surface PM mass concentration (Xia et al., 2017; Kong et al., 2020), carbonaceous aerosol properties (Cao et al., 2003; Lan et al., 2011), and related chemical apportionment (Liu et al., 2008; Huang et al., 2011) based on some short-term intensive campaigns. Recently, Fang et al. (2019) investigated the spatial-temporal characteristics of PM concentrations in the Guangdong–Hong Kong–Macao Greater Bay Area (GBA) of China using daily observations data during 2015–2017. It was emphasized that there are different major air quality issues in the GBA cities due to the differences in pollution sources, meteorological factors, and synergic pollution control policy.

Previous studies are mainly based on observations of short-term field campaigns (Ansmann et al., 2005; Cheng et al., 2008; Hu et al., 2008; Xiao et al., 2011; Yue et al., 2013; Kong et al., 2020), which shed new light on the processes of the formation, maintenance, and dilution of air pollution as a result of comprehensive observations of air quality. Long-term operational observation is also of high significance in showing how air quality evolves as a result of anthropogenic and natural processes, especially recording potential changes in air quality as a result of the implementation of air pollution control measures. Strict implementation of the "Air Pollution Prevention and Control Action Plan" took effect in China in 2013, which provided us a good opportunity to study how PM concentration was impacted by this huge change in anthropogenic emissions. $PM_{2.5}$ concentration in the PRD region was observed to gradually decrease with an average reduction rate of 21% from 2013 to 2017 (Zhang et al., 2019; Lu et al., 2021). The objective of this study is to present a closer look at aerosol evolution during 2011–2018. In order to fulfill this goal, we used three aerosol datasets, i.e., aerosol optical depth (AOD), PM concentration, and visibility at a background site in the PRD. A detailed analysis of variation of AOD, PM, and visibility was presented. Furthermore, we also investigated the influence of meteorological factors and estimated the relationships of AOD, PM, and visibility. The results are necessary for the understanding of the baseline of aerosol properties in PRD and will provide the scientific basis for the adoption of pollution prevention and control measures.

SITE, DATA, AND METHOD

Site

Shenzhen is a rising urban metropolis in the PRD region, with a total area of 1997.47 km^2 and a population of 17.56 million by the end of 2020. It lies along the coast of the South China Sea and is located immediately to the north of Hong Kong. Shenzhen has been experiencing rapid economic development and population growth that probably results in complicated air pollution problems. The sampling site in the study is located at the Shenzhen Xichong Astronomical Observatory (114.56°E, 22.49°N), at the top of a seaside hill with an elevation of 155 m above sea level (ASL). The Xichong observatory is far away from the urban and industrial regions of the PRD, therefore, representing the background level of air quality in the PRD (**Figure 1**).

Observation Data

Aerosol optical depth data are derived from the direct and diffuse solar spectral radiance measured by a CIMEL CE318 sun photometer. The sun photometer measures direct sun and diffuse sky radiances in 15 and 30 min intervals between the spectral ranges of 340–1020 nm, respectively, with a 1.2° field of view (Holben et al., 1998). The AOD products are automatically cloud cleared and quality assured, and have a low uncertainty of 0.01–0.02 in the visible and near-infrared wavelengths (Dubovik et al., 2000). The AOD at 550 nm used in the study was computed using the quadratic fit of AOD to wavelength on a log-log scale. Hourly PM mass concentration is observed by the beta-ray method. An automatic meteorological station is equipped with a set of sensors measuring 1-min visibility (km), temperature (T, °C), relative humidity (RH, %), wind speed (WS, $m{\cdot}s^{-1}$), and precipitation (PR, mm). To eliminate the contamination of precipitation, data obtained under rainy conditions (PR > 0) are removed.

European Centre for Medium-Range Weather Forecasts Atmospheric Reanalysis Data

The boundary layer heights (BLH) and wind vectors at pressure levels from European Centre for Medium-Range Weather Forecasts (ECMWF) reanalysis data (ERA5) are used to analyze the impacts of BLH and wind on the suspended particulate matter and the horizontal visibility. ERA5 is the fifth generation ECMWF atmospheric reanalysis of the global climate, covering the period from January 1950 to the present (https://cds.climate.copernicus.eu/). The data resolve the atmosphere using 137 levels from the surface up to a height of 80 km and has been regreded to a regular grid of 0.25 degrees. The

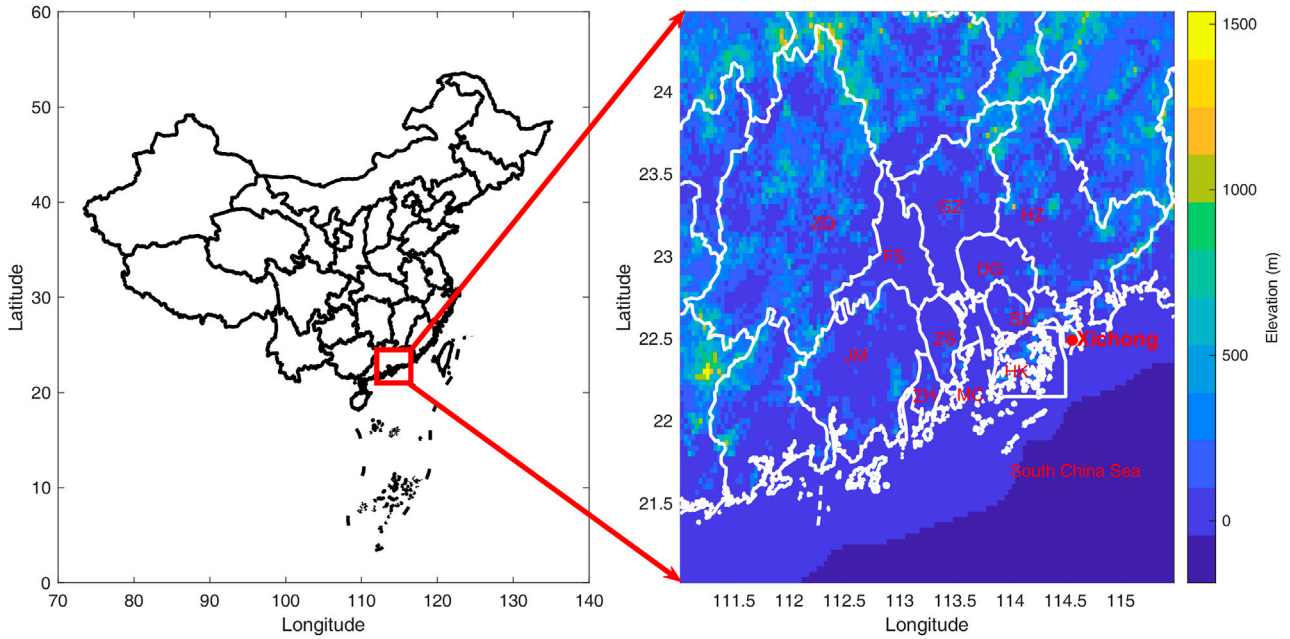

FIGURE 1 | Topography map of the Pearl River Delta region with 11 cities [Zhaoqing (ZQ), Guangzhou (GZ), Huizhou (HZ), Foshan (FS), Dongguan (DG), Jiangmen (JM), Zhongshan (ZS), Shenzhen (SZ), Hong Kong (HK), Zhuhai (ZH), and MC (Macau)] and the location of the Xichong site.

u- and v-components of wind are the eastward and northward components at pressure levels, which indicate the horizontal speed of air moving toward the east and north, respectively. The wind speed (s) in meters per second is calculated using $s = \sqrt{u^2 + v^2}$. The BLH (unit: m) is the depth of air next to the Earth's surface which is most affected by the resistance to the transfer of momentum, heat, or moisture across the surface. The BLH calculation is based on the bulk Richardson number (Vogelezang and Holtslag, 1996).

RESULTS AND DISCUSSIONS

Temporal Variability of Aerosol Optical Depth, PM, and Visibility

The temporal variations in daily PM mass concentrations are presented in **Figure 2A**. Daily averaged PM_{10} ($PM_{2.5}$, PM_1) in **Figure 2A** varies from 1.14 (1.06, 0.22) to 138 (90.8, 80.02) μg/m^3. According to the Chinese ambient air quality standards (GB 3095-2012), the first-level (second-level) limits of daily PM_{10} and $PM_{2.5}$ are 50 μg/m^3 (150 μg/m^3) and 35 μg/m^3 (75 μg/m^3), respectively. It is shown that almost all the daily PM_{10} and $PM_{2.5}$ at Xichong are below the second-level limit but the days over the first-level limit of PM_{10} and $PM_{2.5}$ account for about 8.7% (228 days) and 15.2% (399 days) of the entire study period (2641 days). It is remarkable that a significant reduction in the daily PM mass concentrations occurs after Apr. 2015 at Xichong. Since then, the number of days over the first-level limit of PM_{10} and $PM_{2.5}$ is 22, and 60, respectively, mostly occurring during the winter and spring months.

Figures 2B–G depict the variability of monthly PM mass concentrations, AOD, visibility, and the ratio of PM_1, $PM_{2.5}$, and PM_{10}. Annual means of PM concentrations reached the minimum in 2016, and the values of PM_{10}, $PM_{2.5}$, and PM_1 are 16.5 ± 11.0 μg/m^3, 13.3 ± 10.1 μg/m^3, and 10.8 ± 9.7 μg/m^3, respectively. According to the observational data during 2015–2017 in the PRD, the minima of yearly mean $PM_{2.5}$ (<28 μg/m^3), PM_{10} (<46 μg/m^3), and AQI (<56) were also found in Shenzhen in 2016 (Fang et al., 2019). The mean AOD in 2016 is 0.30 ± 0.14, lower than in other years possibly because of the following reasons: First, the observation data is not available in April when the highest aerosol loading of the year generally occurs (**Figure 3A**). Second, the higher wind speed (>3.5 m/s) at 850 hPa (**Supplementary Figure S2B**) lasted throughout the spring and summer except August and September, which are favorable for the dispersion of aerosols and result in a lower AOD. Finally, the precipitation amount (>200 mm) during the wet season except July is larger than that in other years (**Supplementary Figure S2A**), which implies a stronger wet removal of aerosols.

The linear trends in PM mass concentrations, visibility, and AOD during the study period are also given in **Figures 2B–F**. Negative trends in PM_{10}, $PM_{2.5}$, and PM_1 are significant at a 95% confidence level with the magnitudes of −2.13, −1.82, and −1.37 yr^{-1}, respectively. Moreover, a downward trend of −0.038 yr^{-1} in AOD is also found in **Figure 2F** although it is statistically insignificant. The decrease in aerosol loadings at Xichong is attributed to the strict environmental regulations for improving air quality (http://www.mee.gov.cn/ywgz/fgbz/fl/201404/t20140425_271040.shtml), including the regulations and

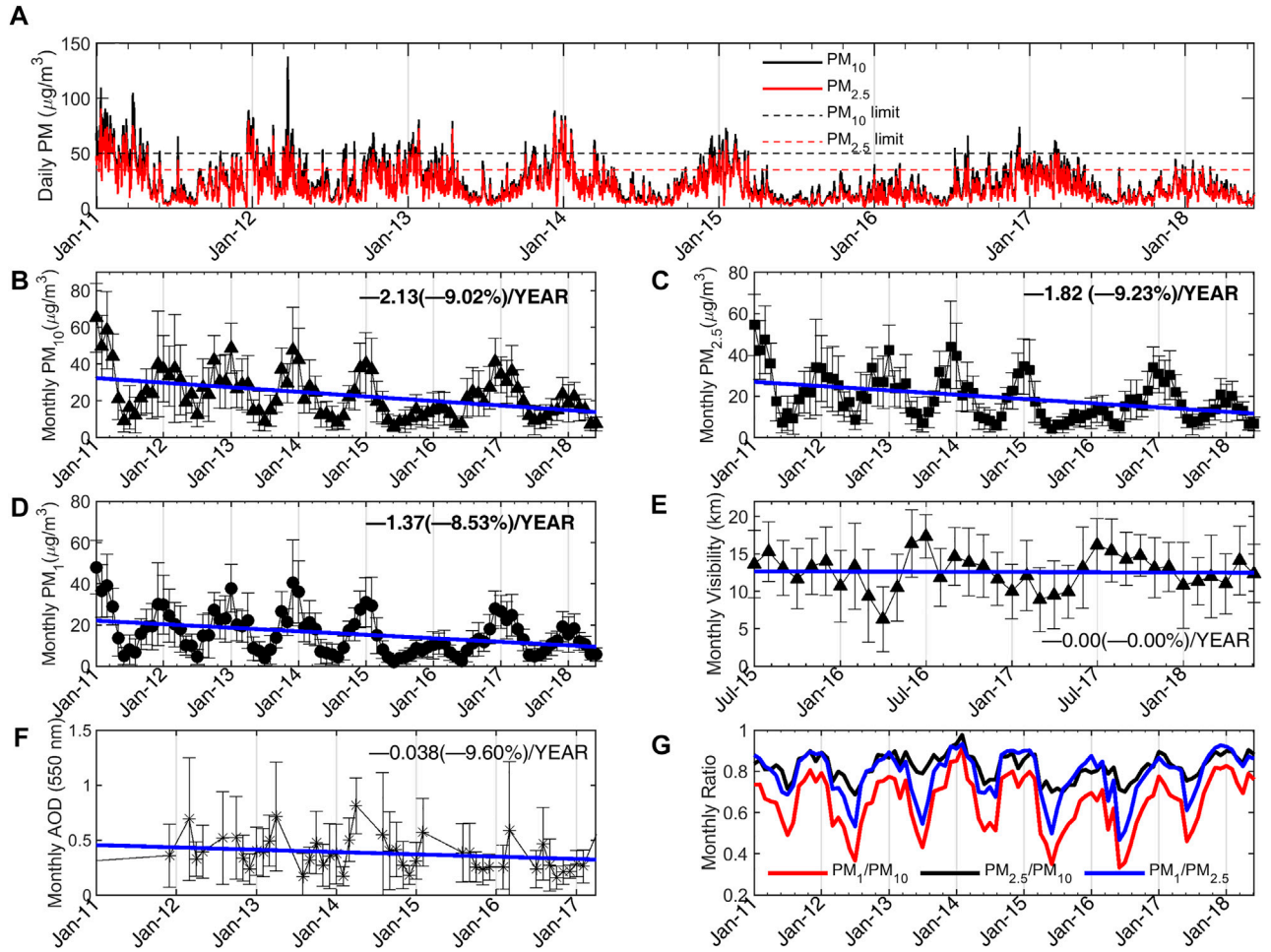

FIGURE 2 | Time series of daily PM_{10} and $PM_{2.5}$ mass concentrations from Jan. 2011 to June 2018 **(A)**, variability of monthly PM concentrations **(B–D)**, visibility **(E)**, AOD **(F)**, and ratios of PM **(G)** at Xichong site. The statistical parameters in the figures are linear trends of monthly PM, visibility and AOD. Bold font indicates trends are statistically significant at the 95% confidence level.

measures of emission reduction in power plants, combustion facilities, vehicles, ports, and ships (http://www.sz.gov.cn/zfgb/2013/gb852/201309/t20130929_2217840.htm). The relatively short-term observations of visibility might not be enough to handle the interannual variation. The trend in visibility cannot be derived from the study.

Table1 listed the means of PM mass concentrations at different sites in the PRD during the same period. The data of PM mass concentration are available from Dec.2013 to Jun. 2018 (https://www.aqistudy.cn/historydata). The multi-year averaged mass concentrations of PM_{10}, $PM_{2.5}$, and PM_1 at Xichong during the study period are 23.7 ± 12.6 μg/m^3, 19.7 ± 11.0 μg/m^3, and 16.1 ± 10.1 μg/m^3, respectively. The averaged mass concentrations of PM_{10} and $PM_{2.5}$ observed in 19 ground-based monitoring sites around Shenzhen during Mar. 2013–Feb. 2014 were 85 and 43 μg/m^3, respectively (Xia et al., 2017). The averaged mass concentrations of PM_{10} and $PM_{2.5}$ during the same period at Xichong were 26.7 ± 13.0 μg/m^3 and 23.2 ± 11.9 μg/m^3, which indicate that the polluting levels of particulate matters at Xichong were much lower than those of urban sites in Shenzhen. The PM mass concentrations at Xichong are the lowest in all the sites in the PRD region (**Table 1**), which suggested that the air masses are relatively clean because the Xichong site is far away from the urban and industrial emission.

The averaged PM_1/PM_{10}, $PM_1/PM_{2.5}$, and $PM_{2.5}/PM_{10}$ ratios from Jan. 2011 to Jun. 2018 are 0.65, 0.78, and 0.82, respectively. The extents of variation in the monthly mean of PM_1/PM_{10}, $PM_1/PM_{2.5}$, and $PM_{2.5}/PM_{10}$ ratios are 0.33–0.91, 0.47–0.93, and 0.69–0.98. The mean ratio of $PM_{2.5}$ to PM_{10} at the Xichong site is the highest in all the observations in the PRD (**Table 1**). In addition to primary emission sources, the ratio of PM_{10} and $PM_{2.5}$ can be significantly affected by secondary aerosol formation in the atmosphere (Kong et al., 2017; Munir, 2017; Fan et al., 2021). Secondary aerosols contribute significantly to PM mass concentrations, especially $PM_{2.5}$ concentrations (Zhao et al., 2018; Fan et al., 2020; Spandana et al., 2021). The high ratios of $PM_{2.5}$ to PM_{10} suggest that aerosol pollution at Xichong is mainly caused by fine particles more from anthropogenic sources

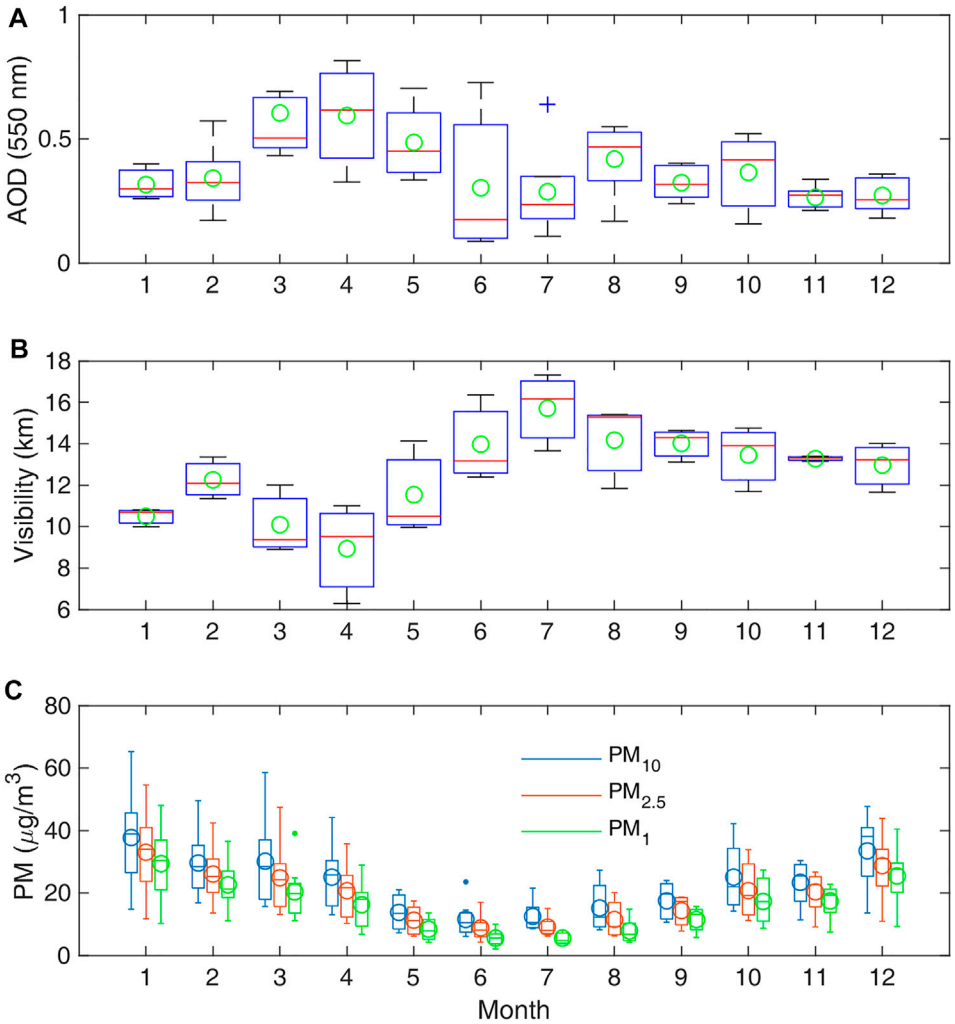

FIGURE 3 | Boxplot of monthly averaged AOD **(A)** from Jan. 2011 to Jun. 2017, visibility **(B)** from Jul. 2015 to Jun. 2018, and PM mass concentrations **(C)** from Jan. 2011 to Jun. 2018 at Xichong. The ends of the boxes, the ends of the whiskers, and the short line across each box represent the 25th and 75th percentiles, the 5th and 95th percentiles, and the median, respectively. The means are represented by the circles.

TABLE 1 | Mean PM mass concentration values observed in PRD during Dec. 2013 to Jun. 2018.

City	PM_{10} (μg/m^3)	$PM_{2.5}$ (μg/m^3)	$PM_{2.5}/PM_{10}$
Dongguan	53.8 ± 16.5	38.8 ± 14.2	0.72
Foshan	62.3 ± 22.0	40.8 ± 16.1	0.65
Guangzhou	60.5 ± 16.8	40.0 ± 13.9	0.66
Huizhou	51.8 ± 13.8	30.4 ± 10.4	0.58
Shenzhen	48.7 ± 17.4	29.9 ± 12.6	0.61
Zhuhai	48.6 ± 20.5	30.8 ± 16.0	0.63
Zhaoqing	62.6 ± 19.9	43.1 ± 17.9	0.69
Zhongshan	50.1 ± 20.7	33.9 ± 15.9	0.68
Xichong	19.4 ± 10.5	16.3 ± 9.5	0.84

(Chu et al., 2015; Kong and Yi, 2015). The site is relatively far away from the downtown of Shenzhen, but the air quality at Xichong is still affected by human activities. The PM_1/PM_{10} and $PM_1/PM_{2.5}$ ratios exhibit a remarkable reduction in summer because the hygroscopic growth of a large fraction of submicrometer particles under higher RH may increase the proportion of $PM_{2.5}$ (Zhao et al., 2018; Wang et al., 2020; Fan et al., 2021).

All the PM ratios in **Figure 2G** have distinct seasonal characteristics, with lower values in the summer but higher values during the autumn and winter months. The mean ratios of PM_1 to $PM_{2.5}$ are greater than 0.83 during the autumn and winter months, which means the mass of $PM_{2.5}$ is dominated by particles with a diameter of <1.0 μm. The PM_1/PM_{10}, $PM_1/PM_{2.5}$, and $PM_{2.5}/PM_{10}$ ratios exhibit a remarkable reduction in summer with the seasonal means of 0.52, 0.67, and 0.76 due to the hygroscopic growth of a large fraction of submicrometer particles under higher RH.

Figure 3 exhibits the statistical distribution of AOD 1) from Jan. 2011 to Jun. 2017, visibility 2) from Jul. 2015 to Jun. 2018,

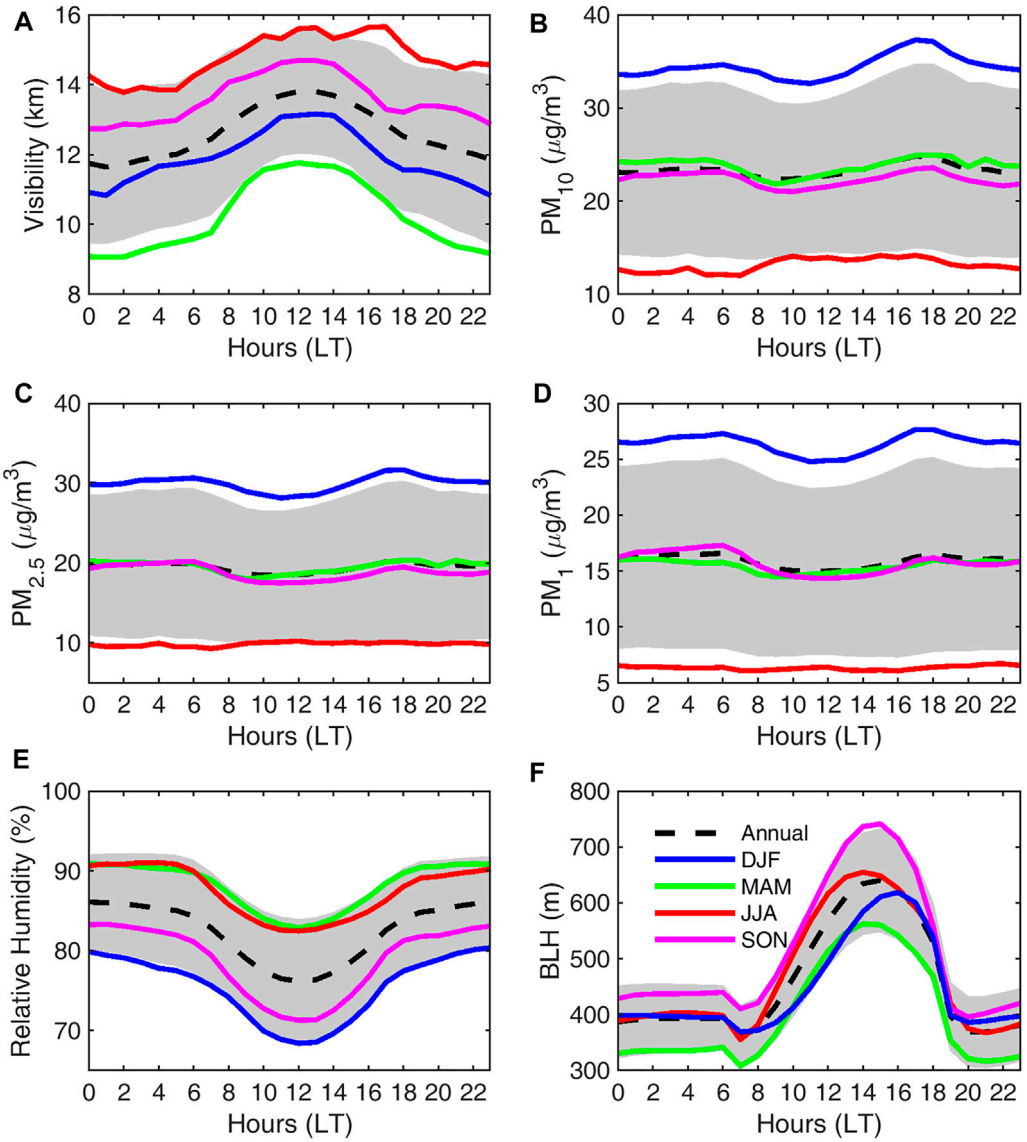

FIGURE 4 | The diurnal variations in multi-year averaged visibility **(A)**, PM_{10} **(B)**, $PM_{2.5}$ **(C)**, PM_1 **(D)**, RH **(E)**, and BLH **(F)** for four seasons at Xichong.

and PM mass concentrations 3) from Jan. 2011 to Jun. 2018 at Xichong. AOD reached its maximum during the spring months with the mean values of 0.61, 0.59, and 0.49 in March, April, and May, respectively. The monthly mean visibility varies from 6.3 ± 4.3 to 17.3 ± 2.9 km. The mean (±σ) of visibility during the study period is 12.6 ± 2.3 km at Xichong. The PM concentrations were higher in the winter and spring months but lower during the summer and autumn months. The peak values of PM mass concentrations were observed in January when the monthly mean of PM_{10}, $PM_{2.5}$, and $PM_{1.0}$ was 37.8, 33.0, and 29.4 μg/m^3, respectively. The PM concentrations reached the lowest values in June when the monthly mean of PM_{10}, $PM_{2.5}$, and $PM_{1.0}$ was 11.6, 8.8, and 5.6 μg/m^3, respectively.

The seasonality of the visibility is inversed to those of PM mass concentrations and AOD. The visibility was higher during the summer and autumn months and lower during the winter and spring months. The highest AODs in spring correspond to the lowest visibility in March and April with the monthly means of 10.1 and 8.9 km. The highest visibility appeared in July with a monthly mean value of 15.7 km, which corresponds to the lowest AOD of 0.29 and the lowest PM_1 and $PM_{2.5}$ concentrations.

Diurnal Variation of PM, Visibility, RH, and Boundary Layer Heights

The height of the boundary layer (BLH) determines the volume available for pollution dispersion and transport in the atmosphere (Yang et al., 2012). **Figure 4** shows the diurnal variations in multi-year averaged visibility, PM_{10}, $PM_{2.5}$, PM_1, RH, and BLH for four seasons at Xichong. The visibility, relative humidity, and BLH

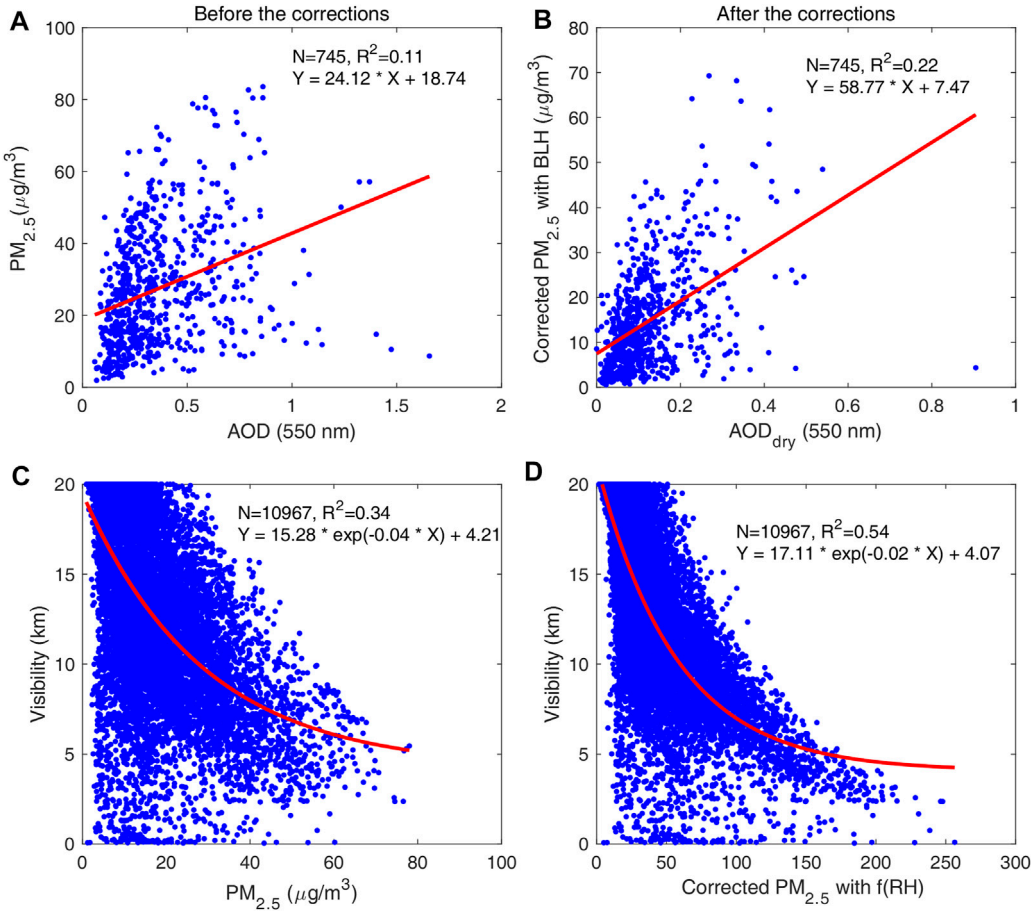

FIGURE 5 | Scatter plots of AOD vs. $PM_{2.5}$ **(A,B)** and $PM_{2.5}$ vs. visibility **(C,D)** at Xichong. The left panel is before the corrections of RH and BLH; the right panel is after the corrections of RH and BLH.

show significant diurnal cycles. The visibility reaches the maximum value (13.6 km) at noon and then decreases from 14:00 LT and drops to the minimum (11.8 km) during the night. Relative humidity shows an opposite diurnal cycle to that of visibility, with a higher RH (~86%) during the night and a lower RH at noon (76%). Most atmospheric aerosols are externally mixed with respect to hygroscopicity and consist of more and less hygroscopic sub-fractions (Cheng et al., 2008; Cubison et al., 2008; Swietlicki et al., 2008; Meier et al., 2009; Yan et al., 2009). Water, absorbed by hygroscopic or deliquescent aerosols, makes a substantial contribution to visibility reduction (Swietlicki et al., 2008; Chen et al., 2014; Li et al., 2017). Therefore, in addition to the chemical composition of the particulate matter, the ambient RH also has a substantial impact on visibility (Deng et al., 2008a; Yang et al., 2015; Wang X. et al., 2019).

The diurnal variations of PM concentrations show a two-peak pattern. The first peak occurs at 6:00 LT, and the mean values of PM_{10}, $PM_{2.5}$, and PM_1 are 23.4, 20.1, and 16.6 μg/m^3, respectively; the second peak occurs at 18:00 LT, and the mean values of PM_{10}, $PM_{2.5}$, and PM_1 are 24.9, 20.3, and 16.5 μg/m^3. The diurnal variation of PM pollutants can be controlled by many factors, including emission, chemical reactions, and meteorological conditions (Sun et al., 2015; Tao et al., 2015; Du et al., 2020). Zhang and Cao (2015) used a long-term dataset of surface $PM_{2.5}$ concentrations measured at 190 cities of China and found that the diurnal variation of the $PM_{2.5}$-to-CO ratio (an excellent tracer for excluding the influence of primary combustion emissions) consistently displayed a pronounced peak during the afternoon (about 16:00 LT). This indicates that the secondary formation process plays an important role in PM concentrations, especially in the afternoon when the photochemical activities are relatively strong (Huang et al., 2011; Zhou et al., 2014; Du et al., 2020). A more detailed explanation of the diurnal variation of PM concentrations is subject to further studies including more comprehensive observations of the chemical of PM and its precursors. The diurnal variations of $PM_{2.5}$ and PM_1 concentrations are flattened in summer compared to those of other seasons.

In addition to pollutant emissions and topographic conditions, the spatial and temporal distribution of PM is mainly affected by meteorological conditions in the troposphere, especially in the atmospheric boundary layer (ABL) (Li et al., 2017; Song et al., 2017; Chen et al., 2018; Su et al., 2018; Wei et al., 2018). Pollutants

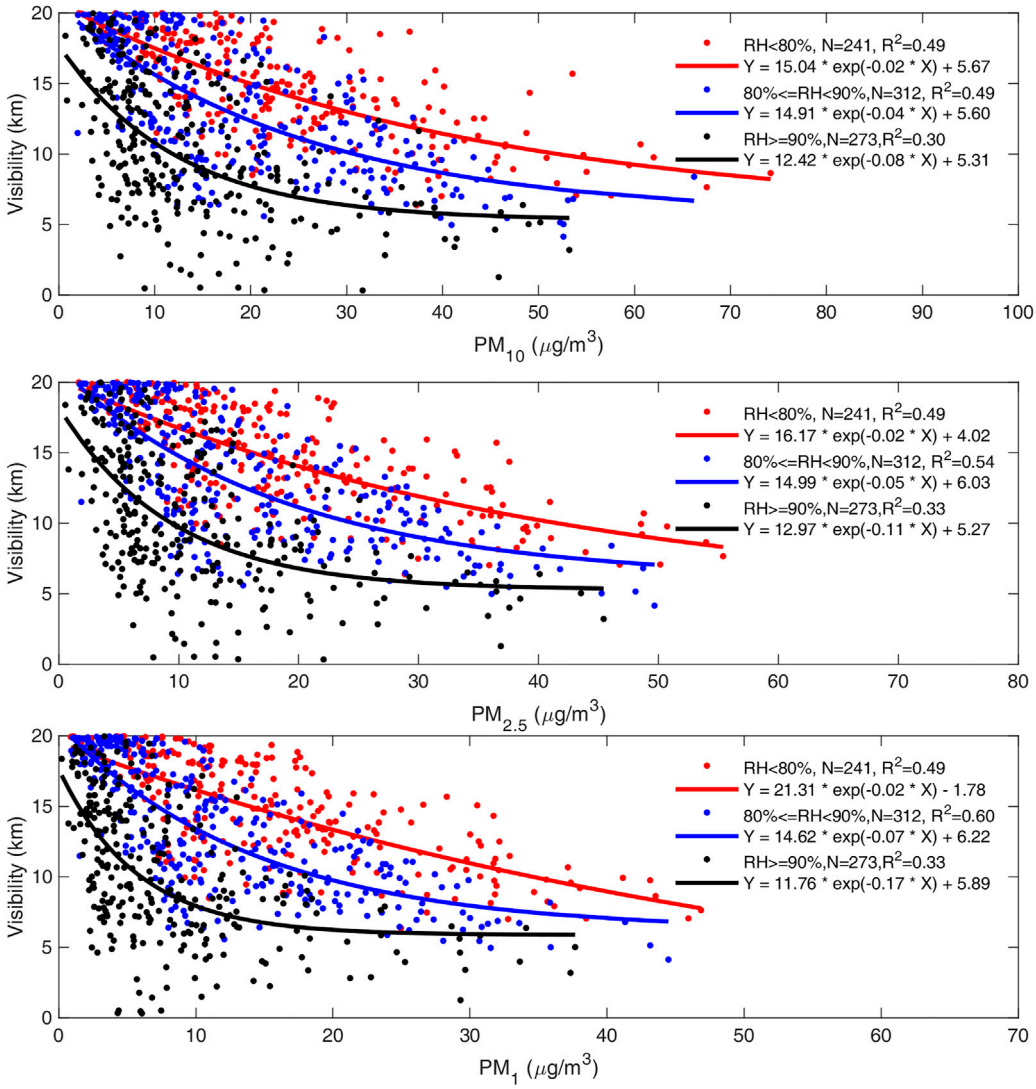

FIGURE 6 | The exponential function fitting between visibility and PM mass concentrations in different RH ranges at Xichong.

within this layer are fully mixed and vertically dispersed due to convection or mechanical turbulence (Seibert et al., 2000). The BLH begins increasing after sunrise (7:00 LT) and reaches a peak with a value of 640 m at 14:00 LT and then decreases to 370 m at 20:00 LT. The BLH determines the volume available for pollution dispersion and transport in the atmosphere. Low BLH and weak turbulence strengthen the accumulation of air pollutants (Petaja et al., 2016; Miao et al., 2018). When the BLH is lower, higher concentrations of pollutants can accumulate, which result in lower visibility. So the diurnal cycles of the BLH exhibit similar patterns to those of visibility.

Relating Aerosol Optical Depth, Visibility, and PM Concentrations

The increase in PM concentration generally leads to reduced visibility (Deng et al., 2008a; Cheng et al., 2008; Li et al., 2017; Wang G. et al., 2019; Kong et al., 2020) and rising AOD (Xiao et al., 2016; Shahzad et al., 2013; 2018). However, the relationship between PM concentration and visibility as well as AOD is complex and nonlinear because of the variability in the particle size distribution, mixing state, and chemical composition of aerosols (Wang X. et al., 2019). The relationship between the AOD and PM can be used to derive the PM concentrations from satellite observations of AOD (Li et al., 2005; Green et al., 2009; van Donkelaar et al., 2010). **Figure 5A** showed the scatter plots of hourly-averaged AOD vs. $PM_{2.5}$. The correlation between AOD and PM is very low, with the coefficients of determination being only 0.11. AOD is the column-integrated aerosol extinction coefficient, while PM observations represent near-surface PM concentration. The relationship between AOD and PM concentrations is, therefore, influenced by the relative humidity, the BLH, and the vertical distribution of aerosol (Dehghan et al., 2017;

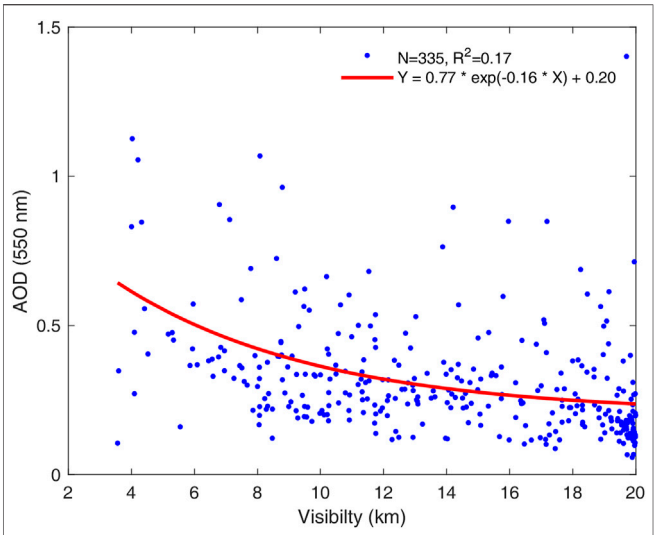

FIGURE 7 | Nonlinear regression fit between AOD and visibility at Xichong.

Shahzad et al., 2018; Filonchyk et al., 2019). The vertical and humidity corrections should be carefully considered in order to better characterize the relationship between AOD and PM. Following the previous studies (Wang et al., 2010; Zheng et al., 2013; Zheng et al., 2017), the column-integrated PM concentrations are first corrected by the BLH as follows:

$$PM_{column} = PM \times BLH. \quad (1)$$

In addition, PM concentrations are measured under a dry condition with the RH <35%. But the hygroscopic growth of particles significantly affects AOD. The effect of relative humidity on AOD has to be considered in order to get a more reliable AOD and PM relationship. Hygroscopic growth factor, f (RH), is one of the most used parameters in describing variations of the aerosol sizes at different ambient RHs (Kotchenruther et al., 1999; Zheng et al., 2013). So, a dehydration adjustment proposed by Zheng et al. (2017) is applied to get the dry condition AOD as follows:

$$AOD_{dry} = \frac{AOD}{f(RH)}. \quad (2)$$

f (RH) can be expressed as follows:

$$f(RH) = 1 + a\left(\frac{RH}{100}\right)^{b}, \quad (3)$$

where a and b are empirical coefficients determined by the aerosol types. The empirical coefficients are based on the previous studies of hygroscopic growing factors in the PRD region (Liu et al., 2008). In the atmosphere, the RH often increases with height within PBL (Zheng et al., 2017; Zhou et al., 2020). This could definitely affect the dehydration adjustment of AOD in **Eqs 2**, **3**. Currently, the surface RH is used to do the adjustment, and the vertical variation in RH has not been considered, which could cause the dry condition AOD to be somehow overestimated compared to its true value.

Figure 5B exhibited the linear regression between hourly-averaged AOD and $PM_{2.5}$ mass concentrations with the vertical and humidity corrections. There is a moderate correlation with an R value of 0.47 between $PM_{2.5}$ and AOD after these corrections, with the coefficients of determination ~0.22 at a 95% confidence level. The RMSE decreased from 14.7 (without corrections) to 8.8 (with correction). There are several factors resulting in the weak correlation between PM and AOD at Xichong. The aerosol loading is relatively low in the background site, and the variation ranges of PM and AOD are narrower compared to those in the urban sites. Generally, higher correlation coefficients were observed at urban sites than at suburban sites (Zheng et al., 2013). In addition, the AOD_{dry} is adjusted based on surface RH, and the vertical variation in RH has not been considered. The AOD_{dry} obtained here could somehow deviate from its true value (Zheng et al., 2017). After the vertical and humidity corrections, the correlative coefficients R between PM_{10}, PM_1, and AOD are 0.44, and 0.46 at a 95% confidence level, respectively.

PM mass concentrations are also corrected using the hygroscopic growth factor in order to consider the effect of humidity on the PM mass concentrations. **Figures 5C, D** showed the scatter plots of $PM_{2.5}$ vs. visibility before and after humidity correction. There is a significant anti-correlation between PM and visibility because the increase of surface PM concentrations impairs the horizontal visibility. There are significant improvements in the correlations between PM and visibility after humidity corrections. The data points are more compact with the determination coefficient R^2 increasing from 0.34 (without correction) to 0.54 (with correction). The relationship between PM_{10}, PM_1, and visibility is similar to that of $PM_{2.5}$ and visibility.

It is known that relative humidity is the most influencing factor on the visual impairment in the context of high aerosol mass loading (Chen et al., 2014). The formation of secondary aerosol species could be enhanced under high-humidity conditions (Yu et al., 2005; Hennigan et al., 2008). Additionally, fine hydrophilic aerosols could increase to a larger size by taking ambient water vapor, resulting in a higher extent of light extinction and visibility deterioration (Xiao et al., 2011; Liu et al., 2012). **Figure 6** shows the variation of visibility with relative humidity and the PM mass concentrations. RH was classified into three ranges: RH ≥90%, 90% > RH ≥ 80%, and RH <80%. It can be seen that the visibility decreases significantly with increasing RH. Moreover, the visibility decreases in a nonlinear tendency with the increase of PM mass concentrations. The highest correlation between visibility and PM concentrations is observed in the RH range of 80–90%, with the coefficients of determination being 0.49, 0.54, and 0.60 for visibility vs. PM_{10}, $PM_{2.5}$, and PM_1, respectively. Under excessively high RH (>90%), the variation of visibility becomes not significant when the mass concentrations of PM_{10}, $PM_{2.5}$, and PM_1 are greater than 40, 30, and 20 μg/m^3.

The relationship between AOD and visibility is illustrated in **Figure 7**. There is a clear anti-correlation between AOD and visibility, although the coefficient of determination of exponential fitting was only 0.17. The higher aerosol loading in the atmosphere results in increased extinction of light and hence

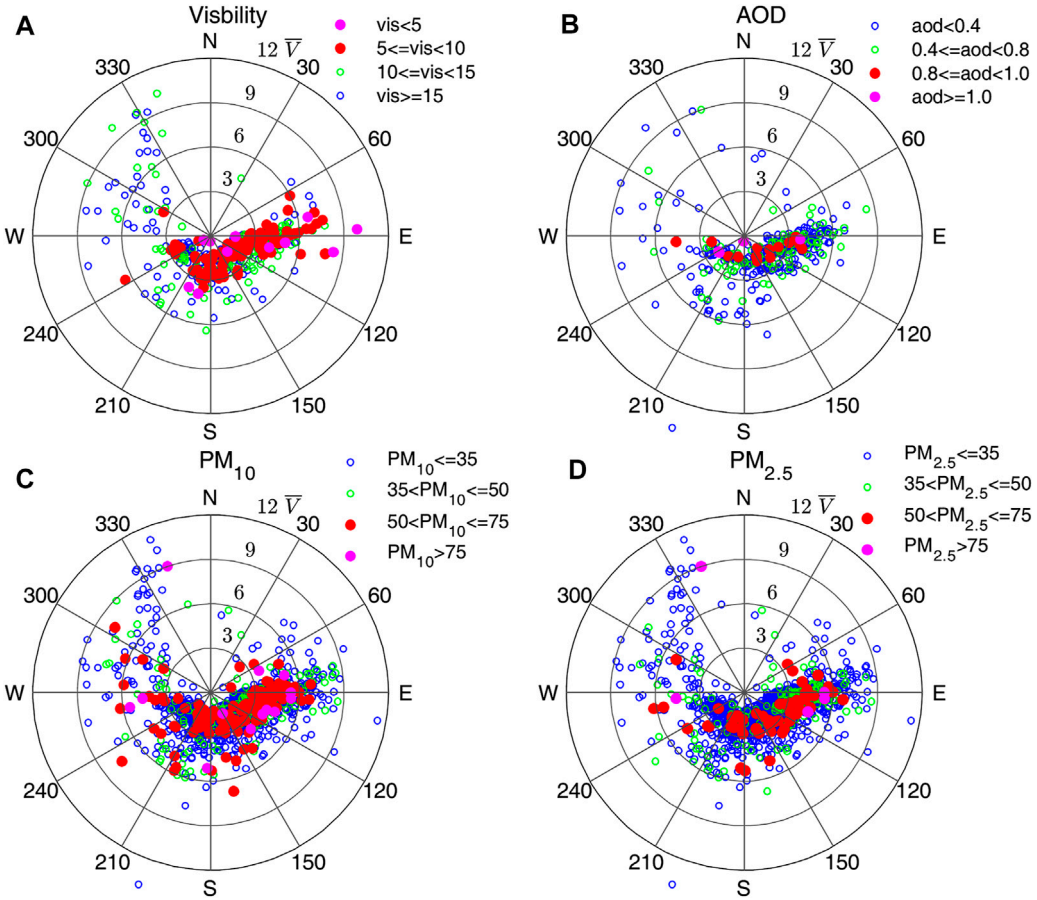

FIGURE 8 | Wind rose as scatter plots with different ranges of daily visibility **(A)**, AOD **(B)**, PM_{10} **(C)**, and $PM_{2.5}$ **(D)** at Xichong.

decreases visibility. In addition to the aerosol loading, the effect of meteorological conditions on visibility is also very important (Wu et al., 2007; Deng et al., 2008b). The effects of humidity and BLH on visibility are significant as previous discussion. We also investigated the effects of ambient temperature and surface pressure on visibility, AOD, and PM mass concentrations. Visibility, AOD, and PM mass concentrations show strong independence on ambient temperature and surface pressure with R^2 less than 0.03 at a 95% confidence level.

Effect of Wind on Aerosol Optical Depth, PM, and Visibility

Wind direction and speed have an important effect on the transport of air pollutants (Yang et al., 2017; Meng et al., 2019; Liu et al., 2020). The influence of surface wind speed and direction on AOD, PM, and visibility is investigated in the section. **Figure 8** shows the relationships of surface wind speed, direction, and daily visibility (a), AOD (b), PM10 (c), and PM2.5 (d). At Xichong, low visibility and high aerosol loading tend to appear at a low wind speed. About 80% of the low visibility (VIS <5 km), high PM mass concentrations (PM_{10} > 50 μg/m^3, $PM_{2.5}$ > 50 μg/m^3) and 100% of high aerosol loading (AOD>1.0) occur on days when the wind speed is less than 5 m/s. The dominant wind direction is concentrated at easterly and southerly wind on low-visibility and high-AOD days.

Backward trajectory analysis is an effective method to clarify the transport of air parcels in the atmosphere (Cheng et al., 2015). We calculated and clustered backward trajectories of air mass using the Hybrid Single-Particle Lagrangian Trajectory (HYSPLIT) model developed by the Air Resources Laboratory of the National Oceanic and Atmospheric Administration (NOAA), United States (Stein et al., 2015). **Figure 9** shows the clustered 72-h backward trajectories ending at 1500 m, 1000 m, and 500 m in January (a–c), April (d–e), July (f–h), and October (i–l) calculated by the HYSPLIT model. The airflows from the west and northwest directions occupy about 80% at Xichong in winter. The airflows from the south directions increase to over 50% during the spring and summer months. The airflows from the southwest increase significantly in spring and summer, especially at higher heights (1000 m and 1500 m), which verify the effects of air pollutants transported from Southeastern Asia on the air quality at Xichong. The air mass mainly from northeast directions in autumn, especially at lower heights (500 m), contributes to the degradation of visibility and enhancement of PM mass concentrations at Xichong.

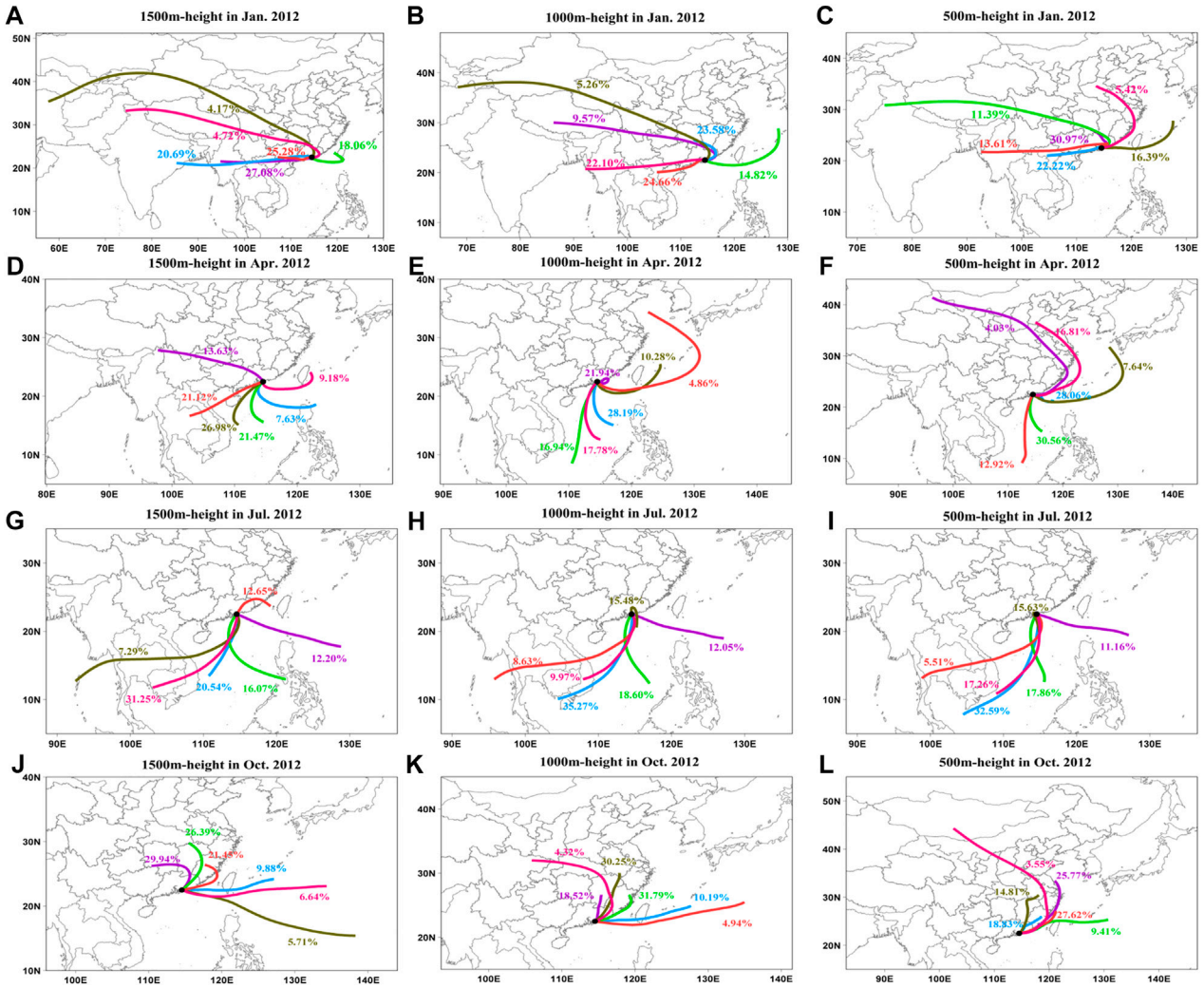

FIGURE 9 | Clustered 72-h backward trajectories of air mass ending at 1500 m (left panel), 1000 m (middle panel), and 500 m (right panel) in January **(A–C)**, April **(D–F)**, July **(G–I)**, and October **(J–L)** 2012, calculated by the Hybrid Single-Particle Lagrangian Trajectory (HYSPLIT) model.

CONCLUSION

Based on the observations of AOD, visibility, and PM mass concentrations during the period of 2011–2018 at Xichong, a long-term analysis of the parameters relative to the air quality is performed. The mean (±σ) of visibility and AOD during the study period is 12.6 ± 2.3 km and 0.38 ± 0.07, respectively. The multi-year averaged mass concentrations of PM_{10}, $PM_{2.5}$, and PM_1 during the study period are 23.7 ± 12.6 μg/m^3, 19.7 ± 11.0 μg/m^3, and 16.1 ± 10.1 μg/m^3, respectively. The daily PM_{10} and $PM_{2.5}$ at Xichong are lower than those in other sites in the PRD because the air masses are relatively cleaner; almost all the daily PM concentrations are below the second-level limit of Chinese ambient air quality standards (GB 3095-2012), which suggested that they may represent the air quality of the background level in the PRD region. Negative trends in PM_{10}, $PM_{2.5}$, and PM_1 are significant at a 95% confidence level with the magnitudes of −2.13, −1.82, and −1.37 yr^{-1}, respectively. The decrease in aerosol loadings at Xichong is attributed to the strict environmental regulations for improving air quality.

AOD reached its maximum during the spring months with the mean values of 0.61, 0.59, and 0.49 in March, April, and May, respectively. The peak and the lowest values of PM mass concentrations were observed in January and June, respectively. The averaged PM_1/PM_{10}, $PM_{2.5}/PM_{10}$, and $PM_1/PM_{2.5}$ ratios during the study period are 0.65, 0.78, and 0.82, respectively. The ratio of PM_{10} and $PM_{2.5}$ can be significantly affected by secondary aerosol formation in the atmosphere (Kong et al., 2017; Munir, 2017; Fan et al., 2021). Secondary aerosols contribute significantly to PM mass concentrations, especially $PM_{2.5}$ concentrations (Zhao et al., 2018; Fan et al., 2020; Spandana et al., 2021). The high ratios of $PM_{2.5}$ to PM_{10} suggest that aerosol pollution at Xichong is mainly caused by fine particles more from anthropogenic sources (Chu et al.,

2015; Kong and Yi, 2015). The PM_1/PM_{10} and $PM_1/PM_{2.5}$ ratios exhibit a remarkable reduction in summer because the hygroscopic growth of a large fraction of submicrometer particles under higher RH may increase the proportion of $PM_{2.5}$ (Zhao et al., 2018; Wang et al., 2020; Fan et al., 2021). The seasonality of the visibility is inversed to those of PM mass concentrations and AOD at Xichong. The visibility was higher during the summer and autumn months and lower during the winter and spring months.

The visibility and PM concentrations show significant diurnal cycles. The visibility reaches its maximum values at noon and then drops to its minimum during the night, which is similar to the diurnal variation of BLH. The diurnal variations of PM concentrations show a two-peak pattern possibly caused by the more active photochemistry process due to the increasing solar radiation during the daytime. A more detailed explanation of the diurnal variation of PM concentrations is subject to further studies including more comprehensive observations of the chemical of PM and its precursors.

AOD, visibility, and PM mass concentrations are physically related. There is a clear anti-correlation between AOD and visibility at the Xichong site, although the coefficient of determination of exponential fitting was only 0.17. The highest correlation between visibility and PM concentrations is observed in the RH range of 80–90%, with the coefficients of determination being 0.49, 0.54, and 0.60 for visibility vs. PM_{10}, $PM_{2.5}$, and PM_1, respectively. Under excessively high RH (>90%), the variation of visibility becomes insignificant when the mass concentrations of PM_{10}, $PM_{2.5}$, and PM_1 are greater than 40, 30, and 20 $\mu g/m^3$.

At Xichong, low visibility and high aerosol loading tend to appear with a low wind speed. About 80% of the low visibility (VIS <5 km), high PM mass concentrations (PM_{10} > 50, $PM_{2.5}$ > 50) and 100% of high aerosol loading (AOD >1.0) occur on days when the wind speed is less than 5 m/s. The dominant wind direction is concentrated at easterly and southerly wind in low-visibility and high-AOD days. Understanding of variability of surface particle concentration and column-integrated aerosol loading at multiple temporal scales at this background site in the PRD region would provide a scientific basis for the adoption of pollution prevention and control measures.

DATA AVAILABILITY STATEMENT

The original contributions presented in the study are included in the article/**Supplementary Material**, further inquiries can be directed to the corresponding author.

AUTHOR CONTRIBUTIONS

XF, XX, and HC contributed to the conceptualization. XF contributed to methodology, formal analysis, and writing—original draft preparation. XX and HC contributed to reviewing and editing. YZ contributed to software. JL contributed to validation. HY and HL contributed to data curation. All authors have read and agreed to the published version of the manuscript.

FUNDING

This research was supported by the National Natural Science Foundation of China granting (42030708, 41775033), the Strategic Priority Research Program of the Chinese Academy of Sciences (XDA17040511), and the Opening Foundation of Key Laboratory of Atmosphere Sounding, China Meteorological Administration and CMA Research Centre on Meteorological Observation Engineering Technology (U2021Z03).

ACKNOWLEDGMENTS

We appreciate the open-access data released by European Centre for Medium-Range Weather Forecasts. We also thank Yaqiang Wang for developing the GIS software for meteorological data (MeteoinfoMap, http://www.meteothink.org).

SUPPLEMENTARY MATERIAL

The Supplementary Material for this article can be found online at: https://www.frontiersin.org/articles/10.3389/fenvs.2022.893408/full#supplementary-material

REFERENCES

Ansmann, A., Engelmann, R., Althausen, D., Wandinger, U., Hu, M., Zhang, Y. H., et al. (2005). High Aerosol Load Over the Pearl River Delta, China, Observed with Raman Lidar and Sun Photometer. *Geophys. Res. Lett.* 32 (13), L13815. doi:10.1029/2005gl023094

Cao, J., Lee, S. C., Ho, K. F., Zhang, X. Y., Zou, S. C., Fung, K., et al. (2003). Characteristics of Carbonaceous Aerosol in Pearl River Delta Region, China during 2001 Winter Period. *Atmos. Environ.* 37 (11), 1451–1460. doi:10.1016/s1352-2310(02)01002-6

Chen, J., Qiu, S., Shang, J., Wilfrid, O. M. F., Liu, X., Tian, H., et al. (2014). Impact of Relative Humidity and Water Soluble Constituents of PM2.5 on Visibility Impairment in Beijing, China. *Aerosol Air Qual. Res.* 14 (1), 260–268. doi:10.4209/aaqr.2012.12.0360

Chen, Y., An, J., Sun, Y., Wang, X., Qu, Y., Zhang, J., et al. (2018). Nocturnal Low-Level Winds and Their Impacts on Particulate Matter over the Beijing Area. *Adv. Atmos. Sci.* 35 (12), 1455–1468. doi:10.1007/s00376-018-8022-9

Cheng, Y. F., Wiedensohler, A., Eichler, H., Heintzenberg, J., Tesche, M., Ansmann, A., et al. (2008). Relative Humidity Dependence of Aerosol Optical Properties and Direct Radiative Forcing in the Surface Boundary Layer at Xinken in Pearl River Delta of China: An Observation Based Numerical Study. *Atmos. Environ.* 42 (25), 6373–6397. doi:10.1016/j.atmosenv.2008.04.009

Cheng, T., Xu, C., Duan, J., Wang, Y., Leng, C., Tao, J., et al. (2015). Seasonal Cariation and Difference of Aerosol Optical Properties in Columnar and Surface Atmospheres Over Shanghai. *Atmos. Environ.* 123, 315–326. doi:10.1016/j.atmosenv.2015.05.029

Chu, B., Liu, T., Zhang, X., Liu, Y., Ma, Q., Ma, J., et al. (2015). Secondary Aerosol Formation and Oxidation Capacity in Photooxidation in the Presence of Al2O3

Seed Particles and SO2. *Sci. China Chem.* 58 (9), 1426–1434. doi:10.1007/s11426-015-5456-0

Cubison, M. J., Ervens, B., Feingold, G., Docherty, K. S., Ulbrich, I. M., Shields, L., et al. (2008). The Influence of Chemical Composition and Mixing State of Los Angeles Urban Aerosol on CCN Number and Cloud Properties. *Atmos. Chem. Phys* 8 (18), 5649–5667. doi:10.5194/acp-8-5649-2008

Dehghan, M., Omidvar, K., Mozafari, K., and Mazidi, A. (2017). Estimation of Relationship Between Aerosol Optical Depth, PM10 and Visibility in Separation of Synoptic Codes, as Important Parameters in Researches Connected to Aerosols; Using Genetic Algorithm in Yazd. *Int. J. Environ. Sci. Nat. Res.* 7 (4). doi:10.19080/IJESNR.2017.07.5557

Deng, X., Tie, X., Wu, D., Zhou, X., Bi, X., Tan, H., et al. (2008a). Long-term Trend of Visibility and its Characterizations in the Pearl River Delta (PRD) Region, China. *Atmos. Environ.* 42 (7), 1424–1435. doi:10.1016/j.atmosenv.2007.11.025

Deng, X., Tie, X., Zhou, X., Wu, D., Zhong, L., Tan, H., et al. (2008b). Effects of Southeast Asia Biomass Burning on Aerosols and Ozone Concentrations over the Pearl River Delta (PRD) Region. *Atmos. Environ.* 42 (36), 8493–8501. doi:10.1016/j.atmosenv.2008.08.013

Du, Q., Zhao, C., Zhang, M., Dong, X., Chen, Y., Liu, Z., et al. (2020). Modeling Diurnal Variation of Surface PM_{2.5} Concentrations over East China with WRF-Chem: Impacts from Boundary-Layer Mixing and Anthropogenic Emission. *Atmos. Chem. Phys.* 20 (5), 2839–2863. doi:10.5194/acp-20-2839-2020

Dubovik, O., Smirnov, A., Holben, B. N., King, M. D., Kaufman, Y. J., Eck, T. F., et al. (2000). Accuracy Assessments of Aerosol Optical Properties Retrieved from Aerosol Robotic Network (AERONET) Sun and Sky Radiance Measurements. *J. Geophys. Res.* 105 (D8), 9791–9806. doi:10.1029/2000jd900040

Fan, H., Zhao, C. F., and Yang, Y. K. (2020). A Comprehensive Analysis of the Spatio-Temporal Variation of Urban Air Pollution in China during 2014-2018. *Atmos. Environ.* 220, 117066. doi:10.1016/j.atmosenv.2019.117066

Fan, H., Zhao, C. F., Yang, Y. K., and Yang, X. C. (2021). Spatio-Temporal Variations of the PM2.5/PM10 Ratios and its Application to Air Pollution Type Classification in China. *Front. Environ. Sci.* 9. doi:10.3389/fenvs.2021.692440

Fang, X., Fan, Q., Liao, Z., Xie, J., Xu, X., and Fan, S. (2019). Spatial-temporal Characteristics of the Air Quality in the Guangdong–Hong Kong–Macau Greater Bay Area of China during 2015-2017. *Atmos. Environ.* 210, 14–34. doi:10.1016/j.atmosenv.2019.04.037

Filonchyk, M., Yan, H. W., Zhang, Z. R., Yang, S. W., Li, W., and Li, Y. M. (2019). Combined Use of Satellite and Surface Observations to Study Aerosol Optical Depth in Different Regions of China. *Sci. Rep.* 9, 6174. doi:10.1038/s41598-019-42466-6

Green, M., Kondragunta, S., Ciren, P., and Xu, C. (2009). Comparison of GOES and MODIS Aerosol Optical Depth (AOD) to Aerosol Robotic Network (AERONET) AOD and IMPROVE PM2.5Mass at Bondville, Illinois. *J. Air & Waste Manag. Assoc.* 59 (9), 1082–1091. doi:10.3155/1047-3289.59.9.1082

Hennigan, C. J., Bergin, M. H., Dibb, J. E., and Weber, R. J. (2008). Enhanced Secondary Organic Aerosol Formation Due to Water Uptake by Fine Particles. *Geophys. Res. Lett.* 35 (18). doi:10.1029/2008gl035046

Holben, B. N., Eck, T. F., Slutsker, I., Tanre, D., Buis, J. P., Setzer, A., et al. (1998). AERONET - A Dederated Instrument Network and Data Archive for Aerosol Characterization. *Remote Sens. Environ.* 66 (1), 1–16. doi:10.1016/S0034-4257(98)00031-5

Hu, M., Wu, Z., Slanina, J., Lin, P., Liu, S., and Zeng, L. (2008). Acidic Gases, Ammonia and Water-Soluble Ions in PM2.5 at a Coastal Site in the Pearl River Delta, China. *Atmos. Environ.* 42 (25), 6310–6320. doi:10.1016/j.atmosenv.2008.02.015

Huang, X.-F., He, L.-Y., Hu, M., Canagaratna, M. R., Kroll, J. H., Ng, N. L., et al. (2011). Characterization of Submicron Aerosols at a Rural Site in Pearl River Delta of China Using an Aerodyne High-Resolution Aerosol Mass Spectrometer. *Atmos. Chem. Phys.* 11 (5), 1865–1877. doi:10.5194/acp-11-1865-2011

Kong, L., Hu, M., Tan, Q., Feng, M., Qu, Y., An, J., et al. (2020). Aerosol Optical Properties under Different Pollution Levels in the Pearl River Delta (PRD) Region of China. *J. Environ. Sci.* 87, 49–59. doi:10.1016/j.jes.2019.02.019

Kong, L., Xin, J., Liu, Z., Zhang, K., Tang, G., Zhang, W., et al. (2017). The PM2.5 Threshold for Aerosol Extinction in the Beijing Megacity. *Atmos. Environ.* 167, 458–465. doi:10.1016/j.atmosenv.2017.08.047

Kong, W., and Yi, F. (2015). Convective Boundary Layer Evolution From Lidar Backscatter and its Relationship with Surface Aerosol Concentration at a Location of a Central China Megacity. *J. Geophys. Res. Atmos.* 120 (15), 7928–7940. doi:10.1002/2015jd023248

Kotchenruther, R. A., Hobbs, P. V., and Hegg, D. A. (1999). Humidification Factors for Atmospheric Aerosols off the Mid-Atlantic Coast of the United States. *J. Geophys. Res.* 104 (D2), 2239–2251. doi:10.1029/98jd01751

Lan, Z.-J., Chen, D.-L., Li, X., Huang, X.-F., He, L.-Y., Deng, Y.-G., et al. (2011). Modal Characteristics of Carbonaceous Aerosol Size Distribution in an Urban Atmosphere of South China. *Atmos. Res.* 100 (1), 51–60. doi:10.1016/j.atmosres.2010.12.022

Li, C., Lau, A. K.-H., Mao, J., and Chu, D. A. (2005). Retrieval, Validation, and Application of the 1-km Aerosol Optical Depth from MODIS Measurements Over Hong Kong. *IEEE Trans. Geosci. Remote Sens.* 43 (11), 2650–2658. doi:10.1109/tgrs.2005.856627

Li, Y., Huang, H. X. H., Griffith, S. M., Wu, C., Lau, A. K. H., and Yu, J. Z. (2017). Quantifying the Relationship between Visibility Degradation and PM2.5 Constituents at a Suburban Site in Hong Kong: Differentiating Contributions from Hydrophilic and Hydrophobic Organic Compounds. *Sci. Total Environ.* 575, 1571–1581. doi:10.1016/j.scitotenv.2016.10.082

Liu, X., Cheng, Y., Zhang, Y., Jung, J., Sugimoto, N., Chang, S.-Y., et al. (2008). Influences of Relative Humidity and Particle Chemical Composition on Aerosol Scattering Properties during the 2006 PRD Campaign. *Atmos. Environ.* 42 (7), 1525–1536. doi:10.1016/j.atmosenv.2007.10.077

Liu, X., Zhang, Y., Cheng, Y., Hu, M., and Han, T. (2012). Aerosol Hygroscopicity and its Impact on Atmospheric Visibility and Radiative Forcing in Guangzhou during the 2006 PRIDE-PRD Campaign. *Atmos. Environ.* 60, 59–67. doi:10.1016/j.atmosenv.2012.06.016

Liu, X., Zhang, Y., Wen, M., Wang, J., Jung, J., Chang, S.-y., et al. (2010). A Closure Study of Aerosol Hygroscopic Growth Factor during the 2006 Pearl River Delta Campaign. *Adv. Atmos. Sci.* 27 (4), 947–956. doi:10.1007/s00376-009-9150-z

Liu, Y., He, J., Lai, X., Zhang, C., Zhang, L., Gong, S., et al. (2020). Influence of Atmospheric Circulation on Aerosol and its Optical Characteristics in the Pearl River Delta Region. *Atmos.* 11 (3). doi:10.3390/atmos11030288

Lu, M., Zheng, J., Huang, Z., Wu, C., Zheng, C., Jia, G., et al. (2021). Insight into the Characteristics of Carbonaceous Aerosols at Urban and Regional Sites in the Downwind Area of Pearl River Delta Region, China. *Sci. Total Environ.* 778, 146251. doi:10.1016/j.scitotenv.2021.146251

Ma, Y., Lu, K., Chou, C. C.-K., Li, X., and Zhang, Y. (2017). Strong Deviations from the NO-NO2-O3 Photostationary State in the Pearl River Delta: Indications of Active Peroxy Radical and Chlorine Radical Chemistry. *Atmos. Environ.* 163, 22–34. doi:10.1016/j.atmosenv.2017.05.012

Meier, J., Wehner, B., Massling, A., Birmili, W., Nowak, A., Gnauk, T., et al. (2009). Hygroscopic Growth of Urban Aerosol Particles in Beijing (China) during Wintertime: a Comparison of Three Experimental Methods. *Atmos. Chem. Phys.* 9 (18), 6865–6880. doi:10.5194/acp-9-6865-2009

Meng, C., Cheng, T., Bao, F., Gu, X., Wang, J., Zuo, X., et al. (2020). The Impact of Meteorological Factors on Fine Particulate Pollution in Northeast China. *Aerosol. Air Qual. Res.* 20, 1618–1628. doi:10.4209/aaqr.2019.10.0534

Miao, Y., Liu, S., Guo, J., Huang, S., Yan, Y., and Lou, M. (2018). Unraveling the Relationships between Boundary Layer Height and PM2.5 Pollution in China Based on Four-Year Radiosonde Measurements. *Environ. Pollut.* 243, 1186–1195. doi:10.1016/j.envpol.2018.09.070

Munir, S. (2017). Analysing Temporal Trends in the Ratios of PM2.5/PM10 in the UK. *Aerosol Air Qual. Res.* 17 (1), 34–48. doi:10.4209/aaqr.2016.02.0081

Petäjä, T., Järvi, L., Kerminen, V. M., Ding, A. J., Sun, J. N., Nie, W., et al. (2016). Enhanced Air Pollution via Aerosol-Boundary Layer Feedback in China. *Sci. Rep.* 6, 18998. doi:10.1038/srep18998

Seibert, P., Beyrich, F., Gryning, S. E., Joffre, S., Rasmussen, A., and Tercier, P. (2000). Review and Intercomparison of Operational Methods for the Determination of the Mixing Height. *Atmos. Environ.* 34 (7), 1001–1027. doi:10.1016/s1352-2310(99)00349-0

Shahzad, M. I., Nichol, J. E., Campbell, J. R., and Wong, M. S. (2018). Assessment of MODIS, OMI, MISR and CALIOP Aerosol Products for Estimating Surface Visual Range: A Mathematical Model for Hong Kong. *Remote Sens.* 10 (9). doi:10.3390/rs10091333

Shahzad, M. I., Nichol, J. E., Wang, J., Campbell, J. R., and Chan, P. W. (2013). Estimating Surface Visibility at Hong Kong From Ground-Based LIDAR, Sun Photometer and Operational MODIS Products. *J. Air Waste Manag. Assoc.* 63 (9), 1098–1110. doi:10.1080/10962247.2013.801372

Song, C., Wu, L., Xie, Y., He, J., Chen, X., Wang, T., et al. (2017). Air Pollution in China: Status and Spatiotemporal Variations. *Environ. Pollut.* 227, 334–347. doi:10.1016/j.envpol.2017.04.075

Spandana, B., Srinivasa Rao, S., Upadhya, A. R., Kulkarni, P., and Sreekanth, V. (2021). PM2.5/PM10 Ratio Characteristics over Urban Sites of India. *Adv. Space Res.* 67 (10), 3134–3146. doi:10.1016/j.asr.2021.02.008

Stein, A. F., Draxler, R. R., Rolph, G. D., Stunder, B. J. B., Cohen, M. D., and Ngan, F. (2015). NOAA's HYSPLIT Atmospheric Transport and Dispersion Modeling System. *Bull. Amer. Meteor. Soc.* 86, 2059–2077. doi:10.1175/BAMS-D-14-00110.1

Su, T., Li, Z., and Kahn, R. (2018). Relationships between the Planetary Boundary Layer Height and Surface Pollutants Derived from Lidar Observations over China: Regional Pattern and Influencing Factors. *Atmos. Chem. Phys.* 18 (21), 15921–15935. doi:10.5194/acp-18-15921-2018

Sun, Y., Du, W., Wang, Q., Zhang, Q., Chen, C., Chen, Y., et al. (2015). Real-Time Characterization of Aerosol Particle Composition above the Urban Canopy in Beijing: Insights into the Interactions between the Atmospheric Boundary Layer and Aerosol Chemistry. *Environ. Sci. Technol.* 49 (19), 11340–11347. doi:10.1021/acs.est.5b02373

Swietlicki, E., Hansson, H.-C., Hämeri, K., Svenningsson, B., Massling, A., McFiggans, G., et al. (2008). Hygroscopic Properties of Submicrometer Atmospheric Aerosol Particles Measured with H-TDMA Instruments in Various Environments-A Review. *Tellus B Chem. Phys. Meteorology* 60 (3), 432–469. doi:10.1111/j.1600-0889.2008.00350.x

Tao, J., Zhang, L., Gao, J., Wang, H., Chai, F., and Wang, S. (2015). Aerosol Chemical Composition and Light Scattering during a Winter Season in Beijing. *Atmos. Environ.* 110, 36–44. doi:10.1016/j.atmosenv.2015.03.037

van Donkelaar, A., Martin, R. V., Brauer, M., Kahn, R., Levy, R., Verduzco, C., et al. (2010). Global Estimates of Ambient Fine Particulate Matter Concentrations from Satellite-Based Aerosol Optical Depth: Development and Application. *Environ. Health Perspect.* 118 (6), 847–855. doi:10.1289/ehp.0901623

Vogelezang, D. H. P., and Holtslag, A. A. M. (1996). Evaluation and Model Impacts of Alternative Boundary-Layer Height Formulations. *Boundary-Layer Meteorol.* 81 (3-4), 245–269. doi:10.1007/bf02430331

Wang, G., Deng, X.-J., Wang, C.-L., Zhang, X.-Y., Yan, H.-H., Chen, D.-H., et al. (2019a). A New and Detailed Assessment of the Spatiotemporal Characteristics of the SO2 Distribution in the Pearl River Delta Region of China and the Effect of SO2 Emission Reduction. *Aerosol Air Qual. Res.* 19 (8), 1900–1910. doi:10.4209/aaqr.2019.03.0135

Wang, J., Xu, X. G., Spurr, R., Wang, Y. X., and Drury, E. (2010). Improved Algorithm for MODIS Satellite Retrievals of Aerosol Optical Thickness Over Land in Dusty Atmosphere: Implications for Air Quality Monitoring in China. *Remote Sens. Environ.* 114 (11), 2575–2583. doi:10.1016/j.rse.2010.05.034

Wang, M., Chen, Y., Fu, H., Qu, X., Li, B., Tao, S., et al. (2020). An Investigation on Hygroscopic Properties of 15 Black Carbon (BC)-containing Particles from Different Carbon Sources: Roles of Organic and Inorganic Components. *Atmos. Chem. Phys.* 20 (13), 7941–7954. doi:10.5194/acp-20-7941-2020

Wang, X., Zhang, R., and Yu, W. (2019b). The Effects of PM 2.5 Concentrations and Relative Humidity on Atmospheric Visibility in Beijing. *J. Geophys. Res. Atmos.* 124 (4), 2235–2259. doi:10.1029/2018jd029269

Wei, W., Zhang, H., Wu, B., Huang, Y., Cai, X., Song, Y., et al. (2018). Intermittent Turbulence Contributes to Vertical Dispersion of PM_{2.5} in the North China Plain: Cases from Tianjin. *Atmos. Chem. Phys.* 18 (17), 12953–12967. doi:10.5194/acp-18-12953-2018

Wu, D., Deng, X., Li, F., and Tan, H. (2007). Effect of Atmospheric Haze on the Deterioration of Visibility over the Pearl River Delta. *J. Meteorological Res.* 21 (2), 215–223.

Wu, Z., Zhang, Y., Zhang, L., Huang, M., Zhong, L., Chen, D., et al. (2019). Trends of Outdoor Air Pollution and the Impact on Premature Mortality in the Pearl River Delta Region of Southern China during 2006-2015. *Sci. Total Environ.* 690, 248–260. doi:10.1016/j.scitotenv.2019.06.401

Xia, X., Qi, Q., Liang, H., Zhang, A., Jiang, L., Ye, Y., et al. (2017). Pattern of Spatial Distribution and Temporal Variation of Atmospheric Pollutants during 2013 in Shenzhen, China. *Ijgi* 6 (2), 2. doi:10.3390/ijgi6010002

Xiao, R., Takegawa, N., Zheng, M., Kondo, Y., Miyazaki, Y., Miyakawa, T., et al. (2011). Characterization and Source Apportionment of Submicron Aerosol with Aerosol Mass Spectrometer during the PRIDE-PRD 2006 Campaign. *Atmos. Chem. Phys.* 11 (14), 6911–6929. doi:10.5194/acp-11-6911-2011

Xiao, Z. Y., Jiang, H., and Song, X. D. (2016). Aerosol Optical Thickness Over Pearl River Delta Region, China. *Int. J. Remote Sens.* 38 (1), 258–272. doi:10.1080/01431161.2016.1264024

Yan, P., Pan, X., Tang, J., Zhou, X., Zhang, R., and Zeng, L. (2009). Hygroscopic Growth of Aerosol Scattering Coefficient: A Comparative Analysis between Urban and Suburban Sites at Winter in Beijing. *Particuology* 7 (1), 52–60. doi:10.1016/j.partic.2008.11.009

Yang, J. X., Lau, A. K. H., Fung, J. C. H., Zhou, W., and Wenig, M. (2012). An Air Pollution Episode and its Formation Mechanism during the Tropical Cyclone Nuri's Landfall in a Coastal City of South China. *Atmos. Environ.* 54, 746–753. doi:10.1016/j.atmosenv.2011.12.023

Yang, W., Ji, Y., Lin, H. T., Yang, Y., Kang, S. B., and Yu, J. Y. (2015). "Ambient Occlusion via Compressive Visibility Estimation," in 2015 Ieee Conference on Computer Vision and Pattern Recognition (Cvpr), Boston, MA, USA, 7-12 June 2015, 3882–3889.

Yang, Y., Russell, L. M., Lou, S. J., Liao, H., Guo, J. P., Liu, Y., et al. (2017). Dust-Wind Interactions Can Intensify Aerosol Pollution Over Eastern China. *Nat. Comm.* 8, 15333. doi:10.1038/ncomms15333

Yu, L. E., Shulman, M. L., Kopperud, R., and Hildemann, L. M. (2005). Characterization of Organic Compounds Collected during Southeastern Aerosol and Visibility Study: Water-Soluble Organic Species. *Environ. Sci. Technol.* 39 (3), 707–715. doi:10.1021/es0489700

Yu, M., Zhu, Y., Lin, C. J., Wang, S., Xing, J., Jang, C., et al. (2009). Effects of Air Pollution Control Measures on Air Quality Improvement in Guangzhou, China. *J. Environ. Manage* 244, 127–137. doi:10.1016/j.jenvman.2019.05.046

Yue, D. L., Hu, M., Wang, Z. B., Wen, M. T., Guo, S., Zhong, L. J., et al. (2013). Comparison of Particle Number Size Distributions and New Particle Formation between the Urban and Rural Sites in the PRD Region, China. *Atmos. Environ.* 76, 181–188. doi:10.1016/j.atmosenv.2012.11.018

Zhang, Q., Zheng, Y., Tong, D., Shao, M., Wang, S., Zhang, Y., et al. (2019). Drivers of Improved PM 2.5 Air Quality in China from 2013 to 2017. *Proc. Natl. Acad. Sci. U.S.A.* 116 (49), 24463–24469. doi:10.1073/pnas.1907956116

Zhang, Y. H., Hu, M., Zhong, L. J., Wiedensohler, A., Liu, S. C., Andreae, M. O., et al. (2008). Regional Integrated Experiments on Air Quality over Pearl River Delta 2004 (PRIDE-Prd2004): Overview. *Atmos. Environ.* 42 (25), 6157–6173. doi:10.1016/j.atmosenv.2008.03.025

Zhang, Y. L., and Cao, F. (2015). Fine Particulate Matter (PM 2.5) in China at a City Level. *Sci. Rep.* 5, 14884. doi:10.1038/srep14884

Zhao, C., Li, Y., Zhang, F., Sun, Y., and Wang, P. (2018). Growth Rates of Fine Aerosol Particles at a Site Near Beijing in June 2013. *Adv. Atmos. Sci.* 35 (2), 209–217. doi:10.1007/s00376-017-7069-3

Zheng, C., Zhao, C., Zhu, Y., Wang, Y., Shi, X., Wu, X., et al. (2017). Analysis of Influential Factors for the Relationship between PM_{2.5} and AOD in Beijing. *Atmos. Chem. Phys.* 17 (21), 13473–13489. doi:10.5194/acp-17-13473-2017

Zheng, J., Che, W., Zheng, Z., Chen, L., and Zhong, L. (2013). Analysis of Spatial and Temporal Variability of PM10 Concentrations Using MODIS Aerosol Optical Thickness in the Pearl River Delta Region, China. *Aerosol Air Qual. Res.* 13 (3), 862–876. doi:10.4209/aaqr.2012.09.0234

Zhou, S., Wang, T., Wang, Z., Li, W., Xu, Z., Wang, X., et al. (2014). Photochemical Evolution of Organic Aerosols Observed in Urban Plumes from Hong Kong and the Pearl River Delta of China. *Atmos. Environ.* 88, 219–229. doi:10.1016/j.atmosenv.2014.01.032

Zhou, S., Wu, L., Guo, J., Chen, W., Wang, X., Zhao, J., et al. (2020). Measurement Report: Vertical Distribution of Atmospheric Particulate Matter within the Urban Boundary Layer in Southern China - Size-Segregated Chemical Composition and Secondary Formation through Cloud Processing and

Heterogeneous Reactions. *Atmos. Chem. Phys.* 20 (11), 6435–6453. doi:10.5194/acp-20-6435-2020

Conflict of Interest: The authors declare that the research was conducted in the absence of any commercial or financial relationships that could be construed as a potential conflict of interest.

Publisher's Note: All claims expressed in this article are solely those of the authors and do not necessarily represent those of their affiliated organizations, or those of the publisher, the editors, and the reviewers. Any product that may be evaluated in this article, or claim that may be made by its manufacturer, is not guaranteed or endorsed by the publisher.

frontiers | Frontiers in Environmental Science

ORIGINAL RESEARCH
published: 30 May 2022
doi: 10.3389/fenvs.2022.901754

An Integrated Approach to Characterize Temporal–Spatial Variations in $PM_{2.5}$ Concentrations at the Ground Level and Its Implication on Health Impact Assessments

*Ming-Shing Ho[1,2], Ming-Yeng Lin[1], Jung-Der Wang[3], Li-Hao Young[4], Hui-Tsung Hsu[4], Bing-Fang Hwang[4] and Perng-Jy Tsai[1]**

[1]Department of Environmental and Occupational Health, College of Medicine, National Cheng Kung University, Tainan, Taiwan, [2]Labor Standards Inspection Office, Labor Affairs Bureau, Kaohsiung City Government, Kaohsiung, Taiwan, [3]Department of Internal Medicine, National Cheng Kung University Hospital, College of Medicine, National Cheng Kung University, Tainan, Taiwan, [4]Department of Occupational Safety and Health, College of Public Health, China Medical University, Taichung, Taiwan

OPEN ACCESS

Edited by:
Jianhuai Ye,
Southern University of Science and Technology, China

Reviewed by:
Xin Wang,
Southern University of Science and Technology, China
Fuzhen Shen,
University of Reading, United Kingdom

***Correspondence:**
Perng-Jy Tsai
pjtsai@mail.ncku.edu.tw

Specialty section:
This article was submitted to Atmosphere and Climate, a section of the journal Frontiers in Environmental Science

Received: 22 March 2022
Accepted: 19 April 2022
Published: 30 May 2022

Citation:
Ho M-S, Lin M-Y, Wang J-D, Young L-H, Hsu H-T, Hwang B-F and Tsai P-J (2022) An Integrated Approach to Characterize Temporal–Spatial Variations in $PM_{2.5}$ Concentrations at the Ground Level and Its Implication on Health Impact Assessments. Front. Environ. Sci. 10:901754. doi: 10.3389/fenvs.2022.901754

Although $PM_{2.5}$ concentrations measured by the governmental air quality monitoring station (AQMS) have been widely used for conducting exposure assessments, it might be not able to reflect the residents' exposures, especially for those associated with ground emissions. The present study was conducted in a city area for 1 year. A mobile monitoring station (MMS) was established to measure the $PM_{2.5}$ concentrations at the ground level. A significant linear relationship (R^2 = 0.53) was found between the MMS-measured concentrations and the corresponding concentrations obtained from the AQMS (15 m above the ground level), and the former was ~ 1.11 times (95% CI: 1.08-1.15) in magnitude higher than that of the latter. To characterize the spatial variation of the area, the MMS-measured values were further classified into three different regions. A consistent trend was found in the present study for all collected data as industry region ≒ urban region > harbor region. The aforementioned results clearly indicate that the residents' ambient $PM_{2.5}$ exposures do have spatial differences. Seven-year AQMS-measured concentrations (i.e., $AQMS_{7\text{-yr}}$) were used to establish the long-term $PM_{2.5}$ concentrations at the ground level (i.e., $MMS_{7\text{-yr}}$) of the three different regions using the linear regression equations obtained from the MMS and AQMS. Health impact functions and local health data were used to quantify the $PM_{2.5}$-attributable health burden for both $AQMS_{7\text{-yr}}$ and $MMS_{7\text{-yr}}$, respectively. Results show that the former is ~ 10.4% lower in magnitude than the latter in the estimated lung cancer death attributed fraction (AF). In particular, the decrease of unit $PM_{2.5}$ ($\mu g/m^3$) would lead to a 0.75 and 0.71% decrease in the estimated AF of lung cancer death for $AQMS_{7\text{-yr}}$ and $MMS_{7\text{-yr}}$, respectively. As a result, directly using $AQMS_{7\text{-yr}}$ would lead to an underestimation of ~ 1,000 lung cancer deaths annually in Taiwan in comparison with those using $MMS_{7\text{-yr}}$. The aforementioned results clearly indicate the importance of characterizing ground-level exposures for assessing the health impact of residents, and the methodology developed by the present study would be helpful for solving the aforementioned problem.

Keywords: PM2.5, mobile monitoring station, air quality monitoring station, exposure assessment, health impact assessment

INTRODUCTION

It has been reported that air pollution is responsible for ~ 2.9 million deaths per year accounting for ~ 35% of all environmental pollution-related deaths (Fuller et al., 2019). The International Agency for Research on Cancer (IARC) has classified outdoor air pollution as Group 1 carcinogen (i.e., carcinogenic to humans) (Straif et al., 2013). Among various particulate matters (PMs), many pieces of evidence have shown that $PM_{2.5}$ (i.e., PM with a particle size less than 2.5 μm) has a much stronger impact on human health than those with greater particle sizes (Environmental Protection Agency U.S, 2019). $PM_{2.5}$ is responsible for many adverse health effects, including lung cancer, chronic obstructive pulmonary disease (COPD), ischemic heart disease (IHD), strokes, and acute lower respiratory infections (ALRIs). (Mustafic et al., 2012; Forouzanfar et al., 2016; Monrad et al., 2017). Therefore, the control of atmospheric $PM_{2.5}$ concentrations has been considered as the primary concern in many countries. However, it should be noted that the initiation of appropriate abatement strategies for $PM_{2.5}$ should start with knowing the correct $PM_{2.5}$ exposure levels and health impact on the residents in the target area. Considering the existence of the intrinsic spatial and temporal variations in residents' $PM_{2.5}$ exposure concentrations, developing suitable exposure assessment (EA) methodologies has become an important issue in the environmental health science field.

At present, the methodologies used for conducting $PM_{2.5}$ EA can be classified into two categories: the non-ground level (also called macroenvironment) and ground level (microenvironment) (Straif et al., 2013; Dias and Tchepel, 2018; Li et al., 2018; Caplin et al., 2019; Environmental Protection Agency U.S, 2019). For non-ground-level EA methods, exposure data can be obtained from governmental air quality monitoring stations (AQMS) (i.e., fixed monitoring stations), model estimation, satellite remote sensing, etc. (Ozkaynak et al., 2013; Environmental Protection Agency U.S, 2019). The aforementioned methodologies are widely used in conducting EA on a large scale (such as on the whole country level, or even across-country level) and assuming the uniformity of $PM_{2.5}$ concentrations in each divided subarea. For example, $PM_{2.5}$ AQMS data from many countries were collected by the World Health Organization (WHO) for assessing the global exposure and health burden assuming the uniformity of $PM_{2.5}$ concentrations at a city level (W.H.O., 2012). However, the aforementioned methods might not be feasible for conducting $PM_{2.5}$ EA in a small area (such as at a city level) because the spatial heterogeneity might have a significant impact on the residents' $PM_{2.5}$ exposure concentrations (Fishbain et al., 2017; Malings et al., 2020).

It is known that urban traffic accounts for >50% of the total PM_{10} emissions. In comparison with PM_{10}, urban traffic has an even greater contribution to $PM_{2.5}$ concentrations at the ground level (Han and Naeher, 2006). The main traffic emission sources include road traffic, airport, and port operations (Kingham et al., 2013; Mazaheri et al., 2018). Among them, urban ground $PM_{2.5}$ concentrations are mainly influenced by road traffic contributed by both traffic exhaust and non-traffic exhaust (e.g., brake wear and road dust) (Jeong et al., 2019). Considering the proximity of residents to ground $PM_{2.5}$ emission sources (such as traffic), higher exposure concentrations at the ground level are expected than those obtained from the non-ground level (e.g., AQMS). Therefore, many methodologies have been developed to measure ground-level $PM_{2.5}$ concentrations (such as the mobile monitoring station (MMS) (Hankey and Marshall, 2015; Okokon et al., 2017; Lin et al., 2018; Cheng et al., 2019; Shen and Gao, 2019), air box (Lee et al., 2019; Lin et al., 2020), and modeling estimation (Hu et al., 2016; Jung et al., 2018)) for better characterizing residents' exposures in the small area of interest. Although the air box and modeling methods are less expensive and provide real-time information, many limitations are involved if they are used for conducting EA, including the accuracy and reliability of the collected data (Cabada et al., 2004; Snyder et al., 2013; Castell et al., 2017; Morawska et al., 2018; Williams et al., 2019; Li et al., 2020; Zamora et al., 2020; Environmental Protection Agency U.S, 2021). For the MMS, it has been found to be more accurate and reliable than the aforementioned two methodologies. On the condition of the existence of an AQMS in the target area, the use of the MMS method provides the possibility for better characterizing spatiotemporal personal exposures in a given microenvironment by combining with the AQMS data (Hankey and Marshall, 2015; Droge et al., 2018; Piotrowicz and Polednik, 2019).

In Taiwan, at least one AQMS is installed in every city or township for characterizing $PM_{2.5}$ concentrations in different areas. Although concentrations obtained from the AQMS provide longitudinal information of the area, however, they are inadequate to characterize the residents' $PM_{2.5}$ exposures in different regions of the area because of their intrinsic spatial heterogeneity (Borge et al., 2016). Therefore, developing new monitoring strategies with the aid of long-term AQMS data to characterize the residents' both temporal and spatial exposures has become an important issue for conducting $PM_{2.5}$ EAs. In principle, the development of predicting models between $PM_{2.5}$ concentrations of the AQMS and MMS would be helpful for establishing the residents' long-term $PM_{2.5}$ exposure concentrations at the ground level in different regions. However, it should be noted that before the establishment of the aforementioned predicting models, possible interference factors should be considered, including meteorological factors (e.g., temperature, humidity, (RH), wind speed, etc.) (Ye et al., 2018; Zhang et al., 2018; Lee et al., 2020; Rittner et al., 2020; Yousefian et al., 2020; Yang et al., 2022) and other co-emission pollutants (e.g., primary pollutants of NO_2, SO_2 etc. and secondary pollutants of O_3) (Saraswat et al., 2013; Zhang et al., 2018; Guo et al., 2019).

Since $PM_{2.5}$ concentration plays a significant role in human health, conducting a health impact assessment (HIA) would provide better evidence to help decision-makers for developing proper control strategies (W.H.O., 2022). For any given air pollutant, the calculation of the burden of disease (BOD) is widely adopted for conducting the HIA (van der Kamp and

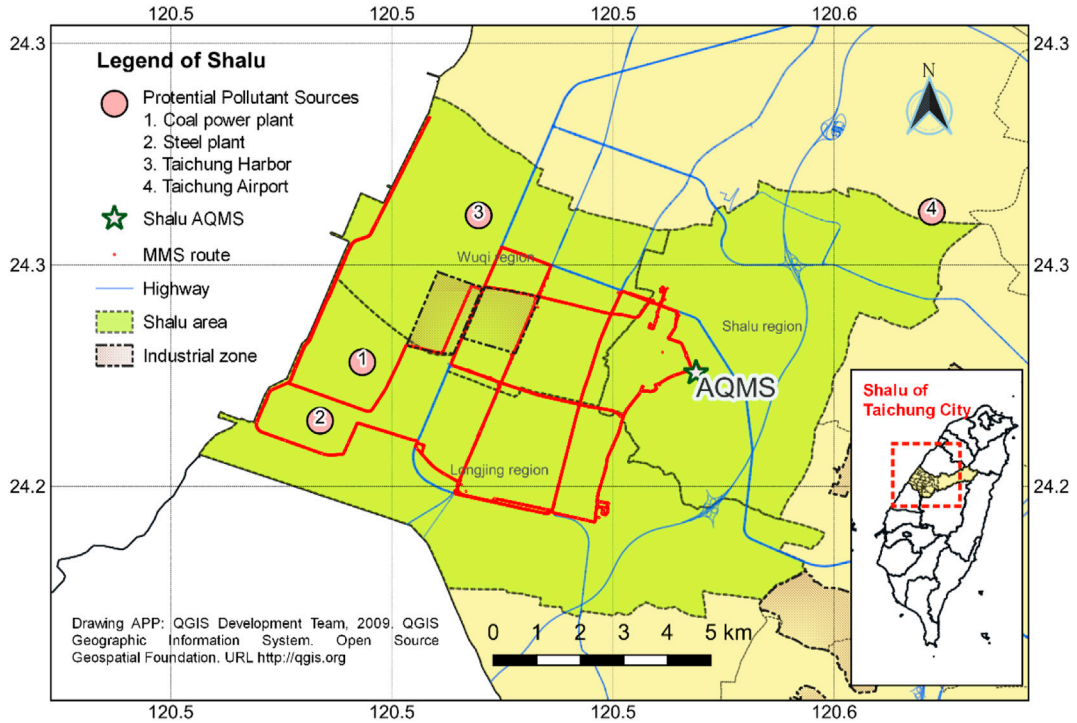

FIGURE 1 | Location of Taichung City and the study area, Shalu.

Bachmann, 2015; W.H.O., 2016; Maji et al., 2017; Malmqvist et al., 2018; Wu et al., 2018). In principle, four components should be collected for conducting the HIA: the exposure and reference concentrations of the air pollutant of interest, the resultant health outcomes, associated concentration–response functions (CRFs) and attributed fractions (AFs), and incidence rate (IR) of the health effect. CRFs can be determined using the novel Global Exposure Mortality Model (GEMM). If the exposure and reference concentrations of the air pollutant of interest were measured, the CRF can be determined, and finally, the burden of disease associated with the given air pollutant can be estimated (Ostro and WHO, 2004). This process has been widely adopted by WHO and others for conducting HIAs associated with $PM_{2.5}$ exposures.

The present study is set out to establish an effective methodology for assessing $PM_{2.5}$ exposures at the ground level in an urban region. Considering the existence of an AQMS, an MMS was established to collect concentrations of $PM_{2.5}$ at the ground level of different regions of the study area to characterize its spatial variation. Since continuous longitudinal data were collected by the AQMS, the AQMS data were used to determine the temporal variation in $PM_{2.5}$ concentrations in the study area. By combining the obtained MMS data with AQMS results, both temporal and spatial variations in $PM_{2.5}$ concentrations were characterized. Finally, HIAs were conducted to quantify the $PM_{2.5}$-attributable health burden for those data simply considering the temporal variation (i.e., directly obtained from the AQMS) and those considering both temporal and spatial variations (i.e., by combining both those directly obtained from the AQMS and measured by the MMS) of different regions of the study area. The obtained $PM_{2.5}$-attributable health burdens were used for showing the importance of characterizing temporal and spatial variations in conducting $PM_{2.5}$ exposure and HIAs.

MATERIALS AND METHODS

Study Area

The whole study was conducted in the Shalu area (including Shalu, Wugi, and Longjing districts with a total area of 95 km^2), located in west Taichung City (the second largest city in Taiwan), with a population of 220,000 residents, 216,000 vehicles (locomotives accounting for ~ 58%), and five industrial/science parks (~ 1,300 manufacturing industries) in 2014. From 2014–2019, there were 5.1, 5.7, and 13.7% increases annually for the number of residents, vehicles, and manufacturing industries, respectively. The region is adjacent to three main traffic roads including one highway (Chen et al., 2015), comprising one coal-fired power plant, one big steel factory, and one harbor located on the west (Kuo et al., 2014) (**Figure 1**).

$PM_{2.5}$ Monitoring Stations

On the north-western side of the Shalu area, one AQMS (latitude: 24.22563, longitude: 120.5688.) operated by the Taiwan EPA has been installed. In the present study, an MMS was established to collect concentrations of $PM_{2.5}$ at the ground level of different regions of the study area.

TABLE 1 | Basic information for the AQMS and MMS used in the present study for measuring $PM_{2.5}$ concentrations.

Station	AQMS	MMS
Station height	15 m above the ground level	Ground level
Monitoring instrument	BAM-1020 (beta-rays)	DUSTTRAK II Aerosol Monitor 8,530 (90° light scattering)
Monitoring frequency	per hour	real-time (1s–1 h)
Monitoring resolution	2 $\mu g/m^3$	1 $\mu g/m^3$
Calibrated concentrations by reference to FRM/FEM[a] method	$AQMS_c$ = 0.96*AQMSm-9.33 (R^2 = 0.92) (Environmental Protection Administration, T.R.O.C, 2020)	MMS_c = 0.33*MMS_m + 2.25 (R^2 = 0.859) (Yanosky et al., 2002; TSI_Incorporated, 2013)

[a]*FRM/FEM, Federal Reference Methods/Federal Equivalent Methods.*

The Air Quality Monitoring Station

The AQMS is 15 m above the ground level with a sampling inlet at 19.5 m in height. The main monitoring items include fine suspended particulates ($PM_{2.5}$), coarse suspended particulates (PM_{10}), carbon monoxide (CO), sulfur dioxide (SO_2), ozone (O_3), nitrogen dioxide (NO_2), and meteorological data (UVB, rainfall, wind direction and wind speed, temperature, and humidity). The installed $PM_{2.5}$ monitoring instrument (model BAM-1020, Met One Instruments Inc., Grands Pass, OR) uses beta-rays for detecting the relative concentration of $PM_{2.5}$ (detection range: 0–10 mg/m^3, resolution: 2 $\mu g/m^3$, beta-ray source: C-14, filter paper: glass fiber, capture efficiency: 0.3 μm particulate matter> 99.999%, sampling flow rate: 16.7 LPM) once per hour automatically.

The Mobile Monitoring Station

An electric car (LUXGEN MPV EV+, battery module: lithium-ion) was chosen as a mobile platform for the MMS to avoid influences from vehicle self-emissions. The MMS is equipped with a DUSTTRAK II Aerosol Monitor (model 8,530, TSI Inc., St. Paul, MN, United States; detection range: 0.001–150 mg/m^3, resolution: 1 $\mu g/m^3$, sampling flow rate: 3 L/min, time resolution: one reading per second) to monitor $PM_{2.5}$ real-time concentrations and a GPS to record the latitude–longitude information. To prevent collected samples from being affected by road contaminants, the sampling inlet of the MMS is set at a height of 2.2 m and air samples are collected isokinetically. **Table 1** shows the information on the station height, monitoring instrument, data collection frequency, and resolution for both the AQMS and MMS. Considering the intrinsic differences in the monitoring instruments of the AQMS and MMS, both the collected data (i.e., $AQMS_m$ and MMS_m) were calibrated (i.e., $AQMS_c$ and MMS_c) by reference to the Federal Reference Methods/Federal Equivalent Methods (FRM/FEM) (Environmental Protection Agency U.S, 2022).

Sampling Campaign

A sampling route ~ 80 km in length was designed for the MMS to collect $PM_{2.5}$ concentrations in the study area. Samplings were conducted from September 2013 to August 2014 covering the four seasons. For each sampling day, samplings were conducted approximately from 6:00 to 17:00 and 18:00 to 23:00 during the daytime and nighttime, respectively. Details of the MMS and its QA/QC can be found in our previous work (Lin et al., 2018). To compare with AQMS-collected data (i.e., hourly data), all MMS-collected data were further processed as the hourly average values. All collected MMS data in the study area were classified into three regions as follows based on the obtained GPS records: the urban region, industrial region, and harbor region (**Figure 2**). **Table 2** shows the details of the whole MMS sampling campaign. In the present study, the corresponding AQMS data were also recorded in accordance with the aforementioned MMS sampling campaign.

Statistic Methods

Since the obtained $PM_{2.5}$ concentrations were lognormally distributed, logarithmic conversion was applied to both AQMS and MMS data. *One-way ANOVA/paired t/t-tests* were applied to examine the differences between the MMS and the AQMS in seasons, day/night, commute periods, and different areas.

To develop predicting models for establishing residents' long-term $PM_{2.5}$ exposure concentrations at the ground level in different regions, MMS-measured data were compared with those obtained from the AQMS. Before the establishment of the aforementioned predicting models, possible interference factors were first identified, including three atmospheric variables [temperature (TEMP), relative humidity (RH), and wind speed (WS)], three primary pollutants (CO, NO_x, and SO_2), and one secondary pollutant (O_3) according to literature reviews (Cabada et al., 2004; Borge et al., 2016; Mazaheri et al., 2018; Adams et al., 2020; Liu et al., 2020). The hierarchical regression analysis was used to further confirm interference factors for the final predicting models. All data aggregation and statistics were performed using the Excel 365 software (Microsoft), R software (R x64 3.6.2) (R-Core-Team, 2019), and SPSS17 (IBM SPSS, 2008).

Conducting Health Impact Assessment

In the present study, ground-level $PM_{2.5}$ concentrations derived from predicting models were used for deriving the $PM_{2.5}$ mortality hazard ratio (HR) through the application of the GEMM as follows:

$$\mathbf{HR} = \mathbf{GEMM}(\mathbf{z}) = \boldsymbol{exp}[\boldsymbol{\theta} * \mathbf{log}(\mathbf{z}/\boldsymbol{\alpha} + 1)/(1 + \boldsymbol{exp}[-(\mathbf{z} - \boldsymbol{\mu})/\mathbf{v}])], \quad (1)$$

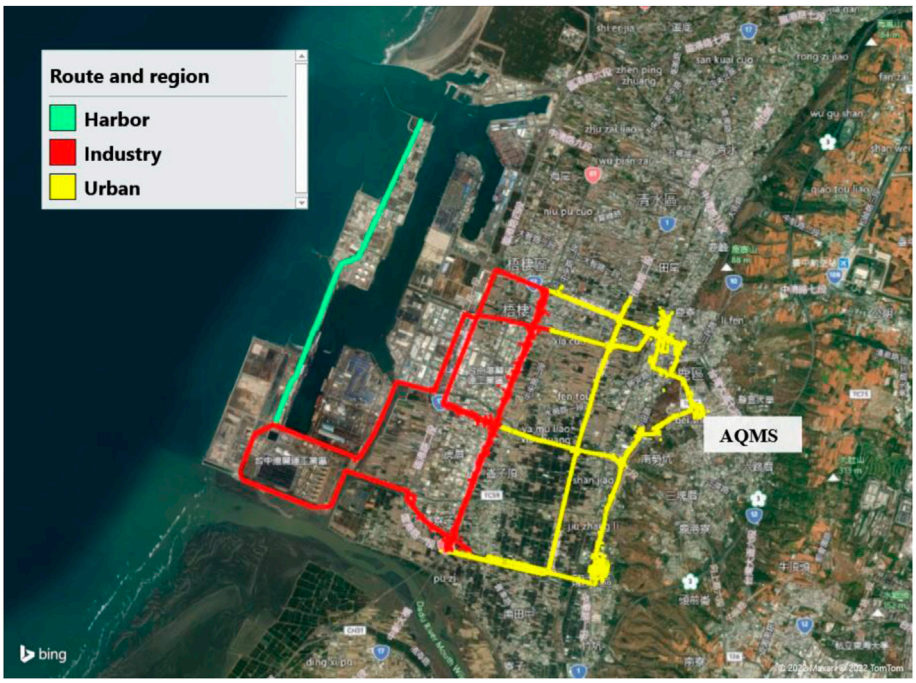

FIGURE 2 | MMS sampling route in the three regions: urban (yellow), industrial (red), and harbor regions (green).

TABLE 2 | Description of the whole MMS sampling campaign classified into the whole sampling days/hours by the season, day/night, rush/non-rush, and area.

	n	Season[a]				Day/night[b]		Rush_or_not[c]		Region		
		Fall	Winter	Spring	Summer	Daytime	Nighttime	Rush	Non-rush	Urban	Industry	Harbor
Days	59	16	19	8	19	56	49	58	41	59	—	—
Hours	694	148	233	78	235	465	229	584	110	330	248	116

[a]*Fall: Sep. 2013—Nov. 2013; winter: Dec. 2013–Feb. 2014; spring: Mar. 2014-May 2014; summer: Jun. 2014-August. 2014.*
[b]*Daytime: am 06–pm 17; nighttime: pm 18–am 05.*
[c]*Rush hour: am7-9 and pm18-20; non-rush hour: excluding rush hours.*

TABLE 3 | Values for the parameter used in the GEMM.

Cause of death	Age range	Parameters				
		θ	SE θ[a]	α	μ	ν
Lung cancer	>25	0.2942	0.06147	6.2	9.3	29.8
LRI	>25	0.4468	0.11735	6.4	5.7	8.4
COPD	>25	0.251	0.06762	6.5	2.5	32
Stroke	>25	0.272	0.07697	6.2	16.7	23.7
IHD	>25	0.2969	0.01787	1.9	12	40.2

[a]*SE, standard error of θ, which is used for 95%CI, uncertainty estimation. Parameters quoted from GEMM, study (with Chinese male cohort) (Burnett et al., 2018).*

where z = max (0, C - C_{rf}), C = the exposed $PM_{2.5}$ concentration, and C_{rf} = the counterfactual $PM_{2.5}$ concentration (=2.4 $\mu g/m^3$).

θ, SEθ, α, μ, and ν = parameters can be determined based on the cause of death (for the present study: lung cancer) by referring to **Table 3**.

Since the mortality probability of lung cancer is quite small, the resultant HR could serve as a surrogate for the relative risk (RR) (Burnett et al., 2018). The attributed fraction for the population (AF) of lung cancer can be calculated as follows (Ostro and WHO, 2004):

$$\mathbf{AF} = (\mathbf{RR} - 1)/\mathbf{RR}. \quad (2)$$

RESULTS AND DISCUSSION

Comparisons of AQMS- and MMS-Measured $PM_{2.5}$ Concentrations

$PM_{2.5}$ concentrations of the whole sampling year, seasonal, diurnal, and rush/non-rush hour obtained from both the AQMS and MMS are compared and shown in **Table 4**. From the whole sampling year aspect, MMS results (GM = 25.9 $\mu g/m^3$; 95% CI = 24.8–27.1 $\mu g/m^3$) are significantly higher than those of

TABLE 4 | Comparison of $PM_{2.5}$ concentrations of the whole sampling year, seasonal, diurnal, and rush/non-rush hour for data obtained from both the AQMS and MMS.

Temporal/spatial	Description	n	MMS	AQMS	MMS/AQMS[a]
			GM (95% CI) μg/m3		Ratio (95% CI)
Season					
Fall	Sep. 2013–November. 2013	148	18.5 (17.3-19.8)	22.2 (21.0-23.6)	0.83 (0.79-0.87)
Winter	Dec. 2013–February. 2014	233	33.1 (30.3-36.2)	29.3 (27.1-31.7)	1.13 (1.08-1.19)
Spring	Mar. 2014–May 2014	78	32.3 (29.4-35.6)	38.6 (35.7-41.8)	0.84 (0.78-0.90)
Summer	Jun. 2014–August. 2014	235	23.4 (21.8-25.1)	16.1 (15.2-17.1)	1.45 (1.38-1.53)
Rush hour					
Rush	(am7-9) and (pm18-20)	584	26.7 (25.4-28.0)	23.7; (22.6-24.8)	1.13 (1.09-1.17)
Non-rush	Excluding rush hours	110	22.4 (20.1, 24.9)	21.4; (19.4-23.6)	1.05 (0.97-1.13)
Diurnal					
Daytime	Hour: 06-17	465	26.8 (25.4-28.3)	23.0 (21.8-24.2)	1.17 (1.12-1.21)
Nighttime	Hour: 18-05	229	24.3 (22.5-26.2)	23.9 (22.3-25.6)	1.01 (0.96-1.08)
Region					
Urban	Dense residential area	330	27.0 (25.3-28.7)	22.3 (20.9-23.7)	1.21 (1.16-1.26)
Industry	Factory area	248	26.7 (24.8-28.7)	24.4 (22.8-26.2)	1.09 (1.03-1.16)
Harbor	Taichung harbor area	116	21.9 (19.5, 24.5)	23.9 (21.4, 26.6)	0.92 (0.84-1.00)
Whole	—	694	25.9 (24.8-27.1)	23.3 (22.3-24.3)	1.11 (1.08-1.15)

[a]*Ratio of MMS/AQMS = exp (ln_MMS–ln_AQMS).*

the AQMS (GM = 23.3 $\mu g/m^3$; 95% CI = 22.3–24.3 $\mu g/m^3$) (t-test; $p < 0.01$). The former is 1.23 times (95% CI = 1.18-1.27) higher in magnitude than the latter. The aforementioned result is not so surprising since the MMS was much closer to $PM_{2.5}$ emission sources (such as traffic) than the AQMS (Wu et al., 2014). In addition, our results are also consistent with previous studies. For example, a study conducted in Boston's Chinatown (near a highway) shows that the increase of building elevation from 0 to 35 m would result in a decrease of the $PM_{2.5}$ mass concentration by 5.1% (Wu et al., 2014). Another study conducted in Pittsburgh, Pennsylvania, shows that the annual MMS is higher than the annual average of the AQMS (14.6 and 10.2 $\mu g/m^3$, respectively) (Li et al., 2016). Here, it should be noted that the latter study was simply conducted in the 2013 winter and 2014 summer (i.e., does not cover four seasons), and hence no statistical significance could be found.

For seasonal $PM_{2.5}$ mass concentrations, MMS results are statistically significantly higher than those of the AQMS in both summer (GM = 23.4 and 16.1 $\mu g/m^3$, 95% CI = 21.8–25.1 and 15.2–17.1 $\mu g/m^3$, respectively; paired t-test; $p < 0.001$) and winter (GM = 33.1 and 29.3 $\mu g/m^3$, 95% CI = 30.3–36.2 and 27.1–31.7 $\mu g/m^3$, respectively; paired t-test; $p < 0.001$). However, an opposite trend is found in both spring (GM = 32.3 and 38.6 $\mu g/m^3$, 95% CI = 29.4–35.6 and 35.7–41.8 $\mu g/m^3$, respectively; paired t-test; $p < 0.001$) and fall (GM = 18.5 and 22.3 $\mu g/m^3$, 95% CI = 17.3–19.8 and 21.0, 23.6 $\mu g/m^3$, respectively; paired t-test; $p < 0.001$). The opposite trend found in spring and fall might be associated with the lower atmospheric boundary layer, and more significant temperature inversions were found in these two seasons (Ye et al., 2018; Yousefian et al., 2020).

Since the MMS was more proximal to traffic $PM_{2.5}$ emission sources than the AQMS, as expected, we found that the MMS rush hour results (GM = 26.7 $\mu g/m^3$, 95% CI: 25.4–28.0 $\mu g/m^3$) are significantly higher than those of the AQMS (GM = 23.7 $\mu g/m^3$, 95% CI = 22.6–24.8 $\mu g/m^3$) (paired sample t-test; $p < 0.001$). Although the same trend can also be found for data collected during non-rush hours, however, no statistical significance is found in the present study (GM = 22.4 and 21.4 $\mu g/m^3$, 95% CI = 20.1–24.9 and 19.4–23.6 $\mu g/m^3$ for the MMS and AQMS, respectively; paired t-test; $p = 0.234$). Obviously, the aforementioned result could be due to less traffic density during non-rush hours. The aforementioned reason can also be used to explain the diurnal sampling results. Here, the daytime sampling results show that those of the MMS are significantly higher than those of the AQMS (GM = 26.8 and 23.0 $\mu g/m^3$, 95% CI = 25.4–28.3 and 21.8–24.2 $\mu g/m^3$, respectively; paired t-test; $p < 0.001$)). Although nighttime sampling results for the MMS are higher than those of the AQMS, no statistical significance is found in the present study (GM = 24.3 and 23.9 $\mu g/m^3$, 95% CI = 22.5–26.2 and 22.3–25.6 $\mu g/m^3$, respectively; paired t-test; $p = 0.635$).

Comparisons of $PM_{2.5}$ Concentrations of the Urban, Industry, and Harbor Regions Obtained From the MMS and Those Simultaneously Obtained From the AQMS

Table 4 shows the $PM_{2.5}$ concentrations of the urban, industry, and harbor regions, and the whole Shalu area data obtained from the MMS. No significant difference (ANOVA post hoc test, $p = 0.978$) could be found between $PM_{2.5}$ concentrations of the urban region (GM = 27.0 $\mu g/m^3$, 95% CI = 25.3–28.7 $\mu g/m^3$) and industry region (GM = 26.7 $\mu g/m^3$, 95% CI = 24.8–28.7 $\mu g/m^3$). Considering that the dimension of the whole Shalu area is less than 100 km^2, the geographical adjacency of both regions might lead to a similarity in their

$PM_{2.5}$ concentrations. On the other hand, both $PM_{2.5}$ concentrations of the aforementioned two regions were significantly higher than those of the harbor region (GM = 21.9 $\mu g/m^3$, 95% CI = 19.5–24.5 $\mu g/m^3$) ug/m^3 (ANOVA post hoc test; $p < 0.01$). It could be due to fewer ground-level pollution sources in the harbor region than that in others. In addition, its remote location from the other two regions and the effect of the monsoon wind direction could also be considered contributors (Cheng and Hsu, 2019).

For the comparison purpose, $PM_{2.5}$ concentrations of the urban, industry, and harbor regions obtained from the MMS were compared with those simultaneously obtained from the AQMS. For both urban and industrial regions, the MMS concentration (GM = 27.0 and 26.7 $\mu g/m^3$, 95% CI = 25.3-28.7 and 24.8–28.7 $\mu g/m^3$, respectively) is significantly higher than that of the AQMS (GM = 22.3 and 24.4 $\mu g/m^3$, 95% CI = 20.9-23.7 and 22.8–26.2 $\mu g/m^3$, respectively) (paired t-test; $p < 0.001$). For the harbor region, however, the MMS concentration (GM = 21.9 $\mu g/m^3$, 95% CI = 19.5–24.5 $\mu g/m^3$) is significantly less than that of the AQMS (GM = 23.9 $\mu g/m^3$, 95% CI = 21.4–26.6 $\mu g/m^3$) (paired t-test; $p = 0.046$). The aforementioned results might be because of the existence of fewer ground-level pollution sources in the harbor region. For both urban and industrial regions, the $PM_{2.5}$ concentration of the MMS is respectively 1.21 and 1.09 times higher in magnitude than that of the AQMS. The aforementioned results might be because the urban region is proximal to traffic pollution sources, and the industrial region is mainly affected by pollution sources associated with manufacturing and heavy truck emission.

Establishing the Relationship Between $PM_{2.5}$ Concentrations of the AQMS and MMS

Multivariate linear regression (MLR) analyses (hierarchical regression) were conducted to identify variables used for establishing predicting models through examining the variability and collinearity of candidate interference factors. The statistical significance can be found for the four factors, CO, SO_2, WS, and AQMS $PM_{2.5}$ concentrations. The aforementioned four factors were first included for establishing predicting models (R^2 = 0.58). Considering that the total contribution of SO_2, CO, and WS to R^2 is less than 7%, they were removed from the prediction models pragmatically for practical reasons (see **Supplementary Table S1**). The ignorance of the aforementioned factors is consistent with previous studies conducted in Lubbock, Texas (Kelley et al., 2020), Tianjin, Beijing, and Hebei provinces in China (Zhang et al., 2018). Considering the intrinsic difference in $PM_{2.5}$ concentrations of the urban, industrial, and harbor regions, predicting models were established not only based on the data collected from the whole area but also each individual region. The resultant predicting models are shown as follows:

Whole area:

$$\ln\_MMS = 0.839 + 0.768*\ln\_AQMS,\ (RMSE = 1.50\mu g/m^3, R^2 = 0.54;\ n = 694). \quad (3)$$

Urban region:

$$\ln\_MMS = 0.691 + 0.839*\ln\_AQMS,\ (RMSE = 1.42\mu g/m^3, R^2 = 0.65;\ n = 330). \quad (4)$$

Industrial region:

$$\ln\_MMS = 1.037 + 0.703*\ln\_AQMS,\ (RMSE = 1.55\mu g/m^3, R^2 = 0.45;\ n = 248). \quad (5)$$

Harbor region:

$$\ln\_MMS = 0.714 + 0.747*\ln\_AQMS,\ (RMSE = 1.55\mu g/m^3, R^2 = 0.51;\ n = 116). \quad (6)$$

Figures 3A–D show the scatter plots of the MMS and AQMS for data collected from the whole study area, urban, industrial, and harbor regions, respectively. The R^2 obtained from the present study is comparable with another study for predicting outdoor personal exposures using nearby AQMS $PM_{2.5}$ concentrations (Miller et al., 2019). In the present study, the ANOVA (post hoc test) was performed to examine if there is a statistical significance among the four predicting models (See **Supplementary Table S2**). Results show that no significant difference can be found among the three predicting models for the whole area, urban region, and industrial region; however, the slope of the predicting model for the harbor region was significantly lower than that of others (all $p < 0.05$). The aforementioned results are consistent with a study conducted in Guangzhou, China, where the relationship between AQMS $PM_{2.5}$ concentrations and personal exposure varies greatly from district to district (Jahn et al., 2013). Here, it should be noted that it would be more reasonable to have one predicting model for both urban and industrial regions from a statistical point of view. However, considering the intrinsic difference in the emission sources of the aforementioned two regions, using two separate predicting models could be feasible to meet practical purposes. In the present study, the established four predicting models were adopted for predicting the residents' exposures and further for conducting health impact analyses of each individual region and the whole area.

Health Impact Assessment for Each Individual Region and the Whole Area

Seven-year (2013–2019) AQMS-measured concentrations (i.e., $AQMS_{7\text{-}yr}$) were used to establish the long-term $PM_{2.5}$ concentrations at the ground level (i.e., $MMS_{7\text{-}yr}$) of the whole area and the three different regions using **Eqs 3–6**, respectively (**Table 5**). Health impact functions and local health data were used to quantify the $PM_{2.5}$-attributable health burden for both $AQMS_{7\text{-}yr}$ and $MMS_{7\text{-}yr}$, respectively. The above ground-level

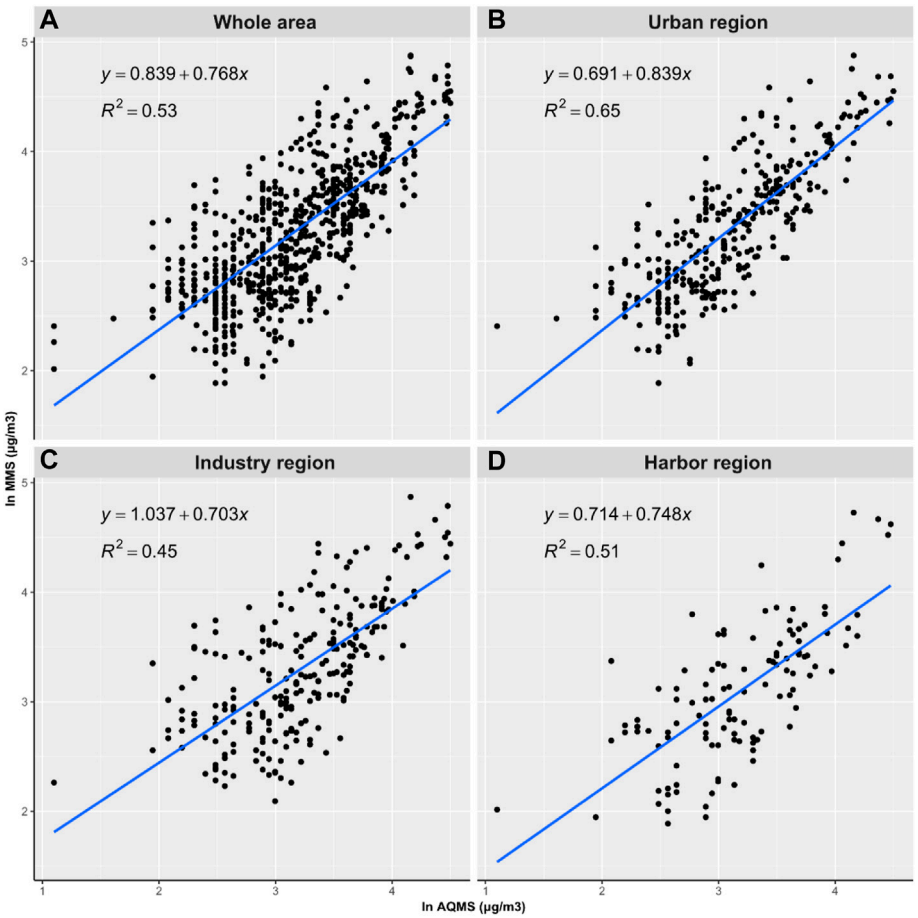

FIGURE 3 | Scatter plots of the MMS and AQMS for the **(A)** whole area, **(B)** urban region, **(C)** industry region, and **(D)** harbor region.

$PM_{2.5}$ concentrations together with the parameter values shown in **Table 3** for lung cancer were applied to the GEMM (**Eq. 1**) for deriving the $PM_{2.5}$ mortality hazard ratio (HR). Since the mortality probability of lung cancer is small, the HR obtained from the present study was used as a surrogate for the relative risk (RR) (Burnett et al., 2018). **Table 5** also shows the lung cancer-attributed fraction (AF) of the population using **Eq. 2**. Results show that both $AQMS_{7\text{-yr}}$ and $MMS_{7\text{-yr}}$ decreased from 2013–2019, and the former is lower than the latter. As a result, the same downward trend can also be seen in the estimated RR and AF over the years.

For the whole area, AQMS $PM_{2.5}$ concentrations from 2013–2019 are, in total, decreased by 56% (i.e., from 35.4 to 15.4 $\mu g/m^3$), the resultant decrease for the RR was 20% (i.e., from 1.45 to 1.19) and AF was 48% (i.e., from 0.31 to 0.16). Therefore, reducing the AQMS $PM_{2.5}$ concentrations (i.e., $AQMS_{7\text{-yr}}$) has a high contribution to the lung cancer AF. Here, it should be noted that even if the yearly average AQMS $PM_{2.5}$ concentration meets the government and WHO $PM_{2.5}$ interim targets 3 and 4 (i.e., 15 and 10 μg/m3, respectively) (W.H.O., 2021), the resultant AFs still cannot be ignored (= 16 and 11%, respectively). Similar results can also be seen in $MMS_{7\text{-yr}}$ [i.e., $PM_{2.5}$ concentrations decreased by 47% in total (i.e., from 35.8 to 18.9 $\mu g/m^3$), RR by 15% (i.e., from 1.46 to 1.24), and AF by 39% (i.e., from 0.31 to 0.19)]. Even if the yearly average AQMS $PM_{2.5}$ concentration meets the government and WHO $PM_{2.5}$ interim targets 3 and 4, the estimated $MMS_{7\text{-y}}$ (i.e., 18.5 and 13.6, respectively) would lead to even higher AFs (=19 and 14%, respectively) in comparison with the corresponding values (= 16 and 11%, respectively) associated with AQMS $PM_{2.5}$ concentrations.

Table 5 also shows the estimated annual mean of $PM_{2.5}$ concentrations at the ground level ($MMS_{7\text{-yr}}$) of the urban, industrial, and harbor regions, and the corresponding attributed fraction of the population (AF) for lung cancer. The trend in the decrease of $PM_{2.5}$ concentrations from 2013 to 2019 and the decrease in the resultant RR are similar to those found in the whole area. Moreover, it can also be seen that if $AQMS_{7\text{-yr}}$ is used for estimating the AF for residents in the Shalu area, an average underestimation of 10.4% was yielded in comparison with those using $MMS_{7\text{-yr}}$. The decrease of unit $PM_{2.5}$ concentration would lead to the decrease in the AF of lung cancer by 0.75 and 0.71% in $AQMS_{7\text{-yr}}$ and $MMS_{7\text{-yr}}$, respectively. By applying **Eq. 3** to the whole Taiwan area, directly using $AQMS_{7\text{-yr}}$ would lead to an underestimation of

TABLE 5 | Annual mean of $PM_{2.5}$ concentrations of $AQMS_{7\text{-}yr}$ and the ground level (MMS7-yr) of the whole Shalu area and their derived relative risks (RRs) and the attributed fraction of the population (AF).

	Year							WHO interim target [d]	
	2013	2014	2015	2016	2017	2018	2019	Target 3	Target 4
$PM_{2.5}$ ($\mu g/M^3$)									
$AQMS_{7\text{-}yr}$ [a]	35.4	28.7	19.3	21.5	19.3	18.9	15.4	15	10
$MMS_{7\text{-}yr}$ [b]									
Whole area	35.8	30.5	22.5	24.4	22.5	22.1	18.9	18.5	13.6
Urban	39.8	33.4	23.9	26.2	23.9	23.5	19.8	19.4	13.8
Industry	34.6	29.9	22.6	24.4	22.6	22.3	19.3	18.9	14.2
Harbor	29.3	25.1	18.6	20.2	18.6	18.3	15.7	15.4	11.4
RR (95%CI) [c]									
AQMS	1.45 (1.25, 1.69)	1.37 (1.2, 1.55)	1.24 (1.14, 1.36)	1.27 (1.15, 1.4)	1.24 (1.14, 1.36)	1.24 (1.13, 1.35)	1.19 (1.11, 1.28)	1.19 (1.11, 1.27)	1.12 (1.07, 1.17)
Whole area	1.46 (1.25, 1.7)	1.39 (1.21, 1.59)	1.28 (1.16, 1.42)	1.31 (1.17, 1.46)	1.28 (1.16, 1.42)	1.28 (1.16, 1.42)	1.24 (1.13, 1.35)	1.23 (1.13, 1.34)	1.17 (1.1, 1.25)
Urban	1.51 (1.28, 1.79)	1.43 (1.23, 1.65)	1.3 (1.17, 1.45)	1.33 (1.18, 1.5)	1.3 (1.17, 1.45)	1.3 (1.17, 1.44)	1.25 (1.14, 1.37)	1.24 (1.14, 1.36)	1.17 (1.1, 1.25)
Industry	1.44 (1.24, 1.68)	1.38 (1.21, 1.58)	1.29 (1.16, 1.43)	1.31 (1.17, 1.46)	1.29 (1.16, 1.43)	1.28 (1.16, 1.42)	1.24 (1.14, 1.36)	1.24 (1.13, 1.35)	1.18 (1.1, 1.26)
Harbor	1.37 (1.21, 1.56)	1.32 (1.18, 1.48)	1.23 (1.13, 1.35)	1.26 (1.14, 1.38)	1.23 (1.13, 1.35)	1.23 (1.13, 1.34)	1.2 (1.11, 1.29)	1.19 (1.11, 1.28)	1.14 (1.08, 1.2)
AF (95% CI)									
AQMS	0.31 (0.2, 0.41)	0.27 (0.17, 0.36)	0.2 (0.12, 0.26)	0.21 (0.13, 0.29)	0.2 (0.12, 0.26)	0.19 (0.12, 0.26)	0.16 (0.1, 0.22)	0.16 (0.1, 0.22)	0.11 (0.07, 0.15)
Whole area	0.31 (0.2, 0.41)	0.28 (0.18, 0.37)	0.22 (0.14, 0.3)	0.24 (0.15, 0.32)	0.22 (0.14, 0.3)	0.22 (0.14, 0.29)	0.19 (0.12, 0.26)	0.19 (0.12, 0.26)	0.14 (0.09, 0.2)
Urban	0.34 (0.22, 0.44)	0.3 (0.19, 0.39)	0.23 (0.14, 0.31)	0.25 (0.16, 0.33)	0.23 (0.14, 0.31)	0.23 (0.14, 0.31)	0.2 (0.12, 0.27)	0.2 (0.12, 0.27)	0.15 (0.09, 0.2)
Industry	0.31 (0.19, 0.4)	0.28 (0.17, 0.37)	0.22 (0.14, 0.3)	0.24 (0.15, 0.32)	0.22 (0.14, 0.3)	0.22 (0.14, 0.3)	0.2 (0.12, 0.26)	0.19 (0.12, 0.26)	0.15 (0.09, 0.21)
Harbor	0.27 (0.17, 0.36)	0.24 (0.15, 0.32)	0.19 (0.12, 0.26)	0.2 (0.13, 0.27)	0.19 (0.12, 0.26)	0.19 (0.12, 0.25)	0.16 (0.1, 0.22)	0.16 (0.1, 0.22)	0.12 (0.07, 0.17)

[a] *The annual average concentration of $PM_{2.5}$ (a large amount of data is assumed to be normal distribution) and the data are from the official annual report of TEPA (Environmental Protection Administration,T.R.O.C, 2021).*

[b] *Regression prediction.*

[c] *GEMM prediction.*

[d] *WHO global air quality guidelines (2021) (W.H.O., 2021).*

~ 1,000 lung cancer deaths annually in Taiwan during the period from 2013 to 2019 in comparison with those using $MMS_{7\text{-}yr}$ (See **Supplementary Figure S3**). The aforementioned results further strengthen the importance of developing methodologies for predicting $PM_{2.5}$ concentrations at the ground level.

Limitations and Future Implications

Considering that there were annual increases in the number of residents, vehicles, and manufacturing industries from 2014 to 2019, it would be more reasonable to establish predicting models based on data collected from the same period of time. In the present study, although before the establishment of the predicting models, possible interference factors were identified (including atmospheric variables, primary pollutants, and secondary pollutants), which would lead to the developed predicting models becoming more suitable for complicated pollution scenarios. Nevertheless, the establishment of the prediction model in the present study is simply based on data collected from 2013 to 2014 for practical reasons. The aforementioned factor should be considered a limitation of the present study. Moreover, possible interference factors in the present study were considered as those affecting $PM_{2.5}$ concentrations. The selection of possible interference factors was based on the results of literature reviews and available information collected by the AQMS. Indeed, some VOCs are known to be associated with the formation of secondary aerosols, which will also affect the concentrations of $PM_{2.5}$. However, considering no VOC information could be obtained from the AQMS, only three atmospheric variables, three primary pollutants, and one secondary pollutant were selected. The aforementioned deficiency might explain the R^2 of the predicting models falling to the range 0.45–0.65. We believe that the addition of some VOCs might increase the magnitude of R^2 of the predicting models. The aforementioned factor can also be considered a limitation of the present study.

This study was set out to develop an integrated approach for effectively predicting $PM_{2.5}$ exposures for residents at the ground level *via* the combination of the concentrations measured across different seasons and regions using the MMS and those obtained

from the nearby fixed-site AQMS. Our results strongly suggest that using the ground-level concentrations would be more accurate in assessing residents' health impacts than those directly obtained from the AQMS. Since the AQMS has been intensively installed in many countries, AQMS data have been widely used for pollution alerts for residents, policy-making for pollution control strategies, and global disease burden assessment. Therefore, the methodology developed from the present study would provide us with a feasible approach for predicting the ground-level concentrations which will effectively enhance the value of the AQMS installed in many countries. Moreover, the approach developed from the present study will be also beneficial to the epidemiological research field for better assessing health outcomes associated with residents' $PM_{2.5}$ exposures.

CONCLUSION

In this study, we presented a methodology for assessing the $PM_{2.5}$ exposures of residents and their health impacts at a city level. We found that there is a significant linear relationship between MMS-measured ground-level concentrations and the corresponding concentrations obtained from the AQMS of the area, and the former is higher than that of the latter. A consistent trend in $PM_{2.5}$ exposures associated with the spatial difference was found as industry region ≅ urban region > harbor region. Our results clearly indicate that residents' ambient $PM_{2.5}$ exposures do exist with spatial differences in both vertical and horizontal spaces. The health impact assessment results show that the use of AQMS data would lead to an underestimation of ~ 10.4% in magnitude in the estimated lung cancer death attributed fraction (AF) in comparison with those using ground-level exposure concentrations. Similarly, directly using the former would lead to an underestimation of ~ 1,000 lung cancer deaths annually in Taiwan during the period from 2013 to 2019, in comparison with those using the latter. The present study clearly indicates the importance of developing methodologies for predicting residents' ground-level $PM_{2.5}$ exposure concentrations in conducting exposure and health impact assessments.

DATA AVAILABILITY STATEMENT

The raw data supporting the conclusions of this article will be made available by the authors, without undue reservation.

AUTHOR CONTRIBUTIONS

Study design: P-JT and M-YL. Field data collection: M-SH, M-YL, L-HY, H-TH. Statistical analyses: M-SH, B-FH, and J-DW. Manuscript preparation: M-SH and P-JT.

ACKNOWLEDGMENTS

The authors would like to thank the National Health Research Institute in Taiwan for funding this research project. The author M-YL has the same contribution to this research project as the corresponding author.

SUPPLEMENTARY MATERIAL

The Supplementary Material for this article can be found online at: https://www.frontiersin.org/articles/10.3389/fenvs.2022.901754/full#supplementary-material

REFERENCES

Adams, M. D., Massey, F., Chastko, K., and Cupini, C. (2020). Spatial Modelling of Particulate Matter Air Pollution Sensor Measurements Collected by Community Scientists while Cycling, Land Use Regression with Spatial Cross-Validation, and Applications of Machine Learning for Data Correction. *Atmos. Environ.* 230, 10. doi:10.1016/j.atmosenv.2020.117479

Borge, R., Narros, A., Artíñano, B., Yagüe, C., Gómez-Moreno, F. J., De La Paz, D., et al. (2016). Assessment of Microscale Spatio-Temporal Variation of Air Pollution at an Urban Hotspot in Madrid (Spain) through an Extensive Field Campaign. *Atmos. Environ.* 140, 432–445. doi:10.1016/j.atmosenv.2016.06.020

Burnett, R., Chen, H., Szyszkowicz, M., Fann, N., Hubbell, B., Pope, C. A., 3rd, et al. (2018). Global Estimates of Mortality Associated with Long-Term Exposure to Outdoor Fine Particulate Matter. *Proc. Natl. Acad. Sci. U.S.A.* 115, 9592–9597. doi:10.1073/pnas.1803222115

Cabada, J. C., Khlystov, A., Wittig, A. E., Pilinis, C., and Pandis, S. N. (2004). Light Scattering by Fine Particles during the Pittsburgh Air Quality Study: Measurements and Modeling. *J. Geophys. Res.-Atmos.* 109 (D16), 1–13. doi:10.1029/2003jd004155

Caplin, A., Ghandehari, M., Lim, C., Glimcher, P., and Thurston, G. (2019). Advancing Environmental Exposure Assessment Science to Benefit Society. *Nat. Commun.* 10, 1236. doi:10.1038/s41467-019-09155-4

Castell, N., Dauge, F. R., Schneider, P., Vogt, M., Lerner, U., Fishbain, B., et al. (2017). Can Commercial Low-Cost Sensor Platforms Contribute to Air Quality Monitoring and Exposure Estimates? *Environ. Int.* 99, 293–302. doi:10.1016/j.envint.2016.12.007

Chen, P., Bi, X., Zhang, J., Wu, J., and Feng, Y. (2015). Assessment of Heavy Metal Pollution Characteristics and Human Health Risk of Exposure to Ambient PM2.5 in Tianjin, China. *Particuology* 20, 104–109. doi:10.1016/j.partic.2014.04.020

Cheng, F.-Y., and Hsu, C.-H. (2019). Long-Term Variations in PM2.5 Concentrations under Changing Meteorological Conditions in Taiwan. *Sci. Rep.* 9, 6635. doi:10.1038/s41598-019-43104-x

Cheng, Y.-H., Ninh, X.-H., and Yeh, S.-L. (2019). Dominant Factors Influencing the Concentrations of Particulate Matters inside Train Carriages Traveling in Different Environments in the Taipei Mass Rapid Transit System. *Aerosol Air Qual. Res.* 19, 1579–1592. doi:10.4209/aaqr.2018.09.0335

Dias, D., and Tchepel, O. (2018). Spatial and Temporal Dynamics in Air Pollution Exposure Assessment. *Int. J. Environ. Res. Public Health* 15, 558. doi:10.3390/ijerph15030558

Dröge, J., Müller, R., Scutaru, C., Braun, M., and Groneberg, D. (2018). Mobile Measurements of Particulate Matter in a Car Cabin: Local Variations, Contrasting Data from Mobile versus Stationary Measurements and the Effect of an Opened versus a Closed Window. *Ijerph* 15, 2642. doi:10.3390/ijerph15122642

Environmental Protection Administration, T.R.O.C (2020). *Manual Monitoring of Fine Fine Suspended Particles [Online]*. Taipei Taiwan. Available at: https://airtw.epa.gov.tw/CHT/EnvMonitoring/Central/spm.aspx (Accessed May 5, 2019).

Environmental Protection Administration, T.R.O.C (2021). *Yearly Reports of Air Monitoring [Online]*. Teipei, Taiwan: EPA. Available at: https://www.epa.gov.tw/Page/672FA2BDDEAA22C7/71fedbd8-9829-49e0-b02b-0addb5bd470a?msclkid=1aaa7477a97811ec8a50451d458a7bb7 (Accessed Mar 5, 2020).

Environmental Protection Agency U.S. (2021). *Air Sensor Toolbox [Online]*. EPA. Available at: https://www.epa.gov/air-sensor-toolbox (Accessed Mar 2, 2021).

Environmental Protection Agency U.S. (2022). *EPA Scientists Develop and Evaluate Federal Reference & Equivalent Methods for Measuring Key Air Pollutants [Online]*. EPA. Available at: https://www.epa.gov/air-research/epa-scientists-develop-and-evaluate-federal-reference-equivalent-methods-measuring-key (Accessed Sep 1, 2019).

Environmental Protection Agency U.S. (2019). *Integrated Science Assessment (ISA) for Particulate Matter*. Washington, DC: U.S. Environmental Protection Agency. (Final Report, Dec 2019).

Fishbain, B., Lerner, U., Castell, N., Cole-Hunter, T., Popoola, O., Broday, D. M., et al. (2017). An Evaluation Tool Kit of Air Quality Micro-sensing Units. *Sci. Total Environ.* 575, 639–648. doi:10.1016/j.scitotenv.2016.09.061

Forouzanfar, M. H., Afshin, A., Alexander, L. T., Anderson, H. R., Bhutta, Z. A., Biryukov, S., et al. (2016). Global, Regional, and National Comparative Risk Assessment of 79 Behavioural, Environmental and Occupational, and Metabolic Risks or Clusters of Risks, 1990-2015: a Systematic Analysis for the Global Burden of Disease Study 2015. *Lancet* 388, 1659–1724. doi:10.1016/S0140-6736(16)31679-8

Fuller, R., Sandilya, K., and Hanrahan, D. (2019). *Pollution and Health Metrics: Global, Regional and Country Analysis*. GAHP, Global Alliance on Health and Pollution.

Guo, H., Gu, X., Ma, G., Shi, S., Wang, W., Zuo, X., et al. (2019). Spatial and Temporal Variations of Air Quality and Six Air Pollutants in China during 2015-2017. *Sci. Rep.* 9, 15201. doi:10.1038/s41598-019-50655-6

Han, X., and Naeher, L. P. (2006). A Review of Traffic-Related Air Pollution Exposure Assessment Studies in the Developing World. *Environ. Int.* 32, 106–120. doi:10.1016/j.envint.2005.05.020

Hankey, S., and Marshall, J. D. (2015). On-bicycle Exposure to Particulate Air Pollution: Particle Number, Black Carbon, PM 2.5 , and Particle Size. *Atmos. Environ.* 122, 65–73. doi:10.1016/j.atmosenv.2015.09.025

Hu, L., Liu, J., and He, Z. (2016). Self-Adaptive Revised Land Use Regression Models for Estimating PM2.5 Concentrations in Beijing, China. *Sustainability* 8, 786. doi:10.3390/su8080786

Jahn, H. J., Kraemer, A., Chen, X.-C., Chan, C.-Y., Engling, G., and Ward, T. J. (2013). Ambient and Personal PM2.5 Exposure Assessment in the Chinese Megacity of Guangzhou. *Atmos. Environ.* 74, 402–411. doi:10.1016/j.atmosenv.2013.04.011

Jeong, C.-H., Wang, J. M., Hilker, N., Debosz, J., Sofowote, U., Su, Y., et al. (2019). Temporal and Spatial Variability of Traffic-Related PM2.5 Sources: Comparison of Exhaust and Non-exhaust Emissions. *Atmos. Environ.* 198, 55–69. doi:10.1016/j.atmosenv.2018.10.038

Jung, C.-R., Hwang, B.-F., and Chen, W.-T. (2018). Incorporating Long-Term Satellite-Based Aerosol Optical Depth, Localized Land Use Data, and Meteorological Variables to Estimate Ground-Level PM2.5 Concentrations in Taiwan from 2005 to 2015. *Environ. Pollut.* 237, 1000–1010. doi:10.1016/j.envpol.2017.11.016

Kelley, M. C., Brown, M. M., Fedler, C. B., and Ardon-Dryer, K. (2020). Long-term Measurements of PM2.5 Concentrations in Lubbock, Texas. *Aerosol Air Qual. Res.* 20, 1306–1318. doi:10.4209/aaqr.2019.09.0469

Kingham, S., Longley, I., Salmond, J., Pattinson, W., and Shrestha, K. (2013). Variations in Exposure to Traffic Pollution while Travelling by Different Modes in a Low Density, Less Congested City. *Environ. Pollut.* 181, 211–218. doi:10.1016/j.envpol.2013.06.030

Kuo, P.-H., Tsuang, B.-J., Chen, C.-J., Hu, S.-W., Chiang, C.-J., Tsai, J.-L., et al. (2014). Risk Assessment of Mortality for All-Cause, Ischemic Heart Disease, Cardiopulmonary Disease, and Lung Cancer Due to the Operation of the World's Largest Coal-Fired Power Plant. *Atmos. Environ.* 96, 117–124. doi:10.1016/j.atmosenv.2014.07.024

Lee, C.-H., Wang, Y.-B., and Yu, H.-L. (2019). An Efficient Spatiotemporal Data Calibration Approach for the Low-Cost PM2.5 Sensing Network: A Case Study in Taiwan. *Environ. Int.* 130, 104838. doi:10.1016/j.envint.2019.05.032

Lee, M., Lin, L., Chen, C.-Y., Tsao, Y., Yao, T.-H., Fei, M.-H., et al. (2020). Forecasting Air Quality in Taiwan by Using Machine Learning. *Sci. Rep.* 10, 4153. doi:10.1038/s41598-020-61151-7

Li, H. Z., Dallmann, T. R., Gu, P., and Presto, A. A. (2016). Application of Mobile Sampling to Investigate Spatial Variation in Fine Particle Composition. *Atmos. Environ.* 142, 71–82. doi:10.1016/j.atmosenv.2016.07.042

Li, J., Mattewal, S. K., Patel, S., and Biswas, P. (2020). Evaluation of Nine Low-Cost-Sensor-Based Particulate Matter Monitors. *Aerosol Air Qual. Res.* 20, 254–270. doi:10.4209/aaqr.2018.12.0485

Li, Z., Fung, J. C. H., and Lau, A. K. H. (2018). High Spatiotemporal Characterization of On-Road PM2.5 Concentrations in High-Density Urban Areas Using Mobile Monitoring. *Build. Environ.* 143, 196–205. doi:10.1016/j.buildenv.2018.07.014

Lin, M.-Y., Guo, Y.-X., Chen, Y.-C., Chen, W.-T., Young, L.-H., Lee, K.-J., et al. (2018). An Instantaneous Spatiotemporal Model for Predicting Traffic-Related Ultrafine Particle Concentration through Mobile Noise Measurements. *Sci. Total Environ.* 636, 1139–1148. doi:10.1016/j.scitotenv.2018.04.248

Lin, Y.-C., Chi, W.-J., and Lin, Y.-Q. (2020). The Improvement of Spatial-Temporal Resolution of PM2.5 Estimation Based on Micro-Air Quality Sensors by Using Data Fusion Technique. *Environ. Int.* 134, 105305. doi:10.1016/j.envint.2019.105305

Liu, X., Schnelle-Kreis, J., Zhang, X., Bendl, J., Khedr, M., Jakobi, G., et al. (2020). Integration of Air Pollution Data Collected by Mobile Measurement to Derive a Preliminary Spatiotemporal Air Pollution Profile from Two Neighboring German-Czech Border Villages. *Sci. Total Environ.* 722, 137632. doi:10.1016/j.scitotenv.2020.137632

Maji, K. J., Arora, M., and Dikshit, A. K. (2017). Burden of Disease Attributed to Ambient PM2.5 and PM10 Exposure in 190 Cities in China. *Environ. Sci. Pollut. Res.* 24, 11559–11572. doi:10.1007/s11356-017-8575-7

Malings, C., Tanzer, R., Hauryliuk, A., Saha, P. K., Robinson, A. L., Presto, A. A., et al. (2020). Fine Particle Mass Monitoring with Low-Cost Sensors: Corrections and Long-Term Performance Evaluation. *Aerosol Sci. Technol.* 54, 160–174. doi:10.1080/02786826.2019.1623863

Malmqvist, E., Lisberg Jensen, E., Westerberg, K., Stroh, E., Rittner, R., Gustafsson, S., et al. (2018). Estimated Health Benefits of Exhaust Free Transport in the City of Malmö, Southern Sweden. *Environ. Int.* 118, 78–85. doi:10.1016/j.envint.2018.05.035

Mazaheri, M., Clifford, S., Yeganeh, B., Viana, M., Rizza, V., Flament, R., et al. (2018). Investigations into Factors Affecting Personal Exposure to Particles in Urban Microenvironments Using Low-Cost Sensors. *Environ. Int.* 120, 496–504. doi:10.1016/j.envint.2018.08.033

Miller, K. A., Spalt, E. W., Gassett, A. J., Curl, C. L., Larson, T. V., Avol, E., et al. (2019). Estimating Ambient-Origin PM2.5 Exposure for Epidemiology: Observations, Prediction, and Validation Using Personal Sampling in the Multi-Ethnic Study of Atherosclerosis. *J. Expo. Sci. Environ. Epidemiol.* 29, 227–237. doi:10.1038/s41370-018-0053-x

Monrad, M., Sajadieh, A., Christensen, J. S., Ketzel, M., Raaschou-Nielsen, O., Tjønneland, A., et al. (2017). Long-Term Exposure to Traffic-Related Air Pollution and Risk of Incident Atrial Fibrillation: A Cohort Study. *Environ. Health Perspect.* 125, 422–427. doi:10.1289/ehp392

Morawska, L., Thai, P. K., Liu, X., Asumadu-Sakyi, A., Ayoko, G., Bartonova, A., et al. (2018). Applications of Low-Cost Sensing Technologies for Air Quality Monitoring and Exposure Assessment: How Far Have They Gone? *Environ. Int.* 116, 286–299. doi:10.1016/j.envint.2018.04.018

Mustafic, H., Jabre, P., Caussin, C., Murad, M. H., Escolano, S., Tafflet, M., et al. (2012). Main Air Pollutants and Myocardial Infarction: a Systematic Review and Meta-Analysis. *JAMA* 307, 713–721. doi:10.1001/jama.2012.126

Okokon, E. O., Yli-Tuomi, T., Turunen, A. W., Taimisto, P., Pennanen, A., Vouitsis, I., et al. (2017). Particulates and Noise Exposure during Bicycle, Bus and Car Commuting: A Study in Three European Cities. *Environ. Res.* 154, 181–189. doi:10.1016/j.envres.2016.12.012

Ostro, B.WHO (2004). *Outdoor Air Pollution: Assessing the Environmental Burden of Disease at National and Local Levels*. Geneva: World Health Organization.

Özkaynak, H., Baxter, L. K., Dionisio, K. L., and Burke, J. (2013). Air Pollution Exposure Prediction Approaches Used in Air Pollution Epidemiology Studies. *J. Expo. Sci. Environ. Epidemiol.* 23, 566–572. doi:10.1038/jes.2013.15

Piotrowicz, A., and Polednik, B. (2019). Exposure to Aerosols Particles on an Urban Road. *J. Ecol. Eng.* 20, 27–34. doi:10.12911/22998993/105329

R-Core-Team (2019). *R: A Language and Environment for Statistical Computing*. 2 ed. Vienna: R Foundation for Statistical Computing. R x64 3.6.

Rittner, R., Gustafsson, S., Spanne, M., and Malmqvist, E. (2020). Particle Concentrations, Dispersion Modelling and Evaluation in Southern Sweden. *Sn Appl. Sci.* 2, 15. doi:10.1007/s42452-020-2769-1

Saraswat, A., Apte, J. S., Kandlikar, M., Brauer, M., Henderson, S. B., and Marshall, J. D. (2013). Spatiotemporal Land Use Regression Models of Fine, Ultrafine, and Black Carbon Particulate Matter in New Delhi, India. *Environ. Sci. Technol.* 47, 12903–12911. doi:10.1021/es401489h

Shen, J., and Gao, Z. (2019). Commuter Exposure to Particulate Matters in Four Common Transportation Modes in Nanjing. *Build. Environ.* 156, 156–170. doi:10.1016/j.buildenv.2019.04.018

Snyder, E. G., Watkins, T. H., Solomon, P. A., Thoma, E. D., Williams, R. W., Hagler, G. S. W., et al. (2013). The Changing Paradigm of Air Pollution Monitoring. *Environ. Sci. Technol.* 47, 11369–11377. doi:10.1021/es4022602

IBM SPSS (2008). *SPSS Statistics for Windows*. version 17.0. Chicago: SPSS Inc.

Straif, K., Cohen, A., and Samet, J. (2013). *Air Pollution and Cancer*. Lyon: International Agency for Research on Cancer, IARC.

Tsi Incorporated (2013). *Rationale for Programming a PCF of 0.38 for Ambient Monitoring (EXPMN-007) A4 [Online]*. Minnesota USA: TSI Incorporated. Available at: https://www.tsi.com/products/aerosol-and-dust-monitors/dust-monitors/dusttrak-ii-aerosol-monitor-8530/ (Accessed May 18, 2020).

Van Der Kamp, J., and Bachmann, T. M. (2015). Health-related External Cost Assessment in Europe: Methodological Developments from ExternE to the 2013 Clean Air Policy Package. *Environ. Sci. Technol.* 49, 2929–2938. doi:10.1021/es5054607

W.H.O. (2022). *Health Impact Assessment [Online]*. World Health Organization. Available at: https://www.who.int/health-topics/health-impact-assessment#tab=tab_1 (Accessed Sep 1, 2019).

W.H.O. (2016). *Health Risk Assessment of Air Pollution: General Principles*. Geneva: World Health Organization.

W.H.O. (2012). *Sustainable Development Goals Target 11.6 [Online]*. World Health Organization. Available at: https://indicators.report/targets/11-6/ (Accessed Sep 1, 2019).

W.H.O. (2021). *WHO Global Air Quality Guidelines: Particulate Matter (PM2.5 and PM10), Ozone, Nitrogen Dioxide, Sulfur Dioxide and Carbon Monoxide*. Geneva: World Health Organization.

Williams, R., Duvall, R., Kilaru, V., Hagler, G., Hassinger, L., Benedict, K., et al. (2019). Deliberating Performance Targets Workshop: Potential Paths for Emerging PM2.5 and O3 Air Sensor Progress. *Atmos. Environ. X* 2, 100031. doi:10.1016/j.aeaoa.2019.100031

Wu, C.-D., Macnaughton, P., Melly, S., Lane, K., Adamkiewicz, G., Durant, J. L., et al. (2014). Mapping the Vertical Distribution of Population and Particulate Air Pollution in a Near-Highway Urban Neighborhood: Implications for Exposure Assessment. *J. Expo. Sci. Environ. Epidemiol.* 24, 297–304. doi:10.1038/jes.2013.64

Wu, T.-Y., Chung, C.-H., Lin, C.-N., Hwang, J.-S., and Wang, J.-D. (2018). Lifetime Risks, Loss of Life Expectancy, and Health Care Expenditures for 19 Types of Cancer in Taiwan. *Clep* 10, 581–591. doi:10.2147/clep.s155601

Yang, X., Xiao, D., Bai, H., Tang, J., and Wang, W. (2022). Spatiotemporal Distributions of PM2.5 Concentrations in the Beijing–Tianjin–Hebei Region from 2013 to 2020. *Front. Environ. Sci.* 10, 843862. doi:10.3389/fenvs.2022.842237

Yanosky, J. D., Williams, P. L., and Macintosh, D. L. (2002). A Comparison of Two Direct-Reading Aerosol Monitors with the Federal Reference Method for PM2.5 in Indoor Air. *Atmos. Environ.* 36, 107–113. doi:10.1016/s1352-2310(01)00422-8

Ye, W.-F., Ma, Z.-Y., and Ha, X.-Z. (2018). Spatial-temporal Patterns of PM2.5 Concentrations for 338 Chinese Cities. *Sci. Total Environ.* 631-632, 524–533. doi:10.1016/j.scitotenv.2018.03.057

Yousefian, F., Faridi, S., Azimi, F., Aghaei, M., Shamsipour, M., Yaghmaeian, K., et al. (2020). Temporal Variations of Ambient Air Pollutants and Meteorological Influences on Their Concentrations in Tehran during 2012-2017. *Sci. Rep.* 10, 292. doi:10.1038/s41598-019-56578-6

Zamora, M. L., Rice, J., and Koehler, K. (2020). One Year Evaluation of Three Low-Cost PM2.5 Monitors. *Atmos. Environ.* 235, 117615. doi:10.1016/j.atmosenv.2020.117615

Zhang, N., Huang, H., Duan, X., Zhao, J., and Su, B. (2018). Quantitative Association Analysis between PM2.5 Concentration and Factors on Industry, Energy, Agriculture, and Transportation. *Sci. Rep.* 8, 9461. doi:10.1038/s41598-018-27771-w

Conflict of Interest: The authors declare that the research was conducted in the absence of any commercial or financial relationships that could be construed as a potential conflict of interest.

Publisher's Note: All claims expressed in this article are solely those of the authors and do not necessarily represent those of their affiliated organizations, or those of the publisher, the editors, and the reviewers. Any product that may be evaluated in this article, or claim that may be made by its manufacturer, is not guaranteed or endorsed by the publisher.

frontiers | Frontiers in Environmental Science

TYPE Mini Review
PUBLISHED 19 July 2022
DOI 10.3389/fenvs.2022.864818

OPEN ACCESS

EDITED BY
Lang Liu,
Northwestern Polytechnical University, China

REVIEWED BY
Eduardo Landulfo,
Instituto de Pesquisas Energéticas e Nucleares (IPEN), Brazil

*CORRESPONDENCE
Jie Zhang,
jzhang35@albany.edu
Qianqian Sun,
sqqufhefei@163.com

SPECIALTY SECTION
This article was submitted to Atmosphere and Climate, a section of the journal Frontiers in Environmental Science

RECEIVED 28 January 2022
ACCEPTED 29 June 2022
PUBLISHED 19 July 2022

CITATION
Fang T, Zhang X, Zhang J, Wang J and Sun Q (2022), The prospected air quality measurements for further unconventional natural gas developments in China based on the United States experience.
Front. Environ. Sci. 10:864818.
doi: 10.3389/fenvs.2022.864818

The prospected air quality measurements for further unconventional natural gas developments in China based on the United States experience

Tao Fang[1], Xiaomeng Zhang[2], Jie Zhang[3]*, Junfeng Wang[4] and Qianqian Sun[5]*

[1]College of Economics and Management, Hefei University, Hefei, China, [2]PetroChina (Tianjin) International Petroleum Exploration & Development Technology Co, Ltd, Tianjin, China, [3]Atmospheric Sciences Research Center, University at Albany, State University of New York, Albany, NY, United States, [4]Jiangsu Key Laboratory of Atmospheric Environment Monitoring and Pollution Control, School of Environmental Science and Engineering, Nanjing University of Information Science and Technology, Nanjing, China, [5]School of Biology, Food and Environment, Hefei University, Hefei, China

The technological innovation of horizontal drilling and high-volume hydraulic fracturing has promoted the development of unconventional natural gas (UNG) production worldwide, and hence has aroused public concern about the air pollution it may bring about. In this study, we have provided (1) an overview of the study on air pollutants from UNG emissions in the USA, focusing on both the air pollutant characterization and their related observation technologies/platforms; and (2) the potential air quality measurements of UNG development emerging in China. This study will provide useful information for Chinese environmental researchers and the local governments to deal with related air quality issues.

KEYWORDS

unconventional natural gas development, air pollution, air quality measurements, China, United States

Introduction

Nature gas is accounting for more percentage of the world's energy supply from 20% in 2000 to 23% in 2019 (https://www.iea.org), due to its relatively less environmental impact and more economic advantages compared to oil and coal (Finkel et al., 2013). To seek "energy independence," unconventional natural gas (hereafter referred to as UNG, which originates from shale, sandstone, etc.) production has been promoted extensively in the USA during recent years at the major basins containing shale gas (i.e., Marcellus Shale Play at Appalachian Basin; Fayetteville Shale Play at Arkoma Basin; Barnett Shale Play at Ft. Worth Basin, etc. Figure 1), benefiting from the significant technological innovation of the horizontal drilling and the high-volume hydraulic fracturing techniques (Finkel et al., 2013; Wang and Krupnick, 2013; Moore et al., 2014; Allshouse et al., 2017; Helmig, 2020). From 2007 to 2019, the annual UNG production increased from about 560×10^8 m^3 to 7900×10^8 m^3 with an enhancement

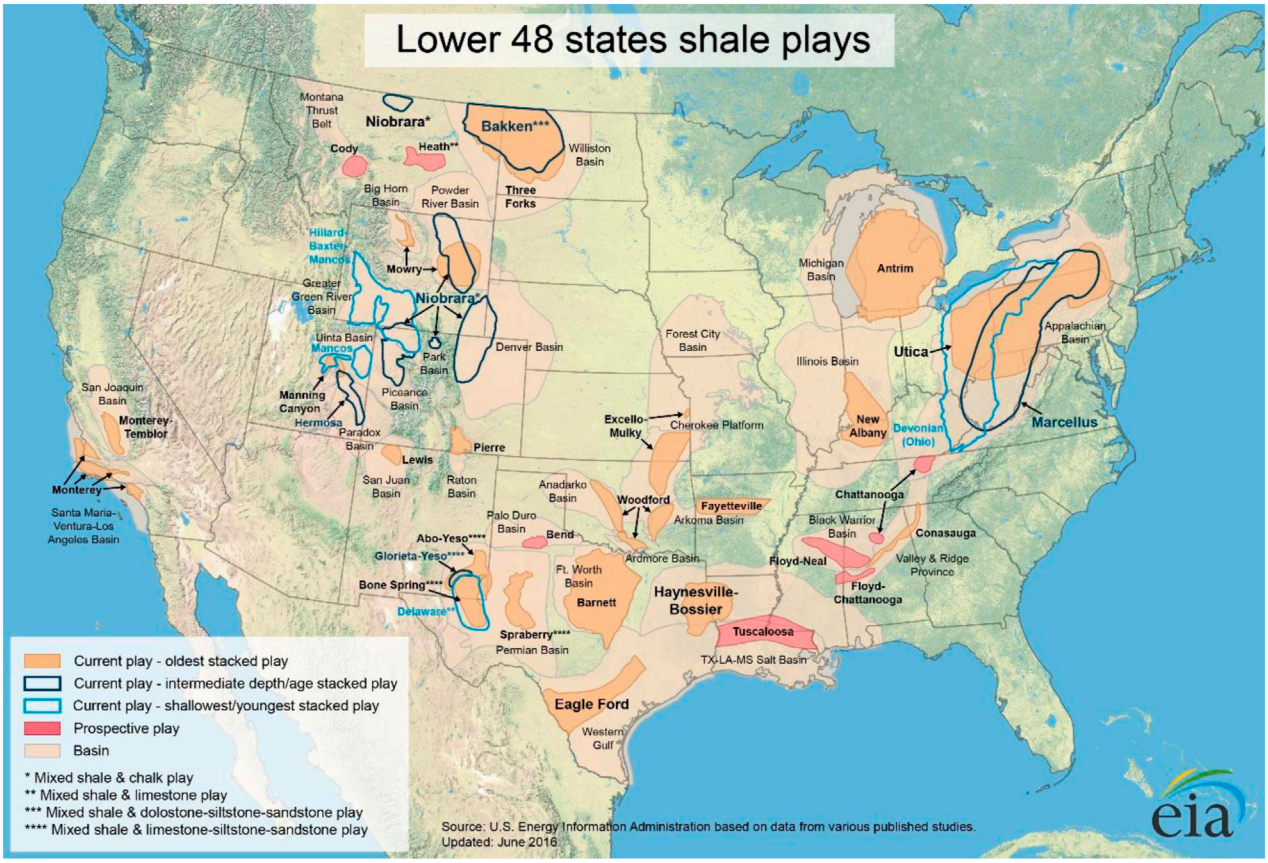

FIGURE 1
The U.S. lower 48 states shale oil and natural gas maps [source: U.S. Energy Information Administration (June 2016)].

factor of about 14 (http://www.eia.gov/naturalgas/). However, the surge of UNG development is accompanied by a significant increase in air pollutants emissions (McKenzie et al., 2012, Shonkoff et al., 2014; Allen, 2016; Kort et al., 2016), including carbon monoxide (CO), nitrogen oxides (NOx), volatile organic compounds (VOCs, Gilman et al., 2013; Bunch et al., 2014; Helmig, 2020; Pétron, et al., 2014), primary particulate matter (PM), and their related secondary productions (i.e., ozone and secondary organic aerosols (SOA), Kemball-Cook et al., 2010; Pacsi et al., 2015; Lee et al., 2015; Liggio et al., 2016; Cheadle et al., 2017; Pozzer et al., 2020). Public concern about the air pollutants has risen with the growth of the UNG development, which has expanded into urban residential areas and has promoted related scientific studies (Pacsi et al., 2015; Adgate et al., 2014; Field et a., 2014; Vinciguerra et al., 2015; McMullin et al., 2018; McKenzie et al., 2019).

China has the most abundant shale gas resources with a total amount of 31×10^{12} m^3, which is about 1.5 times of global shale gas reserves of the United States (https://www.eia.gov/analysis/studies/worldshalegas/). Although UNG production has quickly picked up in China, the annual UNG production of the USA is still about 40 times that of China in 2020 (7900×10^8 vs 200×10^8 m^3 (Sun et al., 2021). Under the most recent Chinese government energy policy, UNG production is expected to increase continually and reach 2200×10^8 m^3 in 2040 (Zou et al., 2017; IEA, 2020). With the surge of UNG production, the UNG wells will inevitably expand into human communities, especially in the Sichuan Basin (Ma and Xie, 2018; He et al., 2020; Nie et al., 2020, Figure 2) which is also a population cluster with two megacities-Chongqing and Chengdu, and the subsequent air quality issues could occur. Taking the fact into consideration, we organized this study to summarize the main air pollution issues detected during the USA UNG developments and their related measurement technologies, which can provide useful guidance for Chinese environmental researchers and the local governments to better understand the air pollution-related to UNG developments.

Air pollutants from UNG production in the USA

The air pollutants caused by UNG production are mainly focused on VOCs species [including methane and Non-methane volatile organic compounds (NMVOCs)] and their related

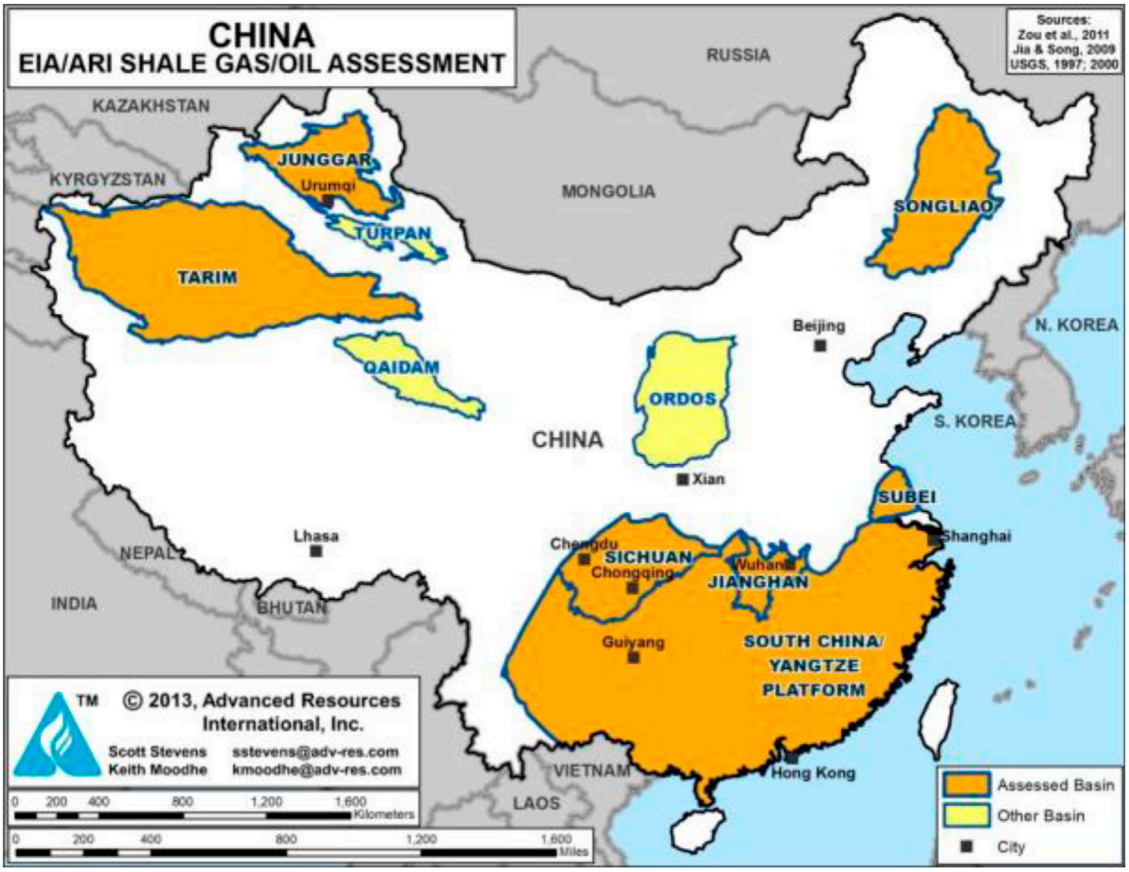

FIGURE 2
China's most prospective shale gas basins [Source: U.S. Energy Information Administration (September 2015)].

secondary productions (including Ozone and SOA) due to their clear effect on the radiative forcing (methane) and on the human health (NMVOCs, Ozone and SOA).

Methane

Methane (CH_4) is the second-most anthropogenic greenhouse gas (after CO_2) for its effect on radiative forcing, with significant emissions from UNG operations (Helmig, 2020). Methane emissions from UNG operations were shown to be about 23 times greater than from conventional ones, due to the larger size and higher production rate of UNG (Omara et al., 2016). The reportedly estimated annual CH_4 emissions from UNG production of the main shale regions were about 158 Gg from Denver-Julesburg Basin in 2015 (Peischl et al., 2018), 270 Gg from Bakken Shale Play at Williston Basin in 2014 (Peischl et al., 2015), 131 Gg from Marcellus Shale Play at Appalachian Basin in 2013 (Peischl et al., 2015), 342 Gg from the Fayetteville Shale Play at Arkoma Basin (Peischl et al., 2015), 525 Gg from the Barnett at Ft. Worth Basin in 2013 (Karion et al., 2015), and 700 Gg from the Haynesville Shale Play at Texas-Louisiana Salt Basin (Peischl et al., 2015). The locations of each region are shown in Figure 1. Besides the CH_4 emissions from the gathering/processing plants and well pads during UNG production, CH_4 could also be emitted from the gathering pipeline, which was used to transport gases to a processing facility or a transmission line (Zimmerle et al., 2017).

Non-methane volatile organic compounds

NMVOCs from UNG production contain hazardous compounds (benzene, toluene, ethylbenzene, and xylenes (BTEX)) and other compounds (Shonkoff et al., 2014; Bolden et al., 2015), which act as precursors to O_3 and secondary organic aerosol (SOA) (Liggio et al., 2016; McDuffie et al., 2016). Enhanced NMVOCs mixing ratios near the UNG wells have been observed with variable VOCs emission rates under different

well operations (namely, drilling, fracking, coiled tubing, and flowback) (Hecobian et al., 2019). The concentration of hazardous BTEX is reported to be as high as 500 ppb downwind of oil and gas wastewater disposal facilities, which highlights the importance of monitoring BTEX concentrations during UNG operations (Helmig, 2020).

O_3 and $PM_{2.5}$

O_3 and $PM_{2.5}$ are classified as two air pollutants on the EPA list, whose high concentration levels can cause serious harm to the human health, respiratory system in particular (Anenberg et al., 2010). The elevated level of VOCs and NOx from the UNG emissions are precursors to O_3 and SOA (Liggio et al., 2016; McDuffie et al., 2016). A number of studies have linked UNG production to nearby O_3 exceedances, even in winter (Edwards et al., 2014). The studies at the Denver basin showed about 20 ppb of O_3 enhancement (Benedict et al., 2019) and about 38% of SOA (Bahreini et al., 2018) being associated with VOCs and NOx emitted from UNG production.

Prospected air quality measurements in China

The measured air pollutants from the US shale plays based on the previous studies will be useful for narrowing the Chinese environmental researchers' focus and comparing the different emission rates of the air pollutants due to the different types of the shale basins comparing China and the United States. The measurements used in the USA also highlighted the necessity of the integration of multiple platforms for the air pollutants, including the (1) site observation platform, (2) mobile lab, drone, and airplane observation platform, and (3) satellite observation platform, for a better understanding the air pollutants emissions, while, the platforms and the related instruments mentioned below will quickly help the environmental researchers build their suitable platforms.

Site observation platform

Large-sized temporarily fixed observation sites, generally modified from mobile shelters (EPA, 2017), are most commonly used, which could support numerous monitors with a stable power supply for long-term measurements, such as (1) the commercial on-site instruments for O_3, NO/NO_2, $PM_{2.5}$ (e.g., 2B Model 205 O_3 Analyzer, Thermo Model 42C NO/NO_2/NOx Analyzer, GRIMM EDM 180 FEM $PM_{2.5}$ Monitor), (2) the mass spectrometry technology-based instruments for VOCs species [e.g., IONICON Proton-transfer-reaction mass spectrometry (PTR-MS), Thermo thermal desorption gas chromatography-mass spectrometry (TD-GC-MS)] and aerosol species [e.g., Aerodyne Aerosol mass spectrometry (AMS)], (3) the laser technology-based instruments for VOCs species [e.g., Aerodyne quantum cascade lasers (QCLs)], (4) the LiDARs for $O_3/PM_{2.5}$ vertical profiles, (5) VOCs canister collection system for further high-sensitivity VOC species analysis, and (6) the meteorological sensors (e.g. temperature, RH, wind speed, wind direction, solar radiance, precipitation). In addition to the larger temporarily fixed sites, temporary smaller sites with low-energy and low-cost sensors have also been established and widely used (https://www.epa.gov/air-sensor-toolbox/evaluation-emerging-air-sensor-performance), which could compensate for the shortcomings of the larger fixed sites (e.g., lack of mobility, high cost to deploy quick-response situations or wide range). When equipped with a photoionization detector (PID) trigger system (Hecobian et al., 2019), the temporary smaller site can capture the high VOC plume using small canisters, which could provide useful information for the VOCs identification from UNG emissions.

Mobile lab, drone, and airplane observation platform

The mobile lab, generally converted from a van or a truck, can carry the above instruments to conduct on-road measurements using a multi-battery system or power generated from the engine (Boanini et al., 2021). The mobile lab could be used to capture the transport of air pollutant plumes, estimate the emission flux based on circle-route measurements, observe the spatial concentration distribution of air pollutants, act as a fixed site at some high concentration spots, etc (Mohr et al., 2011; von der Weiden-Reinmüller et al., 2014; Huang et al., 2020; Zhang J et al., 2020). However, given the terrain or the UNG factory regulations, the mobile lab could miss some areas. In this case, an unmanned aerial vehicle (UAV) carrying light-weight sensors could be used for such region observations and also for concentration vertical profile measurements (McKinney et al., 2019). The airplane platform could be used for large-scale observation, but the number of flights or aircraft could be limited due to the high cost.

Satellite observation platform

Satellite observations could provide temporary and spatial concentration variation of some species, such as NOx, CH_4, O_3, etc, which could be used to evaluate the influence of UNG emissions on a large scale (Jacob et al., 2016; Goldberg et al., 2019; Varon et al., 2019). Combining the model simulation using existing emission inventories and comparing it with the current satellite observations, the current species emission rate could be estimated (Zhang Y et al., 2020), which would be very useful for updating the existing emission inventories.

Conclusion

Benefiting from the horizontal drilling and hydraulic fracturing techniques innovation, the USA has experienced the boom of the UNG development and reached its goal of "energy independence." However, UNG development in China is still in its infancy and has a great potential for rapid growth, which will inevitably result in air pollution, as has been seen in the Denver Basin. These issues should be given top priority due to the clean air action from the current Chinese government. The studies on the air quality in the USA for the UNG-related air pollutant emissions provide solid knowledge, either on the air pollutants characterization or their related observation technologies/platforms, which can provide very useful guidance for Chinese environmental researchers and the local governments to deal with the air quality issues caused by the further surging of UNG production.

Author contributions

Conceptualization, formal analysis, TF and JZ; investigation, resources, TF, XZ, SQ, and JF; writing—original draft preparation, TF; writing—review and editing, XZ, SQ, and JZ. All authors have read and agreed to the published version of the manuscript.

Funding

This research was funded by a domestic visiting program for outstanding young people in Colleges, grant number "gxgnfx2020027".

Conflict of interest

Author XZ is employed by PetroChina (Tianjin) International Petroleum Exploration &Development Technology Co., Ltd.

The remaining authors declare that the research was conducted in the absence of any commercial or financial relationships that could be construed as a potential conflict of interest.

Publisher's note

All claims expressed in this article are solely those of the authors and do not necessarily represent those of their affiliated organizations, or those of the publisher, the editors and the reviewers. Any product that may be evaluated in this article, or claim that may be made by its manufacturer, is not guaranteed or endorsed by the publisher.

References

Allen, D. T. (2016). Emissions from oil and gas operations in the United States and their air quality implications. *J. Air Waste Manag. Assoc.* 66, 549–575. doi:10.1080/10962247.2016.1171263

Allshouse, W. B., Adgate, J. L., Blair, B. D., and McKenzie, L. M. (2017). Spatiotemporal industrial activity model for estimating the intensity of oil and gas operations in Colorado. *Environ. Sci. Technol.* 51 (17), 10243–10250. doi:10.1021/acs.est.7b02084

Anenberg, S. C., Horowitz, L. W., Tong, D. Q., and West, J. J. (2010). An estimate of the global burden of anthropogenic ozone and fine particulate matter on premature human mortality using atmospheric modeling. *Environ. Health Perspect.* 118 (9), 1189–1195. doi:10.1289/ehp.0901220

Bahreini, R., Ahmadov, R., McKeen, S. A., Vu, K. T., Dingle, J. H., Apel, E. C., et al. (2018). Sources and characteristics of summertime organic aerosol in the Colorado front range: Perspective from measurements and WRF-chem modeling. *Atmos. Chem. Phys.* 18, 8293–8312. doi:10.5194/acp-18-8293-2018

Benedict, K. B., Zhou, Y., Sive, B. C., Prenni, A. J., Gebhart, K. A., Fischer, E. V., et al. (2019). Volatile organic compounds and ozone in rocky mountain national park during FRAPPE. *Atmos. Chem. Phys.* 19, 499–521. doi:10.5194/acp-19-499-2019

Boanini, C., Mecca, D., Pognant, F., Bo, M., and Clerico, M. (2021). Integrated mobile laboratory for air pollution assessment: Literature review and cc-TrAIRer design. *Atmosphere* 12 (8), 1004. doi:10.3390/atmos12081004

Bolden, A. L., Kwiatkowski, C. F., and Colborn, T. (2015). New look at BTEX: Are ambient levels a problem? *Environ. Sci. Technol.* 49 (9), 5261–5276. doi:10.1021/es505316f

Bunch, A. G., Perry, C. S., Abraham, L., Wikoff, D. S., Tachovsky, J. A., Hixon, J. G., et al. (2014). Evaluation of impact of shale gas operations in the Barnett Shale region on volatile organic compounds in air and potential human health risks. *Sci. Total Environ.* 468–469, 832–842. doi:10.1016/j.scitotenv.2013.08.080

Cheadle, L. C., Oltmans, S. J., Pétron, G., Schnell, R. C., Mattson, E. J., Herndon, S. C., et al. (2017). Surface ozone in the Colorado northern Front Range and the influence of oil and gas development during FRAPPE/DISCOVER-AQ in summer 2014. *Elem. Sci. Anth* 5, 61. doi:10.1525/elementa.254

Edwards, P. M., Brown, S. S., Roberts, J. M., Ahmadov, R., Banta, R. M., deGouw, J. A., et al. (2014). High winter ozone pollution from carbonyl photolysis in an oil and gas basin. *Nature* 514, 351–354. doi:10.1038/nature13767

EPA (2017). *Quality assurance handbook for air pollution measurement systems, volume II, ambient air quality monitoring program*. Available at: https://www3.epa.gov/ttnamti1/files/ambient/pm25/qa/Final%20Handbook%20Document%201_17.pdf.

Finkel, M., Hays, J., and Law, A. (2013). The shale gas boom and the need for rational policy. *Am. J. Public Health* 103 (7), 1161–1163. doi:10.2105/AJPH.2013.301285

Gilman, J. B., Lerner, B. M., Kuster, W. C., and de Gouw, J. A. (2013). Source signature of volatile organic compounds from oil and natural gas operations in northeastern Colorado. *Environ. Sci. Technol.* 47 (3), 1297–1305. doi:10.1021/es304119a

Goldberg, D. L., Lu, Z., Streets, D. G., de Foy, B., Griffin, D., McLinden, C. A., et al. (2019). Enhanced capabilities of TROPOMI NO_2: Estimating NOx from north American cities and power plants. *Environ. Sci. Technol.* 53, 12594–12601. doi:10.1021/acs.est.9b04488

He, Z. L., Nie, H. K., Hu, D., Jiang, T. X., Wang, R. Y., Zhang, Y., et al. (2020). Geological problems in the effective development of deep shale gas: A case study of upper ordovician wufeng-lower silurian longmaxi formations in Sichuan Basin and its PeripheryHighly elevated atmospheric levels of volatile organic compounds in the Utah basin, Utah. *Acta Pet. sin.environ. Sci. Technol.* 4148 (4), 3794707–3914715. doi:10.7623/syxb202004001Helmig10.1021/es405046r

Hecobian, A., Clements, A. L., Shonkwiler, K. B., Zhou, Y., MacDonald, L. P., Hilliard, N., et al. (2019). Air toxics and other volatile organic compound emissions from unconventional oil and gas development. *Environ. Sci. Technol. Lett.* 6 (12), 720–726. doi:10.1021/acs.estlett.9b00591

Helmig, D. (2020). Air quality impacts from oil and natural gas development in Colorado. *Elem. Sci. Anth* 8, 4. doi:10.1525/elementa.398

Huang, Y., Li, A., Wagner, T., Wang, Y., Hu, Z., Xie, P., et al. (2020). The quantification of NOx and SO_2 point source emission flux errors of mobile differential optical absorption spectroscopy on the basis of the Gaussian dispersion model: A simulation study. *Atmos. Meas. Tech.* 13, 6025–6051. doi:10.5194/amt-13-6025-2020

IEA (2020). *World energy outlook 2020*. Paris: IEA. Available at: https://www.iea.org/reports/world-energy-outlook-2020.

Jacob, D. J., Turner, A. J., Maasakkers, J. D., Sheng, J., Sun, K., Liu, X., et al. (2016). Satellite observations of atmospheric methane and their value for quantifying methane emissions. *Atmos. Chem. Phys.* 16, 14371–14396. doi:10.5194/acp-16-14371-2016

Karion, A., Sweeney, C., Kort, E. A., Shepson, P. B., Brewer, A., Cambaliza, M. O. L., et al. (2015). Aircraft-based estimate of total methane emissions from the Barnett Shale Region. *Environ. Sci. Technol.* 49 (13), 8124–8131. doi:10.1021/acs.est.5b00217

Kemball-Cook, S., Bar-Ilan, A., Grant, J., Parker, L., Jung, J. G., Santamaria, W., et al. (2010). Ozone impacts of natural gas development in the Haynesville Shale. *Environ. Sci. Technol.* 44 (24), 9357–9363. doi:10.1021/es1021137

Lee, L., Wooldridge, P. J., deGouw, J., Brown, S. S., Bates, T. S., Quinn, P. K., et al. (2015). Particulate organic nitrates observed in an oil and natural gas production region during wintertime. *Atmos. Chem. Phys.* 15, 9313–9325. doi:10.5194/acp-15-9313-2015

Liggio, J., Li, S. M., Hayden, K., Taha, Y. M., Stroud, C., Darlington, A., et al. (2016). Oil sands operations as a large source of secondary organic aerosols. *Nature* 534, 91–94. doi:10.1038/nature17646

Ma, X. H., and Xie, J. (2018). The progress and prospects of shale gas exploration and development in southern Sichuan Basin, SW China. *Petroleum Explor. Dev.* 45 (1), 172–182. doi:10.1016/S1876-3804(18)30018-1

McDuffie, E. E., Edwards, P. M., Gilman, J. B., Lerner, B. M., Dube, W. P., Trainer, M., et al. (2016). Influence of oil and gas emissions on summertime ozone in the Colorado Northern Front Range. *J. Geophys. Res. Atmos.* 121, 8712–8729. doi:10.1002/2016JD025265

McKenzie, L. M., Crooks, J., Peel, J. L., Biafr, B. D., Brindley, S., Allshouse, W. B., et al. (2019). Relationships between indicators of cardiovascular disease and intensity of oil and natural gas activity in Northeastern Colorado. *Environ. Res.* 170, 56–64. doi:10.1016/j.envres.2018.12.004

McKenzie, L. M., Witter, R. Z., Newman, L. S., and Adgate, J. L. (2012). Human health risk assessment of air emissions from development of unconventional natural gas resources. *Sci. Total Environ.* 424, 79–87. doi:10.1016/j.scitotenv.2012.02.018

McKinney, K. A., Wang, D., Ye, J., de Fouchier, J. B., Guimarães, P. C., Batista, C. E., et al. (2019). A sampler for atmospheric volatile organic compounds by copter unmanned aerial vehicles. *Atmos. Meas. Tech.* 12, 3123–3135. doi:10.5194/amt-12-3123-2019

Moore, C., Zielinska, B., Pétron, G., and Jackson, R. B. (2014). Air impacts of increased natural gas acquisition, processing, and use: A critical review. *Environ. Sci. Technol.* 48 (15), 8349–8359. doi:10.1021/es4053472

Nie, H. K., Li, D. H., Liu, G. X., Lu, Z. Y., Hu, W., Wang, R. Y., et al. (2020). An overview of the geology and production of the fuling shale gas Field, Sichuan Basin, China. *Energy Geosci.* 1 (3–4), 147–164. doi:10.1016/j.engeos.2020.06.005

Omara, M., Sullivan, M. R., Li, X., Subramanian, R., Robinson, A. L., Presto, A. A., et al. (2016). Methane emissions from conventional and unconventional natural gas production sites in the Marcellus shale basin. *Environ. Sci. Technol.* 50 (4), 2099–2107. doi:10.1021/acs.est.5b05503

Pacsi, A. P., Kimura, Y., McGaughey, G., McDonald-Buller, E. C., and Allen, D. T. (2015). Regional ozone impacts of increased natural gas use in the Texas power sector and development in the eagle ford shale. *Environ. Sci. Technol.* 49, 3966–3973. doi:10.1021/es5055012

Peischl, J., Eilerman, S. J., Neuman, J. A., Aikin, K. C., deGouw, J., Gilman, J. B., et al. (2018). Quantifying methane and ethane emissions to the atmosphere from Central and Western U.S. oil and natural gas production regions. *J. Geophys. Res. Atmos.* 123, 7725–7740. doi:10.1029/2018JD028622

Peischl, J., Ryerson, T. B., Aikin, K. C., de Gouw, J. A., Gilman, J. B., Holloway, J. S., et al. (2015). Quantifying atmospheric methane emissions from the Haynesville, Fayetteville, and northeastern Marcellus shale gas production regions. *J. Geophys. Res. Atmos.* 120, 2119–2139. doi:10.1002/2014JD022697

Pétron, G., Karion, A., Sweeney, C., Miller, B. R., Montzka, S. A., Frost, G. J., et al. (2014). A new look at methane and nonmethane hydrocarbon emissions from oil and natural gas operations in the Colorado Denver-Julesburg Basin. *J. Geophys. Res. Atmos.* 119 (11), 6836–6852. doi:10.1002/2013JD021272

Pozzer, A., Schultz, M. G., and Helmig, D. (2020). Impact of U.S. Oil and natural gas emission increases on surface ozone is most pronounced in the central United States. *Environ. Sci. Technol.* 54 (19), 12423–12433. doi:10.1021/acs.est.9b06983

Shonkoff, S. B., Hays, J., and Finkel, M, L. (2014). Environmental public health dimensions of shale and tight gas development. *Environ. Health Perspect.* 122, 787–795. doi:10.1289/ehp.1307866

Sun, C., Nie, H., Dang, W., Chen, Q., Zhang, G., Li, W., et al. (2021). Shale gas exploration and development in China: Current status, geological challenges, and future directions. *Energy fuels.* 35 (8), 6359–6379. doi:10.1021/acs.energyfuels.0c04131

Varon, D. J., McKeever, J., Jervis, D., Maasakkers, J. D., Pandey, S., Houweling, S., et al. (2019). Satellite discovery of anomalously large methane point sources from oil/gas production. *Geophys. Res. Lett.* 46, 13507–13516. doi:10.1029/2019GL083798

von der Weiden-Reinmüller, S. L., Drewnick, F., Crippa, M., Prévôt, A. S. H., Meleux, F., Baltensperger, U., et al. (2014). Application of mobile aerosol and trace gas measurements for the investigation of megacity air pollution emissions: The paris metropolitan area. *Atmos. Meas. Tech.* 7, 279–299. doi:10.5194/amt-7-279-2014

Wang, Z., and Krupnick, A. A. (2013). Retrospective review of shale gas development in the United States: What led to the boom? *Resour. Future*, DP13–12.

Zhang J, J., Ninneman, M., Joseph, E., Schwab, M. J., Shrestha, B., Schwab, J. J., et al. (2020). Mobile laboratory measurements of high surface ozone levels and spatial heterogeneity during LISTOS 2018: Evidence for sea-breeze influence. *J. Geophys. Res. Atmos.* 125 (11). doi:10.1029/2019JD031961

Zhang Y, Y., Gautam, R., Pandey, S., Omara, M., Maasakkers, J. D., Sadavarte, P., et al. (2020). Quantifying methane emissions from the largest oil-producing basin in the United States from space. *Sci. Adv.* 6, eaaz5120. eaaz5120. doi:10.1126/sciadv.aaz5120

Zimmerle, D. J., Pickering, C. K., Bell, C. S., Heath, G. A., Nummedal, D., and Pétron, G. (2017). Gathering pipeline methane emissions in Fayetteville shale pipelines and scoping guidelines for future pipeline measurement campaigns. *Elem. Sci. Anthropocene* 5, 70. doi:10.1525/elementa.258

Zou, C., Zhao, Q., Dong, D., Yang, Z., Qiu, Z., Liang, F., et al. (2017). Geological characteristics, main challenges and future prospect of shale gas. *J. Nat. Gas Geoscience* 2, 273–288. doi:10.1016/j.jnggs.2017.11.002

frontiers | Frontiers in Environmental Science

TYPE Original Research
PUBLISHED 29 August 2022
DOI 10.3389/fenvs.2022.945870

OPEN ACCESS

EDITED BY
Qian Zhang,
Xi'an University of Architecture and Technology, China

REVIEWED BY
Prashant Rajput,
Banaras Hindu University, India
Chunlei Han,
Binzhou Medical University, China

*CORRESPONDENCE
Baoqing Sun,
sunbaoqing@vip.163.com
Zheng Zhu,
ching1262006@126.com

†These authors have contributed equally to this work

SPECIALTY SECTION
This article was submitted to Atmosphere and Climate, a section of the journal Frontiers in Environmental Science

RECEIVED 17 May 2022
ACCEPTED 26 July 2022
PUBLISHED 29 August 2022

CITATION
Gan H, Cheng L, Zhai Y, Wang Y, Hu H, Zhu Z and Sun B (2022), Deaths and disability-adjusted life years burden attributed to air pollution in China, 1990–2019: Results from the global burden of disease study 2019. *Front. Environ. Sci.* 10:945870. doi: 10.3389/fenvs.2022.945870

Deaths and disability-adjusted life years burden attributed to air pollution in China, 1990–2019: Results from the global burden of disease study 2019

Hui Gan[1†], Long Cheng[2†], Yingying Zhai[3†], Yimin Wang[1], Haisheng Hu[1], Zheng Zhu[1*] and Baoqing Sun[1*]

[1]Department of Allergy and Clinical Immunology, Department of Laboratory, National Center for Respiratory Medicine, National Clinical Research Center for Respiratory Disease, State Key Laboratory of Respiratory Disease, Guangzhou Institute of Respiratory Health, The First Affiliated Hospital of Guangzhou Medical University, Guangzhou, China, [2]Department of Medical Affairs, Tongji Hospital, Tongji Medical College, Huazhong University of Science and Technology, Wuhan, China, [3]Department of Pediatrics, The First Affiliated Hospital of Guangzhou Medical University, Guangzhou, China

Background: The impact of deaths and disability-adjusted life years (DALYs) caused by air pollution in China has not been well elucidated. We aimed to analyze the association of air pollution with deaths and DALYs in the Chinese population.

Methods: We extracted data on burden due to deaths and disability-adjusted life years attributed to air pollution in the previous 30 years in China from the Global Burden of Disease (GBD) study 2019 and performed a comprehensive analysis and summary.

Results: 1.85 (95% UI: 1.57–2.17) million Chinese people lost their lives as a result of air pollution in 2019, a slight decrease from 1990. In 2019, the disability-adjusted life years (DALYs) caused by air pollution in China was 42.51 (95% UI: 36.34–49.48) million, a 30.2% decrease from 1990. From 1990 to 2019, both age-standardized death rate (ASDR) and age-standardized DALYs due to air pollution in China showed a significant year-on-year downward trend. Air pollution–related deaths and DALYs occurred mostly in people over the age of 50 years. Stroke, ischemic heart disease, and chronic obstructive pulmonary disease were attributed the maximum death burden due to air pollution in China in 2019.

Conclusion: Over the past 30 years, air pollution has brought a heavy disease burden to China, and in the future, joint efforts are required to improve the air quality.

KEYWORDS

air pollution, China, DALYs, GBD 2019, global burden of disease study

Introduction

Air pollution is one of the most severe environmental issues that threatens public health all around the world (Landrigan et al., 2018). It is well known that air pollution is associated with premature death and diseases (Lelieveld et al., 2015). Air pollution increases the risk of mortality from respiratory diseases such as chronic obstructive pulmonary disease, pneumonia, and asthma (Garshick, 2014; Chen et al., 2017; Pirozzi et al., 2018; Liu Y et al., 2019). Air pollution is also associated with an increased number of hospital visits for allergic rhinitis, asthma, and IgE-mediated allergy (Villeneuve et al., 2007; Hu et al., 2020; Hou et al., 2021). Furthermore, air pollution exposure increases the risk of young children being hospitalized for respiratory diseases (Huang et al., 2022), which lead to increased airway obstruction in adolescence (Milanzi et al., 2018).

The World Health Organization (WHO) reported that air pollution kills an estimated 7 million people every year globally (World Health Organization, 2022). Recent data have shown that all of the global population (99%) breathe air that exceeds WHO guideline limits and contain high levels of pollutants (World Health Organization, 2022). Due to the tremendous increase in its energy consumption and to emissions of air pollutants as a result of the extraordinary economic and industrial developments, China encounters serious air pollution problems that result in health problems (Watts, 2005; Guan et al., 2009). According to a 2005 report, a third of its urban residents are exposed to harmful polluted air, and more than 400,000 people die prematurely every year because of air pollution in China (Watts, 2005). The air quality of most regions in China has improved following the release and implementation of the Air Pollution Prevention and Control Action Plan in 2013 (The State Council of the People's Republic of China, 2013; Guo et al., 2017). However, research on the disease burden and changing trends in the past decades caused by air pollution in China is lacking.

The aim of the present study is to better understand the scale of harm caused by air pollution in China. For this purpose, we analyzed air pollution–attributable disease burden in China, based on the data on deaths and disability-adjusted life years (DALYs) from GBD 2019. We also investigate the different kinds of disease burden caused by the different kinds of air pollution.

Methods

Study data

Data on deaths, DALYs, and estimated annual percentage change (EAPC) as a consequence of air pollution in China were derived from an online data source tool, the Global Health Data Exchange (GHDx) query tool (http://ghdx.healthdata.org/gbd-results-tool), which is a global collaboration that uses various kinds of available epidemiological data to provide a comparative assessment of health loss from 369 diseases and different health risks across 204 countries and territories (GBD 2019 Diseases and Injuries Collaborators, 2020). The details about the study design and methods of GBD studies have been extensively described in the existing GBD literature (Global Burden of Diseases, 2016; GBD 2019 Risk Factors Collaborators, 2020).

Data analysis

Data from the literature reviews and national surveys were used by GBD collaboration to estimate the non-death burden due to air pollution. Bayesian meta-regression with DisMod-MR 2.1, which is a tool evaluating the epidemiology of a disease, was then used to estimate the incidence and prevalence of different diseases by location, year, sex, and age in all the sources. Death burden attributed to air pollution was analyzed using vital registration and surveillance data from the cause-of-death database. The deaths were distributed to different causes according to the ICD code mappings (Global Burden of Diseases, 2016; GBD 2019 Diseases and Injuries Collaborators, 2020; GBD 2019 Risk Factors Collaborators, 2020).

A secondary descriptive analysis was conducted with regard to the burden of deaths and DALYs due to air pollution in China from 1990 to 2019, and the findings were investigated further. The disease burden for both genders and different kinds of air pollution were also compared. The uncertainty intervals (UIs) were defined as the 2.5th and 97.5th values of the posterior distributions as previously descripted (Barendregt et al., 2003; Ferrari et al., 2013).

Results

Deaths and disability-adjusted life years attributable to air pollution in China

The number of deaths due to air pollution in China was 1.90 (95% UI: 1.59–2.19) million in 1990 and 1.85 (95% UI: 1.57–2.17) million in 2019, which is a slight decrease of 2.6% as compared to 1990. There are certain differences between genders when comparing between 1990 and 2019. In 1990, air pollution killed 0.98 (95% UI: 0.80–1.16) million men as compared to 0.92 (95% UI: 0.74–1.08) million women. In 2019, air pollution killed 1.09 (95% UI: 0.87–1.34) million men, an increase since 1990, while the number of deaths was 0.76 (95% UI: 0.61–0.94) million for women, which is a moderate drop as compared to 1990 (Table 1).

DALYs represent the total health burden of a disease, which are the years of lives lost (YLLs) due to premature mortality and years of healthy lives lost due to disabilities (YLDs). In 2019, the DALYs caused by air pollution in China was 42.51 (95% UI:

TABLE 1 Deaths and DALYs attributable to air pollution in China in 1990 and 2019.

	Death cases (95% UI), million		EAPC (95% UI), %	DALYs (95% UI), million		EAPC (95% UI), %
	1990	2019		1990	2019	
Both	1.90 (1.59–2.19)	1.85 (1.57–2.17)	−0.03 (−0.21 to 0.21)	60.91 (51.58–69.88)	42.51 (36.34–49.48)	−0.30 (−0.43 to −0.13)
Male	0.98 (0.80–1.16)	1.09 (0.87–1.34)	0.11 (−0.15 to 0.43)	2.69 (27.03–38.16)	25.61 (14.09–20.06)	−0.22 (−0.39 to 0.00)
Female	0.92 (0.74–1.08)	0.76 (0.61–0.94)	−0.17 (−0.36 to 0.08)	8.21 (23.28–32.78)	42.51 (20.64–31.21)	−0.40 (−0.53 to −0.25)

DALYs, disability-adjusted life years; EAPC, estimated annual percentage change; UI, uncertainty interval. Results are rounded up to two decimal places.

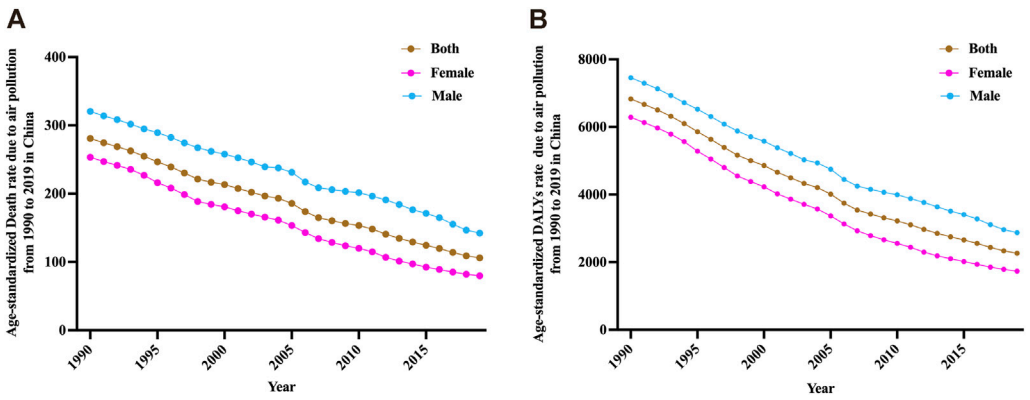

FIGURE 1
Age-standardized disease burden due to air pollution in China from 1990 to 2019. Age-standardized death **(A)** and DALYs **(B)** rate. DALYs, disability-adjusted life years.

36.34–49.48) million, a 30.2% decrease from 1990. In 2019, the DALYs of both males and females had decreased since 1990, with a larger decrease seen in females (Table 1).

From 1990 to 2019, both age-standardized death and DALYs rate caused by air pollution in China showed a significant year-on-year downward trend. The decline was almost the same across genders (Figure 1).

Disease burden of different age groups due to air pollution in China

We further analyzed the disease burden caused by air pollution in the different age groups in China. The age-standardized death rate and DALYs of four different age groups (0–14, 15–49, 50–69, and 70+ years) were analyzed.

From 1990 to 2019, air pollution has had a greater impact on the older age groups, especially those over the age of 70 years. More than 90% of the ASDR caused by air pollution occur among people over the age of 50 years (Figure 2).

In the past 30 years, the health burden of air pollution on the four different age groups has gradually declined, both the age-standardized DALYs rate and ASDR have decreased year after year (Figures 2A,B). However, from 1990 to 2019, the proportion of health burden caused by air pollution to people in the middle and older age groups (50–69 and 70+ years) has increased year after year among all the age groups (Figures 2C,D). In particular, the ASDR caused by air pollution is more prominent in the middle-aged and older age groups. These data indicate that the elderly are more vulnerable to air pollution.

Death due to different diseases caused by air pollution in China

Seven major diseases have been effected by air pollution and have led to death of patients in China. The ASDR of these diseases due to air pollution was ranked in 1990 as follows: chronic obstructive pulmonary disease, stroke, lower respiratory infections, ischemic heart disease, tracheal, bronchus and lung cancer, neonatal disorders, and diabetes mellitus. In 2019, the ranking order of these seven diseases had changed. The ASDR of the seven diseases caused by air pollution ranked from high to low was as follows: stroke, ischemic heart disease, chronic

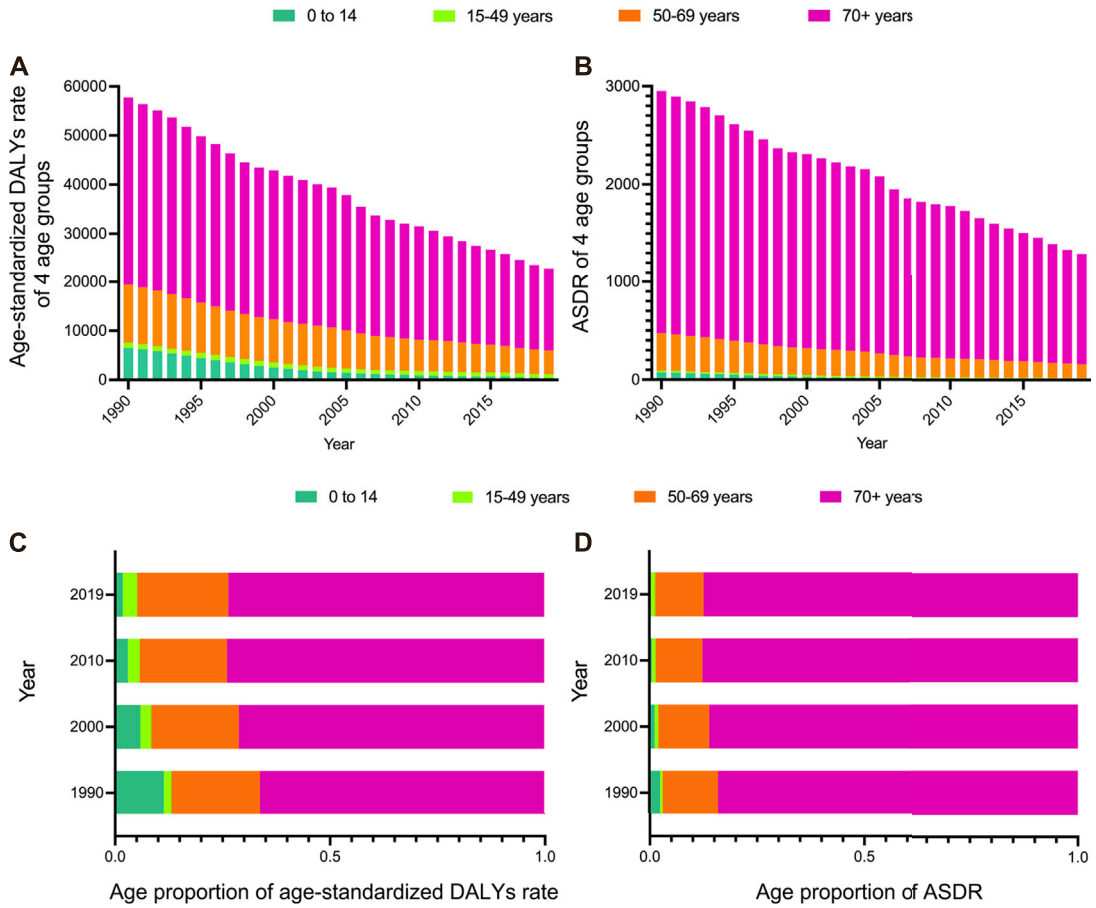

FIGURE 2
Age-standardized death and DALYs rate of different age groups due to air pollution in China from 1990 to 2019. **(A)** Age-standardized DALYs rate of four age groups from 1990 to 2019. **(B)** ASDR of four age groups from 1990 to 2019. **(C)** Four age proportions of age-standardized DALYs rate in 1990, 2000, 2010, and 2019. **(D)** Four age proportions of the ASDR in 1990, 2000, 2010, and 2019.

obstructive pulmonary disease, tracheal, bronchus, and lung cancer, lower respiratory infections, diabetes mellitus, neonatal disorders (Figure 3). In 2019, the ASDR of all the seven diseases caused by air pollution had decreased as compared to 1990. Lower respiratory infections, chronic obstructive pulmonary disease, neonatal disorders, and stroke had the most significant declines, by 87.98%, 80.62%, 77.89%, and 51.35%, respectively. However, the decline rates of diabetes mellitus; tracheal, bronchial, and lung cancer; and ischemic heart disease were slightly lower, declining by 0.46%, 3.5%, and 6.48%, respectively (Figure 3).

In the past 30 years, the ASDR of different types of diseases caused by air pollution in China had shown different trends. Before 2008, chronic obstructive pulmonary disease (COPD) was the leading cause of death due to air pollution. However, stroke rose to be the leading cause of death after 2008, while COPD declined to be the second leading cause. Lower respiratory infections were the third leading cause of air pollution–related deaths from 1990 to 1992, but their ASDR has continued to decline since then, while that of ischemic heart disease has ascended becoming the third leading cause of air pollution–related deaths. It is worth noting that the ASDR of ischemic heart disease; tracheal, bronchial, and lung cancers; and diabetes mellitus caused by air pollution has remained almost unchanged in the past 30 years, while that of the other four diseases has decreased significantly (Figure 4).

Rates and trends of age-standardized death and disability-adjusted life years caused by different kinds of air pollution in China

As a major type of air pollution, particulate matter pollution which includes ambient (outdoor) particulate

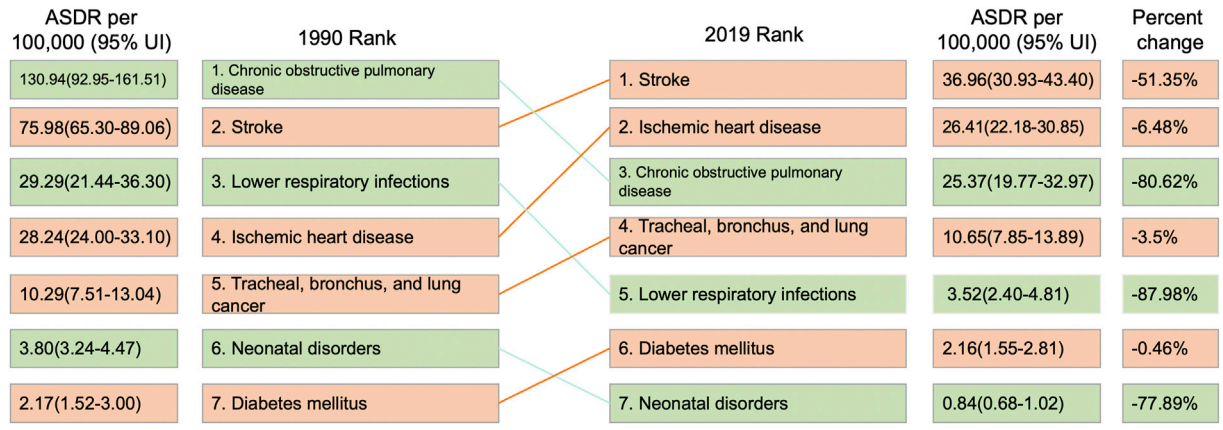

FIGURE 3
ASDR, ranking, and percent change of top seven diseases caused by air pollution in China in 1990 and 2019 (per 100,000). The ASDR of seven kinds of diseases caused by air pollution is ranked. Green block shows the diseases with decreased ranking and the orange block shows the diseases with increased ranking.

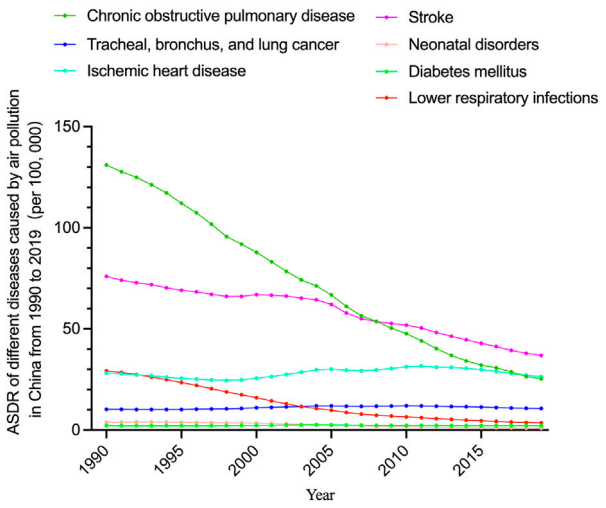

FIGURE 4
Trends of ASDR (per 100,000) of different diseases caused by air pollution from 1990 to 2019 in China.

matter pollution and household (indoor) air pollution from solid fuels led to the topmost health burden in China in both 1990 and 2019. In 1990, age-standardized DALYs rates caused by particulate matter pollution was 6707.77 (95% UI: 5652.42–7691.16)/100,000 and had decreased remarkably to 2214.48 (95% UI: 1908.94–2560.04)/100,000 in 2019, with an EAPC of −0.67% (95% UI: −0.73% to −0.59%). In 1990, the ASDR caused by particulate matter pollution was 272.71 (95% UI: 227.33–317.08)/100,000, and it declined markedly to 102.01 (95% UI: 86.97–119.37)/100,000 in 2019 (Table 2).

Three subtypes of air pollution were included in the GBD 2019 database: ambient ozone pollution, ambient particulate matter pollution, and household air pollution from solid fuels. Ambient particulate matter pollution and household air pollution from solid fuels make up particulate matter pollution, which is caused by particles with an aerodynamic diameter less than 2.5 μm. Household air pollution exposure involves fine particulate matter that comes from burning fuels inside homes with limited ventilation.

The ASDR caused by household air pollution from solid fuels had been the largest among the three kinds of air pollution in 1990. However, in 2019, ambient particulate matter pollution led to the largest ASDR, and it was the only subtype of air pollution that drove an increase in the ASDR, with an EAPC of 0.05% (95% UI: −0.37% to 1.06%) (Table 2). The age-standardized DALYs rates caused by household air pollution from solid fuels were the largest in 1990 at 4891.23 (95% UI: 3392.98–6308.02)/100,000. However, it declined dramatically to 471.13 (95% UI: 249.37–789.01)/100,000 in 2019. In 2019, ambient particulate matter pollution caused the largest age-standardized DALYs rate among the three subtypes of air pollution, and the age-standardized DALYs rate was 1743.35 (95% UI: 1438.42–2035.93)/100,000 in 2019, with the smallest decline as compare to that in 1990 (Table 2).

From the perspective of trend in the past 30 years, age-standardized death and DALYs rate related to particulate matter pollution and household air pollution from solid fuels were dramatically decreased. Age-standardized death and DALYs rate caused by ambient ozone pollution has slightly shrunk. However, ambient particulate matter pollution has led to an increase in age-standardized death and DALYs rate (Figure 5). Before 2003, household air pollution from solid fuels accounted for the largest proportion of age-standardized

TABLE 2 Age-standardized death and DALYs rate and their EAPC due to different kinds of air pollution in China from 1990 to 2019.

	Age-standardized DALYs rate (95% UI), per 100,000		EAPC (95% UI), %	ASDR (95% UI), per 100,000		EAPC (95% UI), %
	1990	2019		1990	2019	
Air pollution	6827.99 (5761.12–7795.08)	2265.40 (1949.97–2614.84)	−0.67 (−0.73 to −0.59)	280.80 (235.78–323.85)	105.92 (90.23–124.03)	−0.62 (−0.69 to −0.53)
Particulate matter pollution	6707.77 (5652.42–7691.16)	2214.48 (1908.94–2560.04)	−0.67 (−0.73 to −0.59)	272.71 (227.33–317.08)	102.01 (86.97–119.37)	−0.63 (−0.69 to −0.53)
Ambient ozone pollution	280.56 (120.49–451.97)	77.14 (35.34–124.93)	−0.73 (−0.78 to −0.54)	18.85 (8.22–30.36)	5.91 (2.73–9.65)	−0.69 (−0.74 to −0.50)
Ambient particulate matter pollution	1816.53 (884.75–2993.10)	1743.35 (1438.42–2035.93)	−0.04 (−0.43 to 0.90)	77.15 (38.47–126.56)	81.28 (67.18–96.13)	0.05 (−0.37 to 1.06)
Household air pollution from solid fuels	4891.23 (3392.98–6308.02)	471.13 (249.37–789.01)	−0.90 (−0.95 to −0.84)	195.56 (133.63–258.34)	20.73 (10.49–35.26)	−0.89 (−0.94 to −0.83)

DALYs, disability-adjusted life years; EAPC, estimated annual percentage change; UI, uncertainty interval. Results are rounded up to two decimal places.

death and DALYs rate among the three types of air pollution (ambient particulate matter pollution, ambient ozone pollution, and household air pollution from solid fuels), but after 2003, ambient particulate matter pollution ranked first. This may be caused by many factors such as changes in human lifestyles, changes in industrial production, and changes in climatic conditions and environmental protection.

Discussion

Air pollution is a global public environmental problem, which poses a major threat to public health. The negative health effects of air quality are a particular concern for sensitive populations, such as those with heart and lung disease, the elderly, and the children (Wang et al., 2022). Studies have shown that improving air quality has a positive effect on improving people's health (Broome et al., 2015; Yang and Zhang, 2018). In 2013, China passed legislation to further strengthen environmental protection and improve air quality as an important measure, and it has achieved positive results (Huang et al., 2018; Maji et al., 2020).

From the data of GBD 2019, we have concluded that air pollution creates a huge health burden in China. Around 1.85 (95% UI: 1.57–2.17) million Chinese people had lost their lives as a result of air pollution in 2019, a slight decrease from 1990. There is abundant evidence that air pollution not only brings direct harm to human health, for example, air pollution exposure directly increases the hospitalization rate (Gu et al., 2020), but also brings health damage and increases death (Carvalho, 2019; Verhoeven et al., 2021; Zhao et al., 2021). At the same time, air pollution also affects human activities. For example, air pollution limits human outdoor activities and physical exercise (Hu et al., 2017; Tainio et al., 2021). In addition, air pollution also has a direct or indirect impact on human economic activities and social development, thus further affecting human health (Husain Tahir et al., 2021). Air pollution causes significantly more deaths in men than in women and in the elderly than the youth. It is possible that men are more likely to work outdoors and are therefore more vulnerable to the health damage caused by air pollution. Furthermore, air pollution is the main risk factor of human chronic respiratory and cardiovascular diseases, and these diseases are more likely to occur in men and in the elderly population (Sierra-Vargas and Teran, 2012; Liu S et al., 2019; Rajak and Chattopadhyay, 2020).

Thanks to the improvement in air quality and advancement in medical care in China, the age-standardized death and DALYs rate caused by air pollution have decreased significantly in the past 30 years. Air pollution had led to 42.51 (95% UI: 36.34–49.48) million DALYs in 2019 in China, a 30.2% decrease from 1990. Air pollution can be prevented and ameliorated despite its enormous negative impact on human health. Reducing pollution from the source can have a rapid and

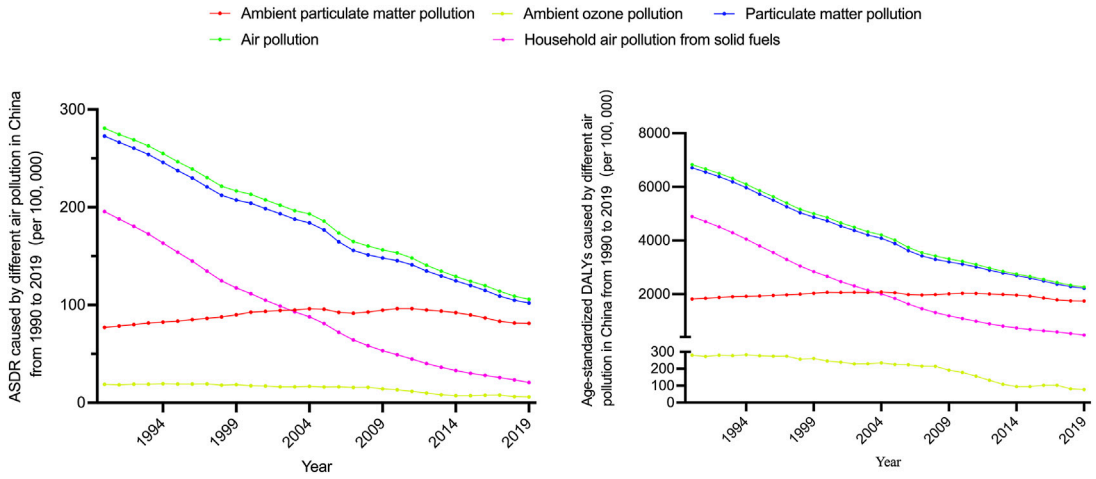

FIGURE 5
Age-standardized death and DALYs rate (per 100,000) caused by different kinds of air pollution in China from 1990 to 2019.

significant impact on health (Schraufnagel et al., 2019). In the past few decades, through government legislation, enterprises, and public participation, China's air quality has improved to a certain extent, thus improving people's health (Zeng et al., 2019; Zou et al., 2019). But China's air pollution is still at a high level, and it is also one of the most polluted countries in the world (World Health Organization, 2016). Therefore, China still urgently needs to work on cleaner air and better human health in the future.

Our research reveals that air pollution mainly provoked harm in seven kinds of diseases, that is, stroke, ischemic heart disease, chronic obstructive pulmonary disease; tracheal, bronchial, and lung cancers; lower respiratory infections; diabetes mellitus; and neonatal disorders. The ASDR caused by chronic obstructive pulmonary disease due to air pollution ranked the first in 1990, but it shifted to stroke in 2019. This indicates that in China, the damage caused by air pollution with regard to the cardiovascular system exceeds that caused to the respiratory system. This may be the reason for the aging of the population and lifestyle changes in China (Moran et al., 2008).

Particulate matter pollution is the largest source of air pollution in China and mainly includes pollutants from fossil fuel consumption, environmental particulate matter pollution, and environmental ozone pollution. These pollutants are mainly related to human lifestyle and industrial production. In the past 30 years, the sources of air pollution have also changed greatly, and its impact on human health is also changing. In recent years, people have paid more and more attention to the development of green, clean, and renewable energy. In China, the use of clean energy is already at the forefront of the world (Hannah Ritchie et al., 2020). However, due to China's large base of air pollution, huge population, and vast territory, improving air quality still requires a lot of work and investment in China.

Through a comprehensive analysis of the GBD 2019 data, this article systematically demonstrates the disease burden caused by air pollution in China over the past 30 years. But there are some limitations. First of all, we could not obtain data from different regions of China due to the limitation of the data sources. Due to China's vast territory and uneven development, and huge differences between regions, there may be large differences in air pollution in different geographical locations, but we have not been able to compare and analyze them. Secondly, the composition of air pollution is extraordinarily complex (Ghio et al., 2012), such as sulfur dioxide, nitrogen dioxide, ozone, nitric oxide etc., but we cannot obtain detailed data on the composition of air pollution in China for research. Finally, there are various sources of air pollution, such as factories, automobiles, home life, animal husbandry, etc., and these are also affected by climate, vegetation coverage, geographical environment, and other aspects, which our study fails to cover. Therefore, more detailed and comprehensive research is needed in the future to assess the health impact of air pollution in China and to analyze the sources and causes of specific air pollution in China to provide better evidence for air pollution prevention and control. Despite these limitations, our research extracts the latest GBD data to comprehensively and systematically analyze the disease and health burden caused by air pollution in China over the past 30 years. This may provide inspiration for the formulation of environmental policies and the health protection strategies for the vulnerable population in China.

Conclusion

Over the past 30 years, air pollution has brought an enormous disease burden to China, resulting in a large number of deaths and health losses. Air pollution mainly damages the respiratory and cardiovascular systems, and people over the age of 50 years are more vulnerable. Particulate matter pollution is the main culprit of health damage caused by air pollution. Although China has made great efforts to improve air quality in the past few decades, more efforts are needed to further control air pollution in the future. Especially for particulate pollution, a long-term mechanism should be established to effectively curb it. In addition, for the elderly, additional attention should be given to reduce health damage caused by air pollution.

Data availability statement

The raw data supporting the conclusion of this article will be made available by the authors, without undue reservation.

Author contributions

HG, BS, LC, YZ, and ZZ designed the study and wrote the manuscript. HG, LC, and HH collected and analyzed the data. YW, ZZ, YZ, and HH provided suggestions for study design and data analysis. BS and ZZ supervised the study. All authors have read and approved the manuscript.

Funding

This work has been supported by the Foundation of State Key Laboratory of Respiratory Disease (No. Z-2022-09).

Acknowledgments

We highly appreciate the great works by the Global Burden of Disease Study 2019 collaborators.

Conflict of interest

The authors declare that the research was conducted in the absence of any commercial or financial relationships that could be construed as a potential conflict of interest.

Publisher's note

References

Barendregt, J. J., Van Oortmarssen, G. J., Vos, T., and Murray, C. J. (2003). A generic model for the assessment of disease epidemiology: the computational basis of DisMod II. *Popul. Health Metr.* 1 (1), 4. doi:10.1186/1478-7954-1-4

Broome, R. A., Fann, N., Cristina, T. J., Fulcher, C., Duc, H., and Morgan, G. G. (2015). The health benefits of reducing air pollution in Sydney, Australia. *Environ. Res.* 143, 19–25. doi:10.1016/j.envres.2015.09.007

Carvalho, H. (2019). Air pollution-related deaths in Europe - time for action. *J. Glob. Health* 9 (2), 020308. doi:10.7189/jogh.09.020308

Chen, R., Yin, P., Meng, X., Liu, C., Wang, L., Xu, X., et al. (2017). Fine particulate air pollution and daily mortality. A nationwide analysis in 272 Chinese cities. *Am. J. Respir. Crit. Care Med.* 196 (1), 73–81. doi:10.1164/rccm.201609-1862oc

Ferrari, A. J., Charlson, F. J., Norman, R. E., Flaxman, A. D., Patten, S. B., Vos, T., et al. (2013). The epidemiological modelling of major depressive disorder: application for the global burden of disease study 2010. *PLoS One* 8 (7), e69637. doi:10.1371/journal.pone.0069637

Garshick, E. (2014). Effects of short- and long-term exposures to ambient air pollution on COPD. *Eur. Respir. J.* 44 (3), 558–561. doi:10.1183/09031936.00108814

GBD 2019 Diseases and Injuries Collaborators (2020). Global burden of 369 diseases and injuries in 204 countries and territories, 1990-2019: a systematic analysis for the global burden of disease study 2019. *Lancet* 396 (10258), 1204–1222. doi:10.1016/S0140-6736(20)30925-9

GBD 2019 Risk Factors Collaborators (2020). Global burden of 87 risk factors in 204 countries and territories, 1990-2019: a systematic analysis for the global burden of disease study 2019. *Lancet* 396 (10258), 1223–1249. doi:10.1016/S0140-6736(20)30752-2

Ghio, A. J., Carraway, M. S., and Madden, M. C. (2012). Composition of air pollution particles and oxidative stress in cells, tissues, and living systems. *J. Toxicol. Environ. Health Part B* 15 (1), 1–21. doi:10.1080/10937404.2012.632359

Global Burden of Diseases (2016). Global, regional, and national life expectancy, all-cause mortality, and cause-specific mortality for 249 causes of death, 1980-2015: a systematic analysis for the global burden of disease study 2015. *Lancet* 388 (10053), 1459–1544. doi:10.1016/S0140-6736(16)31012-1

Gu, J., Shi, Y., Zhu, Y., Chen, N., Wang, H., Zhang, Z., et al. (2020). Ambient air pollution and cause-specific risk of hospital admission in China: A nationwide time-series study. *PLoS Med.* 17 (8), e1003188. doi:10.1371/journal.pmed.1003188

Guan, D., Peters, G. P., Weber, C. L., and Hubacek, K. (2009). Journey to world top emitter: An analysis of the driving forces of China's recent CO2emissions surge. *Geophys. Res. Lett.* 36 (4), L04709. doi:10.1029/2008gl036540

Guo, H., Cheng, T. H., Gu, X. F., Wang, Y., Chen, H., Bao, F. W., et al. (2017). Assessment of PM2.5 concentrations and exposure throughout China using ground observations. *Sci. Total Environ.* 601, 1024–1030. doi:10.1016/j.scitotenv.2017.05.263

Hannah RitchieMax Roserand Pablo Rosado (2020) *Energy*. England: Our World in data. Access to: https://ourworldindata.org/energ.

Hou, X., Huang, H., Hu, H., Wang, D., Sun, B., and Zhang, X. D. (2021). Short-term exposure to ambient air pollution and hospital visits for IgE-mediated allergy: A time-stratified case-crossover study in southern China from 2012 to 2019. *EClinicalMedicine* 37, 100949. doi:10.1016/j.eclinm.2021.100949

Hu, L., Zhu, L., Xu, Y., Lyu, J., Imm, K., and Yang, L. (2017). Relationship between air quality and outdoor exercise behavior in China: a novel mobile-based study. *Int. J. Behav. Med.* 24 (4), 520–527. doi:10.1007/s12529-017-9647-2

Hu, Y., Xu, Z., Jiang, F., Li, S., Liu, S., Wu, M., et al. (2020). Relative impact of meteorological factors and air pollutants on childhood allergic diseases in Shanghai, China. *Sci. Total Environ.* 706, 135975. doi:10.1016/j.scitotenv.2019.135975

Huang, J., Pan, X., Guo, X., and Li, G. (2018). Health impact of China's air pollution prevention and control action plan: an analysis of national air quality monitoring and mortality data. *Lancet Planet. Health* 2 (7), e313–e323. doi:10.1016/s2542-5196(18)30141-4

Huang, Z. H., Liu, X. Y., Zhao, T., Jiao, K. Z., Ma, X. X., Ren, Z., et al. (2022). Short-term effects of air pollution on respiratory diseases among young children in Wuhan city, China. *World J. Pediatr.* 18, 333–342. doi:10.1007/s12519-022-00533-5

Husain Tahir, S., Kousar, S., Ahmed, F., and Rizwan Ullah, M. (2021). Impact of economic freedom on air pollution: configuration analysis of asia-pacific region. *Environ. Sci. Pollut. Res.* 28 (35), 47932–47941. doi:10.1007/s11356-021-13681-4

Landrigan, P. J., Fuller, R., Acosta, N. J. R., Adeyi, O., Arnold, R., Basu, N. N., et al. (2018). The Lancet Commission on pollution and health. *Lancet* 391 (10119), 462–512. doi:10.1016/s0140-6736(17)32345-0

Lelieveld, J., Evans, J. S., Fnais, M., Giannadaki, D., and Pozzer, A. (2015). The contribution of outdoor air pollution sources to premature mortality on a global scale. *Nature* 525 (7569), 367–371. doi:10.1038/nature15371

Liu, S., Li, Y., Zeng, X., Wang, H., Yin, P., Wang, L., et al. (2019). Burden of cardiovascular diseases in China, 1990-2016: Findings from the 2016 global burden of disease study. *JAMA Cardiol.* 4 (4), 342–352. doi:10.1001/jamacardio.2019.0295

Liu, Y., Pan, J., Zhang, H., Shi, C., Li, G., Peng, Z., et al. (2019). Short-term exposure to ambient air pollution and asthma mortality. *Am. J. Respir. Crit. Care Med.* 200 (1), 24–32. doi:10.1164/rccm.201810-1823oc

Maji, K. J., Li, V. O., and Lam, J. C. (2020). Effects of China's current Air Pollution Prevention and Control Action Plan on air pollution patterns, health risks and mortalities in Beijing 2014-2018. *Chemosphere* 260, 127572. doi:10.1016/j.chemosphere.2020.127572

Milanzi, E. B., Koppelman, G. H., Smit, H. A., Wijga, A. H., Oldenwening, M., Vonk, J. M., et al. (2018). Air pollution exposure and lung function until age 16 years: the PIAMA birth cohort study. *Eur. Respir. J.* 52 (3), 1800218. doi:10.1183/13993003.00218-2018

Moran, A., Zhao, D., Gu, D., Coxson, P., Chen, C. S., Cheng, J., et al. (2008). The future impact of population growth and aging on coronary heart disease in China: projections from the coronary heart disease policy model-China. *BMC Public Health* 8, 394. doi:10.1186/1471-2458-8-394

Pirozzi, C. S., Jones, B. E., VanDerslice, J. A., Zhang, Y., Paine, R., 3rd, and Dean, N. C. (2018). Short-term air pollution and incident pneumonia. A case-crossover study. *Ann. Am. Thorac. Soc.* 15 (4), 449–459. doi:10.1513/annalsats.201706-495oc

Rajak, R., and Chattopadhyay, A. (2020). Short and long term exposure to ambient air pollution and impact on health in India: A systematic review. *Int. J. Environ. Health Res.* 30 (6), 593–617. doi:10.1080/09603123.2019.1612042

Schraufnagel, D. E., Balmes, J. R., De Matteis, S., Hoffman, B., Kim, W. J., Perez-Padilla, R., et al. (2019). Health benefits of air pollution reduction. *Ann. Am. Thorac. Soc.* 16 (12), 1478–1487. doi:10.1513/annalsats.201907-538cme

Sierra-Vargas, M. P., and Teran, L. M. (2012). Air pollution: impact and prevention. *Respirology* 17 (7), 1031–1038. doi:10.1111/j.1440-1843.2012.02213.x

Tainio, M., Jovanovic Andersen, Z., Nieuwenhuijsen, M. J., Hu, L., de Nazelle, A., An, R., et al. (2021). Air pollution, physical activity and health: A mapping review of the evidence. *Environ. Int.* 147, 105954. doi:10.1016/j.envint.2020.105954

The State Council of the People's Republic of China (2013). The air pollution prevention and control action plan. Available at: http://wwwgovcn/zwgk/2013-09/12/content_2486773htm (Accessed On April 19th, 2022).

Verhoeven, J. I., Allach, Y., Vaartjes, I. C. H., Klijn, C. J. M., and de Leeuw, F-E. (2021). Ambient air pollution and the risk of ischaemic and haemorrhagic stroke. *Lancet Planet. Health* 5 (8), e542–e552. doi:10.1016/s2542-5196(21)00145-5

Villeneuve, P. J., Chen, L., Rowe, B. H., and Coates, F. (2007). Outdoor air pollution and emergency department visits for asthma among children and adults: A case-crossover study in northern alberta, Canada. *Environ. Health* 6, 40. doi:10.1186/1476-069x-6-40

Wang, A. Q., Zhang, M., and Zhou, S. Y. (2022). Air pollution, environmental violation risk, and the cost of debt: Evidence from China. *Int. J. Environ. Res. Public Health* 19 (6), 3584. doi:10.3390/ijerph19063584

Watts, J. (2005). China: the air pollution capital of the world. *Lancet* 366 (9499), 1761–1762. doi:10.1016/s0140-6736(05)67711-2

World Health Organization (2022). Air pollution. Available from: https://wwwwhoint/health-topics/air-pollution#tab=tab_1 (Accessed date: April 17th, 2022).

World Health Organization (2016). *Ambient air pollution: A global assessment of exposure and burden of disease*. Geneva: World Health Organization.

Yang, J., and Zhang, B. (2018). Air pollution and healthcare expenditure: Implication for the benefit of air pollution control in China. *Environ. Int.* 120, 443–455. doi:10.1016/j.envint.2018.08.011

Zeng, Y., Cao, Y., Qiao, X., Seyler, B. C., and Tang, Y. (2019). Air pollution reduction in China: Recent success but great challenge for the future. *Sci. Total Environ.* 663, 329–337. doi:10.1016/j.scitotenv.2019.01.262

Zhao, S., Liu, S., Hou, X., Sun, Y., and Beazley, R. (2021). Air pollution and cause-specific mortality: A comparative study of urban and rural areas in China. *Chemosphere* 262, 127884. doi:10.1016/j.chemosphere.2020.127884

Zou, B., You, J., Lin, Y., Duan, X., Zhao, X., Fang, X., et al. (2019). Air pollution intervention and life-saving effect in China. *Environ. Int.* 125, 529–541. doi:10.1016/j.envint.2018.10.045

frontiers | Frontiers in Environmental Science

ORIGINAL RESEARCH
published: 31 August 2022
doi: 10.3389/fenvs.2022.949504

Source Apportionment of Elemental Carbon in Different Seasons in Hebei, China

Dongli Hou[1], Xiang Zhang[1], Jiangwei Zhao[1], Jie Qiang[1], Jianguo Wang[1], Peng Wang[1], Qingxian An[1], Yang Wang[2,3], Liwei Wang[1], Shihui Yuan[1] and Feng Zhang[1]**

[1]Hebei Province Ecology Environmental Monitoring Center, Shijiazhuang, China, [2]School of Geographical Sciences, Hebei Normal University, Shijiazhuang, China, [3]State Key Joint Laboratory of Environmental Simulation and Pollution Control, Beijing, China

Black carbon (BC), also termed elemental carbon (EC), is a strong light-absorbing substance. It can disturb the radiation balance between the earth and atmosphere resulting in changing regional and global climate conditions. This study conducted a thorough analysis of EC in Hebei during different seasons and provided comprehensive EC emission data in the Beijing–Tianjin–Hebei (BTH) region for future policy making connected with air pollution mitigation and control. The results showed that the concentration of EC during the sampling period varied from 0.01 to 18.4 μg/m^3 with a mean value of 2.6 ± 2.8 μg/m^3. The EC source apportionment exercise identified four regular emission sources for all seasons, including traffic-related emissions, coal combustion, biomass burning, and mineral dust. Annually, traffic-related emissions were the primary EC contributor with an annual average contribution of 38%, followed by biomass burning (30%) and coal combustion (25%). In addition, the EC mass concentration at Shijiazhuang was also influenced by diverse pollutants from upwind regions. This study shows that traffic emissions are a major contributor to EC mass concentration in Shangjiazhuang and highlights that regional joint control of air pollution is important to local air quality.

Keywords: elemental carbon, source apportionment, Hebei, different seasons, online measurement

OPEN ACCESS

Edited by:
Qiyuan Wang,
Institute of Earth Environment (CAS), China

Reviewed by:
Zhuzi Zhao,
Jiangsu University of Technology, China
Guangxuan Yan,
Henan Normal University, China

****Correspondence:***
Xiang Zhang
1443578002@qq.com
Feng Zhang
hbszdqs@126.com

Specialty section:
This article was submitted to Atmosphere and Climate, a section of the journal Frontiers in Environmental Science

Received: *21 May 2022*
Accepted: *23 June 2022*
Published: *31 August 2022*

Citation:
Hou D, Zhang X, Zhao J, Qiang J, Wang J, Wang P, An Q, Wang Y, Wang L, Yuan S and Zhang F (2022) Source Apportionment of Elemental Carbon in Different Seasons in Hebei, China. Front. Environ. Sci. 10:949504. doi: 10.3389/fenvs.2022.949504

1 INTRODUCTION

Black carbon (BC), also termed elemental carbon (EC), is a strong light-absorbing substance, and based on the thermal detection method, it also embraces elemental carbon (EC) (Bond et al., 2013). BC can disturb the radiation balance between the earth and atmosphere resulting in changes to regional and global climate conditions (IPCC, 2021). BC can go through an aging process in the atmosphere, by mixing with other substances and through chemical reactions. It alters optical properties such as the light-absorbing ability (Bond et al., 2013). At different heights in the atmosphere, BC exerts different climatic effects. BC heats the atmosphere, while by contrast, it cools the earth's surface. This could also impact the planetary boundary height and could, therefore, worsen regional pollution levels (Wang et al., 2018). Furthermore, BC also could exert adverse impacts on human health (Geng et al., 2013; Ji et al., 2019a).

The sources of BC can be classified into natural and anthropogenic sources. Natural sources include natural phenomena such as volcanic eruptions and forest fires, but compared with anthropogenic sources, natural sources have little effect on the long-term changes in the concentration of black carbon aerosols due to their low occurrence since the industrial

revolution. Fossil fuels such as coal and petroleum are the major fossil fuel sources. Biomass burning in rural regions also plays an important role in the global BC inventory (Bond et al., 2013).

Two methods are widely used for identifying the emission sources of BC. One is an offline method, namely, collecting samples in the field and using laboratory analysis such as the 14C method, to identify the sources (Li et al., 2016). The 14C method can provide a good level of accuracy in the results, but limitations, such as high cost and a minimum sample loading required for analysis, hinder its promotion. Another method uses mathematical models such as the Aethalometer (AE) model and a receptor model to apportion BC into its various sources based on its optical features and chemical composition (Rajesh and Ramachandran, 2017; Wang et al., 2020; Liu et al., 2021). Compared with the 14C method, mathematical models are not restricted by sample loadings because online data are also applicable. However, regarding the Aethalometer model, the resultant accuracy heavily depends on the optical parameters used in the model (Zotter et al., 2017). Most studies' optical parameters (Healy et al., 2017; Zhu et al., 2017; Helin et al., 2018) such as the absorption Ångström exponent (AAE) are based on the literature. However, optical parameters are highly variable depending on combustion conditions and the characteristics of the sources (Tian et al., 2019). Thus, there may be uncertainty in using the AE model if the specific parameters are unknown.

A quarter of BC emissions in the world was reported from China (Streets et al., 2001). Previous studies have shown that BC emissions in the BTH region were high (Zhang et al., 2009). Ji et al. (2019a) noted that even though a number of policies on pollution control were active in the BTH region, EC mass concentrations remained high in 2017. A recent study showed that the maximum daily $PM_{2.5}$ in BTH can reach 150 μg/m^3 (Zhang et al., 2022), which exceeds the threshold of $PM_{2.5}$ high pollution level. BC contribution to $PM_{2.5}$ pollution was not negligible (Ji et al., 2017; Ji et al., 2019b). A further analysis of EC and organic carbon (OC) showed that they were highly correlated, indicating they were from the same source (Zhang et al., 2022).

Mao et al. (2020) used a combined method to calculate different source contributions to BC in the atmosphere from 2013 to 2017. The results showed that most pollution happened during winter and the most severe cases were found in the heating season due to residential heating, followed by vehicle emissions. However, due to the clean energy policies introduced and replacing coal combustion with clean energy, both OC and EC have declined since 2017. One study reported that compared with 2017, the mass concentration of EC in the BTH region during 2019 declined from 4.7 μg/m^3 to 3 μg/m^3, mainly due to banning coal combustion (Ji et al., 2022). Regarding regional emission loads in BTH, Liu et al. (2018) found that Hebei was the most important emission source for BC, which contributed 55% and 49% of the EC mass concentration in Beijing and Tianjin cities, respectively. Xiao et al. (2021) conducted a BC source apportionment in Beijing, which revealed that coal combustion, liquid fuel combustion, and biomass burning were the top three BC sources. Combustion of coal and liquid fuel contributed about 82%, with coal combustion making a higher contribution during winter and spring, while liquid fuel had a higher contribution during summer and autumn.

Although much research has been conducted in BTH, few studies have focused on annual source apportionment in Hebei which has been found to be a major source of pollution in other cities like Beijing and Tianjing as noted above. Thus, this study aims to present a thorough analysis of BC in Hebei during different seasons and provide comprehensive BC emission data in the BTH region for future policy-making on air pollution mitigation and control.

2 MATERIALS AND METHODS

2.1 Sampling Site and Data Collection

Hebei Province has 11 cities in total but the urbanization level is not high compared with other mega cities in BHT, reaching 60% in 2020, and the rural area infrastructure is not well-developed. According to the China Energy Statistics Yearbook of 2018, energy consumption in Hebei was about 67% of the total energy consumption of the BTH region, indicating a significant level of pollution in the province. Shijiazhuang City is the provincial capital city of Hebei which has 18 districts and counties. The sampling site was at Hebei University of Economics and Business (114°30′7″, 38°8′23″, **Figure 1**). River passes by the sampling site (~1.5 km away) at the Northeast. Major highways surround the sampling site and the city center is located south of the city. A total of 2951 data points were collected with an hourly resolution during 2020, in January, April, July, and October. The online data include EC, OC, K^+, Mg^{2+}, Ca^{2+}, Cl^-, and the elements (Si, K, Ca, Ti, Mn, Fe, As, Se, Br, Ba, Pb, and Zn).

2.2 Online Measurement

2.2.1 Online OCEC Analyzing

OC and EC were analyzed by using a discontinuous thermal-optical transmittance (TOT) based OC/EC analyzer (RT-4, Sunset Laboratory Inc., Tigard, Oregon, United States). The samples were placed on quartz filters and heated step by step in a non-oxidizing environment of helium (He), where OC is volatilized. In the process, a portion of OC is carbonized into pyrolyzed carbon (OP). The EC is oxidized and decomposes into gaseous oxides under an oxygen mixture (He/O_2) environment where the temperature will be increased gradually. Quantitative inspection was carried out using the ion flame method (FID) and the non-infrared dispersion method (NDIR). During this process, a laser beam was irradiated on the quartz film, so that the intensity of the transmitted light of the laser gradually weakens when OC is carbonized. The transmitted light of the laser will gradually increase when PC and EC decompose in the He/O_2 environment. When the intensity of the transmitted light returns to the initial value, this moment is defined as the OC/EC split point, which means that the amount of carbon detected before this moment is defined as the initial OC and the amount of carbon detected thereafter corresponds to the starting EC. The detection ranges of OC and EC are between 5 and 400 μg/cm^2 and 1 and 15 μg/cm^2. The minimum detection limit is 0.2 μg/cm^2. The maintenance and calibration were strictly performed according to a Standard Operating Procedure issued by China National

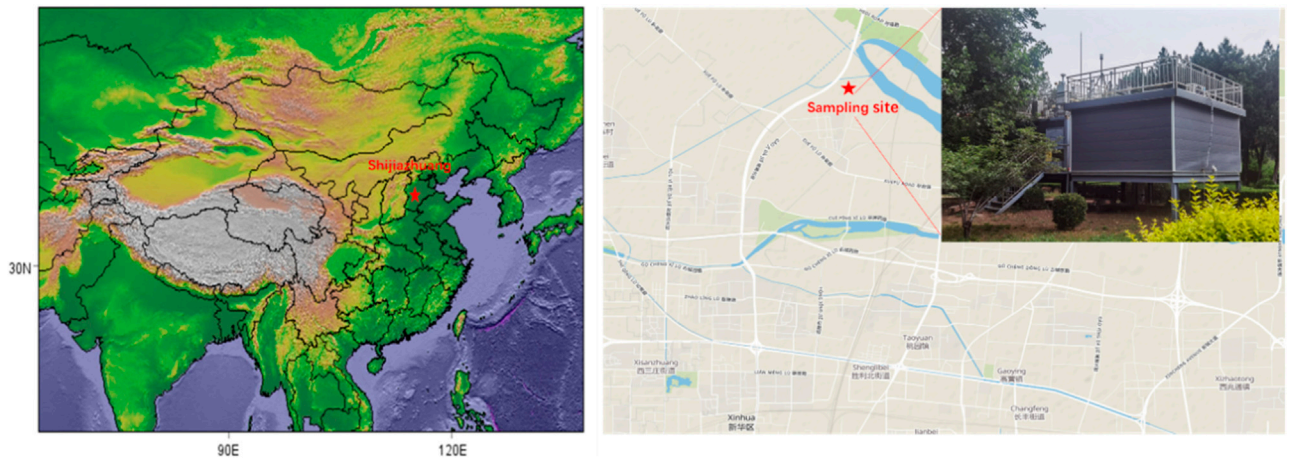

FIGURE 1 | The sampling site of this study.

Environmental Monitoring Center (http://www.cnemc.cn/jcgf/dqhj/202112/t20211223_965048.shtml, in Chinese).

2.2.2 Online Ion Analyzing

An ion chromatography analyzer (URG9000D, ThermoFisher Scientific (China), Shanghai, China) was used to measure the ions levels in $PM_{2.5}$ at a sampling flow of 16.67 L/min. The URG gas sampling device utilizes a wet parallel plate diffusion dissolver and adopts a gas-selective permeability membrane technology. Gaseous pollutants in the air can pass through the membrane into the absorption liquid channel and react with hydrogen peroxide. The kinetic principle of the process is a redox reaction, which ensures the complete absorption of gaseous pollutants. Wet parallel plate diffusion dissolvers can effectively absorb gaseous pollutants in the atmosphere. Absorption efficiency was tested using a permeation tube to generate 1 ppmv of SO_2, and 5 mM H_2O_2 was used as the absorption solution in the dissolver. The maintenance and calibration were strictly performed according to a Standard Operating Procedure issued by China National Environmental Monitoring Center (http://www.cnemc.cn/jcgf/dqhj/202112/t20211223_965048.shtml, in Chinese).

2.2.3 Online Elemental Analyzing

The elements were measured by using an online analyzer for atmospheric heavy metals (XHAM-2000A, Hebei Sailhero Environmental Protection High-tech Co., Ltd., Shijiazhuang, Hebei, China), which was used to measure the element levels in $PM_{2.5}$ at a sampling flow of 16.67 L/min. The monitor collects samples through reel-to-reel (RTR) filter paper strips and performs non-destructive analysis of particles deposited on the filter paper strips by X-ray fluorescence spectroscopy (XRF). The ambient air is sampled by the particle size cutter and drawn onto the filter paper belt. The collected samples are automatically transported to the detection position and the selected metal elements are analyzed using XRF technology. The next sample is taken when the previous sample is being analyzed. Sampling and analysis are performed synchronously and continuously, except during filter tape transport (approximately 20 s). During the study period, daily automatic quality checks are carried out on a regular basis. The maintenance and calibration were strictly performed according to a Standard Operating Procedure issued by China National Environmental Monitoring Center (http://www.cnemc.cn/jcgf/dqhj/202112/t20211223_965048.shtml, in Chinese).

2.2.4 Source Apportionment

EC source apportionment in this study was conducted by using the positive matrix factorization (PMF) model. PMF was developed by Paatero and Tapper (1994). This method has non-negative constraints and optimizes the error estimation of the input data. The input data matrix is divided into a factor profile matrix (F) and factor contribution (G) matrix through the following equation:

$$Xij = \sum_{k=1}^{p} gikfkj + eij, \tag{1}$$

where Xij is the input data matrix, i represents the i^{th} sample, j represents j^{th} species, and k represents the k^{th} factor number; g_{ik} represents the source contribution of the k^{th} factor to the i^{th} sample; f_{kj} is the factor profile of the j^{th} species in the k^{th} factor; and e_{ij} is the residual between the real value and estimated value.

PMF solves F and G by finding the global minimum Q value with the following equation:

$$Q = \sum_{\text{i=1}}^{\text{n}} \sum_{j=0}^{n} \left[\frac{\text{eij}}{\text{uij}} \right]^2, \tag{2}$$

where Q is the sum of the squares of the normalized residuals, e_{ij} represents the residual values, and u_{ij} represents the uncertainties of the input data. The United States Environmental Protection Administration (EPA) PMF version 5.0 was employed for the EC source apportionment in this study. The concentrations of chemical species were inputted into PMF as an input matrix.

2.2.5 Trajectory Cluster Analysis

Trajectories over 72 h and 50 m above the ground over 4 months were calculated using the Hybrid Single-Particle Lagrangian Integrated Trajectory model (HYSPLIT). The HYSPLIT model

is a widely used air-mass trajectory model (Draxler and Hess, 1998). To understand the regional transport impacts on the study site, cluster analysis was applied to the 72 h air mass trajectories. The cluster method used an angle-based distance calculation method, the calculation equations being as follows (Wang et al., 2018):

$$d_{12} = \frac{1}{n}\sum_{i=1}^{n} cos^{-1}\left(0.5 \times \frac{A_i + B_i - C_i}{\sqrt{A_i B_i}}\right), \quad (3)$$

$$A_i = (X_1(i) - X_o)^2 + (Y_1(i) - Y_o)^2, \quad (4)$$

$$B_i = (X_2(i) - X_o)^2 + (Y_2(i) - Y_o)^2, \quad (5)$$

$$C_i = (X_2(i) - X_1(i))^2 + (Y_2(i) - Y_1(i))^2, \quad (6)$$

where d_{12} represents the averaged angle which varies between 0 and π between two trajectories; n denotes the total endpoints, X and Y represent the location of the study site, X1 (Y1) denotes the first trajectory, and X2 (Y2) denotes the second trajectory. The calculation software used is TrajStat developed by Wang et al. (2009). The data used for the calculations were from the Global Data Assimilation System (GDAS, https://www.ready.noaa.gov/gdas1.php). The trajectories associated with EC mass concentration over the 75th percentile were taken as polluted trajectories. The trajectories were drawn on a grid with a resolution of 0.5°.

2.2.6 Potential Source Contribution

To estimate the potential contribution from regional transport, the potential source contribution function (PSCF) was applied to detect the possible contribution regions to EC in Shijiazhuang. High PSCF values indicate that high EC emissions were transported to the study site. The PSCF value of every grid was calculated using the following equation:

$$PSCF_{ij} = \frac{m_{ij}}{n_{ij}}, \quad (7)$$

where m_{ij} denotes endpoints associated with EC concentration which is higher than the criterion set in the model and n_{ij} is the total endpoints of the grid cell. The 75th percentiles of EC from different sources were set as the threshold value of pollution.

To reduce uncertainties caused by a low n_{ij} value, arbitrary weighting factors (w_{ij}) were used during the calculation of PSCF. The values and criteria were taken from the work of Polissar et al. (2001):

$$W_{ij} = \begin{cases} 1 & 80 < n_{ij} \\ 0.7 & 20 < n_{ij} \le 80 \\ 0.42 & 10 < n_{ij} \le 20 \\ 0.05 & n_{ij} \le 10 \end{cases}. \quad (8)$$

3 RESULTS AND DISCUSSION

3.1 Observed Concentrations of EC

Figure 2 illustrates the concentrations of EC and OC as well as the ratio of OC/EC in four different months, January, April, July, and October. The concentration of EC during the sampling period varied from 0.01 to 18.4 μg/m^3 with a mean value of 2.6 ± 2.8 μg/m^3 (**Table 1**). It was much lower than the average annual EC concentration in Shijiazhuang, from December 2016 to November 2017 (5.4 ± 6.5 μg/m^3, Ji et al., 2019a). It could be due to a positive effect of air pollution control actions launched in the BTJ region. The concentration is close to the EC concentration measured in Beijing (3.4 ± 2.3 μg/m^3) from September 2017 to August 2018. Similar to EC, OC in Shijiazhuang was significantly lower compared with the value reported from December 2016 to November 2017. The concentration of OC during the sampling period varied from 0.04 to 50.7 μg/m^3 with a mean concentration of 9.5 ± 9.4 μg/m^3, which was about 58% lower than the OC measured in December 2016—November 2017 (22.8 ± 30.6 μg/m^3, Ji et al., 2019a) and also was lower than that established in the 4-month average. The ratio of OC/EC was 4.7 ± 2.4 from 2016 to 2017. The reduced ratio of OC/EC (4.2 ± 3.0) indicates that from 2017 to 2020, OC in Shijiazhuang has decreased slightly faster than EC. This could be caused by the changed contribution ratios of different emission sources.

Focusing on the variation among different seasons, the concentrations of OC and EC were 22.5 ± 8.7 μg/m^3 and 5.8 ± 3.4 μg/m^3 in January; 3.1 ± 2.9 μg/m^3 and 0.9 ± 0.8 μg/m^3 in April; 4.2 ± 1.9 μg/m^3 and 1.1 ± 0.8 μg/m^3 in July; and 7.4 ± 4.6 μg/m^3 and 2.3 ± 1.5 μg/m^3 in October. The data showed that OC and EC in January were much higher compared with those measured in other seasons. The mass concentration of OC and EC displayed a similar variation pattern over the 4-month period, in the order January > October > July > April, representing higher concentrations in winter and autumn, while lower concentrations occurred in spring and summer. This is consistent with the pattern reported in a previous study (Ji et al., 2019a). Even though the concentrations in winter in 2020 were still the highest of all seasons, the concentration of both OC and EC has been declining significantly, by 52% and 49%, respectively (**Table 1**), compared with winter in 2016–2017. Immediately after the concentration decrease in winter, the decrease in OC and EC in spring was the second largest among the four seasons with a reduction of 7.1 μg/m^3 and 1.8 μg/m^3, respectively. This was followed by decreases in summer and autumn, the concentrations of OC and EC declining by varying degrees, suggesting that the Three-Year Action Plan to Fight Air Pollution since 2018 has worked well in terms of improving air quality.

The diurnal variations over the four seasons demonstrate different patterns. As shown in **Figure 3A**, during winter, the diurnal variation in OC presented high values in the morning and night and low values in the afternoon. EC showed a similar diurnal pattern to OC during winter and a good correlation between OC and EC (R^2 = 0.54, p < 0.1) during winter. This indicates that the majority of OC and EC emissions were likely from the same sources during the winter. However, although the patterns were similar, the hourly mass concentration changes in OC and EC were not in proportion, therefore the ratio of OC/EC varied greatly on a daily basis. The ratio was high in the afternoon and much lower at night. This phenomenon was possibly influenced by meteorological conditions, and less secondary

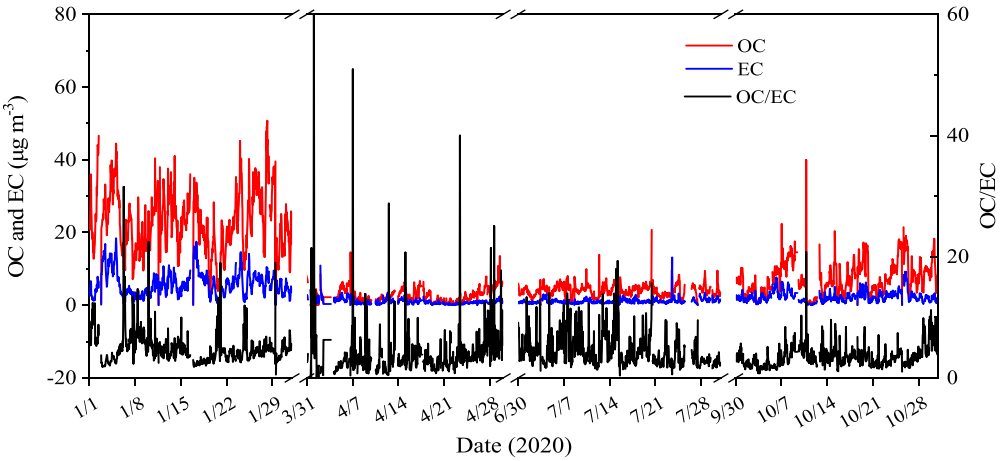

FIGURE 2 | Time series over 4 months for EC, OC, and the OC/EC ratio.

TABLE 1 | Concentrations of OC, EC, and the ratio of OC/EC.

	OC[a] (μg/m^3)	EC[a] (μg/m^3)	Ratio[a]	OC[b] (μg/m^3)	EC[b] (μg/m^3)	Ratio[b]	OC[c] difference	EC[c] difference
Spring	3.1 ± 2.9	0.9 ± 0.8	3.4	10.2	2.7	3.8	7.1	1.8
Summer	4.2 ± 1.9	1.1 ± 0.8	3.8	8.5	2.0	4.3	4.3	0.9
Autumn	7.4 ± 4.6	2.3 ± 1.5	3.2	10.7	3.3	3.2	3.3	1.0
Winter	22.5 ± 8.7	5.8 ± 3.4	3.9	53.3	11.6	4.6	30.8	5.8
Annual	9.5 ± 9.4	2.6 ± 2.8	3.7	22.8 ± 30.6	5.4 ± 6.5	4.2	13.3	2.8

[a]*Note: This study*
[b]*Ji et al., 2019a*
[c]*Difference between data in 2020 and 2017.*

OC was generated at night due to the weak solar radiation and temperature.

Unlike the variation patterns in winter, a clear OC rise was found in spring from 7 to 10 am (**Figure 3B**) which could be caused by traffic emissions. Another rise was found from 18:00 h to 23:00 h which was likely caused by the evening traffic peak and nocturnal planetary boundary layer height (PBLH). With residential heating demand declining in spring, the mass concentration of EC was low at night which is opposite to that in the winter season. The fluctuation of the OC/EC ratio was more frequent than in winter, particularly during daytime, which could be caused by a combination of more varied meteorological conditions and more diverse emission sources. In addition, OC and EC were found weakly correlated (R^2 = 0.25, p < 0.1) in spring.

In summer, as presented in **Figure 3C**, OC decreased from midnight to 6:00 h then rose dramatically to 9:00 h and remained stable to 15:00 h. From 16:00 h to 20:00 h, OC decreased again and then rose to 23:00 h. By contrast, the diurnal variation in EC only fluctuated slightly except from 10:00 h to 14:00 h. This indicates that large quantities of OC and EC emissions may not be from the same source, which can also be confirmed by the weak correlation between OC and EC (R^2 = 0.14, p < 0.1).

Similar to winter, the correlation between OC and EC was relatively higher (R^2 = 0.57, p < 0.1) in the autumn season, indicating that the majority of OC and EC were from the same source. The diurnal variations in OC and EC were almost identical (**Figure 3D**), showing a continuous decrease from midnight to 17:00 h with a small peak at 9:00 h, which was likely formed by the morning traffic peak. From 18:00 h to 23:00 h, the concentration of OC and EC kept rising. This could be caused by the pollution accumulation due to the poor dispersion conditions at night and the evening traffic peak around 19:00 h.

3.2 Source Apportionment of EC in Different Seasons

Five sources of EC were identified by PMF during wintertime shown in **Figure 4**. The first factor was characterized by high loadings of Ca^{2+} (86%), Si (48%), and Ti (43%), widely recognized as associated with mineral dust (Tao et al., 2017; Liu et al., 2021). This factor barely contributed to EC during winter. The second factor showed relatively high loadings of K^+ (32%) and Br (51%). K^+ is a widely recognized marker of biomass burning (Zhao et al., 2021) and a considerable amount of Br is found in biomass burning due to the CH3Br generated in the combustion process (Manö and Andreae, 1994; Artaxo et al., 1998). Thus, this factor

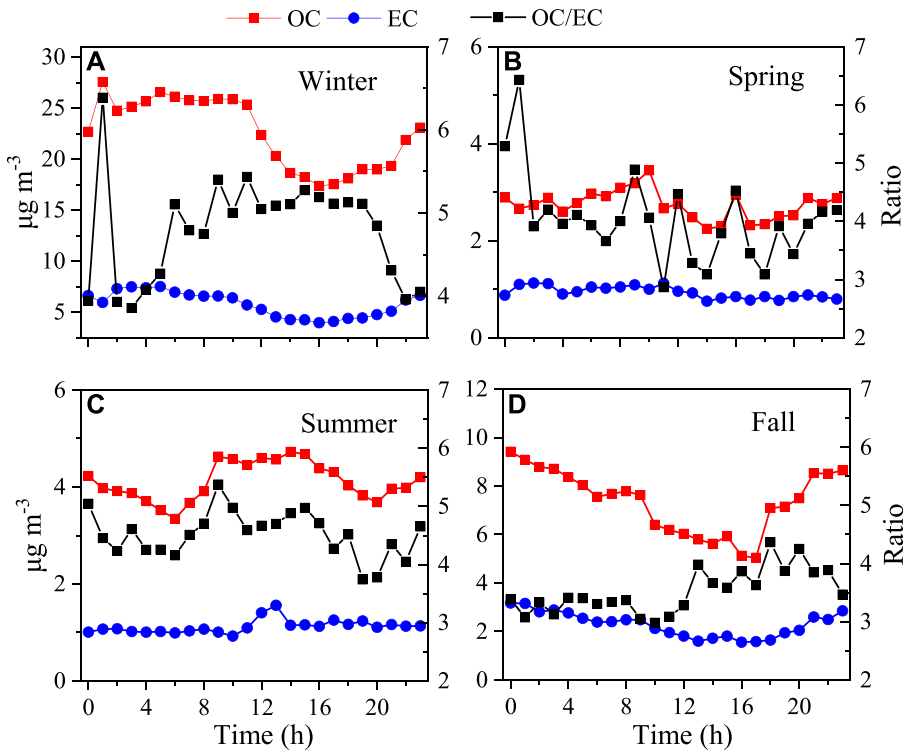

FIGURE 3 | Diurnal variations in OC, EC, and the OC/EC ratios in the four seasons of the year.

was considered to be biomass burning which contributed 19% of EC during winter. The third factor presented a large amount of Mn (81%), Fe (49%), and Zn (43%). Mn is often used as a smoke suppression agent and an additive in vehicles to protect the engine (Lewis et al., 2003). Zn and Fe are widely found in braking and lubricating oil (Alander et al., 2005; Thorpe and Harrison, 2008). In addition, as shown, this factor contributed a noticeable amount of EC (36%), which is consistent with previous studies (Cao et al., 2013). In addition, the diel variation in EC from this factor showed two peaks in morning and evening in traffic busy hours (Supplementary Figure S1). Thus, this factor was identified as traffic-related emissions. The fourth factor showed high loadings of K^+ (53%), Mg^{2+}(72%), Ti (50%), and Ba (64%). K^+, Mg, and Ba are abundant in fireworks (Li et al., 2013; Yadav et al., 2019). Furthermore, EC contributed by this factor was only found to be significant from 24 January 2020 to 29 January 2020, which happened to be the Chinese New Year. Thus, this factor was likely to be the result of firework displays. The last factor was characterized by high loadings of As (43%) and Pb (30%). According to previous studies, high loadings of As and Pb are found in coal combustion (Tan et al., 2017; Liu et al., 2021). Thus, this factor was recognized as resulting from coal combustion which contributed 35% of EC.

Different from the January results, four factors were identified in spring (**Figure 5**). The first one is associated with high loadings of Si (49%), Ca (66%), Ti (55%), and Fe (58%). Thus, this factor stemmed from mineral dust. The second factor showed high loadings of Cl^- (64%), Br (87%), and K (43%). Previous research has reported that Cl^- is also considered a marker of biomass burning (Urban et al., 2012; Zhao et al., 2021). At the same time, levels of OC and EC were also high in this factor with contributions of 38% and 48%, respectively. Thus, this factor was identified as stemming from biomass burning. The third factor is characterized by high loadings of Mn (48%), Zn (90%), and Pb (59%). As explained before, Mn and Zn are commonly found in traffic-related emissions. Although China phased out Pb-containing petroleum, research still finds an alarming amount of Pb associated with vehicular emissions (Xu et al., 2016), and the diel variation showed two peaks in morning and evening in traffic busy hours (Supplementary Figure S1). Therefore, this factor is deemed to be caused by traffic-related emissions, the factor contributing 16% of total EC. The last factor contained relatively higher amount of As (41%), Ti (39%), and EC (35%). As mentioned above, As is widely considered as a marker of coal combustion. Previous studies (e.g., Ji et al., 2019a) showed that coal combustion contributed a considerable amount of EC in Shijiazhuang City. In addition to the abundant amount of Ti found in mineral dust, in urban areas, Ti is also found in manufacturing industries. This factor is likely to be coal combustion for industrial activities, the factor contributing 35% of EC.

Source apportionment for EC during summer also showed four major contributors (**Figure 6**). The first source showed high loadings of Cl^- (62%), K^+ (67%), and Br (59%). Meanwhile, this factor contains moderate loadings of OC (39%) and EC (41%), which are commonly found in the emissions from biomass

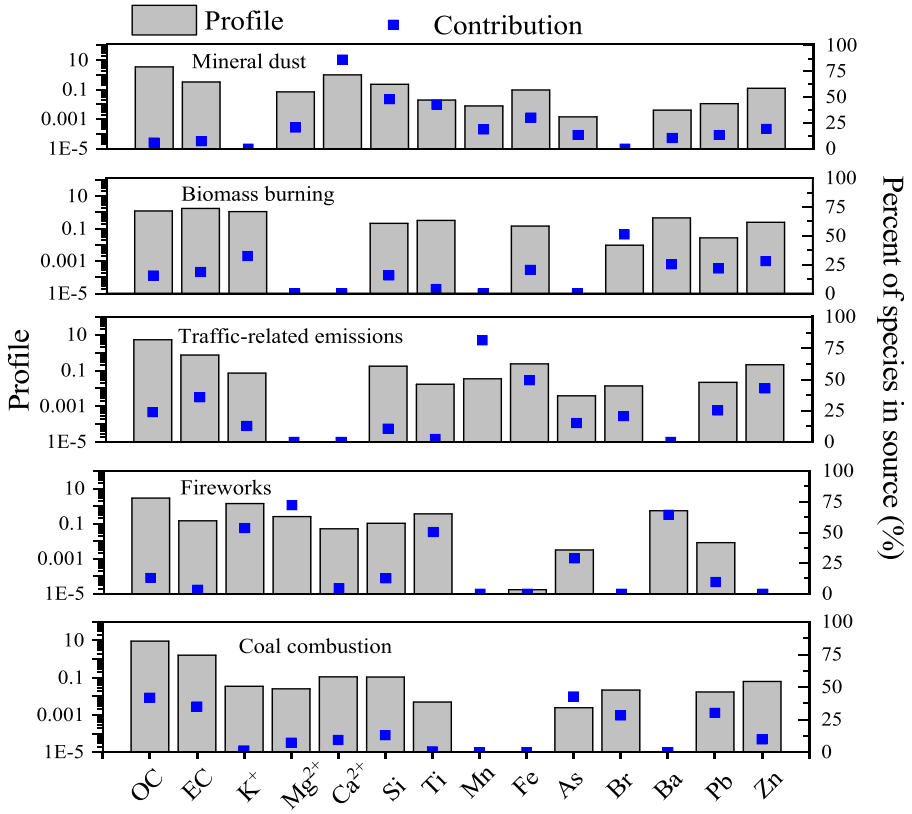

FIGURE 4 | Source apportionment of EC in winter.

burning (Cao et al., 2013). Thus, this factor was identified as biomass burning. The second factor demonstrated a considerable amount of As (66%) and Se (45%). According to Tan et al. (2017), high loadings of Se are also found in coal combustion. As a result, this factor was identified as coal combustion, contributing 10% of EC. The third factor is characterized by a high loading of Mn (78%) and Zn (54%) with a moderate loading of Fe (38%). Furthermore, moderate amounts of OC and EC were found in this factor and the loading of EC was higher than that for OC, which fits the feature of vehicle emissions (Cao et al., 2013), so does the EC diel variation in this factor (Supplementary Figure S2). Thus, this factor was recognized as traffic-related emissions with 35% contributed as EC. The last factor showed high loadings of Ca^{2+} (71%), Si (46%), and Ti (50%), thus, this factor was interpreted as mineral dust. Some 14% of EC was found in this factor which could be due to the resuspension of the deposited EC from other perturbations such as vehicle driving and wind.

Similar to the source apportionment results in summer, source apportionment of EC during autumn showed four major contributing factors (**Figure 7**). The first factor profile showed high loadings of Mg^{2+} (80%), Ca^{2+} (93%), and Si (67%), which indicate mineral dust for this factor. This factor only contributed 6% of EC. The second factor presented a high amount of As (44%), Se (59%), and Pb (59%). As mentioned earlier, these are widely used markers of coal combustion. Thus, this factor is coal combustion, which contributed 19% of EC. The third factor is characterized by high loadings of OC (71%), EC (65%), Mn (48%), Fe (39%), and Zn (56%). These are typical elements reflecting vehicular emissions which can be verified by the EC diel variation (Supplementary Figure S2). The last factor contained high loadings of Cl^- (64%) and K^+ (71%) and a moderate amount of Br (41%), and is recognized as biomass burning with a 10% contribution to EC.

The contributions of the regular four sources varied in different seasons possibly due to the change in meteorological conditions and the variation in emission intensity, although there was a variation in the contribution of different sources in different seasons, traffic-related emissions were the primary EC contributor with an annual averaged contribution of 38% followed by biomass burning (30%) and coal combustion (25%). The contribution of the same source varied greatly in different seasons. As listed in **Table 2**, a significant amount of EC was contributed by traffic-related emissions in autumn (65%), but much less in spring (16%). Biomass burning contributed a considerable amount of EC in spring (48%) and summer (41%), but a relatively small amount in autumn (10%) and winter (19%). This indicates open fires (Supplementary Figure S2) might be the primary emission source for biomass burning instead of residential combustion. By contrast, coal combustion was a major contributor of EC in spring (35%) and winter (35%), which suggests coal combustion could be the primary energy source for residential heating. The contribution from mineral dust varied less dramatically compared with other identified sources, and

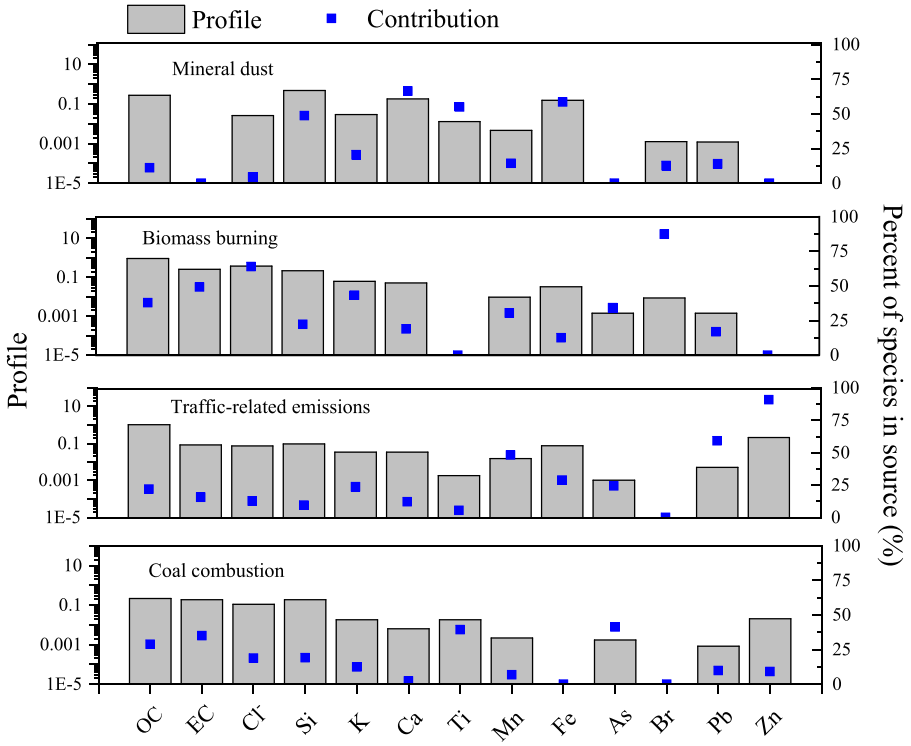

FIGURE 5 | Source apportionment of EC in spring.

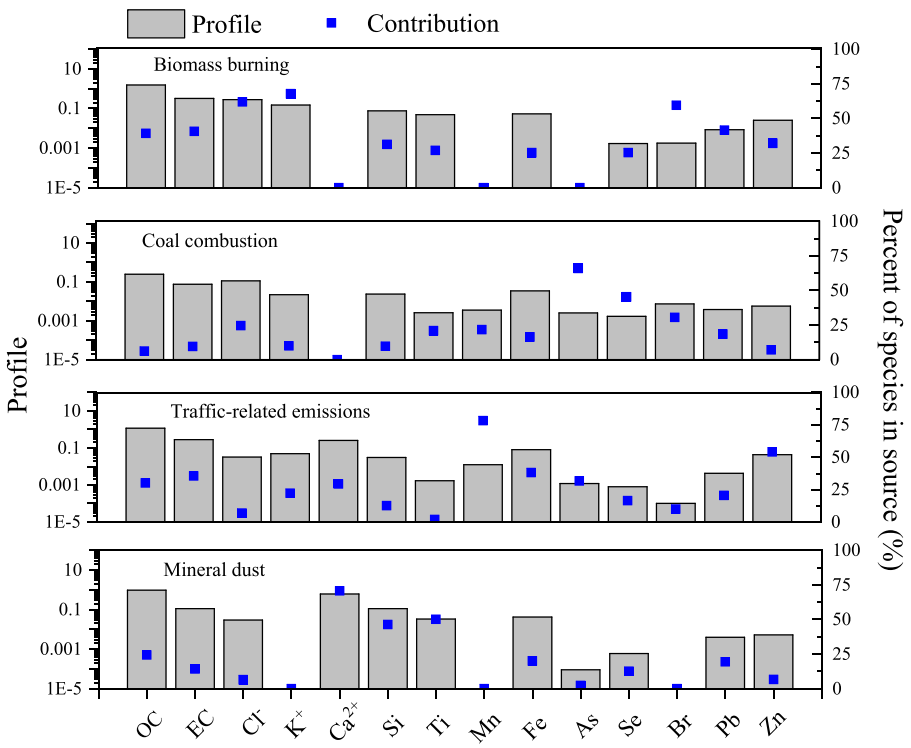

FIGURE 6 | Source apportionment of EC in summer.

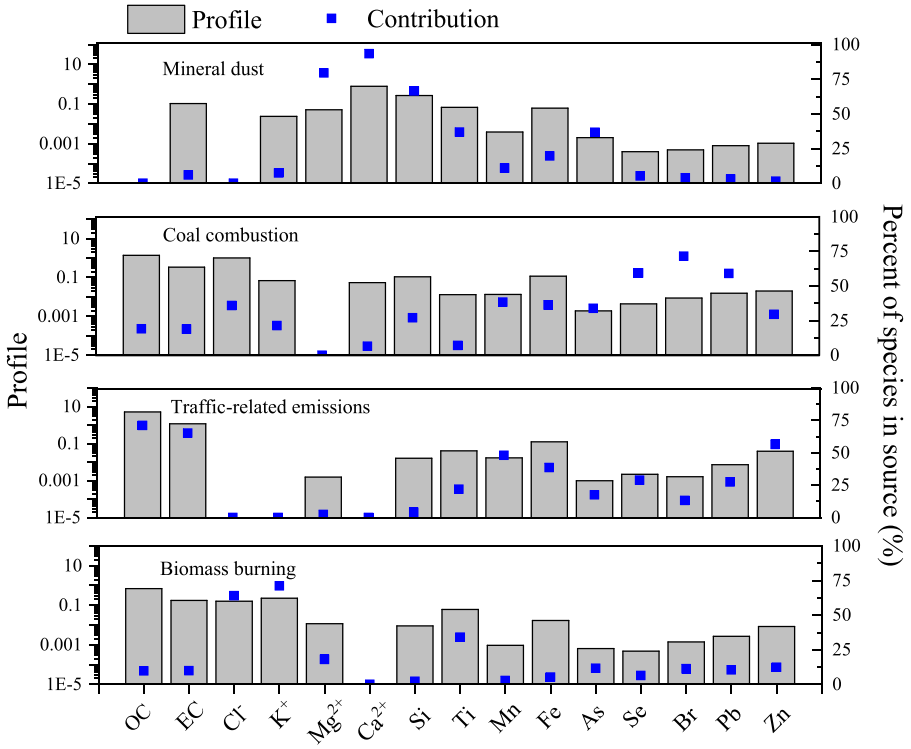

FIGURE 7 | Source apportionment of EC in autumn.

TABLE 2 | Source contributions to EC in different seasons.

	Traffic-related emissions (%)	Biomass burning (%)	Coal combustion (%)	Mineral dust (%)	Fireworks (%)
Spring	16	48	35	1	
Summer	35	41	10	14	
Autumn	65	10	19	6	
Winter	36	19	35	6	4
Average	38	30	25	7	

comparatively speaking, it contributed more in summer. Fireworks were only found to contribute to EC in winter during the Chinese New Year.

3.3 Trajectory Cluster Analysis

Air flow on the one hand can disperse pollutants but on the other, can carry pollutants from upwind regions. Thus, to establish the influence of air masses from different directions in different seasons, 72 h back trajectories of air masses were calculated during the study period on an hourly basis. A cluster analysis was then conducted based on those calculated trajectories. The results showed (**Figure 8**) that air masses were mainly from four clusters but the trajectory contribution ratios varied across the four seasons. As shown in **Figure 8A**, during winter, Cluster No. 3 contains 33% of the total trajectories from a northerly direction. The origin of the air mass 72 h earlier was near the boundary of inner Mongolia. Cluster No. 2 contains 27% of the total trajectories. The origin of Cluster No. 2 was in Shanxi Province and Cluster No. 4 (25%) originated in Hebei Province, passing through Tianjin city. Cluster No. 1 (15%) was also from Hebei Province but the cluster trajectory showed that it was from a northerly direction and close to that province.

In contrast with winter, most of the trajectories in spring were from a northerly direction. As shown in **Figure8B**, 77% of total trajectories were from the north, and 38% of total trajectories originated from outside of China (Cluster No. 3). Of the total trajectories, 39% originated from inner Mongolia (Cluster No. 1 and No. 4). The remaining 23% of trajectories were from Shandong Province (Cluster No.2), passing through Henan Province. During summer, the air mass trajectories were mainly from an easterly direction. As presented in **Figure 8C**, three of four clusters originated in Shandong Province, clearly an important source region. The origin of Cluster No. 1 was very close to the Huanghai Sea coastline. This cluster contains 13% of the total trajectories. Cluster No. 4 has 37% of the total trajectories and Cluster No. 3 has 13%. The remaining cluster (Cluster No. 2) was

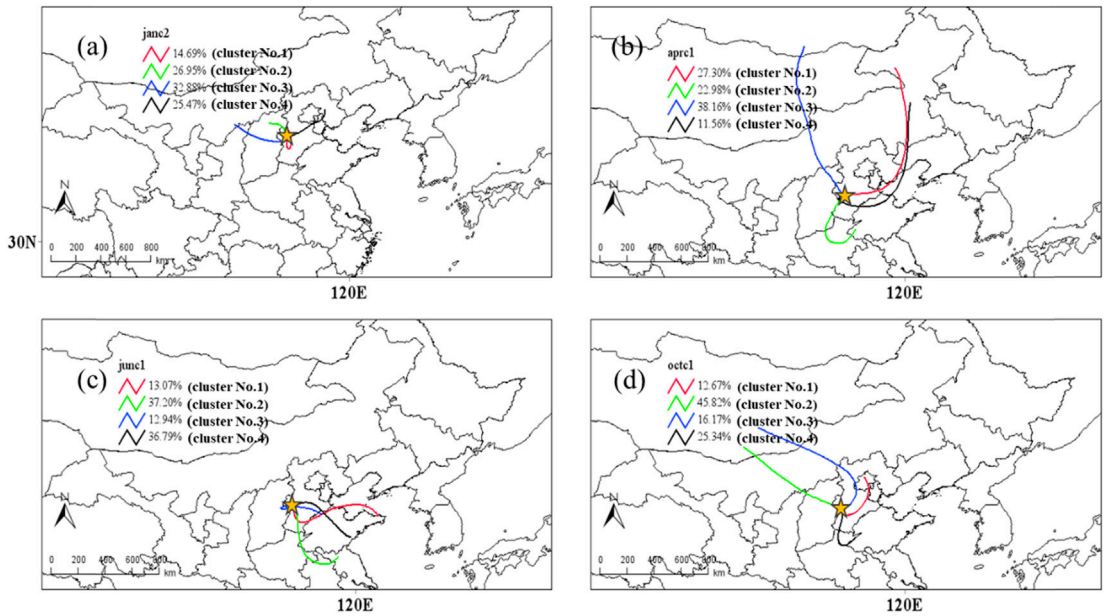

FIGURE 8 | The cluster analysis of the trajectories in **(A)** winter, **(B)** spring, **(C)** summer, and **(D)** autumn.

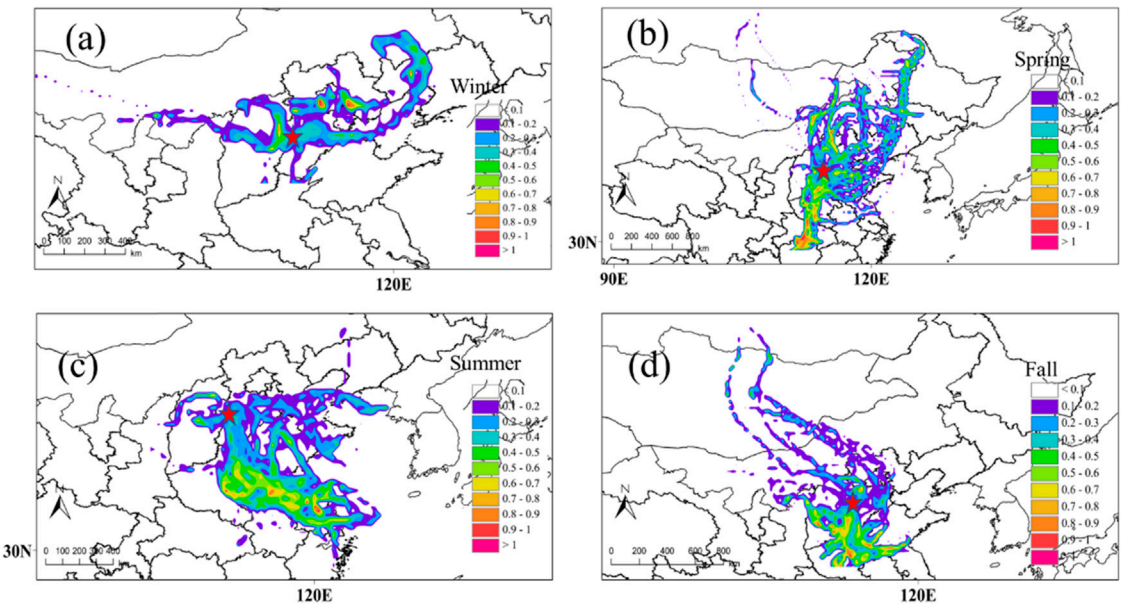

FIGURE 9 | Potential source regions for EC in Shijiazhuang in **(A)** winter, **(B)** spring, **(C)** summer, and **(D)** autumn. The color bar represents PSCF probability. The color circles denote the sampling site.

from Jiangsu Province containing 37% of the total trajectories. Similar to winter, in autumn, the major trajectories were from a northwest direction, originating outside China (**Figure 8D**). Mongolia accounted for 72% of the total trajectories (Cluster No. 2 and No. 3). Some 25% of the total trajectories originate from Shandong Province (Cluster No. 4) and 13% of total trajectories originated from Beijing City (Cluster No. 1).

3.4 Potential Source Region Identification

EC mass concentration is not only influenced by local emissions but also by regional transport. Given the different air mass directions in different seasons, the variations in EC concentration throughout the seasons can be partially ascribed to regional transport. Thus, potential contribution sources were analyzed based on the PSCF results shown in **Figure 9**.

As shown in **Figure 9A**, in winter, the highest potential sources were mainly in the northeast, particular in Beijing and its western region. Although there were policies launched to mitigate air pollution in the BTJ region, as indicated by PSCF, the surrounding regions of Beijing were still potential EC sources. In addition, near the sampling site, Shanxi province also has moderate potential to contribute EC in Shijiazhuang. This could be due to the high consumption and production of coal in Shanxi province, particularly in winter due to the demand for residential heating (Zhang et al., 2014). Much further away, Liaoning and Inner Mongolia could also be potential source areas in winter since coal-fired power plants in north China are mainly located in Inner Mongolia, Shanxi, and Shaanxi provinces (Ji et al., 2019a). In comparison with the surrounding regions, the contribution of EC from Shijiazhuang, itself, showed a moderate potential in winter.

Different from the distribution of the potential EC sources identified in winter, the strongest potential contribution of EC to the sampling site changed to the southern regions, mainly from Hubei, Hunan, and Guizhou provinces in spring (**Figure 9B**). In the north, Shanxi province and Inner Mongolia could also contribute EC to Shijiazhuang when the air mass flow is from a northerly direction. Zhang et al. (2014) conducted an energy survey in Guizhou households and found about 60% of the rural households in Guizhou burned crops on the farmland for fertilizing the land. Coal and firewood were the primary energy sources for residential use in Guizhou. In addition, burning on non-cultivated land was found to be high during spring in north, northeast, and southeast Hubei (Shen et al., 2021). Thus, the high potential contribution to Shijiazhuang from the north in spring could be caused by rural residential energy consumption and open fires (Supplementary Figure S2). This, to a degree, could also explain the high biomass burning levels and coal combustion contributions found in source apportionment in spring, compared with those in other seasons.

In summer, the potential contribution sources changed to Henan, Anhui, and Jiangsu provinces (**Figure 9C**). This is likely associated with the southeast prevailing wind in summer and is consistent with the increased nitrate concentration in Beijing in August found in East China (Ying et al., 2014). Based on Yao et al. (2021), this could be attributed to Henan, since it is one of the largest energy-consuming provinces in China, where coal combustion and biomass burning are the major sources of pollution. Additionally, according to the emission inventory for Jiangsu (Zhou et al., 2017), on-road and non-road transportation contributed notable amounts of EC. Similar to the PSCF revealed in summer, Henan and Aihui were identified as the most likely source of the high contribution to EC concentrations in Shijiazhuang during autumn (**Figure 9D**).

4 CONCLUSION

The concentration of EC during the sampling period varied from 0.01 to 18.4 μg/m^3 with a mean value of 2.6 ± 2.8 μg/m^3. The concentration of OC during the sampling period varied from 0.04 to 50.7 μg/m^3 with a mean concentration of 9.5 ± 9.4 μg/m^3. Both EC and OC were found to be higher in winter and autumn while lower concentrations occurred in spring and summer. The diurnal variations in OC/EC in different seasons indicate the varied contributions from different sources in the four seasons. Winter and autumn presented high mass concentrations of EC and OC during the night, likely due to residential heating and nocturnal PBLH. The EC source apportionment identified four regular emission sources for all seasons: traffic-related emissions, coal combustion, biomass burning, and mineral dust. However, due to the celebration of Chinese New Year Festival, one more emission source was found in winter, which was fireworks. The contributions of the regular four sources varied in different seasons possibly due to changes in meteorological conditions and variations in emission intensity. Annually, traffic-related emissions were the primary EC contributor with an annual average contribution of 38% followed by biomass burning (30%) and coal combustion (25%). The primary source of EC differed according to the season. A significant amount of EC was contributed by vehicle emissions in the autumn (65%) while a considerable amount of EC originated from biomass burning in spring (49%) and summer (41%). Coal combustion was a major contributor of EC in the spring (35%) and winter (35%). In addition to local emission changes, the trajectory cluster analysis and PSCF results indicated that the EC mass concentration in Shijiazhuang was also influenced by a variety of pollutants from upwind regions. In winter, the north China region showed high PSCF values likely due to the coal-fired power plants located there. In spring, high values of PSCF were found in the southwest region near to Shijiazhuang because of extensive firewood burning and open fires (Supplementary Figure S2) in the rural regions. In summer and autumn, high PSCF values were found in the south and southeast area of Shijiazhuang, where transportation contributed notable amounts of EC. This study shows that in general, traffic-related emissions are a major contributor to EC mass concentration in Shangjiazhuang, with emissions in the surrounding cites likely worsen EC pollution in the receptor site. It thus highlights how important regional joint control of air pollution is to local air quality.

DATA AVAILABILITY STATEMENT

The original contributions presented in the study are included in the article/Supplementary Material; further inquiries can be directed to the corresponding authors.

AUTHOR CONTRIBUTIONS

Data curation: DH, XZ, JZ, JW, and FZ; formal analysis: PW and QA; funding acquisition: YW; investigation: JQ and Liwei Liu; methodology: XZ, YW, SY, and FZ; software: JQ; and writing—original draft: DH and JZ.

FUNDING

This project was supported by the special fund of the State Key Joint Laboratory of Environmental Simulation and Pollution Control (Grant No. 22K03ESPCP).

REFERENCES

Alander, T., Antikainen, E., Raunemaa, T., Elonen, E., Rautiola, A., and Torkkell, K. (2005). Particle Emissions from a Small Two-Stroke Engine: Effects of Fuel, Lubricating Oil, and Exhaust Aftertreatment on Particle Characteristics. *Aerosol Sci. Technol.* 39 (2), 151–161. doi:10.1080/027868290910224

Artaxo, P., Fernandas, E. T., Martins, J. V., Yamasoe, M. A., Hobbs, P. V., Maenhaut, W., et al. (1998). Large-scale Aerosol Source Apportionment in Amazonia. *J. Geophys. Res.* 103, 31837–31847. doi:10.1029/98jd02346

Bond, T. C., Doherty, S. J., Fahey, D. W., Forster, P. M., Berntsen, T., DeAngelo, B. J., et al. (2013). Bounding the Role of Black Carbon in the Climate System: A Scientific Assessment. *J. Geophys. Res. Atmos.* 118, 5380–5552. doi:10.1002/jgrd.50171

Cao, J.-J., Zhu, C.-S., Tie, X.-X., Geng, F.-H., Xu, H.-M., Ho, S. S. H., et al. (2013). Characteristics and Sources of Carbonaceous Aerosols from Shanghai, China. *Atmos. Chem. Phys.* 13, 803–817. doi:10.5194/acp-13-803-2013

Draxler, R., and Hess, G. (1998). An Overview of the HYSPLIT_4 Modelling System for Trajectories. *Aust. Meteorol. Mag.* 47, 295–308.

Geng, F., Hua, J., Mu, Z., Peng, L., Xu, X., Chen, R., et al. (2013). Differentiating the Associations of Black Carbon and Fine Particle with Daily Mortality in a Chinese City. *Environ. Res.* 120, 27–32. doi:10.1016/j.envres.2012.08.007

Healy, R. M., Sofowote, U., Su, Y., Debosz, J., Noble, M., Jeong, C.-H., et al. (2017). Ambient Measurements and Source Apportionment of Fossil Fuel and Biomass Burning Black Carbon in Ontario. *Atmos. Environ.* 161, 34–47. doi:10.1016/j.atmosenv.2017.04.034

Helin, A., Niemi, J. V., Virkkula, A., Pirjola, L., Teinilä, K., Backman, J., et al. (2018). Characteristics and Source Apportionment of Black Carbon in the Helsinki Metropolitan Area, Finland. *Atmos. Environ.* 190, 87–98. doi:10.1016/j.atmosenv.2018.07.022

IPCC (2021). Climate Change 2021: The Physical Science Basis. Contribution of Working Group I to the Sixth Assessment Report of the Intergovernmental Panel on Climate Change. Report.

Ji, D., Gao, M., MaenhautHe, W., He, J., Wu, C., Cheng, L., et al. (2019a). The Carbonaceous Aerosol Levels Still Remain a Challenge in the Beijing-Tianjin-Hebei Region of China: Insights from Continuous High Temporal Resolution Measurements in Multiple Cities. *Environ. Int.* 126, 171–183. doi:10.1016/j.envint.2019.02.034

Ji, D., Gao, W., Maenhaut, W., He, J., Wang, Z., Li, J., et al. (2019b). Impact of Air Pollution Control Measures and Regional Transport on Carbonaceous Aerosols in Fine Particulate Matter in Urban Beijing, China: Insights Gained from Long-Term Measurement. *Atmos. Chem. Phys.* 19, 8569–8590. doi:10.5194/acp-19-8569-2019

Ji, D., Li, J., Shen, G., He, J., Gao, W., Tao, J., et al. (2022). Environmental Effects of China's Coal Ban Policy: Results from *In Situ* Observations and Model Analysis in a Typical Rural Area of the Beijing-Tianjin-Hebei Region, China. *Atmos. Res.* 268, 106015. doi:10.1016/j.atmosres.2022.106015

Ji, D., Li, L., Pang, B., Xue, P., Wang, L., Wu, Y., et al. (2017). Characterization of Black Carbon in an Urban-Rural Fringe Area of Beijing. *Environ. Pollut.* 223, 524–534. doi:10.1016/j.envpol.2017.01.055

Lewis, C. W., Norris, G. A., Conner, T. L., and Henry, R. C. (2003). Source Apportionment of Phoenix PM2.5Aerosol with the Unmix Receptor Model. *J. Air & Waste Manag. Assoc.* 53 (3), 325–338. doi:10.1080/10473289.2003.10466155

Li, C., Bosch, C., Kang, S., AnderssonChenZhang, A. P. Q., ChenChen, P. B., Zhang, Q., et al. (2016). Sources of Black Carbon to the Himalayan-Tibetan Plateau Glaciers. *Nat. Commun.* 7, 12574. doi:10.1038/ncomms12574

Li, W., Shi, Z., Yan, C., Yang, L., Dong, C., and Wang, W. (2013). Individual Metal-Bearing Particles in a Regional Haze Caused by Firecracker and Firework Emissions. *Sci. Total Environ.* 443, 464–469. doi:10.1016/j.scitotenv.2012.10.109

Liu, H., Wang, Q., Ye, J., Su, X., Zhang, T., Zhang, Y., et al. (2021). Changes in Source-Specific Black Carbon Aerosol and the Induced Radiative Effects Due to the COVID-19 Lockdown. *Geophys Res. Lett.* 48, e2021GL092987. doi:10.1029/2021GL092987

Liu, X. Y., He, K. B., Zhang, Q., Lu, Z. F., Wang, S. W., Zhang, Y. X., et al. (2018). Analysis of the Origins of Black Carbon and Carbon Monoxide Transported to Beijing, Tianjin, and Hebei in China. *Sci. Total Environ.* 653, 1364–1376. doi:10.1016/j.scitotenv.2018.09.274

Manö, S., and Andreae, M. O. (1994). Emission of Methyl Bromide from Biomass Burning. *Science* 263, 1255–1257. doi:10.1126/science.263.5151.1255

Mao, Y. H., Zhao, X., Liao, H., Zhao, D., Tian, P., Henze, D. K., et al. (2020). Sources of Black Carbon during Severe Haze Events in the Beijing-Tianjin-Hebei Region Using the Adjoint Method. *Sci. Total Environ.* 740, 140149. doi:10.1016/j.scitotenv.2020.140149

Paatero, P., and Tapper, U. (1994). Positive Matrix Factorization: A Non-negative Factor Model with Optimal Utilization of Error Estimates of Data Values. *Environmetrics* 5 (2), 111–126. doi:10.1002/env.3170050203

Polissar, A. V., Hopke, P. K., and Harris, J. M. (2001). Source Regions for Atmospheric Aerosol Measured at Barrow, Alaska. *Environ. Sci. Technol.* 35, 4214–4226. doi:10.1021/es0107529

Rajesh, T. A., and Ramachandran, S. (2017). Characteristics and Source Apportionment of Black Carbon Aerosols over an Urban Site. *Environ. Sci. Pollut. Res.* 24 (9), 8411–8424. doi:10.1007/s11356-017-8453-3

Shen, Y., Jiang, C., Chan, K. L., Hu, C., and Yao, L. (2021). Estimation of Field-Level NOx Emissions from Crop Residue Burning Using Remote Sensing Data: A Case Study in Hubei, China. *Remote Sens.* 13, 404. doi:10.3390/rs13030404

Streets, D. G., Gupta, S., Waldhoff, S. T., Wang, M. Q., Bond, T. C., and Yiyun, B. (2001). Black Carbon Emissions in China. *Atmos. Environ.* 35, 4281–4296. doi:10.1016/S1352-2310(01)00179-0

Tan, J., ZhangZhou, L. X., ZhouLi, X. Y., Duan, J., Li, Y., Hu, J., et al. (2017). Chemical Characteristics and Source Apportionment of PM 2.5 in Lanzhou, China. *Sci. Total Environ.* 601-602, 1743–1752. doi:10.1016/j.scitotenv.2017.06.050

Tao, J., Zhang, L., Cao, J., Zhong, L., Chen, D., Yang, Y., et al. (2017). Source Apportionment of PM2.5 at Urban and Suburban Areas of the Pearl River Delta Region, South China - with Emphasis on Ship Emissions. *Sci. Total Environ.* 574, 1559–1570. doi:10.1016/j.scitotenv.2016.08.175

Thorpe, A., and Harrison, R. M. (2008). Sources and Properties of Non-exhaust Particulate Matter from Road Traffic: A Review. *Sci. Total Environ.* 400 (1-3), 270–282. doi:10.1016/j.scitotenv.2008.06.007

Tian, J., Wang, Q., Ni, H., Wang, M., Zhou, Y., Han, Y., et al. (2019). Emission Characteristics of Primary Brown Carbon Absorption from Biomass and Coal Burning: Development of an Optical Emission Inventory for China. *J. Geophys. Res.-Atmos.* 124, 1879–1893. doi:10.1016/10.1029/2018jd029352

Urban, R. C., Lima-Souza, M., Caetano-Silva, L., Queiroz, M. E. C., Nogueira, R. F. P., Allen, A. G., et al. (2012). Use of Levoglucosan, Potassium, and Water-Soluble Organic Carbon to Characterize the Origins of Biomass-Burning Aerosols. *Atmos. Environ.* 61, 562–569. doi:10.1016/j.atmosenv.2012.07.082

Wang, Q., Cao, J., Han, Y., Tian, J., Zhu, C., Zhang, Y., et al. (2018). Sources and Physicochemical Characteristics of Black Carbon Aerosol from the Southeastern Tibetan Plateau: Internal Mixing Enhances Light Absorption. *Atmos. Chem. Phys.* 18, 4639–4656. doi:10.5194/acp-18-4639-2018

Wang, Q., Liu, H., Wang, P., Dai, W., Zhang, T., Zhao, Y., et al. (2020). Optical Source Apportionment and Radiative Effect of Light-Absorbing Carbonaceous Aerosols in a Tropical Marine Monsoon Climate Zone: the Importance of Ship Emissions. *Atmos. Chem. Phys.* 20, 15537–15549. doi:10.5194/acp-20-15537-2020

Wang, Y. Q., Zhang, X. Y., and Draxler, R. R. (2009). TrajStat: GIS-Based Software that Uses Various Trajectory Statistical Analysis Methods to Identify Potential Sources from Long-Term Air Pollution Measurement Data. *Environ. Model. Softw.* 24, 938–939. doi:10.1016/j.envsoft.2009.01.004

Xiao, H.-W., Huang, L.-L., Xiao, H.-Y., Wu, J.-F., and Wu, J. (2021). Evaluation of Black Carbon Source Apportionment Based on One Year's Daily Observations in Beijing. *Sci. Total Environ.* 773, 145668. doi:10.1016/j.scitotenv.2021.145668

Xu, H., Cao, J., Chow, J. C., Huang, R.-J., Shen, Z., Chen, L. W. A., et al. (2016). Inter-annual Variability of Wintertime PM 2.5 Chemical Composition in Xi'an, China: Evidences of Changing Source Emissions. *Sci. Total Environ.* 545-546, 546–555. doi:10.1016/j.scitotenv.2015.12.070

Yadav, S. K., Kumar, M., Sharma, Y., Shukla, P., Singh, R. S., and Banerjee, T. (2019). Temporal Evolution of Submicron Particles during Extreme Fireworks. *Environ. Monit. Assess.* 191, 191–576. doi:10.1007/s10661-019-7735-2

Yao, R., Li, Z., Zhang, Y., Wang, J., Zhang, S., and Xu, H. (2021). Spatiotemporal Evolution of PM2.5 Concentrations and Source Apportionment in Henan

Province, China. *Pol. J. Environ. Stud.* 30 (5), 4815–4826. doi:10.15244/pjoes/132639

Ying, Q., Wu, L., and Zhang, H. (2014). Local and Inter-regional Contributions to PM2.5 Nitrate and Sulfate in China. *Atmos. Environ.* 94, 582–592. doi:10.1016/j.atmosenv.2014.05.078

Zhang, Q., Streets, D. G., Carmichael, G. R., He, K. B., Huo, H., Kannari, A., et al. (2009). Asian Emissions in 2006 for the NASA INTEX-B Mission. *Atmos. Chem. Phys.* 9, 5131–5153. doi:10.5194/acp-9-5131-2009

Zhang, R., Wei, T., Glomsrød, S., and Shi, Q. (2014). Bioenergy Consumption in Rural China: Evidence from a Survey in Three Provinces. *Energy Policy* 75, 136–145. doi:10.1016/j.enpol.2014.08.036

Zhang, X., Zhang, Z., Xiao, Z., Tang, G., Li, H., Gao, R., et al. (2022). Heavy Haze Pollution during the COVID-19 Lockdown in the Beijing-Tianjin-Hebei Region, China. *J. Environ. Sci.* 114, 170–178. doi:10.1016/j.jes.2021.08.030

Zhao, S., Tian, H., Luo, L., Liu, H., Wu, B., Liu, S., et al. (2021). Temporal Variation Characteristics and Source Apportionment of Metal Elements in PM2.5 in Urban Beijing during 2018-2019. *Environ. Pollut.* 268, 115856. doi:10.1016/j.envpol.2020.115856

Zhou, Y., Zhao, Y., Mao, P., Zhang, Q., Zhang, J., Qiu, L., et al. (2017). Development of a High-Resolution Emission Inventory and its Evaluation and Application through Air Quality Modeling for Jiangsu Province, China. *Atmos. Chem. Phys.* 17, 211–233. doi:10.5194/acp-17-211-2017

Zhu, C.-S., Cao, J.-J., Hu, T.-F., Shen, Z.-X., Tie, X.-X., Huang, H., et al. (2017). Spectral Dependence of Aerosol Light Absorption at an Urban and a Remote Site over the Tibetan Plateau. *Sci. Total Environ.* 590-591, 14–21. doi:10.1016/j.scitotenv.2017.03.057

Zotter, P., Herich, H., Gysel, M., El-Haddad, I., Zhang, Y., Močnik, G., et al. (2017). Evaluation of the Absorption Ångström Exponents for Traffic and Wood Burning in the Aethalometer-Based Source Apportionment Using Radiocarbon Measurements of Ambient Aerosol. *Atmos. Chem. Phys.* 17, 4229–4249. doi:10.5194/acp-17-4229-2017

Conflict of Interest: The authors declare that the research was conducted in the absence of any commercial or financial relationships that could be construed as a potential conflict of interest.

Publisher's Note: All claims expressed in this article are solely those of the authors and do not necessarily represent those of their affiliated organizations, or those of the publisher, the editors, and the reviewers. Any product that may be evaluated in this article, or claim that may be made by its manufacturer, is not guaranteed or endorsed by the publisher.

Advantages of publishing in Frontiers

OPEN ACCESS
Articles are free to read for greatest visibility and readership

FAST PUBLICATION
Around 90 days from submission to decision

HIGH QUALITY PEER-REVIEW
Rigorous, collaborative, and constructive peer-review

TRANSPARENT PEER-REVIEW
Editors and reviewers acknowledged by name on published articles

Frontiers
Avenue du Tribunal-Fédéral 34
1005 Lausanne | Switzerland

Visit us: www.frontiersin.org
Contact us: frontiersin.org/about/contact

REPRODUCIBILITY OF RESEARCH
Support open data and methods to enhance research reproducibility

DIGITAL PUBLISHING
Articles designed for optimal readership across devices

FOLLOW US
@frontiersin

IMPACT METRICS
Advanced article metrics track visibility across digital media

EXTENSIVE PROMOTION
Marketing and promotion of impactful research

LOOP RESEARCH NETWORK
Our network increases your article's readership